รายงานวิจัยฉบับสมบูรณ์

โครงการ: การออกแบบวัสดุสปินครอสโอเวอร์เหล็ก (III): สวิตซ์โมเลกุลสู่อุปกรณ์นาโน

Designed Iron(III) Spin Crossover Materials: From Molecular Switches to Nanodevices

รศ.ดร. เดวิด เจมส์ ฮาร์ดิง และคณะ

เมษายน พ.ศ. 2561

สัญญาทุนเลขที่ RSA5880048

รายงานวิจัยฉบับสมบูรณ์

โครงการ: การออกแบบวัสดุสปินครอสโอเวอร์เหล็ก (III): สวิตซ์โมเลกุลสู่อุปกรณ์นาโน

Designed Iron(III) Spin Crossover Materials: From Molecular Switches to Nanodevices

รศ.ดร. เดวิด เจมส์ ฮาร์ดิง มหาวิทยาลัยวลัยลักษณ์
ผศ.ดร. พิมผกา ฮาร์ดิง มหาวิทยาลัยวลัยลักษณ์

สนับสนุนโดยสำนักงานกองทุนสนับสนุนการวิจัยและมหาวิทยาลัยวลัยลักษณ์

(ความเห็นในรายงานนี้เป็นของผู้วิจัย สกว. และมหาวิทยาลัยวลัยลักษณ์
ไม่จำเป็นต้องเห็นด้วยเสมอไป)

Abstract

This report describes the preparation and characterization of Fe(III) and Co(II) complexes with either spin crossover or single-ion magnetism. Six new ligands have been prepared and fully characterized: Hqsal-5-(3-py), Hqsal-5-(4-py), H_2bqimbd, H_2bpmabd, HnaphEen and HnaphBzen.

The heteroleptic complexes [Fe(qsal-Cl)(qsal-Br)]A·sol have been synthesized by layered diffusion and show SCO behaviour intermediate between the homoleptic systems. Structural studies show mostly LS Fe(III) centres. A related series [Fe(qsal-X)(salpm-X)]A have also been prepared which show only gradual or incomplete SCO.

[Fe(qsal-X)$_2$]OTs·sol, prepared by layered diffusion, show abrupt SCO in all cases with [Fe(qsal-F)$_2$]OTs exhibiting a hysteresis of 50 K. Structures of [Fe(qsal-X)$_2$]OTs reveal 1D π-π chains of the [Fe(qsal-X)$_2$]$^+$ cations, strong halogen bonding between the anion and cation, and high cooperativity. [Fe(qsal-X)$_2$]NTf_2 made from [Fe(qsal-X)$_2$]NO_3 and $LiNTf_2$ with [Fe(qsal-I)$_2$]NTf_2 showing a strongly hysteretic SCO coupled to a change in the confirmation of the triflimide anion. The [Fe(qsal-X)$_2$]$_2$[1,5-npds] and [Fe(qsal-X)$_2$]$_2$[2,6-npds] complexes display either LS and HS character. Despite the large anions most of the structures still contain 1D π-π chains with the Fe(III) centres in the LS state.

The structure of [Fe(qsal-I)$_2$]OTf·EtOH shows extremely large changes in the unit cell parameters consistent with the very wide hysteresis. EPR studies of [Fe(qsal-I)$_2$]OTf show rhombic spectra and strongly temperature dependent *g*-values suggesting an unusual relaxation process. Computational studies of [Fe(qsal-I)$_2$]OTf and [Fe(qsal-Br)$_2$]NO_3 reveal that the short interactions in the former are responsible for the abrupt SCO, while weaker contacts lead to stepped SCO in the latter compound.

The [Fe(qnal)$_2$]A compounds show SCO in the NCS and BPh_4 compounds. Structural studies of [Fe(qnal)$_2$]BPh_4·5H_2O show a HS Fe(III) centre and a combination of π-π and C-H···π interactions leading to strong connectivity. [Fe(qnal)$_2$]BPh_4 also shows the LIESST effect.

Iron(III) SCO nanomaterials have been prepared using the reverse micelle method with NaAOT as a surfactant. [Fe(qsal-I)$_2$]OTf and [Fe(qsal-I)$_2$]NTf_2 nanomaterials exhibit a nanorod morphology while [Fe(qsal-I)$_2$]OTf forms plate like aggregates. [Fe(qsal-I)$_2$]OTf has residual HS at low temperature, while the [Fe(qsal-I)$_2$]NTf_2 nanomaterials exhibit the same magnetic profile as the bulk material.

[Fe(qsal-X)halide] complexes have been made in trying to make Fe(III) SCO dimers. Most of the compounds exhibit halogen bonding between the molecular units to form the extended structure.

[Co(Himap)$_2$] is found to be a single-ion magnet with relaxation via the Raman process. HF-EPR studies and magnetic modelling of [Fe_4(2-Himap)$_6$][NO_3]$_3$ show the compound is a weak SMM with ferromagnetic coupling between the Fe(III) and Fe(II) centres.

The [Fe(naphEen)$_2$]anion·sol compounds are almost all LS only. Structural studies show the [Fe(naphEen)$_2$]$^+$ cations pack into supramolecular squares held together by C-H···O, π-π and C-H···π interactions. [Fe(naphEen)$_2$]BPh_4·H_2O·0.5CH_2Cl_2 shows SCO coupled to a change in the orientation of the ethyl group of one of the naphEen ligands.

The related [Fe(naphBzen)$_2$]A complexes exhibit SCO in most cases with two showing hysteresis. In the [Fe(naphBzen)$_2$]I, a 50% SCO with 20 K hysteresis is observed and a *hidden hysteresis* of 30 K, revealed by light irradiation. [Fe(naphBzen)$_2$]BF_4 exhibits stepped SCO with hysteresis in both steps. Structural studies show remarkably varied packing but strong cation-anion interactions through N-H···anion hydrogen bonds. In systems where the SCO is abrupt, the packing involves 2D sheets linked through N-H···anion and C-H···anion interactions.

บทคัดย่อ

ในรายงานฉบับนี้ได้แสดงถึงรายละเอียดการสังเคราะห์และพิสูจน์เอกลักษณ์สารประกอบเชิงซ้อนเหล็ก(III) และโคบอลต์(II) ที่มีสมบัติทางแม่เหล็กแบบสปินครอสโอเวอร์หรือแม่เหล็กไอออนเดี่ยว รวมไปถึงลิแกนด์ใหม่จำนวน 6 ชนิด คือ Hqsal-5-(3-py), Hqsal-5-(4-py), H_2bqimbd, H_2bpmabd, HnaphEen และ HnaphBzen

สารประกอบเชิงซ้อนเฮเทอโรเลพติก [Fe(qsal-Cl)(qsal-Br)]A·sol ซึ่งสังเคราะห์จากการแพร่ของชั้นสารละลายแสดงสมบัติสปินครอสโอเวอร์ โดยมีสมบัติอยู่ระหว่างสารประกอบโฮโมเลพติก การศึกษาโครงสร้างพบโดยมากโลหะกลางเป็นแบบ LS Fe(III) นอกจากนี้ยังได้ทำศึกษาสารประกอบกลุ่มใกล้เคียงคือ [Fe(qsal-X)(salpm-X)]A พบว่ามีสมบัติสปินครอสโอเวอร์อย่างช้า ๆ หรือแบบไม่สมบูรณ์

สารประกอบเชิงซ้อน [Fe(qsal-X)$_2$]OTs·sol เตรียมโดยการแพร่ของชั้นสารละลายพบสมบัติสปินครอสโอเวอร์แบบฉับพลันทุกสารประกอบ โดย [Fe(qsal-F)$_2$]OTs มีฮีสเทอเรซีสขนาด 50 K โครงสร้างของ [Fe(qsal-X)$_2$]OTs อันตรกิริยาแบบ π-π ทำให้เกิดสายโซ่ของ [Fe(qsal-X)$_2$] แบบ 1D มีพันธะฮาโลเจนที่แข็งแรงระหว่างไอออนบวกและไอออนลบ นอกจานี้ยังมีโคออพเพอร์เรทิวิทีที่สูง สารประกอบ [Fe(qsal-X)$_2$]NTf$_2$ สังเคราะห์จาก [Fe(qsal-X)$_2$]NO$_3$ และ LiNTf$_2$ สารประกอบมีฮีสเทอเรซีสที่แข็งแรงร่วมกับการเปลี่ยนคอนฟอร์เมชันของทริฟลิไมด์ไอออน สารประกอบ [Fe(qsal-X)$_2$]$_2$[1,5-npds] และ [Fe(qsal-X)$_2$]$_2$[2,6-npds] แสดงสมบัติแบบ LS และ HS แม้จะมีไอออนลบขนาดใหญ่แต่โครงสร้างก็ยังเป็นแบบ 1D ผ่านอันตรกิริยาแบบ π-π โดยมีเหล็กแบบ LS

โครงสร้างของสารประกอบ [Fe(qsal-I)$_2$]OTf·EtOH มีการเปลี่ยนแปลงพารามิเตอร์ของหน่วยเซลล์อย่างมากเมื่อมีการเกิดสปินครอสโอเวอร์ที่มีฮีสเทอเรซีสกว้างมาก การศึกษา EPR ของ [Fe(qsal-I)$_2$]OTf พบรอมบิคสเปกตราและค่า g จะขึ้นกับอุณหภูมิเป็นอย่างมากบ่งให้ทราบถึงกระบวนการรีเลกเซชั่นที่ต่างจากทั่วไปเป็นอย่างยิ่ง การคำนวณทางคอมพิวเตอร์พบว่า [Fe(qsal-I)$_2$]NO$_3$ มีอันตรกิริยาที่สั้นกว่า [Fe(qsal-Br)$_2$]OTf ทำให้มีการเกิดสปินครอสโอเวอร์แบบฉับพลันกว่าในขณะที่อันตรกิริยาที่อ่อนกว่าทำให้เกิดสปินครอสโอเวอร์แบบขั้นบันไดในสารประกอบ [Fe(qsal-Br)$_2$]OTf

สารประกอบ Fe(qnal)$_2$]A แสดงสมบัติสปินครอสโอเวอร์ในกรณีที่ A = NSC และ BPh$_4$ การศึกษาโครงสร้างพบว่าสารประกอบ Fe(qnal)$_2$]BPh$_4$·5H$_2$O มี Fe(III) แบบ HS โดยมีอันตรกิริยาแบบ π-π และ C-H···π ที่ทำให้เกิดการต่อกันอย่างแข็งแรง นอกจากนี้สารประกอบยังแสดงสมบัติ LIESST อีกด้วย

วัสดุนาโนสปินครอสโอเวอร์เหล็ก(III) สังเคราะห์ด้วยวิธีรีเวอร์สไมเซลโดยมี NaAOT เป็นสารลดแรงตึงผิว วัสดุนาโน [Fe(qsal-I)$_2$]OTf และ [Fe(qsal-I)$_2$]NTf$_2$ มีลักษณะเป็นแบบแท่งนาโน ขณะที่ [Fe(qsal-I)$_2$]OTf มีลักษณะเป็นแผ่น วัสดุนาโน [Fe(qsal-I)$_2$]OTf แสดงสมบัติแบบ HS ที่อุณหภูมิต่ำ ในขณะที่วัสดุนาโน [Fe(qsal-I)$_2$]NTf$_2$ แสดงสมบัติสปินครอสโอเวอร์เหมือนสารประกอบเชิงซ้อนระดับโมเลกุล

ในการพยายามสังเคราะห์สารประกอบสปินครอสโอเวอร์ไดเมอร์เหล็ก(III) พบว่าผลิตภัณฑ์ที่ได้คือสารประกอบ [Fe(qsal-X)halide] มีพันธะฮาโลเจนระหว่างหน่วยโมเลกุล

สารประกอบ $[Co(Himap)_2]$ แสดงสมบัติแบบแม่เหล็กไอออนเดี่ยวที่มีรีเลกเซชันผ่านกระบวนการทางรามาน การศึกษาเพิ่มเติมด้วยเทคนิค HF-EPR และการจำลองทางโมเลกุลของสประกอบ $[Fe_4(2\text{-}Himap)_6][NO_3]_3$ พบว่าสารประกอบแสดงสมบัติแม่เหล็กโมเลกุลเดี่ยวอย่างอ่อนที่มีเฟอร์โรแมกเนติกคับปลิงระหว่างเหล็ก(II) และ เหล็ก(III)

สารประกอบ [Fe(naphEen)$_2$]anion·sol ส่วนมากเป็นแบบ LS เพียงอย่างเดียว การศึกษาโครงสร้างพบว่า $Fe(naphEen)_2]^+$ มีการจัดเรียงระดับโมเลกุลแบบซูปราโมเลกุลาร์สแควร์ โดยเกิดจากอันตรกิริยาระหว่าง C-H···O, π-π and C-H···π สารประกอบ $Fe(naphEen)_2]BPh_4 \cdot H_2O \cdot 0.5CH_2Cl_2$ เป็นเพียงสารเดียวในกลุ่มนี้ที่แสดงสมบัติสปินครอสโอเวอร์พร้อมกับการเปลี่ยนทิศทางของหมู่อีทิลในโมเลกุลของลิแกนด์ naphEen

สารประกอบ $[Fe(naphBzen)_2]A$ เกิดสปินครอสโอเวอร์เกือบทุกสาร และมีสองชนิดที่มีฮีสเทอเรซีส ในกรณีของ $[Fe(naphBzen)_2]I$ เกิดสปินครอสโอเวอร์ 50% ที่อุณหภูมิ 20 K และมีฮีสเทอเรซีสที่ซ้อนอยู่ที่อุณหภูมิ 30 K โดยจะสามารถเข้าถึงได้ด้วยการกระตุ้นด้วยแสง สารประกอบ $[Fe(naphBzen)_2]BF_4$ เกิดสปินครอสโอเวอร์แบบขั้นบันไดและมีฮีสเทอเรซีสทั้งในสองขั้น การศึกษาโครงสร้างทำให้ทราบกรจัดเรียงที่หลากหลายแต่จะมีอันตรกิริยาที่แข็งแรงของไอออนบวกผ่านพันธะไฮโดรเจน N-H···anion ในระบบที่มีสปินครอสโอเวอร์แบบฉับพลันจะมีการจัดเรียงแบบแผ่น 2D โดยมีอันตรกิริยา N-H···anion และ C-H···anion เชื่อมระหว่างแผ่น

Table of Contents

	Page Number
1. Executive Summary	1
1.1 Proposed Objectives	7
1.2 Achieved Objectives	7
2. Results and Discussion	8
Ligand Synthesis	8
Synthesis of $[Fe(qsal\text{-}Cl)(qsal\text{-}Br)]^+$ complexes	9
Structures of $[Fe(qsal\text{-}Cl)(qsal\text{-}Br)]^+$ complexes	10
Magnetic studies of $[Fe(qsal\text{-}Cl)(qsal\text{-}Br)]^+$ complexes	12
Synthesis and characterization of $[Fe(qsal\text{-}X)(salpm\text{-}X)]^+$ complexes	13
Synthesis and characterization of $[Fe(qsal\text{-}X)_2]OTs$	15
Structural studies of $[Fe(qsal\text{-}X)_2]OTs$	16
Magnetic studies of $[Fe(qsal\text{-}X)_2]OTs$	20
Synthesis and structural studies of $[Fe(qsal\text{-}X)_2]NTf_2$	22
Magnetic studies of $[Fe(qsal\text{-}X)_2]NTf_2$	25
Synthesis and structures of $[Fe(qsal\text{-}X)_2]_2[npds]$ complexes	26
Magnetic studies of $[Fe(qsal\text{-}X)_2]_2[npds]$ complexes	28
Structural studies of $[Fe(qsal\text{-}I)_2]OTf{\cdot}EtOH$	29
EPR spectroscopic studies of $[Fe(qsal\text{-}I)_2]OTf{\cdot}solvent$	31
Computational studies on $[Fe(qsal\text{-}I)_2]OTf$ and $[Fe(qsal\text{-}Br)_2]NO_3$	32
Synthesis of $[Fe(qnal)_2]$anion complexes	34
Structural studies of $[Fe(qnal)_2]BPh_4$	35
Magnetic studies of $[Fe(qnal)_2]$anion complexes	37
Fe(III) SCO nanomaterials	38
Synthesis and structures of [Fe(qsal-X)halide] complexes	45
Magnetic properties of $[Co(2\text{-}Himap)_2]$	46
Magnetic studies and HF-EPR studies of $[Fe_4(2\text{-}Himap)_6][NO_3]_3$	51
Magnetic studies and HF-EPR studies of $[Fe_4(2\text{-}Himap)_6][NO_3]_3$	54
Computational Investigations of Fe(III)-F Complexes	55
Structural studies of $[Fe(naphEen)_2]$anion	56
Magnetic studies of $[Fe(naphEen)_2]$anion	61
Synthesis and structural studies of $[Fe(naphBzen)_2]$anion	63
Magnetic studies of $[Fe(naphBzen)_2]$anion	67
Experimental	69
Synthesis of Hqsal-5-(3-py)	69
Synthesis of H_2bqimbd	69
Synthesis of HnaphEen	69
Synthesis of $[Fe(qsal\text{-}X)_2]A$ (A = sulfonate anions)	70
Synthesis of $[Fe(qsal\text{-}X)_2]NTf_2$	70
Synthesis of $[Fe(naphEen)_2]$anion	70
Synthesis of $[Fe(naphBzen)_2]$anion	71
3. Project Outcomes	71
3.1 Publications	71
3.2 Presentations	72
3.3 Academic collaborations	73
3.4 Academic activities	74

1. Executive Summary

The pyridyl-substituted ligands, Hqsal-5-(3-py) {8-quinolyl[5-(3′-pyridyl)]salicylaldimine} and Hqsal-5-(4-py) {8-quinolyl[5-(4′-pyridyl)]salicylaldimine}, have been synthesized from the corresponding salicylaldehyde and 8-aminoquinoline in near quantitative yield. The dinucleating ligands H_2bqimbd {2-methyl-4,6-bis((quinolin-8-ylimino)methyl)-benzene-1,3-diol} and H_2bpmabd {2-methyl-4,6-bis((pyridylimino)-methyl)benzene-1,3-diol} have also been prepared and are isolable in the case of the former. Reaction of the ligands with simple iron(III) staring materials results in black solids.

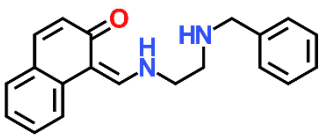

HnaphBzen ligand

Two new ligands HnaphEen {1-{[2-(ethylamino)ethylimino]methyl}-2-naphthol} and HnaphBzen {1-{[2-(benzylamino)ethylimino]methyl}-2-naphthol} have been made from 2-hydroxynaphth-aldehyde and N-alkylaminoethylamine. The ethyl derivative is best prepared *in situ* as it slowly degrades over time. The ligands have been fully characterized by IR, UV-Vis and ^{1}H NMR spectroscopy.

The reaction of Hqsal-Cl and Hqsal-Br with iron(III) gives [Fe(qsal-Cl)(qsal-Br)]A·sol (A = NCS, sol = MeOH **1**; PF_6 **2**; BPh_4, sol = $2CH_2Cl_2$ **3**; OTf, sol = 0.5MeOH **4**) prepared via layered diffusion. The yields are moderate and interestingly in all cases the heteroleptic compounds are the only product. The structures of all the compounds have been determined by X-ray crystallography. In most cases the Fe(III) centres are low spin. The exception is [Fe(qsal-Cl)(qsal-Br)]BPh_4·$2CH_2Cl_2$ for which the structure has been determined at 100, 123 and 267 K showing a LS, mixed HS-LS and HS Fe(III) centre, respectively. Despite the two different qsal-X/Y ligands the packing remains remarkably similar to the homoleptic systems, [Fe(qsal-X)$_2$]A and hence there is significant cooperativity. Magnetic studies indicate that the spin crossover behaviour of [Fe(qsal-Cl)(qsal-Br)]$^+$ is generally intermediate between the homoleptic systems.

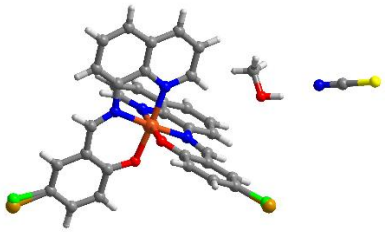

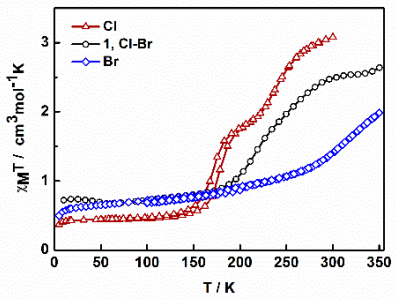

The synthesis of the mixed ligand complexes, [Fe(qsal-X)(salpm-X)]A (X = Cl, A = NO_3 **5**, ClO_4 **6**, NCS **7**; X = Br, A = NO_3 **8**, ClO_4 **9**, NCS **10**) has been achieved by simple mixing of the starting materials followed by slow evapouration. UV-Vis spectroscopy studies confirm that the mixed ligand Fe(III) compounds are the only product. Magnetic studies show that the compounds undergo very gradual or incomplete spin crossover.

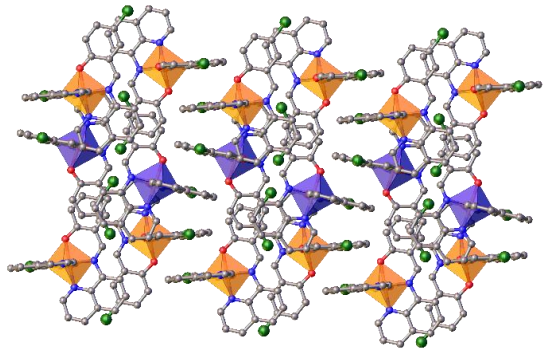

Layered diffusion in EtOH yields black crystals of [Fe(qsal-X)$_2$]OTs·sol, (X = Cl = **11·H_2O** sol = H_2O or none **11**, X = Br **12**, sol = H_2O; X = I **13**, sol = $2H_2O$). The structures of all the compounds show the characteristic 1D π-π chains but in **11·H_2O** these are angled relative to each other while in **11** they are parallel. The compounds also show strong halogen bonding between the cations and the O atom of the OTs anion, being strongest for the iodo. The anions are also linked by bridging water molecules

which add to the high cooperativity in the compounds. The related $[Fe(qsal\text{-}F)_2]OTs{\cdot}0.5EtOH$ **14** compound is made in a similar way with the structure determined at multiple temperatures. As with all other Fe(III) compounds with the qsal-F ligand there are two independent Fe(III) centres in the asymmetric unit. One of these is stubbornly LS between 93 and 293 K while the other undergoes a gradual spin crossover. The presence of the extra independent centre disrupts the normal 1D π-π chains with the chain involving the Fe2 centres more closely resembling supramolecularly connected Fe dimers. The chains are linked through extensive C-H···O contacts and unlike the heavier halogens above there are no halogen bonds.

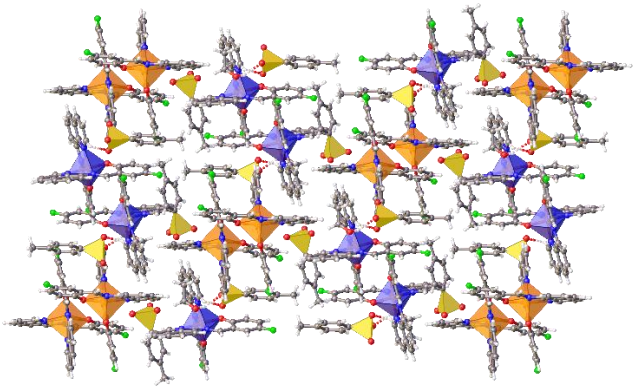

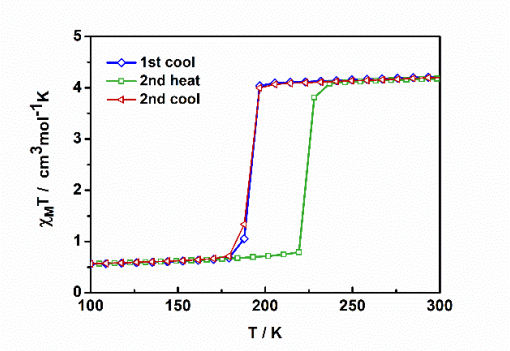

The spin crossover properties of the $[Fe(qsal\text{-}X)_2]OTs$ series are unusual with all members showing abrupt or moderately abrupt spin crossover. $[Fe(qsal\text{-}Cl)_2]OTs$ undergoes a 50% spin transition with $T_{1/2}$ = 230 K. In contrast, $[Fe(qsal\text{-}Br)_2]OTs{\cdot}H_2O$ undergoes SCO from LS to 67% HS at $T_{1/2}$ = 260 K and $[Fe(qsal\text{-}I)_2]OTs{\cdot}2H_2O$ reveals an almost complete crossover at $T_{1/2}$ = 290 K. The results demonstrate an increase in stability for the LS state on descending the halogen group. $[Fe(qsal\text{-}F)_2]OTs$ has an exceeding abrupt SCO with $T_{1/2}(\downarrow)$ = 180 K and $T_{1/2}(\uparrow)$ = 230 K and thus a hysteresis of 50 K. This is one of the widest and squarest hystereses ever observed in SCO chemistry.

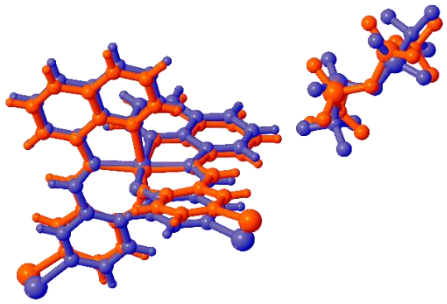

The reaction of $[Fe(qsal\text{-}X)_2]NO_3$ dissolved in MeOH with $LiNTf_2$ gives $[Fe(qsal\text{-}X)_2]NTf_2$ (X = Cl **15**, Br **16**, I **17**). X-ray crystallography reveals that **17** crystallizes in triclinic $P\bar{1}$ while **15** and **16** are found in orthorhombic *Pbca*. Uniquely, **17** shows clear spin crossover with the Fe-N/O bond lengths decreasing by 0.128 Å and 0.024 Å, respectively, upon cooling between 245 and 255 K. The most remarkable feature of the structure is a re-orientation of the SO_2CF_3 group of the triflimide anion coupled to the change in spin change. This is unprecedented in SCO chemistry and may represent a new way to induce SCO. The magnetic properties of **17** are equally impressive with $T_{1/2}(\downarrow)$ = 248 K and $T_{1/2}(\uparrow)$ = 278 K giving a hysteresis of 30 K. This is one of only a handful of SCO compounds to undergo strongly hysteretic SCO close to room temperature.

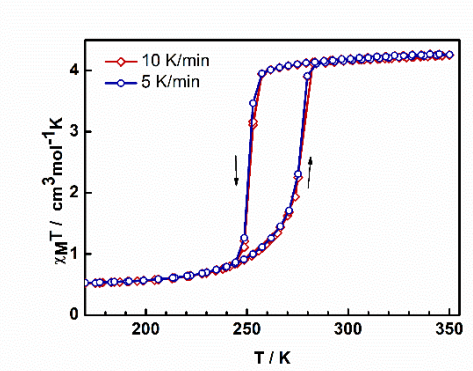

Surprisingly, **15** and **16** are trapped in the LS state which seems to be due to the higher symmetry in which the compounds crystallize. This in turn must relate to the smaller size of the Cl and Br substituents compared to the iodo group.

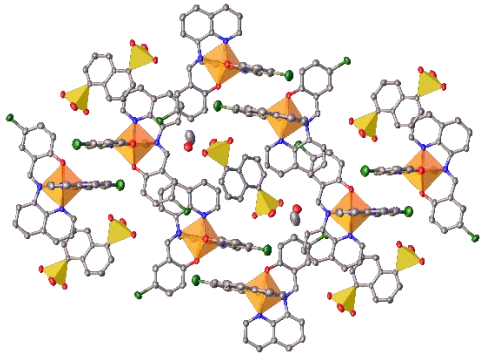

$[Fe(qsal\text{-}X)_2]_2[1,5\text{-}npds]$ (X = Cl **18**, Br **19**, I **20**) and $[Fe(qsal\text{-}X)_2]_2[2,6\text{-}npds]$ (X = Cl **21**, Br **22**, I **23**) are prepared by layered diffusion as black microcrystalline solids. Despite the very large anions the Fe-N/O bond lengths are all typical of the LS state. In **19**, **20** and **23** the $[Fe(qsal\text{-}X)_2]^+$ cations are organized into 1D π-π chains. In contrast, **18**, **21** and **22** are composed of π-π dimers clustered around the anions to give 2D sheets.

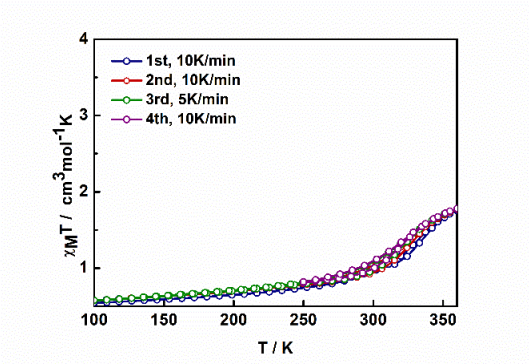

The SCO characteristics of the compounds are generally poor with the $[Fe(qsal\text{-}X)_2]_2[1,5\text{-}npds]$ almost all stuck in the LS state while $[Fe(qsal\text{-}X)_2]_2[2,6\text{-}npds]$ are trapped in the HS state. The results indicate that the shape of the anion can be just as important as the type of anion in directing SCO behaviour.

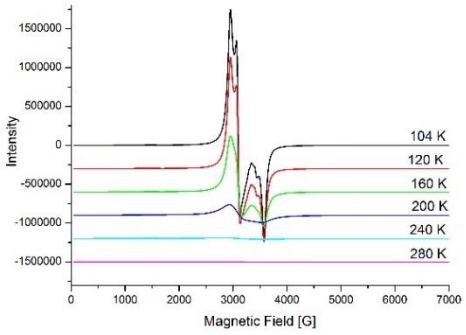

The structure of $[Fe(qsal\text{-}I)_2]OTf{\cdot}EtOH$ **24** at 100 K has been determined and shows that the Fe-N/O bond lengths change by ΔFe–N = 0.170 Å and ΔFe–O = 0.023 Å consistent with full spin crossover. A comparison of the HS and LS structures reveals a remarkably anisotropic distortion with *b* and *c* shortening by 0.845 and 0.499 Å, respectively while *a* lengthens by 0.901 Å. This results in a substantial reduction in the unit cell volume by 6.3%, the largest yet reported for any Fe(III) SCO complex and partly responsible for the large hysteresis in **24**. There is also a significant reorganization of the triflate anion reminiscent of $[Fe(qsal\text{-}I)_2]NTf_2$ which also exhibits large hysteresis.

EPR studies of $[Fe(qsal\text{-}I)_2]OTf$ show a strongly rhombic spectrum and a clear spin transition around 230 K. An interesting feature of the spectra are that the *g*-values are strongly temperature dependent and may suggest a relaxation process is operative.

Computational studies on $[Fe(qsal\text{-}I)_2]OTf$ and $[Fe(qsal\text{-}Br)_2]NO_3$ reveal that in the case of the latter compound there are three spin states close in energy. As a result the compound goes through a symmetry breaking HS-LS intermediate. For $[Fe(qsal\text{-}I)_2]OTf$ only the LS and HS states are close in energy meaning that a first-order spin transition

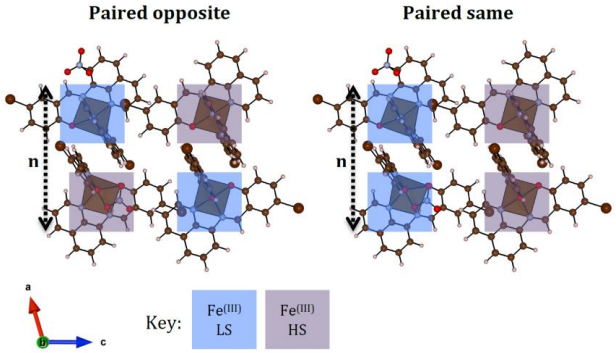

occurs. The reason seems to be due to stronger interactions in $[Fe(qsal\text{-}I)_2]OTf$ compared to $[Fe(qsal\text{-}Br)_2]NO_3$.

$[Fe(qnal)_2]A$ (A = NCS **25**, NO_3 **26** and BPh_4 **27**) are prepared by layered diffusion with the structure of $[Fe(qnal)_2]BPh_4 \cdot 5H_2O$ determined at room temperature. As expected, the Fe(III) centre is HS but unlike the $[Fe(qsal\text{-}X)_2]^+$ series, a combination of π-π and C-H···π interactions form the 1D chain. The BPh_4 anions then decorate the 1D chains and through extensive C-H···π interactions link the 1D chains to form a 2D sheet.

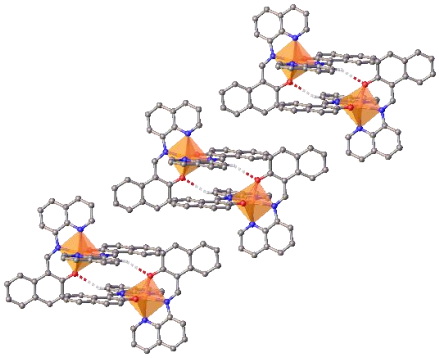

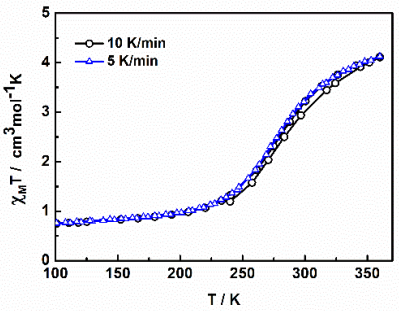

SQUID magnetometric studies show that the NCS and BPh_4 anions exhibit gradual SCO with $T_{1/2}$ = 330 K and 280 K, respectively, while **26** is essentially LS. The lower spin transition temperature of **27** is critical and allows us to observe a very rare case of light induced SCO, or LIESST. The compound also undergoes reverse LIESST making the compound a true light switchable material.

Iron(III) SCO nanomaterials have been prepared using the reverse micelle method with NaAOT as a surfactant. The amount of surfactant, reaction time and the solvent used in the preparation have been explored in $[Fe(qsal)_2]NO_3$. Ideal conditions produce parallelogram shaped materials with length × width × thickness of 1-2 μm × 300-600 nm × 90-110 nm on average. The SQUID profile of the bulk $[Fe(qsal)_2]NO_3$ and the nanomaterials are almost identical. Similar nanosizing of $[Fe(qsal\text{-}I)_2]OTf$ and $[Fe(qsal\text{-}I)_2]NTf_2$ also yield nanomaterials with an average size of 510 ± 27 nm and 709 ± 193 nm, respectively. The $[Fe(qsal\text{-}I)_2]NTf_2$ nanomaterials have a particularly strong nanorod morphology while $[Fe(qsal\text{-}I)_2]OTf$ resembles plate like aggregates. The magnetic profile of $[Fe(qsal\text{-}I)_2]OTf$ shows a reduced hysteresis and 19% of Fe(III) centres that remain HS even at low temperature. In contrast, the $[Fe(qsal\text{-}I)_2]NTf_2$ nanomaterials exhibit the same magnetic profile as the bulk material strongly suggesting that provided that the hysteresis in the bulk sufficiently large nanosizing results in little change. This makes $[Fe(qsal\text{-}I)_2]NTf_2$ an extremely promising material for future device development.

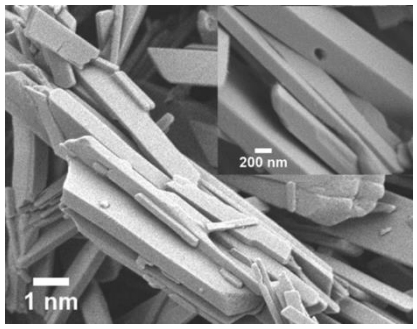

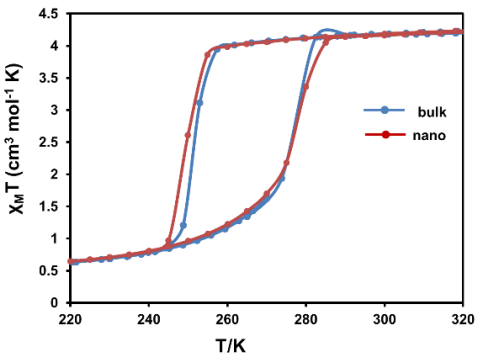

In trying to make Fe(III) SCO dimers we have isolated a range of complexes, $[Fe(qsal\text{-}Br)Cl_2]$ **28**, $[Fe_2(\mu\text{-}OMe)_2F_2(qsal\text{-}Br)_2]\cdot 2MeOH$ **29** and $[Fe_2(\mu\text{-}OMe)_2Cl_2(qsal\text{-}I)_2]$ **30**. $[Fe(qsal\text{-}Br)Cl_2]$ has a square-pyramidal geometry and halogen bonds that link to form the extended structure. Halogen bonds are also a feature of the structure of **30** linking

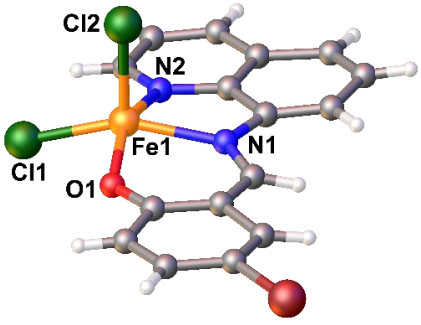

the individual dimers. The related $[Fe_2(\mu\text{-}OMe)_2F_2(qsal\text{-}Br)_2]\cdot 2MeOH$ dimer exchanges the halogen bond for hydrogen bonds between the coordinated fluorides and the MeOH molecules.

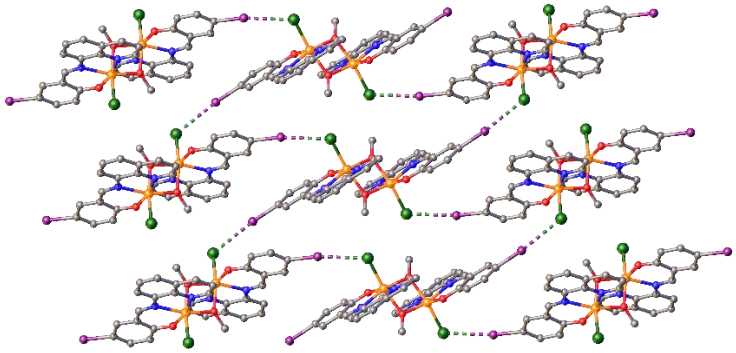

The magnetic properties of $[Co(Himap)_2]$ **31** have been studied and show that D = +36.7 cm^{-1}; E = 2.0 cm^{-1}; g = 2.11, 2.48, 2.12. Computational studies reveal that the ligand splits the *d*-orbitals creating a gap of *ca*. 100 cm^{-1} for the lowest energy transition. Further modelling of the *ac* magnetic data suggests that the barrier to the reversal of magnetization is 14 K. Moreover, MOLCAS calculations indicate that for this Single-Ion Magnet the dominant relaxation pathway is via the Raman process.

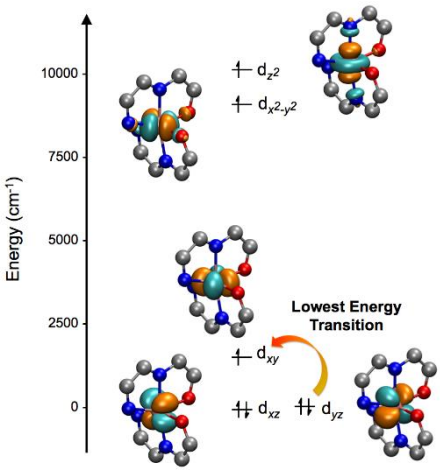

HF-EPR studies and magnetic modelling of $[Fe_4(2\text{-}Himap)_6][NO_3]_3$ **32** reveals that weak ferromagnetic coupling (J = +2.77 cm^{-1}, D = -7.09 cm^{-1}) between the peripheral and central Fe centres. The compound is also a weak SMM. The HF-EPR studies confirm that D is –ve but the spectra are very complex and difficult to interpret with certainty.

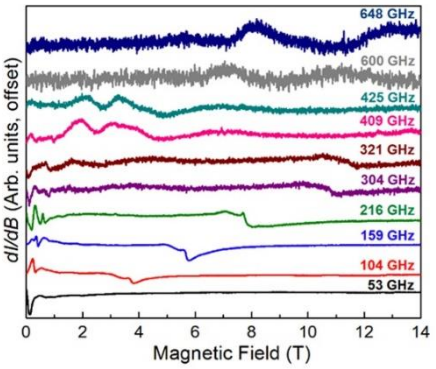

The iron(III) complexes, [Fe(naphEen)$_2$]anion·sol (anion = F, **33**; Cl, **34**; Br **35**; I **36**; BF_4 **37**; NO_3 **38**; ClO_4 **39**; PF_6 **40**; BPh_4 **41**; OTf **42**; NTf_2 **43**; 1,5-npds **44**; 2,6-npds **45** and terephthalate **46**) were synthesized by reacting two equivalents of HnaphEen, made *in situ*, with FeX_3 giving reasonable yields. The fluoride complex exhibits an unusual equilibrium between [Fe(naphEen)$_2$]F and [Fe(naphEen)$_2$F] where the fluoride acts a counteranion or ligand, respectively.

Structural studies of the majority of the complexes reveal two independent LS Fe(III) centres. In the case of $[Fe(naphEen)_2]Br\cdot H_2O$, heating results in a phase change to give $[Fe(naphEen)_2]Br\cdot 0.5H_2O$ and three independent Fe(III) centres but no spin crossover. The anions are held by the cations in an embrace by a pair of N-H···X interactions. The $[Fe(naphEen)_2]^+$ cations pack into supramolecular squares held together by C-H···O, π-π and C-H···π interactions. These in turn are stacked into ABAB layers with each layer containing a single Fe(III) centre. The solvent and anion are located in 'butterfly' shaped holes between the $[Fe(naphEen)_2]^+$ cations.

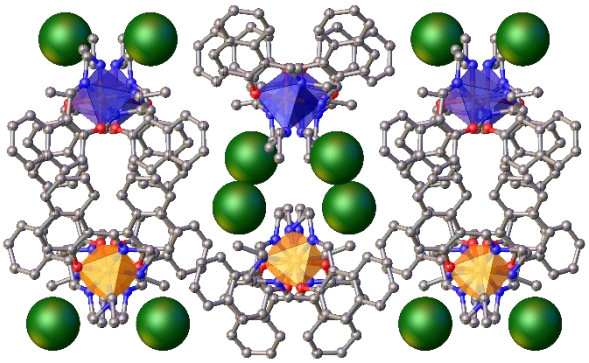

The most interesting structure is $[Fe(naphEen)_2]BPh_4 \cdot H_2O \cdot 0.5CH_2Cl_2$ **41** which has been determined at 123, 173, 198, 223 and 293 K. The Fe-N/O bond lengths reveal a complete SCO over this temperature range. Intriguingly, the ethyl group of one of the naphEen ligands rotates as the SCO proceeds. To the best of our knowledge this is the first such example in iron(III) SCO chemistry. The packing in **41** is unique in the $[Fe(naphEen)_2]^+$ series as the large BPh_4 anion disrupts the normal packing noted above. Similar disruption is caused by the 1,5-npds and 2,6-npds anions resulting instead in ladders with the anions located between the ladders.

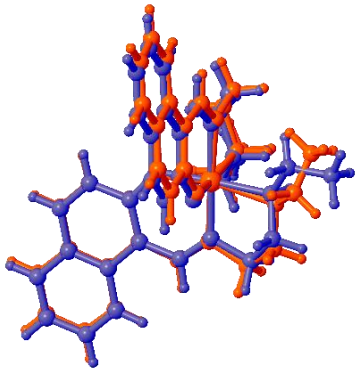

Magnetic studies confirm that the compounds are mostly trapped in the LS state the exception being the ClO_4, PF_6, and 2,6-npds compounds which exhibit gradual SCO. In the case of **41** the SCO is from the HS state but is incomplete even at 100 K suggesting solvent loss compared to the crystal structure.

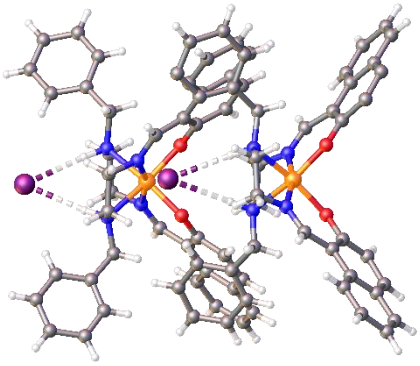

The $[Fe(naphBzen)_2]A$ (A = F **47**, Cl **48**, Br **49**, I **50**, BF_4 **51**, NO_3 **52**, ClO_4 **53**, PF_6 **54**) compounds were prepared in good yields as dark green crystals. The structures of **47**, **48**, **50** and **52** contain two independent Fe(III) centres, while the others all have a single Fe(III) centre. The Fe-N/O bond lengths are in most cases short at low temperature and increase upon heating, a clear indication of spin crossover. In the case of $[Fe(naphBzen)_2]Cl$ the Fe-N/O bond lengths indicate that SCO occurs between a [LS-LS] and [LS/HS-HS] while for $[Fe(naphBzen)_2]Br$ a transition between a [LS/HS-HS] and a [HS-HS] state is found. In $[Fe(naphBzen)_2]NO_3$ a gradual transition occurs from a [LS-HS] to a [LS/HS-HS] state. The lack of complete SCO in any of these compounds suggests that the high symmetry prevents access to the full HS state. In contrast, in $[Fe(naphBzen)_2]I$ SCO occurs between a [HS-LS] to [HS-HS] state while **54** shows a gradual SCO between 200 and 350 K as evidenced by subtle changes in the Fe-N/O bond lengths.

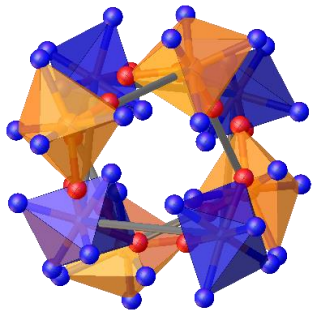

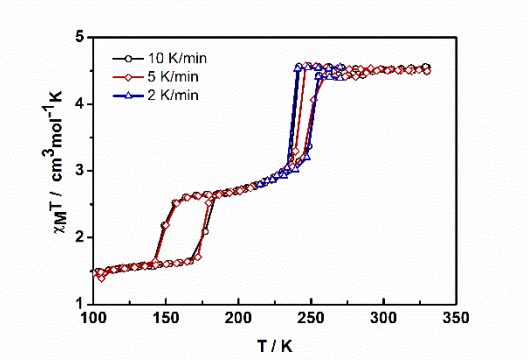

Magnetic susceptibility studies show SCO in all compounds. In the case of **48** and **49** the hysteresis is quite wide but involves only 15-20% SCO. In contrast, **50** exhibits a stable 50% SCO with a hysteresis of 20 K with $T_{1/2}(\uparrow)$ = 135 K and $T_{1/2}(\downarrow)$ = 115 K. $[Fe(naphBzen)_2]I$ also undergoes a unique reverse-LIESST and light-induced thermal hysteresis revealing a hidden hysteresis of 30 K. In $[Fe(naphBzen)_2]BF_4$ an unprecedented stepped SCO from 25% HS to 50% HS with $T_{1/2}(\uparrow)$ = 177 K and $T_{1/2}(\downarrow)$ = 149 K and consequently a hysteresis of 28 K. A 50% HS plateau of *ca*. 70 K exists before $\chi_M T$ increases again to the full HS state with $T_{1/2}(\uparrow)$ = 252 K and $T_{1/2}(\downarrow)$ = 239 K (ΔT = 13 K). The complexes **52** and **54** exhibit gradual SCO, the former going from *ca*. 50% HS to *ca*. 80 HS%. Compound **54** undergoes a gradual but very linear SCO from 100% LS at 200 K to ca. 60% HS at 350 K.

1.1 Proposed Objectives

1. To prepare two new dinucleating ligands and a pair of pyridyl substituted ligands, Hqsal-5-(3-py) and Hqsal-5-(4-py).
2. To prepare [Fe(qsal-X)(qsal-Y)]A and [Fe(qsal-X)(salpm-X)]A SCO complexes and evaluate how these heteroleptic compounds compare with $[Fe(qsal\text{-}X)_2]A$ (A = anion).
3. To prepare SCO complexes which may act as ligands, $[Fe(qsal\text{-}5\text{-}(3\text{-}py))_2]A$ and $[Fe(qsal\text{-}5\text{-}(4\text{-}py))_2]A$ (A = anion). Use these to create supramolecular and coordination SCO polymers.
4. To prepare a series of Fe(III) spin crossover dimers exploring their structural chemistry and determining if the SCO and magnetic exchange are coupled.
5. Utilize $[Fe(qsal\text{-}I)_2]OTf$ in the preparation of SCO nanomaterials.
6. To train Thai students in spin crossover chemistry providing them with much needed STEM skills.
7. To publish 6-7 high impact publications based upon this research.

1.2 Achieved Objectives

1. Both the dinucleating, H_2bqimbd and H_2bpmabd, and the pyridyl substituted ligands Hqsal-5-(3-py) and Hqsal-5-(4-py) have been prepared and fully characterized.
2. A series of heteroleptic [Fe(qsal-X)(qsal-Y)]A and [Fe(qsal-X)(salpm-X)]A (A = anion) SCO complexes have been prepared and almost completely characterized.
3. Four new series $[Fe(qsal\text{-}X)_2]OTs{\cdot}sol$ (sol = none or nH_2O), $[Fe(qsal\text{-}X)_2]NTf_2$, $[Fe(qsal\text{-}X)_2]_2[1,5\text{-}npds]$ and $[Fe(qsal\text{-}X)_2]_2[2,6\text{-}npds]$ have been prepared and completely characterized.
4. Three new complexes $[Fe(qnal)_2]A$ (A = NCS, NO_3, BPh_4) have been prepared and characterized.
5. Nanomaterials of $[Fe(qsal)_2]A$ (A = NO_3, NCS), $[Fe(qsal\text{-}I)_2]OTf$ and $[Fe(qsal\text{-}I)_2]NTf_2$ have been prepared and the impact of concentration, reaction time and surfactant has been explored.
6. A new ligand HnaphEen and Fe(III) complexes $[Fe(naphEen)_2]A$ (A = F, Cl, Br, I, BF_4, ClO_4, PF_6, NO_3, OTf, BPh_4, NTf_2, 1,5-npds, 2,6-npds, terephthalate) have been prepared and completely characterized.
7. A new ligand HnaphBzen and the Fe(III) complexes $[Fe(naphBzen)_2]A$ (A = F, Cl, Br, I, BF_4, NO_3, ClO_4, PF_6) have been prepared and characterized.
8. Three undergraduate DPST students and two PhD students have worked on the project.
9. The work has been presented at international conferences, and at postgraduate seminars in Australia.
10. 9 high impact ISI publications and one book chapter have been published in the course of this project.

2. Results and Discussion

Ligand Synthesis

The pyridyl-substituted ligands, Hqsal-5-(3-py) and Hqsal-5-(4-py), have been successfully synthesized from the appropriate salicylaldehyde in CH_2Cl_2. The yields of the ligands are almost quantitative but the yield of the starting aldehyde remains low as column chromatography is required to obtain the aldehyde from the Suzuki coupling in pure form. ^{1}H-NMR spectroscopy confirms the purity of the ligand with peaks for the pyridine, quinoline and the phenyl groups all in their expected positions (Table 1). The asymmetry of the 3-pyridine ligand is particularly clear with 4 different proton environments observable. The compounds show strong similarity in their quinoline and imine proton shifts, consistent with the large distance from the pyridyl group.

Table 1 ^{1}H-NMR spectroscopic data for Hqsal-5-(4-py), Hqsal-5-(3-py), H_2bqimbd and HnaphEen.

Compound	δ (ppm)[a]
Hqsal-5-(3-py)	14.21 (s, 1H, OH), 9.02 (dd, $1H_{quin}$, J_{HH} = 4.5, 1.2), 8.90 (s, $1H_{imine}$), 8.84 (s, $1H_{py}$), 8.63 (d, $1H_{py}$, J_{HH} = 3.9), 7.85-7.76 (m, $4H_{quin+py+phenyl}$), 7.62-7.37 (m, $4H_{quin}$), 7.13-7.09 (m, $2H_{py+phenyl}$)
Hqsal-5-(4-py)	14.02 (s, 1H, OH), 9.00 (dd, $1H_{quin}$, J_{HH} = 4.2, 1.2), 8.93 (s, $1H_{imine}$), 8.65 (d, $2H_{py}$, J_{HH} = 6.0), 7.77 (d, $1H_{quin}$, J_{HH} = 7.8), 7.64-7.46 (m, $6H_{quin+phenyl}$), 7.13 (d, $2H_{py}$, J_{HH} = 8.4), 7.08 (d, $1H_{phenyl}$, J_{HH} = 9.0)
H_2bqimbd	15.26 (s, 2H, OH), 9.03 (dd, $2H_{quin}$, J_{HH} = 4.8, 1.5), 8.86 (s, $2H_{imine}$), 8.20 (dd, $2H_{quin}$, J_{HH} = 7.4, 1.5), 7.73 (dd, $2H_{quin}$, J_{HH} = 7.8, 1.8), 7.61-7.46 (m, $6H_{quin}$), 7.43 (s, H_{phenyl}), 2.31 (s, 3H, CH_3)
HnaphEen	8.82 (br s, 1H, N-H), 7.88 (d, $1H_{naph}$, J_{HH} = 8.4), 7.69 (d, $1H_{naph}$, J_{HH} = 8.7), 7.62 (d, $1H_{naph}$, J_{HH} = 8.1), 7.44 (t, $1H_{naph}$, J_{HH} = 8.4), 7.24 (t, $1H_{naph}$, J_{HH} = 8.1), 6.93 (d, $1H_{naph}$, J_{HH} = 8.7), 5.30 (s, $1H_{=CH}$), 3.75 (s, $2H_{N\text{-}\underline{CH2}\text{-}CH2}$), 3.00 (s, $2H_{N\text{-}CH2\text{-}\underline{CH2}}$), 2.73 (q, $2H_{N\text{-}\underline{CH2}\text{-}CH3}$, J_{HH} = 7.2), 1.33 (t, $2H_{N\text{-}CH2\text{-}\underline{CH3}}$, J_{HH} = 7.2)

[a] J values in Hz in $CDCl_3$.

The dinucleating ligands H_2bqimbd and H_2bpmabd have also been prepared and characterized by IR and ^{1}H-NMR spectroscopy. The reaction is a little slower than the tridentate Hsalpm and Hqsal ligands requiring a small amount of acid and heating to obtain clean products, particularly when aminoquinoline is used. The reason for the lack of data on the pyridyl analogue is that it is oily and thus difficult to work with, a feature shared with the Hsalpm ligands. Consequently, we prepare this ligand *in situ* for subsequent complex synthesis. The IR and ^{1}H-NMR spectroscopic data are consistent with the proposed ligand with a single imine and CH_3 peaks. The IR shows a C=N stretch at 1630 cm^{-1}, typical of such Schiff bases.

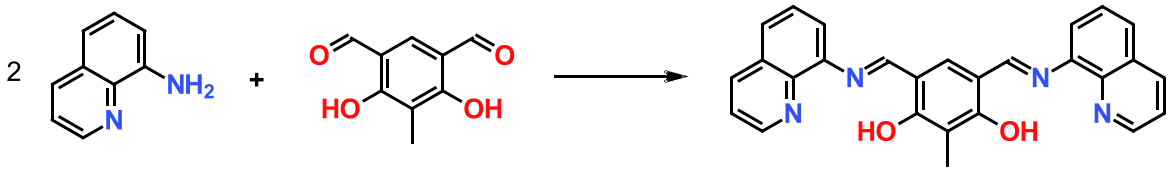

Scheme 1 Synthesis of H_2bqimbd.

Finally, we have prepared another ligand by reacting N-ethylaminoethylamine with 2-hydroxy-1-naphaldehyde (Scheme 2). This ligand contains a large π-cloud and a free N-H which would be expected to engage in H-bonding.

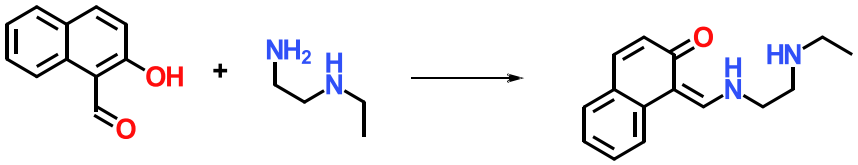

Scheme 2 Synthesis of HnaphEen.

The IR shows a C=O stretch at 1632 cm^{-1} which is very strong unlike imine stretches which tend to be weaker. The ^{1}H-NMR also shows a lack of an O-H stretch again strongly suggesting that the ligand is in the keto-amino tautomeric form in solution. A further ligand we have prepared in this family is HnaphBzen, where the ethyl group is replaced by a benzyl group. The ligand is prepared simply from 2-hydroxynaphthaldehyde as a bright yellow microcrystalline solid (Scheme 3).

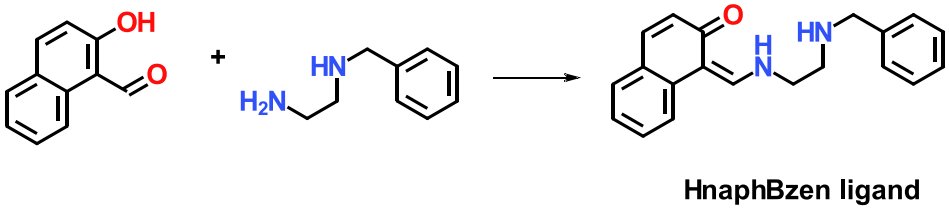

Scheme 3 Synthesis of HnaphBzen.

Synthesis of [Fe(qsal-Cl)(qsal-Br)]$^{+}$ complexes

[Fe(qsal-Cl)(qsal-Br)]A·sol (A = NCS, sol = MeOH **1**; PF_6 **2**; BPh_4, sol = $2CH_2Cl_2$ **3**; OTf, sol = 0.5MeOH **4**) have been prepared via layered diffusion in moderate yields (Scheme 4). The compounds are black with IR spectra showing imine stretches between 1598-1602 cm^{-1} and typical of qsal-Cl/Br ligands. The NCS, PF_6 and OTf anions are also evident in the IR spectra (Table 2).

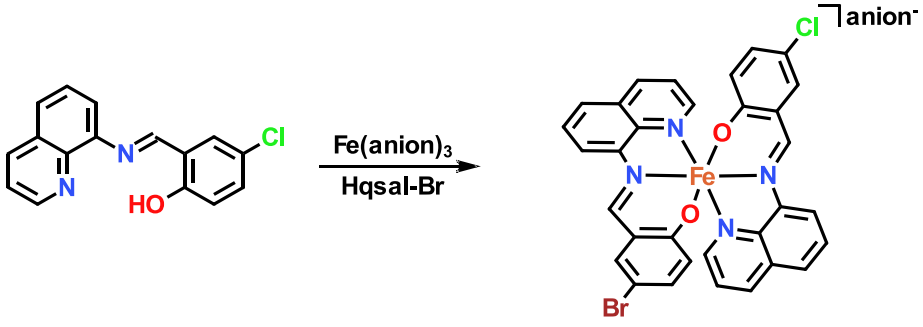

Scheme 4 Synthesis of [Fe(qsal-Cl)(qsal-Br)]$^{+}$.

TGA analysis of the compounds reveals a mass of 3.9% for **1** between 70-100 °C consistent with one MeOH (4.3% expected). Similarly, **3** displays a 13.7% mass loss beginning at 50 °C and complete at 90 °C, indicative of two molecules of CH_2Cl_2 (14.7%). The other complexes showed no mass until much higher temperatures and in the case of **4** suggests that the MeOH is readily lost, something confirmed by elemental analysis.

Table 2 Physical and IR spectroscopic data [Fe(qsal-Cl)(qsal-Br)]A·sol.

Compound	% yield	Colour	IR (cm^{-1})[a]		
			$\nu_{C=N}$	ν_{ArH}	ν_{anion}
[Fe(qsal-Cl)(qsal-Br)]NCS·MeOH **1**	43	Black	1619	3054	2055
[Fe(qsal-Cl)(qsal-Br)]PF_6 **2**	38	Black	1614	3056	843
[Fe(qsal-Cl)(qsal-Br)]BPh_4·$2CH_2Cl_2$ **3**	45	Black	1619	3057	-
[Fe(qsal-Cl)(qsal-Br)]OTf·0.5MeOH **4**	35	Black	1614	3054	1297, 1164, 1084

[a] Complexes were determined in KBr

Structures of [Fe(qsal-Cl)(qsal-Br)]$^+$ complexes

Structures of all the mixed-ligand complexes have been determined, in some cases at multiple temperatures. The compounds all crystallize in triclinic $P\bar{1}$ except **4** which is in monoclinic $P2_1/c$. In all cases the Cl and Br substituents are crystallographically disordered over the two sites. This has been modelled with either fixed or variable occupancy and in both cases yields a 1:1 ratio of the qsal-Cl and qsal-Br ligands. Interestingly, only [Fe(qsal-Cl)(qsal-Br)]PF_6 has two Fe(III) centres in the asymmetric unit with the other compounds having a single Fe(III) site (Figure 1). By comparison, the compositions of the homoleptic compounds are [Fe(qsal-$X)_2$]NCS·MeOH, [Fe(qsal-$X)_2$]PF_6, [Fe(qsal-$X)_2$]OTf·sol (X = Cl, sol = none; X = Br, sol = 0.5 MeOH) and [Fe(qsal-$X)_2$]BPh_4·sol (X = Cl, sol = H_2O; X = Br, sol = CH_2Cl_2).

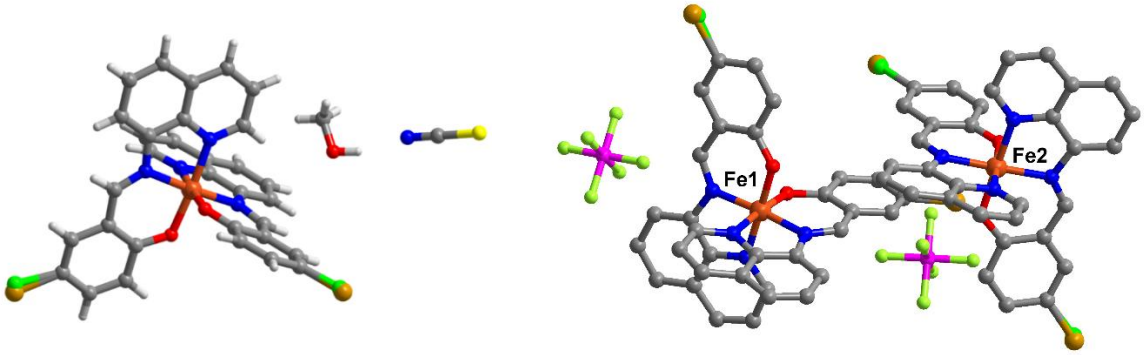

Figure 1 The asymmetric unit of [Fe(qsal-Cl)(qsal-Br)]NCS·MeOH and [Fe(qsal-Cl)(qsal-Br)]PF_6.

The Fe-N/O bond lengths of [Fe(qsal-Cl)(qsal-Br)]A (A = NCS, PF_6, OTf) at 123 K are between 1.945-1.969 Å and 1.850-1.880 Å, respectively indicative of LS Fe(III) (Table 3). The octahedral distortion parameters confirm the spin state assignment. Interestingly, in **2** the Fe-N/O bond lengths of the two Fe(III) centres are very similar but the distortion parameters are subtly different. This may suggest that only one of the Fe centres is able to undergo spin crossover.

Table 3 Fe-N/O bond lengths and octahedral distortion parameters of **1**, **2** and **4** at 123 K (Å, °).

	NCS	**OTf**		**PF_6**	
Fe1-O1	1.879(5)	1.880(3)	1.844(3)	Fe2-O3	1.855(3)
Fe1-O2	1.878(5)	1.879(3)	1.855(3)	Fe2-O4	1.858(3)
$Fe1\text{-}O_{av}$	1.878(5)	1.880(3)	1.850(3)	$Fe2\text{-}O_{av}$	1.856(3)
Fe1-N1	1.965(6)	1.948(2)	1.936(4)	Fe2-N5	1.940(4)
Fe1-N2	1.986(6)	1.962(3)	1.950(4)	Fe2-N6	1.952(4)
Fe1-N3	1.949(6)	1.946(3)	1.940(4)	Fe2-N7	1.933(4)
Fe1-N4	1.975(6)	1.962(3)	1.976(4)	Fe2-N8	1.956(4)
$Fe1\text{-}N_{av}$	1.969(6)	1.954(3)	1.950(4)	$Fe2\text{-}N_{av}$	1.945(4)
Σ	47	50	43	Σ	52
Θ	67	71	63	Θ	69

The most interesting member in this series is $[Fe(qsal\text{-}Cl)(qsal\text{-}Br)]BPh_4{\cdot}2CH_2Cl_2$ where we have been able to determine the structure at three different temperatures. At 100 K the Fe-N/O bond distances are short and characteristic of a LS centre while at 123 K the Fe-N/O bond lengths elongate but are intermediate between HS and LS, termed INT (Table 4). Note that by intermediate we mean a mixture of the HS and LS states and not the intermediate S = 3/2 spin state. Only at 267 K are the Fe-N/O bonds and Σ and Θ indicative of full HS character. This suggests either gradual or stepped spin crossover is present in this compound.

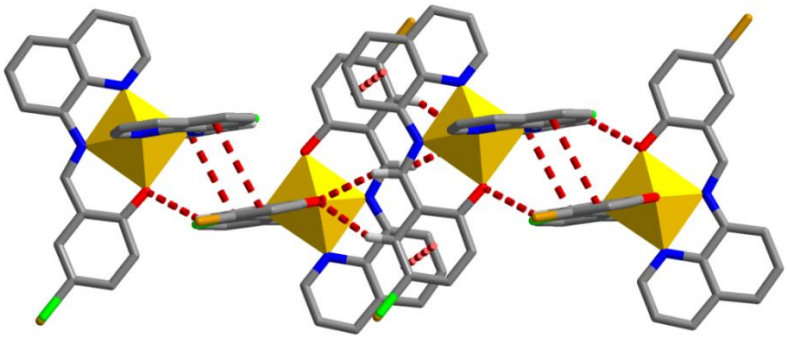

Figure 2 View of the π-π interactions in [Fe(qsal-Cl)(qsal-Br)]NCS·MeOH.

The packing in **1**, **3** and **4** involves a pair of orthogonal π-π interactions which link the cations to form a 1D chain (Figure 2). The plane-to-plane distances vary from 3.13-3.32 Å and are typical of $[Fe(qsal\text{-}X)_2]^+$ complexes (Table 5). In **2** the packing is substantially altered with two types of π-π interaction that form Fe1-Fe1 and Fe2-Fe2 dimers. The type A interaction is 0.13 Å shorter than type B due to the more planar qsal-X ligand in the former dimer. The dimers are linked by further π-π contacts but these have minimal overlap resulting in significantly weaker cooperativity. The 1D chains are connected by a range of other contacts principally C-H···π, C-H···Cl/Br and C-Cl/Br···π forming highly cooperative supramolecular 3D networks (Figure 3). Many of the interactions are present in the homoleptic complexes, $[Fe(qsal\text{-}X)_2]Y$ and reveal that the presence of two different ligands does not significantly impact the supramolecular connectivity.

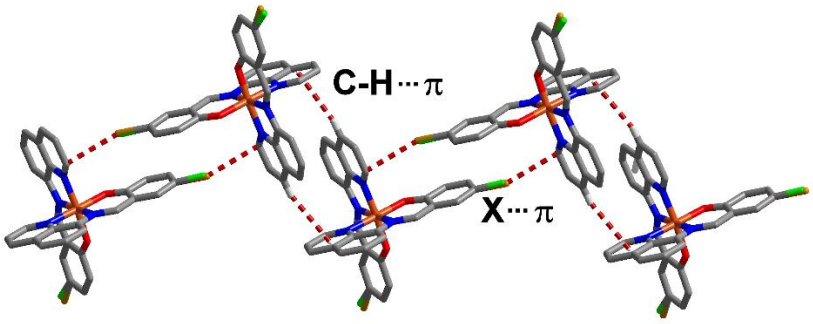

Figure 3 View of the C-H···π and Cl/Br···π interactions that link the 1D chains in **1**.

Table 4 Fe-N/O bond lengths and octahedral distortion parameters of **3** at 100, 123 and 269 K (Å, °).

	100 K	**123 K**	**267 K**
Fe1-O1	1.876(2)	1.888(3)	1.908(3)
Fe1-O2	1.881(2)	1.887(3)	1.904(3)
Fe1-O_{av}	1.879(2)	1.888(3)	1.906(3)
Fe1-N1	1.948(2)	2.045(3)	2.131(4)
Fe1-N2	1.977(2)	2.064(3)	2.150(4)
Fe1-N3	1.951(2)	2.038(3)	2.129(4)
Fe1-N4	1.983(2)	2.077(3)	2.142(4)
Fe1-N_{av}	1.965(2)	2.056(3)	2.138(4)
Σ-Fe1	46	53	75
Θ-Fe1	70	142	209

Magnetic studies of [Fe(qsal-Cl)(qsal-Br)]$^+$ complexes

The magnetic properties of **1**-**4** have been studied between 2-350 K by SQUID magnetometry (Figure 4). To aid comparison, the $\chi_M T$ values of the homoleptic systems are plotted with those of **1**-**4**. In **1** the SCO is gradual reaching a plateau of *ca*. 2.5 $cm^3\ mol^{-1}\ K$ (60% HS) at 280-330 K before beginning increase again. The SCO is more abrupt than [Fe(qsal-Br)$_2$]NCS·MeOH but less than the chloro analogue.[29] The onset of SCO also increases from 150 to *ca*. 200 to *ca*. 270 K in going from the Cl-only to **1** to the Br-only compound. In a similar way **2** exhibits gradual SCO behaviour intermediate between the two homoleptic analogues this time reaching 30% HS at 350 K. In the case of **4** the SCO profile more closely matches that of [Fe(qsal-Cl)$_2$]OTf than [Fe(qsal-Br)$_2$]OTf. In all of these compounds, the structures of the mixed-ligand compounds are virtually identical to the homoleptic [Fe(qsal-X)$_2$]Y systems.

In contrast, [Fe(qsal-Cl)(qsal-Br)]BPh_4·$2CH_2Cl_2$ exhibits a magnetic profile unlike either of the parent complexes perhaps as it contains two CH_2Cl_2 molecules rather than the single CH_2Cl_2 molecule of [Fe(qsal-Br)$_2$]BPh_4 and the H_2O in [Fe(qsal-Cl)$_2$]BPh_4.

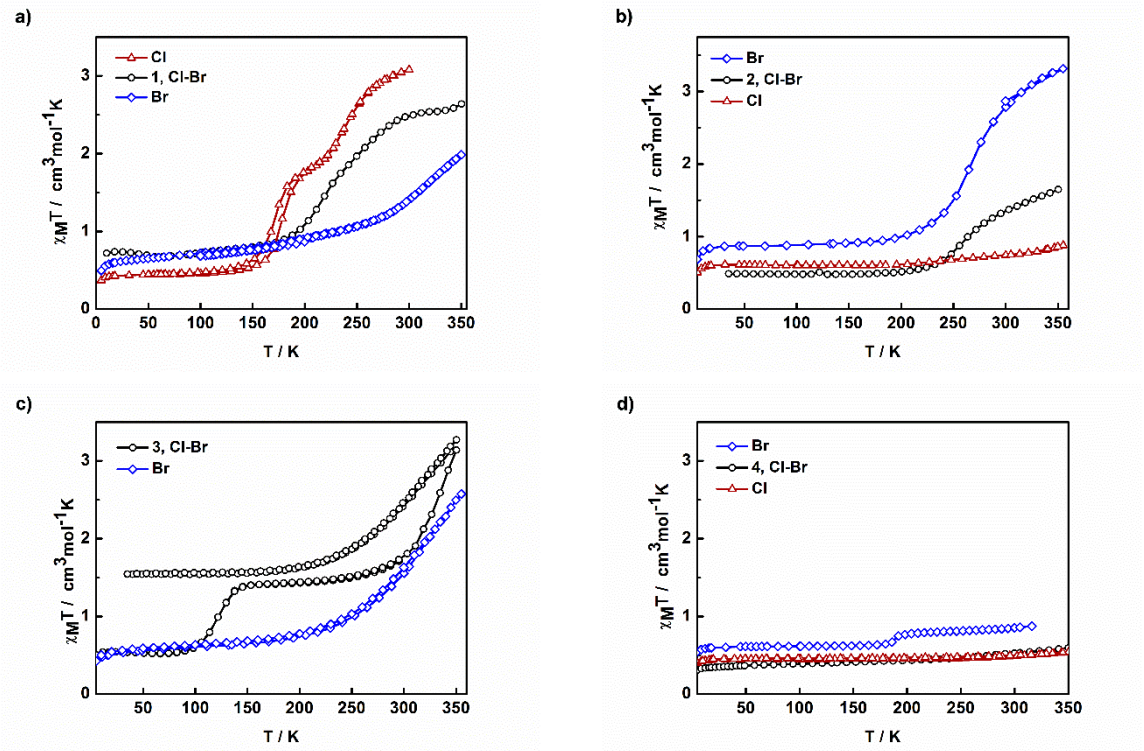

Figure 4 χ_MT versus T plot for [Fe(qsal-Cl)(qsal-Br)]Y where Y are a) NCS, b) PF_6, c) BPh_4, and d) OTf.

In [Fe(qsal-Cl)(qsal-Br)]$BPh_4 \cdot 2CH_2Cl_2$ the sample was quickly cooled to 5 K and then warmed to where 100 K $\chi_M T$ = 0.45 cm^3 mol^{-1} K, consistent with LS Fe(III). Upon further heating $\chi_M T$ increased to 1.40 cm^3 mol^{-1} K, indicative of 30% HS. $\chi_M T$ doesn't increase further until 300 K before an abrupt change is observed with $\chi_M T$ = 3.10 cm^3 mol^{-1} K at 350 K. TGA results indicate that **3** loses both CH_2Cl_2 molecules in the range 320-360 K. Following this loss upon cooling we are unable to return to the full LS state with $\chi_M T$ = 1.50 cm^3 mol^{-1} K down to 30 K. Given the high vacuum of the SQUID measurements it's likely that the SCO here is coupled to partial or complete solvent loss. Comparisons with the structures at 100 and 123 K are consistent with the magnetic studies the one at 267 K is clearly different. The reason for this inconsistency is unclear but discrepancies have also been observed in other solvent sensitive SCO systems of [Fe(qsal-$X)_2$]Y.[12] Overall, the results suggest that provided that the lattice is not greatly impacted by the presence of two different ligands the SCO profile will be intermediate between the parent complexes. However, if a unique lattice is formed the mixed ligand complex can, as hypothesized, yield better SCO characteristics.

Synthesis and characterization of [Fe(qsal-X)(salpm-X)]$^+$ complexes

The synthesis of the mixed ligand complexes, [Fe(qsal-X)(salpm-X)]A (X = Cl, A = NO_3 **5**, ClO_4 **6**, NCS **7**; X = Br, A = NO_3 **8**, ClO_4 **9**, NCS **10**) can be done using the same layered diffusion technique for **1**-**4**. However, this gives rather low yields and mixing of all the components in solution followed by slow evaporation increases the yield while still producing a highly crystalline product (Scheme 5). However, the crystals are small and to date we have no structures in this series. Despite attempts at structural studies at the Australian Synchrotron, we have been unable to obtain any structures for this series.

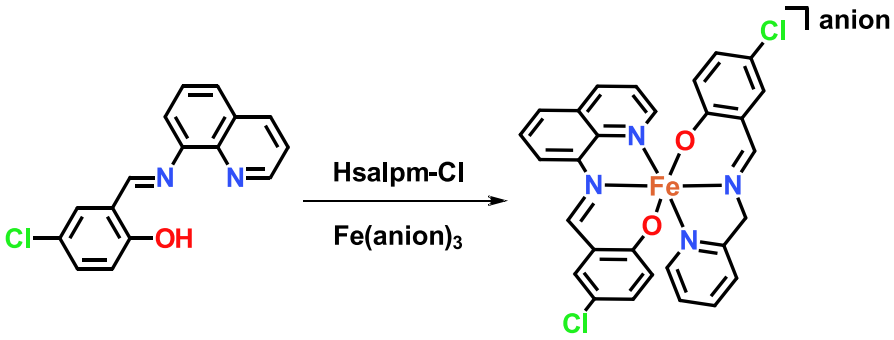

Scheme 5 Synthesis of $[Fe(qsal\text{-}Cl)(salpm\text{-}Cl)]^{+}$.

Table 5 Yield, IR and UV-Vis spectroscopic data for **5**-**10**.

Complex	%yield	IR (cm^{-1})			λ_{max} /nm ($\varepsilon_{max}/M^{-1}cm^{-1}$)
		ν_{C-H}	$\nu_{C=N}$	ν_{anion}	
$[Fe(salpm\text{-}Cl)(qsal\text{-}Cl)]NO_3$ **5**	53	3053(w)	1607(m)	1384(s)	320 (18790), 438 (8420)
$[Fe(salpm\text{-}Cl)(qsal\text{-}Cl)]ClO_4$ **6**	63	3073(w)	1604(s)	1092(s)	325 (18750), 438 (8990)
[Fe(salpm-Cl)(qsal-Cl)]NCS **7**	19	3053(w)	1603(s)	2059(m)	328 (23260), 449 (16930)
$[Fe(salpm\text{-}Br)(qsal\text{-}Br)]NO_3$ **8**	25	3054(w)	1599(s)	1383(s)	324 (17640), 446 (12440)
$[Fe(salpm\text{-}Br)(qsal\text{-}Br)]ClO_4$ **9**	29	3055(w)	1600(s)	1087(s)	324 (24530), 428 (12580)
[Fe(salpm-Br)(qsal-Br)]NCS **10**	32	3053(w)	1600(s)	2051(m)	328)23265(, 450)16875(

The complexes vary in colour more markedly than the parent $[Fe(qsal\text{-}X)_2]^{+}$ complexes suggesting that the colour of the complex may be an indicator of spin state. IR spectroscopy reveals imine stretches at 1599-1607 cm^{-1} that are generally stronger in **8**-**10** than **5**-**7** (Table 5). The anions are also clearly present confirming that no reduction to Fe(II) has occurred.

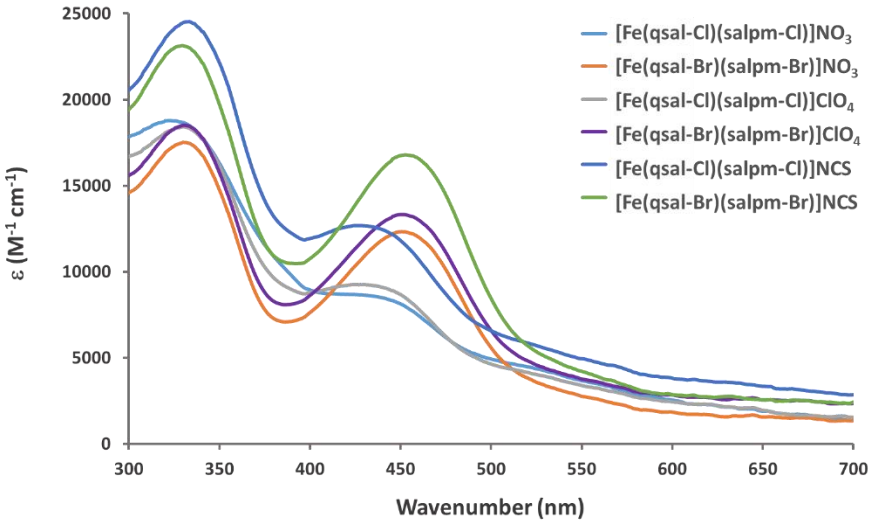

Figure 5 UV-Vis spectra of **5**-**10** in DMF.

UV-Vis spectra of **5**-**10** have been recorded in DMF and are shown in Figure 5. The complexes show broadly similar spectra with the anion clearly influencing the position of the LMCT band which

varies even when the cation is the same, note **8** and **9** where the difference in λ_{max} is almost 20 nm. This suggests that the compounds may undergo spin crossover in solution.

SQUID magnetometric studies of **5**-**8** have been undertaken with the results shown in Figure 6. The thiocyanate complexes have not been explored as the compounds absorb water readily making SQUID analysis problematic. The spin crossover profiles of the $[Fe(qsal\text{-}Cl)(salpm\text{-}Cl)]^+$ series are poor with **5** essentially invariant at ca. 50% HS while **6** shows a modest increase from ca. 33% to 50% HS. A similar gradual profile is observed in **7** this time reaching ca. 66% HS at 350 K. In contrast, **8** goes from almost fully LS to 60% HS with a moderately abrupt transition. The success in other areas of the project lead to us not exploring further anions in this series, although it's likely that abrupt SCO systems can be found provide that the correct anion is present.

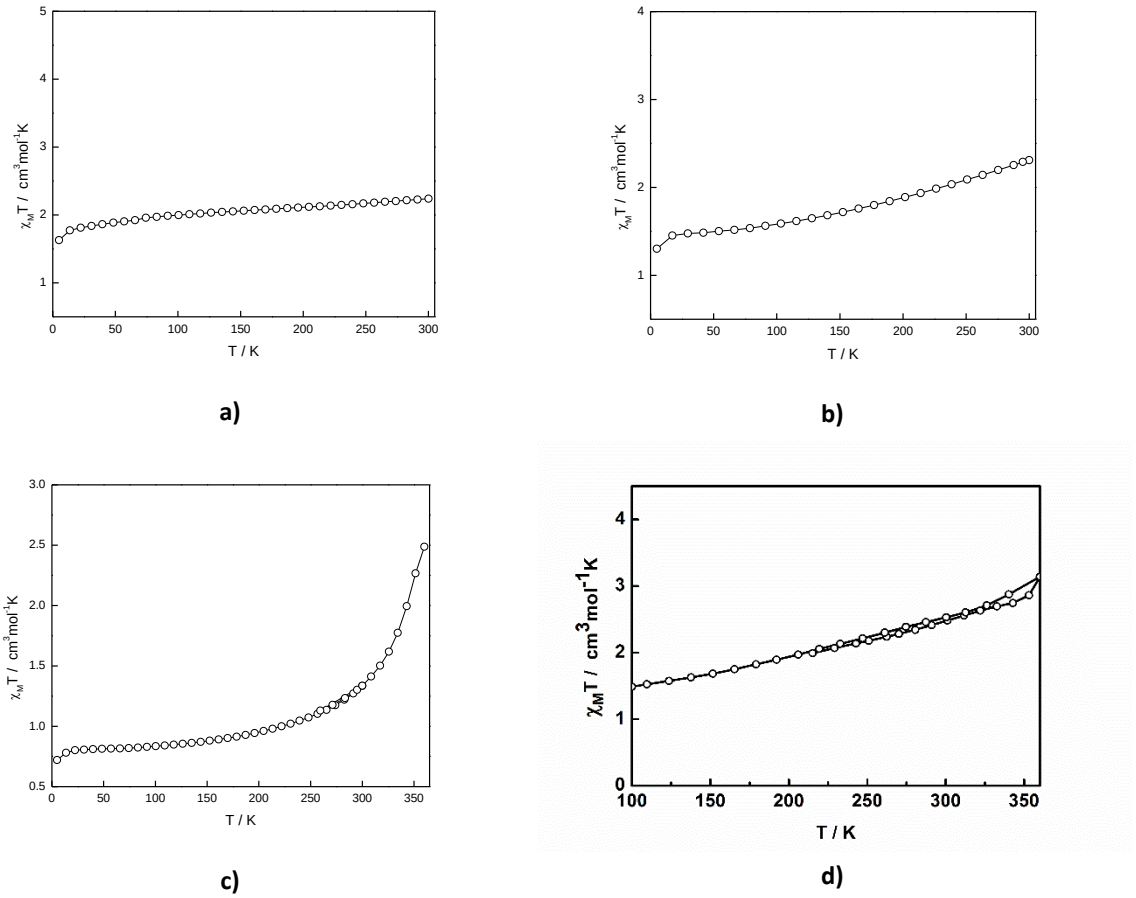

Figure 6 $\chi_M T$ versus T plots for [Fe(qsal-Cl)(salpm-Cl)]A where A are a) NO_3, b) ClO_4 and [Fe(qsal-Br)(salpm-Br)]A where A are c) NO_3 and d) ClO_4.

Synthesis and characterization of $[Fe(qsal\text{-}X)_2]OTs$

Layered diffusion was used to prepare black crystals of $[Fe(qsal\text{-}X)_2]OTs{\cdot}sol$, (X = Cl = **11·$H_2O$** sol = H_2O or none **11**, X = Br **12**, sol = H_2O; X = I **13**, sol = $2H_2O$). This involved the preparation of an EtOH solution of $Fe(OTs)_3$ from $FeCl_3$ and AgOTs. After filtration of the solution it was layered over blank EtOH and a CH_2Cl_2 solution of Hqsal-X (X = Cl, Br, I) in which NEt_3 was added. Black crystals were obtained after 4-5 days. It is should be noted that use of MeOH gave crystals of the Fe(II) complexes, $[Fe(qsal\text{-}X)_2]$ in addition to **11**-**13**.

IR spectroscopic studies of **11**-**13** show stretches at 1599-1601 cm^{-1} indicative of the imine C=N bond (Table 6). These values are *ca*. 14 cm^{-1} lower than the free ligand and consistent with coordination to iron(III). The band for the anion was observed around 1190-1193 cm^{-1}. The stretches found at 3443-3450 cm^{-1} suggest the presence of H_2O, consistent with crystallographic studies.

Table 6 Physical and spectroscopic properties of **11**-**13**.

Compound	**Colour**	**IR (cm^{-1})**[a]			**λ_{max}/nm (ε_{max}/$M^{-1}cm^{-1}$)**[b]
		$\nu_{C=N}$(s)	**ν_{OH}(br)**	**ν_{anion}(vs)**	
[Fe(qsal-Cl)$_2$]OTs **11**	Black	1601	3443	1190	327 (17,565), 431 (9,600)
[Fe(qsal-Br)$_2$]OTs **12**	Black	1599	3450	1192	327 (15,585), 434 (8,350)
[Fe(qsal-I)$_2$]OTs **13**	Black	1598	3448	1193	329 (20,680), 431 (10,040)

[a]As KBr disc [b]In DMF.

Electronic spectra were recorded in DMF giving dark brown solutions. Two intense bands at *ca*. 330 and 430 nm were observed. The band at 330 is assigned as the π-π transition and is slightly lower than the absorption bands (338-360 nm) for the free ligands. The band in the visible region corresponds to a ligand to metal charge transfer (LMCT) from the phenolate p_π to Fe d_{π^*} orbitals. Recent studies on [Fe(qsal-3-OMe)$_2$]$^+$ have suggested that the lower energy transition may be due to the qsal-X ligand. While Hqsal-3-OMe shows a clear band at *ca*. 430 nm, this is not true for the Hqsal-X series and thus we are confident of this assignment for our compounds. In concentrated solutions there is also a band at ~600 nm which may be due to the presence of the LS species in solution.

The spin crossover properties of the complexes in solution were also determined using the Evan's method in DMSO. The χ_MT values were 3.06, 2.59 and 3.03 $cm^3 \cdot mol^{-1} \cdot K$ for **11**, **12** and **13**, respectively. Results indicate that the solutions are in between the LS and HS states being 55-67% HS. Results, however, do not correlate with the size or electronegativity of the halogen, similar to previous findings for [Fe(qsal-X)$_2$]NCS. While [Fe(qsal-Br)$_2$]OTs gives a very similar %HS to [Fe(qsal-Br)$_2$]NCS both **11** and **13** favour the HS state by *ca*. 40% suggesting that the anion does impact SCO behaviour at these concentrations.

Structural studies of [Fe(qsal-X)$_2$]OTs

[Fe(qsal-Cl)$_2$]OTs·H_2O **11·H_2O** crystallizes in the orthorhombic space group *Pcca* at 123 and 300 K, respectively. From the same solution a minor phase of the desolvated complex [Fe(qsal-Cl)$_2$]OTs **11** was observed which at 300 K belongs to the monoclinic space group *Pc*. At 123 and 300 K, the asymmetric unit of **11·H_2O** has one [Fe(qsal-Cl)$_2$]$^+$ cation, a tosylate anion and one molecule of H_2O (Figure 8). Both the anion and the water molecule are disordered at both temperatures. The average Fe-O/N bond lengths for **11·H_2O** are 1.877(6)/1.961(8) Å and 1.877(6)/1.954(7) Å at 123 and 300 K, respectively and clearly LS. However, **11** has Fe-O/N bond distances of 1.915(14)/2.123(17) Å which are characteristic of the HS state (Table 7). The crystal structures of [Fe(qsal-Br)$_2$]OTs·H_2O **12** and [Fe(qsal-I)$_2$]OTs·2H_2O **13** were obtained only at 100 K with both complexes crystallizing in the orthorhombic space group P*ca*2$_1$. Aside from the [Fe(qsal-X)$_2$]$^+$ cation and a tosylate anion, one and two molecules of water were found in the asymmetric units of **12** and **13**, respectively. The average

Fe-O/N bond lengths for **12** are 1.88(2)/1.94(7) Å and 1.88(2) /1.94(7) Å for **13**; indicative of the LS state.

Table 7 Fe-N/O bond lengths of **11**, **11·H₂O**, **12** and **13** at room temperature or 123 K (Å, °).

	1	1·H₂O	2	3
Fe-O1	1.92(1)	1.885(9)	1.86(2)	1.87(1)
Fe-O2	1.91(2)	1.876(9)	1.90(2)	1.90(1)
Fe-N1	2.15(2)	1.98(1)	1.97(2)	1.95(2)
Fe-N2	2.09(2)	1.952(9)	1.90(2)	1.94(2)
Fe-N3	2.12(2)	1.95(1)	1.97(2)	1.95(2)
Fe-N4	2.14(2)	1.96(1)	1.94(2)	1.96(2)
Σ	66.0	50.4	50.4	50.4
Θ	188.8	80.2	77.9	75.0

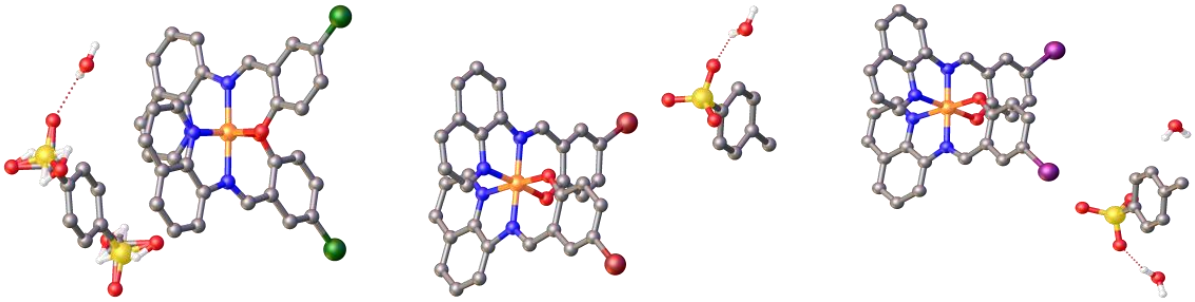

a) **b)** **c)**

Figure 8 View of the asymmetric units of a) **11·H₂O**, b) **12** and c) **13** at low temperature.

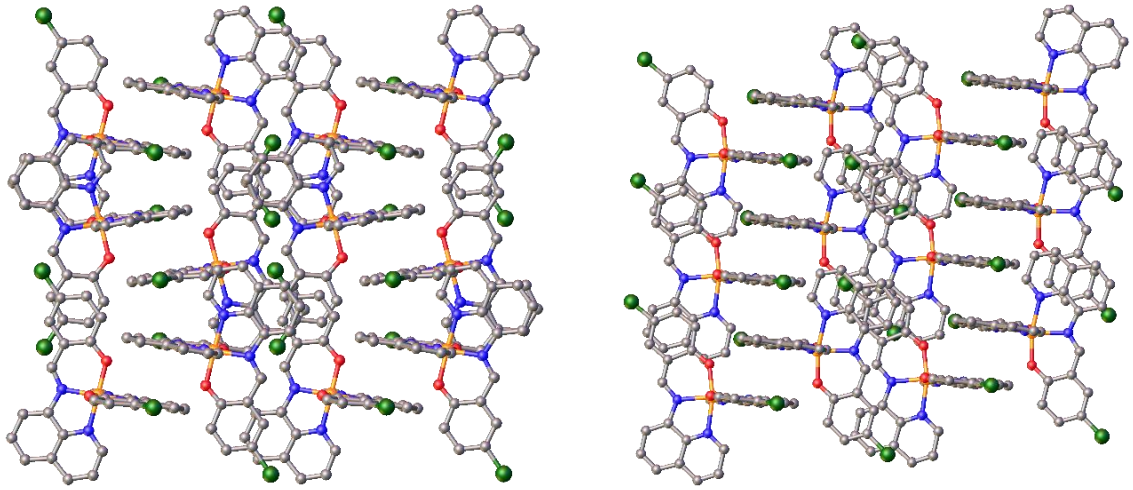

a) **b)**

Figure 9 View of the angled 1D chains in a) [Fe(qsal-Cl)₂]OTs·H₂O and the parallel chains in b) [Fe(qsal-Cl)₂]OTs.

The structures are very similar with the $[Fe(qsal\text{-}X)_2]^+$ cations linked by strong π-π interactions forming 1D chains; the same motif observed in other $[Fe(qsal\text{-}X)_2]^+$ systems. Two types of π-π

interactions are found and the π-π distances range from 3.56-3.99 Å measured from each centroid (3.68 Å for both types in **11·H₂O** at 100 and 300 K, 3.66 Å and 3.56 Å for **1** at 300 K, 3.70 Å and 3.64 Å for **12** and 3.80 and 3.71 Å for **13** at 100 K). The $[Fe(qsal\text{-}X)_2]^+$ units are linked to each other through C-H···O, C-H···X and C-H···π interactions. The C-H···X interactions in particular force the neighbouring chains to be angled relative to each other, 17.0°, 16.3° and 17.4° for **11·H₂O, 12** and **13**, respectively. It follows that are two chains in these systems, alternating throughout the structure (Figure 9a). In contrast, $[Fe(qsal\text{-}Cl)_2]OTs$ has a single chain with each chain parallel to the other (Figure 9b). A further difference in the packing of **11·H₂O** and **11** is the lack of disorder in the tosylate anion for **11** and significant void space in the structure.

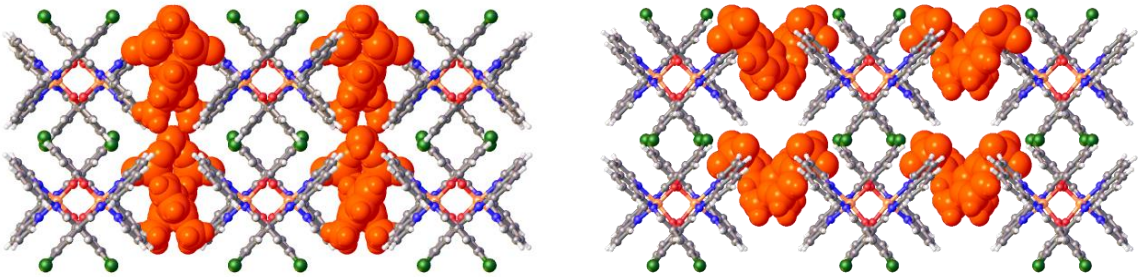

a) **b)**

Figure 10 Molecular packing in a) **11·H₂O** and b) **11** showing the void space in the non-solvated complex. Tosylate anions are highlighted in orange.

Another remarkable feature of these complexes is a strong halogen bond between the oxygen atom of the tosylate anion and the halogen substituent of the $[Fe(qsal\text{-}X)_2]^+$ cation. The strength of these bonds also influences the magnetic properties of the complexes as SQUID magnetometry reveals that all complexes undergo spin crossover with the degree of spin crossover dependent on the substituent. In the case of **11**, **12** and **13**, the distances are 2.86(2) Å (O···Cl), 2.83(2) Å (O···Br) and 2.852(17) Å (O···I), respectively (Figure 11). These are shorter than the van der Waals radii by 0.405 Å for **11**, 0.536 Å for **12** and 0.648 Å for **13**. This is consistent with the larger σ-hole of iodine compared to the lighter halogens. Similar halogen bonding is also observed in $[Fe(qsal\text{-}I)_2[Ni(dmit)_2]\cdot CH_3CN\cdot H_2O$ where the loss of a I···S halogen bond (3.690 Å) is coupled to abrupt SCO.

The final feature of the structure is a hydrogen bonding chain that forms between the tosylate anion and the water molecule. In the case of **13** the extra water molecule is hydrogen bonded to another of the O atoms of the tosylate anion.

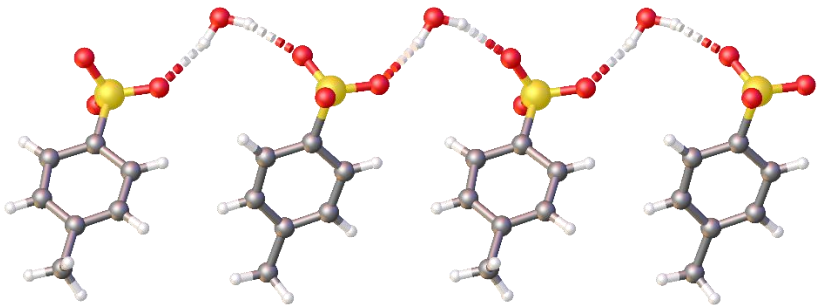

Figure 11 View of the hydrogen bonding chain in $[Fe(qsal\text{-}Br)_2]OTs\cdot H_2O$.

We have also prepared [Fe(qsal-F)$_2$]OTs·0.5EtOH **14** which crystallizes with 2 independent Fe(III) centres, a characteristic of the qsal-F ligand (Figure 12). We have recorded the structure at five different temperatures based on the magnetic data below. The Fe-N/O bond lengths are detailed in Table 8 and suggest that Fe1 is LS throughout this temperature range, while Fe2 undergoes a gradual but complete SCO between 93 and 150 K. A feature of the local coordination environment is that at both metal centres one of the qsal-F ligands is significantly non-planar with this more pronounced at Fe1 than Fe2.

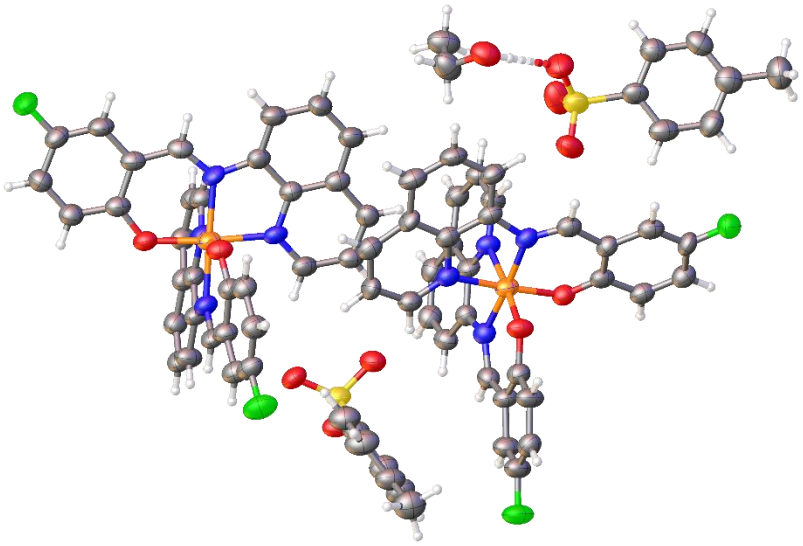

Figure 12 View of the asymmetric unit in [Fe(qsal-F)$_2$]OTs·0.5EtOH **14** at 93 K.

Table 8 Selected bond lengths and octahedral distortion parameters of [Fe(qsal-F)$_2$]OTs·0.5EtOH.

	93 K	**113 K**	**150 K**	**205K**	**293 K**
Fe1-O$_{ave}$	1.871(3)	1.863(3)	1.868(4)	1.861(4)	1.868(4)
Fe1-N$_{ave}$	1.962(4)	1.953(4)	1.964(5)	1.963(5)	1.982(4)
Σ	41.5	41.5	42.7	42.2	43.1
Fe2-O$_{ave}$	1.881(4)	1.877(4)	1.902(4)	1.895(4)	1.898(4)
Fe2-N$_{ave}$	1.972(4)	2.052(5)	2.130(5)	2.127(5)	2.136(4)
Σ	50.5	55.0	74.8	76.3	77.0

In terms of the packing, as with many [Fe(qsal-X)$_2$]$^+$ complexes, 1D chains involving principally π-π interactions are formed (Figure 13). The 1D chains for the Fe2 centre are more similar to those generally found while the Fe1 centre is better described as a series of supramolecular dimers linked through the OTs anions and EtOH molecules, via C-H···O interactions. Interestingly, the organization of the chains is similar to the other [Fe(qsal-X)$_2$]OTs complexes only this time there is more space between neighbouring chains as the anion and solvent molecules are to be found between these chains in **14** (Figure 13). This is clearly a consequence of the 2 independent Fe(III) centres in **14** compared with the other members of the series.

The chains are connected to each other through extensive C-H···O interactions again involving the anion and EtOH molecule (Figure 14). These serve to create a highly cooperative network, despite

the modified packing compared to the other [Fe(qsal-X)$_2$]OTs complexes and once again highlights that the qsal-F system often displays unique packing.

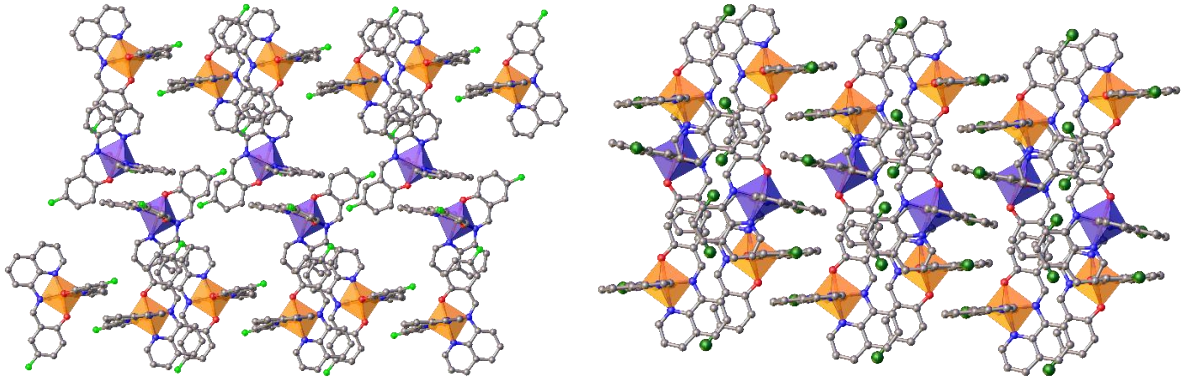

Figure 18 View of the 1D chains formed in [Fe(qsal-F)$_2$]OTs·0.5EtOH (left) and [Fe(qsal-Cl)$_2$]OTs·H$_2$O (right) showing the relative position of the chains.

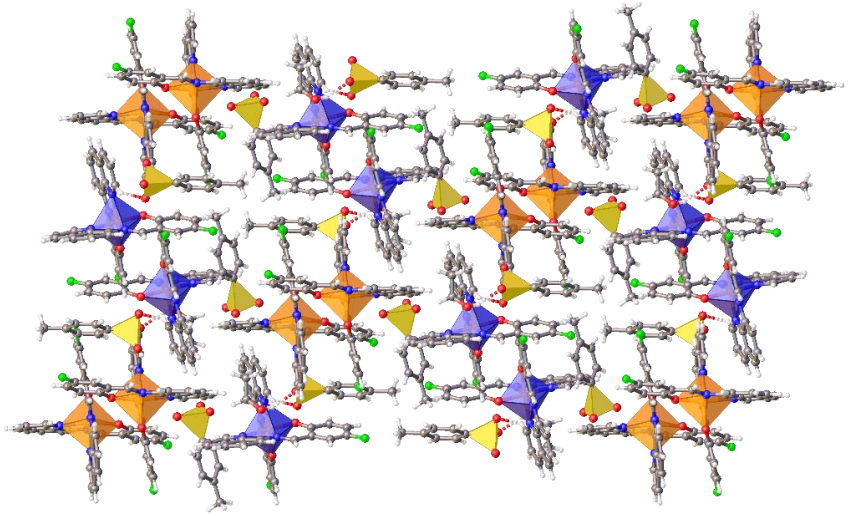

Figure 14 View of the overall packing in **14** viewed down the *a*-axis.

Magnetic studies of [Fe(qsal-X)$_2$]OTs

SQUID magnetometry of **11-14** were undertaken and are presented as χ_MT versus T plots (Figure 15). Attempts to obtain magnetic results for **11·H$_2$O** but were unsuccessful. The magnetic susceptibility data for **11** was collected by warming the sample from 50 to 350 K and cooling from 355 to 150 K. Initial measurements at 50 K show that χ_MT is equal to 2.0 cm^3 K mol^{-1} which upon heating, gradually increased to 2.5 cm^3 K mol^{-1} up to 200 K before increasing more rapidly to reach a value of 4.0 cm^3 K mol^{-1} at 350 K. Although a little lower than the value predicted by the spin only formula, this is still consistent with the full HS state in [Fe(qsal-X)$_2$]$^+$ compounds. Upon cooling the magnetic trace follows the warming mode and suggests that there is no hysteresis in this compound. Magnetic studies of **12** revealed that χ_MT = 0.44 cm^3 K mol^{-1} at 100 K with an abrupt SCO was observed at $T_{½}(\uparrow)$ = 260 K and reaching 3.05 cm^3 K mol^{-1} indicating 67% conversion to HS state. In the cooling mode, a rapid decrease was detected at 250-255 K. As with 12 the small differences in the heating and cooling modes suggests little hysteresis in this compound. In contrast, abrupt SCO with hysteresis was observed in **13**. In the first cycle, χ_MT gradually increased from 0.43 to 0.98 cm^3 K mol^{-1} when the complex was

warmed from 100 to 297 K. There was an abrupt SCO at 330 K with $\chi_M T$ = 3.28 cm^3 K mol^{-1}. Cooling from 350 to 250 K resulted in a hysteresis width of *ca*. 32 K. However, the hysteresis is only apparent with the heating and cooling cycles becoming increasingly close upon repeated cycling (Figure 15c). However, the SCO does become more abrupt and is now centred at *ca*. 290 K. Comparing the transition temperatures of the complexes also revealed that the critical temperature increases as we go down the group. A similar trend was found on the magnetic properties of the complexes of [Fe(qsal-$X)_2$]NCS·sol, (X = Cl, Br sol = MeOH) except for the [Fe(qsal-$I)_2$]NCS which exhibited the low spin state from 100-360 K.

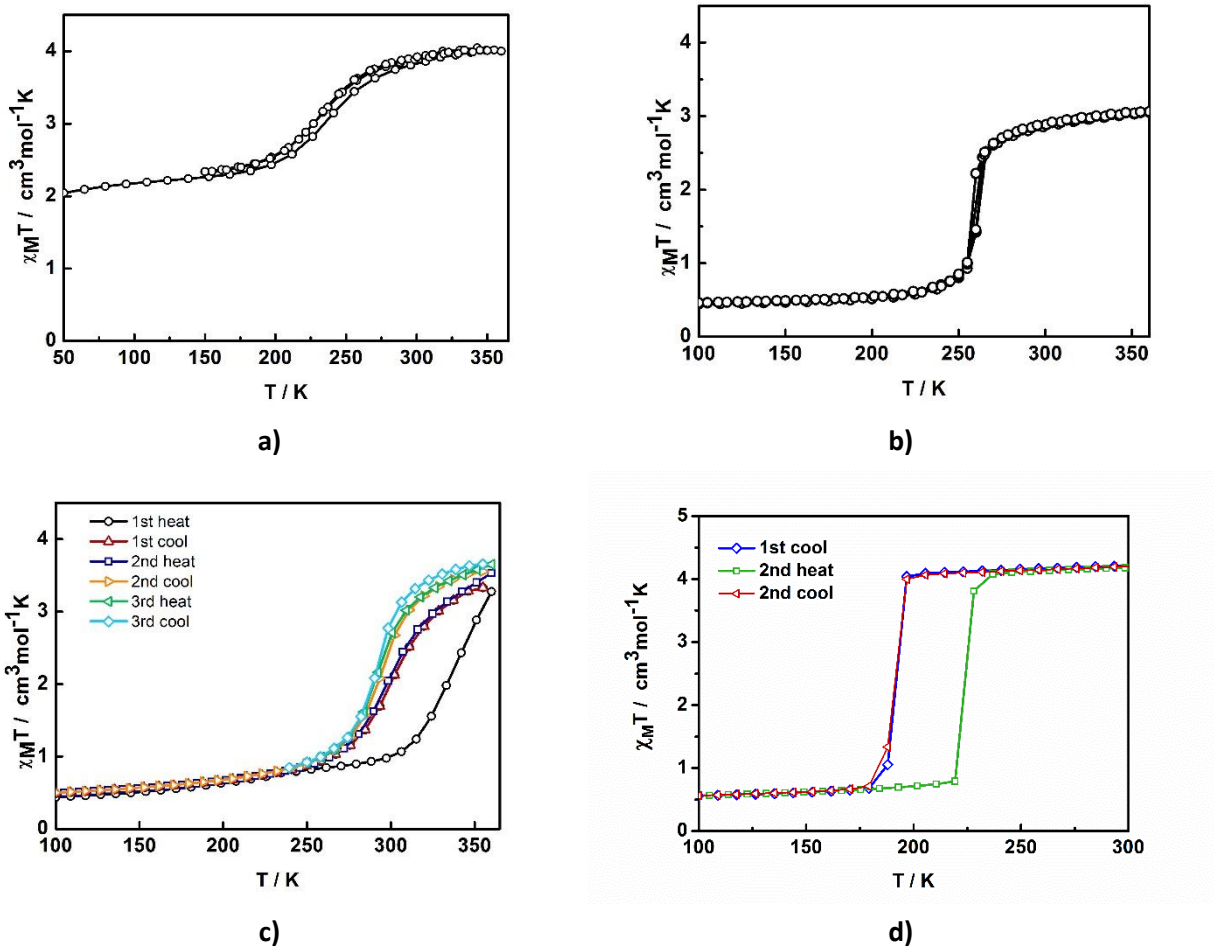

Figure 15 $\chi_M T$ vs. T plot of [Fe(qsal-$X)_2$]OTs with a) **11**, b) **12**, c) **13** and d) **14**.

The final system is **14** for which $\chi_M T$ = 4.10 cm^3 mol^{-1} K at room temperature and consistent with the full HS state (Figure 15d). Cooling results in little change until 185 K when $\chi_M T$ decreases rapidly to 0.60 $cm^3mol^{-1}K$ and is indicative of LS Fe(III). Warming results in another abrupt change at around 220 K returning back to the HS state. As $T_{1/2}(\downarrow)$ = 180 K and $T_{1/2}(\uparrow)$ = 230 K the hysteresis is 50 K centred around 200 K. The hysteresis is also unaffected by scan rate and represents one of the squarest, widest and most stable hystereses in Fe(III) SCO chemistry. The profile contrasts with the SC-XRD study above and indicates that the EtOH is lost in the magnetometer presumably resulting in a different structure. To date we have been unable to obtain crystals of the non-solvated compound.

Synthesis and structural studies of $[Fe(qsal\text{-}X)_2]NTf_2$

One of the original goals of this project was to create nanodevices. With this in mind we have replaced the simple anions used in our $[Fe(qsal\text{-}X)_2]^+$ series with triflimide ($CF_3SO_2\text{-}N\text{-}SO_2CF_3$) which is known to induce liquid crystal behaviour in coordination complexes. The synthesis involves reaction of the isolated $[Fe(qsal\text{-}X)_2]NO_3$ complexes dissolved in MeOH with $LiNTf_2$ to give $[Fe(qsal\text{-}X)_2]NTf_2$ (X = Cl **15**, Br **16**, I **17**) as a precipitate (Scheme 6). Recrystallization from $MeCN\text{-}CH_2Cl_2$ produces extremely fine black needles.

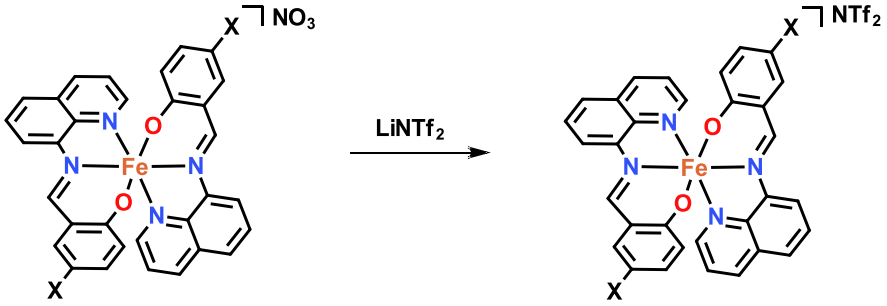

Scheme 6 Synthesis of $[Fe(qsal\text{-}X)_2]NTf_2$.

The crystal structure of $[Fe(qsal\text{-}I)_2]NTf_2$ **17** has been determined through a collaboration with Rigaku/Oxford Diffraction in the UK. They have managed to obtain the structure at three temperatures, 275, 255 and 245 K. At all temperatures, **17** is in triclinic $P\bar{1}$ with the unit cell parameters showing significant changes between 245 and 255 K (Table 9). Specifically, the *a* axis becomes ca. 0.39 Å longer while the *b* and *c* axes both shorten by 0.34 and 0.76 Å, respectively. The unit cell volume also shrinks by 74.8 Å or 4.1% (between 255 and 245 K) making amongst the largest changes yet reported for Fe(III).

Table 9 Unit cell parameters for $[Fe(qsal\text{-}I)_2]NTf_2$ **17** at 245, 255 and 275 K.

	245 K	**255 K**	**275 K**
a (Å)	12.701(1)	12.3138(3)	12.3597(3)
b (Å)	12.434(1)	12.7727(4)	12.7897(3)
c (Å)	12.942(1)	13.6913(4)	13.7188(3)
α (°)	68.75(1)	68.975(3)	68.956(2)
β (°)	78.012(9)	79.325(2)	79.436(2)
γ (°)	68.61(1)	66.548(3)	66.531(3)
Volume ($Å^3$)	1766.9(4)	1841.7(1)	1854.50(9)

A comparison of the bond lengths at the different temperatures reveal that $\Delta Fe\text{-}O_{ave}$ = 0.024 Å and $\Delta Fe\text{-}N_{ave}$ = 0.128 Å which is slightly less than would be expected for complete spin crossover and suggests that a small amount of HS Fe(III) remains at 245 K (Table 10). The cracking of the crystal below 245 K has prevented us from exploring the structure at lower temperatures. Looking at an overlay of the structures at 245 and 255 K it is clear that there is substantial reorganization of the anion coupled with the change in spin state (Figure 16). In the HS state the anion has a *syn* conformation while at 245 K the anion has an intermediate conformation. This conformation is incredibly rare with only 2

other reported examples in the CCDC. Given this large movement in the anion it is perhaps no surprise that the crystal cracks upon spin crossover.

Table 10 Bond lengths (Å) and octahedral distortion parameters (°) for **6** at 245-275 K.

Bond lengths	**245 K**	**255 K**	**275 K**
Fe-O1	1.896	1.909	1.927
Fe-O2	1.888	1.926	1.913
Fe-N2	1.966	2.100	2.110
Fe-N4	1.969	2.097	2.108
Fe-N1	2.003	2.140	2.127
Fe-N3	2.006	2.118	2.148
Σ	50.5	71.7	69.1

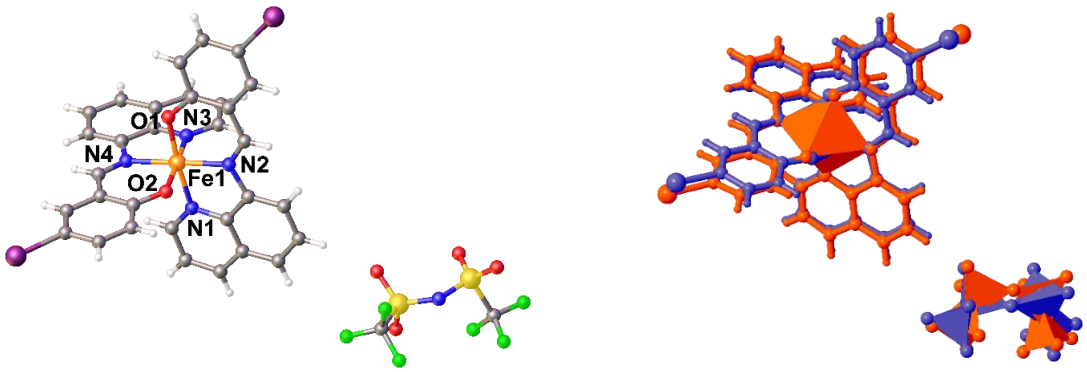

Figure 16 View of the asymmetric unit in **17** (left) and an overlay at 245 (blue) and 255 K (red).

The packing in **17** is almost identical to other $[Fe(qsal\text{-}X)_2]^+$ complexes with π-π interactions between the qsal-I ligands forming a 1D chain. However, unlike previous complexes the P4AE interaction is replaced by a pair of C-H···π interactions to form tightly packed 2D sheets (Figure 17).

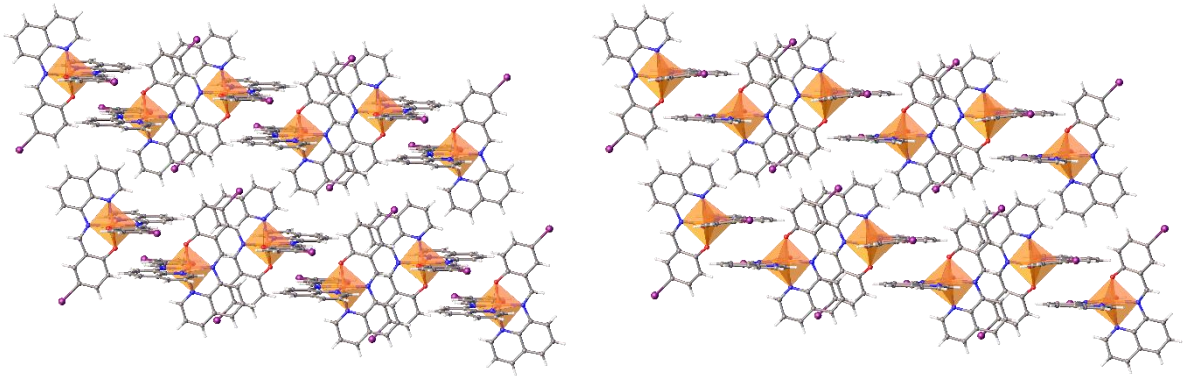

Figure 17 View of the 2D sheets in **17** in the LS (left) and HS (right) states.

A particular feature of this structure is that the 2D sheets are connected not by interactions between the cations but by C-H···O/F and O···π interactions (see the circle in Figure 18). Upon spin crossover, the re-orientation of the SO_2CF_3 group results in the formation of new F···F interactions in the HS state.

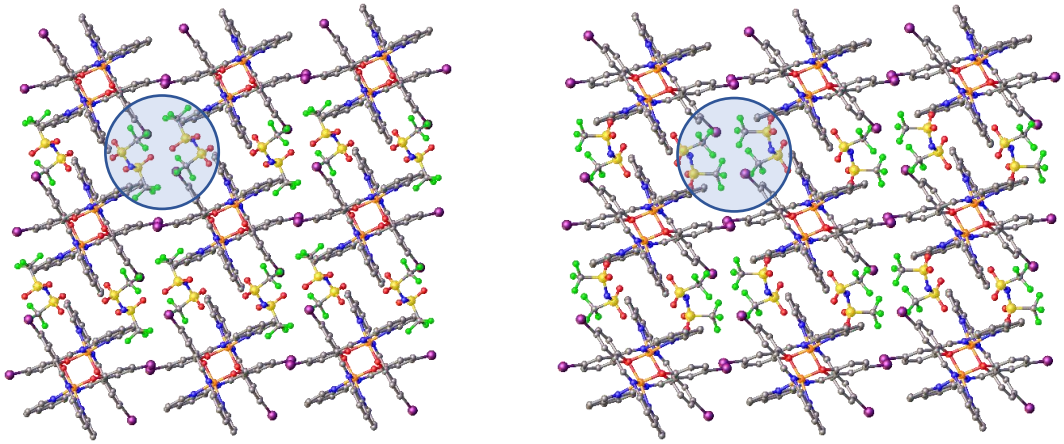

Figure 18 View of the overall packing in **17** in the LS (left) and HS (right) states.

The structures of **15** and **16** have also been determined at 100 and 295 K. These compounds crystallize in orthorhombic *Pbca* also without any solvent in the lattice. The Fe-N/O bond lengths at both temperatures are short and consistent with LS Fe(III), see Table 11. An important difference between the structures of **15** and **16**, and **17** is that at both temperatures the anion has a *syn* conformation unlike the intermediate conformation observed in the LS state of **17**.

Table 11 Bond lengths (Å) and octahedral distortion parameters (°) for **15** and **16** at 100 and 295 K.

Bond lengths	**15-100 K**	**15-295 K**	**16-100 K**	**16-295 K**
Fe-O1	1.885(2)	1.889(2)	1.885(3)	1.884(3)
Fe-O2	1.888(2)	1.888(2)	1.884(3)	1.879(3)
Fe-N1	1.945(3)	1.943(3)	1.943(4)	1.949(4)
Fe-N2	1.973(3)	1.974(3)	1.967(4)	1.970(4)
Fe-N3	1.940(3)	1.949(3)	1.949(4)	1.955(4)
Fe-N4	1.969(2)	1.968(3)	1.970(4)	1.973(4)
Σ	52.4	50.8	47.8	54.1

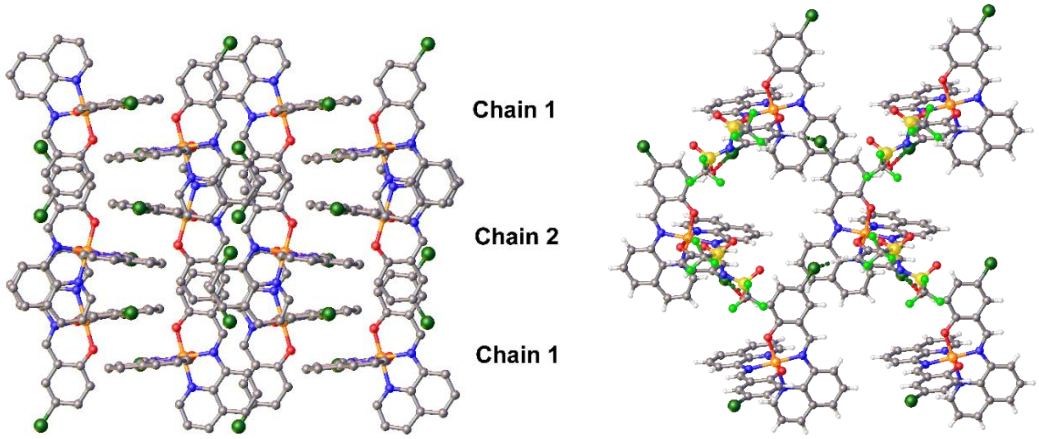

Figure 19 View of a) the angled chains and b) the C-H···X and O···X halogen bonds in [Fe(qsal-Cl)$_2$]NTf$_2$ **15** at 100 K.

Analysing the packing it is evident that while 1D chains are again formed by π-π interactions just like [Fe(qsal-Cl)$_2$]OTs·H$_2$O each chain is angled relative to the other (Figure 19a). This seems to be due in part to the formation of C-H···X (X = Cl, Br) interactions and the presence of O···X halogen bonds involving the triflimide anion (Figure 19b).

Magnetic studies of [Fe(qsal-X)$_2$]NTf$_2$

Magnetic susceptibility measurements of **17** have been performed between 170-350 K at heating and cooling rates of 5 and 10 K min^{-1} (Figure 20). At 170 K χ_MT is 0.52 cm^3 mol^{-1} K and typical of LS Fe^{III}. χ_MT gradually increases upon warming until 270 K when it increases very abruptly reaching 4.19 cm^3 mol^{-1} K at 300 K with $T_{1/2}$ = 278 K and characteristic of HS Fe^{III}. Cooling results in another abrupt transition this time at $T_{1/2}$ = 248 K giving a hysteresis of 30 K. The hysteresis loop is repeatable over successive cycles and shows no scan rate dependence. Photomagnetic measurements reveal that **6** does not undergo LIESST and given the near 100% LIESST in [Fe^{II}(qsal-I)$_2$]·CH$_2$Cl$_2$ this is likely due to the rapid relaxation of the HS state in Fe^{III}. Nevertheless, **6** is one of very few compounds that exhibit abrupt SCO with significant hysteresis close to room temperature.

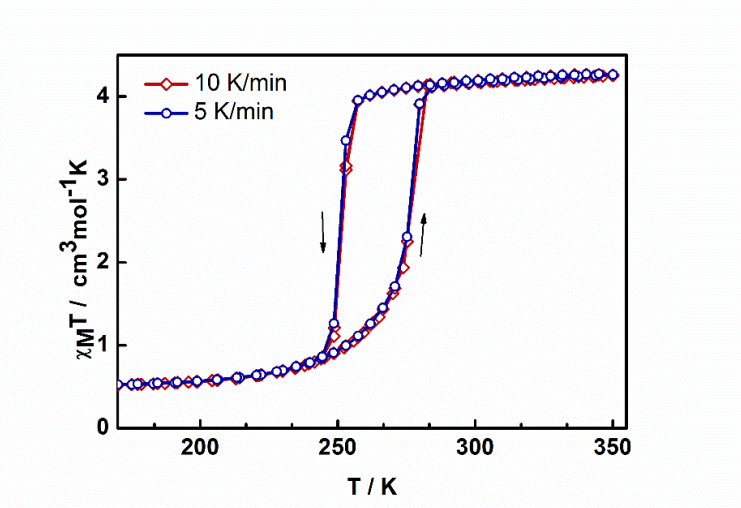

Figure 20 $\chi_M T$ vs. T plot of [Fe(qsal-I)$_2$]NTf$_2$ **17**.

DSC measurements show a peak at 278 K in the warming mode and a peak at 244 K in the cooling mode giving a hysteresis of 34 K and slightly larger than that observed in the magnetic susceptibility studies, something not uncommon in SCO systems. The average enthalpy and entropy values are 5.00 kJ mol^{-1} and 19.5 J mol^{-1} K^{-1}, respectively. The latter is significantly higher than that expected based on electronic considerations only {^{2}T$_2$ to ^{6}A$_1$ transition, Rln(6/2) = 9.13 J mol^{-1} K^{-1}} and suggests strong vibrational contributions to SCO.

To better understand the vibrational contributions to SCO we undertook variable temperature IR and Raman spectroscopic studies between 293 and 228 K (Figure 21). The IR and Raman spectra both show significant changes between 1570-1600 cm^{-1} with the imine stretch moving from 1601 to 1606 cm^{-1} (1594 to 1600 cm^{-1} for the Raman) in going from the HS to the LS state. The most striking difference though is in the S=O stretches in the IR spectra which appear at 1367 and 1381 cm^{-1} in the HS state but are absent in the LS state presumably moving to lower wavenumbers as the anion

undergoes conformational change. The Raman spectra in the cooling and heating modes show considerable differences with the spectra broader between 248-273 K suggesting a mixture of HS and LS states. This is consistent with the slightly more gradual nature of the SCO in this region, upon heating, observed in the magnetic studies of **17** (Figure 20).

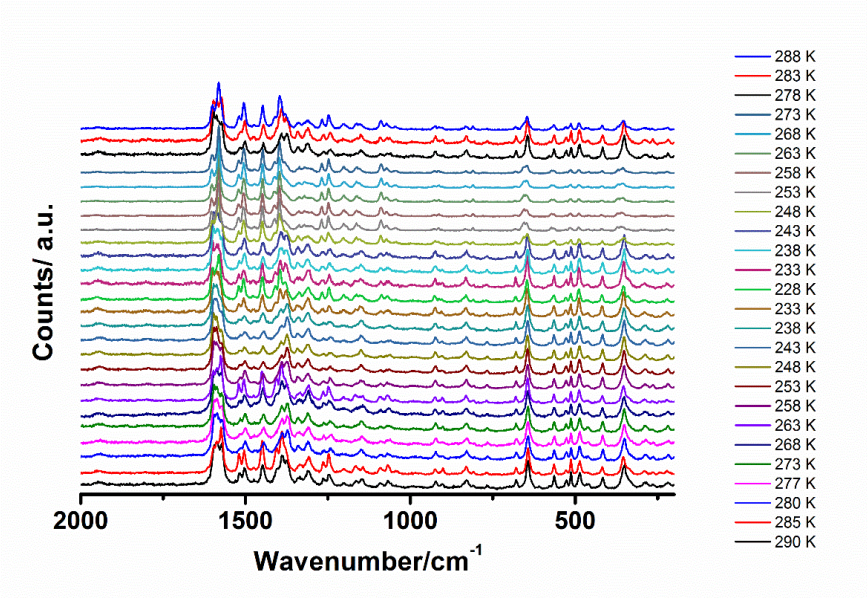

Figure 21 Variable temperature Raman spectra from 290 K → 228 K → 288 K in the cooling and heating modes for **17**.

The magnetic studies of **15** and **16** are less interesting displaying LS only behaviour up to 350 K. It would seem that the change in packing traps the compounds in the LS state. It is noteworthy that the packing in these triflimide complexes mirrors the tosylates above and may suggest that parallel π-π interactions are essential to abrupt SCO.

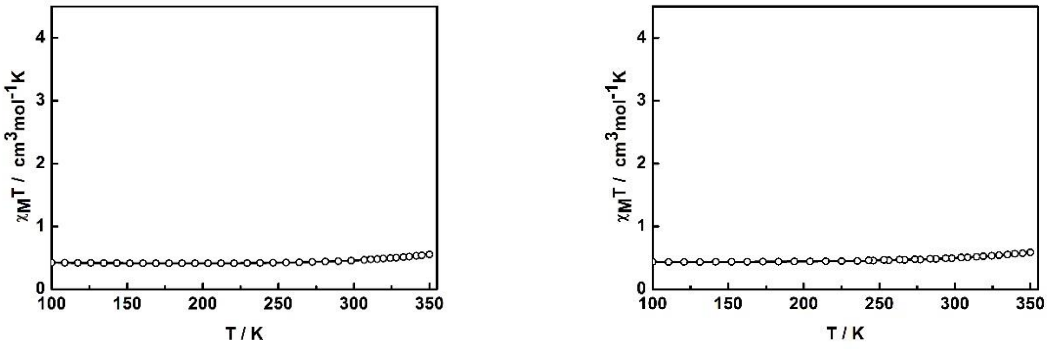

Figure 22 $\chi_M T$ vs. T plots of [Fe(qsal-Cl)$_2$]NTf$_2$ **15** (left) and [Fe(qsal-Br)$_2$]NTf$_2$ **16** (right).

Synthesis and structures of [Fe(qsal-X)$_2$]$_2$[npds] complexes

The success of the [Fe(qsal-X)$_2$]$^+$ complexes led us to prepare [Fe(qsal-X)$_2$]$_2$[1,5-npds] (X = Cl **18**, Br **19**, I **20**) and [Fe(qsal-X)$_2$]$_2$[2,6-npds] (X = Cl **21**, Br **22**, I **23**). The compounds are isolated as black microcrystalline solids in high yields. IR spectroscopic data shows imine stretches at ca. 1600 cm^{-1} while stretches are also observed for the naphthalenedisulfonate SO_3 groups as two bands at 1190 and 1375 cm^{-1}.

Table 12 Physical and spectroscopic properties of **18**-**23**.

Compound	IR (cm^{-1})[a]			λ_{max}/nm ($\varepsilon_{max}/M^{-1}cm^{-1}$)[b]
	$\nu_{C=N}$(s)	ν_{OH}(br)	ν_{anion}(vs)	
$[Fe(qsal\text{-}Cl)_2]_2$[1,5-npds] **18**	1603	3445	1194, 1373	329 (16,600), 432 (9,300)
$[Fe(qsal\text{-}Br)_2]_2$[1,5-npds] **19**	1600	3422	1191, 1367	329 (18,500), 432 (10,400)
$[Fe(qsal\text{-}I)_2]_2$[1,5-npds] **20**	1599	3423	1193, 1369	328 (30,000), 432 (16,200)
$[Fe(qsal\text{-}Cl)_2]_2$[2,6-npds] **21**	1604	3445	1193, 1380	329 (16,600), 432 (9,300)
$[Fe(qsal\text{-}Br)_2]_2$[2,6-npds] **22**	1602	3444	1192, 1378	329 (18,500), 432 (10,400)
$[Fe(qsal\text{-}I)_2]_2$[2,6-npds] **23**	1600	3447	1194, 1376	328 (30,000), 432 (16,200)

[a] As KBr disc [b] In DMSO.

We have fortunately been able to get structures of all the complexes despite the small size of the crystals. The compounds all crystallize in either monoclinic $P2_1/c$ or $P2_1/n$ with a single $[Fe(qsal\text{-}X)_2]^+$ cation, half a naphthalenedisulfonate anion and solvents of crystallization (Figure 23). The Fe-N/O bond lengths are all characteristic of the LS state and show no significant change when heated to room temperature (Table 13).

Table 13 Selected bond lengths for **18-23**.

	18	**19**	**20**	**21**	**22**	**23**
Fe-O1	1.877(3)	1.879(5)	1.876(9)	1.874(3)	1.870(3)	1.875(4)
Fe-O2	1.865(3)	1.886(5)	1.89(1)	1.859(3)	1.851(3)	1.870(4)
$Fe\text{-}O_{ave}$	**1.871(3)**	**1.883(5)**	**1.883(9)**	**1.866(3)**	**1.860(3)**	**1.872(4)**
Fe-N1	1.942(3)	1.967(6)	1.97(1)	1.979(4)	1.986(3)	1.953(4)
Fe-N2	1.978(3)	1.946(6)	1.94(1)	1.940(3)	1.943(3)	1.974(4)
Fe-N3	1.939(3)	1.969(6)	1.98(1)	1.963(5)	1.979(4)	1.969(4)
Fe-N4	1.979(3)	1.956(5)	1.93(1)	1.937(3)	1.948(3)	1.950(4)
$Fe\text{-}N_{ave}$	**1.959(3)**	**1.960(6)**	**1.95(1)**	**1.955(5)**	**1.964(3)**	**1.961(4)**

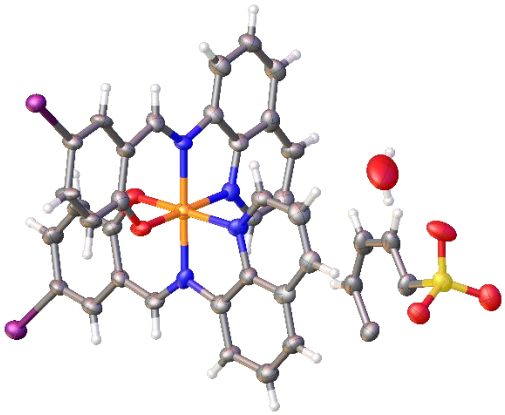

Figure 23 View of the asymmetric unit in $[Fe(qsal\text{-}I)_2]_2$[1,5-npds]·$2H_2O$.

The packing in the structures is remarkably similar in many case to the monoanionic systems, *i.e.* a 1D π-π chain of the $[Fe(qsal\text{-}X)_2]^+$ cations (Figure 24). These 1D chains are then connected via C-H···X (X = Br and I) interactions to give 2D sheets. The anions sit in between these sheets connected principally by C-H···O interactions. This packing pattern exists in **19**, **20** and **23**.

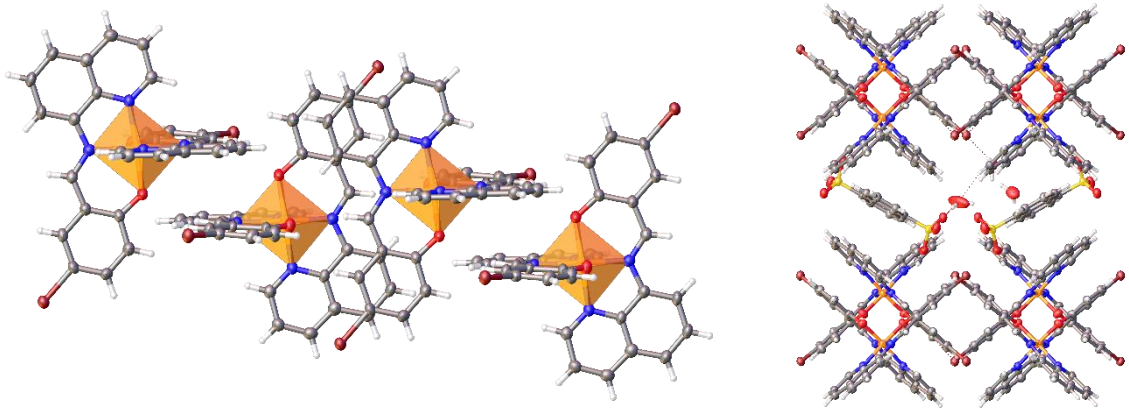

a) **b)**

Figure 24 a) 1D chain of $[Fe(qsal\text{-}X)_2]^+$ cations and b) viewed down the 1D chain.

The packing in **18**, **21** and **22** is different this time involving simple π-π dimers of the $[Fe(qsal\text{-}X)_2]^+$ cations which are clustered around the anions to form 2D sheets (Figure 25). The 2D sheets are then connected via both π-π and C-H···O interactions resulting in a highly cooperative structure. Comparing the two anions the 2,6-npds gives rise to more C-H···π interactions than the 1,5-npds which seems to favour C-H···O interactions to connect with the cations.

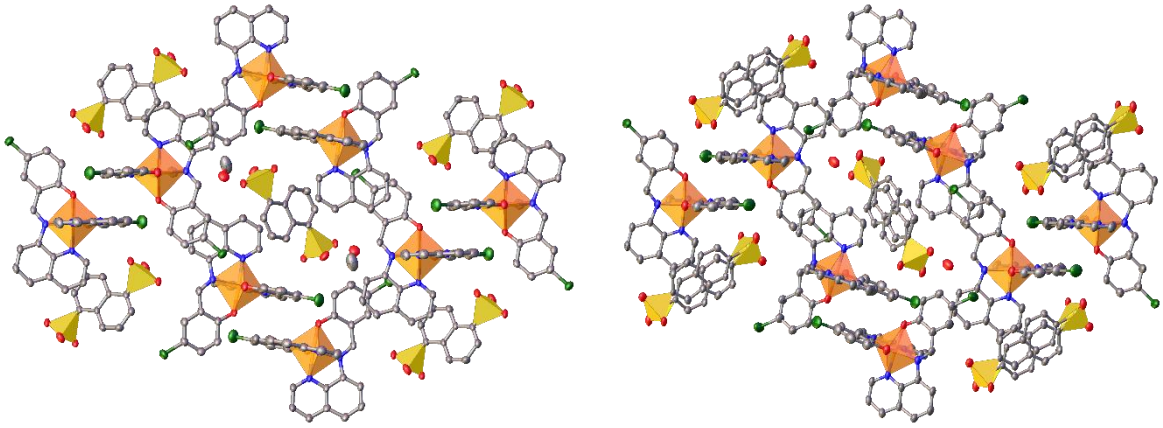

a) **b)**

Figure 25 View of the packing in a) $[Fe(qsal\text{-}Cl)_2]_2[1,5\text{-}npds]\cdot 2MeOH\cdot 2DCM$ and b) $[Fe(qsal\text{-}Cl)_2]_2[2,6\text{-}npds]\cdot 2H_2O$.

Magnetic studies of $[Fe(qsal\text{-}X)_2]_2[npds]$ complexes

The compounds **18**-**23** have all been studied using SQUID magnetometry with $\chi_M T$ vs. T plots presented in Figure 26. The compounds are essentially LS, **18**-**20** or HS, **21-23** only with little or no SCO. It is interesting to note that the 1,5 isomer is LS while the 2,6 isomer is HS and confirms our initial hypothesis that small changes in the anion can have an enormous impact on the magnetic behaviour of the compounds. It is also important to point out that the structures of **21-23** all show LS behaviour

based on X-ray crystallography. The discrepancy is clearly the results of solvent loss during the SQUID measurement and something have encountered before in the $[Fe(qsal\text{-}X)_2]^+$ series.

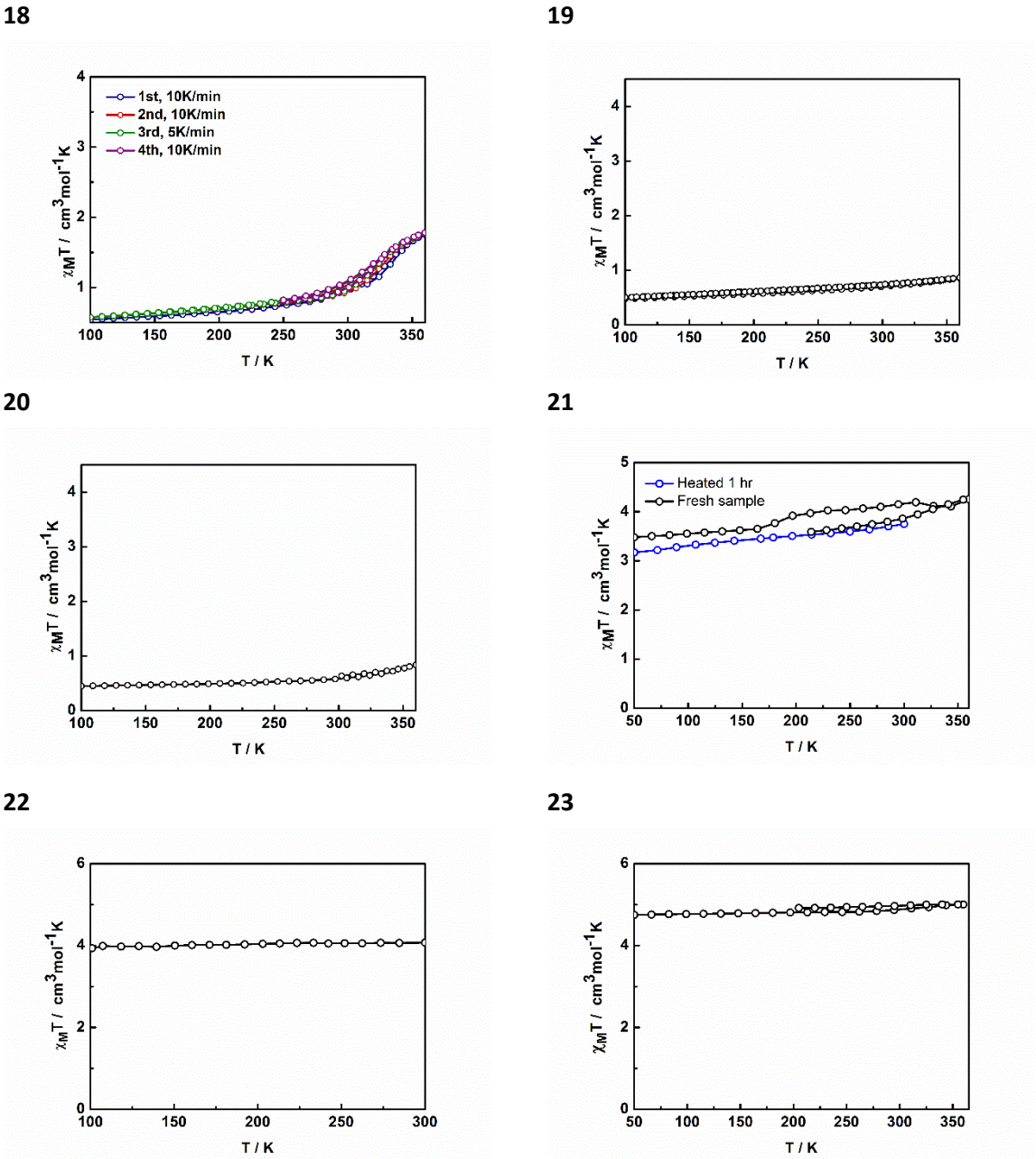

Figure 26 $\chi_M T$ vs. T plots of $[Fe(qsal\text{-}X)_2][1,5\text{-npds}]$ (X = Cl **18**, Br **19**, I **20**) and $[Fe(qsal\text{-}X)_2][2,6\text{-npds}]$ (X = Cl **21**, Br **22**, I **23**).

Structural studies of $[Fe(qsal\text{-}I)_2]OTf{\cdot}EtOH$

As noted in the final report of our previous grant (RSA5580028) the magnetic behaviour of $[Fe(qsal\text{-}I)_2]OTf{\cdot}EtOH$ **24** is extremely varied and depends on sample preparation and age. We have continued to do more work on this compound with Dr Tamsyn Ross at the Australian Synchrotron. As a result of this extra work we have finally been able get the structure of the LS species at 100 K. A comparison of the HS and LS structures reveals a remarkably anisotropic distortion with *b* and *c* shortening by 0.845 and 0.499 Å, respectively while *a* lengthens by 0.901 Å. This results in a substantial

reduction in the unit cell volume by 6.3%, the largest yet reported for any Fe(III) SCO complex and partly responsible for the large hysteresis in **24**. The Fe-N/O bond lengths change by ΔFe–N = 0.170 Å and ΔFe–O = 0.023 Å consistent with full spin crossover (Table 14).

Table 14 Bond lengths (Å) and octahedral distortion parameters (°) for $[Fe(qsal\text{-}I)_2]OTf{\cdot}EtOH$ **24** at 100, 170 and 213 K.

	24-100 K	**24-170 K**	**24-213 K**
$Fe1\text{-}O_{ave}$	1.895(4)	1.908(3)	1.918(6)
$Fe1\text{-}N_{ave}$	1.958(5)	2.119(4)	2.128(7)
Σ	44	60	67
Θ	71	177	200

The packing in the structure closely mirrors our previously reported $[Fe(qsal\text{-}I)_2]OTf{\cdot}MeOH$ with π-π and P4AE interactions combining to give a 2D sheet. However, unlike $[Fe(qsal\text{-}I)_2]OTf{\cdot}MeOH$ there is substantial reorganization of the anion upon spin crossover with the I···O interaction in the HS structure replaced by an O···π interaction (Figure 27). This large movement in the anion is strongly reminiscent of the triflimide in $[Fe(qsal\text{-}I)_2]NTf_2$.

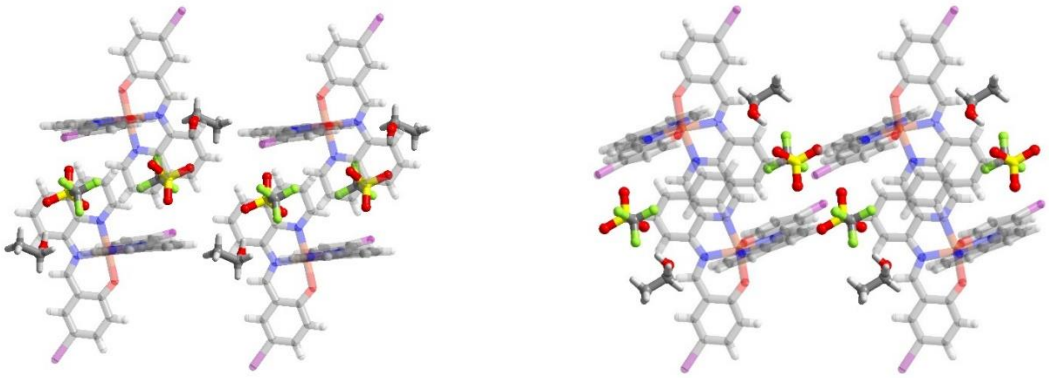

Figure 27 View of the reorientation of the triflate anion in **24** in the LS (left) and HS (right) states.

Further analysis of the VT-PXRD data shows that as expected below 170 K there is a clear phase. Unexpectedly, as well as the LS phase (phase **24b**) and a minority of the sample converts to a phase **24c**. Heating the sample to 300 K converts **24c** into **24a**, the HS phase for which we have a structure. This conversation between **24c** and **24a** is repeated over at least 4 cycles. Given the 2 step SCO observed in the SQUID profile of the fresh sample (Figure 28a) and small changes in the unit cell parameters of **24b** as deduced from the VT-PXRD data it appears that **24b** is a 2 step SCO material (Figure 28b).

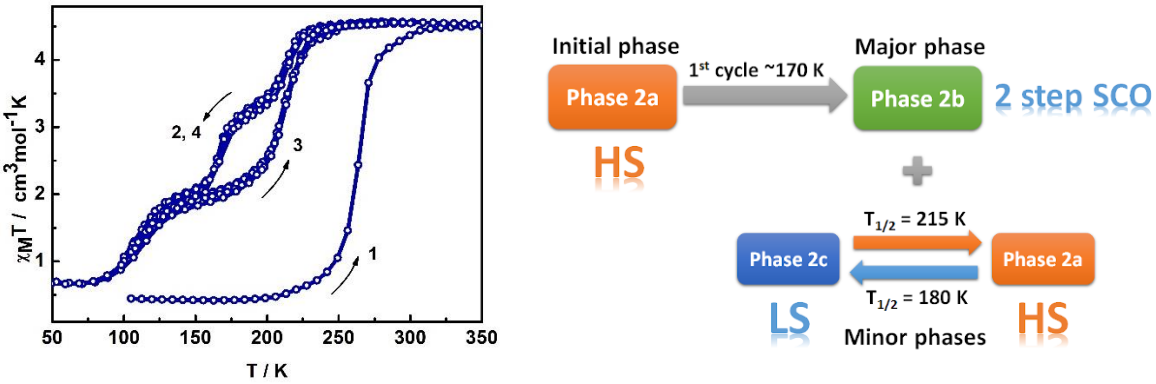

Figure 28 a) $\chi_M T$ versus T plot for [Fe(qsal-I)$_2$]OTf·EtOH and b) summary of the phase changes that occur in **24** from VT-PXRD studies.

EPR spectroscopic studies of [Fe(qsal-I)$_2$]OTf·solvent

Following the publication of the Chemical Science paper we were contacted by Professor Natalia Domracheva of the Kazan Research Centre of the Russian Academy of Sciences, an expert in EPR spectroscopy. Her team have undertaken multiple temperature EPR studies of the propanol solvate and although results are at a preliminary stage the results are already interesting. The spectra are shown in Figure 29. Above 240 K there are no visible peaks in the spectra suggesting that on the HS state exists at this temperature consistent with the SQUID profile of [Fe(qsal-I)$_2$]OTf. It is interesting to note that the HS state is EPR silent, something that is rather rare in Fe(III) SCO chemistry. As the temperature is lowered a strongly rhombic spectrum appears with g_x = 2.31, g_y = 2.18 and g_z = 1.90 consistent with LS Fe(III).

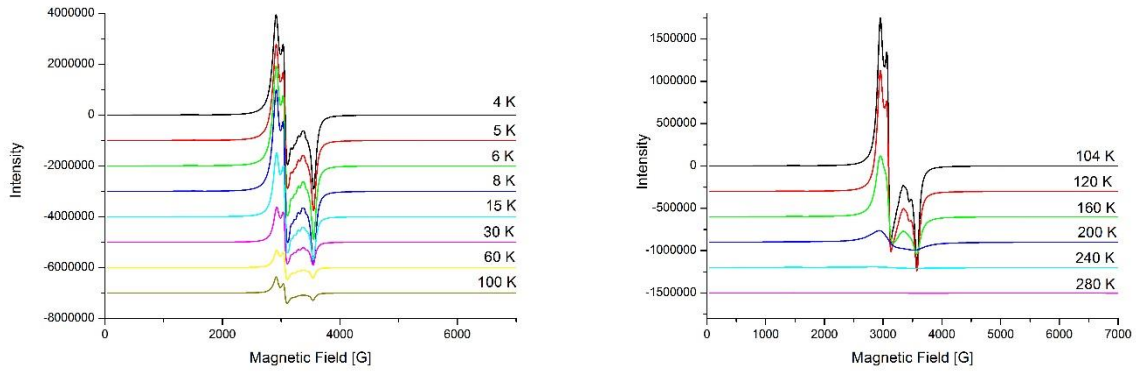

Figure 29 VT-EPR spectra of [Fe(qsal-I)$_2$]OTf, from the propanol solvate.

An interesting feature of the spectra are that the g-values change as the temperature increases (Figure 30). This is very unusual behaviour and may be unprecedented in Fe(III) SCO chemistry. What it suggests is that the qsal-I ligand causes significant deviation from octahedral geometry and that at higher temperatures some kind relaxation process becomes operative resulting in the g-values coalescing. It is also noteworthy that around 230 K, the spin transition temperature, there are subtle changes in g_y. All of these observations are currently being explored further with fitting being undertaken to see if a deeper understanding can be developed.

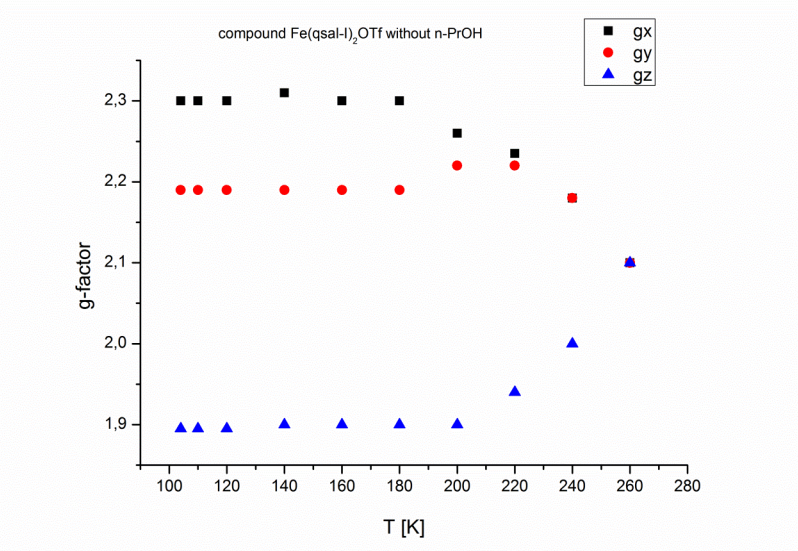

Figure 30 Variation in the g-values with temperature for $[Fe(qsal\text{-}I)_2]OTf$.

Computational studies on $[Fe(qsal\text{-}I)_2]OTf$ and $[Fe(qsal\text{-}Br)_2]NO_3$

In our previous TRF project we discovered two systems $[Fe(qsal\text{-}I)_2]OTf$ and $[Fe(qsal\text{-}Br)_2]NO_3 \cdot 2MeOH$ which undergo abrupt and symmetry breaking spin crossover, respectively. In trying to understand the reason for this stepped spin crossover we have undertaken computational studies with Professor Aron Walsh at the University of Bath, UK (now at Imperial College London).

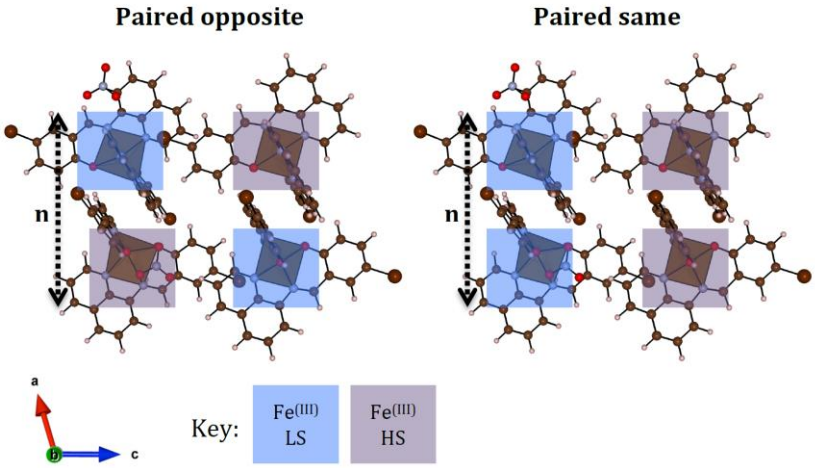

Figure 31 View of the paired opposite and paired same arrangements considered in modelling $[Fe(qsal\text{-}Br)_2]NO_3$.

To try to model the interactions that occur in the solid state unit cells were used with a PBEsol functional which is commonly used for materials. This required a supercomputer and in the case of the symmetry breaking species careful modelling of the spin on neighbouring Fe(III) centres (Figure 31). Note that the paired same is the arrangement observed experimentally. In both systems we also considered whether the Fe(III) centres are ferromagnetically (FM) or anti-ferromagnetically (AFM) coupled. Note that this is for naming purposes only and does not imply actual magnetic coupling.

In the case of $[Fe(qsal\text{-}Br)_2]NO_3$ the results from the calculations are shown below in Table 15. Note that in the unit cell there are two Fe(III) centres at 123 and 280 K while there are four at 175 K. As anticipated the LS state is the most thermodynamically stable with the intermediate state 0.673 eV above that and the full high spin state at 1.352 eV; 0.679 eV above the intermediate state. Thus, there are three energy levels all close in energy and to reach the full HS state it is necessary to go through the intermediate state. It follows that the reason for the stepped spin crossover behaviour is principally electronic. Another feature is that in all cases the FM states are always more stable than the AFM states. Indeed, in the case of the HS state attempts to force an AFM state always led to a spin state change upon convergence. The intermediate states have the added complication of being paired same or paired opposite. Interestingly, only the experimentally observed arrangement of spin states is computationally stable. A view of the four Fe(III) centres and their respective spins is shown in Figure 32.

Table 15 Selected computational parameters for $[Fe(qsal\text{-}Br)_2]NO_3$.

Temperature	**Spin (e per Fe)**	**ΔH (eV per Fe)**	***d* (Fe-Fe) / Å**	***d* (Br-Br) / Å**
*123-FM	0.8, 0.8	0.002	6.900, 7.056	6.898, 11.032
123-AFM	0.8, -0.8	0.013	6.896	5.522, 11.021
175-opposite-FM	0.8, 0.8, 3.9, 3.9 (converged to paired same)	0.672	6.839	5.708, 6.131
175-opposite-AFM	0.8, -0.8, 0.8, -0.8 (converged to low spin)	0.000	6.839	5.708, 6.131
*175-same-FM	0.8, 0.8, 3.9, 3.9	0.673	6.843	5.732, 6.098
175-same-AFM	0.8, -0.8, 0.8, -0.8 (converged to low spin)	0.002	6.890	5.649, 7.102
*280-FM	3.9, 3.9	1.352	6.934	5.793, 10.783
280-AFM	0.8, -0.8 (converged as low spin)	0.021	6.926	5.499, 10.384

* Indicates the experimentally observed arrangement.

Applying the same methodology to $[Fe(qsal\text{-}I)_2]OTf$ yields the results shown in Table 16. This time the results are simple with the FM states are always very much more stable than the AFM states. It follows that the spin transition goes from the LS to the HS state in a single step with no intermediate states as the other states all lie above the HS state.

Table 16 Selected computational parameters for $[Fe(qsal\text{-}I)_2]OTf$.

Temperature	**Spin (e per Fe)**	**ΔH (eV per Fe)**	***d* (Fe-Fe) / Å**	***d* (I-I) / Å**
*LT-FM	0.8, 0.8	0.000	5.952	4.164, 6.061
LT-AFM	0.8, -0.8	2.013	5.863	5.688, 4.513
*RT-FM	3.8, 3.8	1.639	5.383	3.500, 5.692
RT-AFM	3.8, -3.8	3.343	5.496	4.142, 6.083

* Indicates the experimentally observed arrangement.

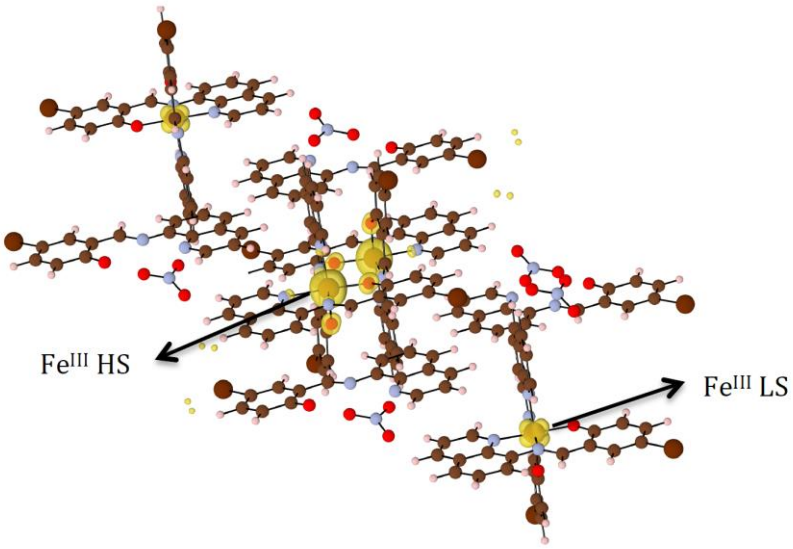

Figure 32 View of the four Fe(III) centres in the intermediate state of $[Fe(qsal\text{-}Br)_2]NO_3$. Note the paired same arrangement of the HS Fe(III) centres.

The reason for this significant difference in behaviour probably lies in the fact that I-H and I-I distances are very much shorter than the Br-H and Br-Br distances in $[Fe(qsal\text{-}Br)_2]NO_3$. In addition, both the Fe-Fe distances and other supramolecular interactions are shorter in $[Fe(qsal\text{-}I)_2]OTf$ (Figure 33). This modifies the electronic structure at the Fe(III) centre resulting in distinct and widely spaced energy levels in $[Fe(qsal\text{-}I)_2]OTf$. It appears that the weaker interactions in $[Fe(qsal\text{-}Br)_2]NO_3$ have the opposite effect resulting in several states at similar energies. This interplay between structural flexibility and rigidity is something also noted in a series of 2D spin crossovers materials currently being investigated by the Kepert-Neville group at the University of Sydney.

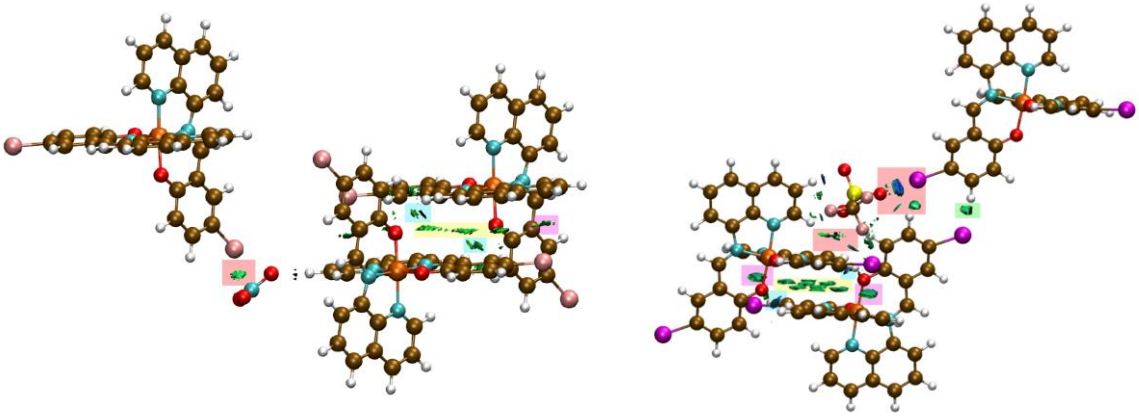

Figure 33 View of the non-covalent interactions in the computed structures of $[Fe(qsal\text{-}Br)_2]NO_3$ (left) and $[Fe(qsal\text{-}I)_2]OTf$ (right).

Synthesis of $[Fe(qnal)_2]$anion complexes

One of the weaknesses of the Fe-qsal system is that it very rarely gives materials that are light activated. In this regard a related ligand to Hqsal is Hqnal with many compounds known to be LIESST active with this ligand. We have therefore prepared $[Fe(qnal)_2]A$ (A = NCS **25**, NO_3 **26** and BPh_4 **27**) using our standard layered diffusion technique. Initial studies showed that compounds crystallize as

very small black needles. However, dropping the concentration slows down the recrystallization and gives larger blocks. In both cases IR spectroscopy shows imine and anion stretches in their expected positions while the UV-Vis spectra show two peaks at *ca*. 340 and 450 nm. The former is assigned to $\pi \rightarrow \pi^*$ transition and the latter is thought to be a LMCT band (Table 17).

Table 17 IR and UV-Vis spectroscopic data of $[Fe(qnal)_2]A$.

Complexes	IR (cm^{-1})			λ_{max} /nm ($\varepsilon_{max}/M^{-1}cm^{-1}$)
	ν_{O-H}	$\nu_{C=N}$	ν_{anion}	
$[Fe(qnal)_2]NCS$ **25**	3422 (w,br)	1613 (s)	2065 (m)	343 (21010), 445 (19815)
$[Fe(qnal)_2]NO_3$ **26**	3408 (w,br)	1614 (m)	1380 (s)	345 (18875), 442 (19560)
$[Fe(qnal)_2]BPh_4$ **27**	3450 (w,br)	1613 (s)	-	342 (24605), 453 (29785)

Structural studies of $[Fe(qnal)_2]BPh_4$

Single crystal X-ray diffraction analysis showed that $[Fe(qnal)_2]BPh_4 \cdot 5H_2O$ **27** crystallized from $MeOH/CH_2Cl_2$ in the triclinic space group $P\bar{1}$. The iron(III) atom is coordinated by four nitrogen and two oxygen atoms from two qnal ligands in an octahedral configuration. The ligands enforce a *cis* configuration around the Fe(III) centre (Figure 34). The Fe–N/O bond lengths in $[Fe(qnal)_2]BPh_4$ range from 1.92-2.15 Å and are consistent with distances for HS Fe(III) at room temperature (Table 18). This is confirmed by the high octahedral distortion parameter. For reasons explained below we are currently trying to get the structure of **27** from the block-like crystals at room and low temperatures.

Table 18 Bond lengths (Å) and octahedral distortion parameters (°) for **27** at 295 K.

Bond lengths	
Fe-O1	1.92
Fe-O2	1.92
Fe-N1	2.10
Fe-N2	2.10
Fe-N3	2.15
Fe-N4	2.14
Σ	74.7

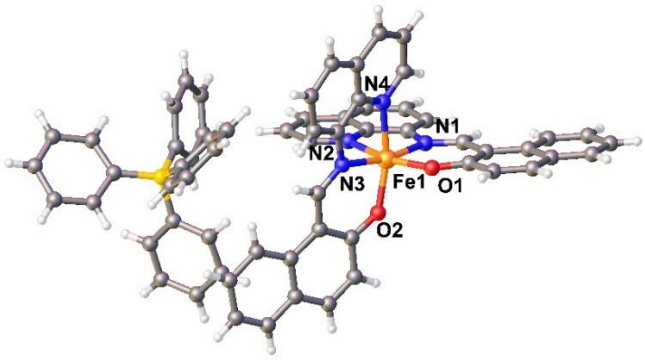

Figure 34 View of the asymmetric unit in **27**.

In terms of packing, $[Fe(qnal)_2]BPh_4$, has a displaced π-π interaction with a centroid-to-centroid distance of 3.7 Å (plane-to-plane distance = 3.42 Å) indicative of a moderately strong π-π interaction. The π-π interaction is supported by a pair of C-H···O contacts giving a dimer. The dimers are then connected by a pair of C-H···π interactions, 2.83 Å forming a 1D chain (Figure 35).

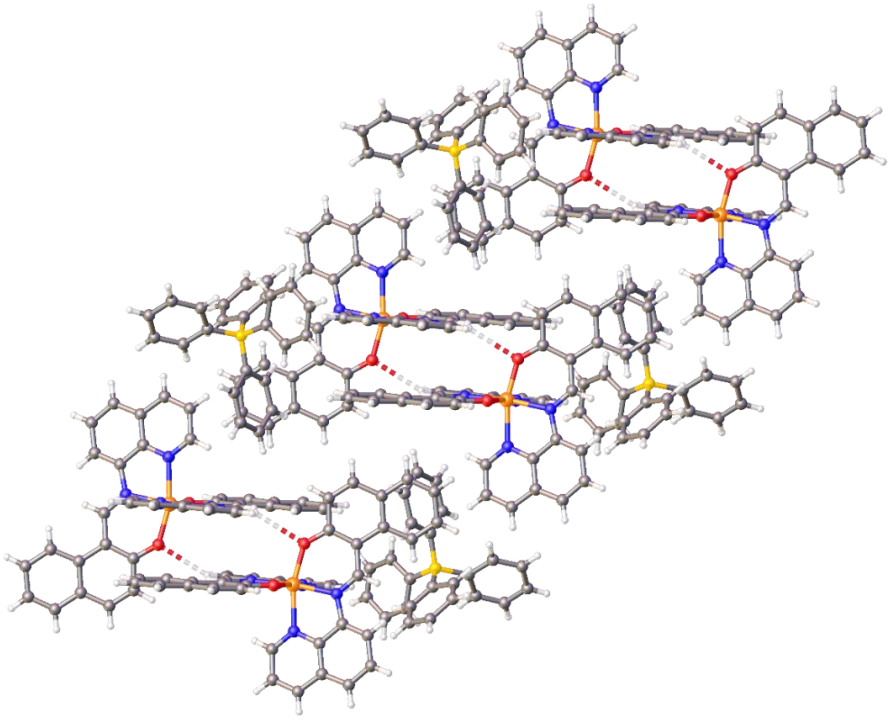

Figure 35 View of π-π interactions in $[Fe(qnal)_2]BPh_4$.

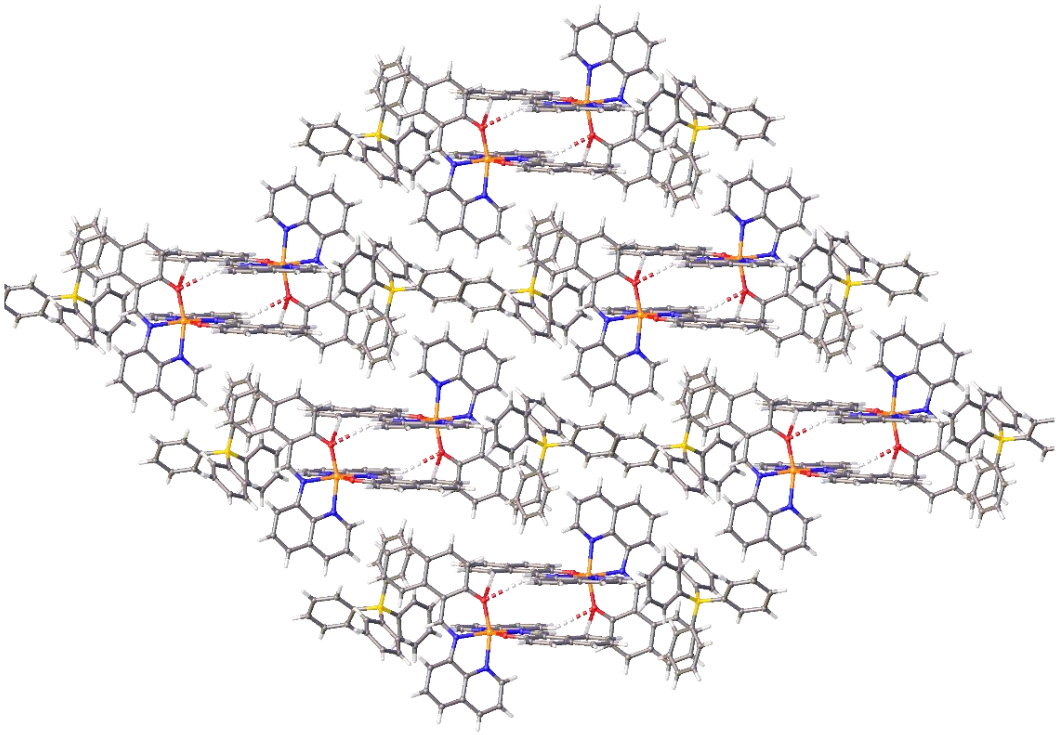

Figure 36 View of the 2D sheets in $[Fe(qnal)_2]BPh_4$.

The 1D chain is decorated by the BPh_4 anions which interact through multiple C-H···π contacts. The BPh_4 anions sit between the 1D chains of the $[Fe(qnal)_2]^+$ cations resulting in a 2D sheet (Figure 36). Beyond this there are no further interactions.

Magnetic studies of $[Fe(qnal)_2]$anion complexes

The SCO profiles of $[Fe(qnal)_2]Y$ have been studied by SQUID magnetometry (Figure 37). The NCS complex is found to undergo moderately abrupt SCO with $T_{1/2}$ = 330 K. The nitrate complex is mostly LS up to 360 K. In contrast to the structural data, $[Fe(qnal)_2]BPh_4 \cdot 5H_2O$ undergoes a gradual and incomplete SCO being approximately 75% HS at 350 K and 20% HS at 100 K. The fact that the full HS state is not achieved at 300 K suggests that some of the water is lost during measurement. We have also noticed that there is a significant difference in the magnetic profile of the blocks and the needles, with the former undergoing a moderately abrupt SCO with $T_{1/2}$ = 280 K (Figure 37d). As with many SCO systems it is clear that the morphology of the crystals can greatly impact the SCO properties.

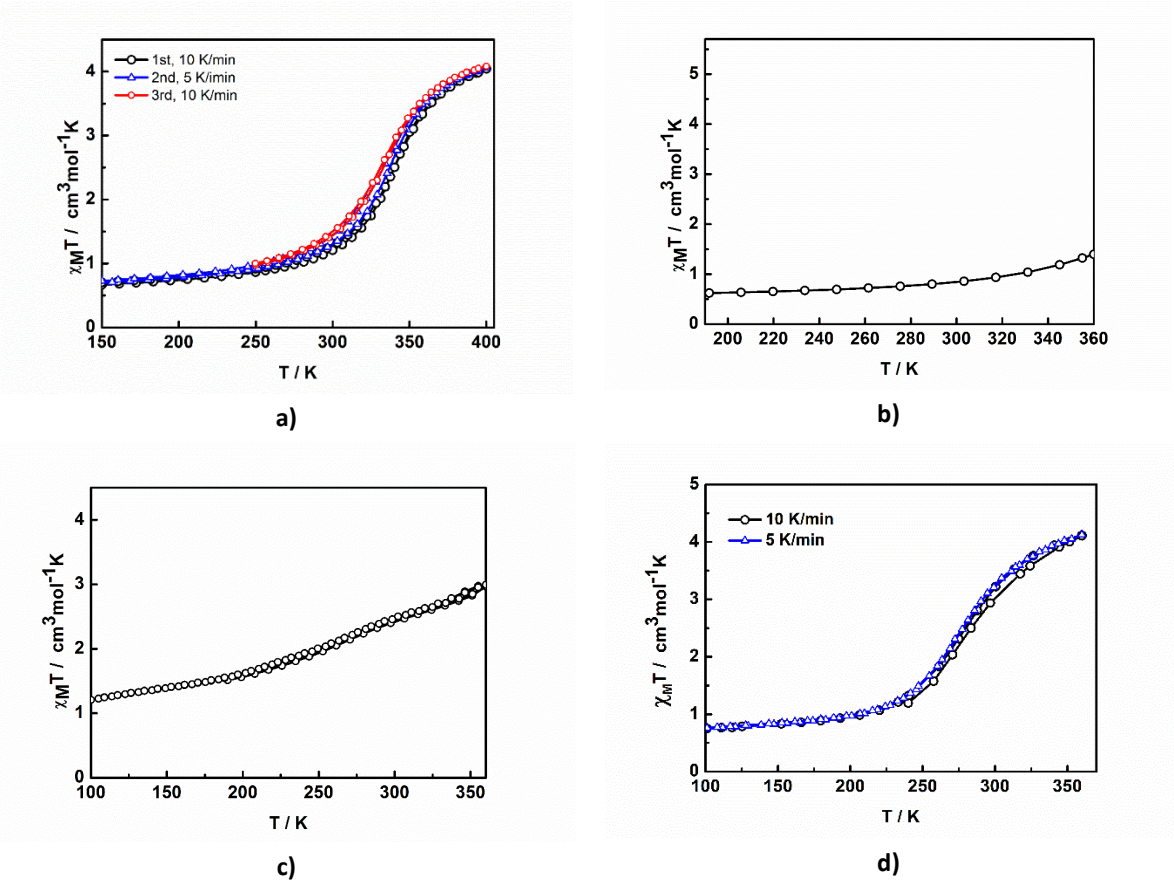

Figure 37 $\chi_M T$ vs. T plots of $[Fe(qnal)_2]$A a) A = NCS, b) NO_3 and c) BPh_4 (needles) and d) BPh_4 (blocks).

Photomagnetic studies of **27** have been undertaken by Dr. Guillaume Chastanet at ICMCB in France. Although the studies are still incomplete, irradiating the sample at 980 nm results in a clear increase in $\chi_M T$ reaching 2.65 $cm^3\ mol^{-1}\ K$ at 10 K (Figure 38). Warming the sample results in a decrease in $\chi_M T$ in two steps reaching the full LS state at *ca*. 50 K. The single state gradual transition observed in the bulk makes this two-step relaxation unprecedented in SCO chemistry. Irradiation at 650 nm results in a return to the LS state showing that **27** is a genuine light switchable material.

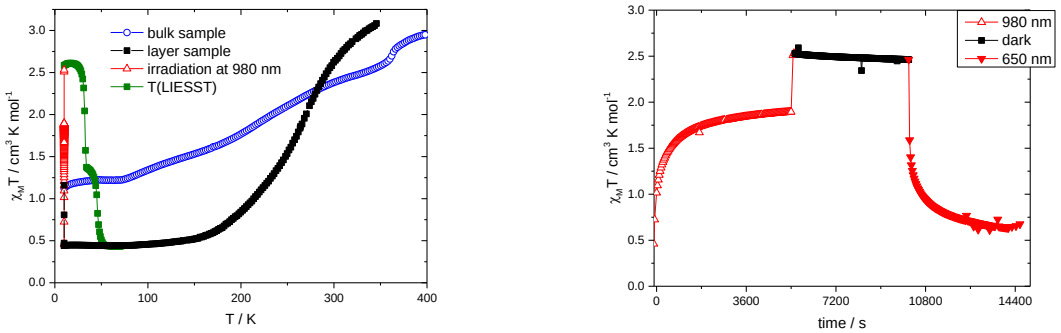

a) b)

Figure 38 Temperature dependence of magnetic susceptibility during the LIESST experiment for **27-needles**.

As noted above, the $[Fe(qnal)_2]BPh_4$ complex can be made as blocks in addition to the needles we initially prepared. The LIESST studies on the blocks show slightly different LIESST behaviour with T_{LIESST} now *ca*. 30 K (Figure 39). However, the LIESST efficiency is increased with $\chi_M T$ now reaching 3.00 cm^3 mol^{-1} K at 10 K. The most notable difference is the loss of the two step relaxation to the LS state. We are currently unclear as to why this occurs but it may relate to differing numbers of water molecules in the needle and block samples.

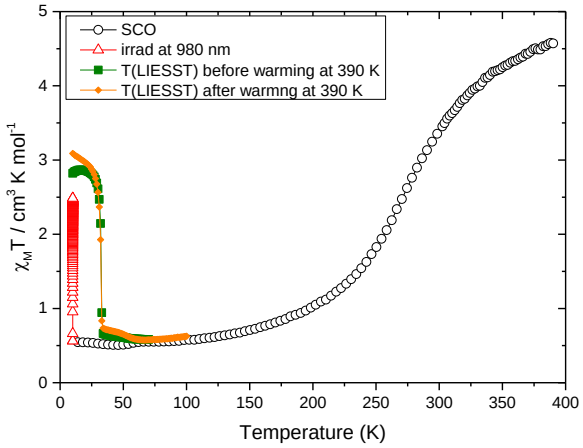

Figure 39 Temperature dependence of magnetic susceptibility during the LIESST experiment for **27-blocks**.

Fe(III) SCO nanomaterials

Fe(III) SCO nanomaterials have been investigated using $[Fe(qsal)_2]NO_3$ as a model as the originally proposed $[Fe(qsal\text{-}I)_2]OTf$ contains the comparatively more expensive qsal-I ligand. As the magnetic behaviour of $[Fe(qsal)_2]NO_3$ is unknown we have prepared the compound in bulk first and obtained a structure of $[Fe(qsal)_2]NO_3 \cdot EtOH$ at 130 K. The Fe-N/O bond lengths are 1.965 and 1.882 Å on average and indicative of LS Fe(III). The packing in the complex consists of strong π-π interactions forming 1D chains. The nitrate interacts strongly with the chain through C-H···O contacts (Figure 40). This suggests strong cooperativity and we hope abrupt SCO.

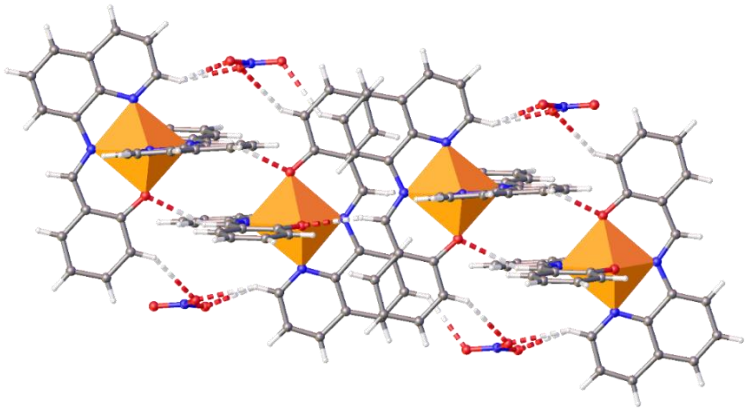

Figure 40 1D chain in $[Fe(qsal)_2]NO_3 \cdot EtOH$ showing the π-π and C-H···O interactions.

To prepare the nanomaterials we have employed the reverse micelle method shown in Figure 41. This involved dissolving Hqsal in MeCN and suspending it a hexane solution containing the surfactant NaAOT, sodium bis(2-ethylhexyl)sulfosuccinate. The $Fe(NO_3)_3$ was dissolved in water and then added to the hexane-surfactant solution. Mixing these two gives the nanoparticles.

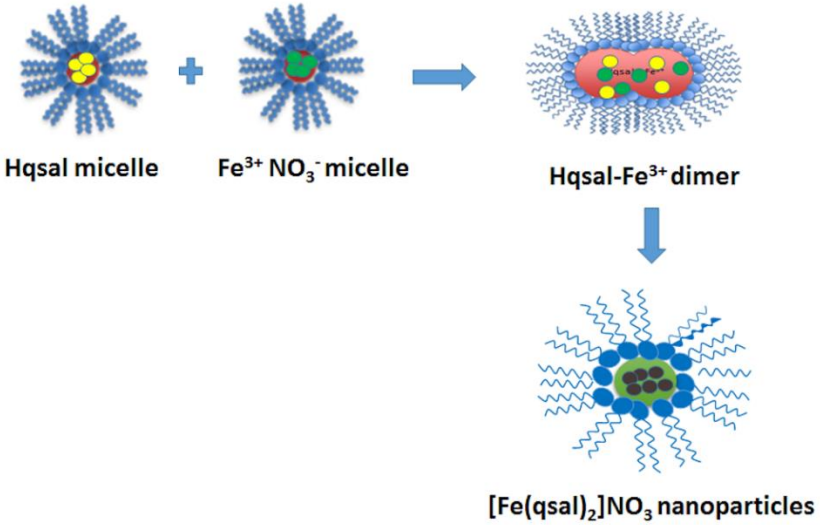

Figure 41 Reverse micelle synthesis of $[Fe(qsal)_2]NO_3$ nanoparticles.

In order to understand the nanoparticle synthesis and ensure that it is repeatable we have explored the amount of surfactant in the aqueous and organic layers as well as reaction time. We began by varying the amount of surfactant in the organic layer (i.e. with Hqsal) from 0.5 g to 4.0 g grams using a reaction time of 24 hours yielding the results shown in Figure 42.

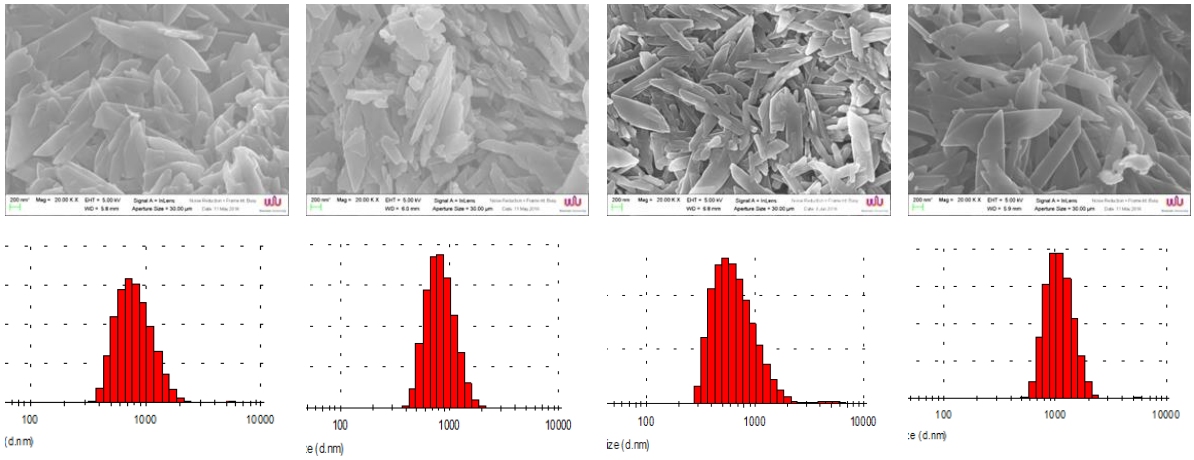

a) **b)** **c)** **d)**

Figure 42 SEM images and DLS profiles of the $[Fe(qsal)_2]NO_3$ nanoparticles by varying the surfactant in the organic layer using a) 0.5 g NaAOT, b) 1.0 g NaAOT, c) 2.0 g NaAOT and d) 4.0 g NaAOT.

Similar experiments keeping the surfactant at 2.0 g in the organic layer and varying the amount in the aqueous layer yields the results shown in Figure 43. The nanoparticles are parallelogram shaped with length × width × thickness of 1-2 μm × 300-600 nm × 90-110 nm on average. It is also evident that the impact of surfactant concentration is greater for the aqueous layer with nanomaterials of two distinct sizes based on DLS measurements. We note that as surfactant concentration increases the nanoparticle size also becomes slightly larger but yields more monodisperse product. The results from these experiments are similar to those reported for $[Fe(salEen\text{-}3\text{-}OMe)_2]PF_6$.

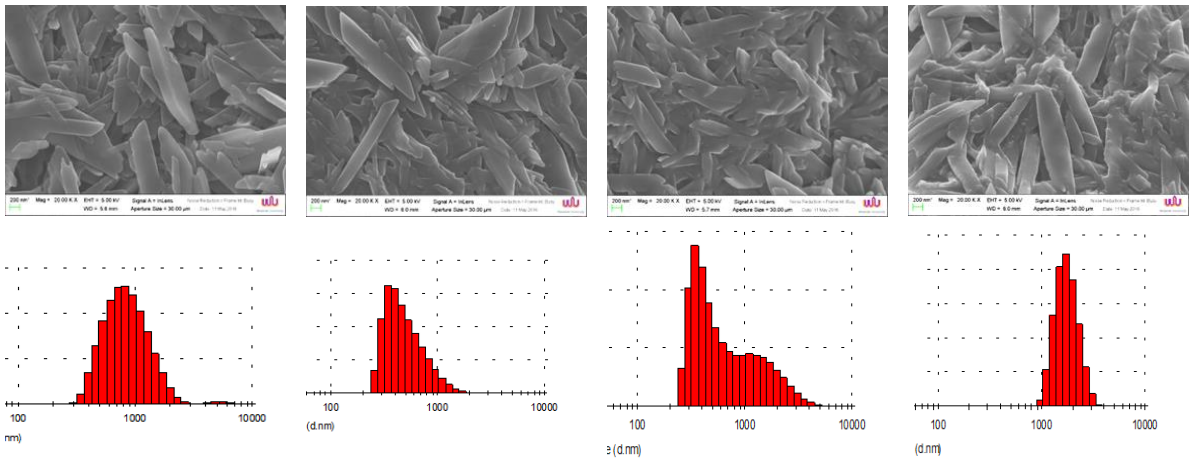

a) **b)** **c)** **d)**

Figure 43 SEM images and DLS profiles of the $[Fe(qsal)_2]NO_3$ nanoparticles by varying the surfactant in the aqueous layer using a) 0.5 g NaAOT, b) 1.0 g NaAOT, c) 2.0 g NaAOT and d) 4.0 g NaAOT.

Regarding reaction time we selected 2.0 g of surfactant in the aqueous and organic layer and then varied the reaction time from 1-48 hours, see Figure 44 for a selection of the SEM and DLS measurements. After 1 hour it is clear that the reaction is not complete and consequently rather an amorphous image is observed in the SEM. After 4 hours parallelogram shapes are now visible in the SEM but two peaks are observed by DLS. Increasing the reaction time to 12 hours produces the

characteristic parallelograms but once again two particles sizes are found by DLS. At 24 hours both SEM and DLS techniques agree that single morphology and size nanomaterials are produced. Interestingly, at 48 hours the SEM shows a loss of morphology resembling the pattern seen after 1 hour. We conclude that in this case 2.0 g of surfactant in both the aqueous and organic layer and a reaction time of 24 hours produce the desired nanomaterials with consistent size and morphology.

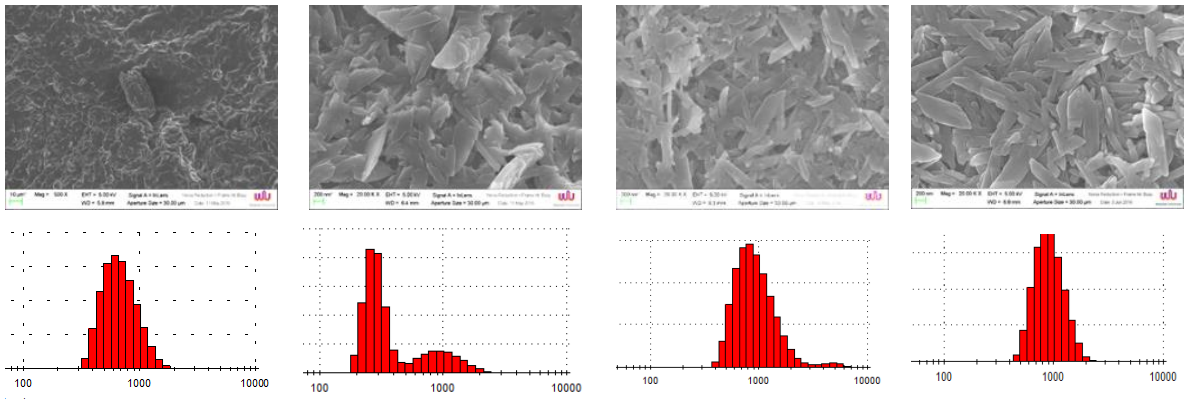

Figure 44 SEM images and DLS profiles of the $[Fe(qsal)_2]NO_3$ nanoparticles by varying the reaction time a) 1 hour, b) 4 hours, c) 12 hours and d) 24 hours.

The SQUID profile of $[Fe(qsal)_2]NO_3$ which shows the compound to be essentially LS up to 350 K (Figure 45). The nanomaterials have also been examined and these show almost identical SCO characteristics strongly suggesting that the nanomaterials maintain the magnetic behaviour of the crystalline systems.

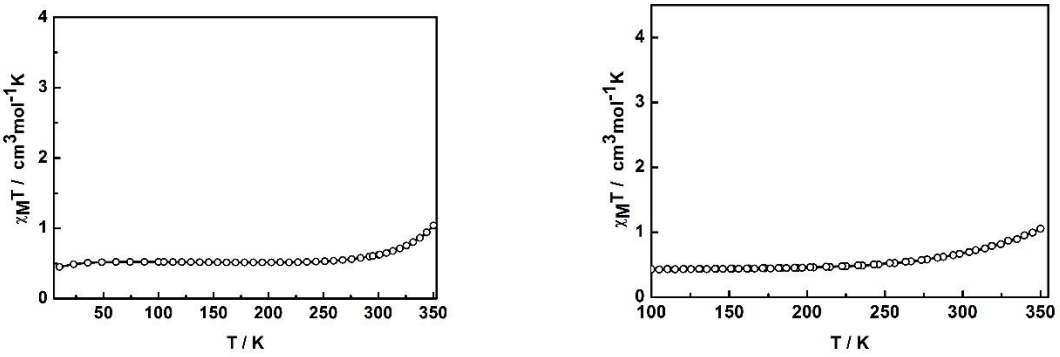

Figure 45 Comparison of the SCO profile of the crystalline (left) and *nano*-$[Fe(qsal)_2]NO_3$ (right).

As the spin crossover profile of $[Fe(qsal)_2]NO_3$ is poor we have also explored nanomaterials of the known compound $[Fe(qsal)_2]NCS$. We have found that reaction times of 12 hours or more give good products but the reaction is very sensitive to the solvent used for the $Fe(NCS)_3$ precursor. In the case of water globular nanomaterials are produced while MeOH gives plate like nanomaterials (Figure 46). Ethanol produces slightly more defined blocks but the best solvent in this case is MeCN where nanocubes are the dominant morphology. The interesting thing about this observation is that nanomaterials when correctly prepared mirror the morphology of the crystalline material.

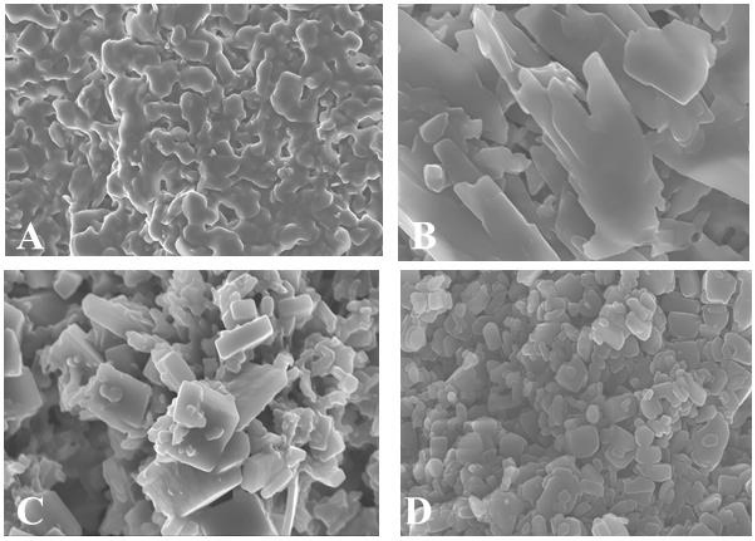

Figure 46 [Fe(qsal)$_2$]NCS nanoparticles prepared using a) water; b) methanol; c) ethanol and d) CH_3CN as solvent for the Fe precursor.

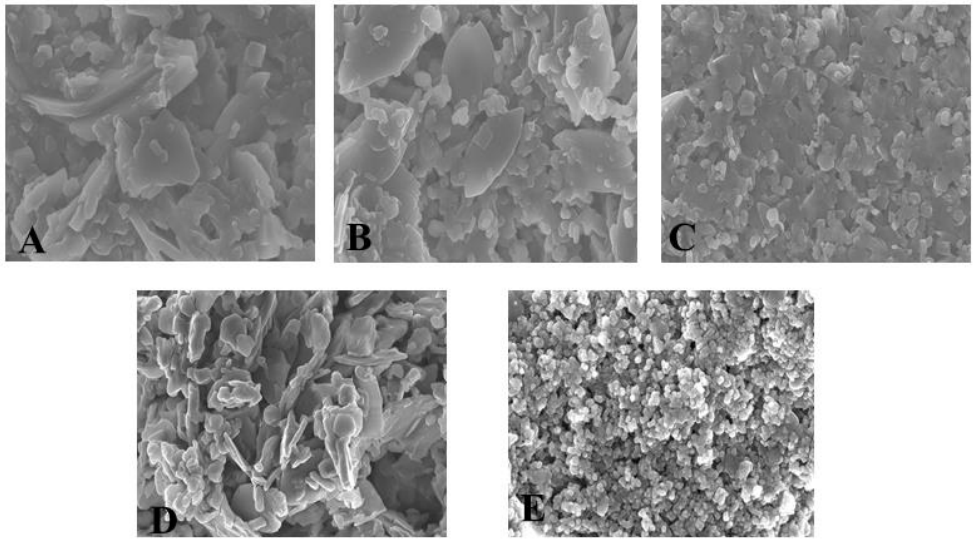

Figure 47 [Fe(qsal)$_2$]NCS nanoparticles washed with a) ethanol (2x); b) EtOH:THF; c) EtOH:hexane; d) EtOH:water and e) hexane.

We have also found that the solvent the nanomaterials are washed with is crucial in terms of both the size and the shape of the resulting nanomaterials. As shown in Figure 47 washing with polar solvents tends to result in aggregation of the nanomaterials while washing with copious amounts of hexane removes most of the surfactant leaving the nanocubes intact.

In addition to the [Fe(qsal)$_2$]NCS nanomaterials we have made nanomaterials of [Fe(qsal-I)$_2$]OTf and [Fe(qsal-I)$_2$]NTf$_2$. The poor solubility of Hqsal-I under the normal conditions we used for [Fe(qsal)$_2$]X (X = NCS, NO_3) have meant that we have had to again survey a number of different solvents to produce high quality nanomaterials. To synthesize [Fe(qsal-I)$_2$]OTf, Hqsal-I was dissolved in DMF and the Fe^{3+} precursor in MeCN. $FeCl_3$ was initially dissolved in MeCN and KOTf was added to the solution. Black solids were obtained after centrifuging and washing with EtOH. SEM micrographs

showed plate like particles which tend to form aggregates. The thin plates seem to combine together and form one big chunk of particle with visible lines that indicate the separate plates (Figure 48a). Similar solvent combination was used in the preparation of $[Fe(qsal\text{-}I)_2]NTf_2$. The Fe^{3+} precursor was prepared using $FeCl_3$ in MeCN. $LiNTf_2$ was then added into the solution before adding into the surfactant solution. Fine, black solids were obtained after washing with EtOH. SEM micrographs revealed rod-like particles measuring *ca*. 100 nm-3 µm long while width and thickness of the particles are shorter. Particle size distribution using DLS showed that the average hydrodynamic diameter for $[Fe(qsal\text{-}I)_2]OTf$ is 510.40 ± 26.53 nm and 709.70 ± 192.8 nm for $[Fe(qsal\text{-}I)_2]NTf_2$ (Figure 48b). The >6.00 polydispersity index (PDI) confirms the presence of nanomaterials with varied sizes with some large, sedimenting particles. The increasing count rate and size also proves that samples aggregate.

IR spectroscopic studies of the nanomaterials show stretches at 1599-1603 cm^{-1} for the C=N bond. Stretches at 1383 for the NO_3^- and 1138-1139 cm^{-1} for the C-F bonds. The S-O bands for the triflate and triflimide are observed at 1030, 1260 and 1373 cm^{-1} and are similar to those found in the bulk materials.

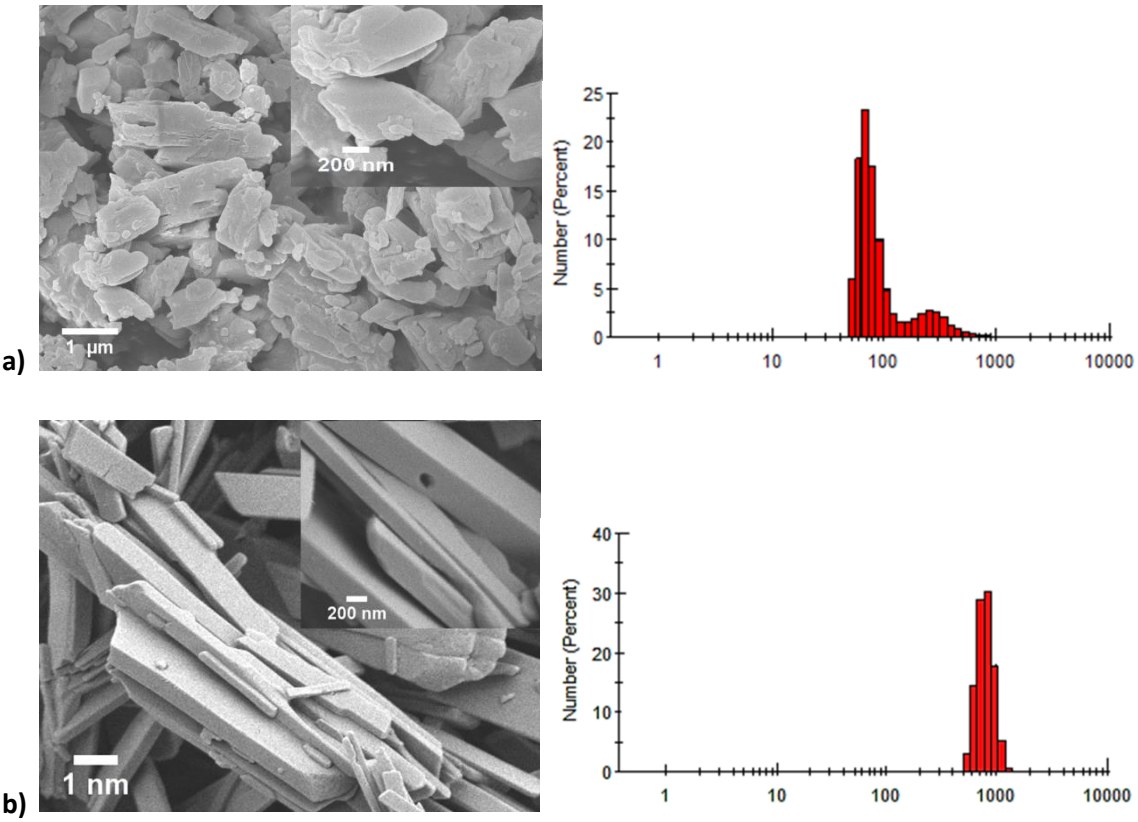

Figure 48 SEM images and DLS size distribution graph for a) $[Fe(qsal\text{-}I)_2]OTf$ and b) $[Fe(qsal\text{-}I)_2]NTf_2$.

Magnetic Studies of $[Fe(qsal\text{-}I)_2]OTf$ and $[Fe(qsal\text{-}I)_2]NTf_2$

Magnetic studies on all samples were conducted using SQUID magnetometry and are presented as $\chi_M T$ versus T plots, see Figures 49 and 50. Abrupt spin crossover with hysteresis similar to the bulk materials are observed for both compounds. At 50 K, the $\chi_M T$ of $[Fe(qsal\text{-}I)_2]OTf$ is found to be 1.20 $cm^3\ mol^{-1}\ K$, slightly higher than is typical of a LS iron(III) centre. An abrupt transition occurs at $T_{½}\uparrow$ = 231 K and $T_{½}\downarrow$ = 227 K giving ΔT = 4 K. This is lower than the bulk material which exhibits an 8 K

hysteresis width ($T_{½}\uparrow$ = 232 K, $T_{½}\downarrow$ = 224 K). Moreover, the amount of HS species at low temperature is relatively larger in the NMs compared with the bulk; 19% in the nanomaterials. This result is typically observed when complexes are nanosized. The narrower hysteresis width is due to the lower cooperativity within the molecules caused by a decrease in the long-range interactions as the particles become smaller. The higher %HS residue maybe attributed to the Fe^{3+} ions located at the surface of the nanomaterials which interact with a trace amount of the surfactant.

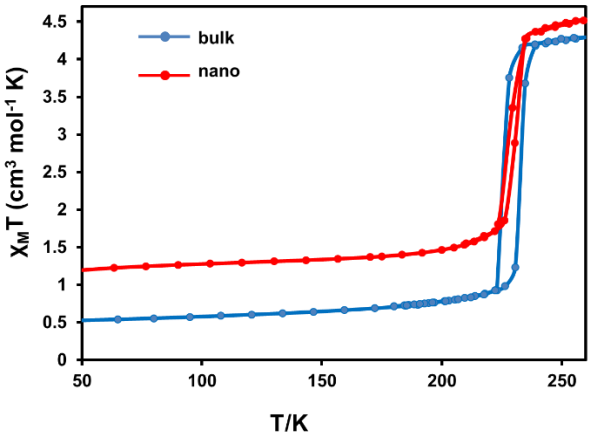

Figure 49 $\chi_M T$ versus T plot of the bulk and nanomaterials of $[Fe(qsal\text{-}I)_2]OTf$.

The magnetic profile of the $[Fe(qsal\text{-}I)_2]NTf_2$ nanomaterials reveals an abrupt transition at $T_{½}\downarrow$ = 248 K and $T_{½}\uparrow$ = 275 K giving a hysteresis width of 27 K, *ca*. 3 K lower than the bulk material. This is reproducible as proven by using 2, 5 and 10 K/min cycling rate (Figure 50). Interestingly, the very small change in the hysteresis width suggests that provided that the hysteresis of the bulk is significant nanosizing results in little change. This is consistent with $[Fe(salen\text{-}3\text{-}OMe)_2]PF_6$ (ΔT = 3 K) which as it is nanosized becomes increasingly more gradual and $[Fe(Htrz)_2(trz)]BF_4$ where the large hysteresis (*ca*. 40 K) is unchanged even at 10 nm.

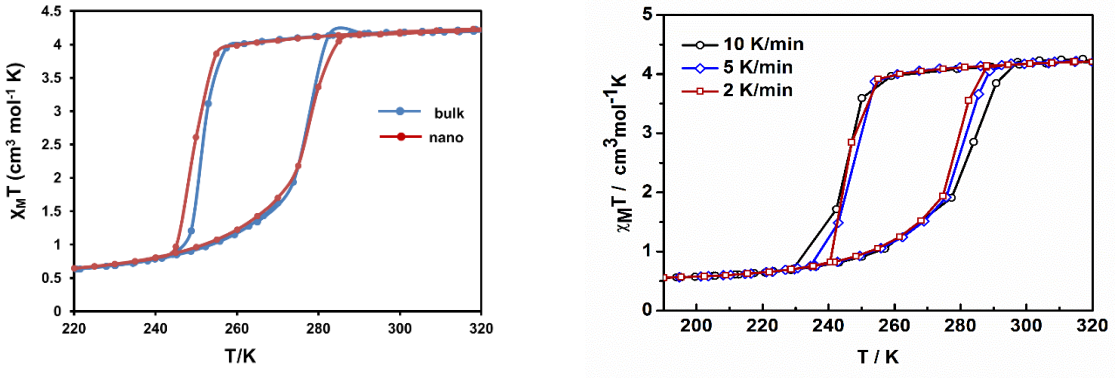

a) **b)**

Figure 50 a) $\chi_M T$ versus T plot of the bulk and nanomaterials of $[Fe(qsal\text{-}I]NTf_2$ and b) $\chi_M T$ versus T plot of the nanomaterials at different cycling rate.

Synthesis and structures of [Fe(qsal-X)halide] complexes

In trying to isolate the Fe(III) spin crossover dimers outlined in the proposal we have inadvertently discovered a number of iron compounds in which only one qsal-X ligand is bound to the Fe(III) centre. The first of these was [Fe(qsal-Br)Cl_2] **28** which is a five coordinate exhibiting an almost perfect square pyramidal geometry, τ = 0.03 (Figure 51).

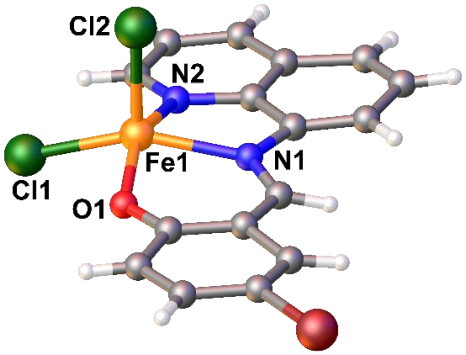

Figure 51 View of the structure of [Fe(qsal-Br)Cl_2].

The packing in this structure is composed of Br···Cl, C-H···Cl and π-π interactions as shown in Figure 52. The halogen bond is particularly strong being almost 0.2 Å shorter than the van der Waal radii, with the Br group acting as the X-bond donor and the chloride as the acceptor. Indeed, it is probably the strength of this halogen bond that favours **28** over the expected octahedral species. While the compound is not expected to show spin crossover the five coordinate geometry may allow **28** to act as a single molecule magnet and this is something we are now exploring.

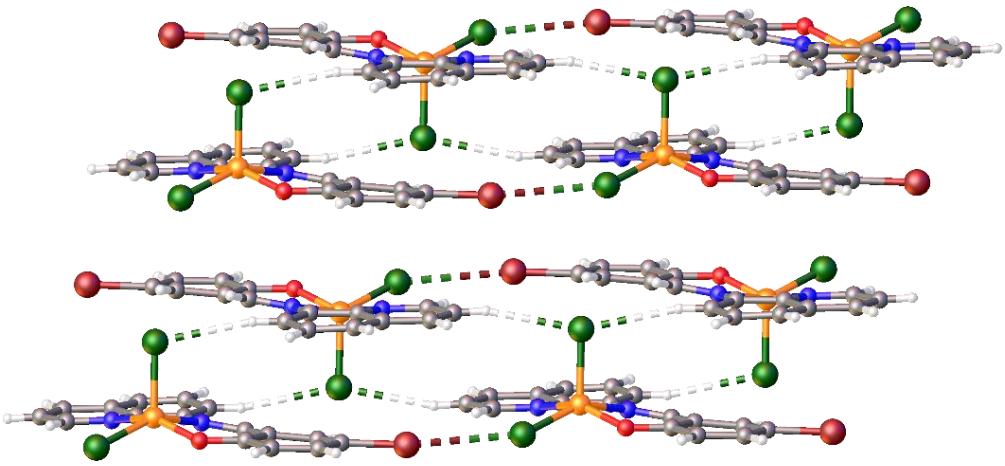

Figure 52 View of the packing in [Fe(qsal-Br)Cl_2] showing the Br···Cl and C-H···Cl interactions.

We have also isolated two related compounds [Fe_2(μ-OMe)$_2F_2$(qsal-Br)$_2$]·2MeOH **29** and [Fe_2(μ-OMe)$_2Cl_2$(qsal-I)$_2$] **30** with crystallize in monoclinic $P2_1/n$ and $P2_1/c$. Both are dimers with **29** containing bridging methoxy groups formed by the deprotonation of MeOH in the basic solution in which the reaction takes place (Figure 53). As with **28** the presence of weak field ligands means that the Fe(III) centres are high spin even at low temperature. The difference between the two structures is the presence of MeOH which is hydrogen bonded to the coordinated fluoride. As they are dimers we would expect magnetic communication between the Fe(III) centres, results in this area are pending.

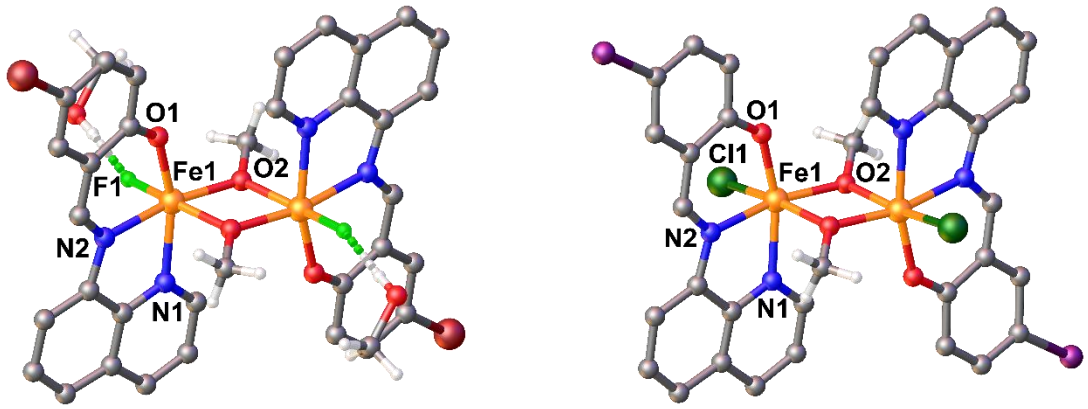

Figure 53 View of the structures of **29** (left) and **30** (right).

Despite the only difference being the presence of methanol in **29** the two compounds exhibit radically different packing. In the case of **29** the key motif is a 1D chain of dimers held together by π-π interactions. In contrast, in **30** 2D sheets are formed by strong I···Cl interactions which are 3.341 Å long (0.39 Å shorter than the van der Waal radii, Figure 54).

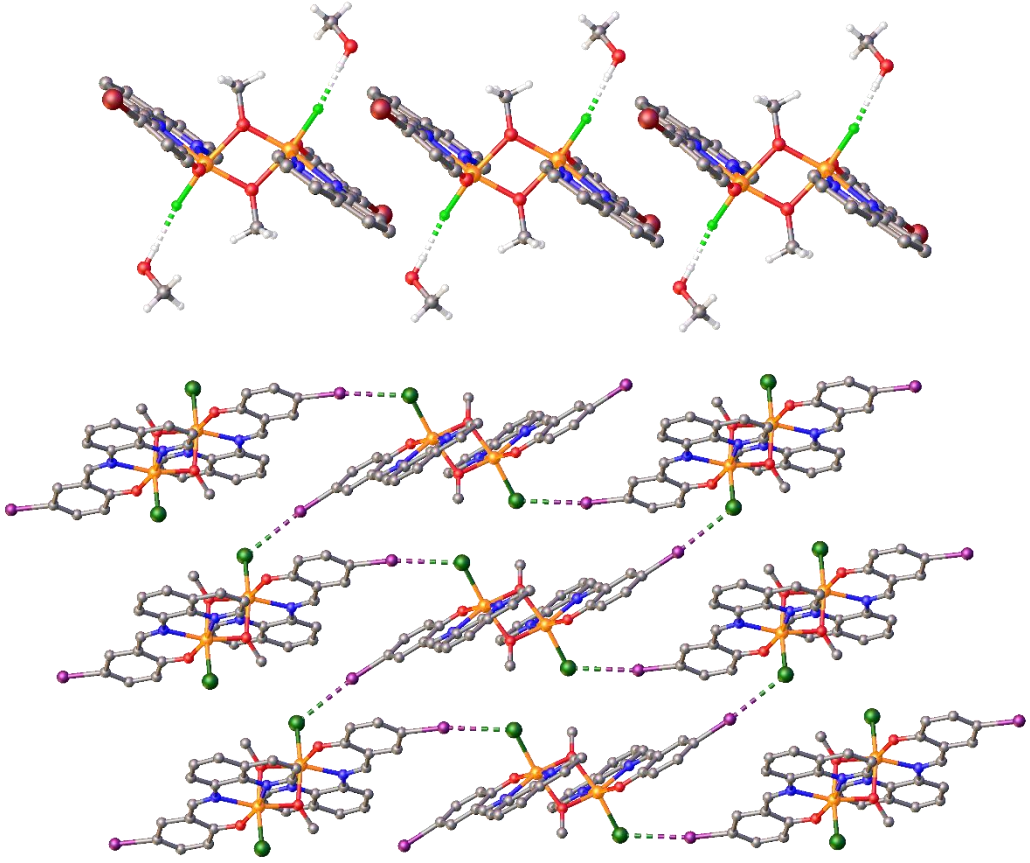

Figure 54 Packing motifs in **29** (top) and **30** (bottom).

Magnetic properties of [Co(2-Himap)$_2$]

Dc magnetic studies were undertaken on [Co(2-Himap)$_2$] **31** between 2-300 K with applied fields of 0.1 T (2-70 K) and 1.0 T (2-300 K). The $\chi_M T$ values are independent of the applied field indicating a lack of magnetic impurity or Zeeman level population effects. At 300 K, $\chi_M T$ = 2.40 cm^3 mol^{-1} K and is

significantly higher than the expected value of 1.875 cm^3 mol^{-1} K for an isolated S = 3/2 Co(II) where g = 2.0. This indicates a considerable orbital angular momentum contribution as expected in a $^4T_{1g}$ system that exhibits magnetic anisotropy. The $\chi_M T$ value for **31** is similar to that reported in other octahedral Co(II) complexes where $\chi_M T$ is in the range 2.30-3.05 cm^3 mol^{-1} K. $\chi_M T$ values remain independent of temperature between 300 and ~100 K suggestive of a large distorted ligand field contribution, and spin-orbit coupling, which transform the $^4T_{1g}$ state into a lowest-energy $^4A_{2g}$ term (compressed tetragonal). Below 80 K $\chi_M T$ decreases rapidly reaching 1.30 cm^3 mol^{-1} K at 2 K which is also indicative of ZFS of the $^4A_{2g}$ state, perhaps combined with remnant orbital degeneracy. The magnetization data reveal that the *M* vs. *H* curve at 2 K becomes almost saturated at higher fields with $M = 2.05\ N\beta$ at 2 K and 5 T. This is lower than the expected value for a S = 3/2 system where g > 2.0, probably because of spin-orbit coupling and magnetic anisotropy in **31**.

There are two approaches currently used to simultaneously fit the $\chi_M T$ vs. *T* and *M* vs *H* plots. The first one assumes that zero field splitting is dominant and uses the giant spin Hamiltonian approach to obtain *D* (and *E*) and *g* values. The second approach uses the Figgis approach that yields ligand field splitting and spin-orbit coupling values. We have used the spin Hamiltonian, shown below, with a spin of 3/2, in the program PHI

$$H = D(S_z^2 - [S(S+1)/3]) + E(S_x^2 - S_y^2) + \mu_B S \cdot g \cdot H \qquad (1)$$

where *D* is the axial zero field splitting (zfs) parameter; *E* is the rhombic zfs, μ_B the Bohr magneton, *H* is the applied dc field. The *g* values were either kept isotropic or anisotropic, although the latter option is more appropriate for a Co(II) complex. The fits were very good for both the $\chi_M T$ vs. *T* and the *M* vs *H* plots at temperatures of 2, 3, 4 and 5.5 K; Figure 55. The parameters obtained from the fits are: *D* = +36.7 cm^{-1}; *E* = 2.0 cm^{-1}; *g* = 2.11, 2.48, 2.12. The use of a negative *D* value gave unrealistic values of *E*, and thus this possibility can be discarded.

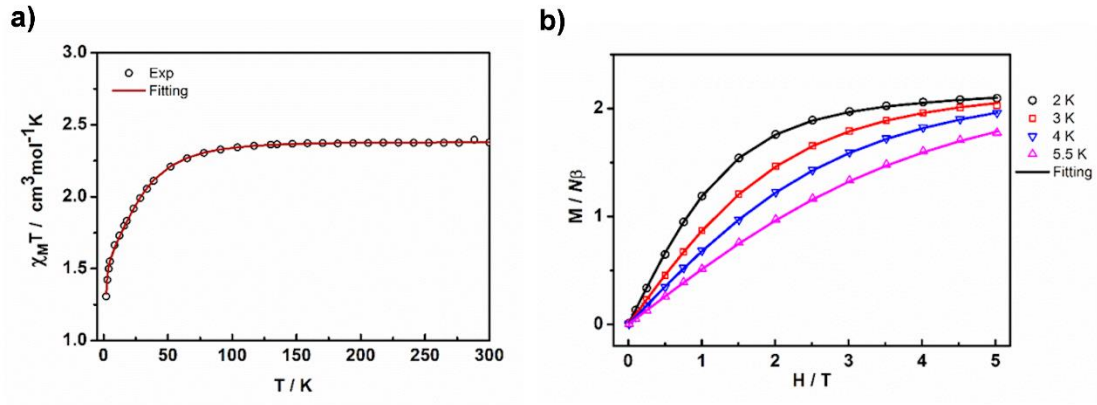

Figure 55 Best fits of a) $\chi_M T$ vs *T* in field of 1 T and of b) *M* vs *H* isotherms using the ZFS Hamiltonian in program PHI[43] with the parameter set given in equation 1.

To better understand and quantify the magnetic anisotropy in **31** we undertook *ab initio* calculations using a multireference methodology; the computed second-order anisotropy parameters and excitation energies are collected in Table 19. These values have been obtained from two different electronic structure calculations using the ORCA and MOLCAS software packages. ORCA produces two sets of results: CASSCF and CASSCF + NEVPT2 (which introduces the dynamic correlation effects), both including spin-orbit contributions. MOLCAS has been employed to provide CASSCF results, including

spin-orbit effects that have been introduced with the SO-RASSI method. Positive, and similar, D values are found with the three methods, as expected for an octahedral Co(II) complex. The best agreement with the experimental data is found with the ORCA/NEVPT2 calculation: D = 39.3 cm^{-1} and E = 1.8 cm^{-1}. In all cases, a 3/2 ground state is found before including spin-orbit effects. Under these conditions, the calculations show the existence of relatively low-lying spin-orbit free excited states (δ in Table 19) with energies around 1000-2000 cm^{-1} above the ground state, which may be responsible for the observed anisotropy. This is also confirmed by the anisotropic g-values for the ground state. Once spin-orbit effects are included a set of Kramers' doublets (KDs, Δ) is obtained; the three methods again produce very similar results, indicating a low-lying KD around 100 cm^{-1} above the ground state, which may participate in the spin relaxation processes (see below). The second KD is located at higher energies in all cases (1200-1800 cm^{-1}) and would not be expected to participate in the spin relaxation mechanism.

Table 19 ORCA/CASSCF, ORCA/CASSCF + NEVPT2, and MOLCAS/CASSCF + RASSI computed D, $|E|$, and g-values for the ground state of **31**. δ and Δ are the computed first excitation energies before and after including the spin-orbit effects, respectively. The Δ-value corresponds to the energy difference between the ground and the first excited Kramers' doublets.

Method	D_{calc} (cm^{-1})	$\|E\|_{calc}$ (cm^{-1})	δ (cm^{-1})	Δ (cm^{-1})	g_{xx}, g_{yy}, g_{zz}
ORCA/CASSCF	50.4	3.1	1339.8	101.3	2.03, 2.45, 2.53
ORCA/NEVPT2	39.3	1.8	1919.8	78.8	2.03, 2.36, 2.41
MOLCAS/CASSCF	48.2	2.8	1439.9	96.8	2.03, 2.45, 2.51

The sign and value of the D parameter can be rationalized using the spin-orbit operator, which couples the ground and excited states. When the excited state results from the excitation between orbitals with the same $|m_l|$ values, the $M_S = \pm 3/2$ components are stabilized and a negative contribution to D is obtained. However, an excitation between orbitals involving a $|\Delta m_l| = 1$ change, *i.e.* stabilizing the $M_S = \pm 1/2$ components, leads to a positive contribution to the D value. **31** displays a distorted octahedral core, which produces the d-orbital splitting shown in Figure 56. This orbital arrangement is obtained with the ORCA/CASSCF + NEVPT2 calculation by using the *ab initio* ligand field theory (AILF) method. We find that the degeneracy of the t_{2g} and e_g orbitals of the regular octahedron is broken in **31**, indicating the transformation of the initial octahedral $^4T_{1g}$ ground state into a lowest-energy $^4A_{2g}$ term, and one of the former clearly moves up in energy (1573.4 cm^{-1}), far from the last doubly occupied orbital (83.9 cm^{-1}). The AILF method allows the identification of these orbitals; the last doubly occupied orbital is d_{yz} (or d_{xz}, because these cannot be distinguished) while the first half-occupied orbital is d_{xy}; since these orbitals have a different $|m_l|$ value *i.e.* ± 1 and ± 2, respectively, the D value should be positive. This contrasts with the similar *mer*-$[Co(L)_2]$ compounds which show negative D values. The difference between the two systems is probably due to the greater distortion towards a trigonal prismatic geometry in *mer*-$[Co(L)_2]$ when compared with **31**, and seems to be caused by H-bonding involving uncoordinated hydroxyl groups on the ligands.

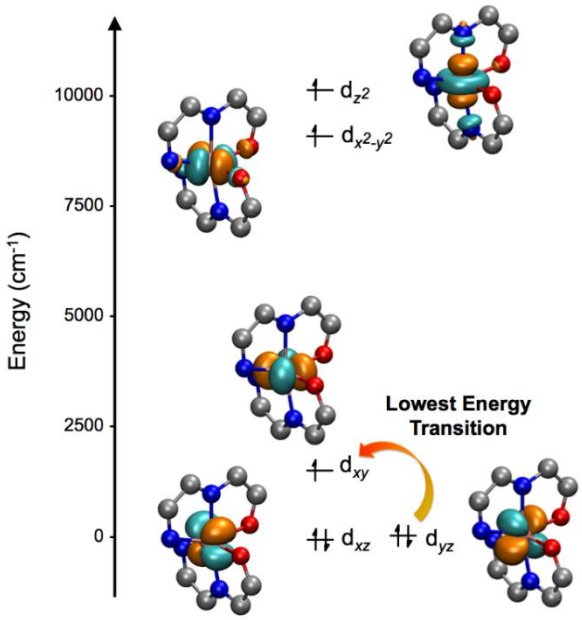

Figure 56 AILF computed d-orbital splitting for **31** (orbital energies: d_{xz} 0.0 cm^{-1}, d_{yz} 83.9 cm^{-1}, d_{xy} 1573.4 cm^{-1}, d_{x2-y2} 9066.1 cm^{-1}, d_{z2} 10150.2 cm^{-1}). Colour code: Co = pink, C = gray, N = blue, O = red; H atoms and parts of the 2-Himap ligand have been omitted for clarity.

The dynamics of magnetization were investigated using *ac*-magnetic measurements. The data were recorded with an applied field of 0.2 T between 2-9 K and 50-1488 Hz (Figure 57a). Under these conditions the out-of-phase magnetization shows a clear peak at higher frequencies, the signature of a single molecule magnet. As with many Co(II) SIMs at zero applied *dc* field there are no signals in the out-of-phase magnetization probably due to efficient quantum tunnelling and consistent with the calculations below.

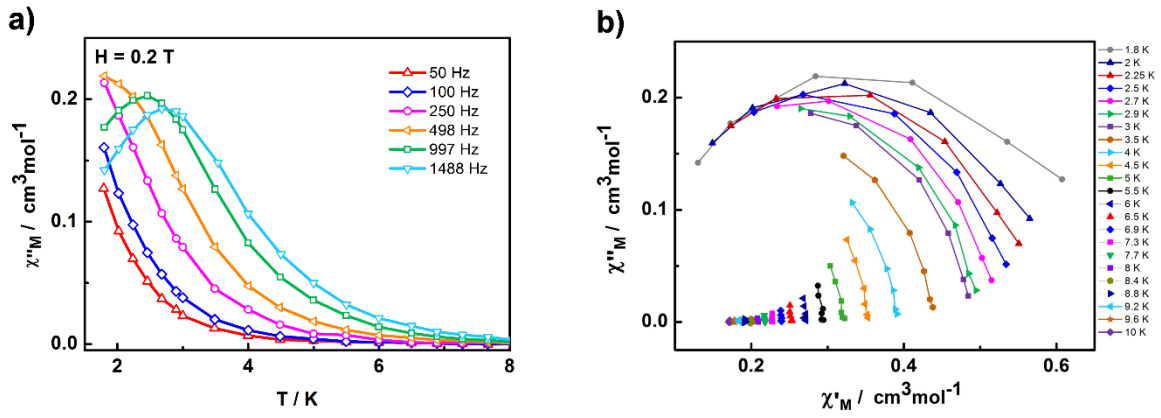

Figure 57 a) Variable-frequency out-of-phase components of the *ac* magnetic susceptibility and b) Cole-Cole plot of **31** the solid lines being best fit.

The program CC-FIT was used to fit the Cole-Cole plots (Figure 57b) that showed semicircles at the lowest temperatures. The α values are 0.24 (1.8 K) to 0.07 (6 K) indicative of deviations from the Debye model and a range of distributions of the relevant relaxation processes. Usually, four mechanisms, as shown in equation 2 are considered, direct, quantum tunnelling, Raman and Orbach:

$$\tau^{-1} = AH^4T + \frac{B_1}{1+B_2H^2} + CT^n + \tau_0^{-1}\exp\left(\frac{-U_{eff}}{kT}\right) \quad (2)$$

A common initial approach is to analyse the temperature dependence of the relaxation time τ values by plotting ln(τ) against 1/T. The best fit for **31** using only an Orbach term gives a U_{eff} value of 14 K. However, as *D* is calculated to be 39.3 cm^{-1} the barrier height, assuming a purely thermal relaxation pathway, should be 78.6 cm^{-1} (2*D*); this is considerably higher than the fitted barrier height. This indicates that the thermal Orbach mechanism is not the main contributor to the temperature dependence. In fact, Co(II) SIMs with positive *D* and limited rhombicity that do exhibit Orbach relaxation are rare, with [Co(tpma)(NCMe)]BF_4 {tpma = tris(pyridylmethyl)amine} a recent example.

The explanation for the occurrence of slow relaxation of magnetization with positive *D* values has recently been explained by a combination of a direct mechanism (due to the presence of very effective hyperfine coupling in an I = 7/2 Co(II) system), a Raman mechanism and a strong nuclear spin-lattice interaction which must also be taken into account. In such a scenario, the temperature dependence of the spin relaxation time can be described by a Raman term and a field-dependent mechanism contribution τ_{FDM}^{-1}

$$\tau^{-1} = \tau_{FDM}^{-1} + CT^n \quad (3)$$

the best fit for **31** is with *C* = 19.12 s^{-1} $K^{-5.10}$, *n* = 5.10 and τ_{FDM}^{-1} 3685.1 s^{-1}. Although, *n* is smaller than the hypothetical *n* = 9 for a Kramers ion, the value is very similar to that reported for other easy-plane Co(II) complexes.

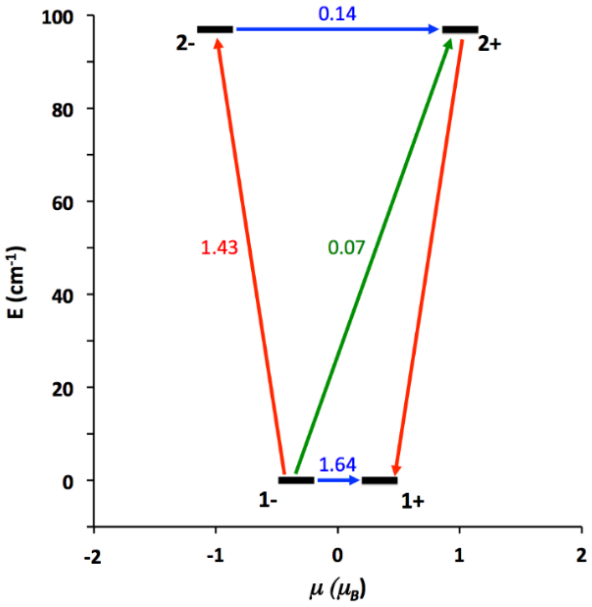

Figure 58 Lowest two Kramers' doublets and *ab initio* computed relaxation mechanism in **31**. The thick black lines imply KDs as a function of their magnetic moment along the main anisotropy axis. Red lines indicate the magnetization reversal mechanism. The blue lines correspond to ground state QTM and thermally assisted-QTM via the first excited KD, and green and purple lines show the possible Orbach relaxation process. The values close to the arrows indicate the matrix elements of the transition magnetic moments (above 0.1 an efficient spin relaxation mechanism is expected).

The computed relative energies of the lowest-lying KDs and the spin relaxation pathways of **31**, obtained with the MOLCAS/CASSCF + RASSI calculation, are shown in Figure 58. The spin relaxation

mechanisms show a plausible pathway *via* direct quantum tunnelling (QTM) in the ground state. The matrix elements of the transition magnetic moments found between states 1- and 1+ is 1.64, much higher than the required value of 0.1 associated with an efficient relaxation mechanism. The second KD may also be accessible (96.8 cm^{-1}) and should able to participate in alternative relaxation pathways, most probably through thermally assisted-QTM. However, the U_{eff} barrier obtained from the fit of the relaxation time (14 K) is much lower than these thermally-activated processes (139 K), and confirms the above fit that the Raman mechanism is the dominant spin relaxation process in an applied field.

Magnetic studies and HF-EPR studies of $[Fe_4(2\text{-Himap})_6][NO_3]_3$

As reported in our previous project we discovered a unique mixed-valence Fe star. Magnetic measurements for $[Fe_4(2\text{-Himap})_6][NO_3]_3$ **32** show $\chi_M T$ = 15.02 cm^3 K mol^{-1} at 300 K with $\chi_M T$ increasing slowly to a maximum of 28.43 cm^3 K mol^{-1} at *ca*. 8 K before decreasing rapidly (Figure 59). The $\chi_M T$ value at 300 K is consistent with one non-interacting Fe^{III} and three non-interacting Fe^{II} centres, and the low temperature data shows evidence of a ferromagnetically coupled ground state. The minor temperature dependence of $\chi_M T$ above 150 suggests that the intramolecular magnetic interactions are relatively weak; this, coupled with the presence of a possible orbital contribution to the magnetic moment of high-spin octahedral Fe^{II} centres make the interpretation of the magnetic data fraught with difficulty. In order to get some insight into the local magnetic properties of the Fe^{II} sites to inform our interpretation, we have performed complete active space self-consistent field spin-orbit (CASSCF-SO) calculations (see ESI for details). These show that the Fe^{II} sites are well-described as S = 2, however are subject to a significant axial zero-field splitting (ZFS, D ~-17 cm^{-1}, $|E/D|$ ~0.12), which arises from close-lying orbtially degenerate states. Interestingly, the main anisotropic axis for each of the Fe^{II} centres lies perpendicular to the plane of the Fe_4 cluster, and points towards the central Fe^{III} centre along a near-two-fold symmetry axis. Given the significant ZFS of the Fe^{II} centres and possibly weak magnetic exchange, it is important to consider the non-collinearity of the local anisotropy axes. Therefore to model our data, we employ the following spin Hamiltonian in PHI:

$$\widehat{H} = -2J_1\hat{S}_1 \cdot \left(\hat{S}_2 + \hat{S}_3 + \hat{S}_4\right) - 2J_2\left(\hat{S}_2 \cdot \hat{S}_3 + \hat{S}_3 \cdot \hat{S}_4 + \hat{S}_4 \cdot \hat{S}_2\right) + D\left({\hat{S}_{z_2}}^2 + {\hat{S}_{z_3}}^2 + {\hat{S}_{z_4}}^2 - {}^1\!/_3\left({\hat{S}_2}^2 + {\hat{S}_3}^2 + {\hat{S}_4}^2\right)\right) + g\mu_B\left(\hat{S}_1 + \hat{S}_2 + \hat{S}_3 + \hat{S}_4\right) \cdot B$$

Here, $\hat{S}_1$ is the spin operator for S = $^5/_2$ of Fe^{III}, $\hat{S}_{2-4}$ are the spin operators for S = 2 Fe^{II}, J_1 and J_2 represent the magnetic coupling between the central Fe^{III} and peripheral Fe^{II} centres (Fe1-Fe2), and the peripheral Fe atoms (Fe2-Fe2), respectively. G is the isotropic g-factor for the cluster, B is the applied magnetic field, and D is the single-ion axial ZFS of the Fe^{II} sites (we ignore E as CASSCF-SO predicts only a small rhombicity); we have rotated the local z-axis of each Fe^{II} site to point towards the central Fe^{III} ion, thus $\hat{S}_{z2-4}$ are non-collinear. There are two possible solutions obtained when fitting the $\chi_M T$ and M vs. B data simultaneously: one with D < 0 (as suggested by CASSCF-SO) and one with D > 0. The former gives J_1 = +2.77 cm^{-1}, J_2 = -0.675 cm^{-1}, g = 1.96 and D = -7.09 cm^{-1} (Figs. 2 and S10-11); while the latter gives J_1 = +2.62 cm^{-1}, and J_2 = -0.738 cm^{-1}, g = 2.03 and D = +14.0 cm^{-1} (Figs. S9-11). Both solutions agree on the nature of the exchange interactions, where we see a weak ferromagnetic exchange between the Fe^{II} and Fe^{III} centres; antiferromagnetic coupling is observed in the related Fe^{III}_4 clusters. While the solution with D > 0 appears to model the high temperature $\chi_M T$ data better than the D < 0 solution, the low temperature magnetisation data (which is more sensitive to the details of

the electronic structure) is better accounted for by the $D < 0$ solution; as $D < 0$ is also suggested by CASSCF-SO, we believe this to be the more likely description.

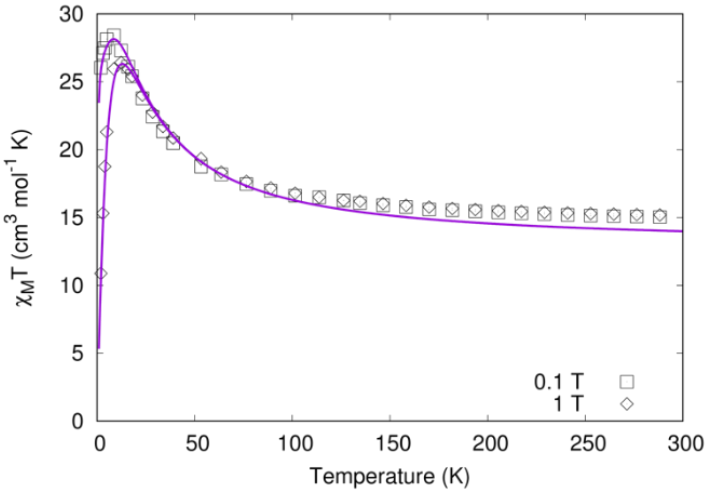

Figure 59 $\chi_M T$ vs. T plot of **32**. The purple lines represent the best fit (D = -7.09 cm^{-1}) with the parameters given in the text.

Given the ferromagnetic ground state and large anisotropy, we conducted *ac* susceptibility measurements to see if **32** showed slow magnetization relaxation and SMM behaviour. Plots of the out-of-phase susceptibilities, χ_M'', as a function of *ac* frequency showed zero values in zero applied *dc* field; however frequency dependent "tails" were noted below 5 K in a static *dc* field of 3000 Oe. This is in contrast with the S = 5 ground state $[Fe^{III}_4(L)_2(dpm)_6]$ stars, L = alkoxide(3-), for which frequency dependent maxima in χ_M'' were observed in zero *dc* field. Thus, our data indicate a lower U_{eff} barrier for **1** compared to the Fe^{III}_4 family of 3.5 – 17 K.

Variable temperature, multi-high-field/frequency EPR measurements were performed on a constrained powder of **32**. Figure 60 shows a series of field-swept *dI*/*dB* spectra recorded at different frequencies in the range from 53 to 648 GHz, and a temperature of 5 K. These can be divided into two groupings: the first set of resonances lie on a straight line that has a slope corresponding a *g*-value of 2.004±0.004, with zero offset (±4 GHz) on the frequency axis; the second grouping of two broad resonances observed at the highest frequencies lie on straight lines that have identical zero-field intercepts of 344±4 GHz, and slopes corresponding to *g*-values of 1.66±0.05 and 2.61±0.06.

The g = 2.004 resonance consists of a sharp inflection superimposed on a broader shoulder. Such a signal suggests a weakly anisotropic species, most likely corresponding to $S = {}^5/_2$ Fe^{III} with an isotropic d^5 electronic configuration. Were such a signal to originate from the Fe^{III} constituent within the Fe_4 cluster, it would imply essentially no exchange coupling to the Fe^{II} centres. On the basis of the magnetic measurements, we feel that this scenario is highly unlikely. Consequently, we attribute the g = 2.00 signal to the Fe^{III} monomer $[Fe(Himap)_2]NO_3$ that is likely present in small quantities in the powder sample, which shows an isotropic magnetic moment. It is difficult to compare the intensity of this signal with the broad high-frequency components because they are never observed within the same frequency/field window. However, one must recall that the *dI*/*dB* traces correspond to the 2nd derivative of the actual spin susceptibility (proportional to the number of spins). Thus, isotropic g = 2.00 resonances are strongly amplified in the *dI*/*dB* traces relative to broad anisotropic ones (see

below). Therefore, it is quite possible the level of contamination in the powder sample is below the 1% level, consistent with the PXRD studies.

We also comment on a series of reproducible features observed close to zero-field (below 1 T) at the lower frequencies (< 320 GHz). The origin of these signals is not presently clear. Similar signals have been observed in samples that undergo magnetic ordering and, hence, strong changes in magnetization at low fields. Again, this is not consistent with the magnetic properties of **32**, therefore likely signifying additional minor contamination of the powder sample.

The considerable zero-field splitting (ZFS) associated with the broad high-frequency signals is indicative of an appreciable magnetic anisotropy. Therefore, we associate these excitations with the coupled Fe_4 cluster **32**. Indeed, the coincidence of the zero-field offsets, and the temperature dependence of the two resonances suggest that they both originate from the ground state of the molecule. The reason there are two resonances is because the measurement was performed on a powder, i.e. they originate from different crystallite orientations within the powder, corresponding to turning points in the orientation dependence of the anisotropic EPR spectrum. As such, the unique zero-field intercept corresponds to the gap between the ground and first excited spin projection states of the cluster. Interestingly, simulations of the energy levels based on the $D < 0$ parameterization obtained from fits to the magnetic data suggest a ZFS of 300 GHz (10 cm^{-1}) from a set of six near-degenerate ground states to a set of six near degenerate excited states; this differs by only 13% from the value deduced by EPR measurements. Meanwhile, the $D > 0$ parameterization is completely inconsistent with the EPR results: simulations predict a ZFS of just 110 GHz (3.7 cm^{-1}) from the ground to first excited states. Therefore, the EPR measurements strongly favour the negative D parameterization. Indeed, given the relatively low information content of the magnetic data and the level of approximation inherent in the model, agreement to within 13% is very good.

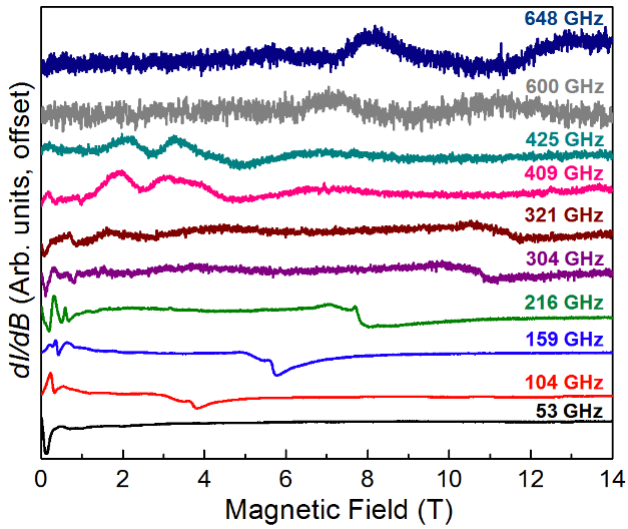

Figure 60 Normalized high-field EPR spectra on a constrained powder of **32**; the spectra were recorded in derivative mode, dI/dB (where I is the absorption intensity), using field modulation and lock-in detection. All measurements were performed at 5 K.

Synthesis and basic characterization of [Fe(naphEen)$_2$]anion

The iron(III) complexes, [Fe(naphEen)$_2$]anion·sol (anion = F, **33**; Cl, **34**; Br **35**; I **36**; BF_4 **37**; NO_3 **38**; ClO_4 **39**; PF_6 **40**; BPh_4 **41**; OTf **42**; NTf_2 **43**; 1,5-npds **44**; 2,6-npds **45** and terephthalate **46**) were synthesized by reacting two equivalents of HnaphEen, made *in situ*, with FeX_3 giving reasonable yields. The complexes are isolated as dark green crystals.

Table 20 IR and UV-Vis spectroscopic data for **33**-**36**.

Compound	IR (cm^{-1})		λ_{max} (nm), ε (M^{-1} cm^{-1}) in CH_2Cl_2
	ν_{N-H}	$\nu_{C=N}$	
[Fe(naphEen)$_2$]F **33**	3130(br)	1617(s)	380 (8230), 425sh (6630), 520 (1940), 684 (1590)
[Fe(naphEen)$_2$]Cl **34**	3088(br)	1616(s)	384 (11750), 420sh (9890), 693 (3500)
[Fe(naphEen)$_2$]Br **35**	3084(br)	1616(s)	383 (12160), 420sh (10100), 696 (3585)
[Fe(naphEen)$_2$]I **36**	3080(br)	1616(s)	384 (9020), 420sh (7620), 701 (2915)

As representative examples spectroscopic data for **33-36** are given in Table 20. IR spectroscopy shows the imine stretch of naphEen is shifted to lower wavenumbers by 16 cm^{-1} on average compared with the free ligand. The N-H stretch moves to higher frequencies by 63 cm^{-1} in **33** and 20 cm^{-1} on average for **34**-**36**. These changes are indicative of coordination of the ligand to Fe(III) and significant hydrogen bonding to the halide anions. The IR spectra also show broad O-H stretches indicating the presence of ethanol or water in the compounds, something confirmed by structural studies.

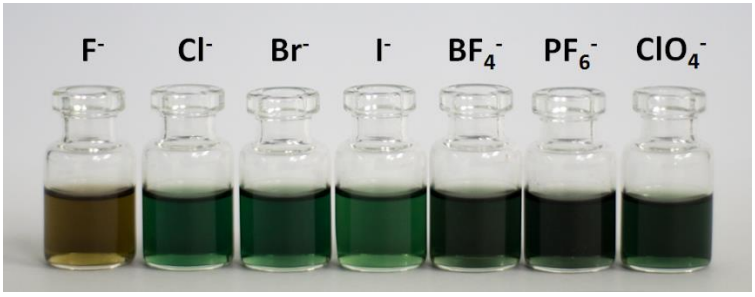

Figure 61 Picture of [Fe(naphEen)$_2$]anion in solution at room temperature.

An interesting feature of these compounds is that the fluoride complex is clearly a different colour in solution, see Figure 61. The UV-Vis spectra of halide complexes in CH_2Cl_2 are shown in Figure 62. All the compounds show three peaks in the UV region, which due to their close similarity with HnaphEen are assigned to $\pi \rightarrow \pi^*$ transitions. In the visible region, **34**-**36** show a single band at *ca*. 700 nm. The intensity of the band and comparison with the closely related [Fe(salEen-X)$_2$]$^+$ (X = H, Br; 3,5-Br) compounds suggest that this band is due to the ligand-to-metal charge transfer transition for low spin Fe(III). The fluoride complex is clearly different with a band at *ca*. 700 nm but an additional band at 520 nm.

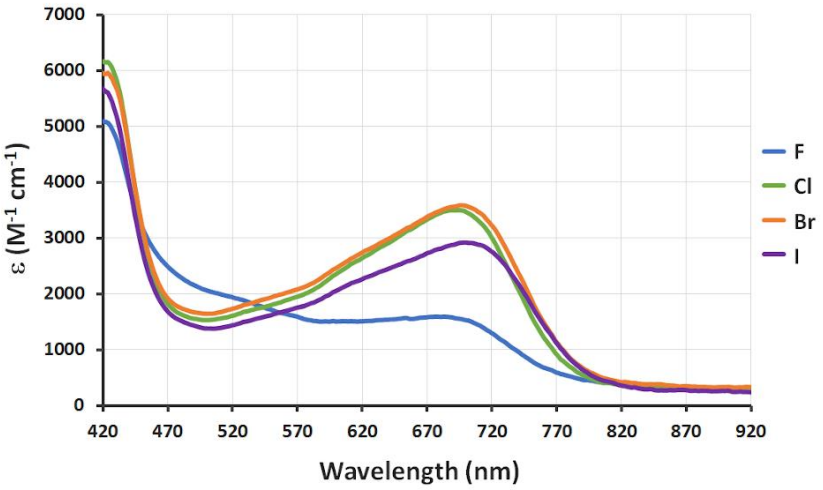

Figure 62 UV-Vis spectra of 0.25 mM $[Fe(naphEen)_2]$halide solutions in CH_2Cl_2 at room temperature.

There are two possible explanations for this, the first being that the band is due to a HS Fe(III) species in solution. The other possibility is that there is an equilibrium between $[Fe(naphEen)_2]F$ and $[Fe(naphEen)_2F]$; the latter having a coordinated F ligand (see Figure 63).

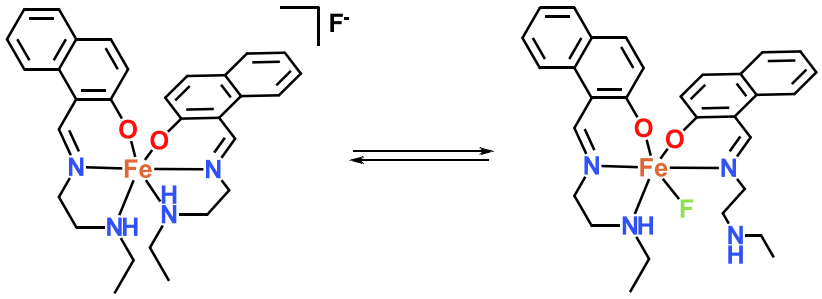

Figure 63 Proposed equilibrium between $[Fe(naphEen)_2]F$ and $[Fe(naphEen)_2F]$.

Computational Investigations of Fe(III)-F Complexes

To investigate the possibility of a $[Fe(naphEen)_2]F$ and $[Fe(naphEen)_2F]$ equilibrium, we have employed density functional theory (DFT) and time-dependent density functional theory (TDDFT) to shed some light on the experimental UV-Vis spectrum of **33**. This work was done in collaboration with Associate Professor Dr. Yuthana Tantirungrotechai at Thammasat University. The $[Fe(naphEen)_2]F$ and $[Fe(naphEen)_2F]$ complexes (see Figure 63) were constructed *in silico* and their UV-Vis spectra were calculated. Based on the HSAB principle and the spectrochemical series, the direct coordination of fluoride to Fe(III) is favourable and leads to HS Fe(III). In contrast, the other halides clearly prefer to act as counteranions only. Figure 64 shows the optimized structure of both $[Fe(naphEen)_2]F$ and $[Fe(naphEen)_2F]$ in solution. The position of the fluoride counteranion in the $[Fe(naphEen)_2]F$ complex was initially identified based on the electrostatic potential of the $[Fe(naphEen)_2]^+$ cation. For $[Fe(naphEen)_2F]$, the F ligand coordinates to Fe(III) which leaves one amino group of the naphEen ligand free.

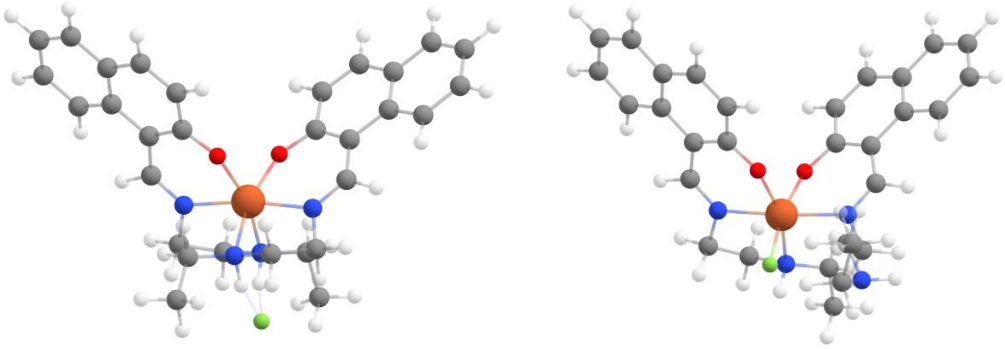

Figure 64 The CPCM-B3LYP*/6-31G(d,p):SDD optimized structures of [Fe(naphEen)$_2$]F and [Fe(naphEen)$_2$F] complexes.

The predicted UV/Vis spectra of [Fe(naphEen)$_2$]F and [Fe(naphEen)$_2$F] are shown in Figure 65. The spectrum of only [Fe(naphEen)$_2$]F in solution, either HS or LS, is ruled out as it yields a transition around 650 nm but cannot reproduce the additional band around 510 nm. Our second hypothesis, that of an equilibrium between [Fe(naphEen)$_2$]F and [Fe(naphEen)$_2$F], is more plausible as a LMCT band is clearly observed for the HS species [Fe(naphEen)$_2$F] at 519 nm which corresponds well to the additional band observed only when fluoride is present. We therefore conclude that the observed spectrum of **33** can be attributed to the equilibrium between [Fe(naphEen)$_2$]F and [Fe(naphEen)$_2$F] in solution.

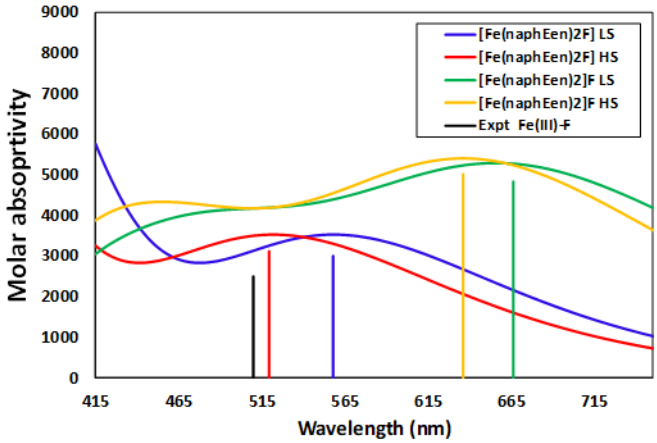

Figure 65 Calculated UV-Vis spectra of [Fe(naphEen)$_2$]F and [Fe(naphEen)$_2$F] complexes in DCM solution using B3LYP*/6-31G(d,p)/SDD method.

Structural studies of [Fe(naphEen)$_2$]anion

The structures of [Fe(naphEen)$_2$]A·sol (sol = H_2O, A = Cl **34**, Br **35**; sol = none, I **36**; sol = $2H_2O$ BF_4 **37**; sol = CH_2Cl_2, NO_3 **38**; sol = $0.5CH_2Cl_2{\cdot}H_2O$, BPh_4 **41**; 1,5-npds **44**; 2,6-npds **45** and terephthalate **46**). The structures of all the compounds have been determined at low and room temperature. In most cases they belong to the monoclinic crystal system but they crystallize in $P2_1/c$ (A = Cl, Br), $C2/c$ (A = BF_4) and most unusually $I2/a$ for the iodide and BPh_4 compounds. The largest anions (**44**-**46**) crystallize in triclinic $P\bar{1}$. In the case of [Fe(naphEen)$_2$]$NO_3{\cdot}CH_2Cl_2$ we find that there are two slightly different phases one with two independent Fe(III) centres, **38a** and the other with a single Fe(III) centre, **38b**.

Interestingly, at room temperature $[Fe(naphEen)_2]Br{\cdot}H_2O$ undergoes a phase change loosing half an equivalent of water and is now in the *C*2/*c* space group. As will be shown below this phase change is a very rare example of a phase change **not** coupled to SCO.

Table 21 Selected bond lengths and octahedral distortion parameters for $[Fe(naphEen)_2]$halide.

	Cl-123 K	**Cl-293 K**	**Br-123 K**	**Br-293 K**	**I**
Fe1-O_{ave}	1.869(4)	1.853(8)	1.880(4)	1.88(3)	1.87(1)
Fe1-N_{imine}	1.924(5)	1.92(1)	1.925(7)	1.96(4)	1.86(3)
Fe1-N_{amine}	2.038(4)	2.029(8)	2.051(7)	2.06(4)	2.09(3)
Σ	38.6	43.7	38.3	25	31.0
Fe2-O_{ave}	1.870(4)	1.859(8)	1.881(4)	1.87(4)	-
Fe2-N_{imine}	1.920(5)	1.92(1)	1.925(7)	1.98(4)	-
Fe2-N_{amine}	2.031(4)	2.019(9)	2.044(6)	2.06(4)	-
Σ	38.0	37.9	36.8	36	-
Fe3-O_{ave}	-	-	-	1.84(4)	-
Fe3-N_{imine}	-	-	-	2.00(4)	-
Fe3-N_{amine}	-	-	-	2.08(5)	-
Σ	-	-	-	32	-

The compounds often crystallize with two independent Fe(III) centres in the asymmetric unit (Figure 66); although one of the phases of $[Fe(naphEen)_2]BF_4{\cdot}2H_2O$, $[Fe(naphEen)_2]NO_3{\cdot}CH_2Cl_2$ and $[Fe(naphEen)_2]I$. The exception is **35** where there are three independent Fe(III) centres in the asymmetric unit. The Fe-N/O bond lengths for almost all compounds are characteristic of the LS state. Even at room temperature most of the compounds show a substantial change in the bond distances suggesting that they do not exhibit SCO up to 293 K. The octahedral distortion parameters are remarkably varied despite the lack of SCO and may suggest that they are not accurate predictors of spin state in these $[Fe(naphEen)_2]^+$ systems.

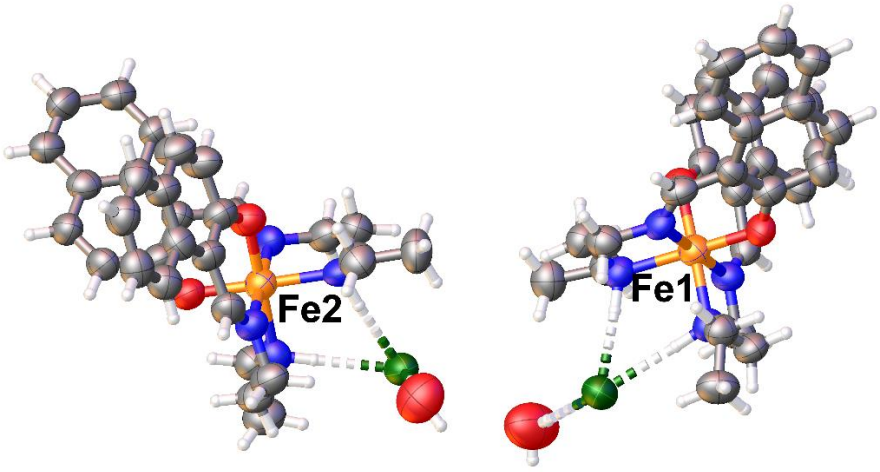

Figure 66 View of the asymmetric unit cell in $[Fe(naphEen)_2]Cl{\cdot}H_2O$ at 123 K.

Table 22 Selected bond lengths (Å) and octahedral distortion parameters (°) for **37** and **38** at 123 K.

	BF_4-123 K	**38a-NO_3-123 K**	**38b-NO_3-123 K**
Fe1-O_{ave}	1.85(1)	1.875(2)	1.898(3)
Fe1-N_{ave} (amine)	2.05(1)	2.045(3)	2.061(4)
Fe1-N_{ave} (imine)	1.93(1)	1.973(3)	1.925(4)
Σ	42.1	37.1	33.8
Fe2-O_{ave}	-	1.870(2)	-
Fe2-N_{ave} (amine)	-	2.048(3)	-
Fe2-N_{ave} (imine)	-	1.922(3)	-
Σ	-	38.8	-

An exception to the above systems is **41** which shows changes in the bond lengths of *ca*. 0.03 Å for the Fe-O bonds and 0.13-0.18 Å for the Fe-N bonds (Table 23). These are consistent with almost complete SCO in the compound (Figure 67). The changes in the Fe-N/O bond distances are on average 0.015 Å (173-123 K), 0.054 Å (198-123 K) and 0.086 Å (223-293 K) and suggest that the SCO occurs principally between 173 and 293 K, i.e. a gradual crossover. The gradual nature of the spin crossover is also evident from the octahedral distortion parameter, Σ.

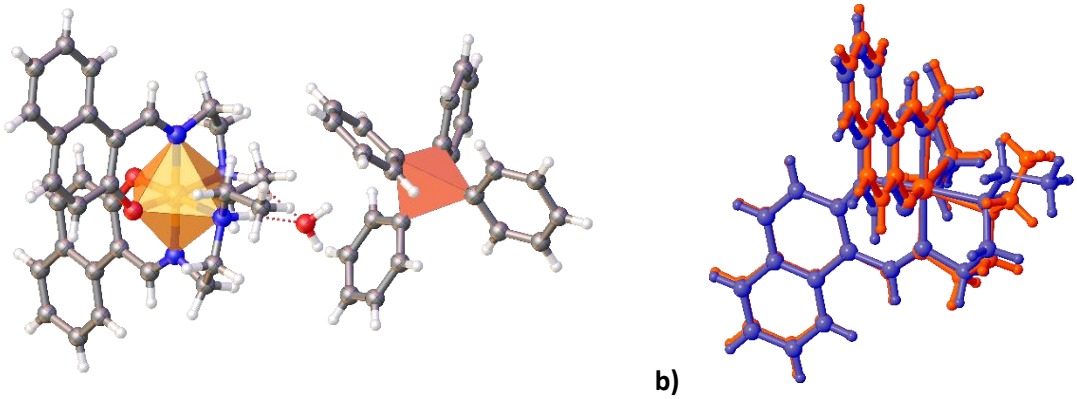

a) **b)**

Figure 67 View of the a) asymmetric unit cell in $[Fe(naphEen)_2]BPh_4 \cdot H_2O \cdot 0.5CH_2Cl_2$ at 123 K and b) an overlay of the structure at 123 and 293 K. The CH_2Cl_2 molecule is omitted for clarity.

One of the most intriguing aspects of the structure is that the ethyl group of the naphEen ligand undergoes a rotation that is coupled to SCO (Figure 67b). Using the structures at 173, 198 and 223 K we are able to show that this change in the orientation of the ethyl group is gradual and not abrupt. This broadly mirrors the changes in the Fe-N/O bond lengths noted above. To the best of our knowledge this is the first time SCO has been found to be coupled to a peripheral group in this way.

Table 23 Selected bond lengths (Å) and octahedral distortion parameters (°) for **41**.

	123K	**173K**	**198K**	**223K**	**293K**
Fe-O1	1.877(3)	1.895(7)	1.890(7)	1.924(6)	1.911(4)
Fe-O2	1.871(3)	1.875(6)	1.889(6)	1.904(6)	1.904(3)
Fe-N1	1.940(4)	1.953(7)	2.003(7)	2.035(7)	2.070(4)
Fe-N2	2.044(4)	2.065(6)	2.118(6)	2.156(6)	2.208(3)

Fe-N3	1.913(4)	1.932(7)	1.978(7)	2.009(7)	2.045(4)
Fe-N4	2.044(4)	2.070(6)	2.145(7)	2.185(6)	2.226(4)
Σ	42.2	44.2	48.6	60.8	71.8

A feature that most of the structures share is that the anion is held in an embrace by the amine hydrogens through N-H···anion interactions (see Figure 68). In all cases the H-bonding is slightly asymmetric and becomes increasingly weak on going from Cl to I. This mirrors the trend found in [Fe(saltrien-OH)]halide and is consistent with the lower electronegativity of the halide on descending the group. The interaction with the BF_4 is particularly strong with H···O contacts less than 2.0 Å and an additional C-H···O interaction holding the anion in place (Figure 68a).

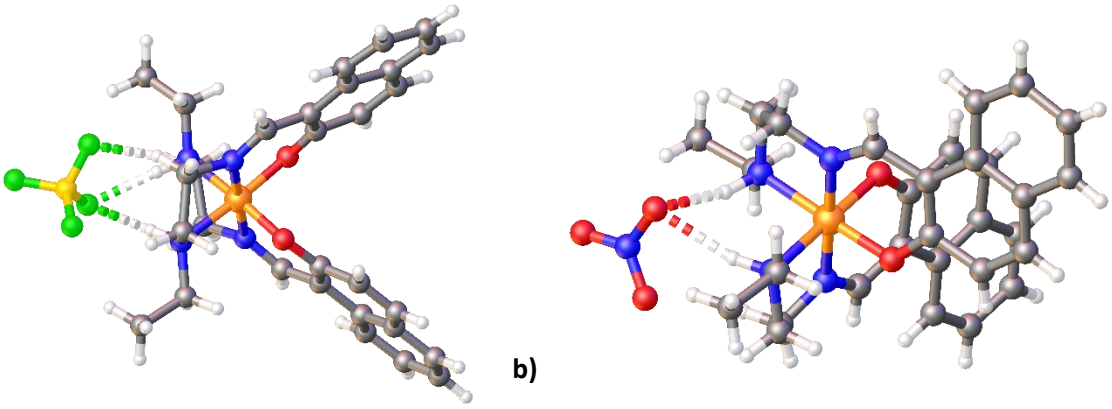

a) **b)**

Figure 68 View of the N-H···anion hydrogen bonds in a) $[Fe(naphEen)_2]BF_4{\cdot}2H_2O$ and b) $[Fe(naphEen)_2]NO_3{\cdot}CH_2Cl_2$.

The packing in the structures is composed of supramolecular Fe squares (Figure 69) linked via a combination of C-H···O, π-π and C-H···π interactions. The C-H···π contacts are generally quite angular and consequently weak. Intriguingly, the π-π interactions only occur in the Fe1 squares while C-H···O contacts link the Fe2 centres in **34** and **35** (at 123 K). The squares connect to form a 2D plane with each plane containing only one type of Fe(III) centre. Surprisingly, even **35-293 K** has these squares despite the extra Fe(III) centre.

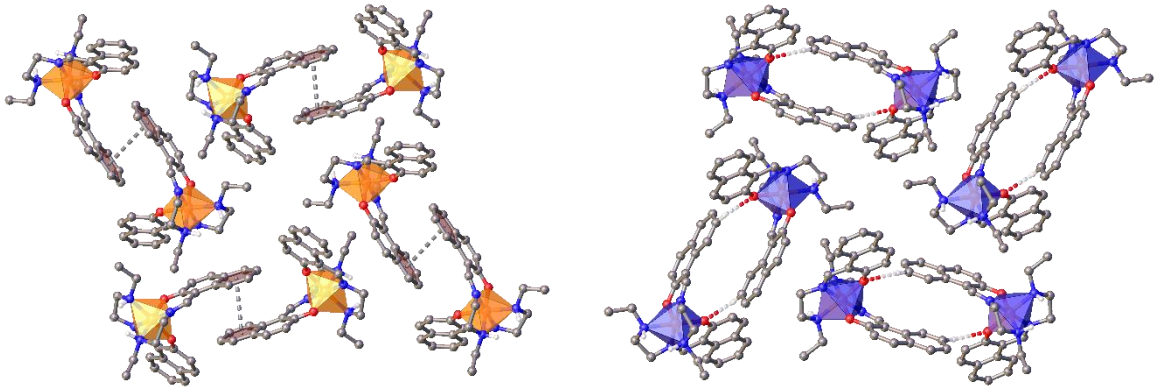

a) **b)**

Figure 69 View of a) the Fe1 and b) Fe2 squares that make up the packing in **34**. The Fe1 and Fe2 centres are coloured orange and purple, respectively.

The 2D planes that are formed from these supramolecular squares are stacked in ABAB layers for **34** and **35-123 K**, while the layers are identical in **36**. Looking at these planes side-on it is clear that the stacking creates a 'Butterfly' shaped pocket where the anions and water molecules reside (Figure 70). Comparing **35-123 K** and **35-293 K** rather than the Fe1 and Fe2 layers in the former each plane contains all three Fe centres with 1D Fe1-Fe2-Fe3 chains. Neighbouring chains run in the opposite direction (Figure 70b). The other difference is that the 'Butterfly' motif is more symmetric at 293 K than at 123 K. The results suggest that despite the relative weakness of the various interactions and the different anions, combined these create a robust motif in the $[Fe(naphEen)_2]^+$ series.

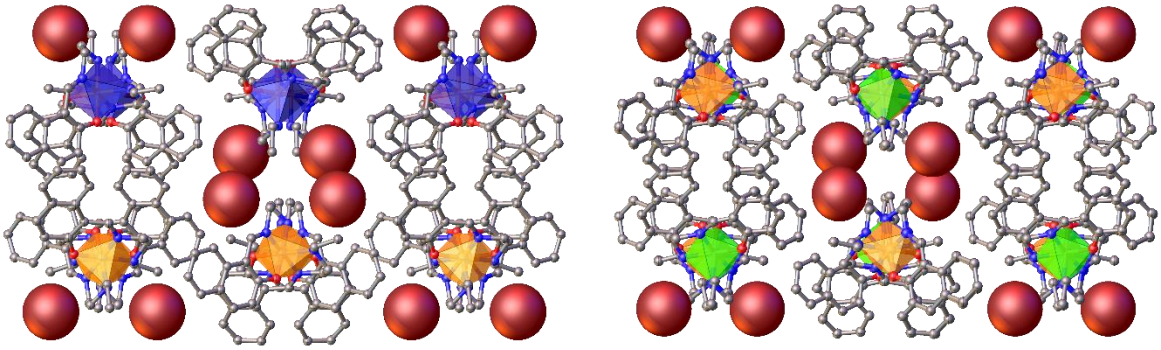

Figure 70 View of the 'Butterfly' motif common to the $[Fe(naphEen)_2]$halide series shown for **35** at a) 123 K (viewed down the *c*-axis) and b) 293 K (viewed along the [101] plane). The Fe1, Fe2 and Fe3 centres are coloured orange, purple and green, respectively.

Very large anions are however able to disrupt this motif. In the case of the naphthalenedisulfonate anions there is an interesting ladder structure of the cations separated by the large anions (Figure 71). The relative positions of the 'ladders' is slightly different for the two anions which seems to be related to optimizing the H-bonding interactions between the dianion and the $[Fe(naphEen)_2]^+$ cations. The cations are mostly linked through multiple C-H···π interactions.

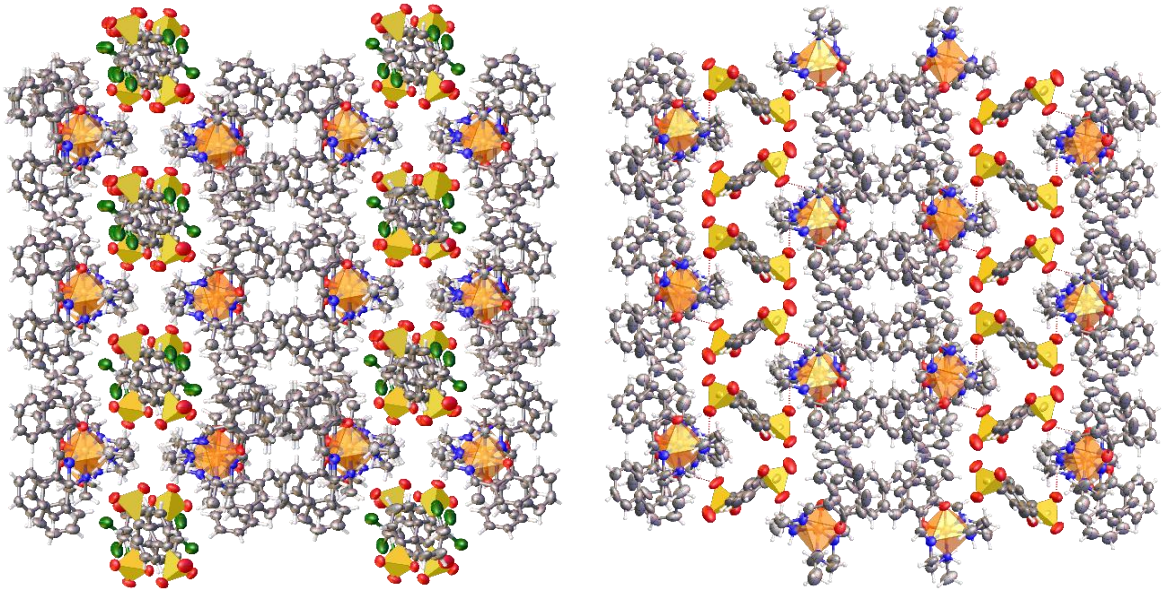

Figure 71 Packing in $[Fe(naphEen)_2]_2$[1,5-npds]·CH_2Cl_2 and $[Fe(naphEen)_2]_2$[2,6-npds].

The packing in the BPh_4 complex differs markedly from all of these systems and instead the cations are generally well separated by the BPh_4 anion. The cations again form ladders but this time are connected to one another through π-π interactions. The anions are interdigitated within these ladders and also between them forming a 2D sheet. It is probably this unique packing arrangement that permits this complex to undergo spin crossover while other members of the family remain stubbornly LS.

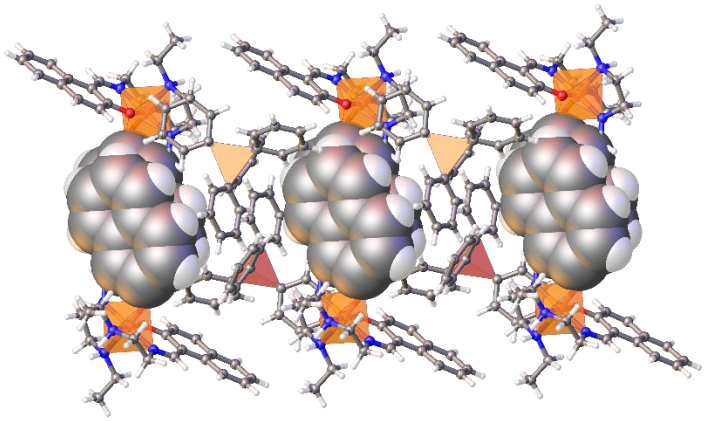

Figure 72 View of the 1D ladders in $[Fe(naphEen)_2]BPh_4 \cdot H_2O \cdot 0.5CH_2Cl_2$.

Magnetic studies of $[Fe(naphEen)_2]$anion

The magnetic studies of $[Fe(naphEen)_2]A$ have been explored using SQUID magnetometry. The results are shown in Figure 73 and confirm that the vast majority of the compounds are trapped in the LS state which the exception of NTf_2 complex which is HS only. The larger anions despite their crystal structures seem to have $\chi_M T$ values slightly above that expected for the full LS state being *ca*. 1.0 cm^3 mol^{-1} K. In the BF_4, ClO_4, PF_6 and 2,6-npds complexes there is a clear and very gradual increase in $\chi_M T$ reaching 2.3, 2.5, 2.8 and 1.8 cm^3 mol^{-1} K, respectively.

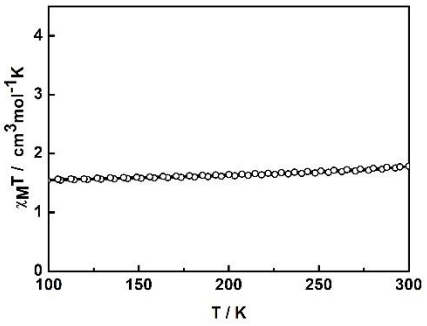

F

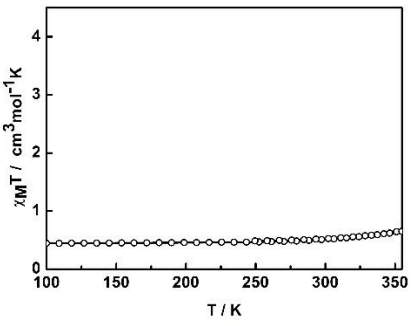

Cl..

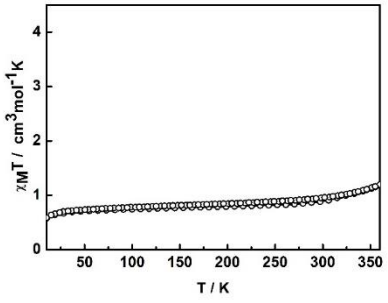

Br

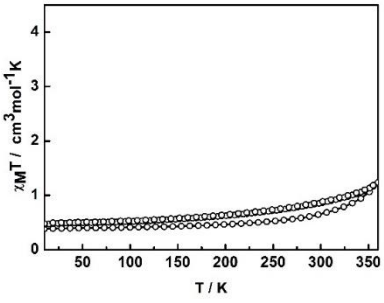

I

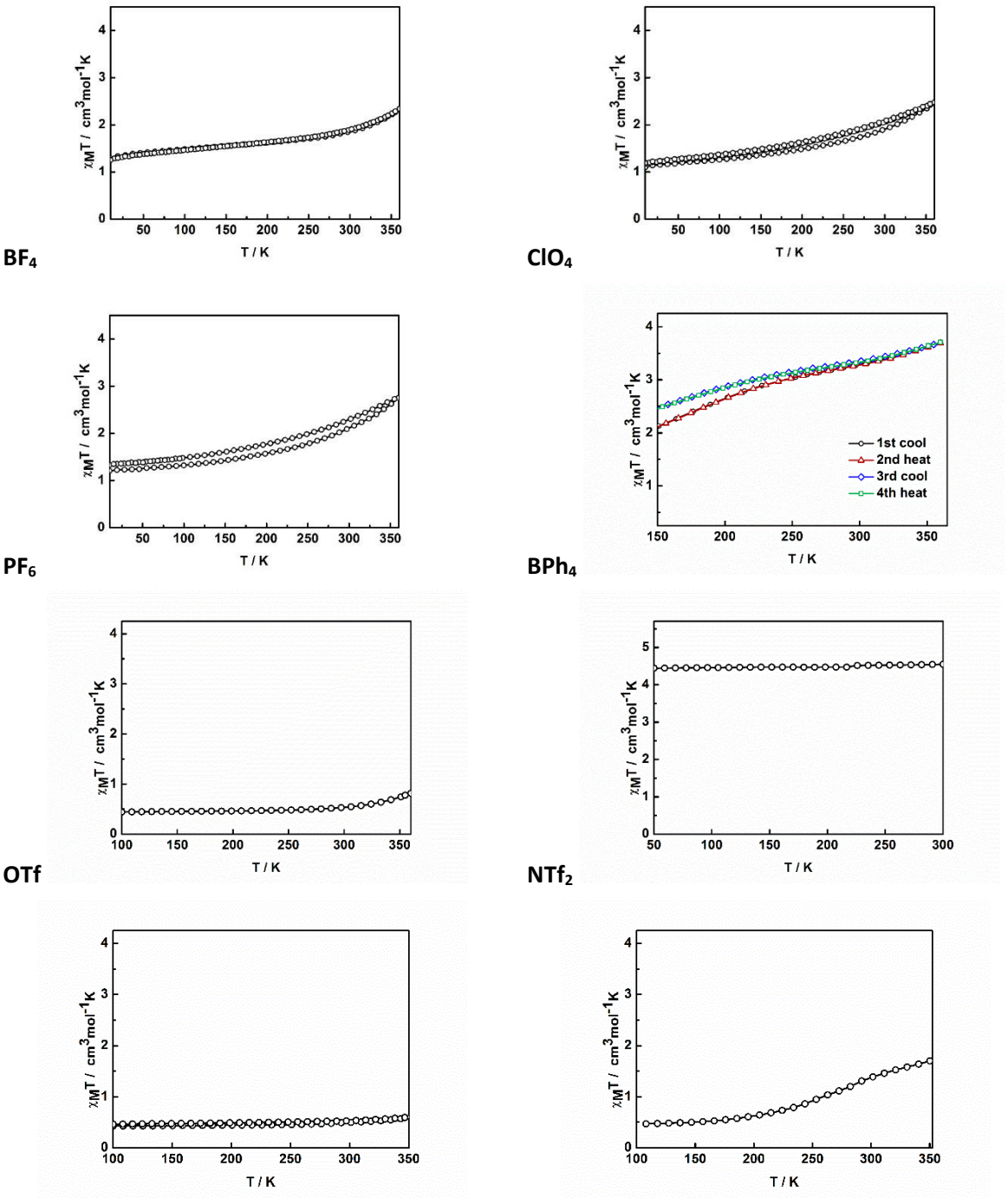

Figure 73 $\chi_M T$ vs. T plots of [Fe(naphEen)$_2$]X.

In the case of the BPh_4 analogue, the SCO is found to be incomplete, this time at both ends. The reason for the difference in the structure which shows complete SCO and the magnetic measurements is probably due to solvent loss during the SQUID measurement.

To explore the behaviour of these complexes without the complicating influence of solvent we have undertaken solution state studies. The VT-NMR studies employing the Evan's method indicate that indeed the compounds are SCO active in $CDCl_3$. The results also show that the degree of SCO is anion dependent with the F being ca. 30% HS at 300 K while the Cl complex is ca. 10% HS at the same

temperature (Figure 74). The PF_6 anion which would be expected to interact most weakly with the cation shows the largest overall change from fully LS to 20% HS. Sadly, due to instrumental limitations we've been unable to explore these at higher temperatures.

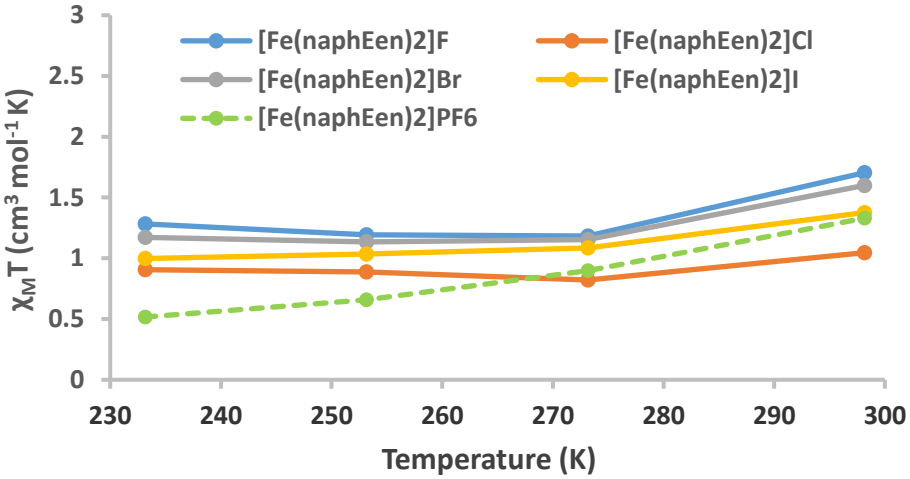

Figure 74 Magnetic profiles of selected [Fe(naphEen)$_2$]anion complexes.

Synthesis and structural studies of [Fe(naphBzen)$_2$]anion

The fact that large anions could lead to SCO in [Fe(naphEen)$_2$]anion series led us to explore a related ligand system which we have termed HnaphBzen, where the ethyl group is replaced by a benzyl group. The ligand has been reacted with a wide range of iron(III) salts yielding [Fe(naphBzen)$_2$]A (A = F **47**, Cl **48**, Br **49**, I **50**, BF_4 **51**, NO_3 **52**, ClO_4 **53**, PF_6 **54**) in good yields. In common with the [Fe(naphEen)$_2$]A complexes above the compounds are dark green but are more crystalline. We have obtained the structure of all compounds except the fluoride and BF_4 derivatives. The compounds **48**, **49** and **52** all crystallize in tetragonal $I4_1/a$, while **53** crystallizes in monoclinic $P2_1/c$ and **54** in orthorhombic *Pbca*. Uniquely, [Fe(naphBzen)$_2$]I **50** crystallizes in monoclinic *Pc*. Compounds **48-50** and **52** all contain 2 Fe(III) centres in the asymmetric unit while **53** and **54** have a single centre (Figure 75). [Fe(naphBzen)$_2$]ClO_4·H_2O·CH_2Cl_2 is interesting in that the compound crystallizes with and without water in the same lattice with the occupancy being ca. 75% for the H_2O solvate.

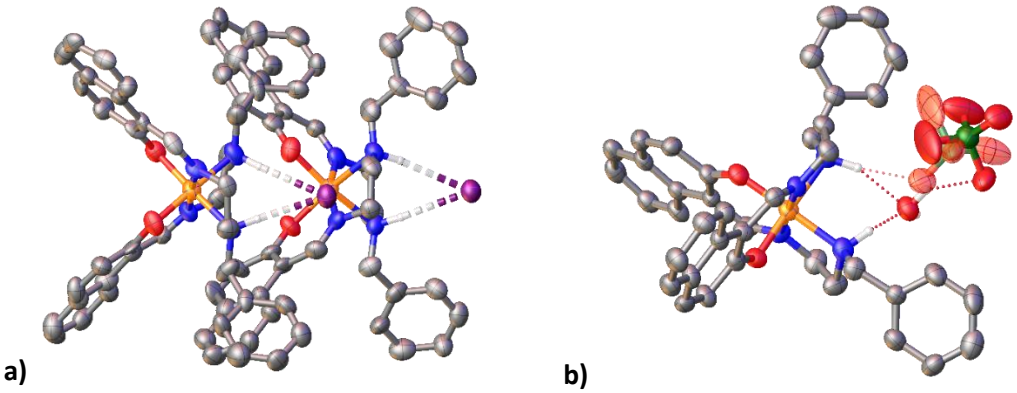

Figure 75 Asymmetric unit of a) [Fe(naphBzen)$_2$]I and b) [Fe(naphBzen)$_2$]ClO_4·H_2O·CH_2Cl_2. In **53** CH_2Cl_2 is omitted in the interest of clarity and the minor ClO_4 anion is shown in lighter colours.

Table 24 Selected bond lengths and octahedral distortion parameters for [Fe(naphBzen)$_2$]anion.

	Cl-150 K	**Cl-340 K**	**Br-150 K**	**Br-350 K**	**NO_3-123 K**	**NO_3-293 K**
Fe1-O_{ave}	1.885(3)	1.879(10)	1.883(7)	1.928(14)	1.933(6)	1.942(5)
Fe1-N_{imine}	1.931(3)	1.989(10)	1.906(8)	1.993(17)	2.066(6)	2.058(5)
Fe1-N_{amine}	2.061(3)	2.135(8)	2.056(8)	2.122(15)	2.167(6)	2.190(5)
Σ	47.1	51.2	51.1	67.8	76.0	77.4
Fe2-O_{ave}	1.889(3)	1.896(9)	1.917(9)	1.908(13)	1.871(5)	1.893(5)
Fe2-N_{imine}	1.973(4)	2.107(10)	2.030(9)	2.071(17)	1.924(6)	1.998(5)
Fe2-N_{amine}	2.088(3)	2.184(9)	2.132(9)	2.176(14)	2.043(6)	2.135(5)
Σ	46.2	74.1	66.5	86.5	50.4	58.6

As **48**, **49** and **52** are isostructural these structures will be discussed first. All the structures have been collected at, at least 2 temperatures. The Fe-N/O bond lengths at low temperatures are in most cases short typically 1.89, 1.91-1.97 and 2.04-2.09 Å for the phenoxide, imine and amine bonds, respectively (Table 24). These values are all suggestive of LS or mostly LS Fe(III) centres. The exception is the Fe1 centre in [Fe(naphBzen)$_2$]NO_3 where the bond lengths are more typical of HS Fe(III). Heating to room temperature, or beyond leads in almost all cases to a lengthening of the Fe-N/O bond lengths consistent with SCO in these systems. In the case of the halide compounds both spin centres undergo changes but these are more pronounced in **48** than in **49**. The Fe2 bond lengths are both characteristic of the full HS state, while Fe1 is still a little too short and suggests a mixture HS and LS, something confirmed by magnetic studies. The [Fe(naphBzen)$_2$]NO_3 Looking at the octahedral distortion parameter, Σ, this varies from 46.2-86.5 and although broadly indicative of the spin state it does not appear to be an accurate predictor. As an example, **48** at 340 K and **49** at 350 K have similar Fe-ligand bond lengths but Σ differs by 16.6°.

The Fe-ligand bond lengths in **50** at 100 K are consistent with LS Fe(III). Heating the crystals to 160 K results in an increase in the Fe1-O and Fe1-N_{imine} and Fe1-N_{amine} bond distances by 0.06, 0.15 and 0.16 Å, respectively (Table 25). In contrast, the Fe2 bond lengths change very little which is unsurprising given that it is already HS at 100 K. We have also collected the structure close to the spin transition at 120 K. Interestingly, the Fe-ligand bond lengths are typical of HS Fe(III) but are actually longer than they are 160 K and are suggestive of subtle change that occur just after (or just before) actual SCO. We have noticed such effects before in [Fe(qsal-I)$_2$]OTf·MeOH. We also find that $\Delta\Sigma$ is *ca*. 30° and is consistent with complete SCO.

The structure of [Fe(naphBzen)$_2$]PF_6 has been determined at 150, 200, 250, 300 and 350 K and shows significant changes only at 250, 300 and 350 K. The SCO is clearly gradual and the bond lengths indicate that even at 350 K it is incomplete. The octahedral distortion parameter shows very small changes even decreasing up to 250 K and is again poorly correlated with spin state.

Table 25 Selected bond lengths and octahedral distortion parameters for **50** and **54**.

	I-100K	**I-120K**	**I-160K**	**PF_6-150K**	**PF_6-200K**	**PF_6-250K**	**PF_6-300K**	**PF_6-350K**
Fe1-O_{ave}	1.885	1.932	1.943	1.876	1.876	1.878	1.89	1.901
Fe1-N_{imine}	1.926	2.082	2.08	1.916	1.923	1.958	1.987	2.007
Fe1-N_{amine}	2.066	2.234	2.227	2.064	2.073	2.095	2.135	2.171
Σ	43.3	75.2	73.3	40	39.5	36.4	42.4	51.4
Fe2-O_{ave}	1.939	1.932	1.941	-	-	-	-	-
Fe2-N_{imine}	2.053	2.067	2.072	-	-	-	-	-
Fe2-N_{amine}	2.266	2.249	2.241	-	-	-	-	-
Σ	65.7	72.2	69.5	-	-	-	-	-

The packing in the three structures is very similar and involves H-bonding of the amine group with the Cl, Br and NO_3 anions. In the case of the nitrate anion, the H-bonds are between two of the three oxygen atoms with the plane of the anion perpendicular to the plane of the N-H bonds. Interestingly, the H-bonds are always asymmetric and seem to be stronger for the HS cation compared with the LS cation.

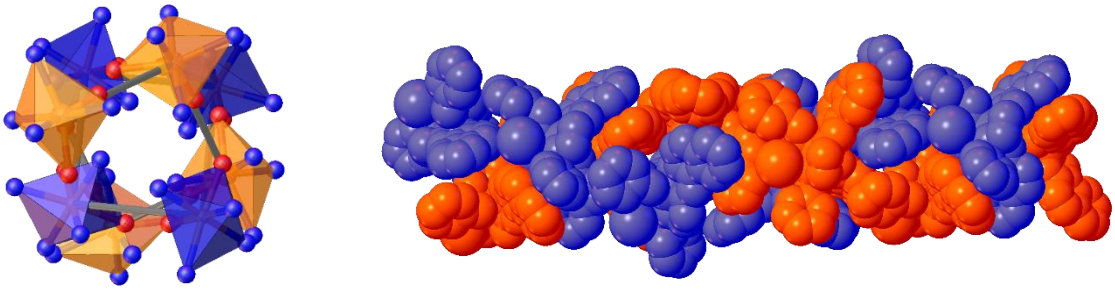

a) **b)**

Figure 76 View of the spiral chains in $[Fe(naphBzen)_2]NO_3$ along the a) *c*-axis and b) *b*-axis at 123 K.

Looking more broadly the cations are linked through a network of C-H···π, C-H···O and angular π-π interactions with each individual Fe centre linked into a helix and wrapped around the helix of the other Fe centres; reminiscent of the two strands in DNA (Figure 76). It appears that this arrangement limits the SCO in $[Fe(naphBzen)_2]NO_3$ as the anion is larger than chloride or bromide and thus only 50% SCO can occur. The shape of the anion is also important as the spherical Cl and Br show unit cell differences of 0.251 and 0.232 Å in the *c*-axis which is coincident with the two helices. By comparison, **52** shows a change of 0.517 Å, twice that of **48** and **49**.

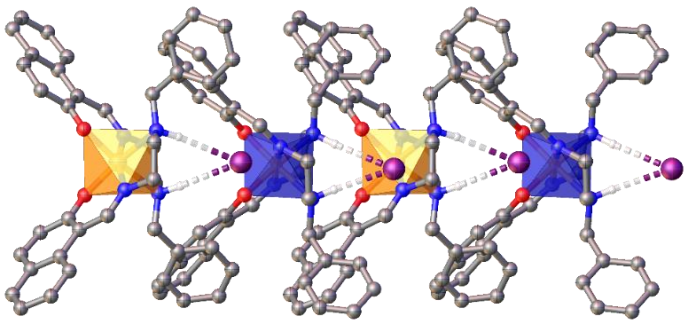

a)

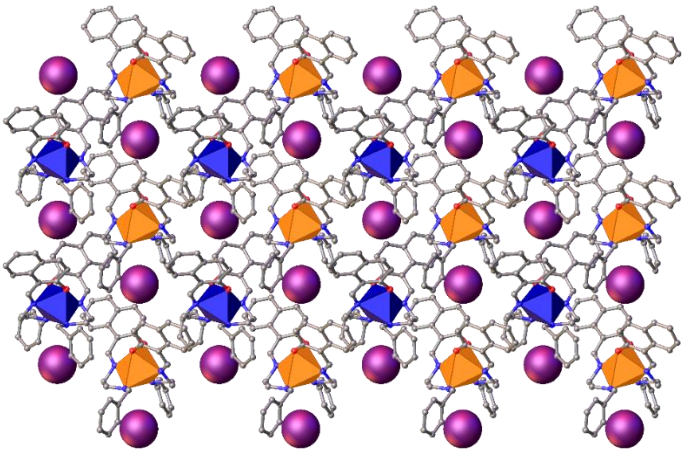

b)

Figure 77 View of a) the ID chain in **50** showing the HS (orange) and LS (blue) centres in the chain and b) the 2D sheets with the iodide shown as a spacefill model.

The packing in $[Fe(naphBzen)_2]I$ **50** is very different and this time involves 1D chains of the cations which at 150 K contain alternating LS and HS centres (Figure 77a). Neighbouring chains are linked via C-H···π interactions to form a 2D sheet with a checkerboard pattern of LS and HS centres (Figure 77b). Further C-H···π interactions then link these sheets to create a highly cooperative supramolecular network. It is noteworthy that the small increase in the radius of Br to I, 1.96 to 2.20 Å, totally changes the structure and greatly increases the cooperativity closely resembling that of the previously reported SCO compound, $[Fe(salEen\text{-}Br)_2]ClO_4$ which also exhibits abrupt SCO.

The packing in **53** is different again and involves a ladder like arrangement of the cations with the ClO_4 anion and CH_2Cl_2 in between the ladders (Figure 78). As with the other members of the series C-H···π interactions are dominant in connecting the $[Fe(naphBzen)_2]^+$ cations.

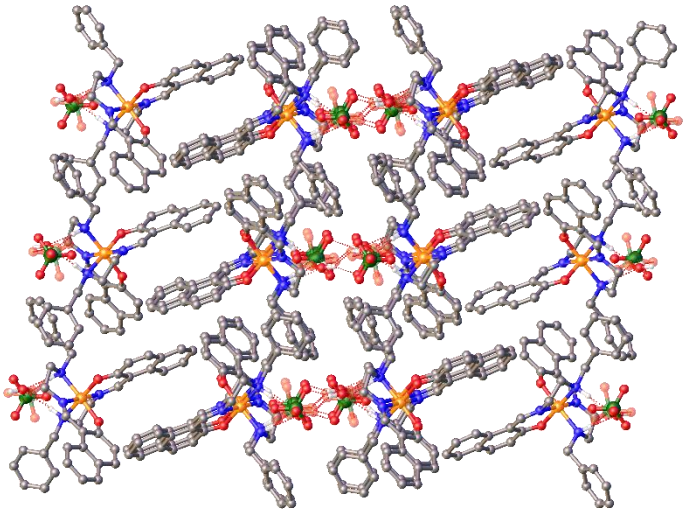

Figure 78 View of the ladders in $[Fe(naphBzen)_2]ClO_4 \cdot H_2O \cdot CH_2Cl_2$.

Finally the packing in **54** consists of 1D chains of the $[Fe(naphBzen)_2]^+$ cations held together by strongly angular C-H···π interactions (Figure 79). Neighbouring chains are connected via C-H···F and C-H···π interactions involving the PF_6 anion and naphthalenyl groups.

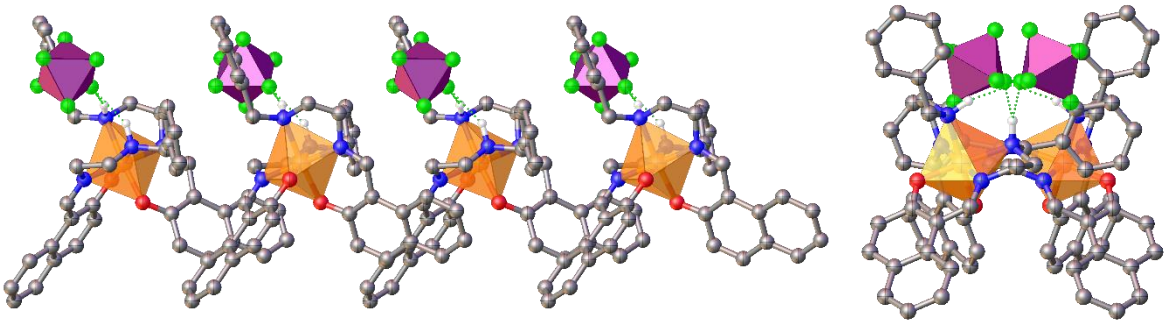

a) b)

Figure 79 View of the 1D chains viewed along the a) *a*-axis and b) *b*-axis in **54** at 150 K.

Magnetic studies of [Fe(naphBzen)$_2$]anion

The compounds **47**-**54** have all been studied using SQUID magnetometry with $\chi_M T$ vs. T plots presented in Figure 80. All the complexes with the exception of the ClO_4 are SCO active, although magnetic studies suggest that the complex is stuck in 50% HS state rather than the LS state found by X-ray crystallography. This is most probably due to solvent loss.

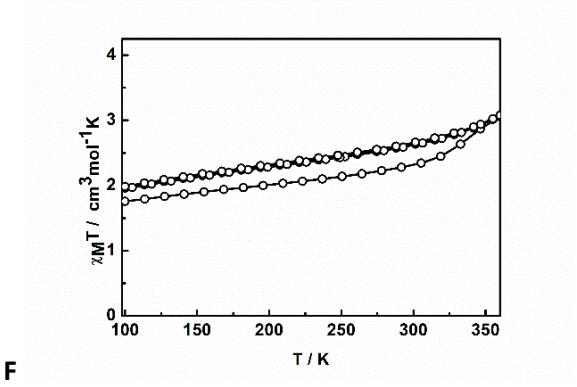

F

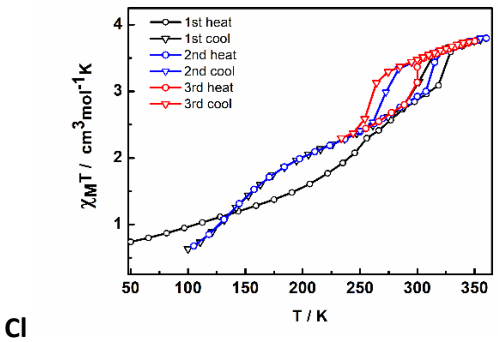

Cl

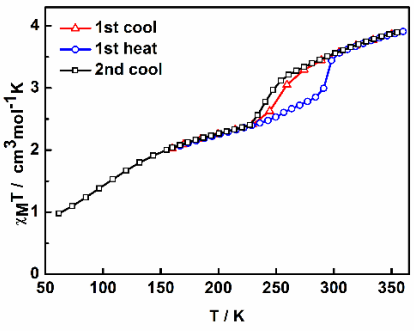

Br

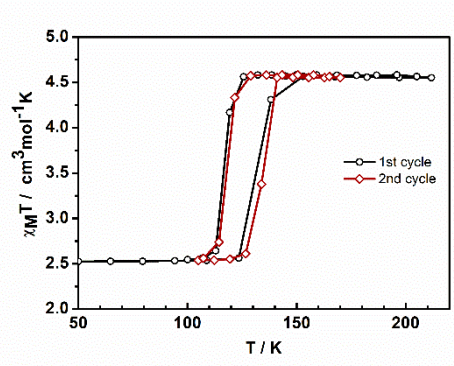

I

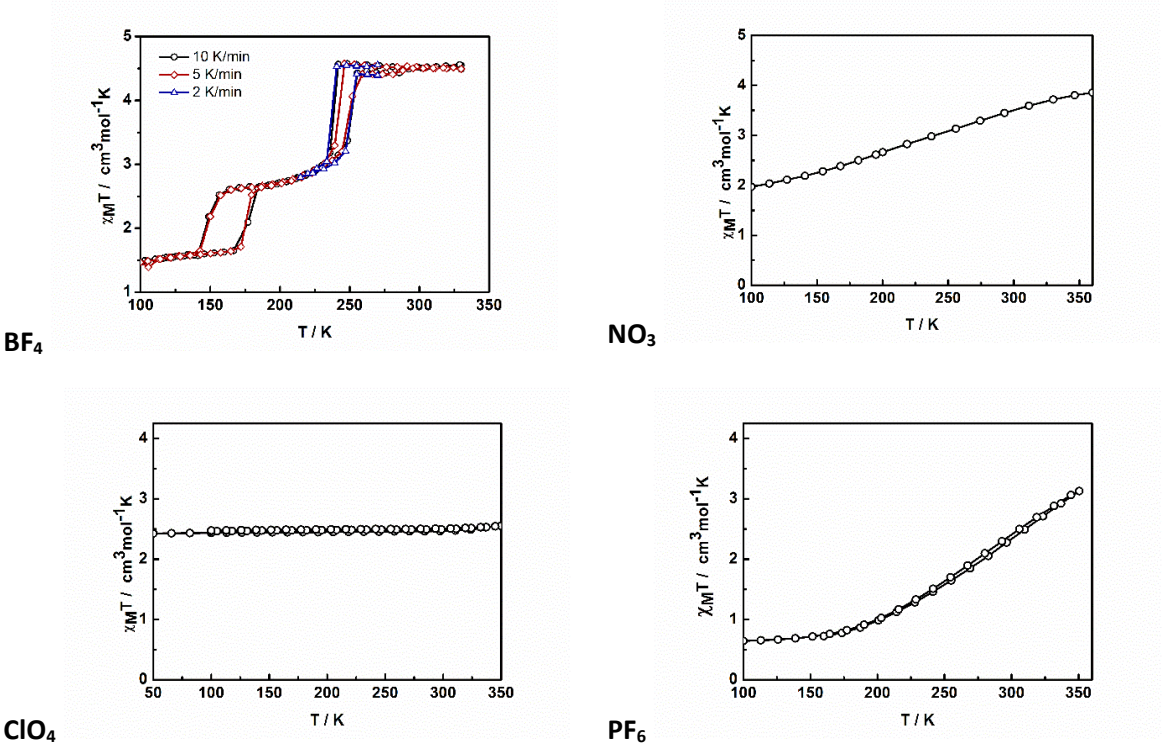

Figure 80 χ_MT vs. T plots of [Fe(naphBzen)$_2$]anion complexes.

Interestingly, [Fe(naphBzen)$_2$]F also shows very little SCO and is predominantly in a 50% HS state. Given the prevalence of 2 independent Fe(III) centres found in the structures we hypothesize that we have a HS and LS centre in **47** and **53**. The remaining halide complexes all show SCO and surprisingly hysteresis. In the case of **48** and **49** the hysteresis is quite wide but involves only 15-20% SCO. In contrast, **50** exhibits a stable 50% SCO with a hysteresis of 20 K with $T_{1/2}(\uparrow)$ = 135 K and $T_{1/2}(\downarrow)$ = 115 K. The presence of hysteresis is uncommon and suggests that the strong 1D chains formed in the structure of **50** are essential to give abrupt SCO.

Very recent results on [Fe(naphBzen)$_2$]I indicate that while the compound does not undergo LIESST. However, irradiation of the sample at 830 or 980 nm shows a reverse-LIESST to a full LS state that is not accessible thermally (Figure 81a). Re-heating results in an increase in χ_MT at $T_{1/2}(\uparrow)$ = 60 K to the [HS-LS] state after which it follows the original magnetic profile. Cooling results in a return to the LS state with $T_{1/2}(\downarrow)$ = 30 K and a hysteresis of 30 K, in what is termed a light-induced thermal hysteresis. This is the first time that *hidden hysteresis* has been discovered in an Fe(III) SCO complex.

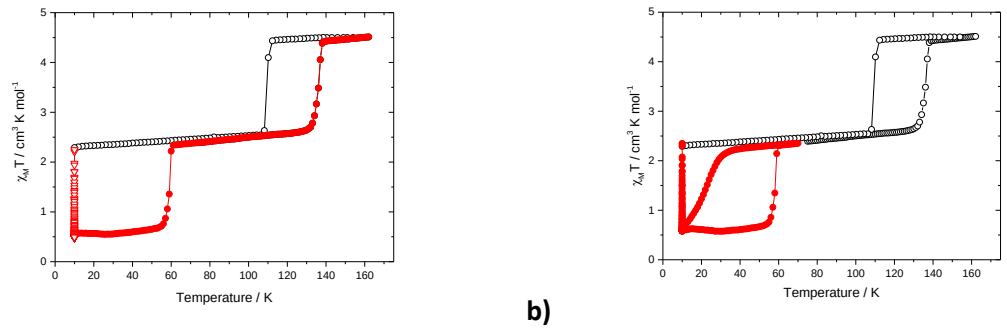

Figure 81 a) Reverse-LIESST and warming curves to 160 K and b) reverse-LIESST and LITH curves showing the hidden hysteresis between the [LS-LS] and [HS-LS] states.

Intriguingly, $[Fe(naphBzen)_2]BF_4$ exhibits an unprecedented stepped SCO from 25% HS to 50% HS with $T_{1/2}(\uparrow)$ = 177 K and $T_{1/2}(\downarrow)$ = 149 K and consequently a hysteresis of 28 K. A 50% HS plateau of *ca*. 70 K exists before $\chi_M T$ increases again to the full HS state with $T_{1/2}(\uparrow)$ = 252 K and $T_{1/2}(\downarrow)$ = 239 K (ΔT = 13 K). To date very few compounds exist where SCO is stepped and even fewer where there is hysteresis in both steps. At this time we don't have the structure so it is unclear to us whether symmetry breaking, a phase change or four independent centres are responsible for the observed SCO.

The complexes **52** and **54** both exhibit gradual SCO, the former going from *ca*. 50% HS to *ca*. 80 HS% and consistent with the structure above. The latter compound undergoes a gradual but very linear SCO from 100% LS at 200 K to ca. 60% HS at 350 K. As the structure contains no solvent it would be expected to reach full HS at around 450 K. The linearity of the SCO could potentially be useful in molecular thermometer using the magnet moment.

Experimental

All chemicals were purchased from TCI Chemicals or Sigma-Aldrich, with the exception of Hqsal-X, (3-pyridyl)-5-salicylaldehyde, (4-pyridyl)-5-salicylaldehyde and 4,6-dihydroxy-5-methylisophthalaldehyde which were made by literature procedures. In the interests of brevity, and because the compounds are prepared similarly, we include only representative syntheses.

Synthesis of Hqsal-5-(3-py)

(3-pyridyl)-5-salicylaldehyde (199 mg, 1.0 mmol) was dissolved in CH_2Cl_2 (10 ml) giving a pale yellow solution. 8-aminoquinoline (144 mg, 1.0 mmol) was added resulting in an almost immediate colour change to orange. The solution was stirred for 2 hours and the solvent removed. The orange oil was triturated with hexane giving an orange solid, 263 mg (81%).

Hqsal-5-(4-py) was prepared in a similar way in 68% yield. The lower yield is due to the higher solubility of the ligand in hexane.

Synthesis of H_2bqimbd

4,6-dihydroxy-5-methylisophthalaldehyde (181 mg, 1.0 mmol) was dissolved in CH_2Cl_2 (10 ml) to give a yellow solution. 8-aminoquinoline (288 mg, 2.0 mmol) was added to the solution causing the solution to turn orange-brown. Stirring for 2 hours resulted in a small amount of solid precipitating. Addition of Et_2O (10 ml) resulted in further brown solid precipitating which was isolated by filtration, 272 mg (63%).

Synthesis of HnaphEen

2-hydroxy-1-naphthaldehyde (172.2 mg, 1 mmol) and N-ethylethylenediamine (104 μl, 1 mmol) were mixed in methanol (10 ml) giving a yellow solution. The solution was stirred for 4 hours and then reduced dryness on a rotary evapourator giving a yellow-orange gum (quantitative yield).

HnaphBzen is isolated in similar way in 94% yield as a bright yellow solid.

Synthesis of [Fe(qsal-X)$_2$]A (A = sulfonate anions)

A solution of Hqsal-F (158.8 mg, 0.6 mmol) in CH_2Cl_2 (3 ml) with NEt_3 (83.1 μL, 0.6 mmol) was placed at the bottom of the tube. A buffer layer of EtOH (3 ml) was placed at the middle. $FeCl_3$ (48.7 mg, 0.3 mmol) was dissolved in EtOH (3 ml) and AgOTs was added (251.5 mg, 0.9 mmol). The mixture was stirred for 3 minutes, filtered and layered over the blank EtOH. Black crystals were obtained after 4-5 days and filtered yielding 90.9 mg (40%).

[Fe(qsal-Cl)$_2$]OTs, [Fe(qsal-Br)$_2$]OTs and [Fe(qsal-I)$_2$]OTs were prepared in a similar way.

In the case of the [Fe(qsal-X)$_2$]$_2$[npds] series, AgOTs was replaced with either sodium 1,5-naphthalenedisulfonate or sodium 2,6-naphthalenedisulfonate giving the six [Fe(qsal-X)$_2$]$_2$[npds] complexes as black crystals.

Synthesis of [Fe(qsal-X)$_2$]NTf$_2$

[Fe(qsal-I)$_2$]NO_3 was prepared by mixing a CH_2Cl_2 solution of Hqsal-I (374 mg, 1.0 mmol) with a MeOH solution of $Fe(NO_3)_3{\cdot}9H_2O$ (202 mg, 0.5 mmol) and then adding NEt_3 (139 μl, 1.0 mmol). This lead to formation of microcrystals of [Fe(qsal-I)$_2$]NO_3 (410 mg, 0.47 mmol) which were isolated by filtration. [Fe(qsal-I)$_2$]NO_3 was dissolved in heated MeOH (8 ml) to give a black solution. $LiNTf_2$ (136 mg, 0.47 mmol) was dissolved in MeOH (2 ml) and added dropwise to the [Fe(qsal-I)$_2$]NO_3 solution resulting in almost immediate precipitation of a dark brown solid which was collected by filtration and washed with cold MeOH (3 x 3 ml). The solid was redissolved in a 1:1 MeCN:CH_2Cl_2 solution (20 ml in total) filtered through celite and then left to evaporate slowly giving thin black needles (304 mg, 60% yield based on [Fe(qsal-I)$_2$]NO_3).

[Fe(qsal-Cl)$_2$]NTf_2 and [Fe(qsal-Br)$_2$]NTf_2 were prepared similarly.

Synthesis of [Fe(naphEen)$_2$]anion

A stirred solution of HnaphEen was prepared from 2-hydroxy-1-naphthaldehyde (104 mg, 0.6 mmol) and N-ethylethylenediamine (63 μl, 0.6 mmol) in ethanol (3 ml) giving a yellow suspension. NEt_3 (84 μl, 0.6 mmol) was added, followed by a solution of $FeCl_3$ (49 mg, 0.3 mmol) in water (5 ml). A green precipitate formed and the reaction was left to stir for 2 hrs. The green solid was filtered through a Buchner funnel, washed with 4 ml water and dried. The solid was dissolved in CH_2Cl_2 (15 ml) and filtered through a celite plug. The solution was evaporated to 3 ml and hexane (10 ml) layered on top. After 10 days dark green crystals formed which were collected, washed with EtOH and Et_2O, 81 mg (43 %).

The remaining [Fe(naphEen)$_2$]anion compounds were prepared in a similar way either from commercially available iron(III) starting materials such as $Fe(NO_3)_3$ or by preparing the appropriate iron(III) salt from $FeCl_3$ and $NaBF_4$, $AgPF_6$, KOTf, $LiNTf_2$, Na_2[1,5-npds], Na_2[2,6-npds] or Na_2[terephthalate]. In all cases recrystallization from CH_2Cl_2-hexane gives the compounds as dark green crystals. The exception is [Fe(naphEen)$_2$]I whose synthesis is detailed below.

Synthesis of [Fe(naphEen)$_2$]I

A stirred solution of HnaphEen was prepared *in situ* from 2-hydroxy-1-naphthaldehyde (172 mg, 1.0 mmol) and N-ethylethylenediamine (105 μl, 1.0 mmol) in EtOH (3 ml). NEt_3 (139 μl, 1.0 mmol) was added, followed by a solution of $Fe(NO_3)_3 \cdot 9H_2O$ (202 mg, 0.5 mmol) in EtOH (3 ml). After 2 hrs of stirring at room temperature the reaction was heated to 60 °C and a hot ethanolic solution of KI (250 mg, 1.5 mmol) added. Heating was discontinued after 2 hrs and the reaction left to cool. The solution was evaporated to 3 ml on a rotary evaporator and water (5 ml) added. The green precipitate that formed was filtered through a Buchner funnel, washed with water (4 ml) and dried for 2 hrs. The solid was dissolved in CH_2Cl_2 (5 ml), filtered and layered with hexane (10 ml). Dark green crystals formed after two weeks which were filtered off and washed with EtOH and Et_2O, 214 mg (57 %).

Synthesis of [Fe(naphBzen)$_2$]anion

A stirred suspension of HnaphBzen was prepared from 2-hydroxy-1-naphthaldehyde (104 mg, 0.6 mmol) and N-benzylethylenediamine (72 μl, 0.6 mmol) in ethanol (3 ml) giving a yellow suspension. NEt_3 (84 μl, 0.6 mmol) was added, followed by a solution of $FeCl_3$ (49 mg, 0.3 mmol) in water (5 ml). A green precipitate formed and the reaction was left to stir for 2 hrs. The green solid was filtered through a Buchner funnel, washed with 4 ml water and dried. The solid was dissolved in CH_2Cl_2 (5 ml) and filtered through a celite plug and hexane (10 ml) layered on top. After 4 days dark green crystals formed which were collected, washed with EtOH and Et_2O, 281 mg (67 %).

The remaining [Fe(naphBzen)$_2$]anion complexes are prepared in a similar way to the corresponding [Fe(naphEen)$_2$]anion compounds.

3. Project Outcomes

3.1 Publications

1. D. Sertphon, P. Harding, K. S. Murray, B. Moubaraki, N. F. Chilton, S. Hill, J. Marbey, H. Adams, C. G. Davies, G. N. L. Jameson and D. J. Harding, Self-assembly of a mixed-valence Fe^{II}-Fe^{III} tetranuclear star, accepted in *Dalton Trans*., 2018, **47**, doi: 10.1039/c8dt01241e (IF = 4.029).
2. D. Sertphon, K. S. Murray, W. Phonsri, J. Jover, E. Ruiz, S. G. Telfer, A. Alkaş, P. Harding and D. J. Harding, Slow relaxation of magnetization in a bis-*mer*-tridentate octahedral Co(II) complex, *Dalton Trans*., 2018, **47**, 859 (IF = 4.029).
3. W. Phonsri, P. Harding, K. S. Murray, B. Moubaraki and D. J. Harding, Spin crossover in mixed ligand iron(III) complexes, *New J. Chem.*, 2017, **41**, 13747 (IF = 3.277).
4. N. Phukkaphan, D. L. Cruickshank, K. S. Murray, W. Phonsri, P. Harding and D. J. Harding, Hysteretic spin crossover driven by anion conformational change, *Chem. Commun*., 2017, **53**, 9801 (IF = 6.319).
5. W. Phonsri, P. Harding, L. Liu, S. G. Telfer, K. S. Murray, B. Moubaraki, T. M. Ross, G. N. L. Jameson and D. J. Harding, Solvent modified spin crossover in an iron(III) complex: phase changes and an exceptionally wide hysteresis, *Chem. Sci*., 2017, **8**, 3949 (IF = 8.668).
6. **Front cover**: J. Sirirak, D. Sertphon, W. Phonsri, P. Harding and D. J. Harding, Comparison of density functionals for the study of the high spin low spin gap in Fe(III) spin crossover complexes, *Int. J. Quantum Chem*., 2017, **117**, e25362 (IF = 2.920).

7. D. J. Harding, P. Harding and W. Phonsri, Spin Crossover in Iron(III) Complexes, *Coord*. *Chem*. *Rev*., 2016, **313**, 38 (IF = 13.324).
8. **Invited article**: P. Insiti, P. Jitthiang, P. Harding, K. Chainok, R. Chotima, J. Sirirak, S. Blackwood, A. Alkaş, S. G. Telfer, and D. J. Harding, Substituent modulated packing in octahedral Ni(II) complexes, *Polyhedron*, 2016, **114**, 242 (IF = 1.926).
9. D. Sertphon, D. J. Harding, P. Harding, K. S. Murray, B. Moubaraki, H. Adams, A. Alkaş and S. G. Telfer, Substituent influenced spin crossover in Fe(III) quinolylsalicylaldiminates, *Eur. J. Inorg. Chem*., 2016, 432 (IF = 2.444).

A book chapter has been written and will be published by Elsevier in June 2018.

1. D. J. Harding, An Overview of Spin Crossover Nanoparticles, in *Novel Magnetic Nanostructures: Unique Properties and Applications*, Edited by E. Rentschler, N. Domracheva and M. Caporali.

Four papers are in preparation:

1. T. Boonprab, P. Harding, K. S. Murray, W. Phonsri, S. G. Telfer, A. Alkaş, R. Ketkaew, Y. Tantirungrotechai, and D. J. Harding, Predominately low spin iron(III) Schiff base complexes: a phase change uncoupled to spin crossover to be submitted to *CrystEngComm*.
2. S. E. Lazaro, P. Harding, S. G. Telfer, W. Phonsri, K. S. Murray and D. J. Harding, Abrupt spin crossover in a series of iron(III) complexes: halogen bonding and the key role of the π-π chains to be submitted to *Inorganic Chemistry*.
3. S. E. Lazaro, P. Harding, U. Boonyang, S. G. Telfer, W. Phonsri, K. S. Murray and D. J. Harding, Reverse micelle synthesis and magnetic properties of iron(III) nanomaterials to be submitted to the *Journal of Materials Chemistry C*.
4. D. Sertphon, P. Harding, K. S. Murray, B. Moubaraki, L. Liu, S. G. Telfer and D. J. Harding, Solvent effects on the spin crossover properties of iron(II) imidazolylimine complexes, invited contribution for a special issue on spin crossover in *Crystals*.

3.2 Presentations

Oral Presentations

1. D. J. Harding, Designed Iron(III) Spin Crossover Materials, PACCON2018, 7th-9th February 2018, Hat Yai, Thailand.
2. S. E. Lazaro, Iron(III) SCO nanoparticles with abrupt transitions, PACCON2018, 7th-9th February 2018, Hat Yai, Thailand.
3. S. E. Lazaro, Abrupt spin crossover in [Fe(qsal-X)$_2$]OTs·solvent, MRS-Thailand 2017, 31st October-3rd November 2017, Chiang Mai, Thailand.
4. Keynote speaker, D. J. Harding, Designing Molecular Switches: A Molecular Magnetism Approach, 12th Joint Conference on Chemistry, 19th-20th September 2017, Semarang, Indonesia.
5. Invited speaker, D. J. Harding, Designing Room Temperature Spin Crossover Materials, 6th Asian Conference on Coordination Chemistry, 23rd-28th July 2017, Melbourne, Australia.
6. D. J. Harding, Solvent modified spin crossover in Fe(III) complexes, 8th Advanced Materials & Nanotechnology conference, 12th-16th February 2017, Queenstown, New Zealand.

7. Workshop Tutor, D. J. Harding, Spin Crossover in Iron(III) Complexes, SANZ-O-MAG2 Workshop, 8th-10th February 2017, University of Otago, Dunedin, New Zealand.
8. Invited speaker, D. J. Harding, Coordination Complexes as Molecular Switches: Adventures in Molecular Magnetism, PACCON2017, 2nd-3rd February 2017, Bangkok, Thailand.
9. Y. Janpathompong, Investigation of Fe(III) spin crossover complexes using X-ray crystallographic studies, PACCON2017, 2nd-3rd February 2017, Bangkok, Thailand.
10. D. Sertphon, Solvent control spin crossover in $[Fe(qsal\text{-}4\text{-}OMe)_2]NCS\cdot solvent$, PACCON2017, 2nd-3rd February 2017, Bangkok, Thailand.
11. D. J. Harding, Spin Crossover in Heteroleptic $[Fe(qsal\text{-}Cl)(qsal\text{-}Br)]^+$ Complexes, 42nd International Conference on Coordination Chemistry, 3rd-8th July 2016, Brest, France.
12. Invited speaker, D. J. Harding, A versatile tridentate Schiff base for spin crossover and high spin self-assembled iron stars, PACCON2016, 9th-11th February 2016, Bangkok, Thailand.
13. D. Sertphon, Base controlled Co^{II} single-ion magnet (SIM) and low spin Co^{III} complex formation, PACCON2016, 9th-11th February 2016, Bangkok, Thailand.
14. Invited speaker, D. J. Harding, Spin Crossover in Heteroleptic $[Fe(qsal\text{-}Cl)(qsal\text{-}Br)]^+$ Complexes, 24th-27th November 2015, Molecular Designs for Advanced Materials: Workshop and Conference, Chiang Mai University, Chiang Mai, Thailand.
15. D. J. Harding, Spin Crossover in Heteroleptic $[Fe(qsal\text{-}Cl)(qsal\text{-}Br)]^+$ Complexes, 6th November 2015, University of Queensland, Australia – seminar.
16. D. J. Harding, Spin Crossover and Single Molecule Magnets of Iron and Cobalt with a Tridentate Schiff Base, 4th and 5th November 2015, University of Melbourne and Queensland University of Technology, Australia – seminar.
17. D. J. Harding, Positional Control of Spin Crossover Behaviour in $[Fe(qsal\text{-}X\text{-}OMe)_2]^+$ Materials: the Importance of π-π Chains, 3rd November 2015, Monash University, Australia – seminar.

Poster presentations

1. S. E. Lazaro, Controlled Synthesis of $[Fe(qsal)_2]NO_3$ Nanoparticles in a Reverse Microemulsion, 8th Advanced Materials & Nanotechnology conference, 12th-16th February 2017, Queenstown, New Zealand.
2. P. Harding, Rare Octahedral Co(II) Single-Ion Magnets, SANZ-O-MAG2 Workshop, 8th-10th February 2017, University of Otago, Dunedin, New Zealand.
3. D. J. Harding, Solution and Solid State Spin Crossover in Iron(III) Complexes, SANZ-O-MAG2 Workshop, 8th-10th February 2017, University of Otago, Dunedin, New Zealand.

3.3 Academic collaborations

The complexity of this project has required us to build new collaborations which are detailed below:

1. Professor Stephen Hill, National High Magnetic Field Laboratory, Florida State University, USA, High-Field EPR spectroscopy studies.
2. Professor Eliseo Ruiz, Universitat de Barcelona, Spain, Computational modelling of magnetic behaviour.
3. Professor Aron Walsh at Imperial College London, UK, Computational materials modelling.
4. Professor Natalia Domracheva at the Kazan Research Centre of the Russian Academy of Sciences, High-field EPR spectroscopy studies of SCO compounds.

5. Dr. Nicholas Chilton, University of Manchester, UK, Computational modelling of magnetic behaviour.
6. Dr. David Turner, Monash University, Australia, Synchrotron X-ray crystallographic studies.
7. Professor Sally Brooker, University of Otago, New Zealand, Iron(III) spin crossover dimers.

3.4 Academic activities

1. Session chair, 43rd Congress on Science and Technology of Thailand, 17th-19th October 2017, Bangkok, Thailand
2. Session chair, 8th Advanced Materials & Nanotechnology conference, 12th-16th February 2017, Queenstown, New Zealand.
3. Poster judge and session chair, SANZ-O-MAG2 Workshop, 8th-10th February 2017, University of Otago, Dunedin, New Zealand.
4. Poster judge, PACCON2017, 2nd-3rd February 2017, Bangkok, Thailand.

Appendix

Dalton Transactions

COMMUNICATION

View Article Online
View Journal

Check for updates

Cite this: DOI: 10.1039/c8dt01241e

Received 30th March 2018,
Accepted 27th April 2018

DOI: 10.1039/c8dt01241e

rsc.li/dalton

Published on 30 April 2018. Downloaded by University of Bath on 03/05/2018 11:19:01.

Self-assembly of a mixed-valence Fe^{II}–Fe^{III} tetranuclear star†

Darunee Sertphon, ‡[a] Phimphaka Harding, [a] Keith S. Murray, [b] Boujemaa Moubaraki,[b] Nicholas F. Chilton, [c] Stephen Hill,[d,e] Jonathan Marbey,[d,e] Harry Adams,[f] Casey G. Davies,[g] Guy N. L. Jameson [g,h] and David J. Harding *[a]

A unique self-assembled mixed-valence Fe^{II}–Fe^{III} tetranuclear star has been comprehensively characterised showing a large magnetic anisotropy at the peripheral Fe^{II} centres, ferromagnetic coupling between the iron centres and field-induced SMM behaviour.

The design and study of transition metal clusters with useful magnetic properties remains a considerable challenge. Single molecule magnets (SMMs) are of particular interest as they exhibit slow relaxation of magnetization with a barrier to spin reversal proportional to the uniaxial magnetic anisotropy and the squared spin of the cluster.[1–8] The magnetic bistability of these clusters potentially permits their use in data storage applications and quantum computation.[9–13] To be useful SMMs must be robust and retain their magnetic bistability when deposited on a surface.[14,15] This is often not the case, for example $[Mn_{12}O_{12}(O_2CR)_{16}(H_2O)_4]$ undergoes reduction upon deposition on Au(111) and loss of SMM behaviour.[16]

A series of particularly robust Fe_4^{III} SMMs was first reported in 1999, and is based on the star shaped $[Fe_4(dpm)_6(OMe)_6]$ (dpm = 2,2,6,6-tetramethyl-3,5-heptanedionate) molecule.[17] Replacing the methoxides with two tripodal ligands, H_3L = R-C$(CH_2OH)_3$ gives $[Fe_4(dpm)_6(L)_2]$ with improved SMM characteristics due to a change in symmetry from C_2 to D_3 resulting in an increase in the helical pitch of the $Fe(O_2Fe)_3$ core, thus increasing the magnetic anisotropy.[18,19] The robustness of these Fe_4 stars has allowed them to be deposited on gold,[20–24] silicon[25] and boron nitride.[26] Unusually, their slow magnetic relaxation is retained on surfaces, which is the first step towards making the above applications a reality.

More recently, tridentate dianionic O,N,O ligands have been used notably the chiral *R* or *S*-2-[(*o*-hydroxyphenyl)-methylideneamino]-2-phenylethanol ligands which impart their chirality on the cluster, $[Fe_4(L')_6]$.[27–29] Varying the substituents on the ligands allows tuning of the magnetic relaxation barrier (U_{eff}) from 0.5–11.0 K.[29] As with $[Fe_4(dpm)_6(L)_2]$, subtle differences in the Fe coordination spheres are responsible for the differing magnetic properties.

Similar stars are formed using the O,N,O donor ligand *N*-methyldiethanolamine (*N*-Me-dea). The star forms by self-assembly of $[Fe(N\text{-Me-dea})_2]^-$ around Fe^{III} to give $[Fe\{Fe(N\text{-Me-dea})_2\}_3]$ with U_{eff} = 14.2 K.[30,31] In an analogous way, Takahashi *et al.*, in an attempt to make spin crossover hybrid materials, instead isolated $[Fe\{Fe(phsal)_2\}_3]$ (phsal = *N*-(2-hydroxyphenyl)-salicylaldimine).[32] Despite its structural similarity to the stars above, it is not a SMM.

In our continuing interest in tridentate N_2O donor ligands we selected 2-((1*H*-imidazol-2-yl)methyleneamino)phenol (2-H_2imap)[33] with the aim of preparing Fe^{III} spin crossover complexes. Unexpectedly, the primary product is a unique mixed-valence Fe^{II}–Fe^{III} star. Herein, we report the structure, magnetic and spectroscopic properties of $[Fe_4(2\text{-Himap})_6][NO_3]_3$ **1**.

Complex **1** was synthesized by layering a MeOH solution of $Fe(NO_3)_3{\cdot}9H_2O$ on top of a warmed solution of the ligand, 2-H_2imap and NEt_3 (see ESI† for details). After one week black crystals of the self-assembled cluster $[Fe_4(2\text{-Himap})_6][NO_3]_3$ **1** are formed. Temperature and time are critical in isolating the cluster, as heating above 40 °C or harvesting the crystals too early gives the Fe^{III} monomer, $[Fe(2\text{-Himap})_2]NO_3{\cdot}0.7MeOH$ **2** (Fig. S1, S2, S8 and Table S1†). IR spectroscopic studies of **1** and **2** reveal imine and nitrate stretches in the expected posi-

[a]*Functional Materials and Nanotechnology Centre of Excellence, Walailak University, Thasala, Nakhon Si Thammarat, 80160, Thailand. E-mail: hdavid@mail.wu.ac.th*
[b]*School of Chemistry, Monash University, Clayton, Victoria, 3800, Australia*
[c]*School of Chemistry and Photon Science Institute, The University of Manchester, Oxford Road, Manchester M13 9PL, UK*
[d]*Florida State University, Department of Physics, Tallahassee, FL 32306, USA*
[e]*National High Magnetic Field Laboratory, 1800 E. Paul Dirac Drive, Tallahassee, FL 32310, USA*
[f]*Department of Chemistry, University of Sheffield, Sheffield, S3 7HF, UK*
[g]*Department of Chemistry & MacDiarmid Institute for Advanced Materials and Nanotechnology, University of Otago, PO Box 56, Dunedin, 9054, New Zealand*
[h]*School of Chemistry, Bio21 Molecular Science and Biotechnology Institute, 30 Flemington Road, The University of Melbourne, Parkville, Victoria 3010, Australia*

†Electronic supplementary information (ESI) available: Experimental details, crystallographic details & figures, magnetic fits and CASSCF-SO calculations details, Mössbauer and EPR spectroscopic figures. CCDC 1830689 and 1830690. For ESI and crystallographic data in CIF or other electronic format see DOI: 10.1039/c8dt01241e

‡Now at: Department of Chemistry, Faculty of Science, Rangsit University, Phaholyothin Rd., Muang, Pathum Thani, 12000, Thailand

Published on 30 April 2018. Downloaded by University of Bath on 03/05/2018 11:19:01.

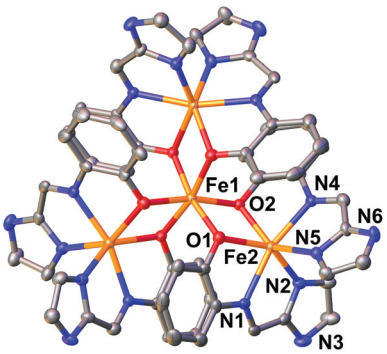

Fig. 1 View of the star shaped cluster $[Fe_4(2\text{-Himap})_6][NO_3]_3$. Hydrogen atoms are omitted for clarity.

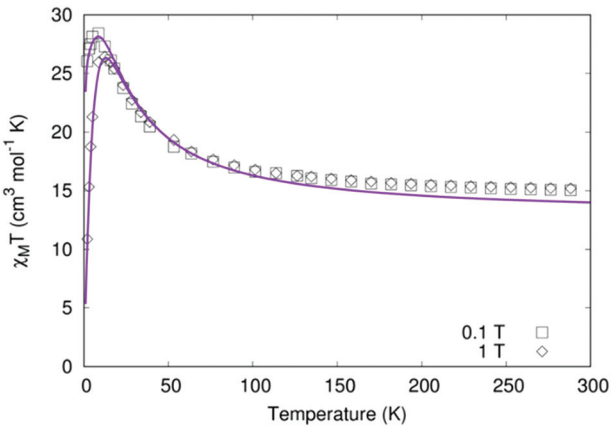

Fig. 2 $\chi_M T$ *vs.* T plot of **1**. The purple lines represent the best fit (D = −7.09 cm^{-1}) with the parameters given in the text.

tions, with $\nu_{C=N}$ being 18 cm^{-1} lower in **2** than for **1**. A similar difference in the imine stretch is observed in the Co^{II}/Co^{III} redox pair $[Co(2\text{-Himap})_2]^{0/+}$.[34] X-ray crystallography reveals that **1** is a star shaped cluster crystallizing in cubic $Pa\bar{3}$ (Fig. 1). PXRD studies indicate that the single crystal structure is representative of the bulk material and ESI-MS studies in MeOH indicate that the cluster is stable in solution (see ESI, Fig. S4 and S5†). The Fe1–O bond lengths are between 1.998–2.005(3) Å while the Fe2–N/O bond distances are much longer, 2.133–2.184(4) Å. This is consistent with the Fe1 and Fe2 centres being Fe^{III} and Fe^{II} respectively. This is, to the best our knowledge, the first example of a mixed-valence Fe star cluster. The Fe1···Fe2 distance is 3.225 Å, while the Fe2···Fe2* distance is 5.586 Å and these are similar to the equivalent distances in other Fe^{III}_4 stars. Each molecule is chiral due to intramolecular π–π interactions between the 2-Himap ligands (Fig. S3†), but as both enantiomers are present the structure overall is achiral.

Mössbauer spectra of **1** were recorded at multiple temperatures and show the presence of two subspectra above 20 K; a quadrupole doublet consistent with HS Fe^{II} and a singlet assigned to the HS Fe^{III} centre (Fig. S6 and Table S2†). The ratio of the intensity of the two species is ~2 : 1, which is lower than the expected 3 : 1 ratio. We believe this is due to differing Lamb–Mössbauer factors of the Fe^{II} and Fe^{III} centres causing the relative intensities of the two species to not be equivalent, particularly at higher temperatures.[35]

As the temperature is lowered the signals broaden, demonstrated by the temperature dependence of the full-width-at-half-maximum (FWHM) values for the transitions (Γ, Fig. S7d†). Below ~15 K, the Fe^{III} signal undergoes intermediate relaxation and broadens, but does not completely collapse into the baseline. In contrast, the Fe^{II} signal remains visible as a distinct quadrupole doublet at all investigated temperatures; these changes mirror the magnetic transition (*vide infra*).

Magnetic measurements for **1** show $\chi_M T$ = 15.02 cm^3 K mol^{-1} at 300 K with $\chi_M T$ increasing slowly to a maximum of 28.43 cm^3 K mol^{-1} at *ca.* 8 K before decreasing rapidly (Fig. 2). The $\chi_M T$ value at 300 K is consistent with one non-interacting Fe^{III} and three non-interacting Fe^{II} centres, and the low temperature data shows evidence of a ferromagnetically coupled ground state. The minor temperature dependence of $\chi_M T$ above 150 K suggests that the intramolecular magnetic interactions are relatively weak; this, coupled with the presence of a possible orbital contribution to the magnetic moment of high-spin octahedral Fe^{II} centres make the interpretation of the magnetic data fraught with difficulty. In order to get some insight into the local magnetic properties of the Fe^{II} sites to inform our interpretation, we have performed complete active space self-consistent field spin–orbit (CASSCF-SO) calculations (see ESI† for details). These show that the Fe^{II} sites are well-described as S = 2, however are subject to a significant axial zero-field splitting (ZFS, $D \sim -17$ cm^{-1}, $|E/D| \sim 0.12$), which arises from close-lying orbitally degenerate states. Interestingly, the main anisotropic axis for each of the Fe^{II} centres lies perpendicular to the plane of the Fe_4 cluster, and points towards the central Fe^{III} centre along a near-two-fold symmetry axis (Fig. S13†). Given the significant ZFS of the Fe^{II} centres and possibly weak magnetic exchange, it is important to consider the non-collinearity of the local anisotropy axes. Therefore to model our data, we employ the following spin Hamiltonian in PHI:[36]

$$\begin{aligned}\hat{H} = &-2J_1\hat{S}_1\cdot(\hat{S}_2+\hat{S}_3+\hat{S}_4) - 2J_2(\hat{S}_2\cdot\hat{S}_3+\hat{S}_3\cdot\hat{S}_4+\hat{S}_4\cdot\hat{S}_2)\\ &+D\left(\hat{S}_{z_2}{}^2+\hat{S}_{z_3}{}^2+\hat{S}_{z_4}{}^2-\frac{1}{3}(\hat{S}_2{}^2+\hat{S}_3{}^2+\hat{S}_4{}^2)\right)\\ &+g\mu_B(\hat{S}_1+\hat{S}_2+\hat{S}_3+\hat{S}_4)\cdot B\end{aligned}$$

here, $\hat{S}_1$ is the spin operator for S = 5/2 of Fe^{III}, $\hat{S}_{2-4}$ are the spin operators for S = 2 Fe^{II}, J_1 and J_2 represent the magnetic coupling between the central Fe^{III} and peripheral Fe^{II} centres (Fe1–Fe2), and the peripheral Fe atoms (Fe2–Fe2), respectively. g is the isotropic g-factor for the cluster, B is the applied magnetic field, and D is the single-ion axial ZFS of the Fe^{II} sites (we ignore E as CASSCF-SO predicts only a small rhombicity); we have rotated the local z-axis of each Fe^{II} site to point towards the central Fe^{III} ion, thus $\hat{S}_{z_{2-4}}$ are non-collinear. There are two possible solutions obtained when fitting the $\chi_M T$ and M *vs.* B

This journal is © The Royal Society of Chemistry 2018

Published on 30 April 2018. Downloaded by University of Bath on 03/05/2018 11:19:01.

data simultaneously: one with $D < 0$ (as suggested by CASSCF-SO) and one with $D > 0$. The former gives J_1 = +2.77 cm^{-1}, J_2 = −0.675 cm^{-1}, g = 1.96 and D = −7.09 cm^{-1} (Fig. 2 and S10, 11†); while the latter gives J_1 = + 2.62 cm^{-1}, and J_2 = −0.738 cm^{-1}, g = 2.03 and D = +14.0 cm^{-1} (Fig. S9–11†). Both solutions agree on the nature of the exchange interactions, where we see a weak ferromagnetic exchange between the Fe^{II} and Fe^{III} centres; antiferromagnetic coupling is observed in the related Fe^{III}_4 clusters. While the solution with $D > 0$ appears to model the high temperature $\chi_M T$ data better than the $D < 0$ solution, the low temperature magnetisation data (which is more sensitive to the details of the electronic structure) is better accounted for by the $D < 0$ solution; as $D < 0$ is also suggested by CASSCF-SO, we believe this to be the more likely description.

Given the ferromagnetic ground state and large anisotropy, we conducted ac susceptibility measurements to see if **1** showed slow magnetization relaxation and SMM behaviour. Plots of the out-of-phase susceptibilities, χ''_M, as a function of ac frequency showed zero values in zero applied dc field; however frequency dependent "tails" were noted below 5 K in a static dc field of 3000 Oe; Fig. S12.† This is in contrast with the S = 5 ground state $[Fe^{III}_4(L)_2(dpm)_6]$ stars, L = alkoxide(3-),[18] for which frequency dependent maxima in χ''_M were observed in zero dc field. Thus, our data indicate a lower U_{eff} barrier for **1** compared to the Fe^{III}_4 family of 3.5–17 K.

Variable temperature, multi-high-field/frequency EPR measurements were performed on a constrained powder of **1**.[37] Fig. 3 shows a series of field-swept dI/dB spectra recorded at different frequencies in the range from 53 to 648 GHz, and a temperature of 5 K. Meanwhile, Fig. S14† plots the positions of the features in the spectra that disperse strongly with magnetic field. These can be divided into two groupings: the first set of resonances lie on a straight line that has a slope corresponding a g-value of 2.004 ± 0.004, with zero offset (±4 GHz) on the frequency axis; the second grouping of two broad resonances observed at the highest frequencies lie on straight lines that have identical zero-field intercepts of 344 ± 4 GHz, and slopes corresponding to g-values of 1.66 ± 0.05 and 2.61 ± 0.06.

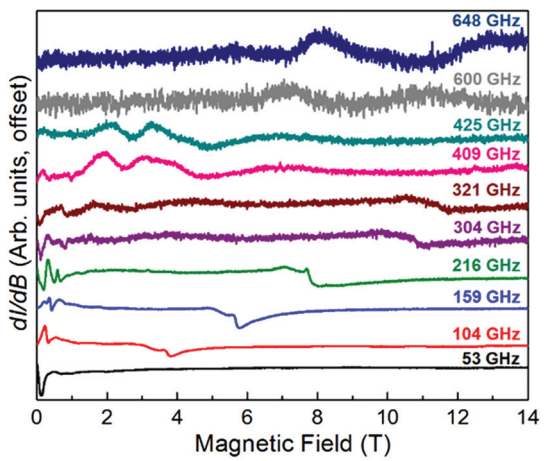

Fig. 3 Normalized high-field EPR spectra on a constrained powder of **1**; the spectra were recorded in derivative mode, dI/dB (where I is the absorption intensity), using field modulation and lock-in detection. All measurements were performed at 5 K.

The g = 2.004 resonance consists of a sharp inflection superimposed on a broader shoulder. Such a signal suggests a weakly anisotropic species, most likely corresponding to S = 5/2 Fe^{III} with an isotropic d^5 electronic configuration.[38] Were such a signal to originate from the Fe^{III} constituent within the Fe_4 cluster, it would imply essentially no exchange coupling to the Fe^{II} centres. On the basis of the magnetic measurements, we feel that this scenario is highly unlikely. Consequently, we attribute the g = 2.00 signal to the Fe^{III} monomer **2** that is likely present in small quantities in the powder sample, which shows an isotropic magnetic moment (Fig. S8†). It is difficult to compare the intensity of this signal with the broad high-frequency components because they are never observed within the same frequency/field window. However, one must recall that the dI/dB traces correspond to the 2nd derivative of the actual spin susceptibility (proportional to the number of spins). Thus, isotropic g = 2.00 resonances are strongly amplified in the dI/dB traces relative to broad anisotropic ones (see below). Therefore, it is quite possible the level of contamination in the powder sample is below the 1% level, consistent with the PXRD studies (Fig. S5†).

We also comment on a series of reproducible features observed close to zero-field (below 1 T) at the lower frequencies (<320 GHz). The origin of these signals is not presently clear. Similar signals have been observed in samples that undergo magnetic ordering and, hence, strong changes in magnetization at low fields. Again, this is not consistent with the magnetic properties of **1**, therefore likely signifying additional minor contamination of the powder sample.

The considerable zero-field splitting (ZFS) associated with the broad high-frequency signals is indicative of an appreciable magnetic anisotropy. Therefore, we associate these excitations with the coupled Fe_4 cluster **1**. Indeed, the coincidence of the zero-field offsets, and the temperature dependence of the two resonances suggest that they both originate from the ground state of the molecule. The reason there are two resonances is because the measurement was performed on a powder, *i.e.* they originate from different crystallite orientations within the powder, corresponding to turning points in the orientation dependence of the anisotropic EPR spectrum. As such, the unique zero-field intercept corresponds to the gap between the ground and first excited spin projection states of the cluster. Interestingly, simulations of the energy levels based on the $D < 0$ parameterization obtained from fits to the magnetic data suggest a ZFS of 300 GHz (10 cm^{-1}) from a set of six near-degenerate ground states to a set of six near degenerate excited states; this differs by only 13% from the value deduced by EPR measurements. Meanwhile, the $D > 0$ parameterization is completely inconsistent with the EPR results: simulations predict a ZFS of just 110 GHz (3.7 cm^{-1}) from the ground to first excited states. Therefore, the EPR measure-

Published on 30 April 2018. Downloaded by University of Bath on 03/05/2018 11:19:01.

ments strongly favour the negative D parameterization. Indeed, given the relatively low information content of the magnetic data and the level of approximation inherent in the model, agreement to within 13% is very good.

In conclusion we have prepared a unique mixed valence Fe^{II}–Fe^{III} tetranuclear star by self-assembly. The star shows weak ferromagnetic coupling between the central and peripheral Fe centres. The star is a weak field-induced SMM with magnetic, EPR and CASSCF-SO studies all suggesting $D = -7.09\ cm^{-1}$ at the peripheral Fe^{II} centres. Preliminary studies suggest that the outer Fe^{II} centres can be replaced with other metal ions and mixed metal stars of this type are now being pursued.

Conflicts of interest

There are no conflicts to declare.

Acknowledgements

We thank the Thailand Research Fund (RSA5580028 and RSA5880048), the Australian Research Council (DP140101013) and the Ramsay Memorial Trust (fellowship to NFC) for funding this research. We also thank the Thailand Research Fund for financial support in the form of a Royal Golden Jubilee scholarship to DS (PHD/0135/2554). A portion of this work was performed at the National High Magnetic Field Laboratory (NHMFL), which is supported by the NSF (DMR-1157490) and the State of Florida. SH also acknowledges the support from the NSF (DMR-1610226).

Notes and references

1 G. Christou, D. Gatteschi, D. N. Hendrickson and R. Sessoli, *MRS Bull.*, 2000, 66–71.
2 S. Dhers, H. L. C. Feltham and S. Brooker, *Coord. Chem. Rev.*, 2015, **296**, 24–44.
3 T. Glaser, *Chem. Commun.*, 2011, **47**, 116–130.
4 S. Goswami, A. K. Mondal and S. Konar, *Inorg. Chem. Front.*, 2015, **2**, 687–712.
5 K. S. Pedersen, J. Bendix and R. Clérac, *Chem. Commun.*, 2014, **50**, 4396–4415.
6 H. Miyasaka, M. Julve, M. Yamashita and R. Clérac, *Inorg. Chem.*, 2009, **48**, 3420–3437.
7 L. Rosado Piquer and E. C. Sañudo, *Dalton Trans.*, 2015, **44**, 8771–8780.
8 D. N. Woodruff, R. E. P. Winpenny and R. A. Layfield, *Chem. Rev.*, 2013, **113**, 5110–5148.
9 M. Affronte, *J. Mater. Chem.*, 2009, **19**, 1731.
10 L. Bogani and W. Wernsdorfer, *Nat. Mater.*, 2008, **7**, 179–186.
11 M. N. Leuenberger and D. Loss, *Nature*, 2001, **410**, 789–793.
12 R. E. P. Winpenny, *Angew. Chem., Int. Ed.*, 2008, **47**, 7992–7994.
13 A. Ardavan, O. Rival, J. J. L. Morton, S. J. Blundell, A. M. Tyryshkin, G. A. Timco and R. E. P. Winpenny, *Phys. Rev. Lett.*, 2007, **98**, 57201.
14 A. Cornia, M. Mannini, P. Sainctavit and R. Sessoli, *Chem. Soc. Rev.*, 2011, **40**, 3076–3091.
15 N. Domingo, E. Bellido and D. Ruiz-Molina, *Chem. Soc. Rev.*, 2012, **41**, 258–302.
16 M. Mannini, P. Sainctavit, R. Sessoli, C. Cartier dit Moulin, F. Pineider, M.-A. Arrio, A. Cornia and D. Gatteschi, *Chem. – Eur. J.*, 2008, **14**, 7530–7535.
17 A. L. Barra, A. Caneschi, A. Cornia, F. De Fabrizi Biani, D. Gatteschi, C. Sangregorio, R. Sessoli and L. Sorace, *J. Am. Chem. Soc.*, 1999, **121**, 5302–5310.
18 S. Accorsi, A.-L. Barra, A. Caneschi, G. Chastanet, A. Cornia, A. C. Fabretti, D. Gatteschi, C. Mortalo, E. Olivieri, F. Parenti, P. Rosa, R. Sessoli, L. Sorace, W. Wernsdorfer and L. Zobbi, *J. Am. Chem. Soc.*, 2006, **128**, 4742–4755.
19 A. Cornia, A. C. Fabretti, P. Garrisi, C. Mortalò, D. Bonacchi, D. Gatteschi, R. Sessoli, L. Sorace, W. Wernsdorfer and A.-L. Barra, *Angew. Chem., Int. Ed.*, 2004, **43**, 1136–1139.
20 M. Mannini, F. Pineider, P. Sainctavit, C. Danieli, E. Otero, C. Sciancalepore, A. M. Talarico, M.-A. Arrio, A. Cornia, D. Gatteschi and R. Sessoli, *Nat. Mater.*, 2009, **8**, 194–197.
21 M. Mannini, F. Pineider, C. Danieli, F. Totti, L. Sorace, P. Sainctavit, M.-A. Arrio, E. Otero, L. Joly, J. C. Cezar, A. Cornia and R. Sessoli, *Nature*, 2010, **468**, 417–421.
22 F. Pineider, M. Mannini, C. Danieli, L. Armelao, F. M. Piras, A. Magnani, A. Cornia and R. Sessoli, *J. Mater. Chem.*, 2010, **20**, 187–194.
23 S. Ninova, V. Lanzilotto, L. Malavolti, L. Rigamonti, B. Cortigiani, M. Mannini, F. Totti and R. Sessoli, *J. Mater. Chem. C*, 2014, **2**, 9599–9608.
24 M. J. Rodriguez-Douton, M. Mannini, L. Armelao, A.-L. Barra, E. Tancini, R. Sessoli and A. Cornia, *Chem. Commun.*, 2011, **47**, 1467–1469.
25 G. G. Condorelli, A. Motta, G. Pellegrino, A. Cornia, L. Gorini, I. L. Fragalà, C. Sangregorio and L. Sorace, *Chem. Mater.*, 2008, **20**, 2405–2411.
26 P. Erler, P. Schmitt, N. Barth, A. Irmler, S. Bouvron, T. Huhn, U. Groth, F. Pauly, L. Gragnaniello and M. Fonin, *Nano Lett.*, 2015, **15**, 4546–4552.
27 Y.-Y. Zhu, X. Guo, C. Cui, B.-W. Wang, Z.-M. Wang and S. Gao, *Chem. Commun.*, 2011, **47**, 8049–8051.
28 Y.-Y. Zhu, T.-T. Yin, S.-D. Jiang, A.-L. Barra, W. Wernsdorfer, P. Neugebauer, R. Marx, M. Dörfel, B.-W. Wang, Z.-Q. Wu, J. Van Slageren and S. Gao, *Chem. Commun.*, 2014, **50**, 15090–15093.
29 Y.-Y. Zhu, C. Cui, K. Qian, J. Yin, B.-W. Wang, Z.-M. Wang and S. Gao, *Dalton Trans.*, 2014, **43**, 11897–11907.
30 R. W. Saalfrank, I. Bernt, M. M. Chowdhry, F. Hampel and G. B. M. Vaughan, *Chem. – Eur. J.*, 2001, **7**, 2765–2769.
31 R. W. Saalfrank, A. Scheurer, I. Bernt, F. W. Heinemann, A. V. Postnikov, V. Schünemann, A. X. Trautwein,

 This journal is © The Royal Society of Chemistry 2018

M. S. Alam, H. Rupp and P. Müller, *Dalton Trans.*, 2006, 2865–2874.
32 K. Takahashi, K. Kawamukai, T. Mochida, T. Sakurai, H. Ohta, T. Yamamoto, Y. Einaga, H. Mori, Y. Shimura, T. Sakakibara, T. Fujisawa, A. Yamaguchi and A. Sumiyama, *Chem. Lett.*, 2015, **44**, 840–842.
33 J. Sanmartín-Matalobos, C. Portela-García, M. Fondo and A. M. García-Deibe, *Cryst. Growth Des.*, 2015, **15**, 4318–4323.
34 D. Sertphon, K. S. Murray, W. Phonsri, J. Jover, E. Ruiz, S. G. Telfer, A. Alkaş, P. Harding and D. J. Harding, *Dalton Trans.*, 2018, **47**, 859–867.
35 P. Gütlich, E. Bill and A. X. Trautwein, *Mössbauer Spectroscopy and Transition Metal Chemistry*, Springer-Verlag, Berlin/Heidelberg, 2011.
36 N. F. Chilton, R. P. Anderson, L. D. Turner, A. Soncini and K. S. Murray, *J. Comput. Chem.*, 2013, **34**, 1164–1175.
37 A. Hassan, L. Pardi, J. Krzystek, A. Sienkiewicz, P. Goy, M. Rohrer and L.-C. Brunel, *J. Magn. Reson.*, 2000, **142**, 300–312.
38 R. J. Holmberg, T. Burns, S. M. Greer, L. Kobera, S. A. Stoian, I. Korobkov, S. Hill, D. L. Bryce, T. K. Woo and M. Murugesu, *Chem. – Eur. J.*, 2016, **22**, 7711–7715.

Published on 30 April 2018. Downloaded by University of Bath on 03/05/2018 11:19:01.

Dalton Transactions

PAPER

Check for updates

Cite this: *Dalton Trans.*, 2018, **47**, 859

Slow relaxation of magnetization in a bis-*mer*-tridentate octahedral Co(II) complex†

Darunee Sertphon, ‡[a] Keith S. Murray, [b] Wasinee Phonsri, [b] Jesús Jover, [c] Eliseo Ruiz,[c] Shane G. Telfer, [d] Adil Alkaş,[d] Phimphaka Harding [a] and David J. Harding *[a]

Received 17th November 2017,
Accepted 11th December 2017

DOI: 10.1039/c7dt04335j

rsc.li/dalton

Reaction of a rigid tridentate ligand *o*-[(1*H*-imidazol-2-yl)methylideneamino]phenol (2-H_2imap) with $Co(ClO_4)_2$ in the presence of NaN_3, or $Co(NO_3)_2$ without a base yields $[Co^{II}(2\text{-Himap})_2]$ **1** and $[Co^{III}(2\text{-Himap})_2]NO_3{\cdot}MeOH$ **2**, respectively. Both complexes exhibit a *mer*-octahedral geometry with the cobalt centre being distorted along an octahedral-trigonal prismatic pathway. The packing in **1** and **2** is dominated by H-bonding forming 2D sheets and 1D chains, respectively. Detailed *dc* and *ac* magnetic studies indicate that **1** is a field-induced single-ion magnet (SIM) with D = 36.7 cm^{-1} and E = 2.0 cm^{-1}. Extensive *ab initio* calculations support these conclusions and suggest that relaxation of the magnetization occurs principally through direct quantum tunnelling in the ground state, with the Raman process dominant in an applied field. This contrasts with the recently reported series of *mer*-$[Co(L)_2]$ (L = monoanionic NNO donor ligand; *Inorg. Chem.*, 2017, **56**, 6056–6066) complexes where D is negative, as these compounds have a more ambiguous geometry, and highlights the importance of supramolecular interactions in subtly altering the coordination sphere thereby impacting the magnetic behaviour.

Introduction

Single molecule magnets are compounds which exhibit slow relaxation of their magnetism of purely molecular origin.[1] They were first discovered in the 1990s and have been extensively investigated as they have a myriad of potential applications.[2–5] Much of the early work focused on metal clusters with the aim of increasing the total spin as the barrier to spin reversal (U_{eff}) depends directly on that term: $U_{eff} = |D|S^2$, where S = the total spin of the complex and D is the axial zero-field splitting (zfs) parameter; when S is a half-integer $U_{eff} = |D|(S^2 - \frac{1}{4})$. While this was successful to some degree many of these larger spin systems still exhibited low barriers due to very small D values. In 2003, Ishikawa and co-workers discovered that the double decker complexes $[LnPc_2][NBu_4]$ (Ln = Tb,Dy) exhibit slow magnetic relaxation, with the Tb(III) complex having a barrier of 230 cm^{-1}.[6] These systems came to be known as single-ion magnets (SIMs)[7–9] and have driven much of the recent research in molecular magnetism. Indeed, very recently a Dy SIM was reported with an impressive blocking temperature of 60 K,[10,11] tantalizingly close to liquid nitrogen temperatures which could make high density data storage a reality with SIMs.

Prior to the advent of single molecule magnetism, cobalt(II) systems were some of the first complexes to be investigated for their ligand field splittings and spin–orbit coupling by Figgis *et al.*[12,13] and Gerloch *et al.*[14] These studies accounted not only for average susceptibility measurements on powders, but also explored single crystal anisotropy, generally measured at temperatures above 77 K by *dc* measurements. Cobalt(II) complexes remain interesting targets as SIMs due to the strong spin–orbit coupling of the metal ion that can, in combination with ligand field effects, lead to high magnetic anisotropy particularly in the orbitally degenerate $^4T_{1g}$ (parent) ground state octahedral species. The first Co(II) SIMs reported were distorted square pyramidal $[\{(2,6\text{-}iPr_2\text{-}PhN{=}CR)_2py\}Co(NCS)_2]$ complexes {R = Me, Ph} in which the Co(II) sitting above the basal plane is vital for observation of SMM behaviour.[15] Shortly afterwards, Long and coworkers reported the complex $[PPh_4]_2[Co(SPh)_4]$ that exhibits D = −70 cm^{-1} and U_{eff} = 21 cm^{-1}.[16] This was the

[a]*Functional Materials and Nanotechnology Centre of Excellence, Walailak University, Thasala, Nakhon Si Thammarat, 80160, Thailand. E-mail: hdavid@mail.wu.ac.th; www.funtechwu.com*
[b]*School of Chemistry, Monash University, Clayton, Victoria, 3800, Australia*
[c]*Departament de Química Inorgànica and Institut de Química Teòrica i Computacional, Universitat de Barcelona, Diagonal 645, E-08028 Barcelona, Spain*
[d]*MacDiarmid Institute for Advanced Materials and Nanotechnology, Institute of Fundamental Sciences, Massey University, Palmerston North, New Zealand*

†Electronic supplementary information (ESI) available: IR and NMR spectra, $\chi_M T$ *vs.* T and M *vs.* H plots, and extra simulations are included. CCDC 1585229 and 1585230. For ESI and crystallographic data in CIF or other electronic format see DOI: 10.1039/c7dt04335j

‡Now at Department of Chemistry, Faculty of Science, Rangsit University, 52/347 Phahonyothin Rd., Muang, Pathum Thani, 12000, Thailand.

first Co(II) SIM to show slow relaxation of magnetization in zero field. Since then a range of tetrahedral systems has been explored and a very diverse range of D values −5 to −160 cm^{-1} and relaxation barriers (14–230 cm^{-1}) has been found. In general, these systems show that use of heavier donor atoms such as S, Se, P or I increases the magnetic anisotropy.[17–21] Geometry is also important, the tight bite angle of the ligand in the tetrahedral Co(II) SIM $[NHEt_3]_2[Co(pdms)]$ {pdms = 1,2-bis(methanesulfonamido)benzene} provides significant axial distortion at the Co(II) centre, leading to large magnetic anisotropy and a relatively high barrier of 230 cm^{-1}.[22] More recently, the linear system [(NHC)Co(NDmp)] (NHC = N-heterocyclic carbene; dmp = dimesitylphenyl), has been reported to have a relaxation barrier as high as 413 cm^{-1}; a new record in transition metal based SIMs.[23]

In contrast to tetrahedral Co(II) SIMs, octahedral systems are much rarer (Table 1), with the first one reported in 2012 by Cano, Pardo and coworkers.[24] Remarkably, in their *cis*-$[Co(dmphen)_2(NCS)_2]$ complex (dmphen = 2,9-dimethyl-1,10-phenanthroline) the value of D was positive (+98 cm^{-1}), implying that the slow relaxation observed is due to transverse, or easy plane (xy) anisotropy. Since then a number of other octahedral systems have been investigated and nearly all of them show positive D values, with the magnitude dependent on the ligands used, the degree of distortion and the *cis* or *trans* geometry adopted by the cobalt centre.[25–35] Nevertheless, the explanation for the occurrence of SMM behaviour, despite positive D parameters, is still not fully understood.[36] Moreover, in employing *mer*-directing ligands Powell *et al.* were able to reverse the sign of D as a result of distortion towards a trigonal prismatic geometry.[37] In trying to better understand the different factors which favour one relaxation mechanism over another in Co(II) SIMs we now report a Co(II) SIM, $[Co(2\text{-}Himap)_2]$ **1**, with a rigid tridentate tight bite angle ligand.

Table 1 Selected examples of octahedral Co(II) complexes with positive D values

Complex	D	U_{eff}/K (H, Oe)	Ref.
cis-$[Co(dmphen)_2(NCS)_2]$	+98	22.9 (2500)	24
$[Co(\mu\text{-}L)(\mu\text{-}OAc)Y(NO_3)_2]$	+47	15.7 (1000)	25
$[Co(abpt)_2(tcm)]$	+48	86.2 (3000)	26
$[Co(acac)_2(H_2O)_2]$	+57	22.6 (various)	36
$[Co(9Accm)_2(py)_2]$	+74	Not given (500)	27
$[Co(9Accm)_2(bipy)]$	+24	Not given (700)	27
$[Co(bpy)_2(ClAn)]\cdot EtOH$	+65.9	16.6 (600)	28
$NEt_4[Co(hfac)_3]$	+118	19.5 (1000)	29
$[Co(pydm)_2][dnbz]_2$	+44	39.0 (400)	33
$[Co(bzpy)_4X_2]$	+106 (X = Cl)		34
	+90.5 (X = NCS)	27.7 (400)	
$[Co(dppm^{O,O})_3][CoBr_4]$	+147	Not given (4000)	35

dmphen = 2,9-dimethyl-1,10-phenanthroline; L = *N*,*N*′,*N*″-trimethyl-*N*,*N*″-bis(2-hydroxy-3-methoxy-5-methylbenzyl)diethylenetriamine; abpt = 4-amino-3,5-bis(2-pyridyl)-1,2,4-triazole; tcm = tricyanomethanide anion; 9Accm = 1,7-bis(9-anthryl)-1,6-heptadiene-3,5-dionate; Cl-An = chloranilate; bzpy = 4-benzylpyridine; $dppm^{O,O}$ = bis(diphenylphosphanoxido)methane; pydm = 2,6-pyridinedimethanol; dnbz = 3,5-dinitrobenzoato; hfac = hexafluoroacetylacetonate.

Results and discussion

Basic characterization and structural studies

The compound, $[Co(2\text{-}Himap)_2]$ **1** was prepared by diffusion of a solution of $Co(ClO_4)_2$ into a solution of the ligand 2-H_2imap[38] with NaN_3 added as a base. The choice of cobalt starting material and base were found to be critical in isolating **1** with $Co(NO_3)_2$ yielding instead the Co(III) compound $[Co(2\text{-}Himap)_2]NO_3\cdot MeOH$ **2** (Scheme 1).

IR spectroscopic studies indicate a strong similarity between the compounds with the imine stretch at 1587 and 1579 cm^{-1} for **1** and **2**, respectively (Fig. S1†). These values are a little lower than those previously reported by Sanmartín-Matalobos *et al.* in $[M(2\text{-}Himap)_2M(2\text{-}H_2imap)_2]^{2+}$ (M = Ni, Cu; 1610–1614 cm^{-1}).[38] The nitrate band is visible only in **2** at 1384 cm^{-1}. ^1H NMR spectroscopic studies of **2** in d^6-DMSO (Fig. S2 in the ESI†) show the typical sharp peaks of diamagnetic Co(III) in the aromatic region attributable to the 2-Himap ligand while the peak at 3.18 ppm is due to the MeOH that crystallizes in the lattice (*vide infra*).

Complex **1** crystallizes in the orthorhombic space group *Pbcn*, while complex **2** crystallizes in the triclinic group $P\bar{1}$. The structures were determined at 296 and 123 K, for **1** and **2** respectively. Crystallographic data are given in Table 2 and the relevant Co–N/O bond lengths and angles are shown in Table 3. The Co–N/O bond lengths are typical for high spin Co(II) in **1**.[28] In contrast, the bond lengths in **2** are on average 0.166 Å (Co–O) and 0.205 Å (Co–N) shorter than those in **1**, indicating that the metal centre is low spin Co(III). This is also confirmed by the octahedral distortion parameters[39,40] which show that **2** has a much more regular octahedral coordination (SHAPE[41] S-O_h parameter for **2** = 0.74) environment than **1** (see Fig. 1). The angle between the two ligands is almost 90° in both compounds and, in the case of **1**, is similar to that found in the related *mer*-$[Co(L)_2]$ systems, (L = monoanionic NNO donor ligands based on 6-hydroxymethyl-pyridin-2-ylcarboxaldehyde) reported by the Powell group.[37] SHAPE analysis[41] shows that **1** is distorted along the octahedral-trigonal prismatic pathway but is closer to octahedral (S-O_h = 3.25) than it is to trigonal prismatic geometry (S-D_{3h} = 9.50). This differs from *mer*-

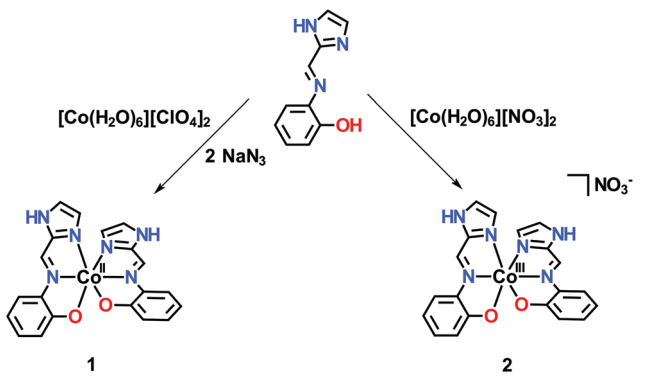

Scheme 1 Synthesis of $[Co(2\text{-}Himap)_2]$ **1** and $[Co(2\text{-}Himap)_2]NO_3$ **2**.

This journal is © The Royal Society of Chemistry 2018

Table 2 Crystallographic data and structure refinement for **1** and **2**

	1	2
Formula	$C_{20}H_{16}CoN_6O_2$	$C_{21}H_{20}CoN_7O_6$
Molecular weight/g mol^{-1}	431.32	525.36
Crystal system	Orthorhombic	Triclinic
Space group	*Pbcn*	*P*$\bar{1}$
a/Å	11.8110(7)	8.4486(5)
b/Å	9.2017(5)	10.2104(7)
c/Å	17.5762(9)	12.8436(9)
α/°	90.00	96.875(7)
β/°	90.00	98.442(7)
γ/°	90.00	101.045(7)
T/K	296	123
Cell volume/Å^3	1910.20(18)	1063.09(13)
Z	4	2
Absorption coefficient/mm^{-1}	0.928	6.836
Reflections collected	6022	6524
Independent reflections, R_{int}	1693, 0.062	2662, 0.0946
Max. and min. transmission	0.746, 0.685	1.00, 0.099
Restraints/parameters	0/136	43/317
Final *R* indices [$I > 2\sigma(I)$]: R_1, wR_2	0.0414, 0.1058	0.0934, 0.2337

Table 3 Selected bond lengths and octahedral distortion parameters (Å, °) for **1** and **2**

	1	2
Co1–O1	2.071(2)	1.897(4)
Co1–O20	—	1.924(6)
Co1–N1	2.070(3)	1.934(5)
Co1–N3	2.159(3)	1.892(6)
Co1–N20		1.950(7)
Co1–N22	—	1.885(6)
Co···Co	7.4862(3)	6.239(2)
		8.157(2)
Σ^a	103.4	49.3
Θ^b	321.4	165.3
Plane-to-plane	88.6	88.7

[a] $\Sigma = \sum_{i=1}^{12} |90 - \alpha_i|$, where α_i are the twelve *cis* N/O–Co–N/O angles.[39] [b] $\Theta = \sum_{i=1}^{24} |60 - \theta_i|$, where θ_i are the 24 unique N/O–Co–N/O angles measured on the projection of two triangular faces of the octahedron along their common pseudo-threefold axis.[40]

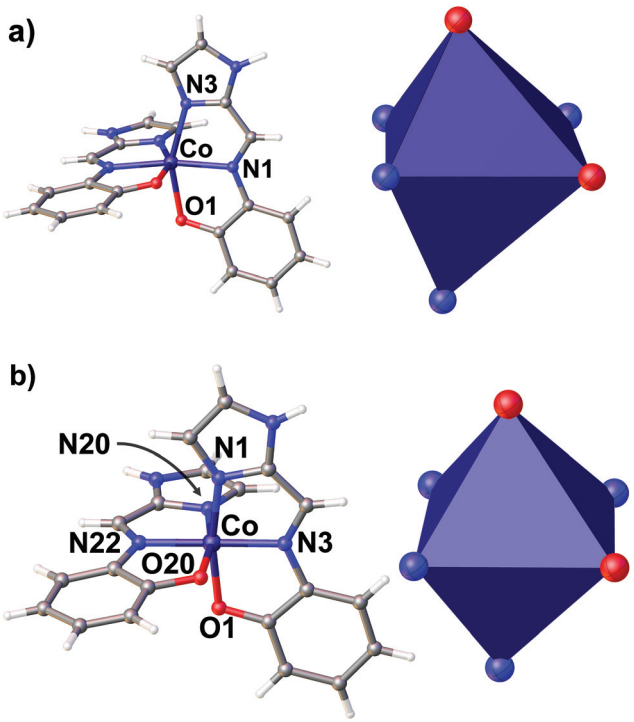

Fig. 1 View of the structures of (a) **1** and (b) **2** showing the key atom labels and the coordination polyhedra of the cobalt centres. Colour code: Co = purple, C = gray, N = blue, O = red.

[Co(L)$_2$] where the geometry is much more ambiguous and intermediate between octahedral and trigonal prismatic (S-O_h = 4.99–5.91; S-D_{3h} = 6.56–7.82) but closely mirrors the Co(II) centre in [Co(μ-L)(μ-OAc)Y(NO$_3$)$_2$].[25]

The individual Co(II) centres in **1** are linked by strong N–H···O hydrogen bonds (N2···O1 = 2.641(4) Å, N2–H2···O1 = 170.0°) involving the imidazole N–H and a phenoxy oxygen atom. The H-bond donors and acceptors are arranged to give a 2D sheet (see Fig. 2). An interesting feature of this structure is that the two [Co(2-Himap)$_2$] enantiomers self-sort into strips, with only one enantiomer present in each strip. This differs from the previously reported [Cd(2-Himap)$_2$] where the enantiomers are arranged into a 1D chain.[42] This difference seems to be due to the greater distortion at the Cd centre that permits π–π interactions which support the N–H···O hydrogen bonds.

The crystal packing of **2** is again dominated by hydrogen bonding this time between the nitrate counteranions, methanol molecules and the [Co(2-Himap)$_2$]$^+$ cations. In addition, there are now π–π interactions {plane-to-plane distance: 3.537(9) Å} which collectively link the [Co(2-Himap)$_2$]$^+$ cations into a 1D chain (Fig. 3). The 1D chains are then linked by C–H···O interactions involving the nitrate anion giving a strongly cooperative 3D supramolecular network.

Magnetic properties of [Co(2-Himap)$_2$]

Dc magnetic studies were undertaken on **1** between 2–300 K with applied fields of 0.1 T (2–70 K) and 1.0 T (2–300 K). These data are presented as $\chi_M T$ *vs.* *T* and magnetization isotherm *M* *vs.* *H* plots in Fig. S3 in the ESI.† The $\chi_M T$ values are independent of the applied field indicating a lack of magnetic impurity or Zeeman level population effects. At 300 K, $\chi_M T$ = 2.40 cm^3 mol^{-1} K and is significantly higher than the expected value of 1.875 cm^3 mol^{-1} K for an isolated *S* = 3/2 Co(II) where *g* = 2.0. This indicates a considerable orbital angular momentum contribution as expected in a $^4T_{1g}$ system that exhibits magnetic anisotropy. The $\chi_M T$ value for **1** is similar to that reported in other octahedral Co(II) complexes where $\chi_M T$ is in the range 2.30–3.05 cm^3 mol^{-1} K.[25–35] $\chi_M T$ values remain independent of temperature between 300 and ~100 K suggestive of a large distorted ligand field contribution, and spin–orbit coupling, which transform the $^4T_{1g}$ state into a lowest-energy $^4A_{2g}$ term (compressed tetragonal). Below 80 K $\chi_M T$ decreases rapidly reaching 1.30 cm^3 mol^{-1} K at 2 K which is also indicative of zfs

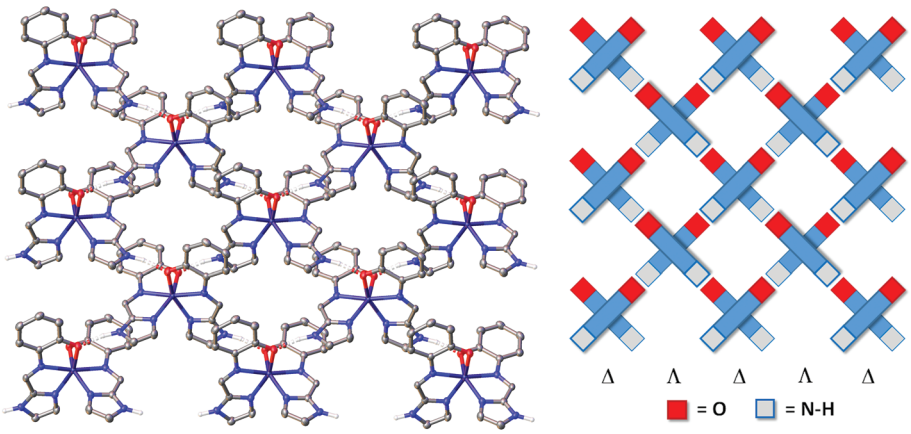

Fig. 2 View of the 2D H-bonding sheet in **1** (left) and a simplified representation of the packing motif (right).

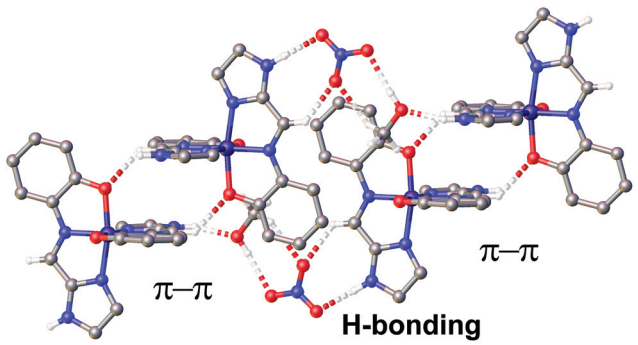

Fig. 3 View of the 1D chain formed by H-bonding and π–π interactions in **2**, for clarity selected H atoms have been removed.

of the $^4A_{2g}$ state, perhaps combined with remnant orbital degeneracy. The magnetization data reveal that the *M vs. H* curve at 2 K becomes almost saturated at higher fields with $M = 2.05N\beta$ at 2 K and 5 T. This is lower than the expected value for a $S = 3/2$ system where $g > 2.0$, probably because of spin–orbit coupling and magnetic anisotropy in **1**.

There are two approaches currently used to simultaneously fit the $\chi_M T$ *vs. T* and *M vs. H* plots. The first one assumes that zero field splitting is dominant and uses the giant spin Hamiltonian approach to obtain *D* (and *E*) and *g* values.[37] The second approach uses the Figgis approach[12,13] that yields ligand field splitting and spin–orbit coupling values.[32,35] We have used the spin Hamiltonian, shown below, with a spin of 3/2, in the program PHI[43]

$$H = D(S_z^2 - [S(S+1)/3]) + E(S_x^2 - S_y^2) + \mu_B S \cdot g \cdot H \quad (1)$$

where *D* is the axial zero field splitting (zfs) parameter; *E* is the rhombic zfs, μ_B the Bohr magneton, *H* is the applied dc field. The *g* values were either kept isotropic or anisotropic, although the latter option is more appropriate for a Co(II) complex. The fits were very good for both the $\chi_M T$ *vs. T* and the *M vs. H* plots at temperatures of 2, 3, 4 and 5.5 K; Fig. 4. The parameters obtained from the fits are: $D = +36.7$ cm^{-1}; $E = 2.0$ cm^{-1}; $g = 2.11, 2.48, 2.12$. The use of a negative *D* value gave unrealistic values of *E*, and thus this possibility can be discarded.

To better understand and quantify the magnetic anisotropy in **1** we undertook *ab initio* calculations using a multireference methodology; the computed second-order anisotropy parameters and excitation energies are collected in Table 4 ($\chi_M T$ *vs. T* and *M vs. H* plots from the simulations are shown in Fig. S4 and S5 in the ESI†). These values have been obtained from two different electronic structure calculations using the ORCA[44] and MOLCAS[45–47] software packages. ORCA produces two sets of results: CASSCF and CASSCF + NEVPT2 (which introduces the dynamic correlation effects), both including spin–orbit contributions. MOLCAS has been employed to provide CASSCF results, including spin–orbit effects that have been introduced with the SO-RASSI method. Positive, and similar, *D* values are found with the three methods, as expected for an octahedral Co(II) complex.[46] The best agreement with the experimental data is found with the ORCA/NEVPT2 calculation: $D = 39.3$ cm^{-1} and $E = 1.8$ cm^{-1}. In all cases, a 3/2 ground state is found before including spin–orbit effects. Under these conditions, the calculations show the existence of relatively low-lying spin–orbit free excited states (δ in Table 4) with energies around 1000–2000 cm^{-1} above the ground state, which may be responsible for the observed anisotropy. This is also confirmed by the anisotropic *g*-values for the ground state. Once spin–orbit effects are included a set of Kramers' doublets (KDs, Δ) is obtained; the three methods again produce very similar results, indicating a low-lying KD around 100 cm^{-1} above the ground state, which may participate in the spin relaxation processes (see below). The second KD is located at higher energies in all cases (1200–1800 cm^{-1}) and would not be expected to participate in the spin relaxation mechanism.

The sign and value of the *D* parameter can be rationalized using the spin–orbit operator, which couples the ground and excited states. When the excited state results from the excitation between orbitals with the same $|m_l|$ values, the $M_S = \pm 3/2$ components are stabilized and a negative contribution to *D* is obtained. However, an excitation between orbitals involving

 This journal is © The Royal Society of Chemistry 2018

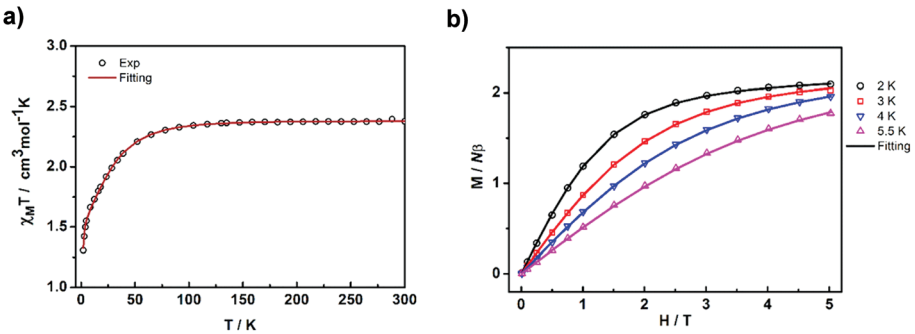

Fig. 4 Best fits of (a) $\chi_M T$ *vs.* *T* in field of 1 T and of (b) *M* *vs.* *H* isotherms using the ZFS Hamiltonian in program PHI[43] with the parameter set given in eqn (1).

Table 4 ORCA/CASSCF, ORCA/CASSCF + NEVPT2, and MOLCAS/CASSCF + RASSI computed *D*, |*E*|, and *g*-values for the ground state of **1**. δ and Δ are the computed first excitation energies before and after including the spin–orbit effects, respectively. The Δ-value corresponds to the energy difference between the ground and the first excited Kramers' doublets

Method	D_{calc} (cm^{-1})	$\|E\|_{calc}$ (cm^{-1})	δ (cm^{-1})	Δ (cm^{-1})	g_{xx}, g_{yy}, g_{zz}
ORCA/CASSCF	50.4	3.1	1339.8	101.3	2.03, 2.45, 2.53
ORCA/NEVPT2	39.3	1.8	1919.8	78.8	2.03, 2.36, 2.41
MOLCAS/CASSCF	48.2	2.8	1439.9	96.8	2.03, 2.45, 2.51

a $|\Delta m_l| = 1$ change, *i.e.* stabilizing the $M_S = \pm 1/2$ components, leads to a positive contribution to the *D* value.[48] **1** displays a distorted octahedral core, which produces the d-orbital splitting shown in Fig. 5. This orbital arrangement is obtained with the ORCA/CASSCF + NEVPT2 calculation by using the *ab initio* ligand field theory (AILF)[49,50] method. We find that the

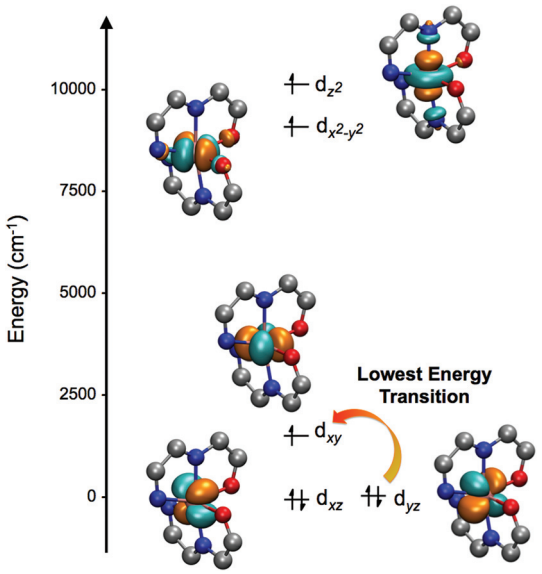

Fig. 5 AILF computed d-orbital splitting for **1** (orbital energies: d_{xz} 0.0 cm^{-1}, d_{yz} 83.9 cm^{-1}, d_{xy} 1573.4 cm^{-1}, $d_{x^2-y^2}$ 9066.1 cm^{-1}, d_{z^2} 10 150.2 cm^{-1}). Colour code: Co = pink, C = gray, N = blue, O = red; H atoms and parts of the 2-Himap ligand have been omitted for clarity.

degeneracy of the t_{2g} and e_g orbitals of the regular octahedron is broken in **1**, indicating the transformation of the initial octahedral $^4T_{1g}$ ground state into a lowest-energy $^4A_{2g}$ term, and one of the former clearly moves up in energy (1573.4 cm^{-1}), far from the last doubly occupied orbital (83.9 cm^{-1}). The AILF method allows the identification of these orbitals; the last doubly occupied orbital is d_{yz} (or d_{xz}, because these cannot be distinguished) while the first half-occupied orbital is d_{xy}; since these orbitals have a different $|m_l|$ value *i.e.* ±1 and ±2, respectively, the *D* value should be positive. This contrasts with the similar *mer*-[Co(L)$_2$] compounds which show negative *D* values.[37] The difference between the two systems is probably due to the greater distortion towards a trigonal prismatic geometry in *mer*-[Co(L)$_2$] when compared with **1**, and seems to be caused by H-bonding involving uncoordinated hydroxyl groups on the ligands.[37]

The dynamics of magnetization were investigated using *ac*-magnetic measurements. The data were recorded with an applied field of 0.2 T between 2–9 K and 50–1488 Hz (Fig. 6a). Under these conditions the out-of-phase magnetization shows a clear peak at higher frequencies, the signature of a single molecule magnet. As with many Co(II) SIMs at zero applied *dc* field there are no signals in the out-of-phase magnetization probably due to efficient quantum tunnelling and consistent with the calculations below.

The program CC-FIT [CC-FIT Copyright 2014, Nicholas F. Chilton] was used to fit the Cole–Cole plots (Fig. 6b) that showed semicircles at the lowest temperatures. The α values are 0.24 (1.8 K) to 0.07 (6 K) indicative of deviations from the Debye model and a range of distributions of the relevant relaxation processes. Usually, four mechanisms, as shown in eqn

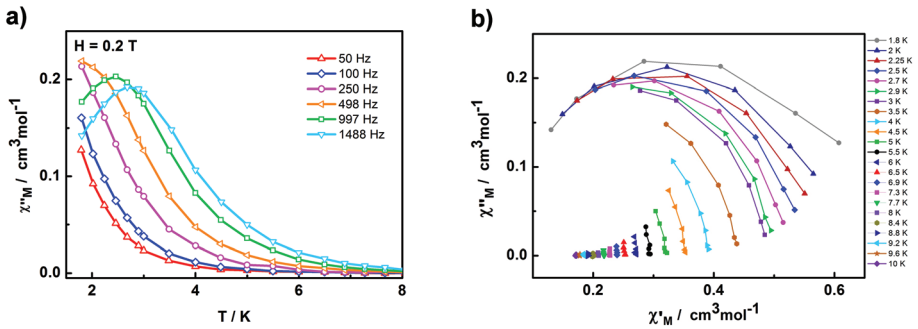

Fig. 6 (a) Variable-frequency out-of-phase components of the *ac* magnetic susceptibility and (b) Cole–Cole plot of **1** the solid lines being best fit.

(2) are considered, direct, quantum tunneling, Raman and Orbach:

$$\tau^{-1} = AH^4T + \frac{B_1}{1 + B_2H^2} + CT^n + \tau_0^{-1}\exp\left(\frac{-U_{\text{eff}}}{kT}\right) \qquad (2)$$

A common initial approach is to analyse the temperature dependence of the relaxation time τ values by plotting $\ln(\tau)$ against $1/T$ (see ESI, Fig. S6†). The best fit for **1** using only an Orbach term gives a U_{eff} value of 14 K. However, as D is calculated to be 39.3 cm^{-1} the barrier height, assuming a purely thermal relaxation pathway, should be 78.6 cm^{-1} ($2D$); this is considerably higher than the fitted barrier height. This indicates that the thermal Orbach mechanism is not the main contributor to the temperature dependence.[24,37,51] In fact, Co(II) SIMs with positive D and limited rhombicity that do exhibit Orbach relaxation are rare, with [Co(tpma)(NCMe)]BF_4 {tpma = tris(pyridylmethyl)amine} a recent example.[52]

The explanation for the occurrence of slow relaxation of magnetization with positive D values has recently been explained by a combination of a direct mechanism (due to the presence of very effective hyperfine coupling in an $I = 7/2$ Co(II) system), a Raman mechanism and a strong nuclear spin–lattice interaction which must also be taken into account.[36] In such a scenario, the temperature dependence of the spin relaxation time (see Fig. 7) can be described by a Raman term and a field-dependent mechanism contribution ${\tau_{\text{FDM}}}^{-1}$

$${\tau}^{-1} = {\tau_{\text{FDM}}}^{-1} + CT^n \qquad (3)$$

the best fit for **1** is with C = 19.12 s^{-1} $\text{K}^{-5.10}$ n = 5.10 and ${\tau_{\text{FDM}}}^{-1}$ 3685.1 s^{-1}. Although, n is smaller than the hypothetical n = 9 for a Kramers ion, the value is very similar to that reported for other easy-plane Co(II) complexes.[53]

The computed relative energies of the lowest-lying KDs and the spin relaxation pathways of **1**, obtained with the MOLCAS/CASSCF + RASSI calculation, are shown in Fig. 8. The spin relaxation mechanisms show a plausible pathway *via* direct quantum tunneling (QTM) in the ground state. The matrix elements of the transition magnetic moments found between states 1− and 1+ is 1.64, much higher than the required value of 0.1 associated with an efficient relaxation mechanism. The second KD may also be accessible (96.8 cm^{-1}) and should able

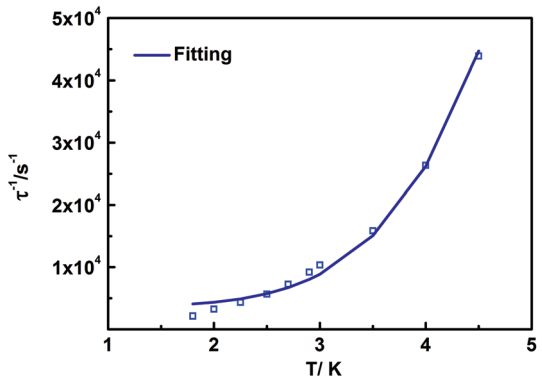

Fig. 7 Relaxation time *vs.* *T* plot and best fit as described using eqn (3) for **1** using *ac* χ''_{M} data in a *dc* field of 0.2 T.

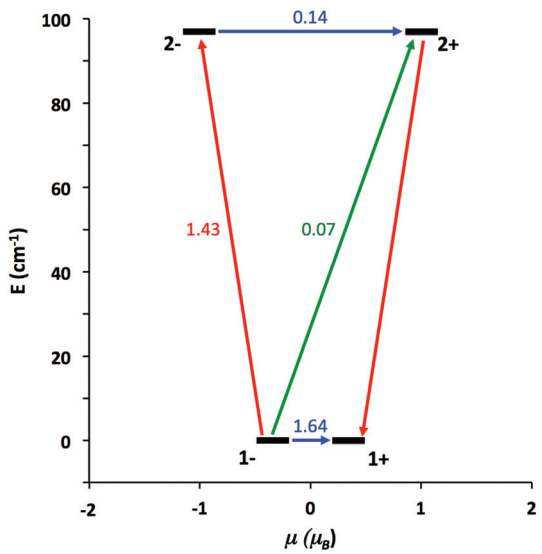

Fig. 8 Lowest two Kramers' doublets and *ab initio* computed relaxation mechanism in **1**. The thick black lines imply KDs as a function of their magnetic moment along the main anisotropy axis. Red lines indicate the magnetization reversal mechanism. The blue lines correspond to ground state QTM and thermally assisted-QTM *via* the first excited KD, and green and purple lines show the possible Orbach relaxation process. The values close to the arrows indicate the matrix elements of the transition magnetic moments (above 0.1 an efficient spin relaxation mechanism is expected).

 This journal is © The Royal Society of Chemistry 2018

to participate in alternative relaxation pathways, most probably through thermally assisted-QTM. However, the U_{eff} barrier obtained from the fit of the relaxation time (14 K) is much lower than these thermally-activated processes (139 K), and confirms the above fit that the Raman mechanism is the dominant spin relaxation process in an applied field.

Conclusions

In summary we have prepared a new Co(II) field-induced SIM featuring a rare meridional geometry. The compound shows a distorted octahedral centre and strong magnetic anisotropy. Subtle differences between **1** and similar systems previously reported result in a positive value for *D*. The difference in the sign of *D* seems to be due to the ambiguous coordination geometry in *mer*-[Co(L)$_2$] caused by H-bonding interactions and re-emphasizes the importance of supramolecular interactions in controlling not only the magnitude but the sign of *D*. In common with other octahedral Co(II) SIMs direct and Raman processes are the dominant relaxation mechanisms. With more flexible ligands and/or different donor sets a more complete picture of the magnetostructural correlations should be forthcoming and efforts along these lines are currently being explored.

Experimental

General remarks

2-H$_2$imap was prepared as previously reported.[38] All other chemicals were purchased from Sigma-Aldrich and used as received. All reactions were performed in air with reagent grade solvents. IR data were measured on a Cary 630 Agilent Technologies IR spectrometer fitted with a Specac Golden Gate diamond ATR. ^{1}H NMR spectra were collected on a Bruker 300 MHz spectrometer in d^6-DMSO at 298 K. Elemental analyses were carried out on a Eurovector EA3000 analyser by staff of the School of Chemistry, University of Bristol, UK. ESI-MS were carried out on a Bruker Daltonics 7.0T Apex 4 FTICR Mass Spectrometer by staff at the National University of Singapore.

Synthesis of [Co(2-Himap)$_2$] 1

A solution of 2-H$_2$imap (0.109 g, 0.5 mmol) in H$_2$O (3 cm^3) with NaN$_3$ (0.065 g, 1.0 mmol) was layered at the bottom of a test tube and then blank MeOH : H$_2$O (1 : 1, 10 mL) was layered in the middle as a buffer layer. Finally, a solution of [Co(H$_2$O)$_6$][ClO$_4$]$_2$ (0.183 g, 0.5 mmol) in MeOH (5 cm^3) was layered on top and the test tube sealed. The solution was left for 2 weeks at room temperature, and red brown crystals were obtained at the buffer layer. The red brown crystals were isolated, washed with diethyl ether (2 × 2 cm^3) and air dried, yield 0.065 g (30%). *m*/*z* (ESI) 429 [Co(2-Himap)$_2$]$^+$. ν_{max} (ATR)/cm^{-1} 1587, 1461, 1384, 1249, 841, 747. Anal. Calc. for **1**·H$_2$O C$_{20}$H$_{18}$N$_6$O$_3$Co: C 53.47; H 4.04; N 18.70. Found: C 53.69; H 3.82; N 19.36%.

Synthesis of [Co(2-Himap)$_2$]NO$_3$·MeOH 2

2-Himap (0.437 g, 2 mmol) was dissolved in MeOH (7 cm^3) and [Co(H$_2$O)$_6$][NO$_3$]$_2$(0.291 g, 1.0 mmol) in MeOH (5 cm^3) added dropwise into the ligand solution. The solution immediately turned deep red with a small amount of dark solid produced. After stirring for 15 minutes the solution was filtered into a test tube and left overnight at room temperature, giving dark crystals. The crystals were isolated by filtration, washed with diethyl ether (2 × 2 cm^3) and air dried, yield 0.331 g (61%). ν_{max} (ATR)/cm^{-1} 3119, 3060, 1579, 1547, 1432, 1310, 1255, 1122, 743. *m*/*z* (ESI) 429 [Co(2-Himap)$_2$]$^+$. Anal. calc. for C$_{21}$H$_{20}$N$_7$O$_6$Co: C, 48.02; H, 3.84; N, 18.66. Found: C, 47.80; H, 3.86; N, 18.63%.

X-ray crystallography

Crystals of **1** and **2** were mounted on a glass fibre using perfluoropolyether oil and in the case of **2** cooled rapidly to 123 K in a stream of cold nitrogen. The diffraction data of **1** were collected on a Bruker APEXII area detector with graphite monochromated MoKα (λ = 0.71073 Å).[54] After data collection an empirical absorption correction (SADABS) was applied.[55] In the case of **2**, data were collected at 123 K on a Rigaku Spider diffractometer equipped with a MicroMax MM007 rotating anode generator, CuK$_\alpha$ radiation (λ = 1.54178 Å), high-flux Osmic multilayer mirror optics, and a curved image-plate detector.[56] The data were integrated and scaled and averaged with FS Process. The structures were then solved by direct methods and refined on all F^2 data using the SHELX suite of programs or OLEX2.[57–59] In all cases non-hydrogen atoms were refined with anisotropic thermal parameters; hydrogen atoms were included in calculated positions and refined with isotropic thermal parameters which were *ca*. 1.2 × (aromatic CH) or 1.5 × (Me, OH) the equivalent isotropic thermal parameters of their parent carbon atoms. Crystallographic data and structure refinement parameters are given in Table 2. All pictures were generated using OLEX2.[60] The CCDC numbers for the X-ray crystallographic data presented in this paper are 1585230 and 1585229 for **1** and **2**,† respectively.

Magnetic measurements

Data were collected using a Quantum Design MPMS 7 SQUID magnetometer under applied fields of 0.1 T (2–70 K) and 1.0 T (2–300 K). The crystalline sample was placed in a gel capsule for all data collection. Magnetization isotherms were collected at 2, 3, 4, 5.5, 10 and 20 K between 0–5 T. Alternating current susceptibility measurements were undertaken in an applied field of 0.2 T between 2–9 K and 50–1488 Hz. All data were corrected for the sample holder and diamagnetic contributions.

Quantum chemical calculations

The calculation of the second-order magnetic anisotropy (or zero-field splitting) parameters (*D* and *E*) has been carried out with two different software packages: MOLCAS 8.0[45–47] and

ORCA.[44] We have employed MOLCAS (along with the SINGLE_ANISO[61,62] code) to carry out a CASSCF calculation of the energy states of the Co(II) complex. After that, the spin–orbit coupling has been introduced, as implemented in the SO-RASSI (Restricted Active Space State Interaction) approach, to mix up these energies and obtain the final energy states. In these calculations we have employed an all electron ANO-RCC basis set:[63–66] Co atoms (6s5p4d2f), N (4s3p2d1f), O (4s3p2d1f), C (3s2p) and H (2s).

A CASSCF calculation was also carried out with ORCA; the dynamic correlation effects were included through the *n*-electron valence state perturbation theory NEVPT2[67–69] method. In all cases the spin–orbit effects were included using the quasi-degenerate perturbation theory (QDPT) and the magnetic anisotropy parameters were obtained using the effective Hamiltonian method. In these calculations all the atoms are described by the def2-TZVPP basis set,[70,71] including the corresponding auxiliary basis sets for correlation and Coulomb fitting. In both sets of calculations, the active space is formed by the seven d electrons of the Co(II) centre and the five d orbitals (7,5); and all the quadruplet (10) and doublet (40) states have been taken into account.

Conflicts of interest

There are no conflicts to declare.

Acknowledgements

We gratefully acknowledge the Thailand Research Fund (RSA5880048) for funding this research and financial support from the Thailand Research Fund in the form of a Royal Golden Jubilee scholarship to D. S. (PHD/0135/2554). K. S. M. thanks the Australian Research Council for a Discovery grant. The research reported here was also supported by the Spanish *Ministerio de Economía y Competitividad* (grant CTQ2015-64579-C3-1-P, MINECO/FEDER, UE). E. R. thanks Generalitat de Catalunya for an ICREA Academia award. J. J. and E. R. gratefully acknowledge the computer resources in the Consorci Serveis Universitaris de Catalunya (CSUC). Declan Wain is thanked for curve fitting. Ivana Borilović is thanked for help with the latest version of the Program PHI and Boujemaa Moubaraki is thanked for magnetic measurements.

Notes and references

1 D. Gatteschi, R. Sessoli and J. Villain, *Molecular Nanomagnets*, Oxford University Press, 2006.
2 R. Sessoli, D. Gatteschi, A. Caneschi and M. A. Novak, *Nature*, 1993, **365**, 141–143.
3 G. Christou, D. Gatteschi, D. N. Hendrickson and R. Sessoli, *MRS Bull.*, 2000, 66–71.
4 R. E. P. Winpenny, *Angew. Chem., Int. Ed.*, 2008, **47**, 7992–7994.
5 G. A. Timco, T. B. Faust, F. Tuna and R. E. P. Winpenny, *Chem. Soc. Rev.*, 2011, **40**, 3067.
6 N. Ishikawa, M. Sugita, T. Ishikawa, S. Y. Koshihara and Y. Kaizu, *J. Am. Chem. Soc.*, 2003, **125**, 8694–8695.
7 G. A. Craig and M. Murrie, *Chem. Soc. Rev.*, 2015, **44**, 2135–2147.
8 S. Gómez-Coca, D. Aravena, R. Morales and E. Ruiz, *Coord. Chem. Rev.*, 2015, **289–290**, 379–392.
9 J. M. Frost, K. L. M. Harriman and M. Murugesu, *Chem. Sci.*, 2016, **6**, 1–22.
10 C. A. P. Goodwin, F. Ortu, D. Reta, N. F. Chilton and D. P. Mills, *Nature*, 2017, **548**, 439–442.
11 F.-S. Guo, B. M. Day, Y.-C. Chen, M.-L. Tong, A. Mansikkamäki and R. A. Layfield, *Angew. Chem., Int. Ed.*, 2017, **56**, 11445–11449.
12 B. N. Figgis, *Introduction to ligand fields*, Wiley-VCH, New York, 1966.
13 B. N. Figgis, M. Gerloch, J. Lewis, F. E. Mabbs and G. A. Webb, *J. Chem. Soc. A*, 1968, 2086.
14 R. B. Bentley, M. Gerloch, J. Lewis and P. N. Quested, *J. Chem. Soc. A*, 1971, 3751–3756.
15 T. Jurca, A. Farghal, P. H. Lin, I. Korobkov, M. Murugesu and D. S. Richeson, *J. Am. Chem. Soc.*, 2011, **133**, 15814–15817.
16 J. M. Zadrozny and J. R. Long, *J. Am. Chem. Soc.*, 2011, **133**, 20732–20734.
17 M. R. Saber and K. R. Dunbar, *Chem. Commun.*, 2014, **50**, 12266–12269.
18 L. Smolko, J. Černák, M. Dušek, J. Miklovič, J. Titiš and R. Boča, *Dalton Trans.*, 2015, **44**, 17565–17571.
19 S. Vaidya, A. Upadhyay, S. K. Singh, T. Gupta, S. Tewary, S. K. Langley, J. P. S. Walsh, K. S. Murray, G. Rajaraman and M. Shanmugam, *Chem. Commun.*, 2015, **51**, 3739–3742.
20 S. Vaidya, S. K. Singh, P. Shukla, K. Ansari, G. Rajaraman and M. Shanmugam, *Chem. – Eur. J.*, 2017, **23**, 9546–9559.
21 J. M. Zadrozny, J. Telser and J. R. Long, *Polyhedron*, 2013, **64**, 209–217.
22 Y. Rechkemmer, F. D. Breitgoff, M. van der Meer, M. Atanasov, M. Hakl, M. Orlita, P. Neugebauer, F. Neese, B. Sarkar and J. van Slageren, *Nat. Commun.*, 2016, **7**, 10467.
23 X.-N. Yao, J.-Z. Du, Y.-Q. Zhang, X.-B. Leng, M.-W. Yang, S.-D. Jiang, Z.-X. Wang, Z.-W. Ouyang, L. Deng, B.-W. Wang and S. Gao, *J. Am. Chem. Soc.*, 2017, **139**, 373–380.
24 J. Vallejo, I. Castro, R. Ruiz-García, J. Cano, M. Julve, F. Lloret, G. De Munno, W. Wernsdorfer and E. Pardo, *J. Am. Chem. Soc.*, 2012, **134**, 15704–15707.
25 E. Colacio, J. Ruiz, E. Ruiz, E. Cremades, J. Krzystek, S. Carretta, J. Cano, T. Guidi, W. Wernsdorfer and E. K. Brechin, *Angew. Chem., Int. Ed.*, 2013, **52**, 9130–9134.
26 R. Herchel, L. Váhovská, I. Potočňák and Z. Trávníček, *Inorg. Chem.*, 2014, **53**, 5896–5898.
27 R. Díaz-Torres, M. Menelaou, O. Roubeau, A. Sorrenti, G. Brandariz-de-Pedro, E. C. Sañudo, S. J. Teat, J. Fraxedas,

 This journal is © The Royal Society of Chemistry 2018

E. Ruiz and N. Aliaga-Alcalde, *Chem. Sci.*, 2016, **7**, 2793–2803.
28 R. Ishikawa, Y. Horii, R. Nakanishi, S. Ueno, B. K. Breedlove, M. Yamashita and S. Kawata, *Eur. J. Inorg. Chem.*, 2016, **2016**, 3220.
29 A. V. Palii, D. V. Korchagin, E. A. Yureva, A. V. Akimov, E. Y. Misochko, G. V. Shilov, A. D. Talantsev, R. B. Morgunov, S. M. Aldoshin and B. S. Tsukerblat, *Inorg. Chem.*, 2016, **55**, 9696–9706.
30 S. Vaidya, S. Tewary, S. K. Singh, S. K. Langley, K. S. Murray, Y. Lan, W. Wernsdorfer, G. Rajaraman and M. Shanmugam, *Inorg. Chem.*, 2016, **55**, 9564–9578.
31 C. Villa-Pérez, I. Oyarzabal, G. A. Echeverría, G. C. Valencia-Uribe, J. M. Seco and D. B. Soria, *Eur. J. Inorg. Chem.*, 2016, **2016**, 4835–4841.
32 J. Walsh, G. Bowling, A.-M. Ariciu, N. Jailani, N. Chilton, P. Waddell, D. Collison, F. Tuna and L. Higham, *Magnetochemistry*, 2016, **2**, 23.
33 D. Valigura, C. Rajnák, J. Moncol, J. Titiš and R. Boča, *Dalton Trans.*, 2017, **46**, 10950–10956.
34 C. Rajnák, J. Titiš, J. Moncol', F. Renz and R. Boča, *Eur. J. Inorg. Chem.*, 2017, **2017**, 1520–1525.
35 F. Varga, C. Rajnak, J. Titis, J. Moncol and R. Boca, *Dalton Trans.*, 2017, **46**, 4148–4151.
36 S. Gómez-Coca, A. Urtizberea, E. Cremades, P. J. Alonso, A. Camón, E. Ruiz and F. Luis, *Nat. Commun.*, 2014, **5**, 4300.
37 Y. Peng, V. Mereacre, C. E. Anson, Y. Zhang, T. Bodenstein, K. Fink and A. K. Powell, *Inorg. Chem.*, 2017, **56**, 6056–6066.
38 J. Sanmartín-Matalobos, C. Portela-García, M. Fondo and A. M. García-Deibe, *Cryst. Growth Des.*, 2015, **15**, 4318–4323.
39 J. K. McCusker, A. L. Rheingold and D. N. Hendrickson, *Inorg. Chem.*, 1996, **35**, 2100–2112.
40 M. Marchivie, P. Guionneau, J. F. Létard and D. Chasseau, *Acta Crystallogr., Sect. B: Struct. Sci.*, 2005, **61**, 25–28.
41 S. Alvarez, *Chem. Rev.*, 2015, **115**, 13447–13483.
42 A. M. García-Deibe, C. Portela-García, M. Fondo, A. J. Mota and J. Sanmartín-Matalobos, *Chem. Commun.*, 2012, **48**, 9915.
43 N. F. Chilton, R. P. Anderson, L. D. Turner, A. Soncini and K. S. Murray, *J. Comput. Chem.*, 2013, **34**, 1164–1175.
44 F. Neese, *Wiley Interdiscip. Rev.: Comput. Mol. Sci.*, 2012, **2**, 73–78.
45 G. Karlström, R. Lindh, P.-Å. Malmqvist, B. O. Roos, U. Ryde, V. Veryazov, P. O. Widmark, M. Cossi, B. Schimmelpfennig, P. Neogrady and L. Seijo, in *Computational Materials Science*, Elsevier, 2003, vol. 28, pp. 222–239.
46 V. Veryazov, P.-O. Widmark, L. Serrano-Andrés, R. Lindh and B. O. Roos, *Int. J. Quantum Chem.*, 2004, **100**, 626–635.
47 F. Aquilante, L. De Vico, N. Ferré, G. Ghigo, P.-Å. Malmqvist, P. Neogrády, T. B. Pedersen, M. Pitoňák, M. Reiher, B. O. Roos, L. Serrano-Andrés, M. Urban, V. Veryazov and R. Lindh, *J. Comput. Chem.*, 2010, **31**, 224–247.
48 S. Gómez-Coca, E. Cremades, N. Aliaga-Alcalde and E. Ruiz, *J. Am. Chem. Soc.*, 2013, **135**, 7010.
49 M. Atanasov, D. Ganyushin, K. Sivalingam and F. Neese, in *Molecular Electronic Structures of Transition Metal Complexes II. Structure and Bonding*, ed. D. M. P. Mingos, P. Day and J. P. Dahl, Springer, Berlin, 2012, pp. 149–220.
50 M. Atanasov, D. Aravena, E. Suturina, E. Bill, D. Maganas and F. Neese, *Coord. Chem. Rev.*, 2015, **289–290**, 177–214.
51 E. A. Buvaylo, V. N. Kokozay, O. Y. Vassilyeva, B. W. Skelton, A. Ozarowski, J. Titiš, B. Vranovičová and R. Boča, *Inorg. Chem.*, 2017, **56**, 6999–7009.
52 T. J. Woods, M. F. Ballesteros-Rivas, S. Gómez-Coca, E. Ruiz and K. R. Dunbar, *J. Am. Chem. Soc.*, 2016, **138**, 16407–16416.
53 M. A. Palacios, J. Nehrkorn, E. A. Suturina, E. Ruiz, S. Gómez-Coca, K. Holldack, A. Schnegg, J. Krzystek, J. M. Moreno and E. Colacio, *Chem. – Eur. J.*, 2017, **23**, 11649–11661.
54 *Bruker APEXII*, Bruker AXS Inc., Madison, USA, 2005.
55 *SADABS and SAINT*, Bruker AXS Inc., Madison, USA, 2013.
56 *Rigaku, Rigaku XRD*, Rigaku Corporation, Tokyo, Japan, 1996.
57 G. M. Sheldrick, *Acta Crystallogr., Sect. A: Found. Crystallogr.*, 2015, **71**, 3–8.
58 G. M. Sheldrick, *Acta Crystallogr., Sect. C: Struct. Chem.*, 2015, **71**, 3–8.
59 L. J. Bourhis, O. V. Dolomanov, R. J. Gildea, J. A. K. Howard and H. Puschmann, *Acta Crystallogr., Sect. A: Found. Adv.*, 2015, **71**, 59–75.
60 O. V. Dolomanov, L. J. Bourhis, R. J. Gildea, J. A. K. Howard and H. Puschmann, *J. Appl. Crystallogr.*, 2009, **42**, 339–342.
61 L. F. Chibotaru, L. Ungur and A. Soncini, *Angew. Chem., Int. Ed.*, 2008, **47**, 4126–4129.
62 L. F. Chibotaru, L. Ungur, C. Aronica, H. Elmoll, G. Pilet and D. Luneau, *J. Am. Chem. Soc.*, 2008, **130**, 12445–12455.
63 B. O. Roos, V. Veryazov and P.-O. Widmark, *Theor. Chem. Acc.*, 2004, **111**, 345–351.
64 B. O. Roos, R. Lindh, P.-Å. Malmqvist, V. Veryazov and P.-O. Widmark, *J. Phys. Chem. A*, 2004, **108**, 2851–2858.
65 B. O. Roos, R. Lindh, P.-Å. Malmqvist, V. Veryazov and P.-O. Widmark, *J. Phys. Chem. A*, 2005, **109**, 6575–6579.
66 B. O. Roos, R. Lindh, P.-Å. Malmqvist, V. Veryazov and P.-O. Widmark, *Chem. Phys. Lett.*, 2005, **409**, 295–299.
67 C. Angeli, R. Cimiraglia, S. Evangelisti, T. Leininger and J.-P. Malrieu, *J. Chem. Phys.*, 2001, **114**, 10252–10264.
68 C. Angeli, R. Cimiraglia and J.-P. Malrieu, *Chem. Phys. Lett.*, 2001, **350**, 297–305.
69 C. Angeli, R. Cimiraglia and J.-P. Malrieu, *J. Chem. Phys.*, 2002, **117**, 9138–9153.
70 F. Weigend and R. Ahlrichs, *Phys. Chem. Chem. Phys.*, 2005, **7**, 3297.
71 F. Weigend, *Phys. Chem. Chem. Phys.*, 2006, **8**, 1057.

NJC

PAPER

Check for updates

Cite this: *New J. Chem.*, 2017, **41**, 13747

Spin crossover in mixed ligand iron(III) complexes†

Wasinee Phonsri, ‡[a] Phimphaka Harding, [a] Keith S. Murray, [b] Boujemaa Moubaraki[b] and David J. Harding *[a]

Received 25th September 2017,
Accepted 18th October 2017

DOI: 10.1039/c7nj03676k

rsc.li/njc

Mixed ligand complexes [Fe(qsal-Cl)(qsal-Br)]Y·sol (Y = NCS, sol = MeOH **1**; PF_6 **2**; BPh_4, sol = $2CH_2Cl_2$ **3**; OTf, sol = 0.5MeOH **4**) have been synthesized. X-ray crystallographic studies of **1**, **2** and **4** at 123 K reveal that the Fe(III) centres are low spin in all cases. In **2** there are two independent Fe(III) centres in the asymmetric unit cell. The structure of **3** has been determined at 100, 123 and 269 K with the Fe centre low spin, mixed spin and mostly high spin, respectively. Packing in the complexes is dominated by π–π interactions which form a 1D chain. C–H···π, C–H···Cl/Br and C–Cl/Br···π interactions link the chains to form highly cooperative supramolecular 3D networks mirroring the homoleptic complexes. SQUID magnetometric studies show almost complete, 50% complete and stepped spin crossover for **1**, **2** and **3** respectively. [Fe(qsal-Cl)(qsal-Br)]OTf·0.5MeOH **4** is low spin up to 350 K. Compared to the homoleptic complexes spin crossover behaviour is mostly intermediate between the $[Fe(qsal\text{-}Cl)_2]^+$ and $[Fe(qsal\text{-}Br)_2]^+$ systems except for **3** where spin crossover characteristics are improved compared to the homoleptic complexes.

Introduction

Iron(III) spin crossover (SCO) complexes have attracted much attention in the last few years due to an increasing number of systems that exhibit abrupt and hysteretic SCO.[1–4] Compared to the more common iron(II) SCO systems,[5–8] iron(III) shows a smaller change in the Fe-ligand bond lengths, limited colour differences between the two spin states and very often no light induced spin crossover (LIESST). Nevertheless, iron(III) compounds are usually more robust and SCO is accessible with a wide range of ligand donor sets.[1] While a range of complexes with different ligands has been reported the most successful systems incorporate tridentate ligands.[9–23] The success of these systems lies in effective control of the supramolecular interactions between the spin centres, known as the cooperativity and essential for abrupt and hysteretic SCO.[24,25] In $[Fe(qsal\text{-}X)_2]^+$ {qsal-X = (*N*-8-quinolyl)-5-X-salicylaldiminate}[9–15] complexes strong π–π interactions are involved while for $[Fe(X\text{-}salEen)_2]^+$ {X-salEen = *N*-ethyl-*N*-(2-aminoethyl)-X-salicylaldiminate}[16–18] and [Fe(5-X-Hthsa)(5-X-thsa)] (5-X-H_2thsa = 5-X-salicylaldehydethiosemicarbazone)[19–23] extensive hydrogen bonding facilitates cooperativity. In these complexes abrupt, symmetry breaking and hysteretic SCO have been reported.

In the search for systems where SCO occurs at room temperature some of us have explored the use of two different ligands. In [Fe(thsa)(qsal)]·sol (sol = 0.4*n*BuOH, 0.5MeCN, 0.5 THF) the MeCN solvate shows a reversible [LS–HS] to [HS–HS] transition with partial loss of MeCN in a single-crystal-to-single-crystal transformation.[26] The halogen substituted analogues [Fe(qsal-X)(thsa)]·*n*MeCN (X = F, *n* = 2.5; X = Cl, Br and I, *n* = 1) are also SCO active but only in the first cycle with [Fe(qsal-F)(thsa)] HS and the Br and I compounds LS.[27] The exception is [Fe(qsal-Cl)(thsa)]·MeCN which after solvent loss exhibits incomplete but hysteretic SCO. In contrast, [Fe(thsa)-(3-OMe-salEen)] shows complete SCO with a very high $T_{1/2}$.[28] In all cases, the mixed ligand complexes exhibit distinct magnetic behaviour not present in the homoleptic analogues. In attempting to more subtly alter the SCO characteristics of these complexes we have now prepared [Fe(qsal-Cl)(qsal-Br)]Y (Y = NCS, PF_6, BPh_4, OTf). The structures and magnetic profiles of the complexes are discussed and comparisons drawn with the homoleptic compounds.

Results and discussion

Synthesis of $[Fe(qsal\text{-}Cl)(qsal\text{-}Br)]^+$ complexes

The compounds [Fe(qsal-Cl)(qsal-Br)]Y·sol (Y = NCS, sol = MeOH **1**; PF_6 **2**; BPh_4, sol = $2CH_2Cl_2$ **3**; OTf, sol = 0.5MeOH **4**) have been prepared *via* layered diffusion in moderate yields (Scheme 1). The compounds are black with IR spectra showing imine

[a] *Functional Materials and Nanotechnology Centre of Excellence (FuNTech), Walailak University, Thasala, Nakhon Si Thammarat, 80160, Thailand. E-mail: hdavid@g-mail.wu.ac.th*

[b] *School of Chemistry, Monash University, Clayton, Victoria, 3800, Australia*

† Electronic supplementary information (ESI) available: TGA results, PXRD diffractograms of **3** and **4**, and supplementary X-ray crystallographic pictures. CCDC 1526771–1526776. For ESI and crystallographic data in CIF or other electronic format see DOI: 10.1039/c7nj03676k

‡ Current address: School of Chemistry, Monash University, Australia.

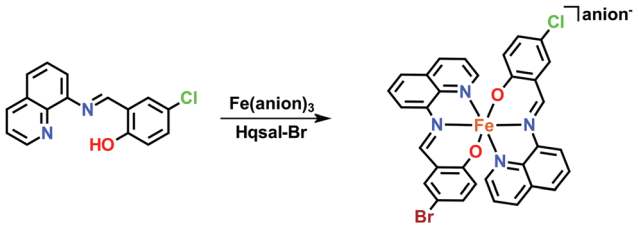

Scheme 1 Synthesis of [Fe(qsal-Cl)(qsal-Br)]$^+$.

stretches between 1598–1602 cm^{-1} and typical of chelated qsal-X ligands.[14,15,29,30] Stretches for the NCS, PF_6 and OTf anions are also evident in the IR spectra (Table 1).

TGA analysis of the compounds reveals a mass loss of 3.9% for **1** between 70–100 °C consistent with one MeOH (4.3% expected, Fig. S1, ESI†). Similarly, **3** displays a 13.7% mass loss beginning at 50 °C and complete at 90 °C, indicative of two molecules of CH_2Cl_2 (14.7%). The other complexes showed no mass loss until much higher temperatures and in the case of **4** suggests that the MeOH is readily lost, something confirmed by elemental analysis.

Structures of [Fe(qsal-Cl)(qsal-Br)]$^+$ complexes

Structures of all the mixed-ligand complexes have been determined, in some cases at multiple temperatures. The compounds all crystallize in triclinic $P\bar{1}$ except **4** which is in monoclinic $P2_1/c$ (Table 2). In all cases the Cl and Br substituents are crystallographically disordered over the two sites. This has been modelled with either fixed or variable occupancy and in both cases yields 1 : 1 ratio of the qsal-Cl and qsal-Br ligands. Interestingly, only [Fe(qsal-Cl)(qsal-Br)]PF_6 has two Fe(III) centres in the asymmetric unit with the other compounds having a single Fe(III) site (Fig. 1). By comparison, the compositions of the homoleptic compounds are [Fe(qsal-X)$_2$]NCS·MeOH, [Fe(qsal-X)$_2$]PF_6, [Fe(qsal-X)$_2$]OTf·sol (X = Cl, sol = none; X = Br, sol = 0.5MeOH) and [Fe(qsal-X)$_2$]BPh_4·sol (X = Cl, sol = H_2O; X = Br, sol = CH_2Cl_2) showing the heteroleptic species are more similar to the [Fe(qsal-Br)$_2$]$^+$ compounds.[31]

As compounds **3** and **4** differ from the homoleptic systems in terms of the solvent present in the lattice and to ensure that the bulk sample is not a mixture of the homoleptic compounds we undertook PXRD studies (Fig. S2 and S3, ESI†). The simulated and real diffractograms show remarkably good agreement and confirm that the crystal structures are reflective of the bulk material.

The Fe–N/O bond lengths of [Fe(qsal-Cl)(qsal-Br)]Y (Y = NCS, PF_6, OTf) at 123 K are between 1.945–1.969 Å and 1.850–1.880 Å, respectively indicative of LS Fe(III) (Table 3). This assignment is supported by the octahedral distortion parameters.[32,33] Interestingly, in **2** the Fe–N/O bond lengths of the two Fe(III) centres are very similar but the distortion parameters are subtly different. This may suggest that only one of the Fe centres is able to undergo spin crossover.

The most interesting member in this series is [Fe(qsal-Cl)(qsal-Br)]BPh_4·2CH_2Cl_2 where we have been able to determine the structure at three different temperatures. At 100 K the Fe–N/O bond distances are short and characteristic of a LS centre while at 123 K the Fe–N/O bond lengths elongate but are intermediate between HS and LS, termed MIX (Table 4). Note that by mixed we mean a mixture of the HS and LS states and not the intermediate S = 3/2 spin state. Only at 267 K are the Fe–N/O bonds and Σ and Θ indicative of full HS character. This suggests either gradual or stepped spin crossover is present in this compound.

The packing in **1**, **3** and **4** involves a pair of orthogonal π–π interactions which link the cations to form a 1D chain (Fig. 2 and Fig. S4–S8, ESI†). The plane-to-plane distances vary from 3.13–3.32 Å and are typical of [Fe(qsal-X)$_2$]$^+$ complexes (Table 5). In **2** the packing is substantially altered with two types of π–π interaction that form Fe1–Fe1 and Fe2–Fe2 dimers. The type A interaction is 0.13 Å shorter than type B due to the more planar qsal-X ligand in the former dimer. The dimers are linked by further π–π contacts but these have minimal overlap resulting in significantly weaker cooperativity. The 1D chains are connected by a range of other contacts principally C–H···π, C–H···Cl/Br and C–Cl/Br···π forming highly cooperative supramolecular 3D networks (Fig. 3). Many of the interactions are present in the homoleptic complexes, [Fe(qsal-X)$_2$]Y and reveal that the presence of two different ligands does not significantly impact the supramolecular connectivity.

Beyond the 1D chains, the packing in **3** is very different with multiple aryl embraces occurring between the [Fe(qsal-Cl)(qsal-Br)]$^+$ chains and the BPh_4^- anions (Fig. 4). Multiple aryl embraces are composed of a combination of C–H···π and π–π interactions in which none of the aryl groups are completely parallel or perpendicular. These interactions have been reported in a wide range of [M(2,2′-bipy)$_3$]$^{n+}$ complexes[34] and are also found in [Fe(qnal-7-OMe)$_2$]BPh_4·2MeOH.[35]

Magnetic studies of [Fe(qsal-Cl)(qsal-Br)]$^+$ complexes

The magnetic properties of **1–4** have been studied between 2–350 K by SQUID magnetometry (Fig. 5). To aid comparison, the $\chi_M T$ values of the homoleptic systems are plotted with those

Table 1 Physical and IR spectroscopic data [Fe(qsal-Cl)(qsal-Br)]Y·sol

Compound	% yield	Colour	IR[a] (cm^{-1})		
			$\nu_{C=N}$	ν_{ArH}	ν_{anion}
[Fe(qsal-Cl)(qsal-Br)]NCS·MeOH **1**	43	Black	1619	3054	2055
[Fe(qsal-Cl)(qsal-Br)]PF_6 **2**	38	Black	1614	3056	843
[Fe(qsal-Cl)(qsal-Br)]BPh_4·2CH_2Cl_2 **3**	45	Black	1619	3057	—
[Fe(qsal-Cl)(qsal-Br)]OTf·0.5MeOH **4**	35	Black	1614	3054	1297, 1164, 1084

[a] Complexes were determined in KBr.

 This journal is © The Royal Society of Chemistry and the Centre National de la Recherche Scientifique 2017

Table 2 Crystallographic data and structure refinement for **1–4**

	1	**2**		**3**		**4**
	123 K	123 K	100 K	123 K	267 K	123 K
Formula	$C_{34}H_{24}BrClFeN_5O_3S$	$C_{32}H_{20}BrClF_6FeN_4O_2P$		$C_{58}H_{44}BBrCl_5FeN_4O_2$		$C_{33.50}H_{20.50}BrClF_3FeN_4O_{3.50}S$
Molecular weight/gmol^{-1}	753.85	808.70	1152.79	1152.79	1152.79	827.31
Crystal system	Triclinic	Triclinic	Triclinic	Triclinic	Triclinic	Monoclinic
Space group	$P\bar{1}$	$P\bar{1}$	$P\bar{1}$	$P\bar{1}$	$P\bar{1}$	$P2_1/c$
a/Å	10.0889(13)	10.3803(6)	13.5484(8)	13.6206(5)	13.719(2)	14.0102(7)
b/Å	12.1516(15)	12.5570(7)	13.5845(6)	13.6929(5)	14.012(3)	19.1475(9)
c/Å	13.1028(18)	23.1729(14)	16.3212(10)	16.2779(6)	16.606(5)	12.2634(5)
α/°	105.885(3)	86.246(3)	97.290(4)	112.954(2)	113.81(2)	90
β/°	98.459(4)	81.312(3)	112.892(5)	96.785(2)	96.164(18)	111.1770(10)
γ/°	98.029(4)	89.492(3)	109.908(5)	110.518(2)	110.831(19)	90
T/K	123(2)	123(2)	100.0(1)	123(2)	267(9)	123(2)
Cell volume/Å^3	1500.6(3)	2979.4(3)	2482.6(3)	2501.27(17)	2609.3(12)	3067.6(2)
Z	2	4	2	2	2	4
Absorption coefficient/mm^{-1}	2.021	2.069	1.428	1.417	1.359	2.287
Reflections collected	9769	26 342	25 868	21 299	26 833	19 857
Independent reflections, R_{int}	6642, 0.0252	13 733, 0.1199	13 308, 0.0346	11 362, 0.0399	13 900, 0.0743	7014, 0.0399
Max. and min. transmission	0.7496 and 0.6296	0.8520 and 0.7894	0.8361 and 0.6349	0.8372 and 0.6368	0.8432 and 0.6478	0.6878 and 0.4312
Restraints/parameters	18/441	8/901	10/667	4/667	4/668	21/506
Final R indices [$I > 2\sigma(I)$]: R_1, wR_2	0.0896, 0.2389	0.0552, 0.0953	0.0491, 0.1092	0.0549, 0.1328	0.0872, 0.2282	0.0532, 0.1357

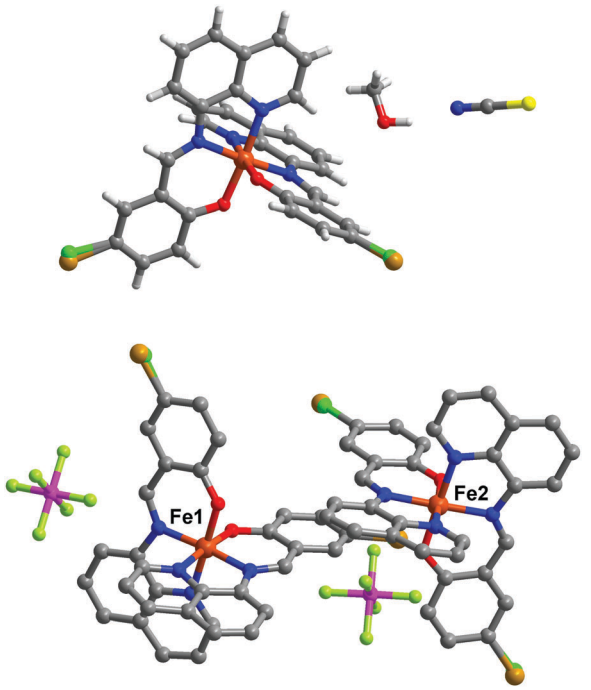

Fig. 1 The asymmetric unit of [Fe(qsal-Cl)(qsal-Br)]NCS·MeOH **1** (above) and [Fe(qsal-Cl)(qsal-Br)]PF_6 **2** (below).

Table 3 Fe–N/O bond lengths and octahedral distortion parameters of **1**, **2** and **4** at 123 K (Å, °)

	NCS-1	OTf-4	PF_6-2		
Fe1–O1	1.879(5)	1.880(3)	1.844(3)	Fe2–O3	1.855(3)
Fe1–O2	1.878(5)	1.879(3)	1.855(3)	Fe2–O4	1.858(3)
Fe1–O_{av}	1.878(5)	1.880(3)	1.850(3)	Fe2–O_{av}	1.856(3)
Fe1–N1	1.965(6)	1.948(2)	1.936(4)	Fe2–N5	1.940(4)
Fe1–N2	1.986(6)	1.962(3)	1.950(4)	Fe2–N6	1.952(4)
Fe1–N3	1.949(6)	1.946(3)	1.940(4)	Fe2–N7	1.933(4)
Fe1–N4	1.975(6)	1.962(3)	1.976(4)	Fe2–N8	1.956(4)
Fe1–N_{av}	1.969(6)	1.954(3)	1.950(4)	Fe2–N_{av}	1.945(4)
Σ	47	50	43	Σ	52
Θ	67	71	63	Θ	69

of **1–4**. In **1** the SCO is gradual reaching a plateau of *ca.* 2.5 cm^3 mol^{-1} K (60% HS) at 280–330 K before beginning to increase again. The SCO is more abrupt than [Fe(qsal-Br)$_2$]NCS·MeOH but less than the chloro analogue.[29] The onset of SCO also increases from 150 to *ca.* 200 to *ca.* 270 K in going from the Cl—only to **1** to the Br—only compound. In a similar way **2** exhibits gradual SCO behaviour intermediate between the two homoleptic analogues this time reaching 30% HS at 350 K. In the case of **4** the SCO profile more closely matches that of [Fe(qsal-Cl)$_2$]OTf than [Fe(qsal-Br)$_2$]OTf. In all of these compounds, the structures of the mixed-ligand compounds are virtually identical to the homoleptic [Fe(qsal-X)$_2$]Y systems.

In contrast, [Fe(qsal-Cl)(qsal-Br)]BPh_4·2CH_2Cl_2 exhibits a magnetic profile unlike either of the parent complexes perhaps as it contains two CH_2Cl_2 molecules rather than the single

Table 4 Fe–N/O bond lengths and octahedral distortion parameters of **3** at 100, 123 and 267 K (Å)

	100 K	123 K	267 K	ΔHS-MIX[a]	ΔHS–LS
Fe1–O1	1.876(2)	1.888(3)	1.908(3)	0.02	0.032
Fe1–O2	1.881(2)	1.887(3)	1.904(3)	0.017	0.023
Fe1–O_{av}	1.879(2)	1.888(3)	1.906(3)	0.018	0.027
Fe1–N1	1.948(2)	2.045(3)	2.131(4)	0.086	0.0183
Fe1–N2	1.977(2)	2.064(3)	2.150(4)	0.086	0.0173
Fe1–N3	1.951(2)	2.038(3)	2.129(4)	0.091	0.0178
Fe1–N4	1.983(2)	2.077(3)	2.142(4)	0.065	0.0159
Fe1–N_{av}	1.965(2)	2.056(3)	2.138(4)	0.082	0.0173
Σ	46	53	75	22	29
Θ	70	142	209	67	139

[a] ΔHS-MIX refers to the difference between the structures at 267 and 123 K.

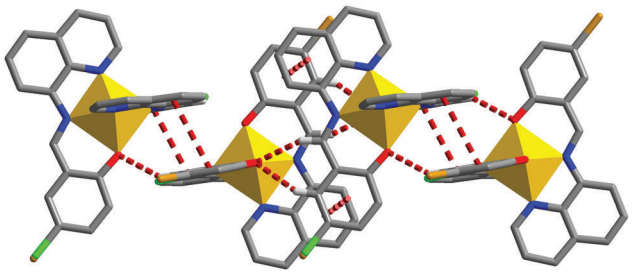

Fig. 2 View of the π–π interactions in **1**.

Table 5 Principal supramolecular contact distances and angles in **1–4** (Å, °)

	1	2	3	4
π–π[a]				
Type A	3.203	3.267 (Fe1–Fe1)	3.240[d] 3.252[e] 3.321[f]	3.248
Type B	3.272	3.393 (Fe2–Fe2)	3.131[d] 3.200[e] 3.322[f]	3.228
Br···π	3.254(8)	3.428(9)	—	—
Cl···π	3.384(5)	3.508(6)	—	—
C–H···Cl1	—	2.922(8)	—	2.857(9)
C–H···Br1	—	2.821(2)	—	2.823(3)
C–H···Cl2	—	2.723(9)	—	2.821(9)
C–H···Br2	—	2.621(3)	—	2.806(2)
α[b]		5.5, 8.5 (Fe1) 11.9, 10.0 (Fe2)	8.8, 23.1[d] 10.0, 24.9[e] 10.9, 25.4[f]	
θ[c]	89.8	83.4 (Fe1) 88.1 (Fe2)	72.6[d] 71.7[e] 72.1[f]	88.3

[a] Plane-to-distances. [b] Angle between the phenyl and quinoline rings. [c] Angle between the two planes of the qsal-X ligands. [d] At 100 K. [e] At 123 K. [f] At 267 K.

CH_2Cl_2 molecule of $[Fe(qsal\text{-}Br)_2]BPh_4$ and the H_2O in $[Fe(qsal\text{-}Cl)_2]BPh_4$.

In $[Fe(qsal\text{-}Cl)(qsal\text{-}Br)]BPh_4{\cdot}2CH_2Cl_2$ the sample was quickly cooled to 5 K and then warmed to 100 K where $\chi_M T$ = 0.45 cm^3 mol^{-1} K, consistent with LS Fe(III). Upon further heating

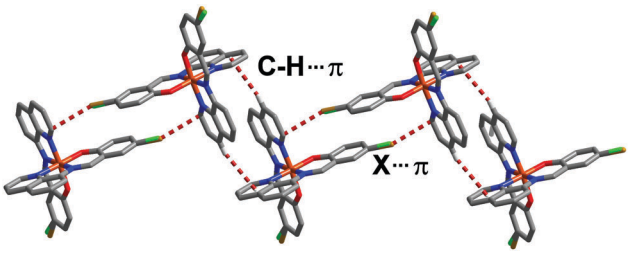

Fig. 3 View of the C–H···π and Cl/Br···π interactions that link the 1D chains in **1**.

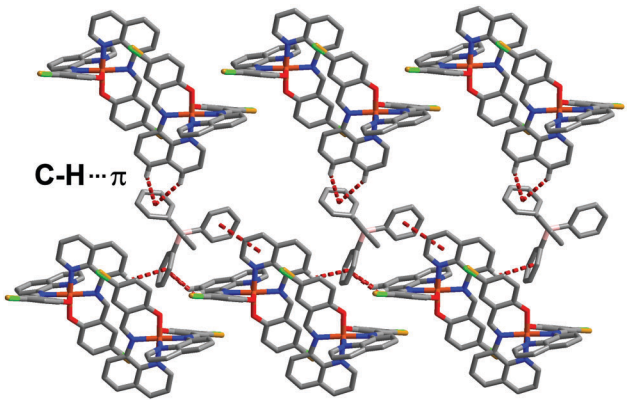

Fig. 4 View of the C–H···π interactions that link the 1D chains in **3**.

$\chi_M T$ increased to 1.40 cm^3 mol^{-1} K, indicative of 30% HS. $\chi_M T$ doesn't increase further until 300 K before an abrupt change is observed with $\chi_M T$ = 3.10 cm^3 mol^{-1} K at 350 K. TGA results (Fig. S1, ESI†) indicate that **3** loses both CH_2Cl_2 molecules in the range 320–360 K. Following this loss upon cooling we are unable to return to the full LS state with $\chi_M T$ = 1.50 cm^3 mol^{-1} K down to 30 K. Given the high vacuum of the SQUID measurements it's likely that the SCO here is coupled to partial or complete solvent loss. Comparisons with the structures at 100 and 123 K are consistent with the magnetic studies the one at 267 K is clearly different. The reason for this inconsistency is unclear but discrepancies have also been observed in other solvent sensitive SCO systems of $[Fe(qsal\text{-}X)_2]Y$.[12] Overall, the results suggest that provided that the lattice is not greatly impacted by the presence of two different ligands the SCO profile will be intermediate between the parent complexes. However, if a unique lattice is formed the mixed ligand complex can as hypothesized yield better SCO characteristics.

Conclusions

In conclusion we have successfully synthesized a series of mixed ligand $[Fe(qsal\text{-}Cl)(qsal\text{-}Br)]^+$ complexes. The heteroleptic complexes are favoured over the homoleptic systems in all cases. X-ray crystallographic studies reveal structures that are more often similar to the $[Fe(qsal\text{-}Cl)_2]^+$ complexes. In most cases the packing is little altered being strongly reminiscent of both parent $[Fe(qsal\text{-}X)_2]^+$ (X = Cl, Br) systems with strong π–π

 This journal is © The Royal Society of Chemistry and the Centre National de la Recherche Scientifique 2017

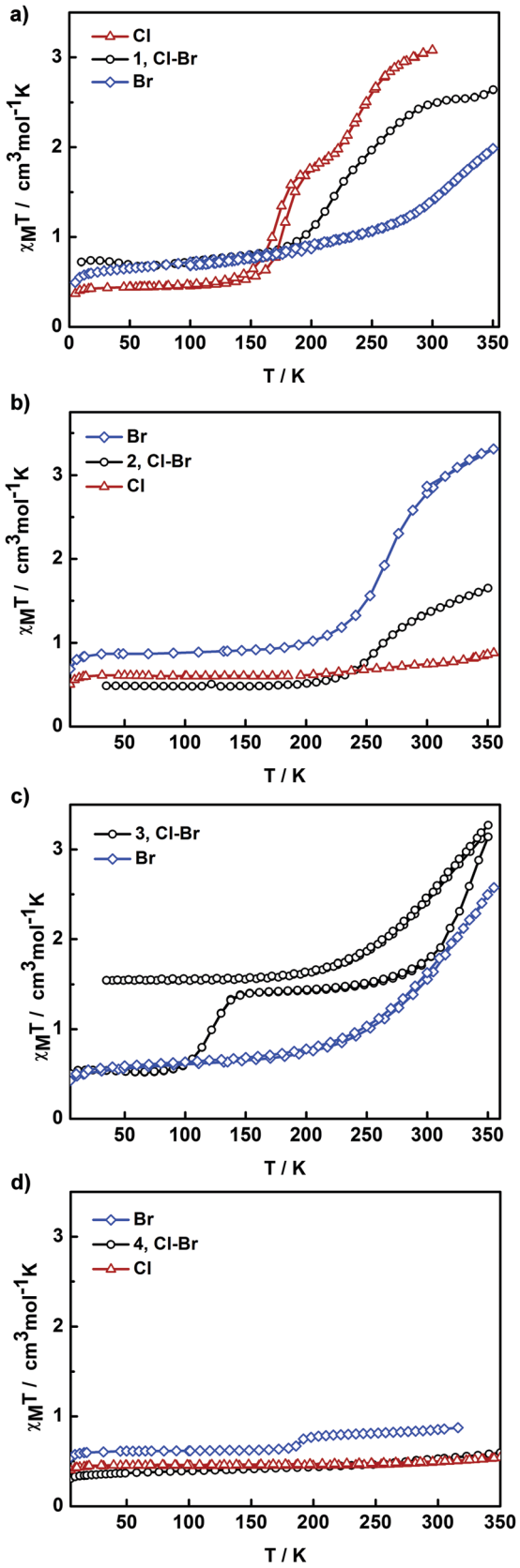

Fig. 5 $\chi_M T$ *versus* T plot for [Fe(qsal-Cl)(qsal-Br)]Y where Y are (a) NCS, (b) PF_6, (c) BPh_4, and (d) OTf.

interactions forming 1D chains. The exception is [Fe(qsal-Cl)-(qsal-Br)]$BPh_4 \cdot 2CH_2Cl_2$ where the presence of CH_2Cl_2 in the lattice, instead of H_2O, significantly impacts the packing resulting in greater cooperativity between the cations and anions. The similarity in packing for **1**, **2** and **4** with the homoleptic complexes results in the spin crossover profile being intermediate between the homoleptic $[Fe(qsal\text{-}X)_2]^+$ systems. In contrast, in **3** the alteration in the packing gives unusual stepped spin crossover behaviour surpassing both $[Fe(qsal\text{-}X)_2]BPh_4 \cdot sol$ complexes. This latter result confirms our earlier studies that mixed ligand complexes provide a valuable strategy in preparing new spin crossover systems.

Experimental

General remarks

All reactions were conducted in air using reagent grade solvents. Hqsal-Cl and Hqsal-Br were synthesized using literature procedures.[36] All other chemicals were purchased from Sigma-Aldrich Chemical Company and used as received. Infrared spectra (as KBr discs) were recorded on a Perkin–Elmer Spectrum One infrared spectrophotometer in the range 400–4000 cm^{-1}. Electronic spectra were recorded on a Shimadzu 1800 UV-visible spectrometer. Elemental analyses were carried out on a Eurovector EA3000 analyser at the School of Chemistry, University of Bristol, UK. ESI-MS were carried out on a Bruker Daltonics 7.0T Apex 4 FTICR Mass Spectrometer at the National University of Singapore.

Synthesis of [Fe(qsal-Cl)(qsal-Br)]NCS·MeOH 1. A solution of Hqsal-Br (65 mg, 0.2 mmol) and Hqsal-Cl (57 mg, 0.2 mmol) in CH_2Cl_2 (2 ml) was added to the bottom of a test tube in which NEt_3 (56 μl, 0.4 mmol) had been added as a base. $FeCl_3$ (31 mg, 0.2 mmol) was dissolved in MeOH (5 ml) and NaNCS (50 mg, 0.6 mmol) added. The solution was stirred for 5 min, filtered and then layered on blank MeOH (3 ml) which had been layered on top of the Hqsal-Cl/Br solution. After 3 days, black crystals formed which were washed with hexane (2 × 1 ml) and air dried; yield 62 mg (43%). *m*/*z* (ESI) 664.0 $[Fe(qsal\text{-}Cl/Br)_2]^+$. Elemental analysis: calcd (found) for $C_{34}H_{24}BrClFeN_5O_3S$: C, 54.17 (53.49); H, 2.79 (3.21); N, 9.70 (9.29)%.

Compounds **2–4** were prepared in a similar manner to **1** using KPF_6, $NaBPh_4$ and $NaCF_3SO_3$, respectively.

[Fe(qsal-Cl)(qsal-Br)]PF_6 2. Black crystals, 38% yield. *m*/*z* (ESI) 664.0 $[Fe(qsal\text{-}Cl/Br)_2]^+$, 144.9 $[PF_6]^-$. Elemental analysis: calcd (found) for $C_{32}H_{20}BrClF_6FeN_4O_2P$: C, 47.53 (47.41); H, 2.49 (2.91); N, 6.93 (6.96)%.

[Fe(qsal-Cl)(qsal-Br)]$BPh_4 \cdot 2CH_2Cl_2$ 3. Black crystals, 45% yield. *m*/*z* (ESI) 664.0 $[Fe(qsal\text{-}Cl/Br)_2]^+$, 319.1 $[BPh_4]^-$. Elemental analysis: calcd (found) for $C_{56}H_{40}BBrClFeN_4O_2$: C, 68.43 (68.46); H, 4.10 (4.33); N, 5.70 (5.58)% (the compound analysed without CH_2Cl_2).

Synthesis of [Fe(qsal-Cl)(qsal-Br)]$CF_3SO_3 \cdot 0.5$MeOH 4. Black crystals, 35% yield. *m*/*z* (ESI) 664.0 $[Fe(qsal\text{-}Cl/Br)_2]^+$, 149.2 $[CF_3SO_3]^-$. Elemental analysis: calcd (found) for $C_{33}H_{20}BrClF_3FeN_4O_5S$: C,

48.76 (48.82); H, 2.48 (3.07); N, 6.89 (6.97)% (the compound analysed without MeOH).

Crystallography

Crystal structures were collected on a Bruker APEXII area detector with graphite monochromated MoKα (λ = 0.71073 Å).[37] After data collection, in each case an empirical absorption correction (SADABS) was applied,[38] and the structures were then solved by direct methods and refined on all F^2 data using the SHELX suite of programs.[39] In all cases non-hydrogen atoms were refined with anisotropic thermal parameters; hydrogen atoms were included in calculated positions and refined with isotropic thermal parameters. Crystal data and data processing parameters for **1–4** are given in Table 2. Pictures were generated using DIAMOND.[40] The CCDC numbers for the X-ray crystallographic data presented in this paper are 1526771 (**1**), 1526772 (**2**), 1526773 (**3**-100 K), 1526774 (**3**-123 K), 1526775 (**3**-267 K) and 1526776 (**4**).†

Magnetic susceptibility studies

Magnetic data were collected using a Quantum Design MPMS 5 SQUID magnetometer under an applied field of 1 T over a temperature range between 340–344 K. The powdered or polycrystalline samples were placed in gel capsules and care was taken to allow long thermal equilibration times at each temperature point; often referred to as settle mode.

Conflicts of interest

There are no conflicts to declare.

Acknowledgements

We thank the Thailand Research Fund (RSA5880048) for funding this research. We also thank the Development and Promotion of Science Talents Project for a PhD scholarship to WP. KSM thanks the Australian Research Council for a Discovery grant.

Notes and references

1 D. J. Harding, P. Harding and W. Phonsri, *Coord. Chem. Rev.*, 2016, **313**, 38–61.
2 M. Nihei, T. Shiga, Y. Maeda and H. Oshio, *Coord. Chem. Rev.*, 2007, **251**, 2606–2621.
3 R. Bertoni, M. Lorenc, A. Tissot, M. L. Boillot and E. Collet, *Coord. Chem. Rev.*, 2015, **282–283**, 66–76.
4 *Spin-Crossover Materials: Properties and Applications*, ed. M. A. Halcrow, John Wiley & Sons, Ltd, Chichester, 2013.
5 P. Gütlich, A. B. Gaspar and Y. Garcia, *Beilstein J. Org. Chem.*, 2013, **9**, 342–391.
6 P. Gütlich and H. A. Goodwin, *Top. Curr. Chem.*, 2004, **233**, 1–47.
7 S. Brooker, *Chem. Soc. Rev.*, 2015, **44**, 2880–2892.
8 K. Senthil and M. Ruben, *Coord. Chem. Rev.*, 2017, **346**, 176–205.
9 S. Hayami, Z.-Z. Gu, H. Yoshiki, A. Fujishima and O. Sato, *J. Am. Chem. Soc.*, 2001, **123**, 11644–11650.
10 S. Hayami, K. Hiki, T. Kawahara, Y. Maeda, D. Urakami, K. Inoue, M. Ohama, S. Kawata and O. Sato, *Chem. – Eur. J.*, 2009, **15**, 3497–3508.
11 K. Fukuroi, K. Takahashi, T. Mochida, T. Sakurai, H. Ohta, T. Yamamoto, Y. Einaga and H. Mori, *Angew. Chem., Int. Ed.*, 2014, **53**, 1983–1986.
12 W. Phonsri, P. Harding, L. Liu, S. G. Telfer, K. S. Murray, B. Moubaraki, T. M. Ross, G. N. L. Jameson and D. J. Harding, *Chem. Sci.*, 2017, **8**, 3949–3959.
13 N. Phukkaphan, D. L. Cruickshank, K. S. Murray, W. Phonsri, P. Harding and D. J. Harding, *Chem. Commun.*, 2017, **53**, 9801–9804.
14 D. J. Harding, W. Phonsri, P. Harding, K. S. Murray, B. Moubaraki and G. N. L. Jameson, *Dalton Trans.*, 2015, **44**, 15079–15082.
15 B. J. C. Vieira, J. C. Dias, I. C. Santos, L. C. J. Pereira, V. da Gama and J. C. Waerenborgh, *Inorg. Chem.*, 2015, **54**, 1354–1362.
16 A. Tissot, R. Bertoni, E. Collet, L. Toupet and M.-L. Boillot, *J. Mater. Chem.*, 2011, **21**, 18347.
17 A. Tissot, P. Fertey, R. Guillot, V. Briois and M.-L. Boillot, *Eur. J. Inorg. Chem.*, 2014, 101–109.
18 A. I. Vicente, A. Joseph, L. P. Ferreira, M. de Deus Carvalho, V. H. N. Rodrigues, M. Duttine, H. P. Diogo, M. E. Minas da Piedade, M. J. Calhorda and P. N. Martinho, *Chem. Sci.*, 2016, **7**, 4251–4258.
19 E. W. T. Yemeli, G. R. Blake, A. P. Douvalis, T. Bakas, G. O. R. Alberda van Ekenstein and P. J. van Koningsbruggen, *Chem. – Eur. J.*, 2010, DOI: 10.1002/chem.201002100.
20 Z.-Y. Li, J.-W. Dai, Y. Shiota, K. Yoshizawa, S. Kanegawa and O. Sato, *Chem. – Eur. J.*, 2013, **19**, 12948–12952.
21 Z.-Y. Li, J.-W. Dai, K. J. Gagnon, H.-L. Cai, T. Yamamoto, Y. Einaga, H.-H. Zhao, S. Kanegawa, O. Sato, K. R. Dunbar and R.-G. Xiong, *Dalton Trans.*, 2013, **42**, 14685–14688.
22 S. Kang, Y. Shiota, A. Kariyazaki, S. Kanegawa, K. Yoshizawa and O. Sato, *Chem. – Eur. J.*, 2016, **22**, 532–538.
23 Z.-Y. Li, H. Ohtsu, T. Kojima, J.-W. Dai, T. Yoshida, B. K. Breedlove, W.-X. Zhang, H. Iguchi, O. Sato, M. Kawano and M. Yamashita, *Angew. Chem., Int. Ed.*, 2016, **55**, 5184–5189.
24 M. A. Halcrow, *Chem. Soc. Rev.*, 2011, **40**, 4119–4142.
25 K. S. Murray and C. J. Kepert, *Top. Curr. Chem.*, 2004, **233**, 195–228.
26 W. Phonsri, C. G. Davies, G. N. L. Jameson, B. Moubaraki and K. S. Murray, *Chem. – Eur. J.*, 2016, **22**, 1322–1333.
27 W. Phonsri, D. S. Macedo, C. G. Davies, G. N. L. Jameson, B. Moubaraki and K. S. Murray, *Dalton Trans.*, 2017, **46**, 7020–7029.
28 W. Phonsri, V. Martinez, C. G. Davies, G. N. L. Jameson, B. Moubaraki and K. S. Murray, *Chem. Commun.*, 2016, **52**, 1443–1446.
29 W. Phonsri, D. J. Harding, P. Harding, K. S. Murray, B. Moubaraki, I. A. Gass, J. D. Cashion, G. N. L. Jameson and H. Adams, *Dalton Trans.*, 2014, **43**, 17509–17518.
30 A. I. S. Neves, J. C. Dias, B. J. C. Vieira, I. S. Santos, M. B. Castelo Branco, L. C. J. Pereira, J. C. Waerenborgh, M. Almeida, D. Belo and V. Da Gama, *CrystEngComm*, 2009, **11**, 2160–2168.

 This journal is © The Royal Society of Chemistry and the Centre National de la Recherche Scientifique 2017

31 W. Phonsri, PhD thesis, Walailak University, 2014.
32 J. K. McCusker, A. L. Rheingold and D. N. Hendrickson, *Inorg. Chem.*, 1996, **35**, 2100–2112.
33 M. Marchivie, P. Guionneau, J. F. Létard and D. Chasseau, *Acta Crystallogr., Sect. B: Struct. Sci.*, 2005, **61**, 25–28.
34 I. Dance and M. Scudder, *J. Chem. Soc., Dalton Trans.*, 1998, 1341–1350.
35 M. Nakaya, K. Shimayama, K. Takami, K. Hirata, A. S. Alao, M. Nakamura, L. F. Lindoy and S. Hayami, *Chem. Lett.*, 2014, **43**, 1058–1060.
36 J. Sirirak, W. Phonsri, D. J. Harding, P. Harding, P. Phommon, W. Chaoprasa, R. M. Hendry, T. M. Roseveare and H. Adams, *J. Mol. Struct.*, 2013, **1036**, 439–446.
37 *Bruker APEXII*, Bruker AXS Inc., Madison, WI, USA, 2005.
38 *SADABS and SAINT*, Bruker AXS Inc., Madison, WI, USA, 2013.
39 G. M. Sheldrick, *Acta Crystallogr., Sect. A: Found. Crystallogr.*, 2008, **64**, 112–122.
40 K. Brandenberg and H. Putz, *DIAMOND, Crystal Impact*, Bonn, Germany, 2006.

ChemComm

COMMUNICATION

Check for updates

Cite this: *Chem. Commun.*, 2017, 53, 9801

Received 1st August 2017,
Accepted 14th August 2017

DOI: 10.1039/c7cc05998a

rsc.li/chemcomm

Hysteretic spin crossover driven by anion conformational change†

Natnaree Phukkaphan,[a] Dyanne L. Cruickshank,[b] Keith S. Murray,[c] Wasinee Phonsri,[c] Phimphaka Harding[a] and David J. Harding*[a]

A new air stable Fe^{III} spin crossover (SCO) complex has been synthesized. The compound undergoes abrupt SCO near room temperature with $T_{1/2}$ (↓) = 244 K and $T_{1/2}$ (↑) = 278 K. Structural studies of the complex in the high spin and low spin state show that the strong cooperativity and thus the wide hysteresis is driven by an unprecedented anionic conformational change.

Molecular bistability is much sought in the development of new materials as two or more states are accessible under a wide range of external stimuli.[1–6] Spin crossover (SCO) complexes are an important family of bistable materials switching between a high spin (HS) and a low spin (LS) state under temperature, pressure or light perturbation.[7–10] It can occur in d^4–d^7 transition metal complexes provided that a suitable ligand field is present but is most commonly studied in iron(II)[11–15] and iron(III)[16,17] complexes.

Our group has been working on one particular ligand system quinolylsalicylaldimine, Hqsal-X which combined with iron(III) gives SCO active materials.[18–22] Our interest in these ligands stems from the report of $[Fe(qsal)_2]NCSe{\cdot}CH_2Cl_2$ which after solvent loss exhibits spin crossover with a hysteresis of 70 K.[23,24] The impressive hysteresis is thought to be due to extensive π–π interactions and in seeking to supplement these we, and others, have been exploring the SCO chemistry of $[Fe(qsal\text{-}X)_2]$anion {qsal-X = (*N*-8-quinolyl)-5-X-salicylaldiminate} systems. In the course of these studies while interesting systems displaying abrupt,[18] symmetry breaking[20] and stepped SCO[19,25] have been discovered the hystereses of these systems remain modest. Moreover, in many cases the SCO behaviour is changeable as a result of solvent loss, polymorphism or other effects.[26] What has become clear is that as with iron(II) SCO complexes multiple factors influence both the abruptness and the cooperativity of the spin crossover.

Of the different factors that affect SCO perhaps the most important is the anion because the different sizes and shapes can lead to significant changes in the crystal lattice and the subsequent magnetic behaviour of the compound.[27] Anions can also be important in driving SCO. One of the first reports of an order–disorder of anion leading to cooperative SCO was in $[Fe(DAPP)(abpt)][ClO_4]_2$ {DAPP = bis(3-aminopropyl)(2-pyridylmethyl)amine, abpt = 4-amino-3,5-bis(pyridin-2-yl)-1,2,4-triazole}.[28] Similar order–disorder of the anion is found in $[Fe\{3\text{-}bpp\text{-}(5\text{-}C_6H_3OH)_2\}_2][ClO_4]_2{\cdot}H_2O{\cdot}2$acetone {3-bpp-(5-$C_6H_3OH)_2$ = 2,6-bis[5-(2′-phenol)pyrazol-3-yl]-pyridine},[29] *fac*-$[Fe(2\text{-}Me\text{-}4\text{-}ima\text{-}n\text{-}Pr)_3]Cl{\cdot}PF_6$ (2-Me-4-ima-*n*-Pr = 2-methylimidazol-4-yl-methylideneamino-*n*-propyl)[30] and $[Mn(sal_2bapen)]PF_6$ {(sal_2bapen = 2,6,9,13-tetraazatetradeca-1,13-diene-1,14-diyl)-bis(phenolate)}.[31] In all the above cases the SCO is abrupt and with hysteresis, up to 40 K for $[Fe\{3\text{-}bpp\text{-}(5\text{-}C_6H_3OH)_2\}_2]\text{-}[ClO_4]_2{\cdot}H_2O{\cdot}2$acetone. Even in stepped SCO systems such as $[Fe(picpzpz)_2][BF_4]_2{\cdot}$MeOH {picpzpz = 3-(2-pyrazinyl)-1-[(2-pyridyl)methyl]pyrazole} the first abrupt SCO step is coupled to an anion order–disorder transition.[32] While in $[Co(4\text{-terpridone})_2][OTf]_2{\cdot}H_2O$ the reverse cooperative SCO is also coupled to an order–disorder of the triflate.[33] Moreover, recent studies have shown that such order–disorder transitions may be induced by high pressure.[34]

It is evident that the anion can have a profound influence on SCO characteristics and help in promoting hysteresis. However, to date there have been no reports of the impact of the anion's conformation on SCO. In this communication we report $[Fe(qsal\text{-}I)_2]NTf_2$ which undergoes an abrupt SCO close to room temperature with a hysteresis of 34 K. We demonstrate that this unusually broad and stable hysteresis is due to an unprecedented anion conformational change in which the anion is ordered in both spin states.

The complex was prepared by adding a MeOH solution of $LiNTf_2$ to a warmed MeOH solution of $[Fe(qsal\text{-}I)_2]NO_3$ resulting in precipitation of $[Fe(qsal\text{-}I)_2]NTf_2$ **1**. Recrystallization by slow evaporation of a $MeCN/CH_2Cl_2$ solution of **1** gives fine black

[a] *Functional Materials and Nanotechnology Center of Excellence, Walailak University, Thasala, Nakhon Si Thammarat, 80160, Thailand. E-mail: hdavid@g-mail.wu.ac.th; Tel: +66-75-672094*
[b] *Rigaku Oxford Diffraction, Kemsing, Sevenoaks, TN15 6QY, UK*
[c] *Monash University, Clayton, Melbourne, Victoria, 3800, Australia*

† Electronic supplementary information (ESI) available: Synthetic procedure, structural pictures, DSC measurements, and IR and Raman spectroscopic details. CCDC 1552831–1552833. For ESI and crystallographic data in CIF or other electronic format see DOI: 10.1039/c7cc05998a

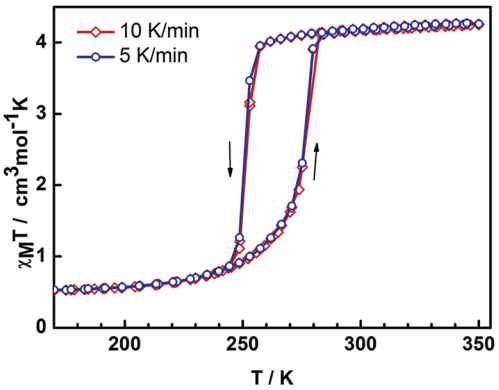

Fig. 1 $\chi_M T$ *vs.* T plot of [Fe(qsal-I)$_2$]NTf$_2$.

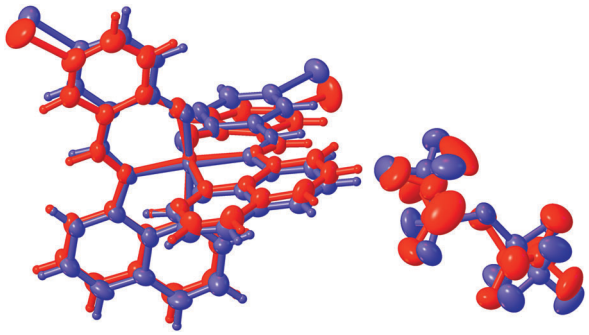

Fig. 2 Overlay of the molecular structures of [Fe(qsal-I)$_2$]NTf$_2$ at 245 K (blue) and 275 K (red) showing the more twisted qsal-I ligands in the HS state and the marked changes in the anion conformation.

needles. The absence of solvent in the lattice and the ability to synthesize the compound in air make **1** an ideal candidate for readily processable SCO materials.

Magnetic susceptibility measurements of **1** have been performed between 170–350 K at heating and cooling rates of 5 and 10 K min^{-1} (Fig. 1). At 170 K $\chi_M T$ is 0.52 cm^3 mol^{-1} K and typical of LS Fe^{III}. $\chi_M T$ gradually increases upon warming until 270 K when it increases very abruptly reaching 4.19 cm^3 mol^{-1} K at 300 K with $T_{1/2}$ = 278 K and characteristic of HS Fe^{III}. Cooling results in another abrupt transition this time at $T_{1/2}$ = 248 K giving a hysteresis of 30 K. The hysteresis loop is repeatable over successive cycles and shows no scan rate dependence. Photomagnetic measurements reveal that **1** does not undergo LIESST and given the near 100% LIESST in [Fe^{II}(qsal-I)$_2$]·CH$_2$Cl$_2$[35] this is likely due to the rapid relaxation of the light induced metastable HS state back to the LS state in Fe^{III}. This has previously been ascribed to the smaller differences in the Fe–ligand bond distances for Fe^{III} compared to Fe^{II} which permits more effective tunneling to the LS state.[36] Nevertheless, **1** is one of very few compounds that exhibit abrupt SCO with significant hysteresis close to room temperature (Table S1, ESI†).[37–39]

DSC measurements show a peak at 278 K in the warming mode and a peak at 244 K in the cooling mode giving a hysteresis of 34 K and slightly larger than that observed in the magnetic susceptibility studies, something not uncommon in SCO systems (Fig. S1, ESI†).[40] The average enthalpy and entropy values are 5.00 kJ mol^{-1} and 19.5 J mol^{-1} K^{-1}, respectively (Table S2, ESI†) and are typical of Fe^{III} systems.[16,17] The latter is significantly higher than that expected based on electronic considerations only {^{2}T$_2$ to ^{6}A$_1$ transition, Rln(6/2) = 9.13 J mol^{-1} K^{-1}} and suggests strong vibrational contributions to the entropy of SCO of *ca.* 10 J mol^{-1} K^{-1}.

To elucidate the structural contributions to SCO the crystal structure was determined at 245, 255 (upon cooling from 275 K) and 275 K. At all temperatures **1** crystallizes in triclinic $P\bar{1}$ with crystallographic data and refinement parameters given in Table S3 (ESI†). The asymmetric unit contains one octahedral Fe^{III} centre coordinated by two meridional qsal-I ligands and a single triflimide anion (Fig. 2). The Fe–N/O bond lengths are 2.099–2.137(4) and 1.918–1.921(4) Å, respectively at 275 and 255 K and characteristic of the HS state.[18,21] As is common in this family of compounds the Fe–N$_{quin}$ bond lengths are *ca.* 0.03 Å longer than the Fe–N$_{imine}$ bonds. At 245 K the bond lengths are very slightly longer than is usual for full LS Fe^{III} (normal LS Fe–N bond lengths = 1.96–1.97 Å)[18,21] suggesting that a small amount HS Fe^{III} is still present at this temperature (Table 1).[18,21] The change in Fe–O bond lengths is 0.028(6) Å while the Fe–N bond distances are 0.137(8) Å confirming that SCO has occurred. This is supported by the change in the octahedral distortion parameters which are $\Delta\Sigma$ = 18.6° and $\Delta\Theta$ = 101° and again indicative of almost complete SCO (Table 1). The final feature of note is the increased non-planarity of the qsal-I ligands upon transition to the HS state. Interestingly, similar changes occur in the strongly hysteretic SCO compound [Fe(qsal-I)$_2$]OTf·EtOH (ΔT = 80 K).[18]

The most striking difference between the HS and LS structures is a remarkable change in the conformation of the triflimide from a *syn* conformation (C–S···S–C torsion angle = 8.7(3)° and 9.3(4)° at 255 and 275 K) in the HS state to an intermediate conformation in the LS state (C–S···S–C torsion angle = 94.5(6)°, see Fig. 3). The *anti* conformation is inaccessible on steric grounds as this would place the CF$_3$ group and the quinoline ring of the qsal-I ligand in the same place. A search of the CCDC reveals that this intermediate conformation

Table 1 Fe–N/O bond lengths, octahedral distortion parameters and supramolecular contact distances (Å) or angles (°) in **1**

T	245 K	255 K	275 K
Fe–O	1.890(6)	1.918(3)	1.921(4)
Fe–N$_{quin}$	2.003(8)	2.130(4)	2.137(4)
Fe–N$_{imine}$	1.967(8)	2.099(4)	2.110(5)
Σ^a	50.4(9)	66.2(4)	69.0(4)
Θ^b	92.9	184.2	193.9
π–π	3.323(8) (type A)	3.316(4) (type A)	3.341(4) (type A)
	3.329(7) (type B)	3.345(3) (type B)	3.336(3) (type B)
C–H···π	2.804(11)	2.695(5)	2.715(6)
O···π	3.013(8)	3.194(4)	3.201(5)
α^c	4.6(3) (type A)	10.2(1) (type A)	10.1(1) (type A)
	6.3(3) (type B)	14.1(1) (type B)	13.9(1) (type B)

^{a} $\Sigma = \sum_{i=1}^{12} |90 - \alpha_i|$, where α_i are the twelve *cis* N/O–Fe–N/O angles.[43] ^{b} $\Theta = \sum_{i=1}^{24} |60 - \theta_i|$, where θ_i are the 24 unique N/O–Fe–N/O angles measured on the projection of two triangular faces of the octahedron along their common pseudo-threefold axis.[44] ^{c} α = the angle between planes of the quinoline and phenolate rings.

 This journal is © The Royal Society of Chemistry 2017

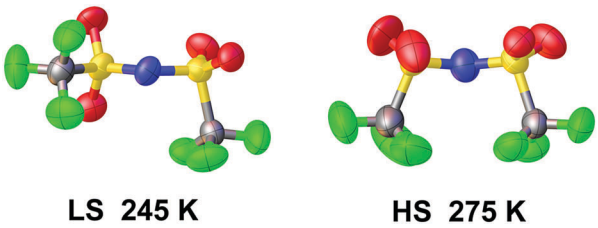

Fig. 3 View of the anion conformational change in **1** between the HS and LS states.

is very rare with only two other examples previously reported.[41,42] The anion is also involved in a O···π interaction involving the quinoline ring that shortens significantly by *ca.* 0.2 Å upon transition to the LS state (see Fig. S2, ESI†).

The packing in **1** mirrors other $[Fe(qsal\text{-}X)_2]^+$ complexes with two types of π–π interactions, type A and B, formed between neighbouring qsal-I ligands forming a 1D chain (Fig. 4 and Fig. S3, ESI†).[18–20] The type A and type B interactions are orthogonal to each other and in contrast to most $[Fe(qsal\text{-}X)_2]^+$ systems, SCO in **1** results in almost no change in the plane-to-plane distance (Table 1). Instead the qsal-I ligands become bent as the Fe^{III} centre becomes HS. The 1D chains are linked by a pair of C–H···π interactions rather than the more common P4AE contacts (Fig. S4, ESI†). Beyond this a combination of C–H···O/F interactions all involving the anion create a 3D supramolecular network. It is notable that when viewed down the 1D π–π chains there is a considerable change in the shape of the central channel from almost square to rhombus like (Fig. S5 and S6, ESI†). The close structural similarity between **1** and other less hysteretic $[Fe(qsal\text{-}X)_2]^+$ systems strongly suggests that the large hysteresis observed here is primarily due to the anionic conformational change.

To better understand the vibrational contributions to SCO we undertook variable temperature IR and Raman spectroscopic studies between 293 and 228 K (Fig. 5 and Fig. S7, S8, ESI†). The IR and Raman spectra both show significant changes between 1570–1600 cm^{-1} with the imine stretch moving from 1601 to 1606 cm^{-1} (1594 to 1600 cm^{-1} for the Raman; Fig. 5 and Fig. S7–S9, ESI†) in going from the HS to the LS state. The most striking difference though is in the S=O stretches in the IR spectra which appear at 1367 and 1381 cm^{-1} in the HS state but are absent in the LS state. The bands presumably move to lower wavenumbers as the anion undergoes conformational change[45] and are now masked by the vibrations of the qsal-I ligand.

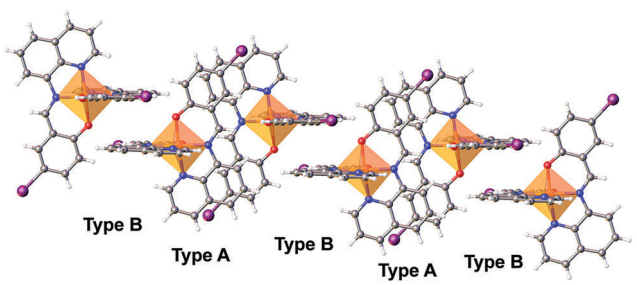

Fig. 4 View of the type A and type B interactions that form the 1D π–π chains in **1**.

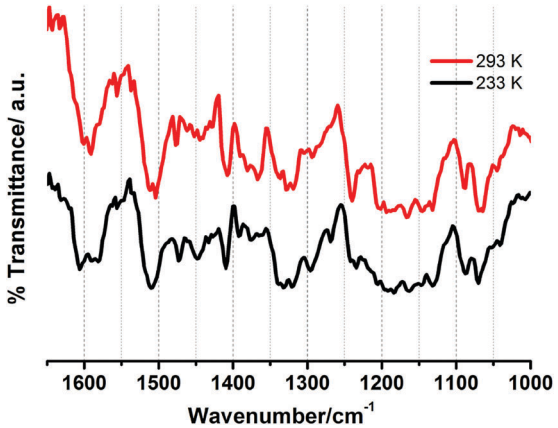

Fig. 5 View of the IR stretches in **1** in the HS (293 K) and LS state (233 K).

The Raman spectra in the cooling and heating modes show considerable differences with the spectra broader in the heating mode suggesting a mixture of HS and LS states (Fig. S9, ESI†). This is consistent with the slightly more gradual nature of the SCO in this region, upon heating, observed in the magnetic studies of **1** (Fig. 1). As in $[Fe(3\text{-}OMe\text{-}salEen)_2]PF_6$ the large changes in the HS and LS IR and Raman spectra in **1** are thought to arise from the significant differences in the skeletal vibrations of the two spin states.[46] This is supported by the fact that $[Fe(qsal\text{-}Br)_2]NO_3{\cdot}2MeOH$ which exhibits far smaller enthalpy and entropy differences shows only very minor changes in the IR spectra of the two spin states.[20]

In summary, we have prepared a solvent free, air-stable Fe^{III} SCO complex which undergoes abrupt SCO close to room temperature with an impressive hysteresis of 34 K. Structural studies indicate that the hysteresis is driven by a unique change in the anion conformation. Given the range of conformationally flexible anions available we believe this new way of achieving cooperativity in a SCO material may be expected to lead to the discovery of further cooperative SCO systems. Efforts along these lines are already underway in these laboratories.

We thank the Thailand Research Fund (RSA5880048) and the Australian Research Council for their generous support of this research. Finlay Shanks at Monash University is thanked for help with IR and Raman studies and Boujemaa Moubaraki for help with magnetic studies. We are also grateful to Dr Guillaume Chastanet at the Institut de Chimie de la Matière Condensée de Bordeaux, Université Bordeaux, France for photomagnetic studies.

Conflicts of interest

There are no conflicts to declare.

Notes and references

1 O. Sato, *Nat. Chem.*, 2016, **8**, 644–656.
2 M. Natali and S. Giordani, *Chem. Soc. Rev.*, 2012, **41**, 4010–4029.
3 R. Klajn, J. F. Stoddart and B. A. Grzybowski, *Chem. Soc. Rev.*, 2010, **39**, 2203–2237.
4 M. D. Manrique-Juárez, S. Rat, L. Salmon, G. Molnár, C. M. Quintero, L. Nicu, H. J. Shepherd and A. Bousseksou, *Coord. Chem. Rev.*, 2015, **308**, 395–408.

5 J. L. Zhang, J. Q. Zhong, J. D. Lin, W. P. Hu, K. Wu, G. Q. Xu, A. T. S. Wee and W. Chen, *Chem. Soc. Rev.*, 2015, **44**, 2998–3022.
6 J. Ferrando-Soria, J. Vallejo, M. Castellano, J. Martínez-Lillo, E. Pardo, J. Cano, I. Castro, F. Lloret, R. Ruiz-García and M. Julve, *Coord. Chem. Rev.*, 2017, **339**, 17–103.
7 K. S. Murray, in *Spin-Crossover Materials: Properties and Applications*, ed. M. A. Halcrow, John Wiley & Sons Ltd., Chichester, 2013, pp. 1–54.
8 M. A. Halcrow, *Chem. Lett.*, 2014, **43**, 1178–1188.
9 V. Ksenofontov, A. B. Gaspar and P. Gütlich, *Top. Curr. Chem.*, 2004, **235**, 23–64.
10 J.-F. Létard, *J. Mater. Chem.*, 2006, **16**, 2550–2559.
11 G. Aromí, L. A. Barrios, O. Roubeau and P. Gamez, *Coord. Chem. Rev.*, 2011, **255**, 485–546.
12 M. A. Halcrow, *Coord. Chem. Rev.*, 2009, **253**, 2493–2514.
13 G. A. Craig, O. Roubeau and G. Aromí, *Coord. Chem. Rev.*, 2014, **269**, 13–31.
14 P. Gütlich, A. B. Gaspar and Y. Garcia, *Beilstein J. Org. Chem.*, 2013, **9**, 342–391.
15 J. Olguín and S. Brooker, *Coord. Chem. Rev.*, 2011, **255**, 203–240.
16 M. Nihei, T. Shiga, Y. Maeda and H. Oshio, *Coord. Chem. Rev.*, 2007, **251**, 2606–2621.
17 D. J. Harding, P. Harding and W. Phonsri, *Coord. Chem. Rev.*, 2016, **313**, 38–61.
18 W. Phonsri, P. Harding, L. Liu, S. G. Telfer, K. S. Murray, B. Moubaraki, T. M. Ross, G. N. L. Jameson and D. J. Harding, *Chem. Sci.*, 2017, **8**, 3949–3959.
19 W. Phonsri, D. J. Harding, P. Harding, K. S. Murray, B. Moubaraki, I. A. Gass, J. D. Cashion, G. N. L. Jameson and H. Adams, *Dalton Trans.*, 2014, **43**, 17509–17518.
20 D. J. Harding, W. Phonsri, P. Harding, K. S. Murray, B. Moubaraki and G. N. L. Jameson, *Dalton Trans.*, 2015, **44**, 15079–15082.
21 K. Fukuroi, K. Takahashi, T. Mochida, T. Sakurai, H. Ohta, T. Yamamoto, Y. Einaga and H. Mori, *Angew. Chem., Int. Ed.*, 2014, **53**, 1983–1986.
22 B. J. C. Vieira, J. C. Dias, I. C. Santos, L. C. J. Pereira, V. da Gama and J. C. Waerenborgh, *Inorg. Chem.*, 2015, **54**, 1354–1362.
23 S. Hayami, Z.-Z. Gu, H. Yoshiki, A. Fujishima and O. Sato, *J. Am. Chem. Soc.*, 2001, **123**, 11644–11650.
24 S. Hayami, K. Hiki, T. Kawahara, Y. Maeda, D. Urakami, K. Inoue, M. Ohama, S. Kawata and O. Sato, *Chem. – Eur. J.*, 2009, **15**, 3497–3508.
25 D. J. Harding, D. Sertphon, P. Harding, K. S. Murray, B. Moubaraki, J. D. Cashion and H. Adams, *Chem. – Eur. J.*, 2013, **19**, 1082–1090.
26 S. Schlamp, B. Weber, A. D. Naik and Y. Garcia, *Chem. Commun.*, 2011, **47**, 7152–7154.
27 M. A. Halcrow, *Chem. Soc. Rev.*, 2011, **40**, 4119–4142.
28 G. S. Matouzenko, A. Bousseksou, S. A. Borshch, M. Perrin, S. Zein, L. Salmon, G. Molnar and S. Lecocq, *Inorg. Chem.*, 2004, **43**, 227–236.
29 G. A. Craig, J. S. Costa, O. Roubeau, S. J. Teat and G. Aromí, *Chem. – Eur. J.*, 2011, **17**, 3120–3127.
30 T. Fujinami, K. Nishi, D. Hamada, K. Murakami, N. Matsumoto, S. Iijima, M. Kojima and Y. Sunatsuki, *Inorg. Chem.*, 2015, **54**, 7291–7300.
31 P. N. Martinho, B. Gildea, M. M. Harris, T. Lemma, A. D. Naik, H. Müller-Bunz, T. E. Keyes, Y. Garcia and G. G. Morgan, *Angew. Chem., Int. Ed.*, 2012, **51**, 12597–12601.
32 B. A. Leita, S. M. Neville, G. J. Halder, B. Moubaraki, C. J. Kepert, J.-F. Létard and K. S. Murray, *Inorg. Chem.*, 2007, **46**, 8784–8795.
33 G. Agustí, C. Bartual, V. Martínez, F. J. Muñoz-Lara, A. B. Gaspar, M. C. Muñoz and J. A. Real, *New J. Chem.*, 2009, **33**, 1262–1267.
34 H. Shepherd, G. Tonge, L. Hatcher, M. Bryant, J. Knichal, P. Raithby, M. Halcrow, R. Kulmaczewski, K. Gagnon and S. Teat, *Magnetochemistry*, 2016, **2**, 9.
35 W. Phonsri, D. S. Macedo, K. R. Vignesh, G. Rajaraman, C. G. Davies, G. N. L. Jameson, B. Moubaraki, J. S. Ward, P. E. Kruger, G. Chastanet and K. S. Murray, *Chem. – Eur. J.*, 2017, **23**, 7052–7065.
36 R. Bertoni, M. Lorenc, A. Tissot, M. L. Boillot and E. Collet, *Coord. Chem. Rev.*, 2015, **282–283**, 66–76.
37 E. Tailleur, M. Marchivie, N. Daro, G. Chastanet and P. Guionneau, *Chem. Commun.*, 2017, **53**, 4763–4766.
38 S. Kang, Y. Shiota, A. Kariyazaki, S. Kanegawa, K. Yoshizawa and O. Sato, *Chem. – Eur. J.*, 2016, **22**, 532–538.
39 B. Weber, W. Bauer and J. Obel, *Angew. Chem., Int. Ed.*, 2008, **47**, 10098–10101.
40 S. Brooker, *Chem. Soc. Rev.*, 2015, **44**, 2880–2892.
41 H. Kim, K. Shin and S. Chang, *J. Am. Chem. Soc.*, 2014, **136**, 5904–5907.
42 Y. E. Türkmen, S. Sen and V. H. Rawal, *CrystEngComm*, 2013, **15**, 4221–4224.
43 J. K. McCusker, A. L. Rheingold and D. N. Hendrickson, *Inorg. Chem.*, 1996, **35**, 2100–2112.
44 M. Marchivie, P. Guionneau, J. F. Létard and D. Chasseau, *Acta Crystallogr., Sect. B: Struct. Sci.*, 2005, **61**, 25–28.
45 I. Rey, P. Johansson, J. Lindgren, J. C. Lassègues, J. Grondin and L. Servant, *J. Phys. Chem. A*, 1998, **102**, 3249–3258.
46 M. Sorai, R. Burriel, E. F. Westrum and D. N. Hendrickson, *J. Phys. Chem. B*, 2008, **112**, 4344–4350.

 This journal is © The Royal Society of Chemistry 2017

Chemical Science

EDGE ARTICLE

Check for updates

Cite this: *Chem. Sci.*, 2017, **8**, 3949

Solvent modified spin crossover in an iron(III) complex: phase changes and an exceptionally wide hysteresis†

Wasinee Phonsri,[a] Phimphaka Harding,[a] Lujia Liu,[b] Shane G. Telfer,[b] Keith S. Murray,[c] Boujemaa Moubaraki,[c] Tamsyn M. Ross,[d] Guy N. L. Jameson[e] and David J. Harding*[a]

Solvent effects in a series of Fe(III) spin crossover (SCO) complexes [Fe(qsal-I)$_2$]OTf·sol (sol = MeOH **1**, EtOH **2**, *n*-PrOH **3**, i-PrOH **4**, acetone **5** and MeCN **6**) are explored. SCO is abrupt in **1** (following MeOH loss) and **2**, gradual for **3** ($T_{1/2}$ = 199 K) and **4** ($T_{1/2}$ = 251 K) and incomplete, even up to 350 K, for **5** and **6**. In [Fe(qsal-I)$_2$]OTf SCO occurs at $T_{1/2}\downarrow$ = 225 K and $T_{1/2}\uparrow$ = 234 K (ΔT = 9 K), while aged samples of **2** exhibit an exceptionally wide hysteresis of 80 K ($T_{1/2}\downarrow$ = 139 K and $T_{1/2}\uparrow$ = 219 K). In contrast, fresh samples of **2** exhibit stepped SCO with hysteresis varying from 2 to 42 K. VT-PXRD (variable temperature powder X-ray diffraction) studies indicate a new phase, **2b**, is formed upon cooling below 180 K along with a minor LS phase **2c**. Phase **2c** and the HS phase **2a** undergo a spin transition at $T_{1/2}\downarrow$ = 180 K and $T_{1/2}\uparrow$ = 215 K with phase **2b** exhibiting two-step SCO. Structural studies in both spin states, except **6**, show the cations are linked through extensive π–π interactions to form 1D chains. A combination of P4AE (parallel fourfold aryl embrace) and I···X (X = I, O, π) interactions create tightly packed 3D supramolecular networks. This study emphasizes that while solvent may result in only small structural changes SCO characteristics can be impacted dramatically.

Received 5th December 2016
Accepted 20th March 2017

DOI: 10.1039/c6sc05317c

rsc.li/chemical-science

Introduction

Switchable molecules are attractive targets in the design of functional nanomaterials.[1–6] In this context spin crossover (SCO) compounds are ideal candidates as they can be switched by a range of stimuli including temperature,[7,8] pressure[9] and light,[10–13] or combinations thereof.[14] As molecular compounds they are easy to prepare and readily tunable. In SCO systems the switching occurs between two electronic states termed high spin (HS) and low spin (LS) that are close in energy. This arises from the splitting of the d-orbitals into a t_{2g} and an e_g set in an octahedral ligand field and, while theoretically possible for a $3d^4$–$3d^7$ electronic configuration, is most widely studied for Fe(II).[8,15–20] However, more recent research has shown that Fe(III) systems can be just as effective and have the advantage over Fe(II) systems of being air stable.[21–23] Moreover, with abrupt hysteretic, symmetry breaking and stepped SCO transitions all reported it is clear that functional devices are becoming a real possibility.

Nevertheless, challenges remain as no system yet exists which has a broad hysteresis at room temperature. In designing SCO complexes careful consideration needs to be given to selecting a ligand with a suitable ligand field strength and ensuring that it will form strong supramolecular contacts in the solid state. The latter is needed for the cooperative processes that underlie hysteretic switching.[24] In addition to the ligand, SCO behaviour is also influenced by the anion[25–32] and the solvent.[33–36] The effect of the anion is particularly pronounced as it often completely alters the solid state packing and consequently impacts SCO behaviour. Solvent effects tend to be more subtle but are less well understood as comparatively few studies exist. In the case of Fe(III) there is only one study of solvent effects in the series [Fe(napet)NCS]·sol (napet = 1-[((2-{3-[2-hydroxy-1-naphthyl)methylideneamino]propylamino}ethylimino)methyl]-2-naphthol); sol = tetrahydrofuran, methanol and 0.5 pyrazine, butanone, DMF, DMSO).[37]

[a]*Functional Materials and Nanotechnology Centre of Excellence (FuNTech), Walailak University, Thasala, Nakhon Si Thammarat, 80160, Thailand. E-mail: hdavid@g-mail.wu.ac.th*

[b]*MacDiarmid Institute for Advanced Materials and Nanotechnology, Institute of Fundamental Sciences, Massey University, Palmerston North, New Zealand*

[c]*School of Chemistry, Monash University, Clayton, Melbourne, Victoria, 3800, Australia*

[d]*Australian Synchrotron, 800 Blackburn Rd, Clayton, Victoria, 3168, Australia*

[e]*Department of Chemistry & MacDiarmid Institute for Advanced Materials and Nanotechnology, University of Otago, PO Box 56, Dunedin, 9054, New Zealand*

† Electronic supplementary information (ESI) available: Crystallographic details, structural figures, VT-PXRD data and figures, Mössbauer spectroscopic data, DSC and TGA results. CCDC 1519938–1519948. For ESI and crystallographic data in CIF or other electronic format see DOI: 10.1039/c6sc05317c

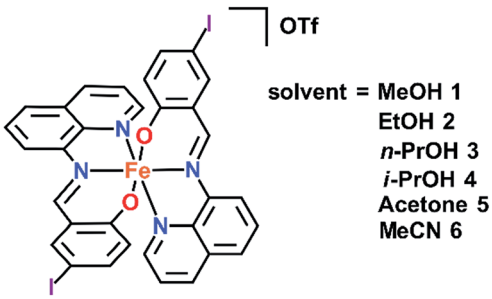

Although, only three of the compounds were SCO active[37] the authors were able to demonstrate that an N–H···O hydrogen bond between the coordinated amine and an oxygen atom from the solvent was responsible for tuning the spin transition temperature. Despite this success only one of the structures was determined in both spin states limiting the conclusions that could be drawn regarding how supramolecular connectivity is altered by SCO.

In our continuing studies on Fe(III) complexes of halogenated quinolylsalicylaldimines (qsal-X) we now report the variation of solvent in [Fe(qsal-I)$_2$]OTf·sol (sol = MeOH **1**,[38] EtOH **2**, *n*-PrOH **3**, i-PrOH **4**, acetone **5**, and MeCN **6**). The structures of all these compounds have been determined by single crystal X-ray diffraction and in many cases the structures of both the high and low spin states have been obtained. This rich data set provides insight into how subtle structural changes radically impact magnetic behaviour. In particular, [Fe(qsal-I)$_2$]OTf·EtOH is sensitive to ageing and sample treatment effects. This results in variable stepped SCO profiles with hysteresis up to 80 K. VT-PXRD studies suggest the different SCO profiles are related to a phase change that occurs following the first spin crossover. While such effects are well described in Fe(II) SCO extended framework systems[39,40] and order–disorder in Fe(II) SCO monomers[41] they are rarely reported in Fe(III).

Results and discussion

Structural overview of [Fe(qsal-I)$_2$]OTf·sol and discussion of Fe(qsal-I)$_2$]OTf·EtOH

The crystal structure of [Fe(qsal-I)$_2$]OTf·MeOH **1**, has previously been reported.[38] In this work, the crystal structures of [Fe(qsal-I)$_2$]OTf·EtOH **2**, [Fe(qsal-I)$_2$]OTf·*n*-PrOH **3**, [Fe(qsal-I)$_2$]OTf·i-PrOH **4**, [Fe(qsal-I)$_2$]OTf·acetone **5**, and [Fe(qsal-I)$_2$]OTf·MeCN **6** have been determined at two temperatures, with the exception of **6** which lost crystallinity at room temperature. The complex magnetic behaviour of [Fe(qsal-I)$_2$]OTf·EtOH **2** led us to determine the structure at 100, 170, 213 and 292 K. The crystallographic data are summarised in Table S1.† Crystals of **2** are found in phase **2a** when prepared at room temperature. Upon cooling below 170 K they shatter explosively due to a phase change to phase **2b** producing very small crystallites. Careful searching and use of synchrotron radiation allowed us to obtain the structure at 100 K, phase **2b**. Similar mechanical instability has recently been reported for [Fe(5-Br-salEen)$_2$]ClO$_4$ (5-Br-salEen = 4-bromo-2-{[2-(ethylamino)ethylimino]methyl}-phenol). In this case it is associated with a "thermosalient" effect unlike in **2**.[42] The structures of **1–6** at all temperatures belong to the triclinic space group $P\bar{1}$. The asymmetric unit contains one molecule of solvent, an [Fe(qsal-I)$_2$]$^+$ cation and a triflate anion, the first such example in Fe(III) SCO chemistry.

As **2** has the most interesting SCO characteristics we will limit the discussion at this stage to this compound. There is a remarkably anisotropic distortion of the unit cell parameters with *b* and *c* shortening by 0.845 and 0.499 Å, respectively from phase **2a** at 292 K to phase **2b** at 100 K while *a* lengthens by 0.901 Å. By comparison, the unit cell parameters in [Fe(5-Br-salEen)$_2$]ClO$_4$ exhibit changes of more than 1.0 Å.[42] Despite our smaller changes in *a*, *b* and *c*, there is a substantial reduction in the unit cell volume by 6.3%, the largest yet reported for any Fe(III) SCO complex.

The Fe centre in **2** is pseudo-octahedral with two meridionally coordinated qsal-I ligands. The Fe–ligand bond lengths for all the compounds are listed in Table 1. At 100 K the Fe–N/O bond lengths in **2b** (average 1.94 Å) are indicative of LS Fe(III).[38,43,44] At 213 and 292 K the Fe–N/O bond lengths for phase **2a** are characteristic of the HS state (average 2.06 Å at 292 K).[38,44] However, at 170 K the bond lengths of phase **2a** are a little shorter than at 213 and 292 K indicating the Fe(III) centre is mostly HS but preparing to undergo SCO. SCO results in changes of ΔFe–N = 0.170 Å and ΔFe–O = 0.023 Å and gives the largest overall change in this series.

The degree of distortion at the Fe centre, as measured by Σ and Θ,[45,46] is $\Delta\Sigma$ (HS-LS) = 23°, while $\Delta\Theta$ = 129° confirming that complete SCO occurs in **2**. Between 170 and 213 K, **2a** shows only small changes in the value of $\Delta\Sigma$ and $\Delta\Theta$, mirroring our previous findings in **1**.[38] As with the Fe–ligand bond lengths, the changes in the coordination sphere are more pronounced in **2** than in any other compound in this series as an overlay of the HS and LS structures for **1** and **2** shows in Fig. 1 (for overlays for **3–5** see Fig. S1†). The large change in unit cell volume, noted above, and the coordination sphere are most likely responsible for the large hysteresis in **2** (*vide infra*).

Magnetic studies of [Fe(qsal-I)$_2$]OTf·EtOH

Magnetic studies of **2** between 50–325 K or 50–350 K indicate that the samples exhibit age and treatment dependent SCO, as shown in Fig. 2. The previously reported magnetic profile of [Fe(qsal-I)$_2$]OTf, formed following MeOH loss from **1**, is included for comparison.[38] Two types of sample were studied, an aged and a fresh sample. Both samples were prepared by layered diffusion of Hqsal-I and NEt$_3$ in CH$_2$Cl$_2$ and Fe(OTf)$_3$ in EtOH. The difference was that the fresh sample was isolated immediately after crystallization was complete (*ca.* 3–4 days). In contrast, for the aged sample the crystals were left in the CH$_2$Cl$_2$/EtOH mother liquor for a further 2 weeks. Both samples analyse for one equivalent of EtOH. For the aged sample at 50 K $\chi_M T$ is 0.5 cm^3 K mol^{-1} and indicative of LS Fe(III), Fig. 2b. The $\chi_M T$ value gradually increases upon heating reaching 1.4 cm^3 K mol^{-1} at 235 K. After that there is an abrupt change ($T_{1/2}\uparrow$ = 252 K) becoming fully HS at 270 K where $\chi_M T$ is 4.42 cm^3 K mol^{-1}. In the cooling mode, $\chi_M T$ decreases beginning at *ca.* 210 K reaching 3.4 cm^3 K mol^{-1} at 170 K before dropping more rapidly

This journal is © The Royal Society of Chemistry 2017

Table 1 Selected Fe–N/O bond lengths (Å) and octahedral distortion parameters (°) for $[Fe(qsal\text{-}I)_2]OTf\cdot sol$

	1[a]-163 K	**1**[a]-293 K	**2b**-100 K	**2a**-170 K	**2a**-213 K	**3**-100 K	**3**-270 K	**4**-163 K	**4**-293 K	**5**-137 K	**5**-293 K	**6**-123 K
Fe1–O1	1.874(8)	1.906(6)	1.900(4)	1.907(3)	1.919(6)	1.883(2)	1.914(3)	1.887(7)	1.908(6)	1.923(6)	1.935(6)	1.868(5)
Fe1–O2	1.878(8)	1.907(7)	1.889(4)	1.908(3)	1.917(6)	1.895(2)	1.922(3)	1.893(7)	1.903(6)	1.915(6)	1.943(7)	1.884(5)
$Fe1–O_{av}$	1.876(8)	1.907(7)	1.895(4)	1.908(3)	1.918(6)	1.889(2)	1.917(3)	1.890(7)	1.906(6)	1.919(6)	1.939(7)	1.876(5)
Fe1–N1	1.965(9)	2.096(7)	1.950(4)	2.101(3)	2.102(7)	1.950(2)	2.107(3)	1.945(8)	2.071(6)	1.953(8)	2.074(8)	1.940(6)
Fe1–N2	1.939(10)	2.145(7)	1.972(5)	2.139(3)	2.143(7)	1.966(3)	2.129(4)	1.967(8)	2.084(6)	1.977(7)	2.109(7)	1.965(6)
Fe1–N3	2.010(10)	2.157(8)	1.939(4)	2.094(3)	2.115(7)	1.966(3)	2.101(3)	1.949(8)	2.067(6)	1.948(8)	2.081(8)	1.937(6)
Fe1–N4	1.948(9)	2.098(7)	1.971(5)	2.142(4)	2.152(7)	1.980(3)	2.158(4)	1.961(8)	2.110(8)	1.986(8)	2.121(7)	1.967(6)
$Fe1–N_{av}$	1.966(10)	2.124(8)	1.958(5)	2.119(4)	2.128(7)	1.966(3)	2.124(4)	1.956(8)	2.083(8)	1.966(8)	2.096(8)	1.952(6)
Σ[b]	43	65	44	60	67	47	65	48	54	41	57	47
Θ[c]	61	189	71	177	200	69	187	71	153	71	160	69

[a] Data taken from ref. 38. [b] $\Sigma = \sum_{i=1}^{12} |90 - \alpha_i|$, where α_i are the twelve *cis* N/O–Fe–N/O angles. [c] $\Theta = \sum_{i=1}^{24} |60 - \theta_i|$, where θ_i are the 24 unique N/O–Fe–N/O angles measured on the projection of two triangular faces of the octahedron along their common pseudo-threefold axis.

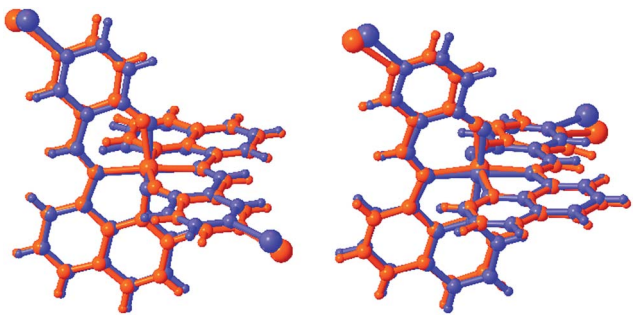

Fig. 1 Overlay of HS (red) and LS (blue) structures of **1** (left) and **2** (right).

to 0.5 cm^3 K mol^{-1} with $T_{1/2}\downarrow = 139$ K. This is consistent with the structure at 170 K which exhibits slightly shorter Fe–N/O bond lengths than at 213 K. In the second heating cycle the spin transition shifts to $T_{1/2}\uparrow = 219$ K. Upon cooling, SCO again occurs in two steps with the step less pronounced in the second cycle (at 160 K, $\chi_M T = 3.26$ and 3.72 cm^3 K mol^{-1} in 1st and 2nd cycle, respectively). Subsequent cycles do not alter the magnetic profile of the complex. Thus, the hysteresis of an aged sample of **2** is 80 K, one of the largest values ever reported for any SCO complex.

Two different magnetic measurements were performed on fresh samples of **2**. Firstly, the fresh sample was slowly cooled from room temperature. The magnetic plot in Fig. 2c shows an abrupt SCO with $T_{1/2}(\downarrow) = 175$ K and $T_{1/2}(\uparrow) = 270$ K in the first cycle. Subsequent cycles reveal two-step SCO with $T_{1/2}(\downarrow) = 213$ and 103 K with a hysteresis of about 1–2 K at each step leading to an unprecedented plateau width of *ca.* 110 K at 2.5 cm^3 K mol^{-1} and consistent with 50% HS.

In the second measurement, the sample was first quenched cooled to 100 K (Fig. 2d). Warming slowly the abrupt change at 270 K observed in the first heating cycle of the slow cooled sample is also present here. However, upon cooling the SCO profile has three steps with an extra step appearing at around 175 K with $\chi_M T = 3.30$ cm^3 K mol^{-1}, indicative of 66% HS. The second step occurs at $T_{1/2}(\downarrow) = 109$ K with $\chi_M T = 2.00$ cm^3 K mol^{-1} and consistent with 33% HS. In contrast, the heating mode is a two-step SCO process going from the LS to the HS state *via* 33% HS intermediate, resulting in an open hysteresis loop of *ca.* 42 K. The complicated SCO plots of **2** and their relationship with the phase changes are explained in the VT-PXRD section.

TGA analysis of **2** shows that it starts to lose EtOH at 353 K with solvent loss complete by 380 K (Fig. S2†). While we cannot absolutely rule out some small degree of solvent loss in fresh samples of **2** we believe that this is minimal as complete removal of EtOH requires heating under vacuum at 100 °C for 1.5 h and even then a cooling and heating cycle is required to give the magnetic profile of $[Fe(qsal\text{-}I)_2]OTf$ (Fig. S3†). Moreover, samples were sealed with Vaseline which also minimizes solvent loss.

DSC measurements of **2** on a fresh sample shows two peaks in the first cycle, one sharp at 277 K and a broader peak at 173 K with $\Delta H = 6.7$ and 7.0 kJ mol^{-1} and $\Delta S = 24$ and 40 J mol^{-1} K^{-1}, respectively (Fig. S4 and S5, Table S2†) closely matching the SCO profile observed in Fig. 2c. These calorimetric values are typical of Fe(III) SCO compounds.[21,23] In the following cycles, the peak at 173 K disappears, mirroring the magnetic studies above. VT-PXRD (*vide infra*) confirms that a phase change takes place at around 170 K. It is noteworthy that there always is a small endothermic peak at 268 K just proceeding the actual SCO possibly associated with some structural pre-organization prior to SCO. In the second cycle, the cooling mode shows only one small peak at 261 K which may correspond to the unusual flexing seen in the VT-PXRD data. The lack of other peaks in the cooling mode may be a due to the small size of the crystallites formed after the first cooling. Similar results have been reported in $[Fe(3\text{-}bpp)(3\text{-}bpp\text{-}Ph\text{-}OMe)][ClO_4]_2\cdot 1.5$-acetone (3-bbp = 2,6-bis{pyrazol-3-yl}pyridine; 3-bpp-Ph-OMe = 2,6-bis{5-(2-methoxyphenyl)pyrazol-3-yl}pyridine)[47] and $[Fe(3\text{-}bpp\text{-}Ph\text{-}OH)_2][ClO_4]_2\cdot 2$-acetone$\cdot H_2O$[48] (3-bpp-Ph-OH = 2,6-bis{5-(2-hydroxyphenyl)pyrazol-3-yl}-pyridine) which show no peaks in the cooling mode despite exhibiting abrupt SCO.

The magnetic studies reveal that samples of **2** are extremely sensitive to sample preparation and ageing. Elemental analysis confirms that both the fresh and aged samples contain one

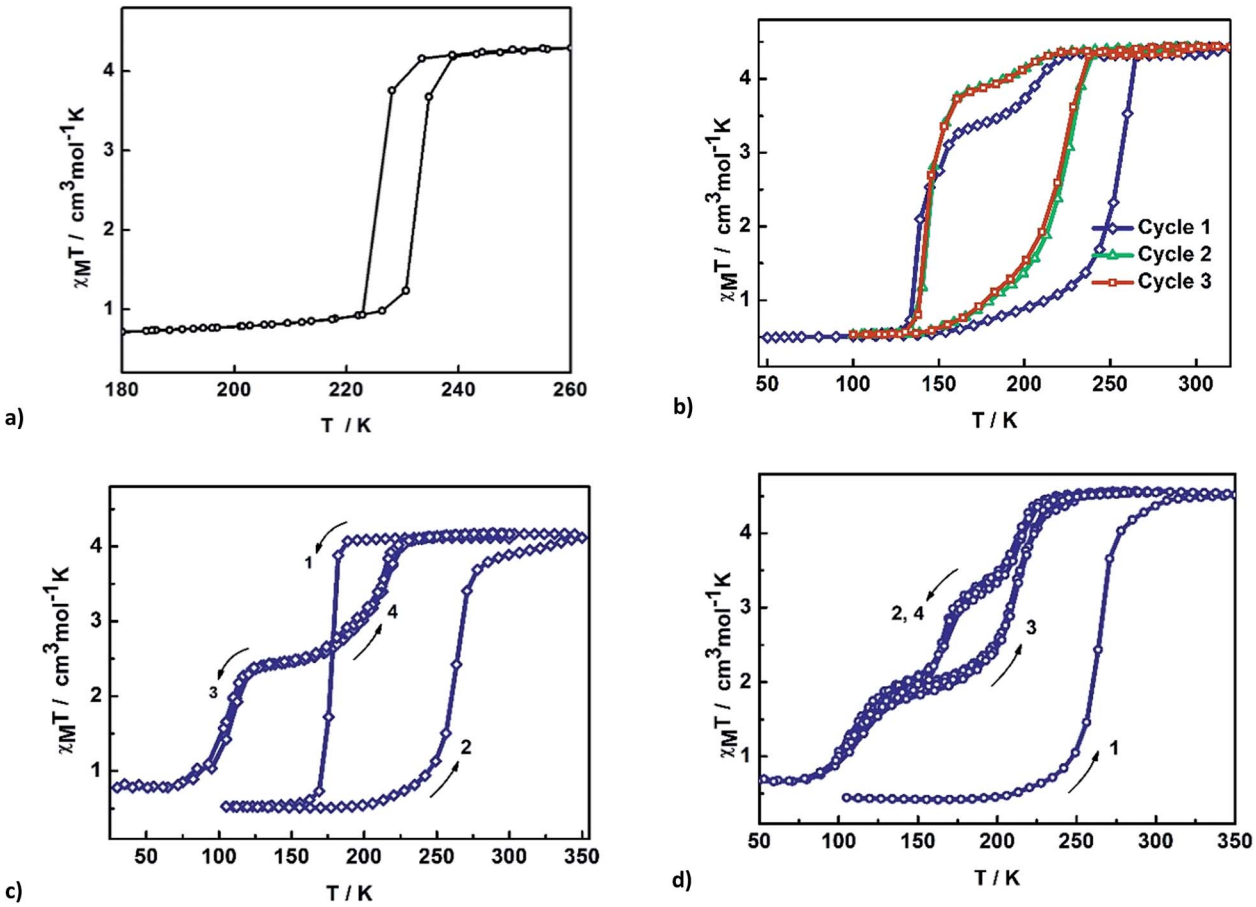

Fig. 2 Thermal variation of $\chi_M T$ *versus* T plot for (a) [Fe(qsal-X)$_2$]OTf, (b) aged EtOH **2**, (c) fresh EtOH **2**, (d) fresh EtOH **2** after flash cooling.

molecule of EtOH. Ageing effects, although uncommon, have been observed in [Fe(qsal)$_2$]NCS and [Fe(3-bpp-Ph-OH)$_2$][ClO$_4$]$_2$·2THF·H$_2$O and are generally found in hysteretic systems.[49,50] As in **2**, ageing of both these compounds results in more complete, abrupt and hysteretic SCO.

Mössbauer spectroscopic studies of [Fe(qsal-I)$_2$]OTf·EtOH

Mössbauer spectroscopy also confirms the different spin states in **2** at different temperatures (Fig. 3). The spectra show that the sample remains LS from 5.3 to 200 K due to the presence of a sharp quadrupole doublet with a wide quadrupole splitting and low isomer shift (Table S3†). By 260 K, although the signal to noise is poor, making fitting of the spectrum impossible, the presence of both HS and LS Fe(III) is visible. At 293 K the sample is fully HS with a broad quadrupole doublet with lower quadrupole splitting and higher isomer shift typical of HS Fe(III). Cooling of the sample reveals a full LS state at 220 K. The difference between the Mössbauer spectroscopic and magnetic data of the fresh sample is probably due to partial solvent loss during the measurement, something previously observed in [Fe(qsal-Br)$_2$]NO$_3$·2MeOH.[51]

VT-PXRD studies of [Fe(qsal-I)$_2$]OTf·EtOH

As the magnetic properties of **2** depend greatly on the sample age and treatment, variable temperature powder X-ray diffraction (VT-PXRD) studies of **2**, using synchrotron radiation, were used to further probe the phase changes that occur. Two experiments were designed and relate to the magnetic data of a freshly prepared sample (Fig. 2c and d). The first experiment started collecting data at high temperature (dataset A) while the other began to collect data only after quenching the sample to 100 K (dataset B). Details of the experiments are shown in Tables S4 and S5† with Pawley fits in Fig. S6 and S7.† Stacked, interpolated diffraction patterns for dataset A and B are shown in Fig. 4.

In the VT-PXRD of dataset A, Fig. 4a, only one phase, that is **2a**, is present at 300 K. On cooling down to 180 K (step 1), a majority phase **2b** and a minority phase **2c** appear while phase **2a** gradually disappears, and is completely gone at *ca.* 164 K. The calculated unit cell parameters from the PXRD patterns of phase **2a** and **2b** are consistent with the single crystal X-ray data of phases **2a** and **2b**, respectively (Tables S6 and S7,† *vide supra*). Unfortunately, attempts to obtain the single crystal X-ray structure of phase **2c** which forms upon shattering have been unsuccessful to date. After cooling to 100 K, the sample was then heated to 300 K (step 2) with phase **2b** remaining the majority phase with the suggested transformation of **2c** into **2a** occurring at around 215–220 K. The transformation of **2a** → **2c** is observed again in the following cooling mode (step 3), at *ca.* 180 K. The persistence of phase **2b** and the transformation of

 This journal is © The Royal Society of Chemistry 2017

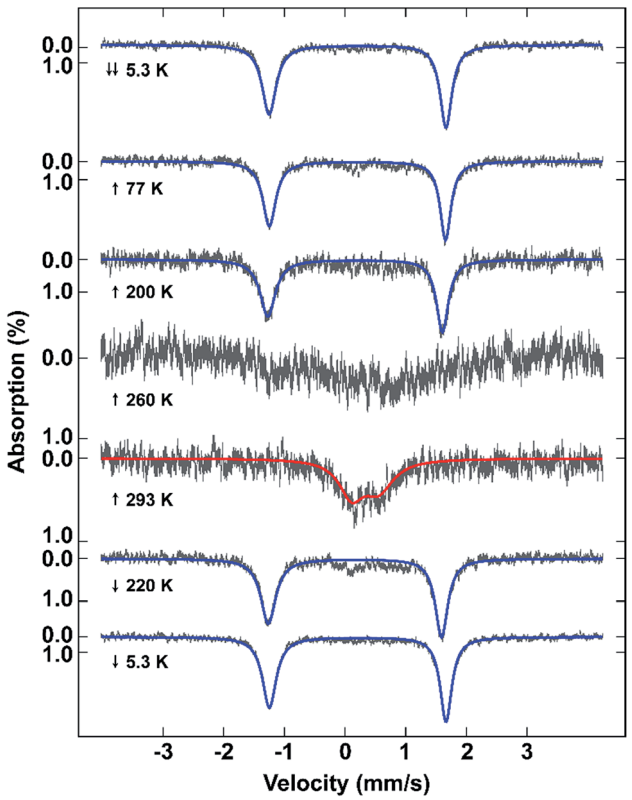

Fig. 3 ^{57}Fe Mössbauer spectra of **2** measured at the temperatures shown with a small magnetic field of 47 mT applied parallel to the γ-ray. The fits to the data are given as blue lines (LS) and red lines (HS).

the minority phase of **2c** ↔ **2a** are repeatable in the following cycles (step 4, Tables S4 and S5†). However, the emergence of the **2b** phase from **2a**, at *ca.* 180 K, takes place only once after the first cooling. As phase **2a** always exists at high temperature and transforms into phase **2c** at low temperature, it suggests that **2a** is the HS phase and **2c** is the LS phase. The temperature-dependent crystallographic phase change behaviour in **2** is summarized in Fig. 5.

For dataset B, Fig. 4b, the sample was initially quench cooled to 100 K. A mixture of phases **2b** (majority) and **2c** (minority) coexist at the beginning which contrasts with only phase **2a** being present in step 1 of dataset A. In the following cycle (steps 1 and 2), the dominant phase is **2b** which always appears together with either **2a** (HS phase) or **2c** (LS phase). Notably, the phase change temperatures between **2a** ↔ **2c** in datasets A and B are similar. However, the relatively weaker intensity of phases **2a** and **2c** in the diffraction patterns of dataset A in comparison to that in dataset B suggest there is a smaller amount of these phases in dataset A. The reason for this behaviour is unclear.

The phase transition from phase **2a** to **2b** at *ca.* 180 K, that is observed only in the first cooling (dataset A), is in accordance with the first abrupt spin transition ($T_{1/2}$ = 175 K) of the magnetic plot shown in Fig. 2c. This also agrees with the peak at 173 K from DSC results that appears distinctly in the first cooling of the experiment. For the heating mode, however, there is no phase change observed in the VT-PXRD data above 260 K where the magnetic plots in Fig. 2c and d show another abrupt SCO ($T_{1/2}$ = 270 K). There is unusual flexing of phase **2b** above 260 K in the VT-PXRD data in both dataset A and B (Fig. 4) and this might be correlated with the abrupt spin change in the magnetic data. For the following cycles, the two step SCO shown in Fig. 2c is believed to be an intrinsic magnetic property of phase **2b**.

As previously mentioned, the VT-PXRD results show relatively small amounts of phase **2a** and **2c** are present in dataset A. These two phases are expected to have minimal contribution to the magnetic plot in Fig. 2c. On the other hand, in dataset B, phases **2a** and **2c** are more pronounced. Consequently, there is

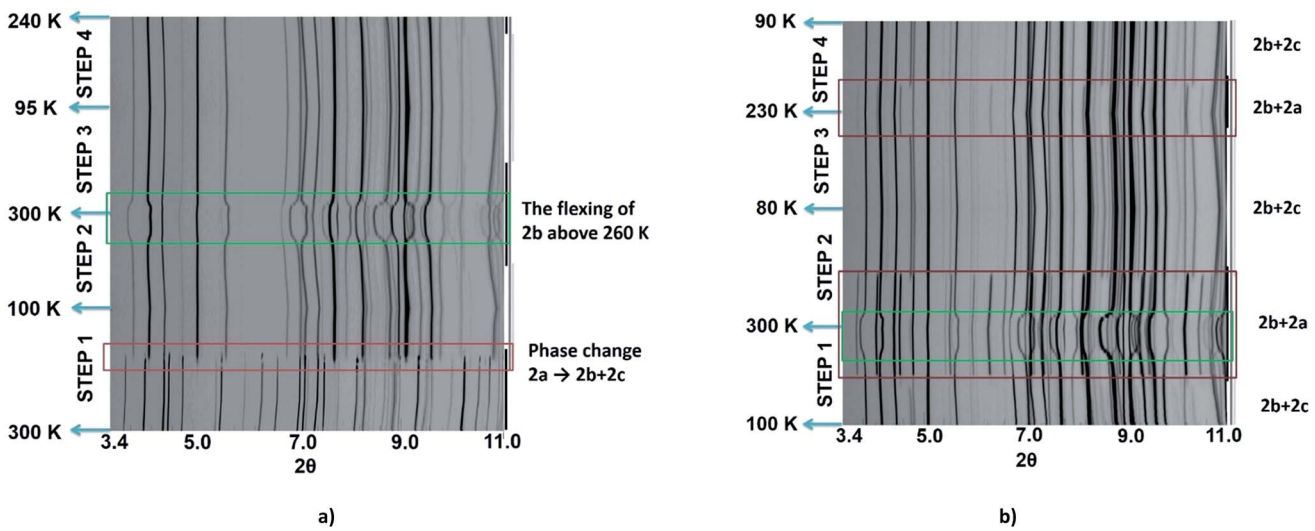

Fig. 4 Stacked, interpolated diffraction patterns of peak evolution in **2** showing the phases that are produced upon repeated heating and cooling cycles for (a) dataset A and (b) dataset B. Highlights of the phase change in the data are in the red frame, showing the presence of phase **2a** in the data. The green box shows an 'unusually large' change in the calculated unit cell parameters of **2b**. Crystallographic phases present at various temperatures (approximate) are depicted by the black (phase **2a**), dark grey (phase **2b**) and light grey (phase **2c**) lines to the right of the stack plot.

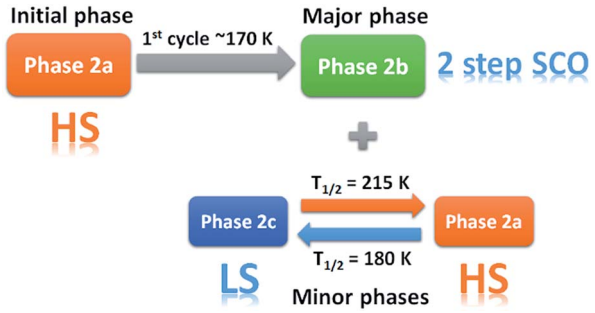

Fig. 5 Summary of the phase changes that occur in **2** from VT-PXRD studies.

Table 2 Spin transition temperatures of $[Fe(qsal\text{-}I)_2]OTf\cdot sol$

Solvent	$T_{1/2}\downarrow$/K	$T_{1/2}\uparrow$/K	ΔT/K	Note
None[a]	225	234	9	
EtOH **2** aged	139	252	113	1st cycle
	139	219	80	2nd cycle
	139	219	80	3rd cycle
n-PrOH **3**	199	199	0	
i-PrOH **4**	251	251	0	
Acetone **5**	331	332	1	
MeCN **6**	315	320	5	

[a] Data from ref. 38.

an extra step in the cooling mode of the magnetic plot at $T_{1/2} \approx$ 175 K (Fig. 2d) which is in the same region as the phase transition between **2a** → **2c**. Overall, the VT-PXRD data correlate well with the observed magnetic behaviour of **2**.

Magnetic studies of $[Fe(qsal\text{-}I)_2]OTf\cdot sol$

The impact of solvent on SCO was investigated by SQUID magnetometry of **3–6**. The results are shown in Fig. 6, while the transition temperatures of **1–6** are shown in Table 2. For **3** and **4**, the packing as well as the supramolecular interactions are almost identical (*vide infra*), resulting in very similar gradual but complete SCO. Heating the sample from 150 K, **3** continuously increases reaching a $\chi_M T$ value of 4.0 cm^3 K mol^{-1} at 275 K. For **4** the SCO is slightly more gradual. This might be due to slight alterations in the supramolecular connectivity with P4AE interactions found in **3** while only C–H···π interactions are found in **4**. The stronger cooperativity in **3** is also believed to be responsible for the lower transition temperature.

In contrast, **5** and **6** show incomplete SCO up to 350 K with a maximum of 70 and 58% HS conversion, respectively. Assuming the SCO is complete at higher temperatures the transition temperature is estimated to be 320–330 K but is rather gradual in both cases, consistent with the lower cooperativity in these compounds.

In this series, it is evident that the alcohols yield more abrupt and complete SCO, presumably due to their ability to hydrogen bond to the anion. However, the other physical properties of the solvents (volume, boiling point, dielectric constant) show no correlation with the abruptness of the SCO or the $T_{1/2}$ of the compounds. It appears that the solvent subtly alters the supramolecular connectivity in the system and it is this that is responsible for particular magnetic profiles we observe. This is explored in more detail in the following section.

Supramolecular packing in $[Fe(qsal\text{-}I)_2]OTf\cdot sol$

To try to better understand the SCO profiles of the different solvates we now examine the cooperativity in these systems. The packing in **1–6** is similar consisting of 1D chains held together by two sets of π–π interactions involving pairs of qsal-I ligands and is common for $[Fe(qsal\text{-}X)_2]^+$ complexes;[35,38,43,51,52] (Tables 3 and S8–S13†). The first set of π–π interactions (type A) contains triflate embraces (Fig. 7). The second set (type B) is supported by weak C–H···O contacts involving the alcohol solvent or C–H···N interactions in the case of MeCN. There are also C–H···O interactions between the aromatic hydrogens and the coordinated phenoxy oxygen atoms which may influence the ligand field provided by the qsal-I ligands.[53]

Upon SCO (LS to HS) the π–π distances increase by on average 0.10 Å, although there is greater range for the type B

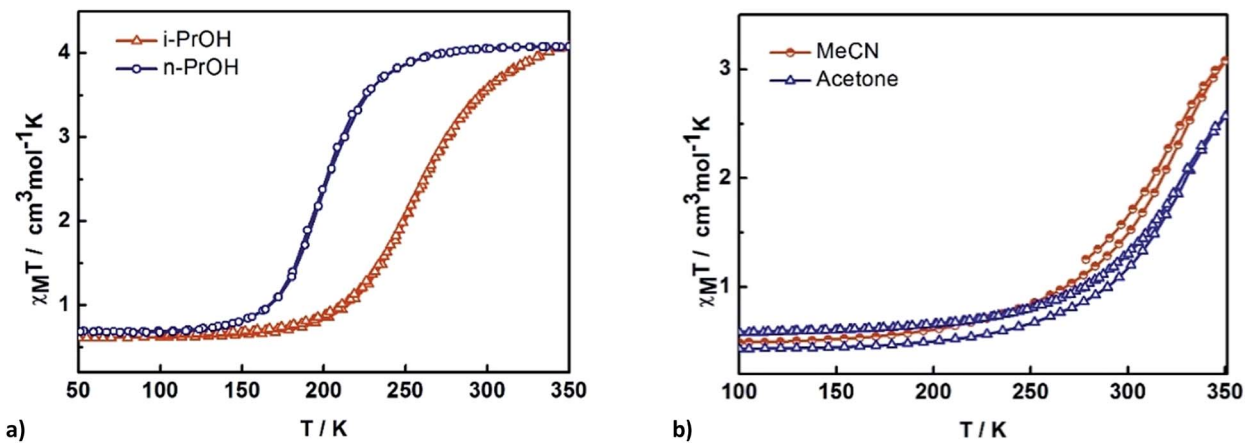

Fig. 6 Thermal variation of $\chi_M T$ *versus* T plot for $[Fe(qsal\text{-}I)_2]OTf\cdot sol$ where sol are (a) *n*-PrOH **3** and i-PrOH **4** and (b) acetone **5** and MeCN **6**.

This journal is © The Royal Society of Chemistry 2017

Table 3 Summary of the principle intermolecular interactions in [Fe(qsal-I)$_2$]OTf·sol

	1 MeOH[a]	**2** EtOH	**3** *n*-PrOH	**4** i-PrOH	**5** Acetone	**6** MeCN
In 1D	π–π, I···π, C–H···O,	π–π, I···π, C–H···O,	π–π, C–H···O	π–π, C–H···O/C	π–π, C–H···O	π–π, I···π, C–H···O
In 2D	P4AE	P4AE	P4AE	C–H···π	P4AE	P4AE
In 3D		I···I (**2a** only)		I···I	I···I	I···π
OTf	C–H···O (OTf)	I···O (OTf, **2a** only)	C–H···O (OTf)	C–H···O (OTf)	C–H···O (OTf)	C–H···O (OTf)
	C–H···F (OTf)	C–H···O (OTf)	C···O (OTf)	C···O (OTf)	C–H···F (OTf)	C–H···F (OTf)
		O···π (**2b** only)	C–H···F (OTf)		I···O (OTf)	I···O (OTf)
					I···F (OTf)	
Solvent	C–H···O (MeOH)	C–H···I (EtOH)	C–H···O (*n*-PrOH)	C–H (i-PrOH)···I	C–H···O (acetone)	C–H···N (MeCN)
		C–H···O (EtOH)	C–H (*n*-PrOH)···I	C–H (i-PrOH)···C	C–H (acetone)···I	
			C (*n*-PrOH)···I			
An–An	F···F (HS only)	F···F	F···F	F···F	O···F, O···S	
Anion–sol	O–H···O	O–H···O	O–H···O, C–H···F/O	O–H···O, C–H···F	C–H···F	C–H···O
Intra-chain/Å[b]	2.74, 2.03[c]	2.72, 2.01[d]	3.04, 2.85	3.11, 2.86	2.74, 2.46	2.92
	$\Delta = -0.71$	$\Delta = -0.71$	$\Delta = -0.19$	$\Delta = -0.25$	$\Delta = -0.28$	
Inter-chain/Å[b]	8.63, 8.83[c]	8.64, 8.71[d]	8.62, 8.82	8.81, 9.00	7.34, 7.61	9.23
	$\Delta = 0.20$	$\Delta = 0.07$	$\Delta = 0.20$	$\Delta = 0.19$	$\Delta = 0.27$	
Inter-plane/Å[b]	12.00, 12.45[c]	12.24, 12.91[d]	12.23, 12.44	12.10, 12.33	13.20, 13.48	10.99
	$\Delta = 0.45$	$\Delta = 0.67$	$\Delta = 0.21$	$\Delta = 0.23$	$\Delta = 0.28$	

[a] Data taken from ref. 38. [b] Low spin (LS), high spin (HS) distances, Δ(HS-LS). [c] At 293 K. [d] At 292 K.

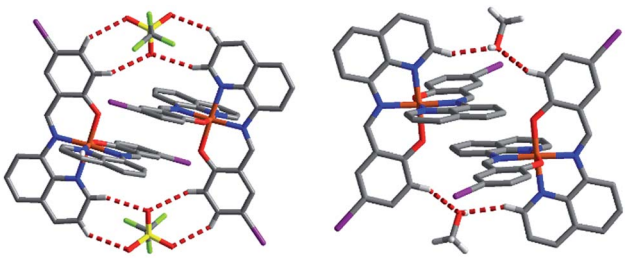

Fig. 7 (a) Type A π–π interactions showing the supporting triflate embraces and (b) type B π–π interactions showing the supporting MeOH interactions of compound **1** at 163 K.

interaction probably as this interaction involves the solvent. Interestingly, even though SCO is incomplete in **5** it shows the largest difference in π–π distances; the reason for this is unclear.

The 1D chains are further connected *via* P4AE (parallel fourfold aryl embrace) interactions[54] to create a 2D network. Uniquely for **4**, the qsal-I ligands are too offset to form a π–π interaction, and only C–H···π interactions are found (Fig. 8, Table S14†). As above the π–π distances lengthen by *ca.* 0.10 Å upon SCO. The C–H···π interactions also increase upon SCO but there appears to be an inverse relationship between the C–H···π and π–π interactions with the largest difference for **5** (*ca.* 0.12 Å, Δπ–π = 0.06 Å) and the smallest for **3** (*ca.* 0.02 Å, Δπ–π = 0.16 Å).

In addition to π–π interactions adjacent planes are linked *via* a weak I···I interaction (see Fig. S8,† a I···π bond is present in **6**). The planes are further linked by weak C–H···O and C–H···F contacts involving the triflate anions resulting in a quasi-3D network. The supramolecular interactions at 230 K for **1** and 170 K for **2a** all show subtle changes, indicative of substantial supramolecular reorganization prior to SCO.

The solvent and triflate interactions for **1–4** are very similar with two alcohol and two triflate anions bound together in a supramolecular circle (see Fig. S9 and Table S15†). The circle is composed of strong alcohol-triflate hydrogen bonds and

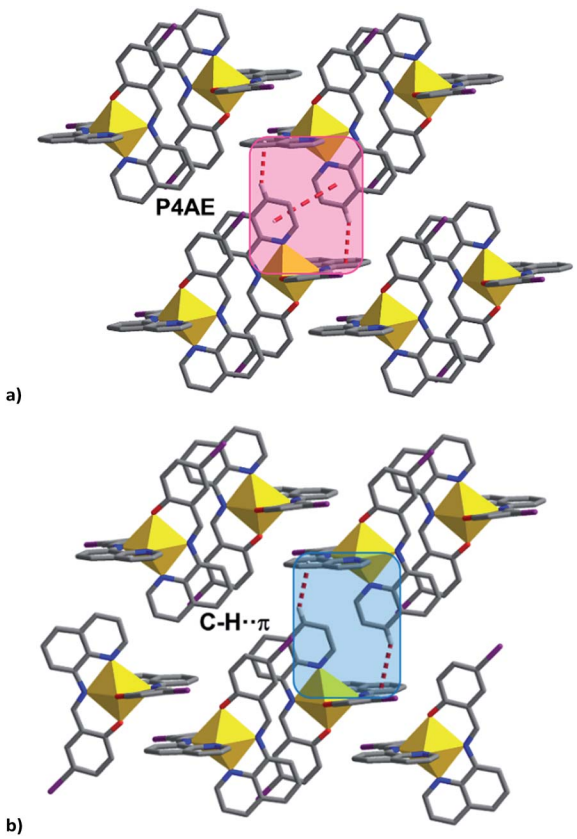

Fig. 8 (a) P4AE interactions in most [Fe(qsal-I)$_2$]OTf·sol complexes, (b) C–H···π interactions in **4** linking the chains into a plane.

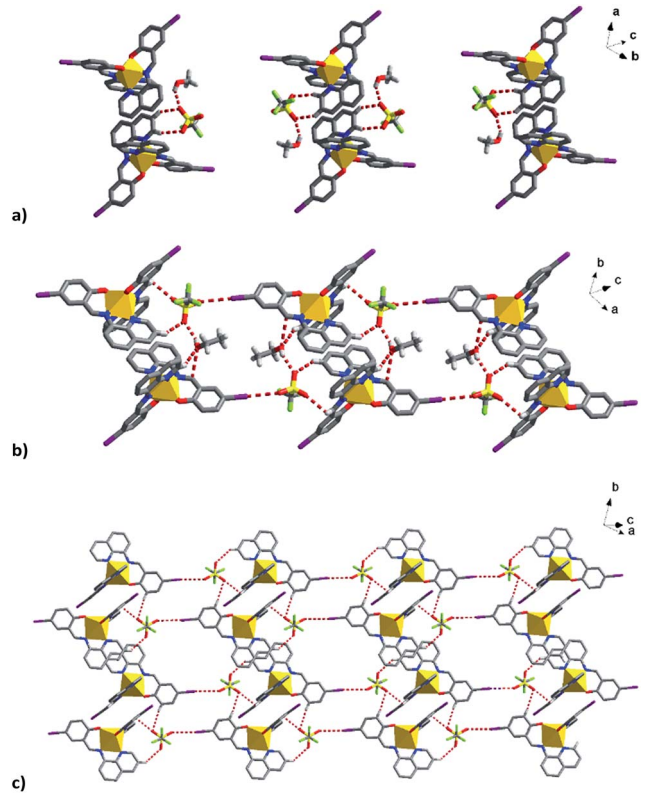

Fig. 9 Supramolecular interactions of the solvent and triflate anions in (a) **1**, (b) **2a** and (c) I···O interactions related to triflate in **2a** bridging the Fe units into a plane.

a F···F interaction[55–57] between the triflate anions. For **1** the latter is stronger at 293 K (2.867 Å) than it is at 163 K (3.005 Å) while for the other complexes it lengthens at high temperature. In **2** the difference between the HS (phase **2a**) and LS (phase **2b**) structures is almost 0.2 Å, consistent with the phase change noted above. For **3** and **4**, there are also C–H···F interactions which are generally weakened by SCO.

In **5** and **6** the solvent and triflate are linked by halogen bonding F···O and C–H···O interactions, respectively (Fig. S10†). The former are particularly strong being *ca.* 0.4 Å shorter than the van der Waals radii of F and O. This change in packing compared to **1–4** is probably responsible for the different SCO behaviour of these two solvates.

The triflate–solvent circles in **1** and **2** bridge the Fe cations that interact *via* π–π interactions as a chain through C–H···F/O interactions (Fig. S11†). In **2a** the Fe cations interact *via* P4AE and I···O interactions involving the triflate anion linking the Fe units in a plane (Fig. 9). This interaction is lost in the **2b** structure following a substantial reorientation of the triflate anion, which results in the formation of a new O···π interaction (3.022 Å, Fig. S12†). At the same time, the P4AE π–π interaction becomes more offset with neighbouring 1D chains shifted relative to each other. Similar supramolecular reorganization is found in $[Fe(qsal\text{-}I)_2][Ni(dmit)_2]\cdot MeCN\cdot H_2O$ where the loss of I···S interactions[44] also gives abrupt and hysteretic SCO.

To gain a better understanding of the 3D packing in these compounds simplified polyhedra packing diagrams have been generated viewed down the 1D π–π chains; **1** is shown in Fig. 10 as a representative example, with **2–6** shown in Fig. S13.† We define three parameters: the intra-chain, inter-chain and inter-plane distances, see Fig. 10. Looking at the different diagrams it is evident that the packing is tightest in **1** and **2**. There is also a large difference in the intra-chain distance in **1** and **2** of 0.71 Å while **3–5** exhibit much smaller values of 0.28–0.19 Å. **1** and **2** also show the smallest intra-chain distance in the HS state in this series. Moreover, the length of the 1D π–π chain, which is coincident with the *b* axis in **1**, **2** and **5** (the *a* axis for **3** and **4**), shortens most in **1** and **2** following SCO to the LS state. This confirms earlier studies that the 1D π–π chains are vital for SCO[34,38,51] and further that large differences between the two spin states will lead to abrupt SCO.[58,59]

The packing in the propanol solvates, **3** and **4**, is almost identical (see Fig. 11), although the intra- and inter-chain distances are slightly shorter in **3** than **4**. This is consistent with the magnetic studies where **4** shows slightly more gradual SCO and a higher transition temperature than **3**.

The acetone and acetonitrile solvates **5** and **6** show the most obvious gaps in the structure with the largest inter-plane and inter-chain distances in this series. These solvents are also unable to hydrogen bond with the anion and combined with the more open packing results in lower cooperativity. Overall, this

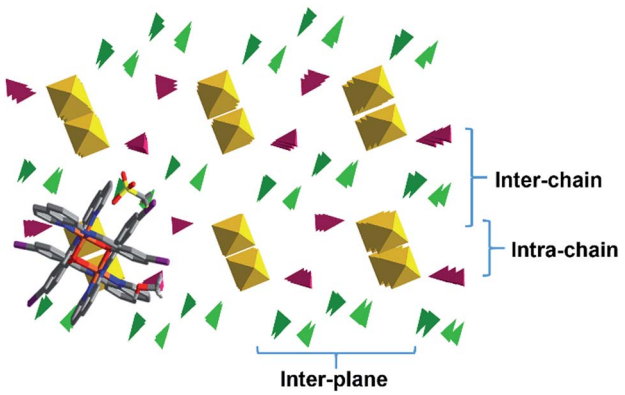

Fig. 10 Simplified packing diagram of **1** showing the intra-chain, inter-chain and inter plane distances with the $[Fe(qsal\text{-}I)_2]^+$ cations shown in yellow, the triflate anions in green and the MeOH molecules in burgundy.

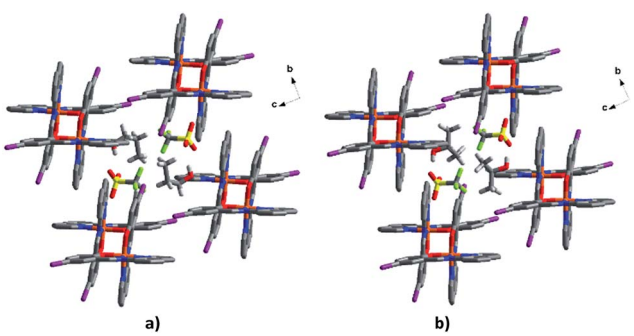

Fig. 11 The packing of the two propanol solvates in (a) **3** and (b) **4**.

This journal is © The Royal Society of Chemistry 2017

analysis reveals that the unique behaviour of **2** appears to be due to unusually tight packing which results in antagonistic interactions that favour a phase change and subsequent stepped SCO. Stepped SCO as a result of tight packing has been reported in $[Fe(qsal\text{-}Br)_2]NO_3\cdot 2MeOH$[51] and a number of Hoffmann-type networks including $[Fe_3^{II}(saltrz)_6(M^{II}(CN)_4)_3]\cdot 8H_2O$ {saltrz = 2-(((4*H*-1,2,4-triazol-4-yl)imino)methyl)-phenol},[60] $\{Fe[(Hg(SCN)_3)_2](4,4'\text{-bipy})_2\}_n$ (ref. 61) and $[Fe(dpsme)\text{-}Pt(CN)_4]\cdot 2/3dpsme\cdot x EtOH\cdot y H_2O$ (dpsme = 4,4′-di(pyridylthio)-methane).[62]

Conclusions

In summary, we have for the first time in Fe(III) SCO chemistry prepared a series of complexes that differ only in the lattice solvent, $[Fe(qsal\text{-}I)_2]OTf\cdot sol$. We have established that solvent provides a simple and valuable tool for tuning SCO properties with $T_{1/2}$ varying over nearly 200 K in **1–6**. The impact of EtOH is particularly stark with samples of **2** showing ageing and sample treatment effects. VT-PXRD studies of fresh samples show a phase change following the first cooling resulting in two-step SCO with the degree of hysteresis dependent on the amount of the minor phases **2a** and **2c** present in the sample. In contrast, the aged sample shows a remarkable hysteresis of 80 K, one of the largest values known in SCO chemistry. Surprisingly, the packing in the compounds is very similar and composed of 1D chains of the $[Fe(qsal\text{-}I)_2]^+$ cations connected by π–π interactions. Additional P4AE and I···X (X = I, O, π) interactions combine to form 3D supramolecular networks. Nevertheless, there are subtle differences which result in very different magnetic behaviour with the shortest intra-chain distances and more extensive interactions associated with more abrupt SCO. Indeed, in the case of **2** these interactions may be antagonistic thereby encouraging a phase change and stepped SCO. The startling impact that solvent has on the SCO characteristics of **1–6** should permit the development of solvent specific sensors. Moreover, the findings from this work would be expected to be applicable to other systems and will greatly aid others in the continuing search for SCO switches that operate at room temperature.

Experimental

Materials and basic characterisation

Hqsal-I was prepared as described previously.[63] All other reagents and solvents were purchased from Sigma-Aldrich Chemical Company or TCI Chemicals and used as received. Elemental analyses were carried out on a Eurovector EA3000 analyser by staff of the School of Chemistry, University of Bristol, UK. ESI-MS were carried out on a Bruker Daltonics 7.0T Apex 4 FTICR Mass Spectrometer by staff at the National University of Singapore. Infrared spectra (as KBr discs) were recorded on a Perkin-Elmer Spectrum One infrared spectrophotometer in the range 400–4000 cm^{-1}.

X-ray crystallography

Crystal data and data processing parameters for the structures of **1–6** are given in Table S1.† Crystals were mounted on a glass fibre using perfluoropolyether oil and the sample cooled to the required temperature in a stream of cold nitrogen. The diffraction data of **1**, **2** (at 170, 213 and 292 K), **4–6** were collected at 108 and 293 K on a Rigaku Spider diffractometer equipped with a MicroMax MM007 rotating anode generator, Cu_α radiation ($\lambda = 1.54178$ Å), high-flux Osmic multilayer mirror optics, and a curved image-plate detector. The data were integrated, scaled and averaged with FS Process.[64] In the case of **3** data were collected on a Bruker APEXII area detector with graphite monochromated MoKα ($\lambda = 0.71073$ Å).[65] After data collection, in each case an empirical absorption correction was applied.[66] In order to collect data for **2** at 100 K, a small amount of the sample was immersed in perfluoropolyether oil on a glass slide at room temperature, and the slide plunged into liquid nitrogen for up to one minute.

The structures were then solved by direct methods and refined on all F^2 data using the SHELX suite of programs[67] or OLEX2.[68] In all cases non-hydrogen atoms were refined with anisotropic thermal parameters; hydrogen atoms were included in calculated positions and refined with isotropic thermal parameters which were *ca.* 1.2 × (aromatic CH) or 1.5 × (Me, CH_2, OH) the equivalent isotropic thermal parameters of their parent carbon atoms. All pictures were generated using either OLEX2 or DIAMOND.[69] The CCDC numbers for the X-ray crystallographic data presented in this paper are 1519938 (**2b**), 1519939 (**2a**-170 K), 1519940 (**2a**-213 K), 1519941 (**2a**-292 K), 1519942 (**3**-100 K), 1519943 (**3**-270 K), 1519944 (**4**-163 K), 1519945 (**4**-293 K), 1519946 (**5**-137 K), 1519947 (**5**-293 K) and 1519948 (**6**).

Magnetic measurements

Data were collected using a Quantum Design MPMS 5 SQUID magnetometer under an applied field of 1 T over the temperature range 30–350 K for **1**, **3–6** and 30–325 K for **2**. The powdered or polycrystalline samples were placed in gel capsules and record at a scanning rate of nominally 10 K min^{-1}. However, care was taken to allow long thermal equilibration times at each temperature point such that the real scan rate was far lower. In the case of **2** Vaseline was used for the fresh and aged samples to ensure minimal solvent loss during the measurement.

Mössbauer spectroscopic studies

^{57}Fe Mössbauer spectra were recorded on a low field Mössbauer spectrometer from SEE Co. (Science Engineering & Education Co., MN). The sample of **2** was enclosed in Vaseline and rapidly frozen in liquid nitrogen. The sample was then placed in the spectrometer running at 5.3 K. This rapidly quenched sample was then warmed slowly to 77 K, 200 K, 260 K and 293 K. The sample was then slowly cooled to 220 K and finally returned to 5.3 K.

Synthesis of $[Fe(qsal\text{-}I)_2]OTf\cdot MeOH$, 1

Hqsal-I (154 mg, 0.4 mmol) was dissolved in CH_2Cl_2 (2 ml) giving an orange solution. NEt_3 (56 μl, 0.4 mmol) was added resulting in a change to dark orange. CH_3OH (3 ml) was layered on top of the Hqsal-I solution. In a separate flask, $FeCl_3$ (34 mg,

0.2 mmol) was dissolved in MeOH (5 ml) giving a yellow solution and AgOTf (155 mg, 0.6 mmol) added resulting in formation of a white powder (AgCl) which was filtered off. The yellow solution of $Fe(OTf)_3$ was then layered on top of the blank CH_3OH and left for 4 days. The black crystals which formed were washed with hexane (2 × 1 ml) and air dried yield 90 mg (47%). $\tilde{\nu}_{max}$(KBr)/cm^{-1} 3067 ($\nu_{Ar\text{-}H}$), 1600 ($\nu_{C=N}$), 1276 ($\nu_{S\text{-}O}$), 1139 ($\nu_{C\text{-}F}$), 1030 ($\nu_{S\text{-}O}$) cm^{-1}. *m*/*z* (ESI) 802.0 $[Fe(qsal\text{-}I)_2]^+$, 149.2 $[CF_3SO_3]^-$. Elemental analysis: calcd (found) for $C_{34}H_{24}F_3FeI_2N_4O_6S$: C, 41.51 (41.76); H, 2.46 (2.39); N, 5.70 (5.84)%.

The synthesis of the other complexes was achieved in a similar fashion by replacing MeOH with the appropriate solvent, *i.e.* EtOH, *n*-PrOH, i-PrOH, acetone and MeCN.

Synthesis of [Fe(qsal-I)$_2$]OTf·EtOH, 2

Aged sample. Prepared in a similar manner to **1** but with the crystals left in the CH_2Cl_2/EtOH mother liquor for 2 weeks. Yield 28%. $\hat{\nu}_{max}$(KBr)/cm^{-1} 3067 ($\nu_{Ar\text{-}H}$), 1600 ($\nu_{C=N}$), 1276 ($\nu_{S\text{-}O}$), 1163 ($\nu_{C\text{-}F}$), 1030 ($\nu_{S\text{-}O}$) cm^{-1}. *m*/*z* (ESI) 801.9 $[Fe(qsal\text{-}I)_2]^+$, 149.1 $[CF_3SO_3]^-$. Elemental analysis: calcd (found) for $C_{35}H_{26}F_3FeI_2N_4O_6S$: C, 42.15 (41.81); H, 2.63 (2.44); N, 5.62 (5.93)%.

Fresh sample. Crystals isolated immediately once crystallization was complete (*ca.* 3–4 days). IR and MS data matched those of the aged sample. Elemental analysis: calcd (found) for $C_{35}H_{26}F_3FeI_2N_4O_6S$: C, 42.15 (42.16); H, 2.63 (2.66); N, 5.62 (5.58)%.

Synthesis of [Fe(qsal-I)$_2$]OTf·*n*-PrOH, 3

Yield 26%. $\tilde{\nu}_{max}$(KBr)/cm^{-1} 3067 ($\nu_{Ar\text{-}H}$), 1601 ($\nu_{C=N}$), 1278 ($\nu_{S\text{-}O}$), 1159 ($\nu_{C\text{-}F}$), 1030 ($\nu_{S\text{-}O}$) cm^{-1}. *m*/*z* (ESI) 801.9 $[Fe(qsal\text{-}I)_2]^+$, 149.1 $[CF_3SO_3]^-$. Elemental analysis: calcd (found) for $C_{36}H_{28}F_3FeI_2N_4O_6S$: C, 42.75 (41.74); H, 2.79 (2.67); N, 5.54 (5.41)%.

Synthesis of [Fe(qsal-I)$_2$]OTf·i-PrOH, 4

Yield 23%. $\tilde{\nu}_{max}$(KBr)/cm^{-1} 3067 ($\nu_{Ar\text{-}H}$), 1601 ($\nu_{C=N}$), 1278 ($\nu_{S\text{-}O}$), 1159 ($\nu_{C\text{-}F}$), 1030 ($\nu_{S\text{-}O}$) cm^{-1}. *m*/*z* (ESI) 801.9 $[Fe(qsal\text{-}I)_2]^+$, 149.1 $[CF_3SO_3]^-$. Elemental analysis: calcd (found) for $C_{36}H_{28}F_3FeI_2N_4O_6S$: C, 42.75 (42.37); H, 2.79 (2.84); N, 5.54 (5.26)%.

Synthesis of [Fe(qsal-I)$_2$]OTf·acetone, 5

Yield 20%. $\tilde{\nu}_{max}$(KBr)/cm^{-1} 3044 ($\nu_{Ar\text{-}H}$), 1596 ($\nu_{C=N}$), 1261 ($\nu_{S\text{-}O}$), 1158 ($\nu_{C\text{-}F}$), 1060 ($\nu_{S\text{-}O}$) cm^{-1}. *m*/*z* (ESI) 801.9 $[Fe(qsal\text{-}I)_2]^+$, 149.1 $[CF_3SO_3]^-$. Elemental analysis: calcd (found) for $C_{36}H_{26}F_3FeI_2N_4O_6S$: C, 42.84 (43.12); H, 2.60 (2.81); N, 5.55 (6.11)%.

Synthesis of [Fe(qsal-I)$_2$]OTf·MeCN, 6

Yield 22%. $\tilde{\nu}_{max}$(KBr)/cm^{-1} 3047 ($\nu_{Ar\text{-}H}$), 1599 ($\nu_{C=N}$), 1299 ($\nu_{S\text{-}O}$), 1159 ($\nu_{C\text{-}F}$), 1042 ($\nu_{S\text{-}O}$) cm^{-1}. *m*/*z* (ESI) 801.9 $[Fe(qsal\text{-}I)_2]^+$, 149.1 $[CF_3SO_3]^-$. Elemental analysis: calcd (found) for $C_{35}H_{23}F_3FeI_2N_5O_5S$: C, 42.36 (43.62); H, 2.33 (2.54); N, 7.06 (7.17)%.

Acknowledgements

We thank the Thailand Research Fund (Grant No. RSA5580028 and RSA5880048) and the National Science and Technology Development Agency (Grant No. P-10-11181) for funding this research. KSM thanks the Australian Research Council for a Discovery Project grant to support this work. Parts of this research were undertaken on the MX2 and PD beamlines with the help of Dr Helen Brand and Dr Alan Riboldi-Tunnicliffe from the Australian Synchrotron, Victoria, Australia.

Notes and references

1 *Spin-Crossover Materials: Properties and Applications*, ed. M. A. Halcrow, John Wiley & Sons, Ltd, Chichester, 2013.
2 R. Klajn, J. F. Stoddart and B. A. Grzybowski, *Chem. Soc. Rev.*, 2010, **39**, 2203.
3 M. Natali and S. Giordani, *Chem. Soc. Rev.*, 2012, **41**, 4010.
4 M. D. Manrique-Juárez, S. Rat, L. Salmon, G. Molnár, C. M. Quintero, L. Nicu, H. J. Shepherd and A. Bousseksou, *Coord. Chem. Rev.*, 2015, **308**, 395–408.
5 J. L. Zhang, J. Q. Zhong, J. D. Lin, W. P. Hu, K. Wu, G. Q. Xu, A. T. S. Wee and W. Chen, *Chem. Soc. Rev.*, 2015, **44**, 2998–3022.
6 O. Sato, *Nat. Chem.*, 2016, **8**, 644–656.
7 K. S. Murray, in *Spin-Crossover Materials: Properties and Applications*, ed. M. A. Halcrow, John Wiley & Sons Ltd., Chichester, 2013, pp. 1–54.
8 P. Gütlich, A. B. Gaspar and Y. Garcia, *Beilstein J. Org. Chem.*, 2013, **9**, 342–391.
9 V. Ksenofontov, A. B. Gaspar and P. Gütlich, *Top. Curr. Chem.*, 2004, **235**, 23–64.
10 A. Hauser, *Top. Curr. Chem.*, 2004, **234**, 155–198.
11 J.-F. Létard, *J. Mater. Chem.*, 2006, **16**, 2550–2559.
12 J.-F. Létard, P. Guionneau and L. Goux-Capes, *Top. Curr. Chem.*, 2004, **235**, 221–249.
13 J.-F. Létard, G. Chastanet, P. Guionneau and C. Desplanches, in *Spin Crossover Materials: Properties and Applications*, ed. M. A. Halcrow, John Wiley & Sons, Ltd, Chichester, 2013, pp. 475–506.
14 M. G. Cowan, J. Olguín, S. Narayanaswamy, J. L. Tallon and S. Brooker, *J. Am. Chem. Soc.*, 2012, **134**, 2892–2894.
15 S. Brooker and J. A. Kitchen, *Dalton Trans.*, 2009, 7331–7340.
16 A. B. Gaspar, M. Seredyuk and P. Gütlich, *J. Mol. Struct.*, 2009, **924–926**, 9–19.
17 M. A. Halcrow, *Coord. Chem. Rev.*, 2009, **253**, 2493–2514.
18 Y. Sunatsuki, R. Kawamoto, K. Fujita, H. Maruyama, T. Suzuki, H. Ishida, M. Kojima, S. Iijima and N. Matsumoto, *Coord. Chem. Rev.*, 2010, **254**, 1871–1881.
19 B. Weber, in *Spin-Crossover Materials: Properties and Applications*, ed. M. A. Halcrow, John Wiley & Sons Ltd., Chichester, 2013, pp. 55–76.
20 G. A. Craig, O. Roubeau and G. Aromí, *Coord. Chem. Rev.*, 2014, **269**, 13–31.
21 M. Nihei, T. Shiga, Y. Maeda and H. Oshio, *Coord. Chem. Rev.*, 2007, **251**, 2606–2621.
22 R. Bertoni, M. Lorenc, A. Tissot, M. L. Boillot and E. Collet, *Coord. Chem. Rev.*, 2015, **282–283**, 66–76.
23 D. J. Harding, P. Harding and W. Phonsri, *Coord. Chem. Rev.*, 2016, **313**, 38–61.

 This journal is © The Royal Society of Chemistry 2017

24 K. S. Murray and C. J. Kepert, *Top. Curr. Chem.*, 2004, **233**, 195–228.
25 S. Hayami, K. Hiki, T. Kawahara, Y. Maeda, D. Urakami, K. Inoue, M. Ohama, S. Kawata and O. Sato, *Chem.–Eur. J.*, 2009, **15**, 3497–3508.
26 D. Sertphon, D. J. Harding, P. Harding, K. S. Murray, B. Moubaraki, J. D. Cashion and H. Adams, *Eur. J. Inorg. Chem.*, 2013, 788–795.
27 A. Tissot, P. Fertey, R. Guillot, V. Briois and M.-L. Boillot, *Eur. J. Inorg. Chem.*, 2014, 101–109.
28 I. Nemec, R. Herchel, R. Boča, Z. Trávníček, I. Svoboda, H. Fuess and W. Linert, *Dalton Trans.*, 2011, **40**, 10090–10099.
29 I. Nemec, R. Herchel, I. Šalitroš, Z. Trávníček, J. Moncol, H. Fuess, M. Ruben and W. Linert, *CrystEngComm*, 2012, **14**, 7015–7024.
30 C. Krüger, P. Augustín, L. Dlháň, J. Pavlik, J. Moncoĺ, I. Nemec, R. Boča and F. Renz, *Polyhedron*, 2015, **87**, 194–201.
31 M. Koike, K. Murakami, T. Fujinami, K. Nishi, N. Matsumoto and Y. Sunatsuki, *Inorg. Chim. Acta*, 2013, **399**, 185–192.
32 K. Hanahara, H. Ono, T. Fujinami, N. Matsumoto and Y. Sunatsuki, *Inorg. Chim. Acta*, 2015, **429**, 93–98.
33 J. C. Dias, B. Vieira, I. C. Santos, L. C. J. Pereira and V. Da Gama, *Inorg. Chim. Acta*, 2009, **362**, 2076–2079.
34 D. J. Harding, D. Sertphon, P. Harding, K. S. Murray, B. Moubaraki, J. D. Cashion and H. Adams, *Chem.–Eur. J.*, 2013, **19**, 1082–1090.
35 B. J. C. Vieira, J. C. Dias, I. C. Santos, L. C. J. Pereira, V. da Gama and J. C. Waerenborgh, *Inorg. Chem.*, 2015, **54**, 1354–1362.
36 T. Shimizu, Y. Komatsu, H. Kamihata, Y. H. Lee, A. Fuyuhiro, S. Iijima and S. Hayami, *J. Inclusion Phenom. Macrocyclic Chem.*, 2011, **71**, 363–369.
37 I. Nemec, R. Herchel and Z. Trávníček, *Dalton Trans.*, 2015, **44**, 4474–4484.
38 D. J. Harding, W. Phonsri, P. Harding, I. A. Gass, K. S. Murray, B. Moubaraki, J. D. Cashion, L. Liu and S. G. Telfer, *Chem. Commun.*, 2013, **49**, 6340–6342.
39 G. J. Halder, K. W. Chapman, S. M. Neville, B. Moubaraki, K. S. Murray, J.-F. Létard and C. J. Kepert, *J. Am. Chem. Soc.*, 2008, **130**, 17552–17562.
40 P. D. Southon, L. Liu, E. A. Fellows, D. J. Price, G. J. Halder, K. W. Chapman, B. Moubaraki, K. S. Murray, J. F. Létard and C. J. Kepert, *J. Am. Chem. Soc.*, 2009, **131**, 10998–11009.
41 T. M. Ross, B. Moubaraki, K. S. Wallwork, S. R. Batten and K. S. Murray, *Dalton Trans.*, 2011, **40**, 10147.
42 A. I. Vicente, A. Joseph, L. P. Ferreira, M. de Deus Carvalho, V. H. N. Rodrigues, M. Duttine, H. P. Diogo, M. E. Minas da Piedade, M. J. Calhorda and P. N. Martinho, *Chem. Sci.*, 2016, **7**, 4251–4258.
43 W. Phonsri, D. J. Harding, P. Harding, K. S. Murray, B. Moubaraki, I. A. Gass, J. D. Cashion, G. N. L. Jameson and H. Adams, *Dalton Trans.*, 2014, **43**, 17509–17518.
44 K. Fukuroi, K. Takahashi, T. Mochida, T. Sakurai, H. Ohta, T. Yamamoto, Y. Einaga and H. Mori, *Angew. Chem., Int. Ed.*, 2014, **53**, 1983–1986.
45 J. K. McCusker, A. L. Rheingold and D. N. Hendrickson, *Inorg. Chem.*, 1996, **35**, 2100–2112.
46 M. Marchivie, P. Guionneau, J. F. Létard and D. Chasseau, *Acta Crystallogr., Sect. B: Struct. Sci.*, 2005, **61**, 25–28.
47 G. Aromí, C. M. Beavers, J. Sánchez Costa, G. A. Craig, G. Mínguez Espallargas, A. Orera and O. Roubeau, *Chem. Sci.*, 2016, **7**, 2907–2915.
48 G. A. Craig, J. S. Costa, O. Roubeau, S. J. Teat and G. Aromí, *Chem.–Eur. J.*, 2011, **17**, 3120–3127.
49 H. Oshio, K. Kitazaki, J. Mishiro, N. Kato and Y. Maeda, *J. Chem. Soc., Dalton Trans.*, 1987, 1341–1347.
50 G. A. Craig, J. S. Costa, O. Roubeau, S. J. Teat and G. Aromí, *Eur. J. Inorg. Chem.*, 2013, **2013**, 745–752.
51 D. J. Harding, W. Phonsri, P. Harding, K. S. Murray, B. Moubaraki and G. N. L. Jameson, *Dalton Trans.*, 2015, **44**, 15079–15082.
52 B. J. C. Vieira, J. T. Coutinho, J. C. Dias, J. C. Nunes, I. C. Santos, L. C. J. Pereira, V. da Gama and J. C. Waerenborgh, *Polyhedron*, 2015, **85**, 643–651.
53 O. Iasco, E. Rivie, R. Guillot, M. Buron-Le Cointe, J.-F. Meunier, A. Bousseksou and M.-L. Boillot, *Inorg. Chem.*, 2015, **54**, 1791–1799.
54 V. Russell, M. Scudder and I. Dance, *J. Chem. Soc., Dalton Trans.*, 2001, 789–799.
55 K. Reichenbächer, H. I. Süss and J. Hulliger, *Chem. Soc. Rev.*, 2005, **34**, 22–30.
56 S. K. Nayak, M. K. Reddy, T. N. G. Row and D. Chopra, *Cryst. Growth Des.*, 2011, **11**, 1578–1596.
57 D. Chopra, *Cryst. Growth Des.*, 2012, **12**, 541–546.
58 M. A. Halcrow, *Chem. Soc. Rev.*, 2011, **40**, 4119–4142.
59 M. A. Halcrow, *Chem. Lett.*, 2014, **43**, 1178–1188.
60 N. F. Sciortino, K. A. Zenere, M. E. Corrigan, G. J. Halder, G. Chastanet, J.-F. Létard, C. J. Kepert and S. M. Neville, *Chem. Sci.*, 2017, **8**, 701–707.
61 E. Trzop, D. Zhang, L. Piñeiro-Lopez, F. J. Valverde-Muñoz, M. Carmen Muñoz, L. Palatinus, L. Guerin, H. Cailleau, J. A. Real and E. Collet, *Angew. Chem., Int. Ed.*, 2016, **55**, 8675–8679.
62 N. F. Sciortino, K. R. Scherl-Gruenwald, G. Chastanet, G. J. Halder, K. W. Chapman, J.-F. Létard and C. J. Kepert, *Angew. Chem., Int. Ed.*, 2012, **51**, 10154–10158.
63 J. Sirirak, W. Phonsri, D. J. Harding, P. Harding, P. Phommon, W. Chaoprasa, R. M. Hendry, T. M. Roseveare and H. Adams, *J. Mol. Struct.*, 2013, **1036**, 439–446.
64 Rigaku, *Rigaku XRD*, Rigaku Corporation, Tokyo, Japan, 1996.
65 *Bruker APEXII*, Bruker AXS Inc., Madison, WI, USA, 2005.
66 *SADABS and SAINT*, Bruker AXS Inc., Madison, WI, USA, 2003.
67 G. M. Sheldrick, *Acta Crystallogr.*, 2008, **A64**, 112–122.
68 O. V. Dolomanov, L. J. Bourhis, R. J. Gildea, J. A. K. Howard and H. Puschmann, *J. Appl. Crystallogr.*, 2009, **42**, 339–342.
69 K. Brandenberg and H. Putz, *DIAMOND, Crystal Impact*, Bonn, Germany, 2006.

Volume 117 | Issue 9 | May 5, 2017

International Journal of QUANTUM CHEMISTRY

www.q-chem.org

WILEY

Received: 13 August 2016 | Revised: 10 January 2017 | Accepted: 2 February 2017

DOI 10.1002/qua.25362

FULL PAPER

WILEY International Journal of QUANTUM CHEMISTRY

Comparison of density functionals for the study of the high spin low spin gap in Fe(III) spin crossover complexes

Jitnapa Sirirak[1] | Darunee Sertphon[2] | Wasinee Phonsri[2†] | Phimphaka Harding[2] | David J. Harding[2]

[1]Department of Chemistry, Faculty of Science, Silpakorn University, Muang, Nakhon Pathom 73000, Thailand

[2]Functional Materials and Nanotechnology Center of Excellence, Walailak University, Nakhon Si Thammarat, Thasala 80160, Thailand

Correspondence
David J. Harding, Functional Materials and Nanotechnology Center of Excellence, Walailak University, Nakhon Si Thammarat, Thasala 80161, Thailand.
Email: hdavid@g-mail.wu.ac.th

Funding information
We thank Walailak University for a Postdoctoral Fellowship to JS, the Thailand Research Fund (RSA5580028 and RSA5880048) and the National Science and Technology Development Agency (grant no.: P-10-11181) for funding this research.

Abstract

A detailed investigation of the accuracy of different quantum mechanical methods for the study of iron(III) spin crossover complexes is presented. The energy spin state gap between the high and low spin states; ΔE(HS-LS) of nine iron(III) quinolylsalicylaldiminate complexes were calculated with nine different DFT functionals, then compared. DFT functionals: B3LYP, B3LYP-D3, B3LYP*, BH&HLYP, BP86, OLYP, OPBE, M06L, and TPSSh were tested with six basis sets: 3-21G*, dgdzvp, 6-31G**, cc-pVDZ, Def2TZVP, and cc-pVTZ. The cations from the X-ray crystal structures of [Fe(qsal-OMe)$_2$]Cl·MeCN·H_2O, [Fe(qsal-OMe)$_2$]Cl·2MeOH·0.5H_2O, [Fe(qsal-OMe)$_2$]BF_4·MeOH, [Fe(qsal-OMe)$_2$]NCS·CH_2Cl_2, [Fe(qsal-F)$_2$]NCS, [Fe(qsal-Cl)$_2$]NCS·MeOH, [Fe(qsal-Br)$_2$]NCS·MeOH, [Fe(qsal-I)$_2$]OTf·MeOH, and [Fe(qsal)$_2$]NCS·CH_2Cl_2 were used as starting structures. The results show that B3LYP, B3LYP-D3, OLYP, and OPBE with a 6-31G**, Def2TZVP, and cc-pVTZ basis set give reasonable results of ΔE(HS-LS) compared with the experimental data. The enthalpy of [Fe(qsal-I)$_2$]$^+$ calculated with an OLYP functional and cc-pVTZ basis set (1.48 kcal/mol) most closely matches the experimental data (1.34 kcal/mol). B3LYP* yields an enthalpy of 5.92 kcal/mol suggesting it may be unsuitable for these Fe(III) complexes, mirroring recent results by Kepp (*Inorg. Chem.*, 2016, *55*, 2717–2727).

KEYWORDS
basis sets, DFT calculations, functionals, iron(III) complexes, spin crossover

1 | INTRODUCTION

Spin crossover is an elegant example of bistability with switching occurring between a high spin (HS) and a low spin (LS) state.[1–4] A particular advantage of these materials is that a variety of external stimuli including temperature, pressure or light may be used to enable switching.[5–7] Moreover, their relative simplicity and ready processability mean that they are attractive targets in the fields of molecular electronics and high density data storage.[8,9]

To be spin crossover active requires that the HS and LS states are close in energy, something that depends on the ligand, the metal and its oxidation state.[10] Accurately computing such spin state energies to enable better design or insight into systems where subtle ligand changes radically alter magnetic behavior is, however, computationally challenging.[11–13] Part of the problem lies in the fact that the spin state gap is often within the error associated with the calculation itself. While computational systems exist which can reduce this error they are typically computationally expensive and often require expert knowledge to use correctly.[14,15] Moreover, semiempirical methods such as CAPST2 have been found to have strong dependence on the value chosen for the ionization potential—electron affinity shift.[16,17]

DFT calculations have become a popular alternative to these time consuming HF methods. While successful to some degree the choice of functional used has been shown to have a significant impact on the energy gap. Thus, pure functionals such BLYP and BP86 invariably favour LS states while hybrid functionals such as B3LYP tend to overstabilize HS states.[18] Another factor shown to be critical for most common functionals is that of the basis sets. Swart has demonstrated that large basis sets are typically required to accurately reproduce experimental data.[19]

In relation to spin crossover compounds, the favouring of the HS state by B3LYP has been compensated for by adjusting the amount of

†Current address: School of Chemistry, Monash University, Clayton, Melbourne, Victoria, 3800, Australia

 © 2017 Wiley Periodicals, Inc.

HF exchange from 20% to 15% which in a large number of Fe(II) SCO systems yields reasonable results.[20] However, Friesner and Hughes recommend against altering the degree of HF exchange instead preferring a local correction model.[21] Moreover, they suggest that the reason for the success of B3LYP* in most Fe(II) SCO systems is due to the commonality of the ligands with most systems using aromatic and imine nitrogen donors. In attempting to address this we have undertaken computational studies on a series of Fe(III) SCO systems[22,23] to see what effects the choice of functional and basis set will have on these systems. The particular system we have chosen to study is [Fe(qsal-X)$_2$]Y (qsal-X = substituted quinolylsalicylaldiminate, Y = anion; see figure below) as structural data, in both the high spin and low spin states, and thermochemical data are known for a number of these compounds permitting comparison with our computational results.[24–30]

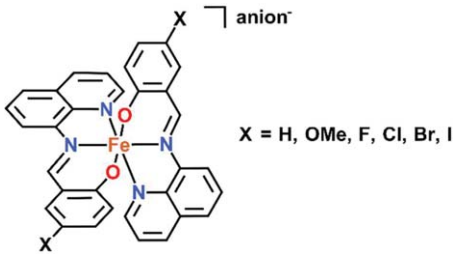

Specifically, we explore eight DFT functionals: B3LYP, B3LYP*, BH&HLYP, BP86, OLYP, OPBE, M06L, and TPSSh and six basis sets: 3-21G*, dgdzvp, 6-31G**, cc-pVDZ, Def2TZVP, and cc-pVTZ to investigate their effects on the energy differences between the high and low spin states; ΔE(HS-LS) and comparisons are drawn between the computed and experimental data.

2 | METHODS

All DFT calculations were performed using the GAUSSIAN 09 package suite[31] Using the X-ray structures as starting structures,[26–28,32] the geometries of the cations of the complexes at the lowest energy LS and HS states were fully optimized with B3LYP and 6-31G(d,p) basis set (except for the iodine atom, where a dgdzvp basis set was used).

Using the optimized structures in the HS and LS state calculated above, single point calculations were performed with seven other DFT functionals including B3LYP*, BH&HLYP, BP86, OLYP, OPBE, M06L, and TPSSh. In the case of B3LYP, we also included dispersion effects using a D3 correction[33] as such effects have recently been shown to be significant in some systems.[34] Six different basis sets: 3-21G*, dgdzvp, 6-31G**, cc-pVDZ, Def2TZVP, and cc-pVTZ were also tested. This approach is justified as beyond the geometric optimization the different functionals and basis sets result in only very minor changes to metal–ligand bond lengths and in the relative energies, as both spin states are affected in the same way by any change in method.[35,36] In the interests of simplicity, solvation, and relativistic effects are not included in the calculations as the differences between the two spin states are typically small.[21] From the electronic energies obtained from the different methods, the spin state energy differences between the high and low spin states ΔE(HS-LS) of these cations were calculated. The differences between the calculated ΔE(HS-LS) with other basis sets and those of cc-pVTZ as well as the mean of these differences from all nine complexes for each method were then calculated in order to investigate the effect of the basis set (Supporting Information Table S3). Moreover, to explore the effect of the functional on ΔE(HS-LS), the differences between the calculated ΔE(HS-LS) with other basis sets and those of cc-pVTZ along with the mean of these differences from all nine complexes for each method were calculated and compared. B3LYP was chosen as a reference functional as its performance for transition metal energetic calculations is generally very good among DFT functionals (Supporting Information Table S4).[21,37]

To obtain the thermal corrections to the enthalpy where zero-point energies were included, vibrational frequencies calculations were also performed with B3LYP, B3LYP-D3, B3LYP*, OLYP, and OPBE methods and 6-31g**, cc-pVDZ, and cc-pVTZ basis sets using the optimized structure of the cation of [Fe(qsal-I)$_2$]OTf·MeOH. Thermal corrections to the enthalpy were added to ΔE(HS-LS) computed using the above methods and compared with the experimental enthalpy.

To more accurately determine how closely the calculated structures matched the experimental ones we also determined the octahedral distortion parameters, Σ and Θ. Σ is defined as the sum of the deviation of the 12 *cis* angles (ϕ) of the complex from 90° (Equation 1),[38] while Θ is the sum of the deviation of the 24 N—Fe—N angles (θ) measured on the projection of two triangular faces of the octahedron along their common *pseudo*-three fold axes from 60° (Equation 2).[39]

$$\Sigma = \sum_{i=1}^{12} |90 - \phi_i| \quad (1)$$

$$\Theta = \sum_{i=1}^{24} |60 - \theta_i| \quad (2)$$

Finally, the frontier orbitals and more particularly the highest occupied molecular orbital (HOMO) and the lowest occupied molecular orbital (LUMO) were calculated with the aim of exploring which molecular orbitals are involved in the bonding between the iron and ligand, and how this is effected by spin crossover.

3 | RESULTS AND DISCUSSION

3.1 | Geometries of spin crossover complexes

The cations from nine X-ray crystal structures [Fe(qsal-OMe)$_2$]Cl·2MeOH·0.5H$_2$O **1**, [Fe(qsal-OMe)$_2$]Cl·2MeCN·H$_2$O **2**, [Fe(qsal-OMe)$_2$]BF$_4$·MeOH **3**, [Fe(qsal-OMe)$_2$]NCS·CH$_2$Cl$_2$ **4**, [Fe(qsal-F)$_2$]NCS **5**, [Fe(qsal-Cl)$_2$]NCS·MeOH **6**, [Fe(qsal-Br)$_2$]NCS·MeOH **7**, [Fe(qsal-I)$_2$]OTf·MeOH **8**, and [Fe(qsal)$_2$]NCS·CH$_2$Cl$_2$ **9** were used as the starting structure for structural optimization at the B3LYP/6-31G** level. Four X-ray structures have the same cation, [Fe(qsal-OMe)$_2$]$^+$ which means that there are four different starting structures of the same cation so results from these four optimized structures can be used to justify the applicability of the method. Moreover, there are four cations, in which their X-ray structures in both high spin and low spin have been reported, which are

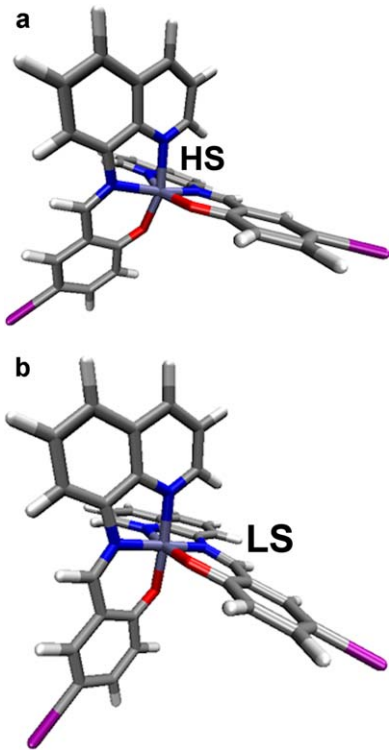

FIGURE 1 View of the molecular structure of $[Fe(qsal\text{-}I)_2]^+$ in the high spin (top) and low spin (bottom) state

$[Fe(qsal\text{-}OMe)_2]^+$, $[Fe(qsal\text{-}F)_2]^+$, $[Fe(qsal\text{-}I)_2]^+$, and $[Fe(qsal)_2]^+$,[25–28,32] permitting further comparison with the calculated structures.

The optimized structures of $[Fe(qsal\text{-}I)_2]^+$ in the HS and LS states are shown in Figure 1. Important bond lengths are listed in Table 1 (bond angles may be found in Supporting Information Table S1) while the octahedral distortion parameters Σ and Θ values are listed in Table 2.

A comparison between the X-ray and the optimized structures, reveals that the bond lengths and angles are similar as can be seen in Tables 1 and Supporting Information S1. The difference between the bond lengths and angles obtained from the X-ray structures and the optimized structures are 0.03 Å and 1.9° on average, respectively, indicating that the calculations are good models of the real structures. A comparison of **1**–**4** where the starting structures contain the same cation, $[Fe(qsal\text{-}OMe)_2]^+$ are extremely similar and further support this conclusion. Similar differences between calculated and crystal structures are observed by Jensen and Cirera in $[Fe(2\text{-}NH_2CH_2py)_3]^{2+}$ with {MAD = 0.009 Å (LS) and 0.041 Å (HS); TPSSh}[40] and Bučko et al. in $[Fe(phen)_2(NCS)_2]$ {MAD = 0.023 Å (LS) and 0.040 Å (HS); PBE + U-D2}.[41]

The degree of distortion around the Fe centre as measured by their $\sum$ and Θ values reveal that the values obtained from the X-ray structures are more similar to those of the optimized structure in the low spin state. This is expected as the exact nature of the distortion that occurs in the high spin state is often difficult to model.[42] Although the exact $\sum$ and Θ values of the optimized and X-ray structures are often significantly different, the differences between the $\sum$ and Θ values from the structures in the high and low spin state {ΔΣ (HS-LS) and ΔΘ (HS-LS)} are very similar. As octahedral distortion parameters are rarely reported, comparisons are difficult but studies on $[Fe(phen)_2(NCS)_2]$ using a PBE + U-D2 method shows that the LS differences are ca. 1° while for the HS state it is much greater at almost 28°.[41] This confirms that our calculations adequately model the $[Fe(qsal\text{-}X)_2]^+$ compounds.

3.2 | Molecular orbital analysis

The frontier orbitals of the optimized structures were also investigated (see Figures S1 and S2 in the Supporting Information). The HOMO and LUMO of the two cations: $[Fe(qsal\text{-}I)_2]^+$ and $[Fe(qsal\text{-}OMe)_2]^+$ in the high and low spin state (HS and LS) are presented as representative examples in Figures 2 and 3, respectively. The HOMO of $[Fe(qsal\text{-}OMe)_2]^+$ in both the HS and LS state has considerable electron density localized on the ligand with a relatively small metal contribution. The

TABLE 1 Comparison of the bond lengths from the X-ray crystal structures and the structures optimized at the B3LYP/6-31G** level

Bond lengths/Å	Structure	1	2	3	4	5	6	7	8	9	MAD[a]
Fe-N_{quin} (HS)	Opt	2.20	2.20	2.20	2.21	2.21	2.20	2.19	2.15	2.22	-
Fe-N_{quin} (HS)	X-ray	2.17	-	-	-	2.14[b]	-	-	2.15	2.16	0.053
Fe-N_{quin} (LS)	Opt	2.01	2.01	2.01	2.01	2.01	2.01	2.01	1.96	2.01	-
Fe-N_{quin} (LS)	X-ray	1.99	1.98	1.97	1.98	1.97	1.97	1.98	1.99	1.99	0.031
Fe-N_{imine} (HS)	Opt	2.15	2.15	2.15	2.14	2.15	2.15	2.16	2.14	2.15	-
Fe-N_{imine} (HS)	X-ray	2.11	-	-	-	2.11[b]	-	-	2.09	2.10	0.045
Fe-N_{imine} (LS)	Opt	1.96	1.96	1.96	1.96	1.96	1.96	1.96	1.93	1.96	-
Fe-N_{imine} (LS)	X-ray	1.95	1.94	1.93	1.94	1.93	1.93	1.96	1.94	1.95	0.018
Fe-O (HS)	Opt	1.90	1.90	1.90	1.90	1.89	1.90	1.90	1.88	1.89	-
Fe-O (HS)	X-ray	1.91	-	-	-	1.90[b]	-	-	1.90	1.90	0.013
Fe-O (LS)	Opt	1.86	1.86	1.86	1.86	1.86	1.86	1.86	1.85	1.86	-
Fe-O (LS)	X-ray	1.88	1.88	1.87	1.87	1.87	1.86	1.88	1.89	1.87	0.016

[a]MAD = Mean absolute deviation; in cases where experimental data are not available these points are ignored.
[b]Fe_2—N/O bond lengths at 270 K are used, taken from Ref. 27.

TABLE 2 The comparison of Σ and Θ of the X-ray crystal structures and the structures optimized at the B3LYP/6-31G** level

	Structure	1	2	3	4	5	6	7	8	9
Σ										
Σ (HS)	Opt	84.1	84.5	84.7	84.6	84.4	85.6	89.4	85.3	88.6
Σ (HS)	X-ray	74.8	-[a]	-[a]	-[a]	73.0	-[a]	-[a]	63.3	69.9
Σ (LS)	Opt	51.9	51.8	51.8	51.7	52.5	52.1	52.5	53.4	53.0
Σ (LS)	X-ray	42.4	42.5	43.6	44.4	40.1	48.2	51.4	42.0	52.1
ΔΣ (HS-LS)	Opt	32.3	32.7	33.0	32.9	31.9	33.5	36.8	31.9	35.6
ΔΣ (HS-LS)	X-ray	32.4	-[a]	-[a]	-[a]	32.9	-[a]	-[a]	21.3	17.8
Θ										
Θ (HS)	Opt	245.0	245.2	245.6	245.6	241.7	245.3	249.9	223.7	247.1
Θ (HS)	X-ray	205.5	-[a]	-[a]	-[a]	198.0	-[a]	-[a]	186.4	203.8
Θ (LS)	Opt	97.3	95.9	95.9	78.8	105.2	94.7	94.6	90.3	95.7
Θ (LS)	X-ray	62.3	64.8	58.8	61.3	80.7	67.1	74.9	61.3	81.0
ΔΘ (HS-LS)	Opt	147.7	149.3	149.7	166.7	136.6	150.6	155.3	133.4	151.3
ΔΘ (HS-LS)	X-ray	143.2	-[a]	-[a]	-[a]	117.3	-[a]	-[a]	125.1	122.8

[a]Structure not available.

HOMO of $[Fe(qsal\text{-}I)_2]^+$ (HS and LS) has more metal character than $[Fe(qsal\text{-}OMe)_2]^+$, a trend also observed for the other $[Fe(qsal\text{-}X)_2]^+$ (X = halogen) complexes. Comparing the HS and LS HOMOs, the HS HOMO is found to be a combination of a Fe $d_{x2\text{-}y2}$ orbital and O and N p-orbitals giving an Fe—O and Fe—N σ* HOMO. In contrast, the LS HOMO exhibits Fe-O π* character. This change is entirely consistent with spin crossover and electrons moving from the e_g set (Fe-ligand σ-orbitals) to the t_{2g} set (Fe-ligand π-orbitals). As expected the LUMOs of all the compounds are principally ligand based with significant electron density on the quinolyl fragment. Unlike the HOMOs the change in spin state has a relatively minor effect on the LUMOs, although there is slightly more metal participation in the LS LUMOs. Overall, the different substituent group have a relatively minor effect on the frontier orbitals consistent with the observation that all these systems undergo spin crossover.

3.3 | Spin state splitting in $[Fe(qsal\text{-}X)_2]^+$

The energy difference between the HS and LS state, Δ*E*(HS-LS) for the complexes calculated using B3LYP, B3LYP-D3, B3LYP*, BHandHLYP, BP86, OLYP, OPBE, M06L, and TPSSh, with four different basis sets each: 6-31G**, cc-pVDZ, cc-pVTZ, and Def2TZVP are presented in Table 3. These values are averages across all the complexes as the results indicate the splitting energies are relatively insensitive to the substituent group (see Supporting Information Table S2). The smaller basis sets 3-21G* and dgdzvp exhibit large standard deviations and are thus presented in Supporting Information Table S3. For all tested functionals and basis sets here, very similar Δ*E*(HS-LS) were obtained from the four different starting structures of $[Fe(qsal\text{-}OMe)_2]^+$. Figure S3 Supporting Information illustrates the comparison of Δ*E*(HS-LS) for $[Fe(qsal\text{-}OMe)_2]^+$ calculated with eight DFT functionals with 6-31G** basis set using four starting structures optimized at the B3LYP/6-31G** level. The lack of any significant difference is to be expected as the starting structures contain the same cation.

A comparison of Δ*E*(HS-LS) for the nine complexes calculated from the methods considered here, reveal similar trends as can be seen in Figure 4 for $[Fe(qsal\text{-}OMe)_2]^+$ and $[Fe(qsal\text{-}I)_2]^+$ as representative examples. The Δ*E*(HS-LS) is clearly sensitive to the DFT functional and the basis set. As can be seen in Supporting Information Tables S2–S3, when a dgdzvp basis set is used with any functional tested here, there

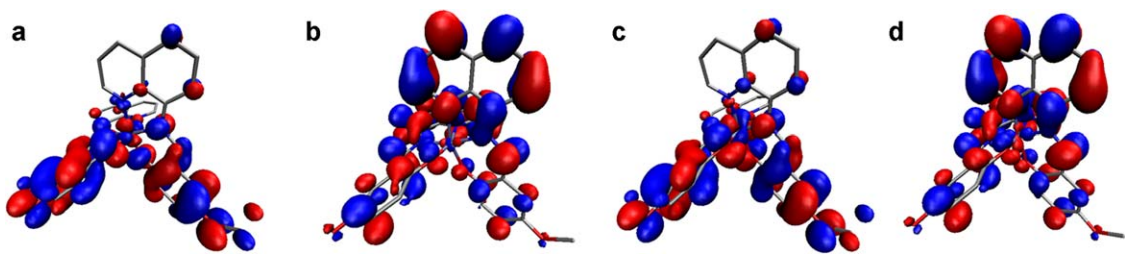

FIGURE 2 HOMO and LUMO of $[Fe(qsal\text{-}OMe)_2]^+$ in the high spin (HS) and low spin (LS) state where a = HOMO in HS, b = LUMO in HS, c = HOMO in LS, and d = LUMO in LS

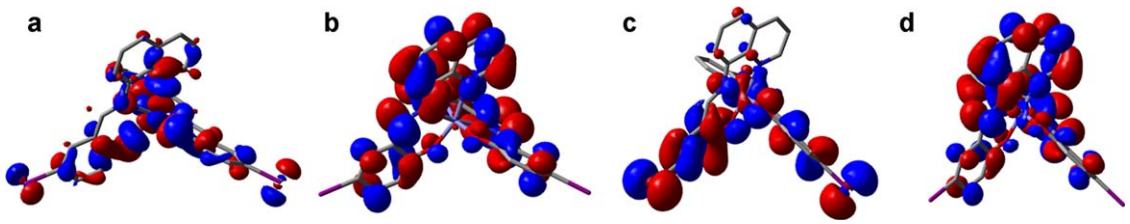

FIGURE 3 HOMO and LUMO of $[Fe(qsal\text{-}I)_2]^+$ in the high spin (HS) and low spin (LS) state where a = HOMO in HS, b = LUMO in HS, c = HOMO in LS, and d = LUMO in LS

is a large increase in ΔE(HS-LS) by 10–17 kcal/mol, compared to those of cc-pVTZ. In contrast, 3-21G* decreases ΔE(HS-LS) by 3–11 kcal/mol. This clearly shows that the dgdzvp and 3-21G* basis sets are too small for accurate calculations of the spin state energy in spin crossover systems, in line with previous reports by Swart et al.[19] The three basis sets 6-31G**, cc-pVTZ, and Def2TZVP give similar spin state splittings to each other, the difference being up to 2.5 kcal/mol but, on average, only 0.68 kcal/mol. We also note that cc-pVTZ and Def2TZVP are particularly close a trend also reported by Swart et al. in calculations on a series of $[M(Tp\text{-}R)_2]^{n+}$ (n = 0, 1, 2) compounds.[43] By comparison, cc-pVDZ yields values consistently lower than these basis sets by about 3 kcal/mol.

Looking at the effect of the functional on ΔE(HS-LS), we ignore the dgdzvp and 3-21G* basis sets due to their aforementioned failure for these spin crossover systems. As illustrated in Supporting Information Tables S2, S4, and Table 3, BH&HLYP and M06L predict negative values of ΔE(HS-LS). It follows that these two functionals favour the HS state too much, resulting in an underestimation of ΔE(HS-LS) by up to 25.2 and 7.6 kcal/mol, respectively. Jensen and Cirera report a similar favouring of the HS state by M06L in $[Fe(acac_2\text{-trien})]^+$ ($acac_2$-trien- = 4-[2-(2-{2-[3-Hydroxy-1-methyl-2-butenylideneamino]ethylamino}ethylamino)ethylimino]-2-penten-2-ol).[40] In contrast, BP86 and TPSSh favour the LS state resulting in a large positive value of HS-LS gap of 21 to 25 kcal/mol and 11 to 14 kcal/mol. The poor performance of TPSSh is puzzling given it's widespread use in iron(II) and cobalt(II) SCO materials[40,44] and suggests that it may be unsuitable for iron(III) spin crossover systems. Indeed, TPSSh has been shown to yield an enthalpy for spin crossover of 7.9 and 9.6 kcal/mol for $[Fe(acac_2\text{-trien}]^+$.[34,40] This is further supported by Bannwarth et al. who also found the LS state is favoured by TPSSh and BP86 in their iron(III) spin crossover compounds, $[Fe(salten)(n\text{-azpy})]BPh_4$ (n = 3, 4; salten = *o*-[(3-{3-[(*o*-Hydroxyphenyl)methylideneamino]propylamino}propylimino)methyl]phenol).[45] B3LYP* also seems to favour the LS state, however, using B3LYP* with cc-pVDZ gives an acceptable value of ΔE(HS-LS) (~5 kcal/mol) with the right sign, for the complexes considered here. Subtle changes in the spin state energy as a result of changes in the basis set has previously been observed by Swart et al.[19] Moreover, the general favouring of the LS state by B3LYP* is consistent with the results of with Friesner and Hughes who recommend against the use of B3LYP* in spin crossover complexes.[21] They argue that the reason B3LYP* is not suitable for all spin crossover complexes is that it was optimized using a narrow training set involving principally aromatic nitrogen donors. The system in this study involves phenoxide O donors to give an N_4O_2 donor set, compared to N_6 commonly found for Fe(II), and may explain why B3LYP* does not perform as well as expected.

As regards the remaining functionals reasonable values for the HS-LS gap (in the range of 1 to 5 kcal/mol) can be obtained from OPBE with any of these four basis sets. In addition, a HS-LS gap of 1.7 to 3.2 kcal/mol is predicted by B3LYP and OLYP with 6-31G**, cc-pVTZ, and Def2TZVP, while with cc-pVDZ these two functionals predict ΔE(HS-LS) to be −0.8 to −0.4 kcal/mol. Hence, among the functionals

TABLE 3 Average spin state splittings, ΔE(HS-LS) for the nine iron complexes, $[Fe(qsal\text{-}X)_2]^+$ calculated with nine functionals with the four largest basis sets (kcal/mol)

Functional	6-31G**	cc-pVDZ	cc-pVTZ	Def2TZVP	Mean	MAX	MIN
B3LYP	3.24	−0.74	2.01	1.67	1.54	3.24	−0.74
B3LYP-D3	3.19	0.12	2.01	1.66	1.75	3.19	0.12
B3LYP*	9.33	5.40	8.30	8.02	7.76	9.33	5.40
TPSSh	14.39	10.83	13.79	13.75	13.19	14.39	10.83
BP86	24.73	21.52	24.69	24.37	23.83	24.73	21.52
BHandHLYP	−21.08	−25.21	−22.97	−23.60	−23.60	−21.08	−25.21
OLYP	3.04	−0.39	3.00	3.10	2.18	3.10	−0.39
OPBE	3.93	1.14	4.79	5.09	3.74	5.09	1.14
M06L	−3.78	−7.57	−4.11	−3.94	−4.85	−7.57	−3.78

considered in this study, OPBE, OLYP, and B3LYP (with or without dispersion) are good choices for computing the ΔE(HS-LS) gap. The results mirror those of Swart who routinely recommends OPBE with a suitably large basis set.[46]

Comparing B3LYP and B3LYP-D3, we find that on average the difference is only 0.20 kcal/mol with a maximum deviation of 0.86 kcal/mol. While dispersion effects can be significant in spin crossover systems they are highly system dependent. In our case, it is possible that as the ligands are rigid and sterically small and there is a smaller structural difference between the two spin states for Fe(III), the dispersion effects are less significant.

3.4 | Experimental and computed enthalpies of spin crossover

For [Fe(qsal-I)$_2$]OTf·MeOH, thermochemical analysis was carried out within the harmonic approximation to estimate the enthalpy associated with the conversion between the HS and LS spin states, to compare

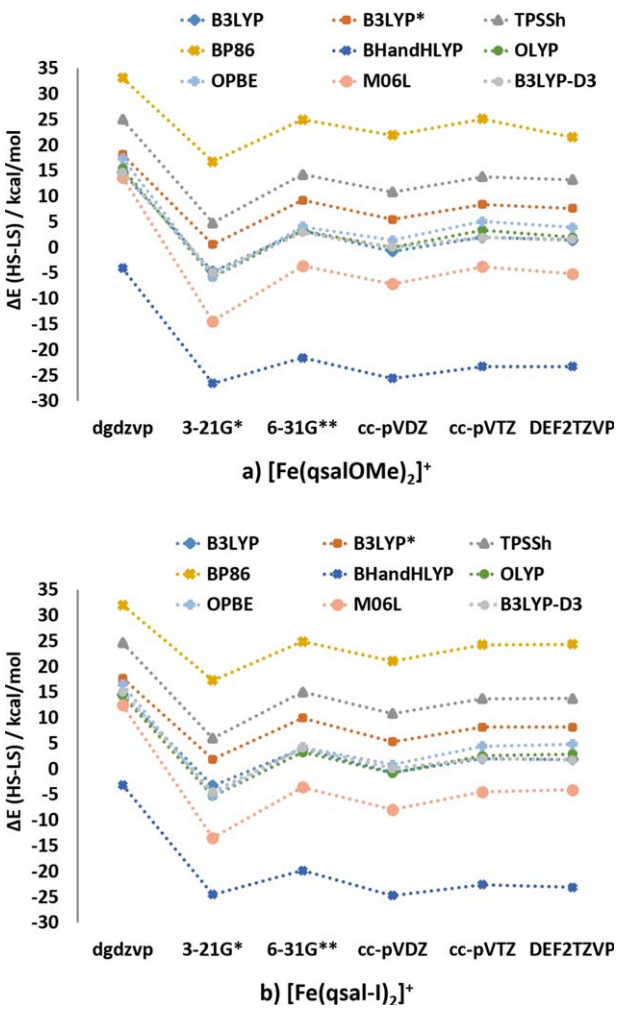

FIGURE 4 Comparison of ΔE(HS-LS) calculated with nine DFT functionals and six basis sets for a) [Fe(qsal-OMe)$_2$]$^+$ and b) [Fe(qsal-I)$_2$]$^+$ using the structures of **1** and **8** optimized at the B3LYP/6-31G** level, respectively

TABLE 4 Experimental and computed enthalpies associated with the conversion between the HS and LS spin states of [Fe(qsal-I)$_2$]$^+$ (kcal/mol)

Method		ΔH(HS-LS) Electronic energy	ΔH(HS-LS) Thermal correction to enthalpy	ΔH(HS-LS)-total
B3LYP	6-31G**	3.94	−1.82	2.12
B3LYP	cc-pVDZ	−0.68	−2.45	−3.14
B3LYP	cc-pVTZ	2.03	−1.30	0.73
B3LYP-D3	6-31G**	4.13	−1.21	2.92
B3LYP-D3	cc-pVDZ	0.10	−3.62	−3.52
B3LYP-D3	cc-pVTZ	2.07	−1.30	0.77
B3LYP*	6-31G**	9.94	−1.83	8.11
B3LYP*	cc-pVDZ	5.31	−2.49	2.82
B3LYP*	cc-pVTZ	8.19	−1.33	6.85
OLYP	6-31G**	3.25	−1.58	1.68
OLYP	cc-pVDZ	−5.29	−1.65	−6.94
OLYP	cc-pVTZ	2.57	−1.09	1.48
OPBE	6-31G**	4.27	−2.68	1.58
OPBE	cc-pVDZ	0.81	−1.57	−0.76
OPBE	cc-pVTZ	4.47	−1.62	2.85
Exp[a]				1.34

[a]Taken from Ref. 27.

with the experimental data. Five functionals: B3LYP, B3LYP-D3, B3LYP*, OLYP, and OPBE along with three basis sets: 6-31G**, cc-pVDZ, and cc-pVTZ were tested. Def2TZVP is not included as the results above shows it produces very similar spin gaps to cc-pVTZ. As shown in Table 4, the thermal corrections for enthalpies calculated from various methods are similar at −1.09 to −3.62 kcal/mol. This closely matches the value reported by Kepp in 30 spin crossover complexes of 2.15 kcal/mol.[34] The electronic energy contribution is strongly dependent on the basis set and as above it is clear that a large basis set is required to accurately model this in spin crossover systems.

The enthalpy calculated with the OLYP functional and cc-pVTZ basis set (1.48 kcal/mol) is the most similar to the experimental data (1.34 kcal/mol), followed by that of OPBE with 6-31G** (1.58 kcal/mol) and B3LYP-D3 with cc-pVTZ (0.77 kcal/mol). By comparison, B3LYP* yields a value of 5.92 kcal/mol which is a little high for Fe(III) spin crossover compounds.[23] While care is needed not to over interpret this result as it based on a single data set, an analysis of the enthalpies of six iron(III) spin crossover compounds in a recent study by Kepp revealed that the enthalpies where on average 7.64 and −0.97 kcal/mol for B3LYP* and B3LYP, respectively (see Supporting Information Table S5).[34] As Kepp's study included zero-point energies, solvation, dispersion, and relativistic effects the close agreement with the current work suggests that our conclusions are justified.

4 | CONCLUSIONS

Using the cations obtained from nine X-ray crystal structures of $[Fe(qsal\text{-}X)_2]^+$ (X = OMe, F, Cl, Br, I, H) the accuracy of different quantum mechanical methods for energetic calculations and the structure optimization of iron(III) spin crossover complexes were investigated. Reasonable results of the spin state splittings, ΔE(HS-LS) can be obtained using B3LYP (with or without dispersion), OLYP, and OPBE functionals with a 6-31G**, cc-pVDZ, cc-pVTZ, and Def2TZVP basis set. Thermodynamic parameters are also correctly predicted with the OLYP functional using a cc-pVTZ basis set (1.48 kcal/mol) giving the most similar enthalpy compared with the experimental data for $[Fe(qsal\text{-}I)_2]^+$ (1.34 kcal/mol). The over favouring of the low spin state by B3LYP* seems to suggest it may not be suitable for use with these iron(III) spin crossover systems, although further work on a broader set of compounds will be needed to confirm this. Hence, these methods are an effective tool for the prediction of spin crossover in iron(III) compounds and will be useful for other researchers seeking to explore more complex theoretical problems in iron(III) spin crossover materials.

ACKNOWLEDGMENTS

We thank Walailak University for a Postdoctoral Fellowship to JS, the Thailand Research Fund (RSA5580028 and RSA5880048) and the National Science and Technology Development Agency (grant no.: P-10-11181) for funding this research.

REFERENCES

[1] M. A. Halcrow, Ed., *Spin-Crossover Materials: Properties and Applications*, Wiley, Chichester **2013**.

[2] P. Gütlich, A. B. Gaspar, Y. Garcia, *Beilstein J. Org. Chem.* **2013**, *9*, 342.

[3] P. Gütlich, H. A. Goodwin, *Top. Curr. Chem.* **2004**, *233*, 1–47.

[4] A. Bousseksou, G. Molnár, L. Salmon, W. Nicolazzi, *Chem. Soc. Rev.* **2011**, *40*, 3313.

[5] V. Ksenofontov, A. B. Gaspar, P. GüTlich, *Top. Curr. Chem.* **2004**, *235*, 23.

[6] J. F. Létard, *J. Mater. Chem.* **2006**, *16*, 2550.

[7] J. F. Létard, G. Chastanet, P. Guionneau, C. Desplanches, in *Spin-Crossover Materials: Properties and Applications* (Ed: M. A. Halcrow), Wiley, Chichester **2013**, pp. 475–506.

[8] J. F. Létard, P. Guionneau, L. Goux-Capes, *Top. Curr. Chem.* **2004**, *235*, 221.

[9] P. Gamez, J. S. Costa, M. Quesada, G. Aromí, *Dalton Trans.* **2009**, 7845.

[10] A. Hauser, *Top. Curr. Chem.* **2004**, *233*, 49.

[11] R. J. Deeth, C. M. Handley, B. J. Houghton, in *Spin-Crossover Materials: Properties and Applications* (Ed: M. A. Halcrow), Wiley, Chichester **2013**, pp. 443–454.

[12] R. J. Deeth, in *Spin States in Biochemistry and Inorganic Chemistry: Influence on Structure and Reactivity* (Eds: M. Swart, M. Costas), Wiley, Oxford, UK **2016**, pp. 85–102.

[13] K. P. Kepp, *Coord. Chem. Rev.* **2013**, *257*, 196.

[14] K. Pierloot, S. Vancoillie, *J. Chem. Phys.* **2008**, *128*, 34104.

[15] L. Daku, F. Aquilante, T. W. Robinson, A. Hauser, *J Chem. Theory Comput.* **2012**, *6*, 4216.

[16] M. Kepenekian, V. Robert, B. Le Guennic, *J. Chem. Phys.* **2009**, *131*, 114702.

[17] M. Radoń, P. Rejmak, M. Fitta, M. Bałanda, J. Szklarzewicz, *Phys. Chem. Chem. Phys.* **2015**, *17*, 14890.

[18] M. Reiher, O. Salomon, B. Artur Hess, *Theor. Chem. Acc.* **2001**, *107*, 48.

[19] M. Güell, J. M. Luis, M. Solà, M. Swart, *J. Phys. Chem. A* **2008**, *112*, 6384.

[20] M. Reiher, *Inorg. Chem.* **2002**, *41*, 6928.

[21] T. F. Hughes, R. A. Friesner, *J. Chem. Theory Comput.* **2011**, *7*, 19.

[22] M. Nihei, T. Shiga, Y. Maeda, H. Oshio, *Coord. Chem. Rev.* **2007**, *251*, 2606.

[23] D. J. Harding, P. Harding, W. Phonsri, *Coord. Chem. Rev.* **2016**, *313*, 38.

[24] S. Hayami, Z. Gu, H. Yoshiki, A. Fujishima, O. Sato, *J. Am. Chem. Soc.* **2001**, *123*, 11644.

[25] S. Hayami, K. Hiki, T. Kawahara, Y. Maeda, D. Urakami, K. Inoue, M. Ohama, S. Kawata, O. Sato, *Chem. Eur. J.* **2009**, *15*, 3497.

[26] D. J. Harding, D. Sertphon, P. Harding, K. S. Murray, B. Moubaraki, J. D. Cashion, H. Adams, *Chem. Eur. J.* **2013**, *19*, 1082.

[27] D. J. Harding, W. Phonsri, P. Harding, I. A. Gass, K. S. Murray, B. Moubaraki, J. D. Cashion, L. Liu, S. G. Telfer, *Chem. Commun.* **2013**, *49*, 6340.

[28] W. Phonsri, D. J. Harding, P. Harding, K. S. Murray, B. Moubaraki, I. A. Gass, J. D. Cashion, G. N. L. Jameson, H. Adams, *Dalton Trans.* **2014**, *43*, 17509.

[29] D. J. Harding, W. Phonsri, P. Harding, K. S. Murray, B. Moubaraki, G. N. L. Jameson, *Dalton Trans.* **2015**, *44*, 15079.

[30] A. I. S. Neves, J. C. Dias, B. J. C. Vieira, I. S. Santos, M. B. Castelo Branco, L. C. J. Pereira, J. C. Waerenborgh, M. Almeida, D. Belo, V. Da Gama, *CrystEngComm* **2009**, *11*, 2160.

[31] M. J. Frisch, G. W. Trucks, H. B. Schlegel, G. E. Scuseria, M. A. Robb, J. R. Cheeseman, G. Scalmani, V. Barone, G. A. Petersson, H. Nakatsuji, X. Li, M. Caricato, A. Marenich, J. Bloino, B. G. Janesko, R. Gomperts, B. Mennucci, H. P. Hratchian, J. V. Ortiz, A. F. Izmaylov, J. L. Sonnenberg, D. Williams-Young, F. Ding, F. Lipparini, F. Egidi, J. Goings, B. Peng, A. Petrone, T. Henderson, D. Ranasinghe, V. G. Zakrzewski, J. Gao, N. Rega, G. Zheng, W. Liang, M. Hada, M. Ehara, K. Toyota, R. Fukuda, J. Hasegawa, M. Ishida, T. Nakajima, Y. Honda, O. Kitao, H. Nakai, T. Vreven, K. Throssell, J. A. Montgomery, Jr., J. E. Peralta, F. Ogliaro, M. Bearpark, J. J. Heyd, E. Brothers, K. N. Kudin, V. N. Staroverov, T. Keith, R. Kobayashi, J. Normand, K. Raghavachari, A. Rendell, J. C. Burant, S. S. Iyengar, J. Tomasi, M. Cossi, J. M. Millam, M. Klene, C. Adamo, R. Cammi, J. W. Ochterski, R. L. Martin, K. Morokuma, O. Farkas, J. B. Foresman, and D. J. Fox, *Gaussian 09 (Revision E.01)*, Gaussian, Inc., Wallingford CT, **2009**.

[32] D. Sertphon, D. J. Harding, P. Harding, K. S. Murray, B. Moubaraki, J. D. Cashion, H. Adams, *Eur. J. Inorg. Chem.* **2013**, 788.

[33] S. Grimme, J. Antony, S. Ehrlich, H. Krieg, *J. Chem. Phys.* **2010**, *132*, 154104.

[34] K. P. Kepp, *Inorg. Chem.* **2016**, *55*, 2717.

[35] K. P. Jensen, B. O. Roos, U. Ryde, *J. Chem. Phys.* **2007**, *126*, 14103.

[36] M. P. Waller, H. Braun, N. Hojdis, M. Bühl, *J. Chem. Theory Comput.* **2007**, *3*, 2234.

[37] M. Swart, R. Groenhof, A. W. Ehlers, K. Lammertsma, *J. Phys. Chem. A* **2004**, *108*, 5479.

[38] J. K. McCusker, A. L. Rheingold, D. N. Hendrickson, *Inorg. Chem.* **1996**, *35*, 2100.

[39] M. Marchivie, P. Guionneau, J. F. Létard, D. Chasseau, *Acta Crystallogr. Sect. B Struct. Sci.* **2005**, *61*, 25.

[40] K. P. Jensen, J. Cirera, *J. Phys. Chem. A* **2009**, *113*, 10033.

[41] T. Bučko, J. Hafner, S. Lebègue, J. G. Ángyán, *Phys. Chem. Chem. Phys.* **2012**, *14*, 5389.

[42] S. Alvarez, *Chem. Rev.* **2015**, *115*, 13447.

[43] M. Gruden-Pavlović, S. Stepanović, M. Perić, M. Güell, M. Swart, *Phys. Chem. Chem. Phys.* **2014**, *16*, 14514.

[44] J. Cirera, F. Paesani, *Inorg. Chem.* **2012**, *51*, 8194.

[45] A. Bannwarth, S. O. Schmidt, G. Peters, F. D. Sönnichsen, W. Thimm, R. Herges, F. Tuczek, *Eur. J. Inorg. Chem.* **2012**, 2776.

[46] M. Swart, *J. Chem. Theory Comput.* **2008**, *4*, 2057.

SUPPORTING INFORMATION

Additional Supporting Information may be found in the online version of this article.

How to cite this article: Sirirak J, Sertphon D, Phonsri W, Harding P, Harding DJ. Comparison of density functionals for the study of the high spin low spin gap in Fe(III) spin crossover complexes. *Int J Quantum Chem.* 2017;117:e25362. https://doi.org/10.1002/qua.25362

Coordination Chemistry Reviews 313 (2016) 38–61

Contents lists available at ScienceDirect

Coordination Chemistry Reviews

journal homepage: www.elsevier.com/locate/ccr

Review

Spin crossover in iron(III) complexes

David J. Harding[a,*], Phimphaka Harding[a], Wasinee Phonsri[b]

[a] Molecular Technology Research Unit, School of Science, Walailak University, Thasala, Nakhon Si Thammarat 80161, Thailand
[b] School of Chemistry, Monash University, Clayton, Victoria 3800, Australia

Contents

1. Introduction 39
2. Monomeric iron(III) SCO systems 39
   2.1. Bidentate ligands 39
      2.1.1. Catecholate systems 39
   2.2. Tridentate ligands 40
      2.2.1. Quinolylsalicylaldimine complexes 40
      2.2.2. Sal-R-en complexes 42
      2.2.3. Thiosemicarbazone complexes 44
      2.2.4. Other complexes 45
   2.3. Tetradentate ligands 46
      2.3.1. Salen ligands 46
      2.3.2. Hapen ligands 47
      2.3.3. Acen ligands 47
   2.4. Pentadentate ligands 47
   2.5. Hexadentate ligands 49
3. Dimeric systems 50
4. Multinuclear systems 50
5. Multifunctional systems 51
   5.1. [Fe(5-X-sal$_2$trien)][Mn{Cr(ox)$_3$}] systems 51
   5.2. [M^{III}(dithiolene)$_2$]$^-$ systems 51
   5.3. Mixed-valence [M^{III}(dithiolene)$_2$]$^-$ systems 52
6. SCO nanomaterials 53
7. Physical characteristics of selected iron(III) SCO systems 54
   7.1. Structural characteristics of SCO 54
      7.1.1. Bond length changes and octahedral distortion 54
      7.1.2. Solvent effects 54
      7.1.3. Anion effects 54
      7.1.4. Supramolecular cooperativity in iron(III) 54
   7.2. Light activation in iron(III) 56
   7.3. Mössbauer spectroscopic studies 57
   7.4. Other techniques 58
8. Conclusions 58
   Acknowledgements 59
   References 59

ARTICLE INFO

Article history:
Received 14 September 2015
Accepted 12 January 2016
Available online 29 January 2016

ABSTRACT

Spin crossover compounds are a diverse class of switchable materials with applications ranging from data storage devices to sensors. Iron(III) spin crossover complexes have received renewed attention over the last 10 years with an increasing number of abrupt and hysteretic spin crossover systems discovered. This review provides a detailed overview of this exciting and increasingly interdisciplinary area of

* Corresponding author. Tel.: +66 75672094.

http://dx.doi.org/10.1016/j.ccr.2016.01.006
0010-8545/© 2016 Elsevier B.V. All rights reserved.

Keywords:
Spin crossover (SCO)
Iron(III) complexes
Magnetic behaviour
Crystal structure
Structure-function relationships

research with a particular focus on the structures of these materials and how this impacts their magnetic performance.

© 2016 Elsevier B.V. All rights reserved.

1. Introduction

Spin crossover (SCO) can occur in transition metal complexes with a d^4–d^7 electron configuration provided that a suitable ligand field is present [1–4]. It involves switching between a high spin (HS) and a low spin (LS) state and may be achieved by changes in temperature and pressure or more rarely light irradiation, termed the LIESST effect [1,4–7]. In the case of iron(III), which has a d^5 electron configuration, the transition occurs from a high spin state ($^6A_1$, $S = 5/2$) to a low spin state ($^2T_2$, $S = 1/2$) [8,9]. This change in magnetic moment and the fact that the switching may occur at or close to room temperature make spin crossover materials ideal candidates for molecular magnetic devices, sensors and as components in multifunctional materials [10,11].

Iron(III) compounds, compared to the more common iron(II) systems [12–16] have the advantage of generally being air stable and thus would be expected to be more amenable to processing in any future devices. Another requirement for workable devices is that the spin crossover is abrupt and occurs with hysteresis ideally greater than 40 K [17,18]. Hysteresis in SCO complexes is the result of strong connectivity between the SCO centres such that the SCO propagates rapidly through the material and is achieved either through coordination bonds or more commonly supramolecular interactions [19]. It follows that successful design of SCO materials requires effective application of crystal engineering principles [20,21].

Spin crossover in iron(III) compounds results in significant shortening of the metal–ligand bonds and averages 0.10–0.13 Å, although this is often distributed unevenly across the coordination sphere [8,9]. Compared with iron(II) complexes where the difference is typically 0.20 Å [1,2] it was long believed that iron(III) compounds could not undergo LIESST as the smaller structural change leads to rapid relaxation of the metastable HS state. However, in 2000 Sato and co-workers reported $[Fe(pap)_2]ClO_4 \cdot H_2O$ which exhibits 80% LIESST due to a combination of π–π interactions and significant distortion at the Fe(III) centre in the HS state [22,23]. This was followed by the discovery in 2001 of $[Fe(qsal)_2]NCSe$ which exhibits abrupt SCO and a hysteresis of 76 K [24,25]. The hysteresis in this case is the result of extensive π–π interactions and following these discoveries research into iron(III) SCO materials has increased dramatically.

Despite the obvious interest in iron(III) spin crossover compounds, surprisingly there has not been a review of iron(III) spin crossover chemistry since 2007 [9] and in that time there have been some significant advances in the field with many more structural studies of compounds in the HS and LS state, the discovery of a substantial number of abrupt and even symmetry breaking SCO systems and the appearance of iron(III) SCO nanomaterials. Consequently, this review will focus on papers from 2007 referring to earlier work only when it is needed to understand more recent developments. We will also exclude iron(III) porphyrin systems from the review as these have been reviewed elsewhere and typically involve a transition from a $S = 3/2$ to $S = 5/2$ spin state [26]. Readers wishing to gain an insight into these earlier reports of iron(III) SCO chemistry are referred to the excellent reviews in 2004 and 2007 by van Koningsbruggen [8] and Oshio [9], respectively. While we have tried to include as many papers as possible published over the last 8 years we are particularly interested in structure–functional relationships in SCO systems and thus there is a focus on papers where structural studies have been performed; we apologise to any authors whose work is not included as a result.

The review is organized according to ligand denticity and then subdivided into ligand type to make it easier for the reader to follow and find information of particular relevance to them. This is followed by an overview of the physical characteristics of iron(III) spin crossover compounds with an emphasis on the insights the most recent findings provide. In this way we hope that this review will serve as an invaluable reference for all those interested in iron(III) SCO chemistry.

2. Monomeric iron(III) SCO systems

2.1. Bidentate ligands

Dithiocarbamate ligands with Fe(III) were the first systems to undergo spin crossover [27,28] and while their SCO behaviour is generally very gradual [8] they continue to be studied. In 2011 Ovchinnikov and co-workers studied a range of $[Fe(S_2CNR_2)_3]$ (R = Me, Et, morpholine) complexes by EPR spectroscopy and concluded that small quantities (0.5–2%) of the solvated $[Fe(S_2CNR_2)_3]$ complex trapped inside a matrix of the non-solvated $[Fe(S_2CNR_2)_3]$ complex showed subtle changes in the EPR spectra indicative of spin crossover [29]. In line with previous reports thoroughly desolvated samples or single crystals are EPR silent between 5 and 300 K. Moreover, Garg et al. demonstrated in a Mössbauer spectroscopic study that the spectra can be resolved into HS and LS doublets [30]. As expected the isomer shift of the LS state is a little lower than the HS state consistent with the more covalent bond in the former. Interestingly, in the case of the alkyl complexes there is a clear increase in the quadrupolar splitting as the molecular weight increases. The same group has also reported the mixed ligand complexes $[Fe(S_2CNEt_2)_2(phen)]NO_3$ and $[Fe(S_2CNEt_2)(phen)_2][NO_3]_2$ in which SCO is gradual according to magnetic and Mössbauer spectroscopic studies [31]. Unfortunately, no structural data has been reported on either of these compounds.

SCO has also been reported in $Na_2(NH_4)[Fe(Hbta)_3] \cdot 3DMF \cdot 2H_2O$ where unusually for Fe(III) there is an N_6 donor set [32]. The SCO is gradual and incomplete even at 400 K and due to decomposition of the complex above this temperature does not reach the full HS state. The structure reveals weak cooperativity between the Fe(III) units as they are separated by the cations and is consistent with the gradual SCO in this system.

2.1.1. Catecholate systems

SCO complexes of Fe(III) frequently possess an N_4O_2 donor set, exemplified by $[(TPA)Fe(Cat\text{-}R)]^+$ (TPA = tris(2-pyridylmethyl) amine) where unusually the oxygen donors come from a (nominally) dianionic catecholate ligand rather than the more common phenoxide. All of the systems show gradual SCO with the transition temperature dependent on the type of catecholate and the anion used (Table 1). Interestingly, both $[(TPA)Fe(cat\text{-}Cl_4)]Y$ ($Y = PF_6$, SbF_6) may be isolated as monoclinic or orthorhombic

polymorphs [33,34]. Surprisingly, despite this the two polymorphs have similar transition temperatures at *ca.* 210 K and 250 K for the PF_6 and SbF_6 polymorphs, respectively. The two polymorphs are different in shape and colour with the orthorhombic platelets deep purple and the monoclinic needles orange. The structures of both polymorphs of [(TPA)Fe(cat-Cl_4)]PF_6 reveal that the changes in the Fe—N/O bond lengths of the orthorhombic polymorph upon SCO are slightly larger than those of the monoclinic one albeit by only 0.01 Å [33]. However, the packing is remarkably similar in both polymorphs with weak interactions between the cations forming layers with the counteranions in between these layers. The weak cooperativity and similarity of the packing are thought to be responsible for the small shift in the transition temperature. These systems have also been investigated using femtosecond optical pump-probe spectroscopy and picosecond X-ray diffraction techniques [35]. In both cases SCO occurs in three steps firstly by excitation into an excited LMCT state followed by relaxation into a metastable HS state within 300 fs. This is followed by molecular swelling resulting in a shock-wave through the crystal leading to crystal expansion within 10 ns–10 μs. Finally, the optical energy is redistributed as heat resulting in further conversion to the HS state which is complete after *ca.* 50 μs. Pressure-induced SCO occurs in [(TPA)Fe(cat-Cl_4)]SbF_6 at 294 K almost 50 K higher than that observed at ambient pressure and is consistent with higher pressure favouring the LS state [36]. The comparative similarity of the thermal and pressure-induced SCO are thought to be due to the weak cooperativity that exists in these complexes.

An ESR spectroscopic study of the related compounds $[(TPA)Fe(Cat\text{-}R)]^+$ in the LS state reveals increasing anisotropy as the substituents on the catecholate ligand become more electron withdrawing [37]. This is due to increasing Fe(II)-semiquinonate character in the Fe(III)-catecholate electronic structure.

Schultz, Popescu and co-workers have recently reported [(TPA)Fe(Cat-NN)]BPh_4 where a nitronylnitroxide radical is attached to the catecholate ligand [38]. The compound undergoes very gradual and incomplete SCO that is virtually identical to the non-radical analogue [(TPA)Fe(Cat-3,5-tBu_2)]BPh_4 suggesting that there is little magnetic exchange between the radical and the Fe d-electrons. X-ray crystallography confirms this with the Fe(III) cations essentially isolated from each other.

Very recently, the TPA ligand has been replaced with bis[(2-pyridyl)methyl]-2-(2-pyridyl)-ethylamine (pmea) to give [(pmea)Fe(Cat)]BPh_4 [39]. The compound undergoes SCO to a 50% HS state compared with [(TPA)Fe(Cat)]BPh_4 where the SCO is complete but in 2 steps. The structure of [(pmea)Fe(Cat)]BPh_4 at high and low temperature is consistent with 50% HS and again shows limited cooperativity which is clearly a feature of $[(TPA)Fe(Cat\text{-}R)]^+$ complexes.

2.2. Tridentate ligands

Tridentate ligands are particularly common in Fe(III) SCO chemistry and are often derived from salicylaldehyde and amines (Fig. 1). This gives a monoanionic N_2O ligand and, with two ligands attached to the Fe centre, results in the N_4O_2 donor set that is such a feature of Fe(III) SCO chemistry (Table 1) [8].

2.2.1. Quinolylsalicylaldimine complexes

As mentioned in the introduction $[Fe(qsal)_2]NCSe$ has one of the widest hysteresis reported for any SCO compound [24,25]. In 2009 Hayami, Sato and co-workers finally succeeded in obtaining the structure of the non-solvated compounds, $[Fe(qsal)_2]NCX$ (X = S, Se) in the HS state [23]. This allowed a direct comparison of the changes at the Fe centre which proved to be on average 0.13 Å and in line with other Fe(III) systems. The presence of solvent in the LS structure sadly prevented a direct comparison of the packing. LIESST studies on $[Fe(qsal)_2]NCX$ revealed only very weak LIESST effects despite the strong π–π interactions.

Subsequent studies on $[Fe(qsal)_2]^+$ complexes have focused, until recently, on varying the anion (anion = I^- [40], N_3^- [41], I_3^- [42,43], $[Fe(qsal)Cl_3]^-$ [40]; see also Section 5.2). A feature of many of these complexes is the presence of 1D chains formed by π–π interactions between neighbouring qsal ligands (Fig. 2). Although not a guarantee of SCO, in systems where SCO does occur it is more likely to be abrupt if these are present. The iodide and $[Fe(qsal)Cl_3]^-$ complexes are trapped in the LS and HS states respectively, based on structural and magnetic susceptibility studies [40]. However, the Mössbauer spectra of $[Fe(qsal)_2]I{\cdot}H_2O$ reveal a change from 77% LS at room temperature to 44% LS at 5.6 K; the origin of this unusual behaviour is currently unclear.

The structure of the azide complex has also been reported at 200 K showing a LS Fe centre but its SCO behaviour is currently unknown [41]. Intriguingly, the triiodide forms two polymorphs α and β [42,43]. The structure of the α-polymorph has been determined in the HS and LS state and shows a slightly smaller change of ΔFe-L = 0.11 Å compared with $[Fe(qsal)_2]NCX$ [23]. The SCO is gradual and incomplete at both ends and this is probably the reason for the smaller change in the Fe–N/O bond lengths. The effect of pressure on both α-$[Fe(qsal)_2]I_3$ and $[Fe(qsal)_2]NCS$ reveals a shift in $T_{1/2}$ to higher temperatures as the pressure is increased consistent with the greater stabilization of the LS state at elevated pressures [42]. Interestingly, in $[Fe(qsal)_2]NCS$ the increase in pressure also results in less complete SCO. The β-polymorph is obtained by precipitation of the product after a few hours, compared with several days via slow diffusion for the α-polymorph. The SCO is now complete, abrupt and with $T_{1/2}\uparrow = 117$ K and $T_{1/2}\downarrow = 92$ K exhibits a hysteresis of 25 K [43]. The structure of the β-polymorph has not yet been reported but emphasizes the importance of polymorphism in SCO chemistry [21].

In 2013, Faulmann and co-workers reported a pair of $[Fe(qsal)_2]^+$ complexes where the anion was $[Fe(CN)_5(NO)]^{2-}$ or $[RuCl_5(NO)]^{2-}$ with the aim of preparing photochromic spin crossover materials [44]. In the case of $[Fe(CN)_5(NO)]^{2-}$ the authors were able to isolate two solvates $[Fe(qsal)_2]_2[Fe(CN)_5(NO)]{\cdot}sol$ (sol = MeOH, 2MeCN) with the MeOH solvate showing gradual 50% SCO while the MeCN solvate exhibits only a minor change in $\chi_M T$ from 2.8 to 2.58 $cm^3\ mol^{-1}$ K. X-ray crystallographic analysis of $[Fe(qsal)_2]_2[Fe(CN)_5(NO)]{\cdot}MeOH$ by Hayami et al. at around the same time reveals that only one of the Fe(III) sites (Fe1) is capable of undergoing SCO [45]. Unusually $[Fe(qsal)_2]_2[Fe(CN)_5(NO)]{\cdot}MeOH$ also exhibits the LIESST effect (Fig. 3). The related complex with the Ru anion undergoes almost complete SCO with a slight hysteresis of 7 K as evidenced by magnetic and Mössbauer spectroscopic studies [44].

The first complexes of a substituted qsal ligand were reported by da Gama et al. in 2009. The complexes, $[Fe(qsal\text{-}3\text{-}OMe)_2]PF_6{\cdot}sol$ (sol = none, $2H_2O$) were trapped either in the HS (H_2O) or LS state (non-solvated) [46]. The X-ray structure of $[Fe(qsal\text{-}3\text{-}OMe)_2]PF_6$ reveals a loss of the 1D π–π chains which are such a common feature of the $[Fe(qsal)_2]^+$ complexes. In contrast, almost all the related $[Fe(qsal\text{-}5\text{-}OMe)_2]Y{\cdot}sol$ (Y = Cl, NCS, BF_4, PF_6, BPh_4) complexes exhibit SCO [47,48]. The MeOH solvate, $[Fe(qsal\text{-}5\text{-}OMe)_2]Cl{\cdot}2MeOH{\cdot}0.5H_2O$, exhibits abrupt half SCO at *ca.* 140 K with a hysteresis of 10 K while the MeCN solvate, $[Fe(qsal\text{-}5\text{-}OMe)_2]Cl{\cdot}MeCN{\cdot}H_2O$ exhibits abrupt stepped SCO at 245 and 275 K with a hysteresis of 5 K in the 1st step via a 2/3 HS intermediate [47]. For the other anions, the SCO is almost complete in the case of NCS and PF_6 but is LS only for BF_4 while the large BPh_4 anion is HS only. X-ray crystallographic analysis of $[Fe(qsal\text{-}5\text{-}OMe)_2]Y$ (Y = Cl, NCS, BF_4) reveals a return of the 1D π–π chains found in many of the qsal systems above and also an additional interaction which links these chains, a parallel four-fold aryl embrace (P4AE, see Fig. 4) [48,49].

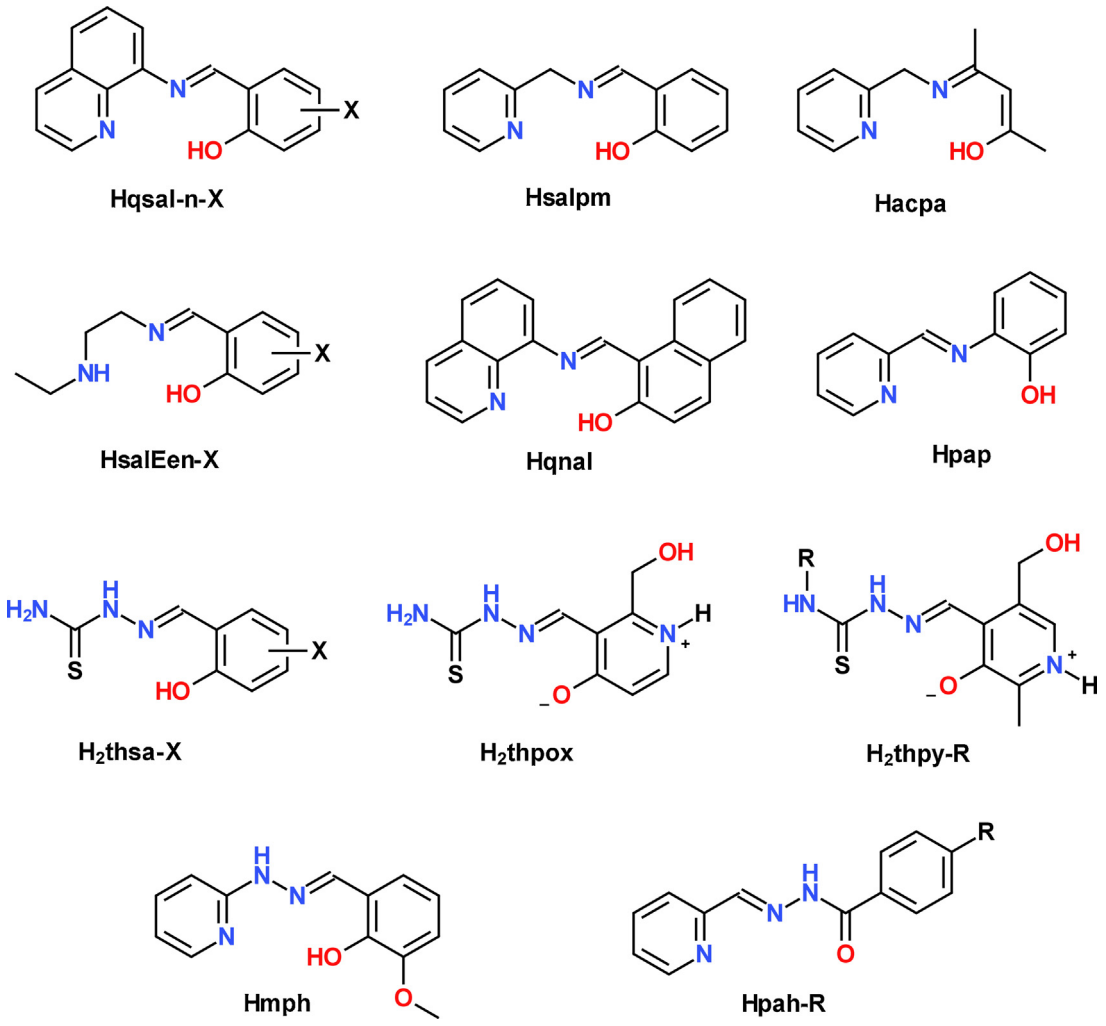

Fig. 1. Structures and abbreviations of the tridentate ligands used in iron(III) SCO systems.

While $[Fe(qsal\text{-}5\text{-}OMe)_2]PF_6{\cdot}CH_2Cl_2$ also contains 1D π–π chains the P4AE interactions are lost and the SCO is now gradual [50]. A remarkable feature of $[Fe(qsal\text{-}5\text{-}OMe)_2]Cl{\cdot}2MeOH{\cdot}0.5H_2O$ is the rare occurrence of a HS and LS Fe centre in the same asymmetric unit which is responsible for the 50% SCO. The substitutional isomers $[Fe(qsal\text{-}4\text{-}OMe)_2]Y$ (Y = ClO_4, NO_3, PF_6, OTf) are all HS except when the anion is OTf where very gradual 25% SCO occurs. The structures reveal strongly distorted qsal-4-OMe ligands, dislocated π–π chains and additional C—H···O interactions which are responsible for the loss of SCO [50].

Substituent effects are also evident in the series $[Fe(qsal\text{-}X)_2]NCS{\cdot}sol$ (X = F, Cl, Br, I) where the F and Cl compounds undergo

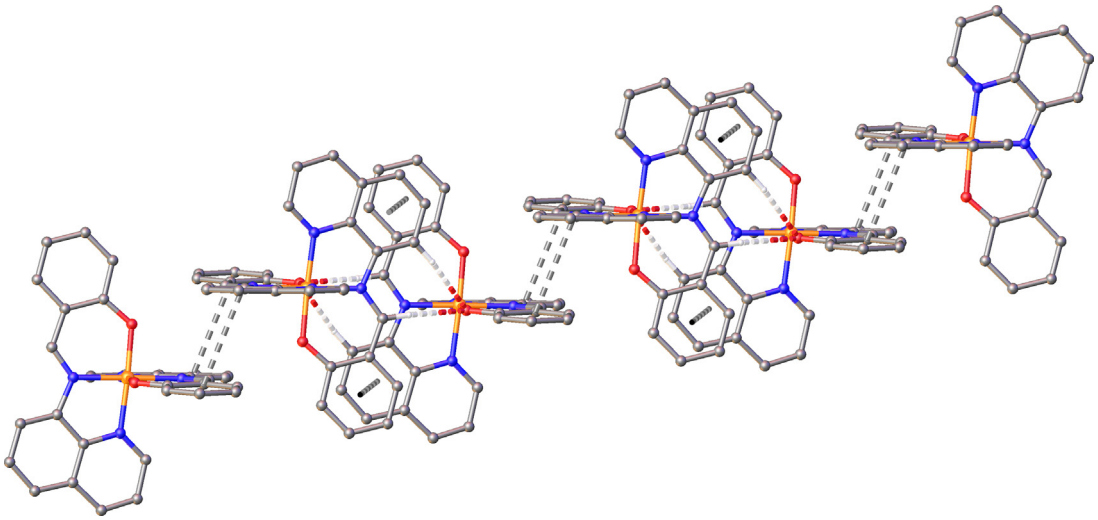

Fig. 2. View of the π–π interactions commonly observed in $[Fe(qsal)_2]^+$ complexes. Drawn from data in Ref. [24].

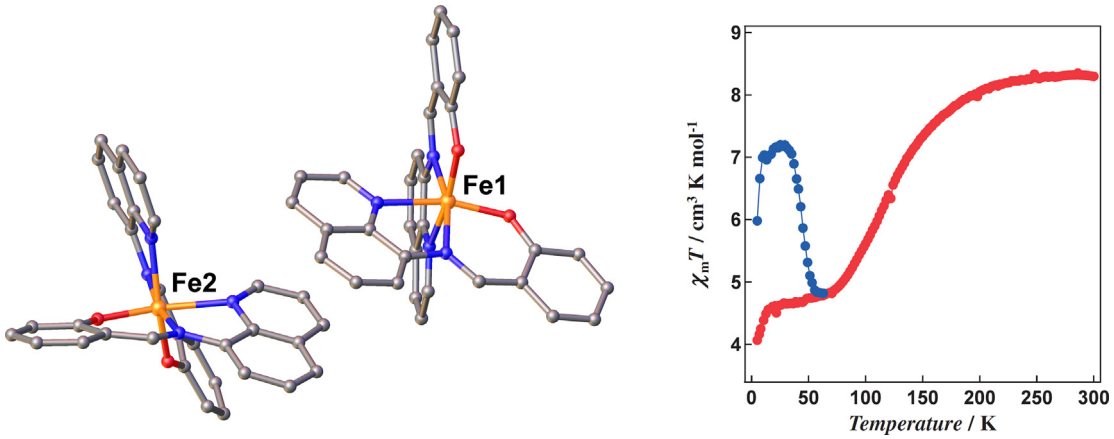

Fig. 3. (a) View of the two independent Fe(III) centres in $[Fe(qsal)_2]_2[Fe(CN)_5(NO)]\cdot MeOH$ (left) [45], (b) magnetic behaviour of $[Fe(qsal)_2]_2[Fe(CN)_5(NO)]\cdot MeOH$ (right, reproduced with permission from Ref. [45]. (Copyright The Chemical Society of Japan, 2013.)

abrupt stepped SCO through a 50% HS intermediate while the Br derivative undergoes a very gradual LS to 50% HS conversion and the iodo derivative is LS up to 300 K [52]. Structures of all the compounds reveal that the F, Br and I complexes contain two independent Fe(III) centres in the asymmetric unit of which both undergo SCO but at different temperatures for $[Fe(qsal\text{-}F)_2]NCS$ while for $[Fe(qsal\text{-}Br)_2]NCS\cdot MeOH$ only one of the Fe centres is SCO active. The stepped SCO in $[Fe(qsal\text{-}Cl)_2]NCS\cdot MeOH$ is harder to understand as there is only one Fe(III) centre in the crystal structure, although it is possible that symmetry breaking occurs in this system.

The importance of cooperativity in $[Fe(qsal\text{-}X)_2]^+$ is highlighted in $[Fe(qsal\text{-}I)_2]OTf\cdot MeOH$ and $[Fe(qsal\text{-}Br)_2]NO_3\cdot 2MeOH$ which exhibit very abrupt and abrupt symmetry breaking SCO, respectively [51,53]. Uniquely, in $[Fe(qsal\text{-}X)_2]^+$ chemistry, hysteresis is present in both steps of $[Fe(qsal\text{-}Br)_2]NO_3\cdot 2MeOH$ being 16 and 5 K in the 1st and 2nd steps, respectively with a 96 K [HS-LS] plateau (see Fig. 5) [51]. The structure of $[Fe(qsal\text{-}I)_2]OTf\cdot MeOH$ shows, to date, the smallest change in unit cell volume for any compound undergoing complete SCO of 20.6 Å^3 [53]. The structure very close to the spin transition temperature reveals subtle reorganization of the coordination and supramolecular sphere prior to actual SCO. This confirms a growing trend in SCO research that abrupt SCO does not require a crystallographic phase change or large changes in volume but rather needs extensive supramolecular interactions [17]. Moreover, it appears that symmetry breaking occurs in $[Fe(qsal\text{-}Br)_2]NO_3\cdot 2MeOH$ because these supramolecular contacts are very short which prevents SCO is a single step [54]. Indeed, loss of solvent yields $[Fe(qsal\text{-}Br)_2]NO_3$ which now undergoes a LS to 50% HS conversion but with an impressive hysteresis of 60 K [51].

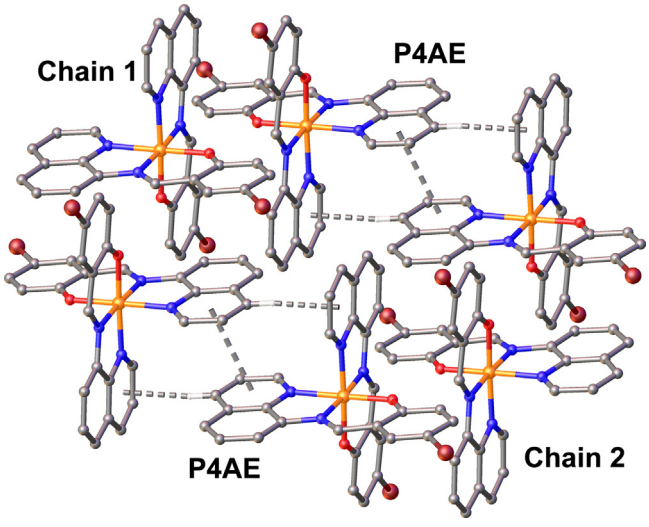

Fig. 4. View of the P4AE interactions that link the 1D π–π chains in $[Fe(qsal\text{-}X)_2]^+$ [51].

The most complex systems employing substituted qsal ligands have been developed by Lemaire et al. The two ligands devised by them were Hqsal-5-(-C≡C-3-th) (3-th = 3-thienyl) [55] and Hqsal-5-(-C≡C-3-terth) (3-terth = 3-terthienyl) [56]. The aim in both cases was to utilize the thienyl group to create polythiophene polymers with SCO groups off the polymer backbone. In the case of $[Fe\{qsal\text{-}5\text{-}(\text{-}C{\equiv}C\text{-}3\text{-}th)\}_2]Y$ (Y = PF_6, NCS, ClO_4) no electropolymerization of the thiophene was observed but SCO was present in all cases, albeit very gradual and incomplete. In the case of the NCS complex, Mössbauer spectroscopic data suggest an extremely rare $S = 5/2$ to $S = 3/2$ transition in a non-heme complex [55]. In contrast, $[Fe\{qsal\text{-}5\text{-}(\text{-}C{\equiv}C\text{-}3\text{-}terth)\}_2]PF_6$ does electropolymerize and the polymer formed undergoes a complete but extremely gradual SCO [56]. The polymer is conducting with the degree of conductivity dependent on temperature suggesting coupling between SCO and electrical conductivity.

More recently, the mixed ligand series [Fe(qsal)(thsa)]·sol (sol = 0.4 *n*-BuOH, 0.5 MeCN, 0.5 THF) has been reported where the BuOH and MeCN solvate undergo 50% SCO [57]. Structural studies of [Fe(qsal)(thsa)]·nMeCN reveal two independent Fe(III) centres with the SCO occurring between a [LS–HS] and [HS–HS] state. Remarkably, during SCO MeCN is lost in a single-crystal-to-single-crystal transformation to give [Fe(thsa)(qsal)]·0.1 MeCN which remains SCO active. Even complete solvent loss does not alter the magnetic behaviour and MeCN can be re-absorbed again without loss of crystallinity or SCO.

2.2.2. Sal-R-en complexes

The tridentate ligands, Hsal-R-en are prepared from N-alkylaminoethylamine and a salicyladehyde derivative. The presence of an NH group on the ligand helps in creating cooperativity through hydrogen bonding. Although a number of alkyl groups have previously been investigated all systems reported since 2007 utilize an ethyl group. $[Fe(salEen)_2]ClO_4$ and $[Fe(salEen)_2]ClO_4\cdot 0.5H_2O$ crystallize simultaneously from the reaction of the ligand and $Fe(ClO_4)_3$ in EtOH [58]. Both compounds undergo gradual SCO with $T_{1/2}$ higher and the SCO more abrupt for the non-solvated form. Crystal structures of both compounds unexpectedly reveal a slightly larger change in the Fe–N/O bond lengths in $[Fe(salEen)_2]ClO_4\cdot 0.5H_2O$ upon SCO. The packing in the

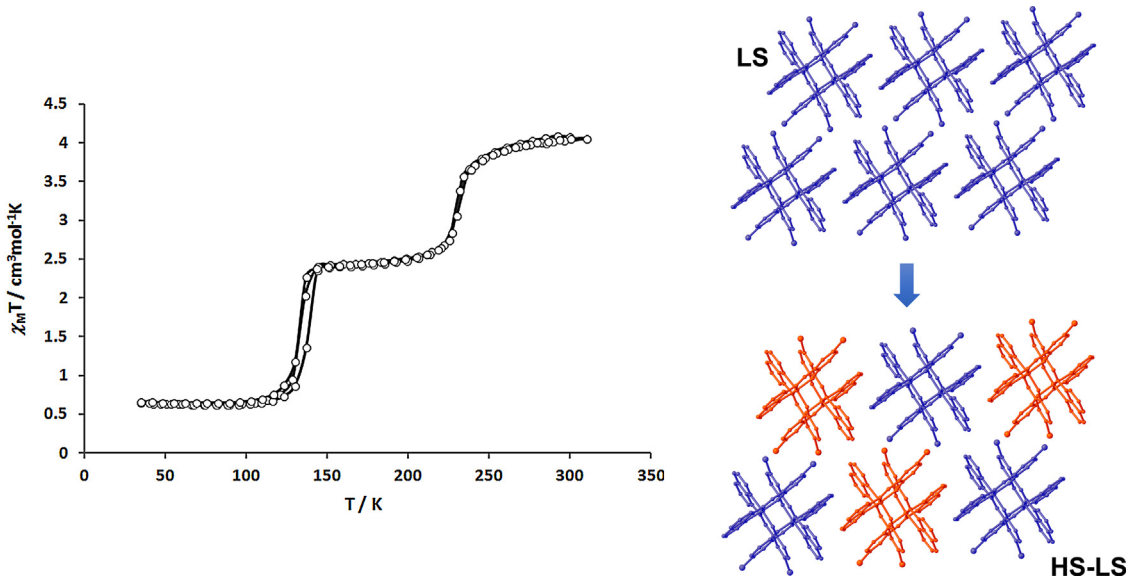

Fig. 5. View of the $\chi_M T$ vs. T plot for [Fe(qsal-Br)$_2$]NO$_3$·2MeOH (left, reproduced with permission from Ref. [51] (Copyright Royal Society of Chemistry, 2015) and the corresponding packing in the LS and [HS–LS] structures.

two structures is defined by strong N—H···anion interactions and is a feature of [Fe(salEen)$_2$]$^+$ complexes; the lack of further significant supramolecular contacts explains the very gradual nature of the SCO in both cases. Similarly, [Fe(salEen)$_2$]$_2$[Fe(CN)$_5$(NO)] undergoes very gradual SCO between 100 and 400 K [44]. Despite the different anions, the packing in the structure is little changed compared with [Fe(salEen)$_2$]ClO$_4$·sol and consequently, there is very weak connectivity between the cationic units but strong cation–anion interactions.

[Fe(3-OMe-salEen)$_2$]PF$_6$ was first prepared in 1981 [59] and undergoes very abrupt SCO at *ca.* 165 K with a hysteresis of 3 K but its structure was only recently published [60]. The structure determined at 300, 200 and 100 K shows a HS, HS and LS Fe(III) centre respectively. The Fe–N/O bond lengths change on average 0.13 Å and are a little larger than in other [Fe(salEen)$_2$]$^+$ complexes. As with [Fe(qsal-I)$_2$]OTf·MeOH, the structure close to $T_{1/2}$ shows a change in cooperativity that supports the abrupt SCO.

The closely related [Fe(4-OMe-salEen)$_2$]Y complexes (Y = NO$_3$, PF$_6$) also exhibit SCO, and when the anion is NO$_3$ this is abrupt with hysteresis (7.5 K) but centred at *ca.* 78 K [61]. The structures of both compounds have been determined in the HS and LS state revealing 2 independent Fe(III) centres for [Fe(4-OMe-salEen)$_2$]PF$_6$ and a single Fe(III) site for [Fe(4-OMe-salEen)$_2$]NO$_3$. This has a dramatic impact on the packing with a 2D supramolecular network formed by a combination of N—H···O, C—H···O interactions involving the NO$_3$ anions and partial overlap of the aromatic part of the 4-OMe-salEen ligands for [Fe(4-OMe-salEen)$_2$]NO$_3$ (see Fig. 6). In contrast, [Fe(4-OMe-salEen)$_2$]PF$_6$ contains only very weak interactions between the cations resulting in two centres that undergo SCO at similar temperatures, hence its gradual nature.

More recently, Martinho et al. have reported [Fe(3,5-Br$_2$-salEen)$_2$]Y·sol (Y = ClO$_4$, sol = EtOH; Y = BPh$_4$, sol = DMF) of which the BPh$_4$ salt shows very gradual, incomplete SCO while the ClO$_4$ complex is LS up to 350 K [62]. The structure of [Fe(3,5-Br$_2$-salEen)$_2$]BPh$_4$·DMF at 150 K reveals that the Fe(III) centre is LS and unlike most other [Fe(X-salEen)$_2$]$^+$ complexes there are no anion—N—H interactions; hydrogen bonding instead occurring between the NH groups and the DMF carbonyl O atom. This greatly reduces the cooperativity as the DMF is not involved in any further supramolecular interactions, consistent with the gradual SCO observed in this compound.

In 2015, Murray and co-workers reported moderately abrupt spin crossover in the heteroleptic complex [Fe(3-OMe-salEen)(thsa)] at 344 K [63]. The structure in the LS state shows extensive π–π and N—H···N interactions. In comparing [Fe(3-OMe-salEen)(thsa)] with related homoleptic systems the authors

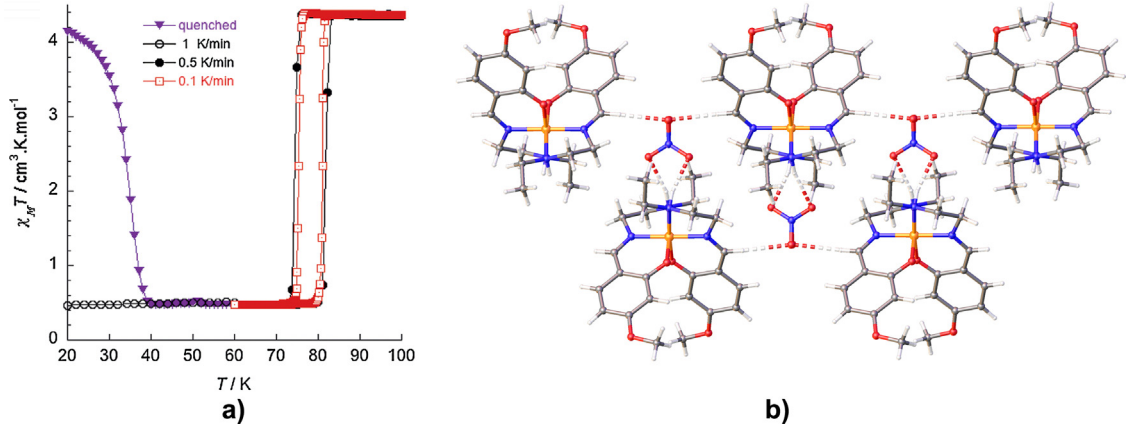

Fig. 6. (a) The magnetic profile (reproduced, slightly modified, with permission from Ref. [61] (Copyright Wiley-VCH, 2014) and (b) packing in [Fe(4-OMe-salEen)$_2$]NO$_3$ showing the 2D supramolecular network.

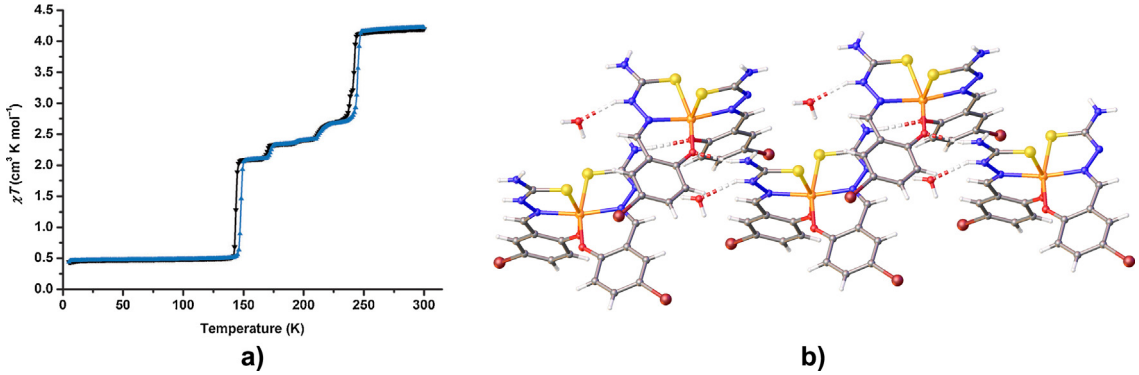

Fig. 7. (a) Multi-step spin crossover in [Fe(5-Br-Hthsa)(5-Br-thsa)]·H_2O (reproduced, slightly modified with permission from Ref. [68] (Copyright Wiley-VCH, 2013) and (b) view of the 1D hydrogen bonding chain at 123 K.

find that stronger π–π interactions lead to higher $T_{1/2}$. The SCO characteristics are improved relative to the parent compounds and represent a new strategy for preparing SCO materials.

2.2.3. Thiosemicarbazone complexes

Thiosemicarbazones, often abbreviated to X-thsa, are planar, readily derivatizable ligands which may be monoanionic or dianionic resulting in SCO complexes of the general formula, [Fe(X-Hthsa)(X-thsa)] or [Fe(X-thsa)$_2$]$^-$. Another unusual aspect of these complexes is that the Fe centre has an $N_2O_2S_2$ donor set rather than the more typical N_4O_2 donor set of other Fe(III) SCO systems. Li[Fe(5-Br-thsa)$_2$]·H_2O undergoes an abrupt SCO at $T_{1/2}\uparrow$ = 329 K and $T_{1/2}\downarrow$ = 292 K and thus a hysteresis of 37 K at its widest point [64]. Mössbauer spectroscopic studies confirm that the SCO is almost complete with a very small amount of LS species remaining at room temperature (*ca.* 3%). Later, the same authors reported a Rietveld refinement of the powder-XRD data showing that despite the large hysteresis there is no change in crystallographic space group [65]. Indeed, the large hysteresis is thought to be due to changes in the hydrogen bonding interactions involving the lattice water molecules. K[Fe(5-Br-thsa)$_2$] exhibits abrupt 2-step hysteretic SCO with ΔT = 69 K in the first cycle and 52 K thereafter [66]. The Fe–N/S bond lengths show a substantial increase upon SCO but unusually the unit cell volume only increases by 29.1 Å^3 and actually *decreases* in the SCO region. The hysteretic SCO is due to high cooperativity imparted by K coordination bonds, K–π interactions and hydrogen bonds forming a 2D network. Using [2-Me-5-Et-pyH]$^+$ results in the SCO moving to *ca.* 220 K and a loss of hysteresis according to ESR spectroscopic studies [67].

The neutral Fe(III) complexes [Fe(5-X-Hthsa)(5-X-thsa)]·nH_2O (X = H, n = 1; X = Cl, n = 1; X = Br, n = 0.5, 1) all exhibit SCO although the abruptness and degree of hysteresis is extremely sensitive to the method of preparation [68–70]. Thus, refluxing 5-Br-H_2thsa, $NHMe_2$ and $Fe(NO_3)_3$ in a MeOH/EtOH/water mixture gives [Fe(5-Br-Hthsa)(5-Br-thsa)]·H_2O which exhibits hysteretic, multi-step symmetry breaking SCO (see Fig. 7) [68] while synthesis of the compound via Li[Fe(5-Br-thsa)$_2$] and subsequent addition of [Hpy]Cl also gives [Fe(5-Br-Hthsa)(5-Br-thsa)]·H_2O but now with abrupt single step SCO [70]. Moreover, using NH_3 gives yet another compound, [Fe(5-Br-Hthsa)(5-Br-thsa)]·0.5H_2O which despite the change in the number of water molecules has a very similar magnetic profile to the compound made with pyridinium [69]. Of these only [Fe(5-Br-Hthsa)(5-Br-thsa)]·H_2O made with $NHMe_2$ has been characterized by single crystal XRD. Below 140 K and above 250 K the structure refines in monoclinic $P2_1/n$ while between these temperatures there is a change in space group to monoclinic P_n. As a consequence there are 2 Fe(III) centres, one HS and one LS, in the intermediate region and one Fe(III) centre at low and high temperatures. The Fe—N and Fe—S bond distances lengthen considerably upon SCO by 0.20 and 0.19 Å, respectively while the Fe—O bond lengths are little changed. The multi-step SCO in the intermediate region is ascribed to subtle changes in the ligand backbone coupled to resonance assisted hydrogen bonding involving the water molecule which very slightly modifies the ligand field. Interestingly, while [Fe(5-Br-Hthsa)(5-Br-thsa)]·H_2O (made with $NHMe_2$) exhibits only 5% LIESST, [Fe(5-Br-Hthsa)(5-Br-thsa)]·0.5H_2O exhibits 100% LIESST and is one of the few Fe(III) complexes to do so.

The impact of synthetic procedure is again evident in [Fe(Hthsa)(thsa)]·H_2O with van Koningsbruggen and co-workers reporting abrupt SCO in 2-steps in the cooling mode and a hysteresis of 12 and 42 K [69] while Floquet et al. [70], using pyridine as a base, report abrupt SCO in a single step with a hysteresis of only 8 K. In the heating mode the SCO occurs at *ca.* 280 K while in the cooling mode SCO occurs at from 230 to 270 K. In contrast, SCO in [Fe(5-Cl-Hthsa)(5-Cl-thsa)]·H_2O is abrupt at *ca.* 230 K with a hysteresis of 1–3 K irrespective of the base used. The structures of [Fe(5-X-Hthsa)(5-X-thsa)]·H_2O (X = H, Cl) at room temperature reveal strong hydrogen bonding between the Fe(III) centres mediated by the water molecules and π–π interactions between neighbouring aryl groups. These are slightly more planar in [Fe(Hthsa)(thsa)]·H_2O than [Fe(5-Cl-Hthsa)(5-Cl-thsa)]·H_2O reflecting the greater cooperativity observed in the former compound. Despite this it is [Fe(5-Cl-Hthsa)(5-Cl-thsa)]·H_2O that displays LIESST (33%) and not [Fe(Hthsa)(thsa)]·H_2O, thought to be due to the halogen group increasing the quantum mechanical tunnelling barrier. DSC studies reveal that ΔH = 10.5–4.3 kJ mol^{-1} and ΔS = 37.6–21.6 J K^{-1} mol^{-1} decreasing on moving from H to Cl to Br but still indicative of a substantial contribution from vibrational modes to the overall entropy and enthalpy.

Substituting one of the N–H groups for an N–Me group gives [Fe(5-Cl-Hthsa-Me)(5-Cl-thsa-Me)]·H_2O which now exhibits 2-step SCO at $T_{1/2}\uparrow$ = 249 and 278 K and $T_{1/2}\downarrow$ = 245 and 270 K and thus hystereses of 4 and 8 K [71]. X-ray crystallographic analysis at 100, 260 and 300 K indicates that the Fe centre is LS, averaged HS/LS and HS, respectively. Surprisingly, introduction of the methyl group results in only minor alterations in the packing which is again dominated by hydrogen bonding and slightly angular π–π interactions (Fig. 8). [Fe(5-Cl-Hthsa-Me)(5-Cl-thsa-Me)]·H_2O also exhibits dielectric anomalies coupled to the spin transition, demonstrating that it acts as a multifunctional material.

A Mössbauer spectroscopic study of [Fe(Hthpu)(thpu)] (H_2thpu = pyruvic acid thiosemicarbazine) has revealed that despite the low $\chi_M T$ = 3.69 cm^3 mol^{-1} K^{-1} the compound is in the full HS state undergoing a spin transition to the full LS state at 225 K. The compound also undergoes LIESST, although this is very modest at 2% [72].

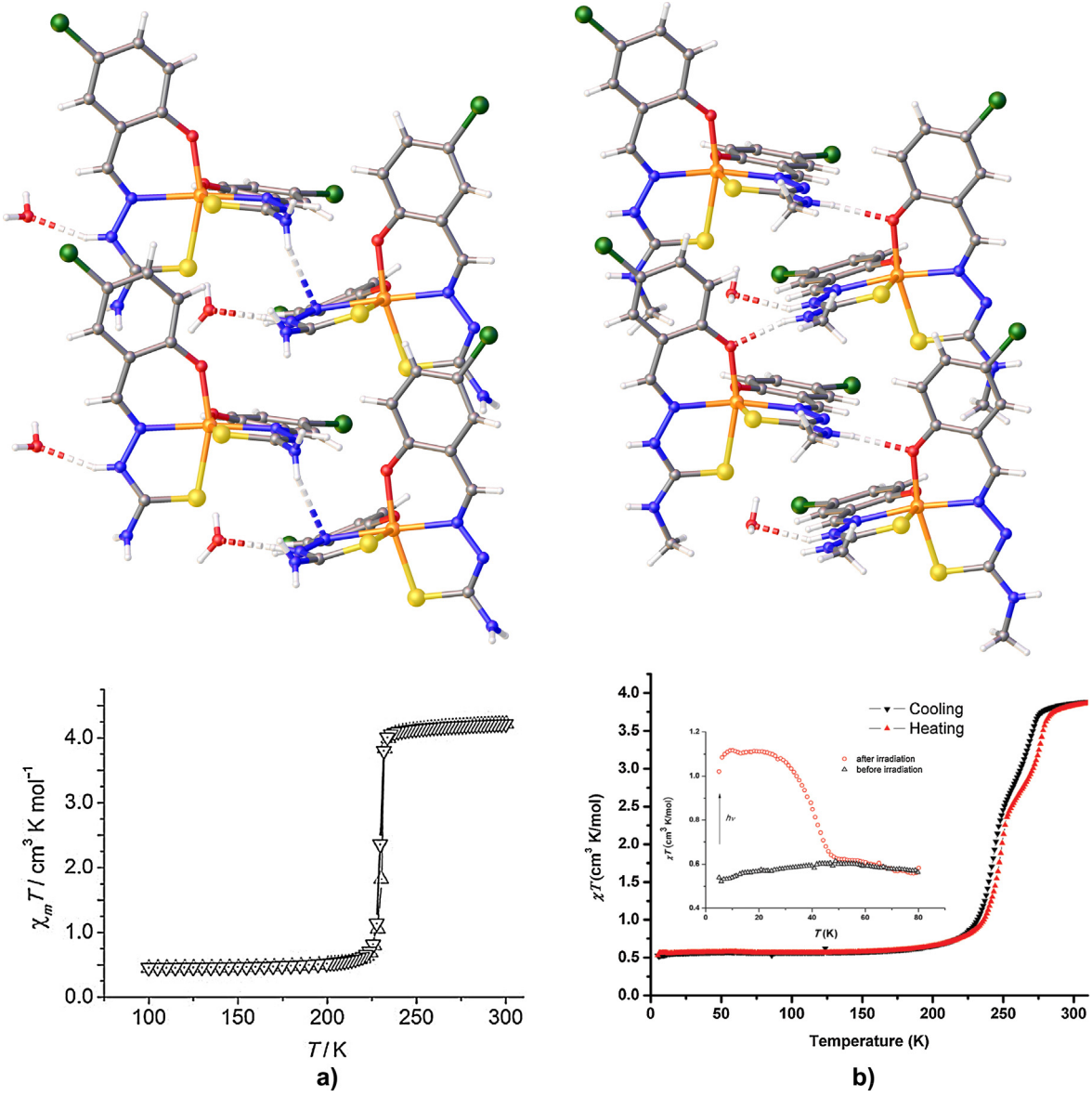

Fig. 8. (a) Comparison of the packing in [Fe(5-Cl-Hthsa)(5-Cl-thsa)]·H_2O (reproduced, slightly modified, with permission from Ref. [69] (Copyright Wiley-VCH, 2010) and (b) [Fe(5-Cl-Hthsa-Me)(5-Cl-thsa-Me)]·H_2O and the magnetic behaviour of the two complexes (reproduced with permission from Ref. [71]. (Copyright Royal Society of Chemistry, 2013.)

Two independent studies by the groups of Floquet and van Koningsbruggen have investigated a series of complexes employing pyridoxal thiosemicarbazone (H_2thpy) namely, A[Fe(thpy)$_2$]·nH_2O (A = NH_4, PPh_4, Na), [73] [Fe(Hthpy)(thpy)]·4.5H_2O, [73] [Fe(Hthpy)(thpy)]·MeOH·3H_2O, [74] [Fe(Hthpox)$_2$]Y·nsol (Y = Cl, NO_3, ClO_4, BPh_4, SO_4; sol = H_2O or MeOH) [73,75] and [Fe(H_2thpy)$_2$][Y]$_3$·nsol (Y = Cl, NO_3; sol = H_2O, EtOH) [73]. Despite the variety of protonated states, different anions and solvents none of the compounds are SCO active being either entirely HS or LS. However, some of the compounds do lose solvent converting to the HS state in the process; naturally this spin change is irreversible. What is clear from this series is that the thiolate ligands exhibit a stronger ligand field than the neutral thione ligand. Structural data for many of the compounds, show extensive hydrogen bonding involving the amide, pyridyl, hydroxyl groups and the lattice water and/or alcohol molecules.

The related compounds [Fe(Me-Hthpy)$_2$][$MeC_6H_4SO_3$]$_3$·EtOH, [75] [Fe(Me-Hthpy)(Me-thpy)]·2H_2O [74] and [Fe(Et-Hthpy)(Et-thpy)]·8H_2O [75] have also been prepared by van Koningsbruggen et al. Once again, none of the compounds undergoes SCO but it is interesting to note that [Fe(Me-H_2thpy)$_2$][$MeC_6H_4SO_3$]$_3$·EtOH is LS while [Fe(H_2thpy)$_2$][NO_3]$_3$·0.5EtOH is HS, although whether this is due to the Me group or the anion is unclear. Structural studies for all complexes show the Fe(III) is LS and once more there is strong hydrogen bonding linking the individual Fe(III) units. However, a distinct difference compared with the [Fe(Hthpy)(thpy)]·sol series is the presence of π–π interactions although these are not as extensive as in the [Fe(X-Hthsa)(X-thsa)]·H_2O series. This suggests that too many supramolecular sites lead to a loss of control of the crystal packing and consequently SCO behaviour.

2.2.4. Other complexes

The remaining complexes do not belong to a particular ligand system but are again often derived from salicylaldehyde or related derivatives. [Fe(salpm)$_2$]ClO_4·0.5EtOH is a particularly interesting example undergoing stepped SCO at 115 and 171 K through a 75% HS intermediate. The initial study of this compound revealed two independent Fe(III) centres at 100, 150 and 294 K with the centres

undergoing sequential SCO [76]. A more recent study by Morgan, Collet, Létard and co-workers revealed, using Mössbauer spectroscopy as a guide, that this explanation is too simplistic and in fact symmetry breaking SCO occurs with not *two* but *four* independent Fe(III) centres in the intermediate region [77]. It follows that at 135 K there are 3HS centres and 1LS centre consistent with the 75%HS intermediate observed in the magnetic data. Cooling results in halving of the unit cell producing two LS centres at 90 K. In addition, the compound undergoes LIESST, also in two steps reflecting the stepped SCO of the thermal transition.

The importance of supramolecular interactions is demonstrated beautifully in a study on $[Fe(acpa)_2]ClO_4$ [78]. The compound can be prepared in two forms, one where the SCO is abrupt, centered at *ca.* 370 K and with a hysteresis of 13 K and the other where it is gradual occurring between 250 and 350 K. The structures of the two polymorphs show tight packing and extensive π–π interactions in the abrupt polymorph, while these are absent in the gradual polymorph.

$[Fe(pap)_2]^+$ compounds hold the distinction of being the first Fe(III) complexes to exhibit LIESST. In 2009, structural comparison of $[Fe(pap)_2]BF_4{\cdot}H_2O$ in the HS state with $[Fe(pap)_2]PF_6{\cdot}MeOH$ which is LS, permitted, at that time, a rare insight into changes in Fe–N/O bond lengths upon SCO. A key feature was the large change in Fe–N/O bond lengths, 0.14 Å on average, and perhaps more significantly the strong structural distortion between the two spin states [23]. These combined give a LIESST activation barrier of 1,079 cm^{-1}, larger even than some Fe(II) SCO compounds and explaining the strong LIESST in $[Fe(pap)_2]ClO_4{\cdot}H_2O$ [79].

A series of compounds closely related to the $[Fe(qsal\text{-}X)_2]^+$ complexes above are $[Fe(qnal)_2]OTf{\cdot}sol$ (sol = MeOH, acetone) [80]. The compounds exhibit abrupt SCO at $T_{1/2}\uparrow = 115$ and $T_{1/2}\downarrow = 104$ K ($\Delta T = 11$ K) and $T_{1/2}\uparrow = 133$ and $T_{1/2}\downarrow = 130$ K ($\Delta T = 3$ K) for the MeOH and acetone solvates, respectively. The structure of $[Fe(qnal)_2]OTf{\cdot}MeOH$ at 80 K reveals a LS Fe(III) centre and π–π interactions formed between the quinolyl and naphthyl rings which are stronger even than those in $[Fe(qsal\text{-}X)_2]^+$ systems. Interestingly, despite the strong structural similarity and packing in the two systems, in contrast with most $[Fe(qsal\text{-}X)_2]^+$ complexes, $[Fe(qnal)_2]OTf{\cdot}sol$ are LIESST active, being 100% in the case of the acetone solvate.

Introduction of a methoxy group on the naphthyl moiety yields $[Fe(qnal\text{-}7\text{-}OMe)_2]Y{\cdot}sol$ (Y = PF_6, sol = acetone; Y = BPh_4, sol = 2MeOH) [81]. Remarkably, $[Fe(qnal\text{-}7\text{-}OMe)_2]BPh_4{\cdot}2MeOH$ has a hysteresis of 110 K at its widest point, the widest for any Fe(III) SCO system. However, in $[Fe(qnal\text{-}7\text{-}OMe)_2]PF_6{\cdot}$acetone the SCO is stepped via an 80% HS intermediate. Structural analysis of $[Fe(qnal\text{-}7\text{-}OMe)_2]PF_6{\cdot}$acetone in the HS and LS state shows an extremely large change in the Fe—O bond lengths by on average 0.08 Å while the change in the Fe—N bond lengths is more modest, 0.12 Å. In both compounds there are again strong π–π interactions which form a 1D chain with the anions linking neighbouring chains; the packing being tighter in the case of the BPh_4 complex. As with $[Fe(qnal)_2]^+$ both compounds undergo almost complete LIESST.

Hydrazone ligands have also been employed to make Fe(III) SCO complexes. The first report was by Gamez, Reedijk and colleagues on $[Fe(mph)_2]ClO_4{\cdot}0.5H_2O{\cdot}0.5MeOH$ which undergoes an unusual

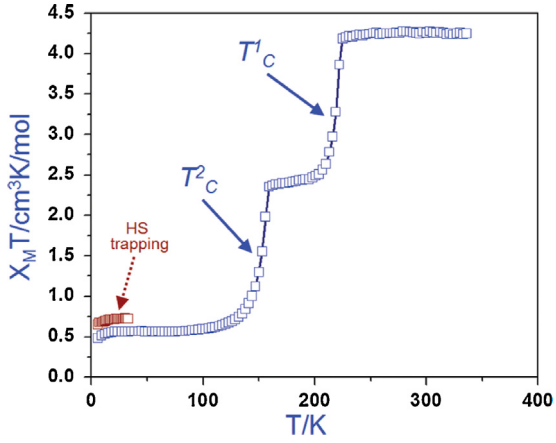

Fig. 9. Magnetic behaviour of $[Fe(mph)_2]ClO_4{\cdot}0.5H_2O{\cdot}0.5MeOH$ (reproduced from Ref. [82] with permission. (Copyright American Chemical Society, 2009.)

abrupt stepped SCO with a 45 K *ca.* 50% HS plateau (Fig. 9) [82]. The structure in the intermediate region shows that despite having two independent Fe(III) centres the Fe–N/O bond lengths are averaged across the two centres being intermediate between full HS and full LS, rather than localized as in many of the systems described above. The packing within the structure consists of H-bonded dimers which are linked to surrounding dimers by π–π interactions leading to 2D sheets.

The pyridyl aroylhydrazone Fe(III) complexes, $[Fe(pah\text{-}R)_2]ClO_4$ (R = H, *t*-Bu) required an unusual 1:1 ratio of Fe and ligand to be isolated; a 1:2 ratio of the Fe and ligand gives only the Fe(II) complex [83]. The SCO is gradual in both cases being incomplete and stepwise for $[Fe(pah)_2]ClO_4$. The structure of $[Fe(pah)_2]ClO_4$ at 100 K reveals two independent LS Fe(III) centres consistent with the stepped SCO.

The final SCO complex with a tridentate ligand is $[Fe(dammithiol)_2]Cl{\cdot}3H_2O$ which uniquely has a N_4S_2 donor set [84]. The compound exhibits a very gradual SCO, incomplete at both ends, from 50% HS at room temperature to 20% HS at 20 K according to Mössbauer spectroscopy. The structure is consistent with a LS Fe(III) centre and shows C—H···O interactions which link the Fe units into a 1D chain.

2.3. Tetradentate ligands

2.3.1. Salen ligands

Much of the most recent work on tetradentate ligands has been done by Matsumoto's group (see Table 2 and Fig. 10). The effect of the anion has been explored in $[Fe(Him)_2(3\text{-}OMe\text{-}salen)]Y{\cdot}H_2O{\cdot}EtOH$ (Y = PF_6, AsF_6, SbF_6) which show abrupt stepped SCO, half-SCO and HS only behaviour, respectively [85]. The SCO occurs at very low temperatures 20–70 K and at 40 K for the PF_6 and AsF_6, respectively. The change in SCO behaviour correlates with the size of the anion with smaller anions permitting more complete SCO. This is consistent with the void in the lattice shrinking upon SCO which can accommodate the PF_6 anion but not the larger SbF_6. Due to the low temperature of the spin crossover only the HS

Fig. 10. Structures and abbreviations of the tetradentate ligands used in iron(III) SCO systems.

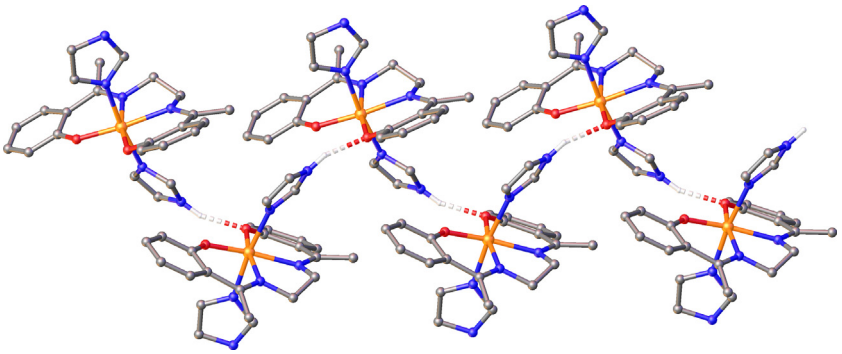

Fig. 11. The 1D hydrogen bonding chain of $[Fe(Him)_2(hapen)]AsF_6$ [87].

structures have been determined but they nevertheless show extensive 2D hydrogen bonding interactions between the Fe cations and the H_2O and EtOH molecules which accounts for the abrupt and hysteretic SCO observed in the PF_6 and AsF_6 systems.

Replacing the methoxy group with an ethoxycarbonyl group yields $[Fe(R\text{-}Im)_2(5\text{-}CO_2Et\text{-}salen)]BPh_4{\cdot}sol$ (R = H, sol = EtOH; R = 1-Me, sol = $0.5H_2O$) [86]. Both exhibit thermochromism in solution changing from red to blue-green but in the solid state only the Him complex is SCO active, although the transition is very gradual with $T_{1/2}$ = 192 K. The structure of the LS and HS forms reveals significant changes in the Fe—N bond lengths by 0.16 Å but unusually no change in the Fe—O bonds. In contrast to the structures above, there are no hydrogen bonding networks but simple hydrogen bonded dimers instead.

2.3.2. Hapen ligands

Closely related to the salen ligands above is the hapen ligand in which 2-hydroxyacetophenone is used instead of salicylaldehyde. The complexes $[Fe(Him)_2(hapen)]Y{\cdot}sol$ (Y = BF_4, ClO_4, PF_6, AsF_6, OTf, BPh_4) show a variety of magnetic behaviours with the smaller anions HS only and the larger anions SCO active [87,88]. The outstanding members of the series are the AsF_6 and PF_6 complexes which exhibit abrupt hysteretic SCO (ΔT = 4.6 K, $T_{1/2}\uparrow$ = 74 K, $T_{1/2}\downarrow$ = 69.4 K) [87] and abrupt SCO at $T_{1/2}$ = 75 K [88], respectively. In both cases the structures show a HS Fe(III) centre with a 1D hydrogen bonding zigzag chain involving the imidazole NH and coordinated phenoxy O atom that links the spin centres (Fig. 11). In its absence, the compounds are trapped in the HS state.

The position of the methoxy substituent on the hapen ligand has also been explored in $[Fe(Him)_2(n\text{-}OMe\text{-}hapen)]PF_6{\cdot}sol$ (n = 4, sol = none; 5, sol = $0.5H_2O$; 6, sol = EtOH) [89]. The 4-OMe and 5-OMe compounds undergo gradual SCO being slightly more abrupt in the former case. Both complexes exhibit thermochromism changing from deep red at room temperature to blue-green at liquid nitrogen temperatures. In contrast, the 6-OMe complex exhibits very incomplete SCO. Structural studies suggest that steric hindrance between the methyl and methoxy group results in greater distortion of the 6-OMe-hapen ligands preventing substantial SCO. The difference in the Fe—N bond lengths is *ca.* 0.14 Å upon SCO, while the Fe—O bond lengths do not change mirroring the trend observed in the $[Fe(Him)_2(salen)]^+$ complexes above. Abrupt SCO ($T_{1/2}$ = 192 K) between a single site HS state (monoclinic C2/c) and a symmetry breaking [HS–HS–HS–LS] state (triclinic $P\bar{1}$) has been reported in $[Fe(Him)_2(4\text{-}OMe\text{-}hapen)]OTf$ [90]. The packing mirrors that of the PF_6 salt with H-bonded chains of $[Fe(Him)_2(4\text{-}OMe\text{-}hapen)]^+$ bridged by the OTf anion. However, the 1D chains are interdigitated in the OTf complex but not the PF_6 analogue and this is probably responsible for the symmetry breaking SCO.

2.3.3. Acen ligands

The complexes $[Fe(acen)(n\text{-}Bu\text{-}im)_2]Y$ (Y = NTf_2, PF_6) both show SCO which is incomplete at 320 K [91]. The NTf_2 salt is an ionic liquid while the PF_6 salt is a crystalline solid. Despite the different anions the SCO profile is remarkably similar but consistent with the lack of cooperativity noted in the structure of $[Fe(acen)(n\text{-}Bu\text{-}im)_2]PF_6$.

2.4. Pentadentate ligands

Pentadentate ligands are usually dianionic Schiff bases with an N_3O_2 donor set with the final N supplied by a terminal ligand (see Fig. 12 and Table 3). The compounds, $[Fe(salten)(n\text{-}py\text{-}N{=}N\text{-}Ph)]BPh_4$ (n = 3, 4) contain photoisomerizable ligands and have been prepared with the aim of determining the effect of isomerisation on SCO characteristics [92]. Both complexes undergo gradual SCO, although it is more abrupt in the 3-py-N=N-Ph complex. In solution, photoisomerization from the *trans* to the *cis* isomer results in essentially no change in the magnetic behaviour.

$[Fe(salten\text{-}3\text{-}OMe)(Me\text{-}Im)]BPh_4$ with a methoxy group on the phenyl ring undergoes gradual SCO with $T_{1/2}$ = 215 K [93]. Structural studies show Fe–N/O bond length changes compatible with SCO with the largest difference for the Fe—N(amine) bond. The packing involves a ribbon of Fe cations connected by C—H···π interactions but surprisingly no hydrogen bonding.

Using an asymmetric ligand with ethylene and propylene linkers rather than two propylene linkers yields a range of complexes many of which undergo SCO. $[Fe(salpet\text{-}R)(NH_2\text{-}tet)]$ (R = H, 5-Cl, 5-Br, 3,5-Br_2) all show SCO although it is very gradual and incomplete even at 400 K [94]. By comparison $[Fe(salten)(NH_2\text{-}tet)]$ is HS at all temperatures. The structure of $[Fe(salpet)(NH_2\text{-}tet)]$ reveals a LS Fe(III) centre and extensive hydrogen bonding between the phenoxy O atoms and the amino N–H groups as well as an N—H···N interaction involving the tetrazole and the salpet N–H group forming a 1D chain. The N—H···O interactions, in particular, may be vital in weakening the ligand field to permit SCO.

The pseudo-halide complexes $[Fe(salpet\text{-}R)X]$ (X = NCS, NCSe, NCO, N_3) are also often SCO active [95–97]. The most abrupt SCO occurs for [Fe(salpet-3-OEt)NCS] with $T_{1/2}\uparrow$ = 84 K and $T_{1/2}\downarrow$ = 82 K and thus ΔT = 2 K, although there is a residual HS fraction even at low temperature [97]. X-ray crystallography shows two independent but structurally similar Fe(III) centres which obviously undergo SCO at the same temperature. The most interesting feature of the structure though, is the strongly asymmetric shortening of the Fe—O bond lengths by 0.01 or 0.07 Å upon SCO. The Fe—O bond distance which lengthens the most is on the propylene side of the Schiff base; this appears to be a feature of these and the [Fe(napet)X] complexes discussed below. The packing again involves H-bonding this time between the N–H amine and the oxygen atom of the ethoxy groups.

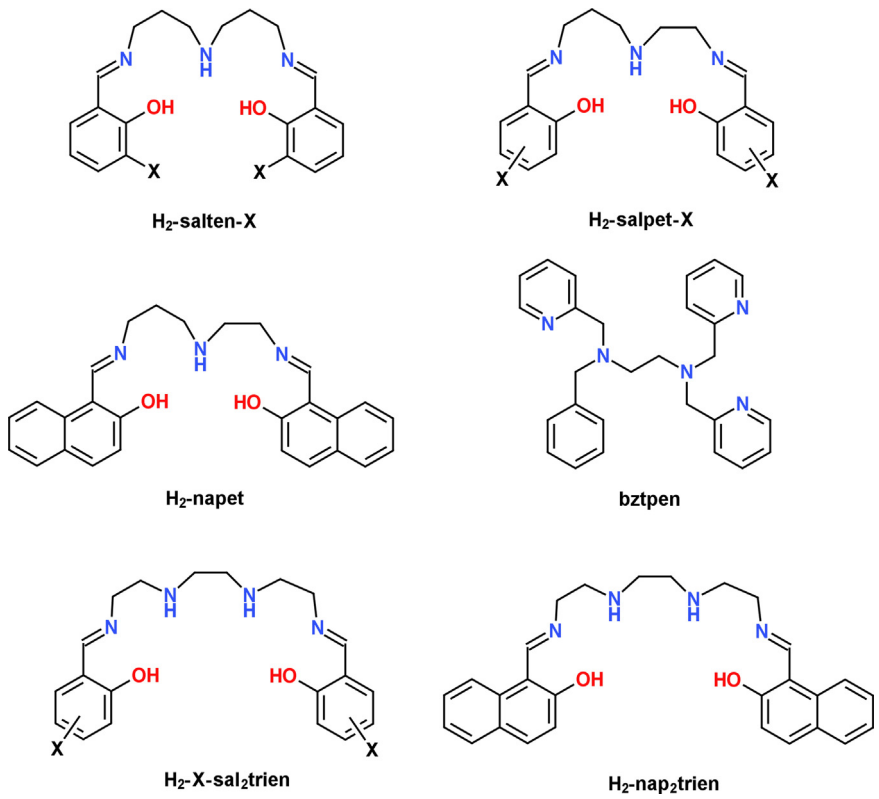

Fig. 12. Structures and abbreviations of the pentadentate and hexadentate ligands used in iron(III) SCO systems.

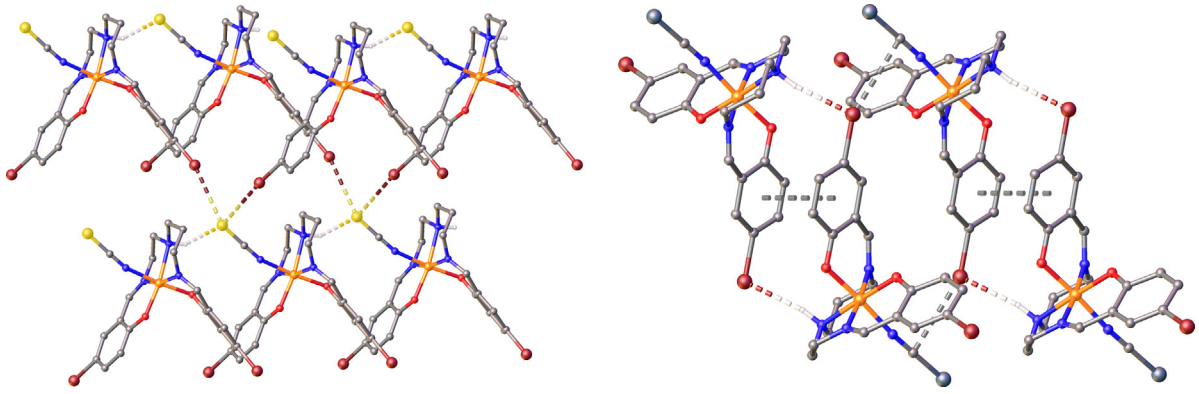

Fig. 13. Comparison of the supramolecular interactions in [Fe(salpet-Br)NCX] {X = S (HS only), Se (SCO)} [95].

[Fe(salpet-Br)X] (X = NCSe, N_3) [95] and [Fe(salpet-Cl)X] (X = NCS, NCSe) [96] show moderately abrupt SCO with $T_{1/2}$ varying from 140 to 320 K being incomplete at lower temperatures for the [Fe(salpet-Br)X] series. Structural data in either the HS or LS state for these compounds reveal once again inequivalent Fe—O bond lengths with a large change in only one of the Fe—O bond lengths. With the exception of [Fe(salpet-Br)N_3], the packing is dominated by N—H···Cl/Br interactions which are reinforced by π–π interactions (see Fig. 13). Additional C—H···Cl/Br interactions coupled with more π–π interactions form a 1D chain. In the case of [Fe(salpet-Br)N_3] the 1D chain is formed exclusively with N—H···N interactions. In either case it is clear that interactions involving the coordinated amine N–H are often key in determining SCO characteristics in [Fe(salpet-R)X] complexes.

[Fe(napet)X]·MeCN (X = NCS, NCSe) [98] and [Fe(napet)X] (X = NCS, NCO, N_3) [97,98] all exhibit quite abrupt SCO with the transition temperature varying from 117 to 174 K. For [Fe(napet)N_3] the SCO is particularly abrupt with $T_{1/2}\uparrow = 122$ K and $T_{1/2}\downarrow = 117$ K and a hysteresis of 5 K [97]. As expected [Fe(napet)NCSe]·MeCN undergoes SCO *ca.* 20 K higher than the NCS analogue [98]. The effect of solvent is evident by comparing [Fe(napet)NCS] and [Fe(napet)NCS]·MeCN where $T_{1/2}$ are 174 and 151 K, respectively. The structures of many of these complexes have been determined in both spin states with Fe–N/O bond length trends matching those of the [Fe(salpet-R)X] complexes. When the Fe—N(amine) bond length is greater than 2.20 Å the compound becomes trapped in the HS state. In terms of the packing, a feature present in all of the [Fe(napet)X] series are N—H···Y (Y = S, N or O) interactions which link the cations to form 1D chains identical to that of [Fe(salpet-Br)N_3]. When MeCN is present this chain is disrupted and N—H···N interactions form instead. Surprisingly, despite the large aromatic rings there is no evidence of π–π interactions in any of the structures.

The impact of solvent on SCO has been explored in a fascinating series of compounds [Fe(napet)NCS]·sol (sol = THF, butanone, DMF, DMSO, acetone), the first systematic structural study of

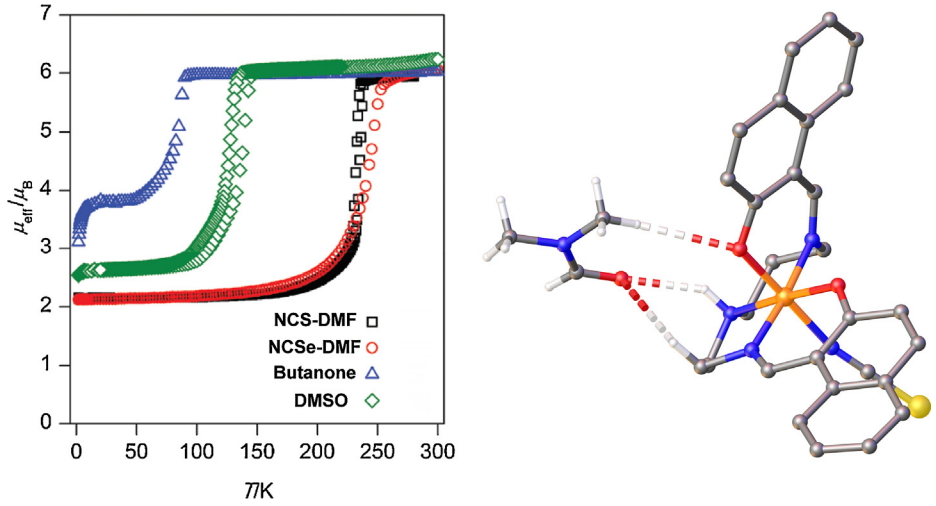

Fig. 14. Magnetic behaviour of [Fe(napet)NCS]·sol and the SCO defining N—H···O interaction in [Fe(napet)NCS]·DMF (reproduced, slightly modified, from Ref. [99]. (Copyright Royal Society of Chemistry, 2015.)

solvent effects in Fe(III) SCO chemistry [99]. All the compounds have N—H···O interactions between the coordinated amine and the oxygen atom of the solvent. The strength of this N—H···O interaction directly correlates with the transition temperature ranging from 84 to *ca.* 230 K. When the N—H···O interaction is longer than 3.0 Å, the complex is no longer SCO active (THF and acetone). In the case of [Fe(napet)NCS]·sol where the solvent is DMF and DMSO hysteresis loops of 3 and 7 K are observed, respectively (Fig. 14). The presence of hysteresis in these compounds is probably due to offset π–π, C—H···π and C—H···O interactions which form a more organized grid than that observed in other [Fe(napet)X] compounds.

Two naphthenyl ligands have been explored using 1-hydroxy-2-acetonaphthone or 2-hydroxy-1-acetonaphthone and reacting it with the asymmetric triamine to give [Fe(*n*-napet-Me)NCS] (*n* = 1 or 2) [96]. Three polymorphs of [Fe(1-napet-Me)NCS] exist with only the α-polymorph undergoing SCO, which unusually is between *S* = 3/2 and *S* = 5/2 spin states at *ca.* 42 K (Δ*T* = 4 K); the other two polymorphs are HS. The α- and γ-polymorphs both contain two independent Fe(III) centres and while for the former there is a bent and a linear NCS ligand, for the latter both are bent. In contrast, the β-polymorph has a single HS Fe(III) centre and a linear NCS ligand. Only in this polymorph is there an extended chain composed of N—H···S interactions between the coordinated amine and the thiocyanate S atom. In the α-polymorph there are no H-bonds while for the γ-polymorph a supramolecular dimer is found. A similar loss of H-bonding interactions occurs in [Fe(1-napet-Me)N_3] which is HS only and in [Fe(2-napet-Me)NCS]. The latter compound undergoes gradual and incomplete SCO with $T_{1/2}$ = 114 K, *ca.* 60 K lower than [Fe(napet)NCS] confirming that the 2-napet-Me ligand generates a weaker ligand field than napet.

Real and co-workers recently reported a series of SCO complexes which uniquely have an N_5O coordination environment, [Fe(btzpen)(OR)][PF_6]$_2$ (R = Me, Et, Pr, n-Bu, i-Bu, CH_2CH_2OH) [100,101]. It seems likely that the two tertiary amine N donors of the btzpen ligand provide a weaker ligand field than the pyridyl N donors making the complexes SCO active. All the compounds exhibit gradual SCO with $T_{1/2}$ increasing from 158 to 284 K as the ionization potential of the alkoxide decreases. The structures of the compounds in the HS and LS states reveal the expected shortening of the Fe—N bond distances between 0.09 and 0.13 Å but a lengthening of the Fe—O bond length by between 0.01 and 0.02 Å upon SCO to the LS state. The overall change in the Fe–N/O bond lengths is slightly less than that of other Fe(III) SCO complexes. The packing shows no significant cation–cation or cation–anion interactions consistent with the gradual SCO observed in these compounds.

2.5. Hexadentate ligands

The first example of symmetry breaking SCO in Fe(III) was reported in 2011 in [Fe(3,5-OMe-sal$_2$bapen)]ClO_4 [102]. The SCO is gradual and incomplete retaining 33% HS character even at low temperature but occurs in two steps with $T_{1/2}$ = 190 and 100 K with slight hysteresis in the latter step. The space group remains the same at all temperatures but trebles in size after the 1st step. This creates two Fe(III) centres one which has 50% occupancy and is LS while the other is HS with 100% occupancy and consequently an overall 67% HS state. The structure below the second step could not be determined but Mössbauer spectroscopic data mirror the magnetic studies with transitions from 100% HS to 2:1 HS:LS to 1:2 HS:LS evident.

Spin crossover has also been explored in [Fe(X-sal$_2$trien)]Y (X = Me, *i*-Pr, *t*-Bu; Y = NO_3, PF_6) [103]. The SCO is gradual and incomplete proceeding to 35–50% completeness except in [Fe(Me-sal$_2$trien)]NO_3·3/2H_2O and [Fe(Me-sal$_2$trien)]PF_6 which are LS and HS, respectively. The structure of [Fe(Me-sal$_2$trien)]PF_6 reveals two unique Fe(III) centres in which the bond lengths and angles differ significantly. This may account for the half-SCO observed in other compounds in this series, although [Fe(*t*-Bu-sal$_2$trien)]NO_3·$C_2H_4Cl_2$ contains only a single HS Fe(III) site at 100 K. However, it should be stressed that it is the non-solvated compound that undergoes SCO. In line with many [Fe(X-sal$_2$trien)]$^+$ complexes, [Fe(*t*-Bu-sal$_2$trien)]NO_3 also undergoes SCO in solution.

In [Fe(4-OH-sal$_2$trien)]Y (Y = Cl, Br and I) the SCO is gradual and incomplete going from the LS state to 20–80% HS being most complete for the iodide complex [104]. The complexes are isostructural and in the LS state, reveal extensive hydrogen bonding between the hydroxyl groups and the halide anions as well as N—H···O interactions which result in a 2D supramolecular network. As expected the hydrogen bonding is strongest for the chloride and weakest for the iodide resulting in the tightest packing for [Fe(4-OH-sal$_2$trien)]Cl and thus the poorest SCO profile. However, in solution all the compounds undergo complete SCO with clear thermochromism going from brown at 298 K to blue at 77 K (see Fig. 15).

Substituting the phenyl groups with imidazolium cations results in a SCO active ionic liquid [Fe(4-(OCH_2-imid-n-Bu)sal$_2$trien)][$(CN)_2N]_3$ with dicyanamide anions. The SCO is modest being 33% HS at 400 K but is reversible and for the first

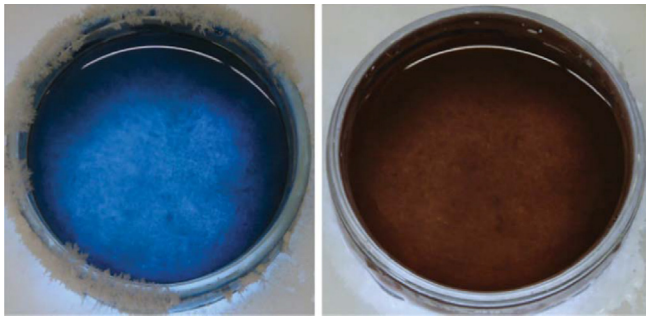

Fig. 15. Thermochromism of [Fe(4-OH-sal$_2$trien)]I in the LS (left) and HS state (right; reproduced with permission from Ref. [104]. (Copyright Royal Society of Chemistry, 2012.)

time in Fe(III) SCO chemistry the ionic liquid is thermally stable [105].

In [Fe(nap$_2$trien)]Y (Y = PF_6, NCS) where naphthenyl groups are used the PF_6 complex is LS up to 300 K [103] while the NCS complex undergoes symmetry breaking SCO that is abrupt in the first (lower temperature) step [106]. The SCO occurs at 142 and 250 K and is much broader in the second step. The structures at 50 and 298 K both contain a single Fe(III) centre which is LS and HS respectively. However, at 150 K the unit cell doubles in size with two Fe(III) centres one HS and the other LS. This type of re-entrant SCO is extremely rare and this was the first time it was reported for Fe(III). The packing within the structure is dominated by N—H···S interactions between the thiocyanate S and neighbouring amines of the nap$_2$trien ligand forming a 1D chain reminiscent of the [Fe(napet)X] and [Fe(salpet)X] systems discussed above.

[Fe($H_{1.5}$tren-imid)][ClO_4]$_{1.5}$ and [Fe(H_2tren-imid)][Co(Htren-imid)][ClO_4]$_3$ also exhibit very incomplete SCO based on Mössbauer spectroscopic studies which are 50% to 60% HS for the Fe only complex and LS to 55% HS for the Fe–Co compound [107]. [Fe($H_{1.5}$tren-imid)][ClO_4]$_{1.5}$ exists as three polymorphs trigonal, hexagonal and cubic. The trigonal polymorph has a 2D sheet supramolecular network while the cubic form is composed of supramolecular tetrahedra. In both cases the networks are held together by N—H···N hydrogen bonds involving the imidazole NH and N atoms.

3. Dimeric systems

Dinuclear systems are almost all based on the pentadentate ligands, salten and salpet [108,109]. In 2007, Matsumoto and co-workers reported [{(salten-3-OMe)Fe}$_2$(μ-bimb)][BPh_4]$_2$ (bimb = 1,4-bisimidazolylbutane) which exhibits gradual 2 step SCO with $T_{1/2}$ = 60 and 90 K [93]. The structure of the HS–HS dimer reveals only weak π–π interactions consistent with the gradual SCO. More recently, the same group has reported two related dimers [{(salten-3-OMe)Fe}$_2$(μ-4,4′-bipy)][BPh_4]$_2$ and [{(N-Me-salten-3-OMe)Fe}$_2$(μ-4,4′-bipy)][BPh_4]$_2$ which exhibit 1 and 2 step SCO, respectively being incomplete in the latter compound [110]. The 2 step SCO is due to the presence of 2 independent Fe(III) centres while in [{(N-Me-salten)Fe}$_2$(μ-4,4′-bipy)][BPh_4]$_2$ the Fe(III) centres are crystallographically equivalent. The change in the Fe–N/O bond lengths in [{(salten-3-OMe)Fe}$_2$(μ-4,4′-bipy)][BPh_4]$_2$ are rather smaller than those observed in the mononuclear compounds being 0.13 and 0.03 Å, respectively. In [{(N-Me-salten-3-OMe)Fe}$_2$(μ-4,4′-bipy)][BPh_4]$_2$ the SCO is incomplete with only one of the independent Fe centres undergoing SCO based on X-ray crystallography, although Mössbauer spectroscopy shows that at 78 K the dimer is 66% LS.

The interplay between possible magnetic exchange between the Fe(III) centres and spin crossover has been explored in a series of compounds [{(N-Me-salten)Fe}$_2$(μ-N-N)][BPh_4]$_2$ {N-N = 1,2-bis(4-pyridyl)ethane (bpe), 1,2-bis(4-pyridyl)ethane (bpea), 1,2-bis(4-pyridyl)propane (bpp), 1,4-phenylenebis (methylene)bis(imidazole)} [108]. Of these only [{(N-Me-salten)Fe}$_2$(μ-bpe)][BPh_4]$_2$ displays SCO although this is incomplete at higher temperatures. [{(N-Me-salten)Fe}$_2$(μ-N-N)][BPh_4]$_2$ (N-N = 4,4′-bipy, bpe) also exhibit thermochromism changing from dark green at low temperature to violet at room temperature. The structures of these compounds reveal crystallographically equivalent Fe(III) centres which are LS when the bridging ligands are bpe and bpea and HS with bpp.

Two asymmetric dimers [(salpet-R)Fe(μ-CN)Fe(salpet-R)]Y (R = H, Y = ClO_4·2H_2O; R = 5-Me-3t-Bu, Y = BPh_4·2MeCN) have been prepared which show gradual but complete SCO for the BPh_4 dimer and very incomplete SCO, from 62% LS to 39% LS for the ClO_4 dimer [111]. As expected, only the N-bound Fe centre undergoes SCO. The structures of the dimers are consistent with the magnetic data and interestingly in the case of the BPh_4 dimer the cyanide bridge is disordered.

The final, and to date only, Fe(III) dimer not utilizing an N_3O_2 ligand are the series [(qsal)Fe(qsal-C≡C-2,2-bith-C≡C-qsal)Fe(qsal)][Y]$_2$ (Y = Cl, NCS, PF_6, ClO_4, see Fig. 16) [112]. The SCO in these dimers is extremely gradual going from almost 100% HS to ca. 50% HS while the ClO_4 salt is incomplete at both ends (20% HS to 56% HS). The lack of structural data means that it's impossible to tell whether the SCO occurs at a single site or at both Fe centres.

4. Multinuclear systems

Multinuclear SCO systems have been prepared with the aim of producing multi-step SCO systems. The trinuclear system [(salpet)Fe(Fe(CN)$_5$NO)Fe(salpet)] shows partial and very gradual SCO in only one of the iron centres [111]. Similarly incomplete SCO is also observed in the Sn(IV) tetramer [{(salpet)Fe}$_4$Sn(CN)$_4$][Cl]$_4$ as evidenced by Mössbauer spectroscopic studies [113]. The largest member of this type is the heptanuclear cluster [Fe^{II}{(CN)Fe^{III}(salpet)}$_6$][Cl]$_2$ for which the SCO is gradual with 4 Fe(III) centres remaining HS even at 20 K [114]. The structure at room temperature is consistent with six HS

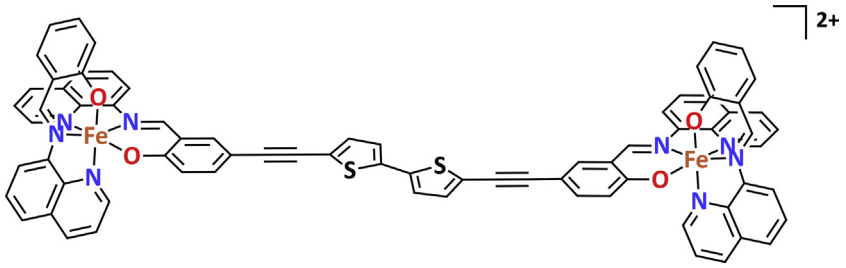

Fig. 16. View of the [(qsal)Fe(qsal-C≡C-2,2-bith-C≡C-qsal)Fe(qsal)][Y]$_2$ dimer [112].

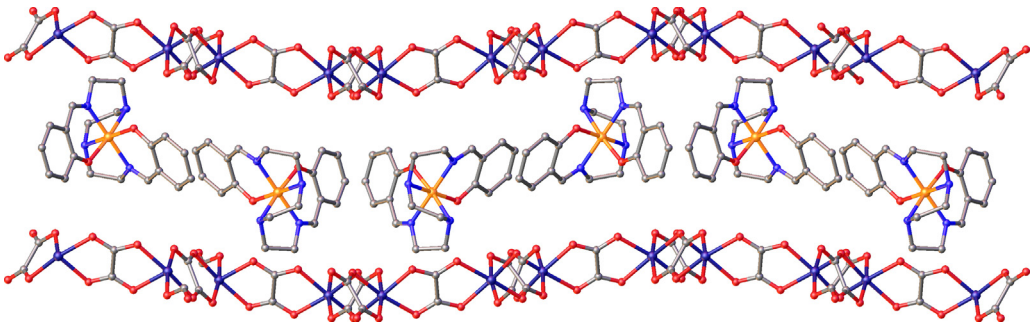

Fig. 17. Layered structure found in many [Fe(5-X-sal$_2$trien)][Mn{Cr(ox)$_3$}]·sol systems [120].

Fe(III) atoms and the close proximity of neighbouring Fe(salpet) units may explain why full SCO cannot be achieved.

In another approach Murray's group have synthesized a large number of 1D polymers [Fe(N_2O_2)L][BPh_4]$_n$ (N_2O_2 = salen, salophen, acen; L = bridging pyridyl or imidazole) with the aim of increasing cooperativity between the iron centres [115]. At almost the same time Matsumoto and co-workers reported {[Fe(acen)L][BPh_4]}$_n$ where L = 1,3-bis(4-pyridyl)propane (bpp) and 1,4-bis(N-imidazole)butane (bimb) [116]. The salen and salophen systems are almost all HS, something that in the former case is thought to be due to the *meso* configuration of the C_2N_2 backbone of the ligand. In contrast, many of the {[Fe(acen)L][BPh_4]}$_n$ systems are SCO active although they are almost all gradual and in some cases SCO is incomplete even at 350 K. The exception is {[Fe(acen)(pin)][BPh_4]}$_n$ (pin = N-(4-pyridyl)-isonicotinamide) where the SCO is relatively abrupt ($T_{1/2}$ = 135 K) possibly due to H-bonding between 1D chains [115]. Structures of {[Fe(acen)(bpp)][BPh_4]}$_n$ and {[Fe(acen)(bimb)][BPh_4]}$_n$ reveal that in spite of their identical formulas the bpp compound contains 2 crystallographically distinct 1D chains while for {[Fe(acen)(bimb)][BPh_4]}$_n$ there is only one. Changes in the Fe–N/O bond lengths are typical of SCO systems being ΔFe-N = 0.14 Å and ΔFe-O = 0.02 Å. In all these systems cooperativity is very poor despite the coordination bonds between the Fe(III) centres. The large anions may be responsible, in part, for the lack of abrupt SCO in these systems and more work is clearly needed.

5. Multifunctional systems

5.1. [Fe(5-X-sal$_2$trien)][Mn{Cr(ox)$_3$}] systems

Materials incorporating SCO centres are attractive targets as the spin crossover may be coupled to other physical properties. An elegant example of this are the series of compounds [Fe(5-X-sal$_2$trien)][Mn{Cr(ox)$_3$}]·sol (X = H, sol = CH_2Cl_2, CH_2Br_2 $CHCl_3$, $CHBr_3$, MeOH; X = Cl, Br, OMe sol = none; X = NO_2, sol = $MeNO_2$·0.5H_2O) where the SCO cation is inserted into a ferromagnetic network [117–123]. The structures are generally composed of alternating layers of the bimetallic [Mn{Cr(ox)$_3$}]$^-$ network with the [Fe(sal$_2$trien)]$^+$ cations intercalated between the layers of the 2D oxalate network (Fig. 17). In [Fe(sal$_2$trien)][Mn{Cr(ox)$_3$}]·sol (sol = CH_2Cl_2, $CHCl_3$, CH_2Br_2, $CHBr_3$) there is coexistence of ferromagnetic ordering at *ca.* 5 K and complete, gradual SCO with $T_{1/2}$ varying from 255 to 142 K [120,122]. Remarkably, all the compounds also undergo LIESST with the degree of LIESST strongly dependent on the solvent, being 40% for $CHCl_3$ and 21% for CH_2Br_2. These hybrid magnets are extremely rare and moreover, demonstrate that cooperative SCO is not a necessary requirement for the observation of LIESST in Fe(III) compounds. The structures in the HS and LS states show changes in the Fe–N/O bond lengths of *ca.* 0.15 and 0.03 Å and are similar to those of simple [Fe(sal$_2$trien)]$^+$ complexes.

The increase in the size of the cations following SCO is reflected in an increase in the distance between the oxalate layers and more extensive C—H···O interactions involving the [Fe(sal$_2$trien)]$^+$ cations which may stabilize the photogenerated metastable HS state. Solvent is critical in these systems and in contrast to the above networks [Fe(sal$_2$trien)][Mn{Cr(ox)$_3$}]·MeOH has a 3D bimetallic oxalate network which results in much more distorted [Fe(sal$_2$trien)]$^+$ units and consequently no SCO [119].

The SCO behaviour of [Fe(n-X-sal$_2$trien)][Mn{Cr(ox)$_3$}]·sol is very variable with the best coexistence of SCO and ferromagnetism occurring in [Fe(5-X-sal$_2$trien)][Mn{Cr(ox)$_3$}]·sol (X = Cl, sol = 0.5$MeNO_2$, X = Br, sol = none) [121] and [Fe(4-Br-sal$_2$trien)][Mn{Cr(ox)$_3$}]$_{0.67}$[Cl]$_{0.33}$·MeOH with 45%, 25% and 90% SCO ($T_{1/2}$ = *ca.* 340 K) respectively [123]. In contrast, [Fe(5-X-sal$_2$trien)][Mn{Cr(ox)$_3$}] where X = NO_2 and OMe, are LS and HS only, respectively [118]. Similarly, [Fe(3-X-sal$_2$trien)][Mn{Cr(ox)$_3$}] (X = Cl, Br, OMe) are essentially trapped in the HS state [123]. The structures are varied with chiral 3D bimetallic oxalate networks formed in [Fe(5-X-sal$_2$trien)][Mn{Cr(ox)$_3$}] (X = Cl, Br) while a 2D network forms for [Fe(4-Br-sal$_2$trien)][Mn{Cr(ox)$_3$}]$_{0.67}$[Cl]$_{0.33}$·MeOH. In the latter case, unusually there is a double layer of [Fe(4-Br-sal$_2$trien)]$^+$ cations in between the anionic oxalate layers. Moreover, unlike the above networks with [Fe(sal$_2$trien)]$^+$, none of the [Fe(n-X-sal$_2$trien)][Mn{Cr(ox)$_3$}]·sol systems exhibit the LIESST effect. This may be due to the more incomplete SCO, higher $T_{1/2}$ or structural differences in the networks.

More recently, the oxalate layers have been replaced by an anilate network to give [Fe(4-X-sal$_2$trien)][Mn{Cr(Cl_2An)$_3$}]·sol (X = H or OH, Cl_2An = chloroanilate), [Fe(5-Cl-sal$_2$trien)][Mn{Cr(Br_2An)$_3$}]·CH_2Cl_2·MeOH·4H_2O·1.5MeCN) (Br_2An = bromoanilate) and [Fe(sal$_2$bapen)][Mn{Cr(Br_2An)$_3$}]·4MeCN (sal$_2$bapen = N,N′-bis(salicylidene)-1,5,8,12-tetraazadodecane) [124]. These networks show ferromagnetic ordering of the anilate networks at *ca.* 10 K but no SCO being either LS or HS only. The structures are similar to those of [Fe(sal$_2$trien)][Mn{Cr(ox)$_3$}]·sol networks being composed of 2D anilate layers with the Fe(III) cations intercalated in between these layers.

Similar anilate networks, [Fe($acac_2$-trien)][Mn{Cr(Cl_2An)$_3$}]·2MeCN and [Fe($acac_2$-trien)][Mn{Cr(Br_2An)$_3$}]·2MeCN show ferrimagnetic ordering at low temperatures but no SCO at the Fe centres [125]. The [Fe($acac_2$-trien)]$^+$ cations are located in hexagonal channels provided by the anilate networks creating 2D materials. Simple Scotch tape micromechanical exfoliation yields nanosheets of the networks. The same method is also applicable to [Fe(sal$_2$trien)][Mn{Cr(ox)$_3$}]·sol despite the 3D network present in this system.

5.2. [M^{III}(dithiolene)$_2$]$^-$ systems

Another strategy towards multifunctional materials involves combining Fe(III) SCO cations with potentially conducting

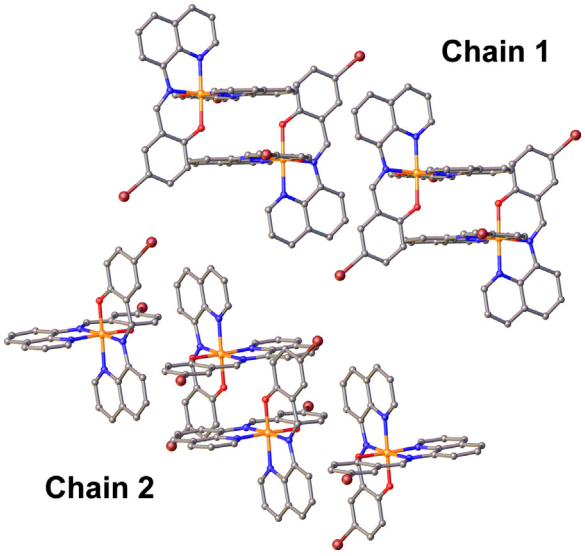

Fig. 18. View of the angular 1D chains in $[Fe(qsal\text{-}5\text{-}Br)_2][Ni(dmit)_2]\cdot CH_2Cl_2$ [132].

anions, $[M^{III}(dithiolene)_2]^-$. The most commonly used cations belong to the $[Fe(qsal\text{-}X)_2]^+$ family of SCO complexes with $[Fe(qsal)_2][Ni(dmit)_2]\cdot 2MeCN$ reported in 2005 [126]. $[Fe(qsal)_2][Ni(dmit)_2]\cdot 2MeCN$ undergoes abrupt and almost complete SCO at 194 K after the first cooling with the compound returning to the HS state at 231 K. This hysteresis is only apparent as subsequent cycles reveal SCO at 231 K in both the heating and warming modes. Despite the large anion, the structure at 273 K is strongly reminiscent of the other $[Fe(qsal)_2]^+$ complexes with 1D chains of the Fe(III) cations formed by orthogonal π–π interactions (see Fig. 2). The $[Ni(dmit)_2]^-$ anions form 1D stacks which sit in between the 1D chains of the $[Fe(qsal)_2]^+$ cations. Loss of solvent gives $[Fe(qsal)_2][Ni(dmit)_2]$ which exhibits very gradual and incomplete SCO (ca. 50% HS at 4 K) [127]. There is complete loss of the 1D $[Fe(qsal)_2]^+$ chains and alternating layers of mixed $[Fe(qsal)_2]^+$ and $[Ni(dmit)_2]^-$ units and $[Ni(dmit)_2]^-$ only stacks. It is clear that as with $[Fe(qsal\text{-}X)_2]^+$ complexes of simple anions the 1D π–π chains are essential for abrupt SCO. Cooperative SCO has been achieved in $[Fe(qsal)_2][Ni(dmise)_2]\cdot 2MeCN$ with SCO occurring at $T_{1/2}\downarrow = 241$ K and $T_{1/2}\uparrow = 256$ K and thus a hysteresis of 15 K [128]. The structure is virtually identical to that of $[Fe(qsal)_2][Ni(dmit)_2]\cdot 2MeCN$ but with the LS structure now available it is clear that in addition to the expected shortening of the Fe–N/O bond lengths (ΔFe-N = 0.169 Å, ΔFe-O = 0.032 Å) there is also reversible slippage of the $[Ni(dmise)_2]^-$ π-dimers.

A number of other anions have been used to prepare $[Fe(qsal)_2][M^{III}(dithiolene)_2]$ systems ($[M^{III}(dithiolene)_2]^- = [Cu^{III}(pds)_2]^-$, $[Au^{III}(pds)_2]^-$ [129], $[Ni(dddt)_2]^-$, $[Ni(pddt)_2]^-$ [130]). Of these only $[Fe(qsal)_2][Ni(dddt)_2]\cdot MeCN\cdot MeOH\cdot H_2O$ exhibits SCO, although it is incomplete and very gradual [130]. The structures of these compounds show high degrees of distortion at the Fe centre caused by significantly non-planar qsal ligands and it is this that is undoubtedly responsible for the lack of SCO in most of these systems. The distortion also results in weak interactions between the $[Fe(qsal)_2]^+$ cations as it is difficult to achieve effective overlap of the aromatic groups.

More recently, Takahashi et al. reported $[Fe(qsal\text{-}5\text{-}I)_2][Ni(dmit)_2]\cdot MeCN\cdot H_2O$ where the spin crossover is coupled to a spin-Peierls-like singlet formation of the paramagnetic $[Ni(dmit)_2]^-$ anions [131]. The SCO is abrupt with a hysteresis of 6 K at *ca.* 150 K. Structural data demonstrate that the SCO and spin-Peierls-like singlet formation are coupled to the reversible loss and formation of I···S interactions between the $[Fe(qsal\text{-}5\text{-}I)_2]^+$ cation and $[Ni(dmit)_2]^-$ anion. Interestingly, the packing of the $[Fe(qsal\text{-}5\text{-}I)_2]^+$ cations is via π–π and C—H···π interactions forming 1D chains rather than the more usual π–π chains. As with $[Fe(qsal)_2][Ni(dmit)_2]\cdot 2MeCN$, the $[Ni(dmit)_2]^-$ anions are present as face-to-face pairs sitting in the channels created by the network formed by the $[Fe(qsal\text{-}5\text{-}I)_2]^+$ cations.

In $[Fe(qsal\text{-}5\text{-}Br)_2][Ni(dmit)_2]\cdot sol$ (sol = CH_2Cl_2, acetone) the acetone solvate shows abrupt SCO with $T_{1/2}\downarrow = 273$ K and $T_{1/2}\uparrow = 286$ K ($\Delta T = 13$ K) while the CH_2Cl_2 solvate exhibits gradual SCO ($T_{1/2}$ *ca.* 270 K) [132]. The structures in the HS and LS states show similar changes in their Fe–N/O bond lengths upon SCO but the packing within the structures is very different. Thus, while both are composed of 1D π–π chains of the cations in the acetone solvate these are identical but in the CH_2Cl_2 solvate neighbouring chains are angled relative to each other resulting in a more open network and therefore lower cooperativity (Fig. 18).

In $[Fe(qsal\text{-}5\text{-}Cl)_2][Ni(dmit)_2]\cdot 2MeCN$ the SCO takes place in two steps at 233 and 256 K and is slightly more abrupt in the 1st lower temperature step [133]. Unusually, the unit cell doubles in size in the region of the spin transition but there is no ordering of the spin centres into HS and LS sites. The packing is virtually identical to that of $[Fe(qsal)_2][Ni(dmit)_2]\cdot 2MeCN$ with closely packed $[Fe(qsal\text{-}5\text{-}Cl)_2]^+$ cations and face-to-face pairs of the $[Ni(dmit)_2]^-$ anions. $[Fe(qsal\text{-}5\text{-}Cl)_2][Ni(\alpha\text{-}tpdt)_2]\cdot MeCN$ is also SCO active although the SCO gradual thought to be due to tight packing between the cation and anionic components of the system [134]. The packing of the $[Fe(qsal\text{-}5\text{-}Cl)_2]^+$ cations involves strong π–π interactions while the anionic units pack at right angles to each other forming zigzag chains. A combination of ferromagnetic and antiferromagnetic interactions results in glassy behaviour with a blocking temperature of 7.5 K. It is interesting to note that in all of these systems clear segregation of the cationic and anionic layers appears to be essential for SCO in $[Fe(qsal)_2][M^{III}(dithiolene)_2]$ materials.

$[Fe(3\text{-}OMe\text{-}salEen)_2][Ni(dmit)_2]\cdot MeOH$ and $[Fe(salEen)_2]_2[Ni(dmit)_2][NO_3]$ both exhibit SCO which is very gradual in the former case ($T_{1/2} = 275$ K) following solvent loss after the 1st heating and incomplete for the latter complex [135]. The structures show segregated cationic and anionic layers with $[Fe(3\text{-}OMe\text{-}salEen)_2]^+$ dimers while the $[Fe(salEen)_2]^+$ cations are linked through N—H···O interactions involving the nitrate anions. The Ni-dithiolene anions form stacks with a greater degree of overlap present in $[Fe(3\text{-}OMe\text{-}salEen)_2][Ni(dmit)_2]\cdot MeOH$. Overall the cooperativity in these systems is very weak.

5.3. *Mixed-valence $[M^{III}(dithiolene)_2]^-$ systems*

Although many of these dithiolene systems were prepared with the aim of producing SCO molecular conductors surprisingly few of the mixed-valence materials have been made. The first, $[Fe(qsal)_2][Ni(dmit)_2]_3\cdot MeCN\cdot H_2O$, was reported in 2006 with the SCO coupled to conductivity of the $[Ni(dmit)_2]$ layers ($\sigma = 2$ S cm^{-1} at 298 K)–the first example of a multifunctional Fe(III) SCO material [136]. The structure shows strong stacking of the $[Ni(dmit)_2]^-$ anions with the $[Fe(qsal)_2]^+$ cations forming a 1D π–π chain aligned with the anionic stacks. Despite this the SCO is rather gradual and incomplete at higher temperatures perhaps hindered by the $[Ni(dmit)_2]^-$ stacks. In 2007, $[Fe(salEen)_2]_2[Ni(dmit)_2]_5\cdot 6MeCN$ was reported, showing gradual but complete SCO between 50 and 300 K. The structures at 290 and 180 K reveal full HS and mostly LS Fe(III) centres, respectively with Fe–N/O bond length changes consistent with incomplete SCO over this temperature range [135]. As with $[Fe(qsal)_2][Ni(dmit)_2]_3$ the anions and cations pack into 1D stacks. However, the conductivity is an order of magnitude lower than $[Fe(qsal)_2][Ni(dmit)_2]_3$ being 0.12 S cm^{-1} at room

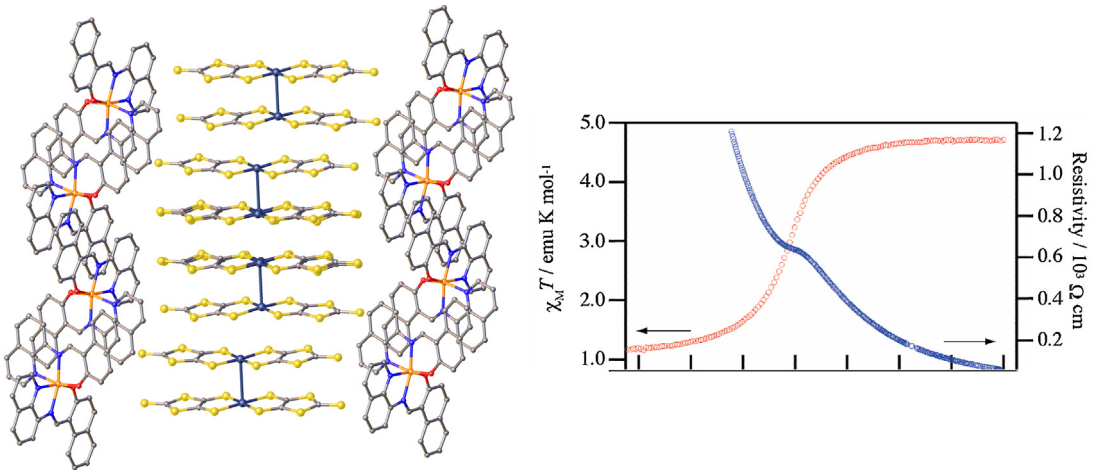

Fig. 19. View of the 1D chains and stacked $[Pd(dmit)_2]^-$ anions in $[Fe(qnal)_2][Pd(dmit)_2]_5$·acetone and the corresponding magnetic and resistivity profile (reproduced from Ref. [137] with permission. (Copyright American Chemical Society, 2008.)

temperature. $[Fe(qnal)_2][Pd(dmit)_2]_5$·acetone is the last compound of this type to be reported [137]. The SCO is moderately abrupt with $T_{1/2}$ = 220 K and shows a clear anomaly in the resistivity at the same temperature as the SCO (Fig. 19). Remarkably, the authors have been able to determine the structure in the LS and HS state which reveals columns of $[Pd(dmit)_2]^-$ and 1D π–π chains of $[Fe(qnal)_2]^+$. Upon SCO there is a considerable change in the Fe–N/O bond lengths (ΔFe-O = 0.03–0.04 Å, ΔFe-O = 0.15–0.18 Å) and more tightly packed $[Fe(qnal)_2]^+$ chains resulting in uniaxial lattice deformation. This in turn impacts the conducting $[Pd(dmit)_2]^+$ layer providing the first structural proof of cooperativity between SCO and conductivity.

6. SCO nanomaterials

SCO nanomaterials remain relatively rare in Fe(III) SCO chemistry and most materials are based on $[Fe(R\text{-}sal_2trien)]^+$. In 2008, Albrecht et al. showed a remarkable dependence of SCO *in solution* on the length of the alkyl chain in $[Fe(4\text{-}OR\text{-}sal_2trien)]NO_3$ with the C_{18} chain showing abrupt SCO ($T_{1/2}$ = 235 K) while the C_6 and C_8 groups are more gradual and incomplete at 200 K [138]. Related complexes with more branched alkyl chains varying in length from C_8 to C_{30} show increasingly abrupt and more complete SCO as the alkyl chains become longer [139] (see Fig. 20). The spin transition temperature is also tuneable over 45 K depending on the length of the alkyl group. The structure of $[Fe(4\text{-}OC_6H_{13}\text{-}sal_2trien)]PF_6$ at 173 K reveals a LS centre and supramolecular organization of the alkyl chains to form polar and non-polar layers [138]. Moreover, SEM studies show that nanorods of $[Fe(4\text{-}OR\text{-}sal_2trien)]^+$ self-assemble into spheres *ca.* 1–3 μm in diameter with these highly organized microstructures thought to be responsible for the cooperative SCO.

In another series of complexes, the sal_2trien ligand was functionalized at the amine nitrogens giving $[Fe(sal_2trien\text{-}(NR)_2)]BF_4$. $[Fe(sal_2trien)]BF_4$ is HS only while increasing the alkyl chain C_6–C_{18} results in compounds exhibiting complete SCO when R = C_{12} and C_{18} [140,141]. As with $[Fe(4\text{-}OR\text{-}sal_2trien)]^+$ increasing the alkyl chain length leads to more abrupt SCO up to C_{12} after which it becomes more gradual again. However, in solution the C_{18} analogue exhibits SCO with a hysteresis of 7 K ($T_{1/2}\downarrow$ = 195 K and $T_{1/2}\uparrow$ = 202 K)–the first observation of hysteretic SCO in solution in any Fe(III) complex. It is interesting to note that in $[Fe(sal_2trien\text{-}(NC_{18}H_{37})_2)]BF_4$ the SCO in the solid state is actually more gradual than that in solution being only 50% complete. The structure of $[Fe(sal_2trien\text{-}(NC_6H_{13})_2)]BF_4$ demonstrates that the half-SCO here is due to two independent Fe(III) centres one of which undergoes SCO while the other remains HS. $[Fe(sal_2trien\text{-}(NC_{12}H_{25})_2)][BF_4]_{0.8}[Br]_{0.2}$ has been used along with an anodic aluminium oxide template to create 1D SCO nanowires [142]. The nanowires undergo SCO but it is slightly less complete than in the bulk material.

Similar dendrimeric SCO materials have been prepared using the salEen ligand framework to make $[Fe(salEen\text{-}OCOR)_2]Cl{\cdot}H_2O$ [143]. The SCO is gradual and incomplete going from 12.5% HS to 70% at

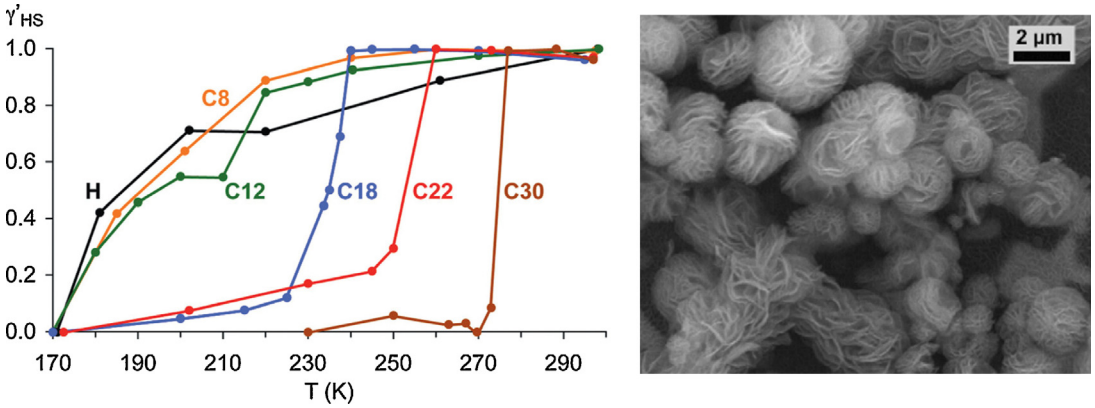

Fig. 20. Magnetic behaviour of $[Fe(4\text{-}OR\text{-}sal_2trien)]NO_3$ (left) and nanostructure (right) of $[Fe(4\text{-}OCH_2C_6H_3\text{-}(OC_{18}H_{37})_2\text{-}sal_2trien)]NO_3$ (reproduced, slightly modified, from Ref. [139] with permission. (Copyright Royal Society of Chemistry, 2012.)

340 K. A detailed ESR study reveals between 4.5 and 50 K antiferromagnetic ordering of the HS and LS Fe(III) centres while between 50 and 200 K a magnetoelectric effect is observed followed by a gradual SCO. Micro and nanomaterials of $[Fe(salEen\text{-}3\text{-}OMe)_2]PF_6$ have been prepared by simple addition of a solution of the complex to an anti-solvent [144]. The microcrystals are needle like while the nanoparticles, *ca.* 18 nm in size, are spherical. As with Fe(II) SCO nanomaterials [145], as the materials become smaller the SCO becomes more gradual with only a minor change in the spin transition temperature, 162 K (bulk) to 153 K (18 nm).

A series of $[Fe(OR\text{-}pap)_2]ClO_4$ ($R = C_8H_{17}$, $C_{10}H_{21}$, $C_{12}H_{25}$, $C_{14}H_{29}$, $C_{16}H_{33}$) dendrimers have been made with the crystal structure of $[Fe(OC_{14}H_{29}\text{-}pap)_2]ClO_4$ determined at 143 K showing a HS Fe(III) centre [146]. As expected the alkyl chains stack next to each other with π–π interactions between the pap ligands forming a 2D plane. Despite this the C_8–C_{14} compounds are all HS and become LS when $R = C_{16}$ with no evidence of significant SCO.

2D nanosheets of $[Fe(qnal)_2]^+$ and $[Fe(qsal)_2]^+$ on graphene oxide and reduced graphene oxide were recently reported by Hayami and co-workers [147]. Only the $[Fe(qnal)_2]^+$ systems are SCO active with the $[Fe(qnal)_2]^+$-reduced graphene oxide showing co-existence of SCO and conductivity, and remarkably LIESST.

7. Physical characteristics of selected iron(III) SCO systems

7.1. Structural characteristics of SCO

7.1.1. Bond length changes and octahedral distortion

As SCO involves moving electrons from the anti-bonding e_g set to the bonding t_{2g} set it is accompanied by a shortening of the Fe–L bond lengths (Tables 4 and 5). Examining all the recent structures reveals that the differences in Fe-L bond lengths vary from *ca.* 0.10–0.13 Å when SCO is complete in line with previous reports concerning iron(III) SCO systems [2,8,9]. However, in contrast with iron(II) compounds where the bond lengths changes are distributed relatively evenly around the Fe centre the changes in Fe(III) are always substantially different. In particular, the Fe—O bonds lengthen by on average only 0.035 Å between the two spin states; in some instances there is no change at all. This compares with an average difference of 0.15 Å for the Fe—N bond distances. But even here there are significant differences depending on whether the N donor is an amine, imine or aromatic nitrogen. Consequently, the average change in Fe-L bond length is too crude a measure to determine if a compound will exhibit abrupt or hysteretic SCO.

Halcrow in a recent review has argued that large changes in octahedral distortion parameters are more often correlated with abrupt SCO [148]. Recent structures reveal that these are remarkably varied with $\Delta\Sigma$ ranging from 2.1 to 47.8. $\Delta\Theta$ is even more variable being 16–148 and is not always correlated with $\Delta\Sigma$ as evidenced by $[TPAFe(cat\text{-}Cl_4)]PF_6$ [33] and the $[Fe(bztpen)(OR)][PF_6]_2$ series [100,101] where despite large $\Delta\Sigma$ values, $\Delta\Theta$ is more modest. This is almost certainly due to the different ligand denticities and donor atoms of the ligands. Nevertheless, trends are clearly evident with both $\Delta\Sigma$ and $\Delta\Theta$ generally higher when the SCO is abrupt and mirror those observed in Fe(II) systems [148]. An interesting exception is $[Fe(Him)_2(4\text{-}OMe\text{-}hapen)]PF_6$ where despite clear SCO based on Fe-L bond lengths $\Delta\Sigma$ and $\Delta\Theta$ are little changed. As has been noted by Halcrow and others [115,148], the conformation of the salen ligand is a more reliable measure of the competency of the Fe(III) to undergo SCO. Moreover, analysis of distortion pathways by Alvarez shows that distortion of octahedral $[Fe(salen\text{-}R)(L)_2]^+$ yields an equatorially vacant pentagonal bipyramid and consequently the O—Fe—O angle is a better measure of this distortion [149]. Thus, it is clear that comparisons of $\Delta\Sigma$ and $\Delta\Theta$ are only valid within specific ligand systems and care is needed in their use.

7.1.2. Solvent effects

Solvent impacts SCO characteristics in some cases quite dramatically for example $[Fe(qsal\text{-}3\text{-}OMe)_2]PF_6{\cdot}nH_2O$ ($n = 0, 2$) where the H_2O solvate is HS only while $[Fe(qsal\text{-}3\text{-}OMe)_2]PF_6$ is LS up to 300 K [46]. However, examining all recent SCO systems it is clear that more often than not different solvents modify the SCO behaviour rather than switching it off. An elegant example is [Fe(napet)NCS]·sol where changing the solvent simplify shifts $T_{1/2}$ [99]. Further insight is provided by [Fe(qsal)(thsa)]·*n*MeCN ($n = 0$, 0.1 and 0.5) where structures for all the compounds reveal that MeCN is progressively lost from a void in the lattice leaving the packing of the Fe(III) centres and consequently the magnetic behaviour unchanged [57]. This suggests that provided that the different solvent, or its loss, does not significantly impact the crystal lattice the SCO behaviour will be modified rather than switched off [47,53,58,68,69]. There is an important caveat, if the solvent tightly fills the void in the lattice then the complex will often be trapped in one spin state [57,99]. Overall, as in Fe(II) complexes [2], the effect of solvent in SCO complexes is still not well understood and whether the solvent will stabilize the LS or HS state cannot be predicted.

7.1.3. Anion effects

The use of different anions in both iron(II) and iron(III) complexes invariably alters their magnetic behaviour. Despite this surprisingly few anions have been explored with NCS, ClO_4, PF_6 and BPh_4 the most common. Moreover, there are comparatively few studies where the anion has been systematically varied. In the $[Fe(qsal\text{-}5\text{-}OMe)_2]Y$ series small anions give LS complexes and intermediate sized anions result in SCO [48]. In contrast, for $[Fe(Him)_2(hapen)]Y$ small anions result in HS behaviour while intermediate to large anions result in SCO active systems [88]. $[FeL][M^{III}(dithiolene)_2]$ complexes often exhibit abrupt and hysteretic SCO (Tables 1–3) possibly due to the fact that the $[M^{III}(dithiolene)_2]^-$ anions are planar and stack into 1D columns thereby increasing cooperativity [126,128,131–133]. It is evident from these examples that there is no general rule and each ligand system is unique in terms of which anions will promote SCO. The reason relates to the different shapes, sizes and supramolecular preferences of the anions which in most cases substantially alter the crystal lattice thereby impacting SCO behaviour. It follows that the effect of the anion on SCO properties is generally more unpredictable than solvent.

7.1.4. Supramolecular cooperativity in iron(III)

As mentioned in the introduction, cooperativity in SCO complexes is mediated by supramolecular interactions. Hydrogen bonding, π–π and C—H···X interactions are the most common supramolecular contacts in iron(III) SCO chemistry (Tables 1–3), and unsurprisingly are also found in Fe(II) [2]. While strong interactions often result in abrupt SCO systems, for instance [Fe(X-Hthsa)(X-thsa)], this is not always the case as evidenced by the $[Fe(X\text{-}salEen)_2]^+$ series. Moreover, abrupt SCO can be achieved with weak π–π interactions, as in $[Fe(qsal\text{-}X)_2]^+$ and $[Fe(qnal)_2]^+$. Interestingly, irrespective of the type of interaction that links the Fe(III) centres abrupt SCO is achieved only when the interactions form 2D sheets. A nice example is $[Fe(qsal\text{-}5\text{-}OMe)_2]Y{\cdot}CH_2Cl_2$ (Y = NCS, PF_6) where loss of the P4AE interaction in going from the NCS to the PF_6 complex results in gradual SCO for the latter [48,50]. Similar behaviour occurs in $[Fe(Him)_2(4\text{-}OMe\text{-}hapen)]Y$ (Y = PF_6, OTf) where the 1D chains are poorly linked in the PF_6 complex (gradual SCO) but closely connected in the OTf analogue (abrupt SCO) [89,90]. Another interesting feature is that many of the complexes

Table 1
SCO behaviour of selected iron(III) complexes with bi- and tridendate ligands.

Compound	Type of SCO	$T_{1/2}$ (K)	ΔT (K)	Principle interactions	Refs.
[(TPA)Fe(cat-Cl_4)]PF_6 (M)	Gradual	214	–	C—H···F	[33]
[(TPA)Fe(cat-Cl_4)]PF_6 (O)	Gradual	203	–	C—H···F	[33]
[(TPA)Fe(cat-Cl_4)]SbF_6	Gradual	250	–	C—H···F	[34]
[(TPA)Fe(cat-NN)]BPh_4	Gradual (I)	*ca.* 150	–	C—H···π	[38]
[(pmae)Fe(cat)]BPh_4	Gradual, 50%	*ca.* 130	–	C—H···π	[39]
[Fe(qsal)$_2$]NCSe	Abrupt	209 (↓), 285 (↑)	76	π–π (2D)	[24,25]
[Fe(qsal)$_2$]NCS	Gradual and abrupt, 2-steps	203 (↓) 210 (↑), 290 (↑)	83, 7	π–π (2D)	[23]
α-[Fe(qsal)$_2$]I_3	Abrupt (m)	240	–	π–π, P4AE	[42]
β-[Fe(qsal)$_2$]I_3	Abrupt	92 (↓), 117 (↑)	25	No structure	[43]
[Fe(qsal)$_2$]$_2$[Fe(NO)$(CN)_5$]	Gradual 50%	122	–	π–π (1D)	[44,45]
[Fe(qsal)$_2$]$_2$[Ru(NO)Cl_5]	Gradual 50%	187 (↓), 190 (↑)	4	No structure	[44]
[Fe(qsal-5-OMe)$_2$]Cl·2MeOH·0.5H_2O	Abrupt 50%	140 (↓), 150 (↑)	10	π–π, P4AE	[47]
[Fe(qsal-5-OMe)$_2$]Cl·MeCN·H_2O	Abrupt - 2 steps	245 (step 1), 275 (step 2)	5 (step 1)	π–π, P4AE	[47]
[Fe(qsal-5-OMe)$_2$]PF_6·sol	Gradual (I)	310 (sol = none) 280 (sol = CH_2Cl_2)	–	π–π (1D, CH_2Cl_2 solvate)	[48,50]
[Fe(qsal-5-OMe)$_2$]NCS·CH_2Cl_2	Abrupt and gradual	305	–	π–π, P4AE	[48]
[Fe(qsal-F)$_2$]NCS	Abrupt and gradual, 2 steps	157 (↓), 170 (↑)	13 (step 1)	π–π, C—H···F	[52]
[Fe(qsal-Cl)$_2$]NCS·MeOH	Abrupt 2 steps	167 (↓), 177 (↑)	10 (step 1)	π–π, P4AE, Cl···π	[52]
[Fe(qsal-Br)$_2$]NCS·MeOH	Gradual 50%	–	–		[52]
[Fe(qsal-Br)$_2$]NO_3·2MeOH	Abrupt, 2 step symmetry-breaking	128 (↓), 144 (↑) 229 (↓), 234 (↑)	16 5	π–π, P4AE	[51]
[Fe(qsal-I)$_2$]OTf	Abrupt	224 (↓), 232 (↑)	8	π–π, P4AE	[53]
[Fe(qsal)$_2$][Ni(dmise)$_2$]·2MeCN	Abrupt	241 (↓), 256 (↑)	15	π–π, C—H···π	[128]
[Fe(qsal-Cl)$_2$][Ni(dmit)$_2$]·2MeCN	Abrupt 2 steps	236, ~260	–	π–π, Cl···π, C—H···S	[133]
[Fe(qsal-Br)$_2$][Ni(dmit)$_2$]·CH_2Cl_2	Gradual	~250	–	π–π, C—H···Br, C—H···S	[132]
[Fe(qsal-Br)$_2$][Ni(dmit)$_2$]·acetone	Abrupt	273 (↓), 286 (↑)	13	π–π, C—H···S	[132]
[Fe(qsal-I)$_2$][Ni(dmit)$_2$]·MeCN·H_2O	Abrupt	150 (↓), 156 (↑)	6	C—H···π, S···I, C—H···S	[131]
[Fe(qsal)(thsa)]·sol	Gradual (I) (sol = 0.4 nBuOH, 0.5 MeCN)	320 (nBuOH), ~300 (MeCN)	–	π–π, N—H···N (MeCN)	[57]
[Fe(salEen)$_2$]ClO_4·sol	Gradual (sol = none, 0.5 H_2O)	155 (0.5 H_2O), 230 (no solvent)	–	π–π (dimer, sol = none), C—H···π (both)	[58]
[Fe(salEen)$_2$]$_2$[Fe(NO)$(CN)_5$]	Gradual	*ca.* 200		C—H···π, C—H···O	[44]
[Fe(3-OMe-salEen)$_2$]PF_6	Abrupt	162.5 (↓), 165.5 (↑)	3	P4AE, N—H···F, C—H···π	[60]
[Fe(4-OMe-salEen)$_2$]PF_6	Gradual	225		N—H···F, C—H···π	[61]
[Fe(4-OMe-salEen)$_2$]NO_3	Abrupt	75.5 (↓), 81 (↑)	7.5	π–π, N—H···O, C—H···O	[61]
[Fe(3,5-Br-salEen)$_2$]BPh_4·DMF	Gradual (I)	–	–	C—H···Br, C—H···π	[62]
[Fe(3-OMe-salEen)(thsa)]	Abrupt (m)	342 (↓), 344 (↑)	2	π–π (dimer), N—H···N	[63]
Li[Fe(5-Br-thsa)$_2$]·H_2O	Abrupt, 2 steps in heating mode	313	39	No structure	[64]
K[Fe(5-Br-thsa)$_2$]	Abrupt, 2 steps	232 (↓, 1st step), 358 (↓, 2nd step), 341 (↑)	52	N—H···O, K–O/S, K···π	[66]
[Fe(Hthsa)(thsa)]·H_2O	Abrupt, 2 steps in cooling mode	232 (↓, 1st step), 262 (↓, 2nd step), 274 (↑)	42 12	N—H···O	[69]
[Fe(5-Cl-Hthsa)(5-Cl-thsa)]·H_2O	Abrupt Abrupt	225 (↓), 228 (↑) 230 (↓), 231 (↑)	3 1	N—H···O	[70][69]
[Fe(5-Br-Hthsa)(5-Br-thsa)]·H_2O	Abrupt, stepped	193 (↓), 195 (↑)	2	No structure	[70]
[Fe(5-Br-Hthsa)(5-Br-thsa)]·H_2O	Abrupt, multistep	144 (↓), 148 (↑) 170 (↓), 173 (↑) 211 (↓), 212 (↑) 238 (↓), 245 (↑)	4 3 1 7	N—H···O	[68]
[Fe(5-Br-Hthsa)(5-Br-thsa)]·0.5H_2O	Abrupt	186 (↓), 188 (↑)	2	No structure	[69]
[Fe(5-Cl-Hthsa-Me)(5-Cl-thsa-Me)]·H_2O	Abrupt, 2 step	245 (↓), 249 (↑) 270 (↓), 278 (↑)	4 8	N—H···O	[71]
[Fe(salpm)$_2$]ClO_4·0.5EtOH	Abrupt (m), 2 steps	115, 171	–	π–π (dimer), C—H···π	[76,77]
[Fe(acpa)$_2$]ClO_4	Gradual and abrupt	265 (gradual), 365 (↓), 378 (↑)	 13	π–π (abrupt)	[78]
[Fe(qnal)$_2$]OTf·MeOH	Abrupt	104 (↓), 115 (↑)	11	π–π	[80]
[Fe(qnal)$_2$]OTf·acetone	Abrupt	130 (↓), 133 (↑)	3	π–π	[80]
[Fe(qnal)$_2$][Pd(dmit)$_2$]$_5$·acetone	Abrupt (m)	220	–	π–π, C—H···S	[137]
[Fe(qnal-7-OMe)$_2$]PF_6·acetone	Abrupt, 2 steps	130 (step 1) 194 (↓), 202 (↑)	–8	π–π, C—H···F	[81]
Fe(qnal-7-OMe)$_2$]BPh_4·2MeOH	Abrupt	194 (↓), 304 (↑)	110	π–π, C—H···π	[81]
[Fe(mph)$_2$]ClO_4·0.5H_2O·0.5MeOH	Abrupt, 2 steps	142 (step 1), 214 (step 2)	–	π–π, N—H···O	[82]
[Fe(pah)$_2$]ClO_4	Multistep (I)	–	–	π–π	[83]
[Fe(pah-*t*-Bu)$_2$]ClO_4	Gradual	280	–	No structure	[83]

I = incomplete, m = moderately.

Table 2
SCO behaviour of selected iron(III) complexes with tetradentate ligands.

Compound	Type of SCO	$T_{1/2}$ (K)	ΔT (K)	Principle interactions	Refs.
$[Fe(Him)_2(3\text{-}OMe\text{-}salen)]PF_6 \cdot H_2O \cdot EtOH$	Abrupt, 2 step	22(↓), 36(↑); 65	14	N—H···O, C—H···F	[85]
$[Fe(Him)_2(3\text{-}OMe\text{-}salen)]AsF_6 \cdot H_2O \cdot EtOH$	Abrupt, 50%	38(↓), 42(↑)	4	N—H···O, C—H···F	[85]
$[Fe(HIm)_2(5\text{-}CO_2Et\text{-}salen)]BPh_4 \cdot EtOH$	Gradual	192	–	C—H···π, C—H···O	[86]
$[Fe(Him)_2(hapen)]BPh_4 \cdot 2MeOH \cdot H_2O$	Very gradual (I)	–	–	C—H···π, N—H···O	[88]
$[Fe(Him)_2(hapen)]OTf \cdot 1.5H_2O$	Gradual (I)	–	–	N—H···O, C—H···O	[88]
$[Fe(Him)_2(hapen)]PF_6 \cdot 2H_2O$	Abrupt	78	–	N—H···O, C—H···F	[88]
$[Fe(Him)_2(hapen)]AsF_6$	Abrupt	69(↓), 74(↑)	5	N—H···O, C—H···F	[87]
$[Fe(Him)_2(4\text{-}OMe\text{-}hapen)]PF_6$	Gradual	150	–	N—H···F, C—H···F	[89]
$[Fe(Him)_2(4\text{-}OMe\text{-}hapen)]OTf$	Abrupt (I)	192(↓), 193(↑)	1	N—H···O, C—H···π	[90]
$[Fe(Him)_2(5\text{-}OMe\text{-}hapen)]PF_6$	Gradual (I)	–	–	N—H···O, C—H···F	[89]
$[Fe(Him)_2(6\text{-}OMe\text{-}hapen)]PF_6$	Gradual (I)	–	–	N—H···O, O—H···O, C—H···F	[89]

I = incomplete, m = moderately.

which contain NCS or NCSe either as ligands, [Fe(napet)NCX]·sol [98,99], or anions, $[Fe(qsal)_2]NCSe$ [23,24] and $[Fe(nap_2trien)]NCS$ [106] more often than not exhibit abrupt SCO. This seems to be due to the presence of extensive C—H···S/Se interactions which are also important in $[Fe(NCS)_2(N\text{-}N)_2]$ SCO systems [150]. The recent discovery of K–π interactions in the hysteretic SCO complex, $K[Fe(Br\text{-}thsa)_2]$ suggests that new supramolecular interactions can be used to improve cooperativity in Fe(III) SCO systems [66]. Despite this particular success, achieving predictable and highly cooperative SCO systems remains a considerable challenge and further work in varying the anion (or cation), ligand types and substituents is needed.

7.2. Light activation in iron(III)

Since 2007, a dozen new LIESST active compounds have been discovered but LIESST still remains relatively uncommon in stark contrast to the many systems for Fe(II) [151]. However, as many of the more abrupt SCO systems have yet to have their photomagnetic behaviour explored it is likely that more LIESST active compounds exist. Despite the small number of systems, T(LIESST) values range from 40 to 100 K and design strategies are becoming clearer [23,44,69,77,80,81,131]. Firstly, larger ΔFe-L values are more likely to result in LIESST as the potential energy wells are further apart thereby increasing the activation energy necessary to relax back to the LS state [151]. Secondly, a high degree of distortion in the HS state also aids LIESST [23] although this must not be too great as the compound may become trapped in the HS state. These two points emphasize that the single coordinate model is not applicable to all light activated SCO complexes and both vibrational and bending modes may need to be considered (Fig. 21). Thirdly, strong interactions while essential for the observation of LIESST in most cases are not a guarantee of it as exemplified by the $[Fe(qsal\text{-}X)_2]^+$ series where despite many hysteretic SCO systems, driven by strong π–π interactions, almost none exhibit LIESST. The reason is thought to be due to an overlap of the LIESST and reverse LIESST bands [23] and emphasizes the need to consider the type of ligand when designing light activated

Table 3
SCO behaviour of selected iron(III) complexes with penta- and hexadendate ligands.

Compound	Type of SCO	$T_{1/2}$ (K)	ΔT (K)	Principle Interactions	Ref.
$[Fe(salten)(n\text{-}py\text{-}N = N\text{-}Ph)]BPh_4$	Gradual (I)	–	–	No structure	[92]
$[Fe(salten\text{-}3\text{-}OMe)(Me\text{-}Im)]BPh_4$	Gradual	215	–	π–π (dimer)	[93]
$[Fe(salpet)(NH_2\text{-}tet)]$	Gradual (I)	–	–	N—H···O, N—H···N	[94]
[Fe(salpet-3-OEt)NCS]	Abrupt	82(↓), 84(↑)	2	C—H···π, C—H···S	[97]
[Fe(salpet-Cl)NCS]	Gradual	280	–	N—H···Cl, π-π, C—H···S	[96]
[Fe(salpet-Cl)NCSe]	Gradual	293	–	N—H···Cl, π-π, C—H···Se	[96]
$[Fe(salpet\text{-}Br)N_3] \cdot MeOH$	Gradual	140	–	N—H···N, C—H···Br	[95]
[Fe(salpet-Br)NCSe]	Gradual	317	–	N—H···Br, π-π, C—H···Se	[95]
[Fe(napet)NCS]	Gradual	174	–	N—H···S, C—H···S	[97]
[Fe(napet)NCS]·MeCN	Abrupt	151	–	N—H···N, C—H···S, C—H···π	[98]
[Fe(napet)NCS]·sol	Abrupt, 50%	84 (sol = butanone)	–	N—H···O, π-π, C—H···π	[99]
	Abrupt (DMF, DMSO)	232(↓), 235(↑) (sol = DMF)	3		
		127(↓), 138(↑) (sol = DMSO)	11		
[Fe(napet)NCSe]·MeCN	Abrupt (m)	170	–	N—H···N, C—H···Se, C—H···π	[98]
[Fe(napet)NCSe]·DMF	Abrupt (m)	244	–	N—H···O, π-π, C—H···π	[99]
[Fe(napet)NCO]	Abrupt (m)	155	–	N—H···O, C—H···π	[98]
$[Fe(napet)N_3]$	Abrupt	117(↓), 122(↑)	5	N—H···N, C—H···π	[98]
α-[Fe(1-napet-Me)NCS]	Abrupt S = 5/2 to 3/2	40(↓), 44(↑)	4	C—H···S, C—H···π	[96]
[Fe(2-napet-Me)NCS]	Gradual (I)	114	–	C—H···S, C—H···π	[96]
$[Fe(bztpen)(OR)][PF_6]_2$	Gradual	158 (OMe), 234 (OEt), 255 (O-nPr), 284 (O-nBu), 278 (O-iBu), 282 (OEtg)	–	–	[100,101]
$[Fe(5\text{-}iPr\text{-}sal_2trien)]PF_6$	Gradual, 50%	157	–	No structure	[103]
$[Fe(5\text{-}tBu\text{-}sal_2trien)]Y$	Gradual, 50% Gradual, 30%	204 –	–	N—H···O, C—H···O	[103]
$[Fe(4\text{-}OH\text{-}sal_2trien)]I$	Gradual 50%	–	–	N—H···O, O—H···I	[104]
$[Fe(3,5\text{-}OMe\text{-}sal_2bapen)]ClO_4$	Gradual, 2 step, symmetry-breaking (I)	*ca.* 110 and 190	–	N—H···O, C—H···O, C—H···π	[102]
$[Fe(nap_2trien)]NCS$	Abrupt and gradual, 2 step symmetry-breaking	142 (step 1), *ca.* 250 (step 2)	–	N—H···S, C—H···π	[106]

I = incomplete, m = moderately.

Table 4
Comparison of the Fe-L bond lengths and distortion parameters for selected iron(III) compounds in the HS and LS state (Å, °).

Compound	ΔFe-O	ΔFe-N	ΔFe-L_{ave}	ΔΣ	ΔΘ	Refs.	Note
Bidentate ligands							
[(TPA)Fe(cat-Cl_4)]PF_6 (M)	0.033	0.160	0.118	40.2	91	[33]	
[(TPA)Fe(cat-Cl_4)]PF_6 (O)	0.046	0.173	0.131	36.4	88	[33]	
Tridentate ligands							
[Fe(qsal)$_2$]NCSe	0.018	0.167	0.117	20.0	123	[24,25]	LS of CH_2Cl_2 solvate
[Fe(qsal)$_2$]NCS	0.003	0.149	0.100	15.5	104	[23]	LS of CH_2Cl_2 solvate
α-[Fe(qsal)$_2$]I_3	0.027	0.148	0.108	26.4	131	[42]	
[Fe(qsal-5-OMe)$_2$]Cl·2MeOH·0.5H_2O	0.033	0.177	0.129	32.3	139	[47]	Two Fe(III) centres
[Fe(qsal-F)$_2$]NCS	0.03	0.164	0.119	33.0	139	[52]	At 200 K, two Fe(III) centres
[Fe(qsal-Br)$_2$]NCS·MeOH	0.039	0.183	0.135	30.0	148	[52]	At 295 K, two Fe(III) centres
[Fe(qsal-Br)$_2$]NO_3·2MeOH	0.021	0.155	0.110	19.5	118	[51]	
[Fe(qsal-I)$_2$]OTf	0.031	0.158	0.116	22.6	128	[53]	
[Fe(qsal)$_2$][Ni(dmise)$_2$]·2MeCN	0.033	0.169	0.124	29.9	140	[128]	
[Fe(qsal-Cl)$_2$][Ni(dmit)$_2$]·2MeCN	0.04	0.157	0.118	36.1	139	[133]	
[Fe(qsal-Br)$_2$][Ni(dmit)$_2$]·CH_2Cl_2	0.036	0.152	0.113	27.3	142	[132]	
[Fe(qsal-Br)$_2$][Ni(dmit)$_2$]·acetone	0.022	0.149	0.107	19.2	119	[132]	
[Fe(qsal-I)$_2$][Ni(dmit)$_2$]·MeCN·H_2O	0.04	0.148	0.112	30.1	129	[131]	
[Fe(salEen)$_2$]ClO_4	0.027	0.132	0.097	11.7	56.3	[58]	
[Fe(salEen)$_2$]ClO_4·0.5H_2O	0.034	0.147	0.109	19.1	84	[58]	
[Fe(salEen)$_2$]$_2$[Fe(NO)(CN)$_5$]	0.024	0.119	0.087	13.3	99	[44]	*ca.* 80% HS at 300 K
[Fe(3-OMe-salEen)$_2$]PF_6	0.051	0.166	0.128	20.8	122	[60]	HS at 200 K
[Fe(4-OMe-salEen)$_2$]PF_6	0.040, 0.035	0.148, 0.132	0.112, 0.100	16.9	101	[61]	Fe1, Fe2
[Fe(4-OMe-salEen)$_2$]NO_3	0.036	0.169	0.125	20.2	118	[61]	293 K nearly full HS
[Fe(salpm)$_2$]ClO_4·0.5EtOH	0.044	0.167	0.126	25.8	129	[76,77]	
[Fe(acpa)$_2$]ClO_4	0.03	0.135	0.100	n/a	n/a	[78]	Gradual polymorph
[Fe(qnal)$_2$]OTf·acetone	0.05	0.12	0.097	n/a	n/a	[80]	
[Fe(qnal-7-OMe)$_2$]PF_6·acetone	0.079	0.119	0.106	18.5	70	[81]	
[Fe(qnal)$_2$][Pd(dmit)$_2$]$_5$·acetone	0.028	0.167	0.121	33.5	144	[137]	
Tetradentate ligands							
[Fe(HIm)$_2$(5-CO_2Et-salen)]BPh_4·EtOH	-0.001	0.157	0.104	2.1	34	[86]	
[Fe(Him)$_2$(4-OMe-hapen)]PF_6	0.000	0.145	0.097	8.7	20	[89]	
Pentadentate ligands							
[Fe(salpet-3-OEt)NCS]	0.040	0.150	0.113	28.2	72	[97]	
[Fe(napet)NCS]	0.044	0.145	0.111	29.3	94	[97]	
[Fe(napet)NCS]·MeCN	0.034	0.142	0.106	25.4	70	[98]	LS is close to $T_{1/2}$
[Fe(napet)NCSe]·MeCN	0.049	0.148	0.115	31.0	107	[98]	
[Fe(napet)NCSe]·DMF	0.051	0.154	0.120	31.3	94	[99]	
[Fe(napet)NCO]	0.058	0.130	0.106	25.7	69	[98]	
[Fe(bztpen)(OMe)][PF_6]$_2$	-0.009	0.116	0.095	28.1	17	[100]	
[Fe(bztpen)(OEt)][PF_6]$_2$	0.015	0.128	0.105	29.2	21	[101]	
[Fe(bztpen)(OPr)][PF_6]$_2$	0.011	0.133	0.108	23.7	16	[101]	
Hexadentate ligands							
[Fe(nap$_2$trien)]NCS	0.022	0.132	0.095	25.0	97	[106]	

SCO systems. In this regard [Fe(qnal-$X)_2$]$^+$ complexes are promising with all compounds exhibiting LIESST suggesting that qnal-X is particularly suitable for light activation [80,81]. Finally, the observation of LIESST in the [Fe(sal$_2$trien)][Mn{Cr(ox)$_3$}]·sol networks [120,122] suggests that provided that 2D and 3D networks of Fe(III) centres can be made these may also be expected to exhibit LIESST.

7.3. Mössbauer spectroscopic studies

Mössbauer spectroscopy so useful in elucidating structural details in Fe(II) SCO systems is much less effective in the case of Fe(III). This stems from the spin interconversion rate often being comparable to the Mössbauer timescale (*ca.* 10–1000 ns) resulting in broader doublets and a loss of detail [9]. Consequently, despite the large number of new SCO systems reported only a third have been studied by Mössbauer spectroscopy. As in Fe(II) systems, the isomer shift, δ and quadrupolar coupling, ΔE_Q are characteristic of the spin state. In the HS state, δ varies between 0.25 and 0.70 mms^{-1} with a small quadrupolar splitting of 0.30–1.00 mms^{-1}, the latter a consequence of the symmetric HS d^5 electronic configuration. By comparison, LS isomer shifts are between 0.05 and 0.40 mms^{-1} with ΔE_Q = 1.90–2.80 mms^{-1}; the larger quadrupolar splitting due to the t_{2g} set being incompletely filled. The slight overlap in the isomer shifts of the two spin states means that both δ and ΔE_Q are needed to correctly identify the spin state.

A particular feature of Fe(III) systems is that, in contrast to Fe(II), the spectra are often asymmetric [47,57,70,77,102,106,132]. This may occur in the HS state, LS state and sometimes both. This asymmetry has been attributed both to bond anisotropy [78] and rapid spin interconversion [47,48,53,106]. In the HS state, as the

Table 5
Comparison of the Fe-L bond lengths and distortion parameters in the HS and LS state for Fe-thsa compounds (Å, °).

Compound	ΔFe-O_{ave}	ΔFe-N_{ave}	ΔFe-S_{ave}	ΔFe-L_{ave}	ΔΣ	ΔΘ	Refs.
K[Fe(5-Br-thsa)$_2$]	0.016	0.198	0.190	0.135	47.8	145	[66]
[Fe(5-Br-Hthsa)(5-Br-thsa)]·H_2O	0.015	0.188	0.192	0.132	40.9	134	[68]
[Fe(5-Cl-Hthsa-Me)(5-Cl-thsa-Me)]·H_2O	−0.01	0.177	0.174	0.114	39.8	133	[71]

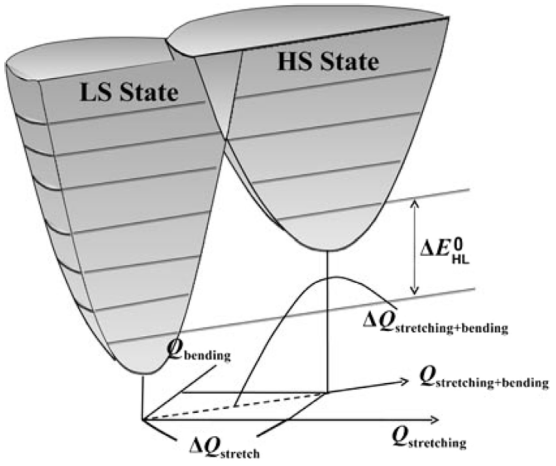

Fig. 21. Potential energy wells of the HS and LS states showing the contribution of stretching and bending (reproduced with permission from Ref. [23]. (Copyright Wiley-VCH, 2009.)

temperature is higher, spin interconversion is the more probable explanation. Indeed, in [Fe(nap_2trien)]NCS the interconversion is so rapid that the HS doublet is replaced by broad singlet [106]. A further problem is that the number of crystallographic Fe(III) sites is rarely correlated with the number of doublets. For instance, [Fe(qsal-$F)_2$]NCS [52] and [Fe(3,5-OMe-sal_2bapen)]ClO_4 [102] contain 2 and 3 sites, respectively but only a single doublet is observed. However, in [Fe(X-Hthsa)(X-thsa)]·sol (X = H, Cl, Br) despite the presence of a single crystallographic Fe(III) site two HS and LS doublets are observed [69]. In some instances Mössbauer spectroscopy can be extremely informative as it was in the identification of [Fe($salpm)_2$]ClO_4·0.5EtOH as a symmetry-breaking SCO compound [77]. Despite this Mössbauer spectroscopy in Fe(III) remains a supplementary technique. Perhaps the greater availability of synchrotron radiation will permit the use of nuclear forward scattering (NFS) or nuclear inelastic scattering (NIS) techniques to give Mössbauer parameters with higher resolution making it more widely applicable to Fe(III) SCO systems.

7.4. Other techniques

EPR spectroscopy can be valuable tool for exploring SCO in Fe(III) systems [9], although few studies have been done since 2007. These confirm earlier reports with the HS state ($S = 5/2$) characterized by a broad signal varying from $g = \sim 4.0–4.5$. The breadth and low intensity of the signal usually prevents observation of hyperfine coupling. In contrast, the LS state is generally sharp with rhombic and tetragonal systems easily distinguishable. In some cases hyperfine coupling is also observable which can provide extra information about the electronic structure of the complex. EPR spectroscopy has been particularly useful in [(TPA)Fe(Cat-R)]$^+$ where the degree of Fe(III)-catecholate character in the electronic structure can be determined [37]. Despite this, EPR spectroscopy remains much under used probably because SCO is more readily characterized by magnetic susceptibility measurements.

An area that has seen significant development in the last 10–15 years is computational modelling of SCO compounds. Several reviews have appeared recently on this subject and although, most studies have focused on Fe(II) SCO chemistry, Fe(III) systems have been considered [152–154]. DFT calculations have become the standard method for calculating the electronic structures of the two spin states and the resulting HS–LS gap. Early on it became clear that large basis sets were vital to adequately model SCO complexes [155]. Thus, basis sets such as 6-311-G** or cc-pVTZ are recommended for Gaussian type and Slater type orbitals, respectively. Extensive studies show that 'pure' functionals tend to overstabilise the LS state while Hartree–Fock (HF) methods favour the HS state [156]. Hybrid functionals fall in between these extremes and are most commonly used particularly B3LYP. In exploring the prototypical SCO complex [Fe($NCS)_2$(phen)$_2$] Reiher adjusted the HF exchange in B3LYP to 15% (termed B3LYP*) giving better agreement with experiment [157]. However, Hughes and Friesner argue that for Fe(III) this actually leads to larger spin state errors and suggest a local orbital correction to B3LYP [158]. In contrast, Jensen recommends TPSSh (10% HF exchange) [159] while Swart suggests OPBE [160] and Neese the double-hybrid orbital B2PLYP [161]. Highly accurate spin state energies have been reported for the CASPT2 method [162]. Although, the study concerned Fe(II) and Co(II) systems it should be applicable to Fe(III) systems but it is time consuming. It is clear that no single functional or method works well with every SCO system and careful validation is required in each case.

Combining molecular mechanics and ligand field parameters using an LFMM approach Deeth has been able to design and screen a series Fe(II) SCO complexes [163]. Now that there is a larger database of Fe(III) SCO systems LFMM studies could potentially lead to new Fe(III) SCO systems. Moreover, as computational methods become more efficient it is likely that structure-function relationships will become clearer permitting more rational design of SCO systems.

8. Conclusions

The last 10 years have seen significant growth in iron(III) SCO chemistry and the appearance of almost 30 hysteretic SCO systems, 12 of which exhibit hystereses greater than 10 K. The spin transition temperature in the various systems is remarkably variable ranging from 20 to 380 K probably due to the wide variety of donor sets, N_4O_2, $N_2O_2S_2$, N_3O_2S and N_5O, capable of supporting SCO. It is increasingly evident that there are more similarities between Fe(II) and Fe(III) SCO chemistry than differences, something previously noted by van Koningsbruggen et al. in 2004 [8]. Most recent research has focused on Schiff bases with tridentate N_2O and ONS ligands particularly effective in accessing abrupt SCO systems. Indeed, half of all symmetry breaking iron(III) SCO systems and [Fe(qnal-7-OMe)$_2$]BPh_4·2MeOH (110 K), which has the widest hysteresis in iron(III) chemistry, contain tridentate ligands. Part of the success of the tridentate ligand class is the effective use of supramolecular interactions including π–π, C—H···π and hydrogen bonding interactions to increase cooperativity. Halogen bonding, now finding widespread use in supramolecular chemistry, remains in its infancy in SCO research but already shows promise with I···S interactions key to the magnetic behaviour of [Fe(qsal-5-I)$_2$][Ni(dmit)$_2$]·MeCN·H_2O. Given the strength and directionality of halogen bonds further research in this area would be expected to yield many abrupt SCO systems.

As the structures of compounds in both spin states has grown it has become increasingly clear that more abrupt SCO is generally associated with larger changes in Fe-ligand bond lengths and greater changes in the distortion at the Fe(III) centre, mirroring the trend observed for iron(II). Moreover, structures close to the spin transition temperature show reorganization of the supramolecular sphere prior to actual SCO. As in Fe(II) SCO chemistry [17] the systems with the most abrupt and hysteretic SCO are mononuclear probably as a result of better control of the supramolecular connectivity in these complexes.

Light activated iron(III) SCO compounds while still rare, are now known for several ligand systems with the qnal ligand class and those incorporating metal dithiolenes the most notable. LIESST has

also been demonstrated in network materials, [Fe(X-sal$_2$trien)]-[Mn{Cr(ox)$_3$}]·sol where there is limited cooperativity and suggests a new strategy for accessing light activated materials with iron(III).

Despite these extraordinary successes, there still remain large gaps in iron(III) SCO chemistry. Dinuclear complexes are confined to two ligand systems neither of which show abrupt SCO in contrast to the many examples in iron(II) chemistry [164–167]. Higher oligomeric systems such as trinuclear, tetranuclear and above are essentially unknown for Fe(III). SCO networks are also extremely limited and no 2D or 3D networks of connected iron(III) SCO centres are yet known. Given the success that has been achieved in iron(II) SCO chemistry with [Fe(py-R)$_2${M(CN)$_4$}] [168,169] this is an area that would be expected to be developed further in the future.

Finally, iron(III) SCO nanomaterials show great potential with abrupt SCO in solution now a reality. Once again the fact that the studies of SCO nanomaterials remain very limited should provide a fruitful area of discovery as iron(III) SCO chemistry moves into a new exciting age of development.

Acknowledgements

We would like to gratefully acknowledge the Thailand Research Fund (RSA5580028 and RSA5880048) for funding our research in iron(III) spin crossover chemistry. We also thank Professor Keith Murray for comments on earlier versions of this manuscript. Structural figures for this review were drawn in OLEX2 [170] with CIF files taken from the CCDC (www.ccdc.cam.ac.uk).

References

[1] M.A. Halcrow, ed., Spin-Crossover Materials: Properties and Applications, John Wiley & Sons, Ltd, Chichester, 2013.
[2] P. Gütlich, A.B. Gaspar, Y. Garcia, Beilstein J. Org. Chem. 9 (2013) 342–391.
[3] P. Gütlich, H.A. Goodwin, Top. Curr. Chem. 233 (2004) 1–47.
[4] A. Hauser, Top. Curr. Chem. 234 (2004) 155–198.
[5] V. Ksenofontov, A.B. Gaspar, P. Gütlich, Top. Curr. Chem. 235 (2004) 23–64.
[6] J.-F. Létard, J. Mater. Chem. 16 (2006) 2550–2559.
[7] A. Cannizzo, C.J. Milne, C. Consani, W. Gawelda, C. Bressler, F. van Mourik, M. Chergui, Coord. Chem. Rev. 254 (2010) 2677–2686.
[8] P.J. van Koningsbruggen, Y. Maeda, H. Oshio, Top. Curr. Chem. 233 (2004) 259–324.
[9] M. Nihei, T. Shiga, Y. Maeda, H. Oshio, Coord. Chem. Rev. 251 (2007) 2606–2621.
[10] J.-F. Létard, P. Guionneau, L. Goux-Capes, Top. Curr. Chem. 235 (2004) 221–249.
[11] P. Gamez, J.S. Costa, M. Quesada, G. Aromí, Dalton Trans. (2009) 7845–7853.
[12] M.A. Halcrow, Coord. Chem. Rev. 253 (2009) 2493–2514.
[13] A.B. Gaspar, M. Seredyuk, P. Gütlich, J. Mol. Struct. 924–926 (2009) 9–19.
[14] Y. Sunatsuki, R. Kawamoto, K. Fujita, H. Maruyama, T. Suzuki, H. Ishida, M. Kojima, S. Iijima, N. Matsumoto, Coord. Chem. Rev. 254 (2010) 1871–1881.
[15] J. Olguín, S. Brooker, Coord. Chem. Rev. 255 (2011) 203–240.
[16] G.A. Craig, O. Roubeau, G. Aromí, Coord. Chem. Rev. 269 (2014) 13–31.
[17] M.A. Halcrow, Chem. Lett. 43 (2014) 1178–1188.
[18] S. Brooker, Chem. Soc. Rev. 44 (2015) 2880–2892.
[19] K.S. Murray, C.J. Kepert, Top. Curr. Chem. 233 (2004) 195–228.
[20] P. Guionneau, Dalton Trans. 43 (2014) 382–393.
[21] J. Tao, R.-J. Wei, R.-B. Huang, L.-S. Zheng, Chem. Soc. Rev. 41 (2012) 703–737.
[22] S. Hayami, Z. Gu, M. Shiro, Y. Einaga, A. Fujishima, O. Sato, J. Am. Chem. Soc. 122 (2000) 7126–7127.
[23] S. Hayami, K. Hiki, T. Kawahara, Y. Maeda, D. Urakami, K. Inoue, M. Ohama, S. Kawata, O. Sato, Chem. Eur. J. 15 (2009) 3497–3508.
[24] S. Hayami, Z. Gu, H. Yoshiki, A. Fujishima, O. Sato, J. Am. Chem. Soc. 123 (2001) 11644–11650.
[25] S. Hayami, T. Kawahara, G. Juhasz, K. Kawamura, K. Uehashi, O. Sato, Y. Maeda, J. Radioanal. Nucl. Chem. 255 (2003) 443–447.
[26] M. Nakamura, Coord. Chem. Rev. 250 (2006) 2271–2294.
[27] L. Cambi, L. Szegö, Chem. Ber. Dtsch. Ges. 64 (1931) 2591–2598.
[28] L. Cambi, L. Szegö, Chem. Ber. Dtsch. Ges. 66 (1933) 656–661.
[29] T.A. Ivanova, O.A. Turanova, I.V. Ovchinnikov, B. Andgheevskii, M. Augustyniak-Jablokow, Appl. Magn. Reson. 40 (2011) 21–30.
[30] A.N. Garg, S. Singhal, K. Chandra, Hyperfine Interact. 185 (2008) 151–157.
[31] S. Singhal, A.N. Garg, K. Chandra, J. Alloy. Compd. 443 (2007) 53–60.
[32] C. Cook, F. Habib, T. Aharen, R. Clérac, A. Hu, M. Murugesu, Inorg. Chem. 52 (2013) 1825–1831.
[33] E. Collet, M.L. Boillot, J. Hebert, N. Moisan, M. Servol, M. Lorenc, L. Toupet, M. Buron-Le Cointe, A. Tissot, J. Sainton, Acta Crystallogr. Sect. B Struct. Sci. 65 (2009) 474–480.
[34] W. Kaszub, M. Buron-Le Cointe, M. Lorenc, M.-L. Boillot, M. Servol, A. Tissot, L. Guérin, H. Cailleau, E. Collet, Eur. J. Inorg. Chem. (2013) 992–1000.
[35] E. Collet, N. Moisan, C. Baldé, R. Bertoni, E. Trzop, C. Laulhé, M. Lorenc, M. Servol, H. Cailleau, A. Tissot, M.-L. Boillot, T. Graber, R. Henning, P. Coppens, M.B.-L. Cointe, Phys. Chem. Chem. Phys. 14 (2012) 6192.
[36] A. Tissot, H.J. Shepherd, L. Toupet, E. Collet, J. Sainton, G. Molnár, P. Guionneau, M.L. Boillot, Eur. J. Inorg. Chem. (2013) 1001–1008.
[37] J.J. Girerd, M.L. Boillot, G. Blain, E. Rivière, Inorg. Chim. Acta 361 (2008) 4012–4016.
[38] C.R. Tichnell, D.A. Shultz, C.V. Popescu, I. Sokirniy, P.D. Boyle, Inorg. Chem. 54 (2015) 4466–4474.
[39] F. Yu, Y.-M. Zhang, A.-H. Li, B. Li, Inorg. Chem. Commun. 51 (2015) 87–89.
[40] B. Djukic, H.A. Jenkins, T. Seda, M.T. Lemaire, Transition Met. Chem. 38 (2012) 207–212.
[41] Y. Kojima, K. Kato, Y. Yamamoto, K. Inoue, S. Hayami, Acta Crystallogr. Sect. E Struct. Rep. 66 (2010) m204.
[42] K. Takahashi, T. Sato, H. Mori, H. Tajima, O. Sato, Physica B 405 (2010) S65–S68.
[43] K. Takahashi, T. Sato, H. Mori, H. Tajima, Y. Einaga, O. Sato, Hyperfine Interact. 206 (2012) 1–5.
[44] C. Faulmann, J. Chahine, L. Valade, G. Chastanet, J.F. Létard, D. De Caro, Eur. J. Inorg. Chem. 5 (2013) 1058–1067.
[45] T. Togo, S.A. Amolegbe, R. Yamaguchi, T. Kuroda-Sowa, M. Nakaya, K. Shimayama, M. Nakamura, S. Hayami, Chem. Lett. 42 (2013) 1542–1544.
[46] J.C. Dias, B. Vieira, I.C. Santos, L.C.J. Pereira, V. Da Gama, Inorg. Chim. Acta 362 (2009) 2076–2079.
[47] D.J. Harding, D. Sertphon, P. Harding, K.S. Murray, B. Moubaraki, J.D. Cashion, H. Adams, Chem. Eur. J. 19 (2013) 1082–1090.
[48] D. Sertphon, D.J. Harding, P. Harding, K.S. Murray, B. Moubaraki, J.D. Cashion, H. Adams, Eur. J. Inorg. Chem. (2013) 788–795.
[49] V. Russell, M. Scudder, I. Dance, J. Chem. Soc., Dalton Trans. (2001) 789–799.
[50] D. Sertphon, D.J. Harding, P. Harding, K.S. Murray, B. Moubaraki, H. Adams, A. Alkaş, S.G. Telfer, Eur. J. Inorg. Chem. (2016) 432–438.
[51] D.J. Harding, W. Phonsri, P. Harding, K.S. Murray, B. Moubaraki, G.N.L. Jameson, Dalton Trans. 44 (2015) 15079–15082.
[52] W. Phonsri, D.J. Harding, P. Harding, K.S. Murray, B. Moubaraki, I.A. Gass, J.D. Cashion, G.N.L. Jameson, H. Adams, Dalton Trans. 43 (2014) 17509–17518.
[53] D.J. Harding, W. Phonsri, P. Harding, I.A. Gass, K.S. Murray, B. Moubaraki, J.D. Cashion, L. Liu, S.G. Telfer, Chem. Commun. 49 (2013) 6340–6342.
[54] M. Shatruk, H. Phan, B.A. Chrisostomo, A. Suleimenova, Coord. Chem. Rev. 289–290 (2015) 62–73.
[55] B. Djukic, P.A. Dube, F. Razavi, T. Seda, H.A. Jenkins, J.F. Britten, M.T. Lemaire, Inorg. Chem. 48 (2009) 699–707.
[56] B. Djukic, M.T. Lemaire, Inorg. Chem. 48 (2009) 10489–10491.
[57] W. Phonsri, C.G. Davies, G.N.L. Jameson, B. Moubaraki, K.S. Murray, Chem. Eur. J. 22 (2016) 1322–1333.
[58] C.-F. Sheu, S.-M. Chen, G.-H. Lee, Y.-H. Liu, Y.-S. Wen, J.-J. Lee, Y.-C. Chuang, Y. Wang, Eur. J. Inorg. Chem. (2013) 894–901.
[59] M.S. Haddad, M.W. Lynch, W.D. Federer, D.N. Hendrickson, Inorg. Chem. 20 (1981) 123–131.
[60] A. Tissot, R. Bertoni, E. Collet, L. Toupet, M.-L. Boillot, J. Mater. Chem. 21 (2011) 18347.
[61] A. Tissot, P. Fertey, R. Guillot, V. Briois, M.-L. Boillot, Eur. J. Inorg. Chem. (2014) 101–109.
[62] P.N. Martinho, A.I. Vicente, S. Realista, M.S. Saraiva, A.I. Melato, P. Brandão, L.P. Ferreira, M.D.D. Carvalho, J. Organomet. Chem. 760 (2014) 48–54.
[63] W. Phonsri, V. Martinez, C.G. Davies, G.N.L. Jameson, B. Moubaraki, K.S. Murray, Chem. Commun. 52 (2016) 1443–1446.
[64] S. Floquet, M.-L. Boillot, E. Rivière, F. Varret, K. Boukheddaden, D. Morineau, P. Négrier, New J. Chem. 27 (2003) 341–348.
[65] S. Floquet, N. Guillou, P. Négrier, E. Rivière, M.-L. Boillot, New J. Chem. 30 (2006) 1621–1627.
[66] S. Kang, Y. Shiota, A. Kariyazaki, S. Kanegawa, K. Yoshizawa, O. Sato, Chem. Eur. J. 22 (2016) 532–538.
[67] A. Krupska, M.A. Augustyniak-Jablokow, V.V. Yablokov, Y.V. Zelentsov, V.A. Ulanov, J. Mrozinski, Acta Phys. Pol. A 110 (2006) 81–95.
[68] Z.-Y. Li, J.-W. Dai, Y. Shiota, K. Yoshizawa, S. Kanegawa, O. Sato, Chem. Eur. J. 19 (2013) 12948–12952.
[69] E.W.T. Yemeli, G.R. Blake, A.P. Douvalis, T. Bakas, G.O.R. Alberda van Ekenstein, P.J. van Koningsbruggen, Chem. Eur. J. (2010), http://dx.doi.org/10.1002/chem.201002100.
[70] S. Floquet, E. Rivière, K. Boukheddaden, D. Morineau, M.L. Boillot, Polyhedron 80 (2014) 60–68.
[71] Z.-Y. Li, J.-W. Dai, K.J. Gagnon, H.-L. Cai, T. Yamamoto, Y. Einaga, H.-H. Zhao, S. Kanegawa, O. Sato, K.R. Dunbar, R.-G. Xiong, Dalton Trans. 42 (2013) 14685–14688.
[72] S. Hayami, K. Hashiguchi, K. Inoue, Y. Maeda, J. Nucl. Radiochem. Sci. 5 (2004) N1–N3.
[73] S. Floquet, M.C. Muñoz, R. Guillot, E. Rivière, G. Blain, J.A. Réal, M.L. Boillot, Inorg. Chim. Acta 362 (2009) 56–64.
[74] E.W.Y. Tido, G.O.R.A. van Ekenstein, A. Meetsma, P.J. van Koningsbruggen, Inorg. Chem. 47 (2008) 143–153.
[75] E.W.Y. Tido, C. Faulmann, R. Roswanda, A. Meetsma, P.J. van Koningsbruggen, Dalton Trans. 39 (2010) 1643–1651.

[76] M.S. Shongwe, B.A. Al-Rashdi, H. Adams, M.J. Morris, M. Mikuriya, G.R. Hearne, Inorg. Chem. 46 (2007) 9558–9568.
[77] K.D. Murnaghan, C. Carbonera, L. Toupet, M. Griffin, M.M. Dîrtu, C. Desplanches, Y. Garcia, E. Collet, J.-F. Létard, G.G. Morgan, Chem. Eur. J. 20 (2014) 5613–5618.
[78] S. Hayami, D. Urakami, Y. Yamamoto, K. Kato, Y. Kojima, S. Nakashima, K. Inoue, Chem. Lett. 39 (2010) 328–329.
[79] H. Ando, Y. Nakao, H. Sato, S. Sakaki, J. Phys. Chem. A 111 (2007) 5515–5522.
[80] T. Shimizu, Y. Komatsu, H. Kamihata, Y.H. Lee, A. Fuyuhiro, S. Iijima, S. Hayami, J. Incl. Phenom. Macrocycl. Chem. 71 (2011) 363–369.
[81] M. Nakaya, K. Shimayama, K. Takami, K. Hirata, A.S. Alao, M. Nakamura, L.F. Lindoy, S. Hayami, Chem. Lett. 43 (2014) 1058–1060.
[82] J. Tang, J. Sánchez Costa, S. Smulders, G. Molnár, A. Bousseksou, S.J. Teat, Y. Li, G.A. van Albada, P. Gamez, J. Reedijk, Inorg. Chem. 48 (2009) 2128–2135.
[83] M.S. Shongwe, S.H. Al-Rahbi, M.A. Al-Azani, A.A. Al-Muharbi, F. Al-Mjeni, D. Matoga, A. Gismelseed, I.A. Al-Omari, A. Yousif, H. Adams, M.J. Morris, M. Mikuriya, Dalton Trans. 41 (2012) 2500–2514.
[84] R. Saha, S. Biswas, I.M. Steele, K. Dey, G. Mostafa, Dalton Trans. 40 (2011) 3166–3175.
[85] K. Hanahara, H. Ono, T. Fujinami, N. Matsumoto, Y. Sunatsuki, Inorg. Chim. Acta 429 (2015) 93–98.
[86] T. Fujinami, D. Hamada, N. Matsumoto, Y. Sunatsuki, R. Irie, Inorg. Chim. Acta 430 (2015) 239–244.
[87] T. Fujinami, M. Koike, N. Matsumoto, Y. Sunatsuki, A. Okazawa, N. Kojima, Inorg. Chem. 53 (2014) 2254–2259.
[88] M. Koike, K. Murakami, T. Fujinami, K. Nishi, N. Matsumoto, Y. Sunatsuki, Inorg. Chim. Acta 399 (2013) 185–192.
[89] T. Fujinami, M. Ikeda, M. Koike, N. Matsumoto, T. Oishi, Y. Sunatsuki, Inorg. Chim. Acta 432 (2015) 89–95.
[90] K. Miyano, T. Nishida, H. Ono, D. Hamada, T. Fujinami, N. Matsumoto, Y. Sunatsuki, Inorg. Chim. Acta 439 (2016) 49–54.
[91] M. Okuhata, Y. Funasako, K. Takahashi, T. Mochida, Chem. Commun. 49 (2013) 7662–7664.
[92] A. Bannwarth, S.O. Schmidt, G. Peters, F.D. Sönnichsen, W. Thimm, R. Herges, F. Tuczek, Eur. J. Inorg. Chem. (2012) 2776–2783.
[93] S. Imatomi, T. Sato, T. Hamamatsu, R. Kitashima, N. Matsumoto, Bull. Chem. Soc. Jpn. 80 (2007) 2375–2377.
[94] R. Herchel, Z. Trávníček, Dalton Trans. 42 (2013) 16279–16288.
[95] C. Krüger, P. Augustín, L. Dlháň, J. Pavlik, J. Moncol', I. Nemec, R. Boča, F. Renz, Polyhedron 87 (2015) 194–201.
[96] C. Krüger, P. Augustín, I. Nemec, Z. Trávníček, H. Oshio, R. Boča, F. Renz, Eur. J. Inorg. Chem. (2013) 902–915.
[97] P. Masárová, P. Zoufalý, J. Moncol, I. Nemec, J. Pavlik, M. Gembický, Z. Trávníček, R. Boča, I. Šalitroš, New J. Chem. 39 (2015) 508–519.
[98] I. Nemec, R. Herchel, R. Boča, Z. Trávníček, I. Svoboda, H. Fuess, W. Linert, Dalton Trans. 40 (2011) 10090–10099.
[99] I. Nemec, R. Herchel, Z. Trávníček, Dalton Trans. 44 (2015) 4474–4484.
[100] N.A. Ortega-Villar, M.C. Muñoz, J.A. Real, Eur. J. Inorg. Chem. (2010) 5563–5567.
[101] N. Ortega-Villar, A.Y. Guerrero-Estrada, L. Pin˜eiro-Loípez, M.C. Mun˜oz, M. Flores-álamo, R. Moreno-Esparza, J.A. Real, V.M. Ugalde-Saldívar, Inorg. Chem. 54 (2015) 3413–3421.
[102] M. Griffin, S. Shakespeare, H.J. Shepherd, C.J. Harding, J.-F. Létard, C. Desplanches, A.E. Goeta, J.A.K. Howard, A.K. Powell, V. Mereacre, Y. Garcia, A.D. Naik, H. Müller-Bunz, G.G. Morgan, Angew. Chem. Int. Ed. 50 (2011) 896–900.
[103] R. Pritchard, S.A. Barrett, C.A. Kilner, M.A. Halcrow, Dalton Trans. (2008) 3159–3168.
[104] I. Nemec, R. Herchel, I. Šalitroš, Z. Trávníček, J. Moncol, H. Fuess, M. Ruben, W. Linert, CrystEngComm 14 (2012) 7015–7024.
[105] A.J. Fitzpatrick, H.M. O'Connor, G.G. Morgan, Dalton Trans. 44 (2015) 20839–20842.
[106] B.J.C. Vieira, J.T. Coutinho, I.C. Santos, L.C.J. Pereira, J.C. Waerenborgh, V. da Gama, Inorg. Chem. 52 (2013) 3845–3850.
[107] G. Brewer, L.J. Alvarado, C.T. Brewer, R.J. Butcher, J. Cipressi, C. Viragh, P.Y. Zavalij, Inorg. Chim. Acta 421 (2014) 100–109.
[108] I. Nemec, R. Boča, R. Herchel, Z. Trávníček, M. Gembický, W. Linert, Montash. Chem. 140 (2009) 815–828.
[109] R. Boča, I. Nemec, I. Šalitroš, J. Pavlik, R. Herchel, F. Renz, Pure Appl. Chem. 81 (2009) 1357–1383.
[110] T. Fujinami, K. Nishi, R. Kitashima, K. Murakami, N. Matsumoto, S. Iijima, K. Toriumi, Inorg. Chim. Acta 376 (2011) 136–143.
[111] I. Šalitroš, R. Boča, L. Dlháň, M. Gembický, J. Kožíšek, J. Linares, J. Moncol, I. Nemec, L. Perašínová, F. Renz, I. Svoboda, H. Fuess, Eur. J. Inorg. Chem. (2009) 3141–3154.
[112] B. Djukic, P.K. Poddutoori, P.A. Dube, T. Seda, H.A. Jenkins, M.T. Lemaire, Inorg. Chem. 48 (2009) 6109–6116.
[113] F. Renz, S. Jung, M. Klein, M. Menzel, A.F. Thünemann, Polyhedron 28 (2009) 1818–1821.
[114] R. Boča, I. Šalitroš, J. Kožíšek, J. Linares, J. Moncol, F. Renz, Dalton Trans. 39 (2010) 2198–2200.
[115] T.M. Ross, S.M. Neville, D.S. Innes, D.R. Turner, B. Moubaraki, K.S. Murray, Dalton Trans. 39 (2010) 149–159.
[116] S. Imatomi, S. Hashimoto, N. Matsumoto, Eur. J. Inorg. Chem. 2009 (2009) 721–726.
[117] M. Clemente-León, E. Coronado, M.C. Giménez-López, A. Soriano-Portillo, J.C. Waerenborgh, F.S. Delgado, C. Ruiz-Pérez, Inorg. Chem. 47 (2008) 9111–9120.
[118] M. Clemente-León, E. Coronado, M. López-Jordà, Dalton Trans. 39 (2010) 4903–4910.
[119] M. Clemente-León, E. Coronado, M. López-Jordà, G. Mínguez Espallargas, A. Soriano-Portillo, J.C. Waerenborgh, Chem. Eur. J. 16 (2010) 2207–2219.
[120] M. Clemente-León, E. Coronado, M. López-Jordà, C. Desplanches, S. Asthana, H. Wang, J.-F. Létard, Chem. Sci. 2 (2011) 1121.
[121] M. Clemente-León, E. Coronado, M. López-Jordà, J.C. Waerenborgh, Inorg. Chem. 50 (2011) 9122–9130.
[122] M. Clemente-León, E. Coronado, M. López-Jordà, J.C. Waerenborgh, C. Desplanches, H. Wang, J.F. Létard, A. Hauser, A. Tissot, J. Am. Chem. Soc. 135 (2013) 8655–8667.
[123] M. Clemente-León, E. Coronado, M. López-Jordà, Eur. J. Inorg. Chem. (2013) 753–762.
[124] A. Abhervé, M. Clemente-León, E. Coronado, C.J. Gómez-García, M. Verneret, Inorg. Chem. 53 (2014) 12014–12026.
[125] A. Abhervé, S. Mañas-Valero, M. Clemente-León, E. Coronado, Chem. Sci. 2 (2015) 4665–4673.
[126] K. Takahashi, H. Cui, H. Kobayashi, Y. Einaga, O. Sato, Chem. Lett. 34 (2005) 1240–1241.
[127] C. Faulmann, S. Dorbes, S. Lampert, K. Jacob, B. Garreau De Bonneval, G. Molnár, A. Bousseksou, J.A. Real, L. Valade, Inorg. Chim. Acta 360 (2007) 3870–3878.
[128] K. Takahashi, H. Mori, H. Kobayashi, O. Sato, Polyhedron 28 (2009) 1776–1781.
[129] J.C. Dias, A. Soriano-Portillo, M. Clemente-Léon, C. Giménez-Saiz, J.R. Galán-Mascarós, C.J. Gómez-García, E. Coronado, Inorg. Chim. Acta 360 (2007) 3843–3847.
[130] X.-M. Li, Y. Ji, C.-F. Wang, J.-L. Zuo, X.-Z. You, J. Coord. Chem. 62 (2009) 1544–1552.
[131] K. Fukuroi, K. Takahashi, T. Mochida, T. Sakurai, H. Ohta, T. Yamamoto, Y. Einaga, H. Mori, Angew. Chem. Int. Ed. 53 (2014) 1983–1986.
[132] B.J.C. Vieira, J.C. Dias, I.C. Santos, L.C.J. Pereira, V. da Gama, J.C. Waerenborgh, Inorg. Chem. 54 (2015) 1354–1362.
[133] B.J.C. Vieira, J.T. Coutinho, J.C. Dias, J.C. Nunes, I.C. Santos, L.C.J. Pereira, V. da Gama, J.C. Waerenborgh, Polyhedron 85 (2015) 643–651.
[134] A.I.S. Neves, J.C. Dias, B.J.C. Vieira, I.S. Santos, M.B. Castelo Branco, L.C.J. Pereira, J.C. Waerenborgh, M. Almeida, D. Belo, V. Da Gama, CrystEngComm 11 (2009) 2160–2168.
[135] C. Faulmann, K. Jacob, S. Dorbes, S. Lampert, I. Malfant, M.-L. Doublet, L. Valade, J.A. Real, Inorg. Chem. 46 (2007) 8548–8559.
[136] K. Takahashi, H.-B. Cui, Y. Okano, H. Kobayashi, Y. Einaga, O. Sato, Inorg. Chem. 45 (2006) 5739–5741.
[137] K. Takahashi, H.-B. Cui, Y. Okano, H. Kobayashi, H. Mori, H. Tajima, Y. Einaga, O. Sato, J. Am. Chem. Soc. 130 (2008) 6688–6689.
[138] C. Gandolfi, C. Moitzi, P. Schurtenberger, G.G. Morgan, M. Albrecht, J. Am. Chem. Soc. 130 (2008) 14434–14435.
[139] C. Gandolfi, G.G. Morgan, M. Albrecht, Dalton Trans. 41 (2012) 3726–3730.
[140] P.N. Martinho, C.J. Harding, H. Müller-Bunz, M. Albrecht, G.G. Morgan, Eur. J. Inorg. Chem. (2010) 675–679.
[141] P.N. Martinho, Y. Ortin, B. Gildea, C. Gandolfi, G. McKerr, B. O'Hagan, M. Albrecht, G.G. Morgan, Dalton Trans. 41 (2012) 7461–7463.
[142] P.N. Martinho, T. Lemma, B. Gildea, G. Picardi, H. Müller-Bunz, R.J. Forster, T.E. Keyes, G. Redmond, G.G. Morgan, Angew. Chem. Int. Ed. 51 (2012) 11995–11999.
[143] N.E. Domracheva, A.V. Pyataev, V.E. Vorobeva, E.M. Zueva, J. Phys. Chem. B 117 (2013) 7833–7842.
[144] A. Tissot, L. Rechignat, A. Bousseksou, M.-L. Boillot, J. Mater. Chem. 22 (2012) 3411.
[145] A. Bousseksou, G. Molnár, L. Salmon, W. Nicolazzi, Chem. Soc. Rev. 40 (2011) 3313–3335.
[146] M. Nakaya, K. Shimayama, K. Takami, K. Hirata, S. Amolegbe, M. Nakamura, L. Lindoy, S. Hayami, Crystals 4 (2014) 104–112.
[147] Y. Murashima, M.R. Karim, N. Saigo, H. Takehira, R. Ohtani, M. Nakamura, M. Koinuma, L.F. Lindoy, K. Kuroiwa, S. Hayami, Inorg. Chem. Front. 2 (2015) 886–892.
[148] M.A. Halcrow, Chem. Soc. Rev. 40 (2011) 4119–4142.
[149] S. Alvarez, Chem. Rev. 115 (2015) 13447–13483.
[150] P. Guionneau, M. Marchivie, G. Bravic, J.-F. Létard, D. Chasseau, Top. Curr. Chem. 234 (2004) 97–128.
[151] J.-F. Létard, G. Chastanet, P. Guionneau, C. Desplanches, in: M.A. Halcrow (Ed.), Spin Crossover Materials: Properties and Applications, John Wiley & Sons, Ltd, Chichester, 2013, pp. 475–506.
[152] R.J. Deeth, C.M. Handley, B.J. Houghton, in: M.A. Halcrow (Ed.), Spin-Crossover Materials: Properties and Applications, John Wiley & Sons, Ltd, Chichester, 2013, pp. 443–454.
[153] R.J. Deeth, in: M. Swart, M. Costas (Eds.), Spin States in Biochemistry and Inorganic Chemistry: Influence on Structure and Reactivity, John Wiley & Sons, Ltd, Oxford, UK, 2016, pp. 85–102.
[154] K.P. Kepp, Coord. Chem. Rev. 257 (2013) 196–209.
[155] M. Güell, J.M. Luis, M. Solà, M. Swart, J. Phys. Chem. A 112 (2008) 6384–6391.
[156] M. Reiher, O. Salomon, B. Artur Hess, Theor. Chem. Acc. 107 (2001) 48–55.
[157] M. Reiher, Inorg. Chem. 41 (2002) 6928–6935.
[158] T.F. Hughes, R.A. Friesner, J. Chem. Theory Comput. 7 (2011) 19–32.
[159] K.P. Jensen, J. Cirera, J. Phys. Chem. A 113 (2009) 10033–10039.

[160] M. Swart, J. Chem. Theory Comput. 4 (2008) 2057–2066.
[161] S. Ye, F. Neese, Inorg. Chem. 49 (2010) 772–774.
[162] L. Daku, F. Aquilante, T.W. Robinson, A. Hauser, J Chem. Theory Comput. 6 (2012) 4216–4231.
[163] R.J. Deeth, A.E. Anastasi, M.J. Wilcockson, J. Am. Chem. Soc. 132 (2010) 6876–6877.
[164] A. Bousseksou, G. Molnár, J.A. Real, K. Tanaka, Coord. Chem. Rev. 251 (2007) 1822–1833.
[165] C.M. Grunert, S. Reiman, H. Spiering, J.A. Kitchen, S. Brooker, P. Gütlich, Angew. Chem. Int. Ed. 47 (2008) 2997–2999.
[166] Y. Garcia, F. Robert, A.D. Naik, G. Zhou, B. Tinant, K. Robeyns, S. Michotte, L. Piraux, J. Am. Chem. Soc. 133 (2011) 15850–15853.
[167] R. Kulmaczewski, J. Olguín, J.A. Kitchen, H.L.C. Feltham, G.N.L. Jameson, J.L. Tallon, S. Brooker, J. Am. Chem. Soc. 136 (2014) 878–881.
[168] M.C. Muñoz, J.A. Real, Coord. Chem. Rev. 255 (2011) 2068–2093.
[169] M.C. Muñoz, J.A. Real, in: M.A. Halcrow (Ed.), Spin-Crossover Materials: Properties and Applications, John Wiley & Sons, Ltd, Chichester, 2013, pp. 121–146.
[170] O.V. Dolomanov, L.J. Bourhis, R.J. Gildea, J.A.K. Howard, H. Puschmann, J. Appl. Cryst. 42 (2009) 339–342.

Polyhedron 114 (2016) 242–248

Contents lists available at ScienceDirect

Polyhedron

journal homepage: www.elsevier.com/locate/poly

Substituent modulated packing in octahedral Ni(II) complexes

Piboonwan Insiti [a], Prapatsorn Jitthiang [a], Phimphaka Harding [a], Kittipong Chainok [b], Ratanon Chotima [c], Jitnapa Sirirak [d], Sebastian Blackwood [e], Adil Alkaş [e], Shane G. Telfer [e], David J. Harding [a,*]

[a] Molecular Technology Research Unit, School of Science, Walailak University, Thasala, Nakhon Si Thammarat 80161, Thailand
[b] Department of Physics, Faculty of Science and Technology, Thammasat University, Khlong Luang, Pathum Thani 12120, Thailand
[c] Department of Chemistry, Faculty of Science, Naresuan University, Phitsanulok 65000, Thailand
[d] Department of Chemistry, Faculty of Science, Silpakorn University, Nakhon Pathom, Thailand
[e] MacDiarmid Institute for Advanced Materials and Nanotechnology, Institute of Fundamental Sciences, Massey University, Palmerston North, New Zealand

ARTICLE INFO

Article history:
Received 22 October 2015
Accepted 14 December 2015
Available online 19 December 2015

Keywords:
Nickel(II) complexes
Schiff bases
Tridentate ligands
Structure
DFT calculations

ABSTRACT

The reaction of $NiCl_2$ with two equivalents of Hqsal-X (Hqsal-X = 5-X-*N*-(8-quinolyl)salicylaldimine) yields the octahedral complexes, $[Ni(qsal)_2]$·MeOH **1** and $[Ni(qsal\text{-}X)_2]$ (X = OMe **2**, Cl **3**, Br **4**, Me **5**, *t*-Bu **6**). UV–Vis spectroscopic studies show that the LMCT band is sensitive to the substituent, ranging from 465 to 520 nm. Crystal structures of $[Ni(qsal)_2]$·MeOH **1** and $[Ni(qsal\text{-}X)_2]$ (X = OMe **2**, Cl **3**, Br **4**) reveal that the Ni centres are octahedral, the qsal-X ligands coordinated with a meridional geometry. The packing in the structures is found to be strongly dependent on the substituent with 1D π–π chains in **3** and **4**, π–π dimers in **2** and a 1D hydrogen bonded chain in **1**. DFT calculations indicate almost identical electronic structures in **1**–**6** suggesting the difference in packing is due to the different supramolecular preferences of the substituent.

© 2015 Elsevier Ltd. All rights reserved.

1. Introduction

Schiff bases are popular ligands often formed by the reaction of amines with salicylaldehyde and related derivatives [1]. As both the amine and the salicylaldehyde can be readily modified, ligands with highly tunable steric and electronic characteristics can be prepared. Consequently, transition metal complexes of these ligands find numerous applications in a diverse set of fields including catalysis [2–5], magnetism [6,7], sensors [8,9], medical imaging [10] and optical materials [11,12]. The most popular Schiff bases continue to be either tetradentate N_2O_2 donors, which occupy the equatorial plane, or hexadentate N_4O_2 donors, which encapsulate first row transition metal ions [1]. By comparison, tridentate ligands have received less attention, and those that have been used typically incorporate simple amines as the terminal coordinating arm. For example, in Ni(II) chemistry, ligands based on *N*,*N*-dimethylethane-1,2-diamine and *N*-methyl-1,3-propanediamine have been extensively studied yielding monomeric [13–17], dimeric [18,19] and even trimeric species [14] depending on the reaction conditions, solvent and supporting anion. Moreover, the ligand may be tridentate [13,14,18] and even bidentate but with a protonated amine arm [14,17].

In contrast to these systems, the chemistry of Schiff bases with potentially coordinating aromatic amines is much less well developed. We are particularly interested in rigid ligands that enforce a meridional configuration on the metal centre, as opposed to the aminopropyl ligands above where even in the tridentate coordination mode both *fac* [13] and *mer* [15,18] configurations are encountered. The ligand system we have been exploring is 5-X-*N*-(8-quinolyl)salicylaldimine, Hqsal-X, which is a planar monoanionic ligand with a large π-surface [20]. Structures of a number of $[M(qsal\text{-}X)_2]^{0/+}$ (M = Mn, Fe, Co) complexes [21–29] reveal a tendency to form π–π interactions and bear a strong resemblance to terpyridyl embraces found in many $[M(terpy)_2]^{2+/3+}$ complexes [30]. In seeking to determine whether this is a general phenomenon for all $[M(qsal\text{-}X)_2]^{0/+}$ compounds and if the substituent group, X, plays any role in the packing we have now prepared a series of $[Ni(qsal\text{-}X)_2]$ complexes many of which have been structurally characterized.

2. Results and discussion

2.1. Synthesis and characterization of $[Ni(qsal\text{-}X)_2]$

The compounds are readily synthesized by adding a MeOH solution of $NiCl_2{\cdot}6H_2O$ to a solution of the Hqsal-X in CH_2Cl_2. Subsequent addition of NEt_3 gives red or brown microcrystals of the

* Corresponding author.

http://dx.doi.org/10.1016/j.poly.2015.12.028
0277-5387/© 2015 Elsevier Ltd. All rights reserved.

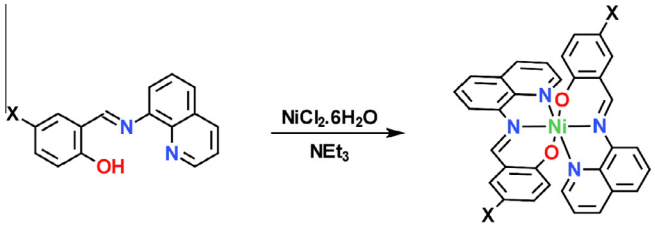

Scheme 1. Synthetic procedure for [Ni(qsal-X)$_2$] 1–6.

products [Ni(qsal)$_2$]·MeOH **1** and [Ni(qsal-X)$_2$] (X = OMe **2**, Cl **3**, Br **4**, Me **5**, *t*-Bu **6**) in good to excellent yields (Scheme 1). The compounds are insoluble in all common organic solvents except DMF and to a lesser extent DMSO. The compounds can also be prepared by diffusion of layered solutions of Hqsal-X in CH_2Cl_2, NEt_3, and Ni(OAc)$_2$·4H$_2$O in MeOH. This latter method gives deep red/brown crystals over two days. It is noteworthy that [Ni(qsal)$_2$]·0.5Me$_2$CO has previously been reported [31], although this compound was prepared from a DMF solution with a few drops of acetone added. This suggests that other solvates of [Ni(qsal)$_2$] may be accessible.

IR spectroscopic studies of **1**–**6** show a strong imine stretch between 1602–1611 cm^{-1} and are similar to values reported in other [M(qsal-X)$_2$]$^{0/+}$ complexes [21,23,25,28]. By comparison, the imine stretch of Hqsal-X is observed at 1615–1630 cm^{-1} with the lower values in **1**–**6** indicative of metal coordination [20,25,32].

The electronic spectra of **1**–**6** were recorded in DMF and are shown in Fig. 1. There are two bands in the spectra. The first occurs at *ca.* 340 nm and is assigned to a $\pi \rightarrow \pi^*$ transition of the qsal-X ligand. The UV–Vis spectra of the free ligands show a single band between 337 and 348 nm and support this assignment. The second band is found between 465 and 520 nm and is consistent with a LMCT transition. Similar results were found for [M(qsal-X)$_2$]$^{0/+}$ (M = Mn, Fe) and confirm that even in DMF the octahedral geometry around the nickel centre is preserved [21,25]. Interestingly, there is a general trend that as the substituent group becomes more electron withdrawing the transition moves to lower wavelengths, with the exception of **1**. Unfortunately, due to the poor solubility of the compounds we were unable to prepare solutions of sufficient concentration to allow us to observe the *d*–*d* transitions (Table 1).

2.2. Description of the structures of [Ni(qsal-X)$_2$]

As noted above, crystals were prepared by layered diffusion crystallizing in the monoclinic space group P2$_1$/c for **1**, while **2**–**4** all crystallize in the monoclinic space group P2$_1$/n. By comparison [Ni(qsal)$_2$]·0.5Me$_2$CO is found in the monoclinic space group C2/c [31]. Selected bond lengths are given in Table 2 while the structures of **2** and **4** are shown in Fig. 2 as representative examples. It should be noted that the poor quality of the diffraction data for **3** result in lower bond length precision, nevertheless the structure is clear and the packing mirrors that in **4** where the data is of far better quality.

As expected, the Ni centre is coordinated by two qsal-X ligands yielding an octahedral geometry and a N_4O_2 donor set. The Ni–N bond lengths vary from 2.019 to 2.120 Å with the bond to the imine nitrogen shorter than that of the quinolyl nitrogen by ~0.07 Å. Differences in Ni–N bond lengths are also observed in [Ni(salMpn-Br)$_2$] (salMpn-Br = 4-Bromo-2-{[3-(methylamino) propylimino]methyl}phenol), although the difference is greater due to the weaker coordinative ability of the amine nitrogen

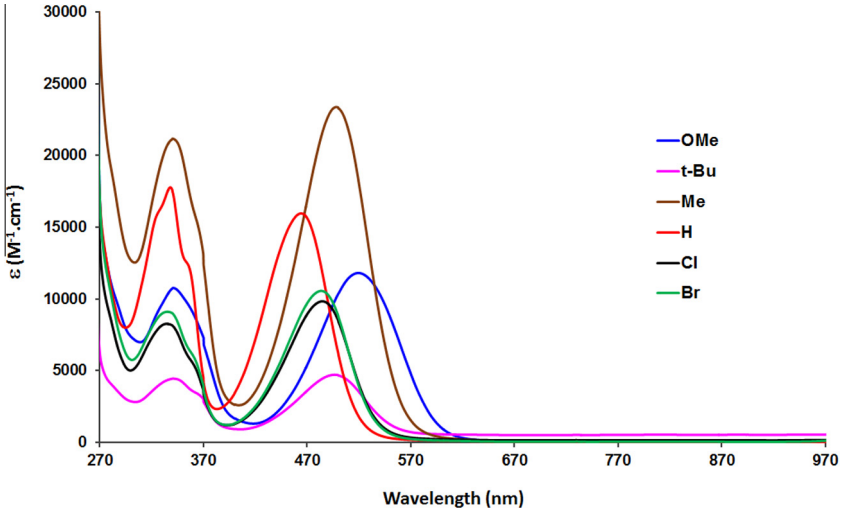

Fig. 1. UV–Vis spectra of **1**–**6** in DMF.

Table 1
Physical, IR and UV–Vis spectroscopic data for **1**–**6**.

Compound	Colour	IR (cm^{-1})			λ_{max} (nm), ε (M^{-1} cm^{-1})
		ν_{C-H}	$\nu_{C=N}$	$\nu_{C=C}$	
[Ni(qsal)$_2$]·MeOH **1**	Brown	2974(w)	1611(s)	1440(m)	330 (sh, 16600), 338 (17760), 353 (sh, 12640), 465 (15960)
[Ni(qsal-OMe)$_2$] **2**	Red	3046(w)	1602(s)	1457(s)	341 (10760), 371 (sh, 6560), 520 (11800)
[Ni(qsal-Cl)$_2$] **3**	Deep-red	3046(w)	1609(s)	1447(s)	336 (8260), 358 (sh, 5730), 485 (9830)
[Ni(qsal-Br)$_2$] **4**	Brown	3046(w)	1608(s)	1448(s)	336 (9100), 358 (sh, 6320), 484 (10560)
[Ni(qsal-Me)$_2$] **5**	Brown	3045(w)	1603(s)	1454(s)	342 (21140), 499 (23370)
[Ni(qsal-*t*-Bu)$_2$] **6**	Red	3040(w)	1602(s)	1456(s)	342 (4440), 363 (sh, 3440),496 (4720)

Table 2
Selected bond lengths and distortion parameters of [Ni(qsal-X)$_2$] **1**–**4** (Å, °).

	1	2	3	4	1·0.5Me$_2$CO[a]
Ni–O1	2.048(2)	2.046(2)	2.039(9)	2.019(2)	2.044(5)
Ni–O2[b]	2.019(2)	2.019(2)	2.018(9)	2.017(2)	2.041(4)
Ni–N1	2.104(2)	2.097(3)	2.096(10)	2.102(2)	2.082(5)
Ni–N2	2.040(2)	2.039(3)	2.026(11)	2.047(2)	2.057(5)
Ni–N3	2.120(2)	2.104(3)	2.089(11)	2.097(2)	2.101(5)
Ni–N4	2.024(2)	2.030(3)	2.019(10)	2.043(2)	2.044(5)
α[c]	17.9	6.2	4.7	4.2	8.4
	16.6	26.5	7.8	8.8	17.1
Σ[d]	53.5	53.7	44.1	44.7	53.9

[a] Data from Ref.
[b] For **2** this is O3 due to the extra O in the ligand.
[c] α = the angle between planes of the quinoline and phenolate rings.
[d] $\Sigma = \sum_{i=1}^{12} |90 - \alpha_i|$, where α_i are the twelve cis N/O–Fe–N/O angles.

[13]. There is also a slight asymmetry between the two qsal-X ligands, particularly evident in the different Ni–O bond lengths. Interestingly, in **4** and **1**·0.5Me$_2$CO the Ni–O bond lengths are almost identical.

It is evident that both ligands are significantly twisted in **1** while they are planar in **3** and **4**. In **2**, one ligand is twisted and the other is planar. This also impacts the degree of distortion at the nickel centre as measured by Σ, the sum of the deviation in the 12 *cis* angles from 90° (where $\Sigma = 0$ represents a perfect octahedron), with a decrease of almost 10° in going from **1** and **2** to **3** and **4**. The difference is clearly influenced by the substituent in the 5-position with the DFT calculations suggesting this is as result of crystal packing forces and not electronic effects (*vide infra*).

The peripheral substituent on the qsal-X ligand is found to dramatically impact the packing in the structures. Thus, in **3** and **4** the principal supramolecular motif is the formation of 1D chains composed of orthogonal π–π interactions supported by C–H···O interactions (Fig. 3). The two interactions are termed Type A and B, and range from 3.53 to 3.33 Å being different from each other by *ca.* 0.13 and 0.15 Å for **3** and **4**, respectively (Table 3). This difference in the plane to plane distances in **3** which are shorter than those of **4** by 0.07 Å may be due to the smaller chloro group which permits closer overlap of the aromatic rings. Such interactions are common in qsal-X complexes and have previously been observed in [Mn(qsal-X)$_2$] [21], [Fe(qsal-X)$_2$]$^+$ [23,26,27] and [Co(qsal-Cl)$_2$]$^+$ [29] complexes.

The 1D chains in **3** and **4** are connected to each other via C–H···X (X = Cl, Br) interactions such that neighbouring chains are slightly angular relative to each other with every second chain identically oriented (Fig. 4). This results in a 2D plane that contains only one type of C–H···Br interaction, in the case of Fig. 4 that

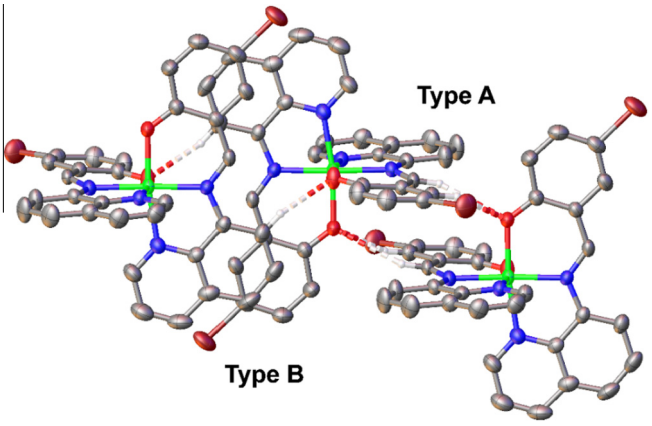

Fig. 3. View of the two orthogonal π–π interactions in [Ni(qsal-Br)$_2$] **4**.

Table 3
Distances of supramolecular interactions in **1**–**4** (Å).

	1	2	3	4
π–π				
Cg1···Cg1 (Type A)	–	3.56	3.64	3.73
Pl-to-Pl	–	3.44	3.46	3.53
Cg2···Cg2 (Type B)	–	–	3.69	3.79
Pl-to-Pl	–	–	3.33	3.39
O1···H24	2.197 (O1···H3B) 2.987 (O1···O3B)	–	2.385	2.419
O2···H10	2.004 (O1···H3A) 2.808 (O1···O3A)	2.539 (O1···H27)	2.663	2.698
O2···H12	2.553 (O2···H24)	2.533 (O1···H25)	2.663	2.673
O3A···H31	2.512	–	–	–
Quinolyl				
Cg3···Cg3	–	–	4.241	4.333
Pl-to-Pl		–	3.554	3.658
Cg4···H22		2.716 (H20)	2.695	2.816
C–H···Halogen				
H15···X1			2.765	2.839
H31···X2			2.904	3.027

involving Br2, with the second set of C–H···Br interactions linking these planes to give a 3D network (see Fig. S1). A final interaction which supports the 3D network are weak fourfold parallel embraces (P4AE [33], see Fig. S2). As with the π–π interactions all the above interactions are slightly stronger in **3** than **4** (Table 2).

The packing in **2** is strongly influenced by the fact that only one of the qsal-OMe ligands is planar with simple π–π dimers forming instead of 1D chains (Fig. 5). Nevertheless, these dimers are linked to each other by a combination of C–H···O interactions, involving

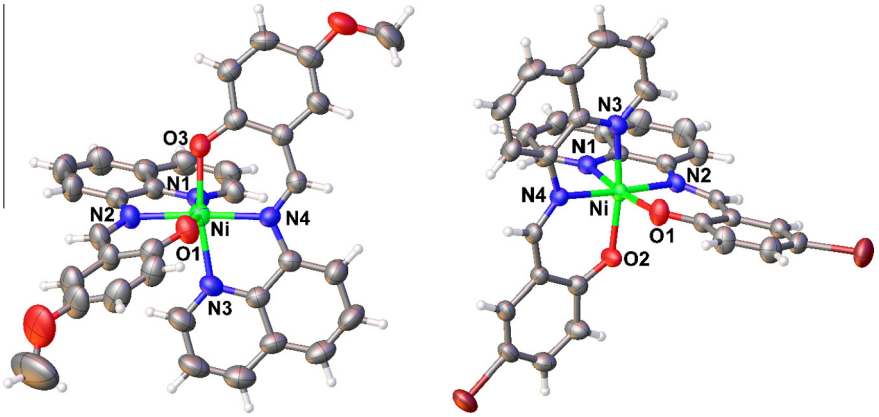

Fig. 2. View of the asymmetric unit of **2** (left) and **4** (right) with ellipsoids shown at 50% probability. Only selected atoms are labeled in the interests of clarity.

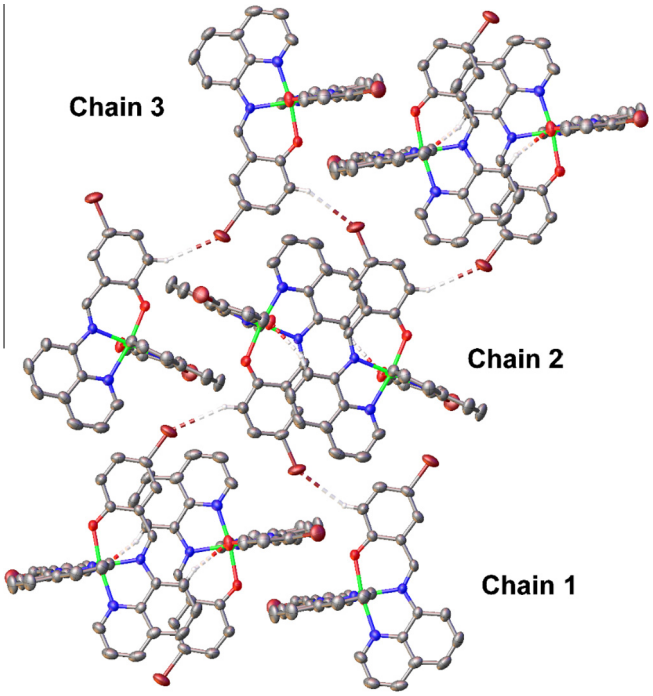

Fig. 4. View of the C–H···Br2 interactions that link the 1D chains in [Ni(qsal-Br)$_2$] **4**.

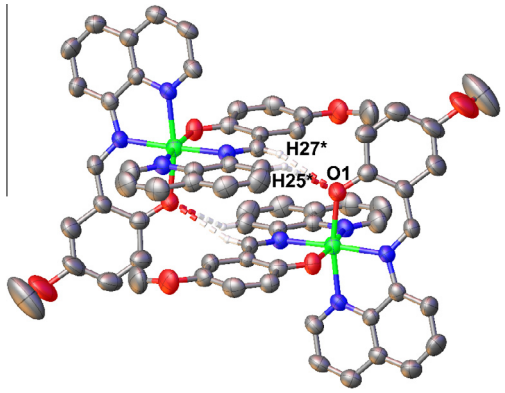

Fig. 5. View of the π–π dimer found in [Ni(qsal-OMe)$_2$] **2**. Only selected atoms are labeled in the interests of clarity.

the coordinated phenolate oxygen and a quinolyl hydrogen, and a pair of C–H···π interactions (see Fig. S3) to give a herringbone packing pattern (Fig. 6). Interestingly, this packing closely resembles that of [Ni(qsal)$_2$]·0.5Me$_2$CO but not [Ni(qsal)$_2$]·MeOH (*vide infra*).

Finally, the packing in [Ni(qsal)$_2$]·MeOH is very different to **2**–**4** with no π–π interactions in the structure. This is unsurprising given that both qsal ligands are non-planar. However, the fact that the packing in [Ni(qsal)$_2$]·0.5Me$_2$CO is almost identical to **2** suggests that for **1** the determining factor in the structure is the solvent. It follows that the substituent is important only in so far as its small size permits inclusion of solvent in the structure. The MeOH molecule is disordered over two sites and is strongly hydrogen bound to one of the phenolate oxygens and through a C–H···O interaction bridges neighbouring [Ni(qsal)$_2$] units. The other phenolate oxygen is involved in a weaker C–H···O interaction forming a 1D chain (Fig. 7). Thus, the change in packing in [Ni(qsal)$_2$]·0.5Me$_2$CO is most probably due to the fact that acetone isn't able to participate in such hydrogen bonding and 2D planes of π–π dimers are observed instead.

2.3. DFT studies

In order to investigate the impact of the substituents of **1**–**6** at the molecular level, DFT calculations were performed with the GAUSSIAN 03 software package [34]. The X-ray crystallographic data of the complexes in **1**–**4** were used as the initial structures for full optimization at the B3LYP/6-31G** level in the gas phase while the geometry optimization of **5** and **6** were performed at the B3LYP/6-31G** level in the gas phase using the modified X-ray structure of **1** as the starting structure.

The comparison of the Ni–N/O bond lengths from the DFT calculations (Table S1) with those found experimentally in the X-ray crystal structures (Table 2) shows that they are in agreement within 0.06 Å, indicating that the calculations accurately model [Ni(qsal-X)$_2$]. The frontier orbitals of **1**–**6** were also examined with the HOMO and LUMO found to be predominately ligand based π* orbitals (Fig. 8; for the remaining complexes see Fig. S4). For **1** and **3**–**4**, the HOMO and LUMO are similar; one qsal-X ligand dominating the HOMO and another qsal-X ligand dominating the LUMO. In contrast, significant electron density is found on both qsal-OMe ligands of **2**.

Given the strong similarity in the electronic structures of the [Ni(qsal-X)$_2$] complexes it seems clear that the differences in the packing motifs for **1**–**4** are due to the differing supramolecular connectivity favoured by the various substituents.

3. Conclusions

In conclusion, we have prepared six closely related [Ni(qsal-X)$_2$] complexes. The different substituents are found to have only a minor effect on the electronic structure of the complexes as evidenced by UV–Vis spectroscopic and DFT computational studies. However, the substituent significantly impacts the packing in the structures with [Ni(qsal-X)$_2$] (X = Cl, Br) favouring the 1D π–π chains that are a feature of many [M(qsal-X)$_2$]$^{0/+}$ complexes. In combination with multiple C–H···Cl/Br interactions 3D supramolecular networks are formed. [Ni(qsal-OMe)$_2$] instead forms simple π–π dimers but links them with C–H···O and C–H···π interactions resulting in a 2D plane. The incorporation of MeOH into the lattice of [Ni(qsal)$_2$] yields another motif this time dominated by strong hydrogen bonds which result in the formation of 1D chains. It is clear from this study that while 1D π–π chains remain a dominant packing motif in the structures of [M(qsal-X)$_2$]$^{0/+}$ complexes it is not the only motif that can form as the packing can be disrupted by stronger supramolecular interactions, such as hydrogen bonding in **1**. The ability of qsal-X ligands to support complexes with other co-ligands and how the X group impacts electrochemical and magnetic properties will be the subject of future studies.

4. Experimental

4.1. General remarks

All manipulations were performed in air with reagent grade solvents. All other chemicals were purchased from Aldrich Chemical Company and used as received. The Hqsal-X ligands were synthesized according to literature procedures [20,25,35,32]. Infrared spectra (as KBr discs) were recorded on a Perkin-Elmer Spectrum One infrared spectrophotometer in the range 400 to 4000 cm^{-1}. Electronic spectra were recorded in DMF at room temperature on a Shimadzu UV-1700 UV–Vis spectrophotometer. Elemental analyses were carried out on a Eurovector EA3000 analyser by staff of the School of Chemistry, University of Bristol, UK. ESI-MS were carried out on a Bruker Daltonics 7.0T Apex 4 FTICR Mass Spectrometer by staff at the National University of Singapore.

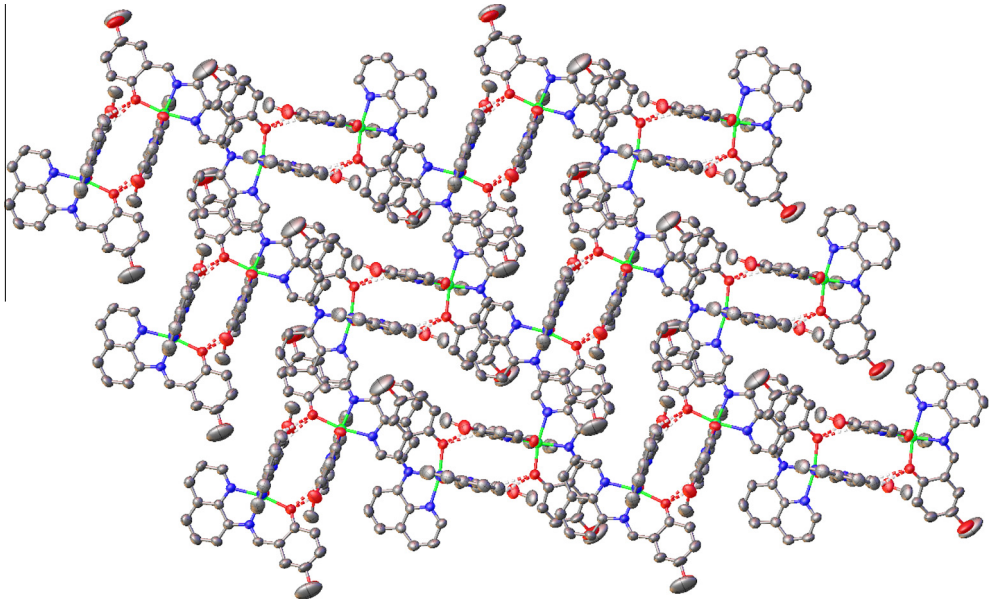

Fig. 6. Herringbone packing pattern in [Ni(qsal-OMe)$_2$] **2**.

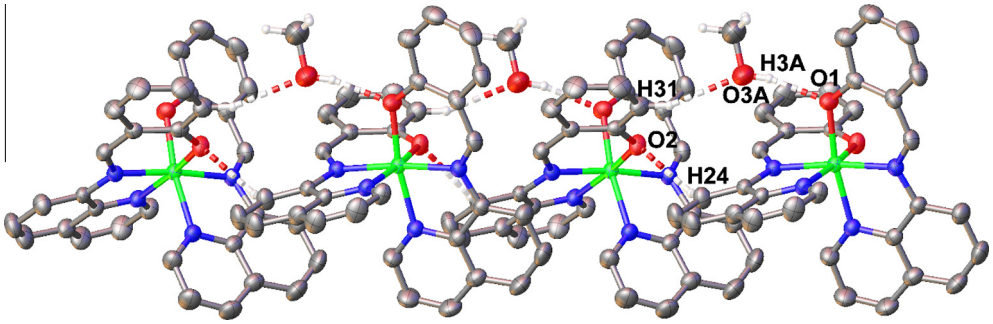

Fig. 7. View of the hydrogen bonding and C–H···O interactions that form the 1D chain in **1**. Only selected atoms are labeled in the interests of clarity.

4.2. Synthesis of [Ni(qsal)$_2$]·MeOH **1**

Hqsal (55 mg, 0.40 mmol) was dissolved in CH_2Cl_2 (10 cm^3) giving an orange solution. In a separate flask $NiCl_2{\cdot}6H_2O$ (48 mg, 0.20 mmol) was dissolved in MeOH (5 mL) to give a light green solution. The Ni(II) solution was added dropwise to the stirred Hqsal solution resulting in a yellow brown solution. NEt_3 (56 µl, 0.40 mmol) was added causing the solution to become browner. After 1 h of stirring the solution was reduced in volume to approximately 5 cm^3, filtered and then washed cold MeOH (5 mL) and Et_2O (10 mL) to give a brown solid, 91.8 mg (83%). IR (KBr): ν_{max} = 1604 ($\nu_{C=N}$). λ_{max} (CH_2Cl_2)/nm (ε/M^{-1} cm^{-1}): 328 (12010), 458 (14210) nm. ESI-MS: *m*/*z*: 553.0 [MH]$^+$. Found (calc. %) for $C_{33}H_{26}NiN_4O_3$: C 67.37 (67.72), H 4.21 (4.48), N 9.36 (9.57).

4.3. Synthesis of [Ni(qsal-OMe)$_2$] 2

2 was prepared in an identical way to **1** using Hqsal-OMe instead of Hqsal yielding deep red microcrystals in 82% yield. IR (KBr): ν_{max} = 1604 ($\nu_{C=N}$). λ_{max} (CH_2Cl_2)/nm (ε/M^{-1} cm^{-1}): 328 (12010), 458 (14210) nm. ESI-MS: *m*/*z*: 613.0 [MH]$^+$. Found (calc. %) for $C_{34}H_{26}NiN_4O_4$: C 66.84 (66.59), H 4.04 (4.27), N 8.57 (9.13).

4.4. Synthesis of [Ni(qsal-Cl)$_2$] 3

3 was prepared in an identical way to **1** using Hqsal-Cl instead of Hqsal yielding red-brown microcrystals in 74% yield. IR (KBr): ν_{max} = 1604 ($\nu_{C=N}$). λ_{max} (CH_2Cl_2)/nm (ε/M^{-1} cm^{-1}): 328 (12010), 458 (14210) nm. ESI-MS: *m*/*z*: 623.0 [MH]$^+$. Found (calc. %) for $C_{32}H_{20}Cl_2NiN_4O_2$: C 61.41 (61.78), H 3.45 (3.24), N 8.89 (9.00).

4.5. Synthesis of [Ni(qsal-Br)$_2$] 4

4 was prepared in an identical way to **1** using Hqsal-Br instead of Hqsal yielding red-brown microcrystals in 69% yield. IR (KBr): ν_{max} = 1604 ($\nu_{C=N}$). λ_{max} (CH_2Cl_2)/nm (ε/M^{-1} cm^{-1}): 328 (12010), 458 (14210) nm. ESI-MS: *m*/*z*: 711.0 [MH]$^+$. Found (calc. %) for $C_{32}H_{20}Br_2NiN_4O_2$: C 54.28 (54.06), H 3.13 (2.83), N 7.52 (7.88).

4.6. Synthesis of [Ni(qsal-Me)$_2$] 5

5 was prepared in a similar way to **1** using Hqsal-Me instead of Hqsal yielding a brown powder in 68% yield. IR (KBr): ν_{max} = 1604 ($\nu_{C=N}$). λ_{max} (CH_2Cl_2)/nm (ε/M$^{-1}\nu$cm^{-1}): 328 (12010), 458 (14210) nm. ESI-MS: *m*/*z*: 581.0 [MH]$^+$. Found (calc. %) for $C_{34}H_{26}NiN_4O_2$: C 70.44 (70.26), H 4.35 (4.51), N 9.28 (9.64).

4.7. Synthesis of [Ni(qsal-tBu)$_2$] 6

6 was prepared in a similar way to **1** using 1.0 mmol of Hqsal-*t*Bu instead of Hqsal yielding a brown powder in 66% yield. IR (KBr): ν_{max} = 1604 ($\nu_{C=N}$). λ_{max} (CH_2Cl_2)/nm (ε/M^{-1} cm^{-1}): 328 (12010), 458 (14210) nm. ESI-MS: *m*/*z*: 665.0 [MH]$^+$. Found (calc. %) for $C_{40}H_{38}NiN_4O_2$: C 71.87 (72.20), H 5.69 (5.76), N 8.09 (8.42).

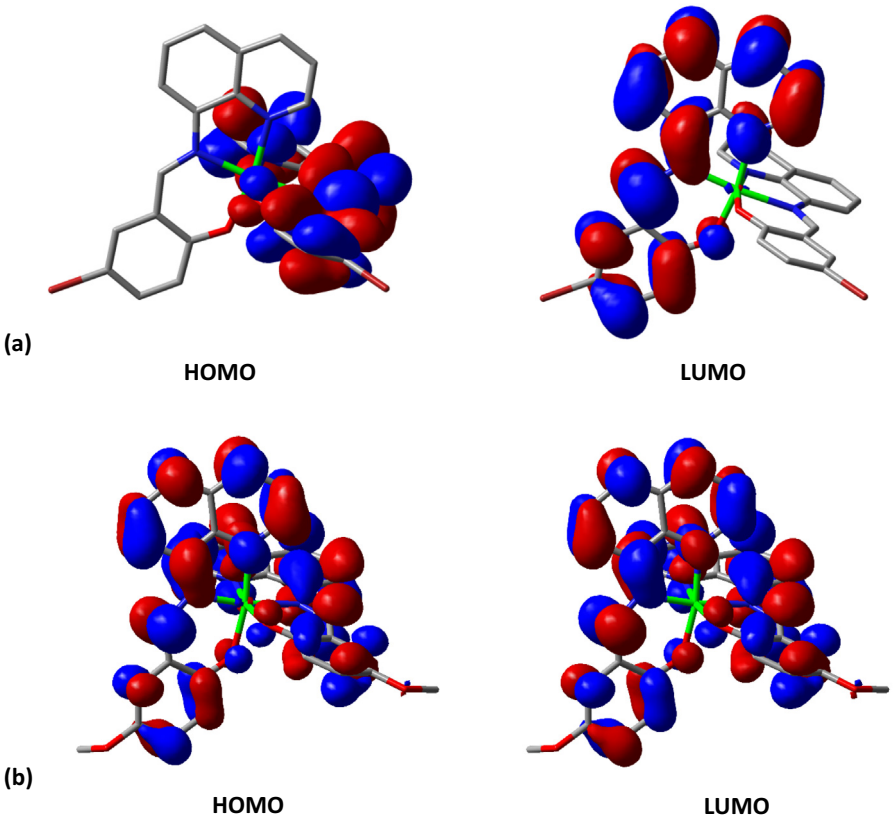

Fig. 8. HOMOs and LUMOs of (a) [Ni(qsal-Br)$_2$] **4**, (b) [Ni(qsal-OMe)$_2$] **2**.

4.8. X-ray crystallography

Crystal data and data processing parameters for the structures of **1**–**4** are given in Table 4. X-ray quality crystals of **1**–**4** were grown by layering a solution of Ni(OAc)$_2$ in MeOH over a solution of Hqsal-X and NEt_3 in CH_2Cl_2. Crystals of **1** and **4** were mounted on a glass fibre using perfluoropolyether oil. The diffraction data of **1** and **4** were collected on a Bruker D8 QUEST CMOS area detector with graphite monochromated Mo K_α (λ = 0.71073 Å) [36]. After data collection, in each case an empirical absorption correction (SADABS) was applied [37]. In the case of **2** and **3**, X-ray crystallographic data were collected at 173 and 293 K on a Rigaku Spider diffractometer equipped with a MicroMax MM007 rotating anode generator, Cu K_α radiation (λ = 1.54178 Å), high-flux Osmic multilayer mirror optics, and a curved image-plate detector [38]. The data were integrated and scaled and averaged with FS Process. The structures were then solved by direct methods and refined on all F^2 data using the SHELX suite of programs [39,40]. In all cases non-hydrogen atoms were refined with anisotropic thermal parameters; hydrogen atoms were included in calculated positions and refined with isotropic thermal parameters which were *ca.* 1.2 × (aromatic CH) or 1.5 × (Me, OH) the equivalent isotropic

Table 4
Crystallographic data and structure refinement for **1**–**4**.

	1	**2**	**3**	**4**
Formula	$C_{33}H_{26}N_4NiO_3$	$C_{34}H_{26}N_4NiO_4$	$C_{32}H_{20}Cl_2N_4NiO_2$	$C_{32}H_{20}Br_2N_4NiO_2$
Molecular weight/g mol^{-1}	585.29	613.30	622.13	711.05
Crystal system	monoclinic	monoclinic	monoclinic	monoclinic
Space group	$P2_1/c$	$P2_1/n$	$P2_1/n$	$P2_1/n$
a (Å)	8.8138(4)	12.6577(3)	10.4314(12)	10.4961(4)
b (Å)	22.6100(11)	11.6898(2)	13.0351(14)	13.1026(4)
c (Å)	13.5734(7)	18.8171(13)	19.0421(19)	19.7332(7)
α (°)	90	90	90	90
β (°)	92.8920(10)	90.420(6)	94.373(7)	94.373(7)
γ (°)	90	90	90	90
T (K)	296(2)	173(2)	293(2)	296(2)
Cell volume (Å^3)	2701.5(2)	2784.2(2)	2581.7(5)	2706.99(16)
Z	4	4	4	4
λ (Å)	0.71073	1.54178	1.54178	0.71073
Absorption coefficient/mm^{-1}	0.761	1.400	3.320	3.708
Reflections collected	33 162	27 865	19 424	34 398
Independent reflections, R_{int}	4951, 0.0827	4732, 0.0483	2687, 0.1208	5530, 0.0515
Minimum and maximum transmission	0.6653, 0.7452	0.544, 1.000	0.617, 1.000	0.383, 0.524
Restraints/parameters	1/381	0/388	0/370	0/370
Final *R* indices [$I > 2\sigma(I)$]: R_1, wR_2	0.0406, 0.0855	0.0484, 0.1015	0.1343, 0.3546	0.0346, 0.0739
CCDC number	1431228	1431229	1431227	1431226

thermal parameters of their parent carbon atoms. All pictures were generated using OLEX2 [41]. Crystals of **3** displayed limited long-range order. Diffraction was observed only to a resolution limit of 1.0 Å. The merging statistics indicated that the dataset was of mediocre quality, which results in elevated R factors and a lack of precision in determining the bond lengths. However, a clear assessment of the molecular structure and intermolecular contacts, as required for this study, can be gleaned from these data.

4.9. DFT calculations

DFT calculations were performed using GAUSSIAN 03 (Revision C.02) and employed the B3LYP density functional [34]. Calculations utilized the 6-31G** basis set with the X-ray crystallographic structures of **1**–**4** used as the starting structures for the optimization of each complex substituting the hydrogen in **1** with a methyl and *t*-butyl for **5** and **6** respectively. Pictures of the HOMO and LUMO were generated with GaussView.

Acknowledgements

We thank the Thailand Research Fund (RSA5580028 and RSA5880048) for funding this work. The Development and Promotion of Science and Technology Talents Project is thanked for undergraduate Scholarships to PI and PJ.

Appendix A. Supplementary data

CCDC 1431228, 1431229, 1431227 and 1431226 contains the supplementary crystallographic data for **1**, **2**, **3** and **4**, respectively. These data can be obtained free of charge via http://www.ccdc.cam.ac.uk/conts/retrieving.html, or from the Cambridge Crystallographic Data Centre, 12 Union Road, Cambridge CB2 1EZ, UK; fax: (+44) 1223-336-033; or e-mail: deposit@ccdc.cam.ac.uk. Supplementary data associated with this article can be found, in the online version, at http://dx.doi.org/10.1016/j.poly.2015.12.028.

References

[1] R. Hernández-Molina, A. Mederos, in: J.A. McCleverty, T.J. Meyer (Eds.), Compr. Coord. Chem. II, 2003, pp. 411–446.
[2] P.G. Cozzi, Chem. Soc. Rev. 33 (2004) 410.
[3] T. Katsuki, Chem. Soc. Rev. 33 (2004) 437.
[4] N.S. Venkataramanan, G. Kuppuraj, S. Rajagopal, Coord. Chem. Rev. 249 (2005) 1249.
[5] X.-B. Lu, D.J. Darensbourg, Chem. Soc. Rev. 41 (2012) 1462.
[6] C. Adhikary, S. Koner, Coord. Chem. Rev. 254 (2010) 2933.
[7] C. Benelli, D. Gatteschi, Chem. Rev. 102 (2002) 2369.
[8] A. Dalla Cort, P. De Bernardin, G. Forte, F. Yafteh Mihan, Chem. Soc. Rev. 39 (2010) 3863.
[9] P.D. Frischmann, M.J. MacLachlan, Chem. Soc. Rev. 42 (2013) 871.
[10] D.E. Reichert, J.S. Lewis, C.J. Anderson, Coord. Chem. Rev. 184 (1999) 3.
[11] P.G. Lacroix, Eur. J. Inorg. Chem. 2001 (2001) 339.
[12] C.J. Whiteoak, G. Salassa, A.W. Kleij, Chem. Soc. Rev. 41 (2012) 622.
[13] A. Bhattacharyya, P.K. Bhaumik, P.P. Jana, S. Chattopadhyay, Polyhedron 78 (2014) 40.
[14] P. Mukherjee, M.G.B. Drew, M. Estrader, A. Ghosh, Inorg. Chem. 47 (2008) 7784.
[15] S. Naiya, S. Biswas, M.G.B. Drew, A. Ghosh, Polyhedron 34 (2012) 67.
[16] D. Parker, E. Stephen Davies, C. Wilson, J. McMaster Inorg. Chim. Acta 360 (2007) 203.
[17] L.W. Xue, G.Q. Zhao, Y.J. Han, L.H. Chen, Q.L. Peng, Acta Crystallogr., Sect. E 66 (2010) m1352.
[18] P. Mukherjee, M.G.B. Drew, C.J. Gómez-García, A. Ghosh, Inorg. Chem. 48 (2009) 5848.
[19] P. Mukherjee, M.G.B. Drew, C.J. Gómez-García, A. Ghosh, Inorg. Chem. 48 (2009) 4817.
[20] J. Sirirak, W. Phonsri, D.J. Harding, P. Harding, P. Phommon, W. Chaoprasa, R.M. Hendry, T.M. Roseveare, H. Adams, J. Mol. Struct. 1036 (2013) 439.
[21] J. Sirirak, D.J. Harding, P. Harding, K.S. Murray, B. Moubaraki, L. Liu, S.G. Telfer, Eur. J. Inorg. Chem. (2015) 2534.
[22] D.J. Harding, W. Phonsri, P. Harding, K.S. Murray, B. Moubaraki, G.N.L. Jameson, Dalton Trans. 44 (2015) 15079.
[23] W. Phonsri, D.J. Harding, P. Harding, K.S. Murray, B. Moubaraki, I.A. Gass, J.D. Cashion, G.N.L. Jameson, H. Adams, Dalton Trans. 43 (2014) 17509.
[24] D.J. Harding, W. Phonsri, P. Harding, I.A. Gass, K.S. Murray, B. Moubaraki, J.D. Cashion, L. Liu, S.G. Telfer, Chem. Commun. 49 (2013) 6340.
[25] D.J. Harding, D. Sertphon, P. Harding, K.S. Murray, B. Moubaraki, J.D. Cashion, H. Adams, Chem. Eur. J. 19 (2013) 1082.
[26] S. Hayami, K. Hiki, T. Kawahara, Y. Maeda, D. Urakami, K. Inoue, M. Ohama, S. Kawata, O. Sato, Chem. Eur. J. 15 (2009) 3497.
[27] B.J.C. Vieira, J.C. Dias, I.C. Santos, L.C.J. Pereira, V. da Gama, J.C. Waerenborgh, Inorg. Chem. 54 (2015) 1354.
[28] O. Iasco, E. Rivie, R. Guillot, M. Buron-Le Cointe, J.-F. Meunier, A. Bousseksou, M.-L. Boillot, Inorg. Chem. 54 (2015) 1791.
[29] X.-J. Luo, C.-H. Zhang, J. Zhou, Y.-C. Liu, Acta Crystallogr., Sect. E Struct. Reports Online 69 (2013) m278.
[30] J. McMurtrie, I. Dance, CrystEngComm 11 (2009) 1141.
[31] H. Xu, Z.P. Ni, X.M. Ren, Q.J. Meng, J. Mol. Struct. 752 (2005) 153.
[32] D. Sertphon, D.J. Harding, P. Harding, K.S. Murray, B. Moubaraki, H. Adams, Aust. J. Chem. 67 (2014) 1574.
[33] V. Russell, M. Scudder, I. Dance, J. Chem. Soc., Dalton Trans. (2001) 789.
[34] M.J. Frisch, G.W. Trucks, H.B. Schlegel, G.E. Scuseria, M.A. Robb, J.R. Cheeseman, J.A. Montgomery Jr., T. Vreven, K.N. Kudin, J.C. Burant, J.M. Millam, S.S. Iyengar, J. Tomasi, V. Barone, B. Mennucci, M. Cossi, G.R. Scalmani, J.A. Pope, Gaussian 03 (Revision C.02), Gaussian Inc., Wallingford, CT, 2004.
[35] J. Wagler, D. Gerlach, G. Roewer, Inorg. Chim. Acta 360 (2007) 1935.
[36] Bruker APEXII, Bruker AXS Inc., Madison, WI, USA, 2014.
[37] SADABS and SAINT, Bruker AXS Inc., Madison, WI, USA, 2003.
[38] Rigaku, Rigaku Corporation, Rigaku XRD, Tokyo, Japan, 1996.
[39] G.M. Sheldrick, Acta Crystallogr., Sect. A64 (2008) 112.
[40] G.M. Sheldrick, Acta Crystallogr., Sect. C Struct. Chem. 71 (2015) 3.
[41] O.V. Dolomanov, L.J. Bourhis, R.J. Gildea, J.A.K. Howard, H. Puschmann, J. Appl. Crystallogr. 42 (2009) 339.

ChemPubSoc Europe

DOI: 10.1002/ejic.201501188

EurJIC European Journal of Inorganic Chemistry

Full Paper

Spin Crossover

Substituent-Influenced Spin Crossover in Fe^{III} Quinolylsalicylaldiminates

Darunee Sertphon,[a] David J. Harding,*[a] Phimphaka Harding,[a] Keith S. Murray,[b] Boujemaa Moubaraki,[b] Harry Adams,[c] Adil Alkaş,[d] and Shane G. Telfer[d]

Abstract: The new ligand Hqsal-4-OMe was synthesized, and four iron(III) complexes, $[Fe(qsal\text{-}4\text{-}OMe)_2]Y{\cdot}CH_2Cl_2$ [Hqsal-4-OMe = 4-methoxy-*N*-(8-quinolyl)salicylaldimine; Y = ClO_4 (**1**), NO_3 (**2**)] and $[Fe(qsal\text{-}4\text{-}OMe)_2]Y$ (Y = PF_6 (**3**), OTf (**4**)] as well as the isomer $[Fe(qsal\text{-}5\text{-}OMe)_2]PF_6{\cdot}CH_2Cl_2$ (**5**), were prepared. UV/Vis spectroscopic studies indicated that the complexes are high-spin in solution and exhibit a ligand-to-metal charge-transfer band around 400 nm. X-ray crystallographic studies on $[Fe(qsal\text{-}4\text{-}OMe)_2]Y{\cdot}CH_2Cl_2$ (Y = ClO_4, NO_3) and $[Fe(qsal\text{-}4\text{-}OMe)_2]PF_6$ at 97 K revealed high-spin Fe^{III} centres with one of the qsal-4-OMe ligands significantly distorted from planarity. In contrast, in **5** the Fe^{III} centre is low-spin at low temperature, and the room-temperature structure of **5** shows about 25 % spin crossover (SCO). The structure of $[Fe(qsal\text{-}4\text{-}OMe)_2]Y{\cdot}sol$ shows weak π–π interactions between neighbouring cations, while **5** exhibits stronger π–π interactions that link it into a 1D chain. SQUID magnetometric studies revealed that **1**–**4** are essentially high-spin, whereas **5** undergoes gradual and almost complete SCO up to 350 K. A combination of distortions to the qsal-4-OMe ligand and intermolecular C–H···O interactions involving both the coordinated phenolate oxygen atom and the OMe group seem to be responsible for the loss of SCO.

Introduction

Spin crossover (SCO) complexes remain the subject of much interest owing to their relative simplicity, ease of modification and wide applicability.[1–5] The basis of SCO is the presence of two magnetic states, termed high-spin (HS) and low-spin (LS), which are close in energy.[1,2] Switching between these states may be accomplished by changes in temperature or pressure, and at lower temperatures by light irradiation.[6] Designing compounds in which the HS and LS states are close in energy involves selecting a ligand with the required ligand field appropriate to the metal concerned. In the case of Fe^{III}, suitable ligands generally have an N_4O_2 donor set with SCO between the $S = 1/2$ (LS) and $S = 5/2$ (HS) spin states.[7,8] While finding a ligand set capable of promoting SCO in a given complex is relatively easy, for the material to have any practical use, the SCO should be abrupt and occur close to room temperature with significant hysteresis. This requires a high degree of co-operativity and is generally achieved by favourable supramolecular contacts.[9–11] It follows that designing hysteretic SCO systems is principally a crystal-engineering challenge.[12] An elegant example of this that is of particular relevance to the current work is $[Fe(qsal)_2]NCSe$ [Hqsal = *N*-(8-quinolyl)salicylaldimine]. This complex exhibits an extremely broad hysteresis of 70 K just below room temperature, which has been ascribed to strong π–π interactions between neighbouring qsal ligands forming tightly packed 2D planes.[13–15]

This success led to a large number of subsequent studies mostly focusing on changing the anion,[16–18] and it was not until 2009 that complexes of substituted qsal-X ligands appeared.[19–22] The first to be reported was $[Fe(qsal\text{-}3\text{-}OMe)_2]PF_6{\cdot}nH_2O$ (n = 0 or 2), in which the water solvate is HS whereas the non-solvated compound is LS.[19] Following this study, in 2013 we reported $[Fe(qsal\text{-}5\text{-}OMe)_2]Y$ (Y = Cl, BF_4, NCS, PF_6 and BPh_4), of which many of the compounds exhibit SCO, in three cases with hysteresis.[23,24] At about the same time Boillot and co-workers reported $[Fe(salEen\text{-}4\text{-}OMe)_2]Y$ (HsalEen = *N*-ethyl-*N*-(2-aminoethyl)salicylaldimine; Y = PF_6, NO_3), which in the case of the nitrate shows improved hysteresis compared to the prototypical compound in this family, $[Fe(salEen\text{-}3\text{-}OMe)_2]PF_6$.[25,26] In both systems it is clear that the position of the substituent is crucial in controlling SCO characteristics. In seeking to better understand how minor structural modifications of the ligand affect SCO, we have now prepared $[Fe(qsal\text{-}4\text{-}OMe)_2]Y$ (Y = ClO_4, NO_3, PF_6, OTf). We demonstrate how this subtle change at the ligand radically impacts both the local

[a] *Molecular Technology Research Unit, Walailak University, Thasala, Nakhon Si Thammarat, 80161, Thailand*
E-mail: hdavid@wu.ac.th
www.mtruwu.com
http://tandfonline.com/tcme
[b] *School of Chemistry, Monash University, Clayton, Melbourne, Victoria, 3800, Australia*
[c] *Department of Chemistry, University of Sheffield, Sheffield, S3 7HF, UK*
[d] *MacDiarmid Institute for Advanced Materials and Nanotechnology, Institute of Fundamental Sciences, Massey University, Palmerston North, New Zealand*

Supporting information and ORCID(s) from the author(s) for this article are available on the WWW under http://dx.doi.org/10.1002/ejic.201501188.

© 2016 Wiley-VCH Verlag GmbH & Co. KGaA, Weinheim

coordination environment and the supramolecular packing and consequently the SCO properties of the compounds in this series.

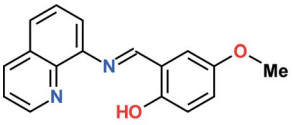

Hqsal-5-OMe

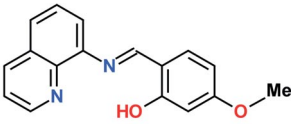

Hqsal-4-OMe

Results and Discussion

Ligand Synthesis

The ligand Hqsal-4-OMe was prepared by our standard procedure from diisopropyl ether.[27] IR and ^{1}H NMR spectroscopic data are consistent with the proposed structure of the ligand (see Supporting Information). Interestingly, the imine stretching frequency is almost 20 cm^{-1} higher than that of the related Hqsal-5-OMe ligand, while the electronic spectrum shows a single $\pi\rightarrow\pi^*$ transition at 340 nm and is essentially identical to that of Hqsal-5-OMe.[23]

Synthesis and Characterization of [Fe(qsal-4-OMe)$_2$]Y

The complexes were all synthesized by layered diffusion of a solution of FeY_3 in MeOH on top of a solution of Hqsal-4-OMe and NEt_3 in CH_2Cl_2. In the case of Y = PF_6 and OTf, the FeY_3 solution was prepared in situ from $FeCl_3$ and an appropriate potassium or silver salt. After 3–5 d, air-stable black or dark brown crystals of the products [Fe(qsal-4-OMe)$_2$]Y·CH_2Cl_2 [Y = ClO_4 (**1**), NO_3 (**2**)] and [Fe(qsal-4-OMe)$_2$]Y [Y = PF_6 (**3**), OTf (**4**)] were isolated. For further comparison, we also synthesized [Fe(qsal-5-OMe)$_2$]PF_6·CH_2Cl_2 (**5**), which is the CH_2Cl_2 solvate of the previously reported [Fe(qsal-5-OMe)$_2$]PF_6.[24] The difference from our previous synthesis lies in the use of $AgPF_6$ instead of KPF_6, which yields a much more crystalline product.[24]

IR spectroscopy revealed stretches between 1601 and 1608 cm^{-1} for **1**–**4** (Table 1), which are typical values for the imine stretch in [Fe(qsal-X)$_2$]$^+$ complexes.[23,24] The stretches of the anions were also readily identified and confirmed the proposed formulation. The UV/Vis spectra of **1**–**4** (Figure 1) were recorded in CH_2Cl_2 and display intense absorption bands at 340 and about 400 nm, which are assigned to $\pi\rightarrow\pi^*$ and ligand-to-metal charge-transfer (LMCT) transitions, respectively, by comparison with the related [Fe(qsal-X)$_2$]$^+$ complexes.[23,24] The minor differences in extinction coefficients reflect the different solubilities of the complexes. The absence of a peak around 830 nm suggests that the complexes are HS in solution at room temperature.[20]

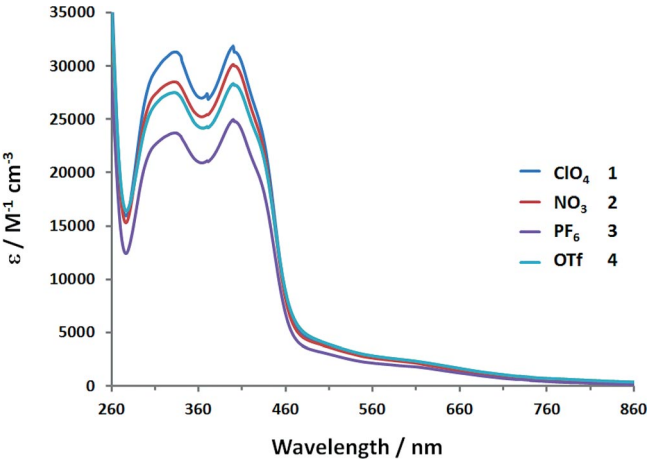

Figure 1. UV/Vis spectra of [Fe(qsal-4-OMe)$_2$]Y in CH_2Cl_2.

Structural Studies on [Fe(qsal-4-OMe)$_2$]Y·Solvent

Crystals of [Fe(qsal-4-OMe)$_2$]ClO_4·CH_2Cl_2 (**1**) and [Fe(qsal-4-OMe)$_2$]NO_3·CH_2Cl_2 (**2**) crystallized from MeOH/CH_2Cl_2 in the triclinic space group $P\bar{1}$ (Figure 2). [Fe(qsal-4-OMe)$_2$]PF_6 (**3**) crystallized in the monoclinic space group $P2_1/n$. The structures were determined at 97 K, and in all cases the Fe centre is six-coordinate with four nitrogen and two oxygen atoms from two meridional qsal ligands, leaving the oxygen atoms *cis* to each other. The Fe–ligand bond lengths and other coordination parameters are given in Table 2. The Fe–N/O bond lengths in **1**–**3** are in the ranges 2.087–2.183 and 1.936–1.904, respectively, and are close to the corresponding distances for the HS Fe^{III} centre in [Fe(qsal-5-OMe)$_2$]Cl·2MeOH·0.5H_2O.[23] However, the Fe–N bond lengths in [Fe(qsal-5-OMe)$_2$]Cl·2MeOH·0.5H_2O are more similar to each other than those in [Fe(qsal-4-OMe)$_2$]$^+$, which may influence the ability of the Fe centre to undergo SCO.

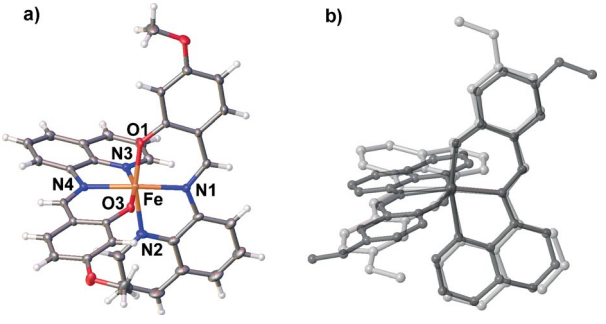

Figure 2. Left: view of the asymmetric unit of [Fe(qsal-4-OMe)$_2$]ClO_4·CH_2Cl_2 **1**; thermal ellipsoids are drawn at 50 % probability. Right: overlay of **1** (light grey) and the HS centre of [Fe(qsal-5-OMe)$_2$]Cl·2MeOH·0.5H_2O (dark grey).

Table 1. Spectroscopic data of **1**–**4**.

Compound	IR [cm^{-1}][a]		λ_{max} [nm] (ε_{max} [M^{-1} cm^{-1}])[b]
	$\nu_{C=N}$	ν_{anion}	
[Fe(qsal-4-OMe)$_2$]ClO_4 (**1**)	1608	1091	340 (24000), 406 (25000)
[Fe(qsal-4-OMe)$_2$]NO_3 (**2**)	1605	1365	340 (27000), 407 (28000)
[Fe(qsal-4-OMe)$_2$]PF_6 (**3**)	1607	845	340 (31000), 406 (32000)
[Fe(qsal-4-OMe)$_2$]OTf (**4**)	1601	1276, 1149	340 (27000), 407 (28000)

[a] As KBr discs. [b] In CH_2Cl_2.

Moreover, in **1**–**3** one of the qsal-4-OMe ligands is significantly distorted, as shown by the angle of 17–23° between the quinoline and phenolate rings. By comparison [Fe(qsal-5-

© 2016 Wiley-VCH Verlag GmbH & Co. KGaA, Weinheim

Table 2. Selected bond lengths [Å] and octahedral distortion parameters [°] for **1**–**3** at 97 K and **5** at 108 and 293 K.

	1-ClO_4	**2**-NO_3	**3**-PF_6	**5**-108	**5**-293
Fe1–O1	1.921(1)	1.920(3)	1.936(2)	1.886(6)	1.895(9)
Fe1–O3	1.923(1)	1.921(3)	1.904(2)	1.881(7)	1.862(8)
Fe1–O_{av}	1.922(1)	1.921(3)	1.920(2)	1.884(7)	1.879(9)
Fe1–N1	2.106(2)	2.107(3)	2.117(3)	1.979(7)	2.04(1)
Fe1–N2	2.164(2)	2.161(4)	2.157(3)	1.94(1)	1.98(1)
Fe1–N3	2.183(2)	2.166(3)	2.182(3)	1.978(8)	2.024(9)
Fe1–N4	2.087(2)	2.096(3)	2.095(3)	1.937(9)	1.98(1)
Fe1–N_{ave}	2.135(2)	2.133(3)	2.139(3)	1.96(1)	2.01(1)
Σ[a]	69.7	68.7	74.9	47.7	50.1
Θ[b]	198.7	195.9	213.9	74.4	107.7
α[c]	19.2	16.7	22.7	1.0	3.1
α	5.3	2.6	3.8	0.9	1.6

[a] $\Sigma = \sum_{i=1}^{12} |90-\alpha_i|$, where α_i are the twelve *cis* N/O–Fe–N/O angles.[29] [b] $\Theta = \sum_{i=1}^{24} |60-\theta_i|$, where θ_i are the 24 unique N/O–Fe–N/O angles measured on the projection of two triangular faces of the octahedron along their common pseudo-threefold axis.[30] [c] α= the angle between the planes of the quinoline and phenolate rings.

OMe)$_2$]Cl·2MeOH·0.5H_2O and **5** (at 293 K, see below) have values of 0.9–5.6°. We have previously shown for [Fe(qsal-5-*t*Bu)$_2$]$^+$ that strong distortions in the qsal-X ligands frequently result in systems in which SCO is switched off.[28] In [Fe(qsal-5-*t*Bu)$_2$]$^+$ the distortion is caused by the large steric bulk of the *t*Bu group, while in the current system the distortion may be due to the solid-state packing, which necessitates ligand distortion for C–H···O interactions to form.

The structure of **5** was determined at 108 and 293 K. At both temperatures the structure belongs to the triclinic space group $P\bar{1}$. The Fe–N/O bond lengths at 108 K are characteristic of LS Fe^{III} and become longer by about 0.03 Å on average at room temperature (Table 2), which suggests the onset of SCO. This is in agreement with magnetic susceptibility studies (see below).[31] As in [Fe(qsal-F)$_2$]NCS,[31] the incomplete SCO (ca. 25 % between 108 and 293 K) is best represented by the octahedral distortion parameter Θ, the change in which is about 33 (cf. $\Delta\Theta$= 128 for complete SCO in [Fe(qsal-I)$_2$]OTf·MeOH).[32]

In addition to the changes at the Fe centre, there are also significant differences in the two unit cells with the *a* and *b* axes increasing in length by about 0.20 Å, while the change in the *c* axis is modest (ca. 0.12 Å). This leads to a change in the unit-cell volume of 64 Å^3 and is comparable with the change that occurs in [Fe(qsal-F)$_2$]NCS between 100 and 200 K, whereby 50 % of the centres undergo SCO.[31]

The solid-state packings in **1** and **2** are very similar with intermolecular π–π interactions forming dimers (Table 3).[33] The twist in the other qsal-4-OMe ligand prevents substantial overlap such that the π–π interaction is replaced by a pair of C–H···O interactions resulting in dislocation of the 1D chain that is such a common feature of [Fe(qsal-5-X)$_2$]$^+$ complexes (Figure 3).[23,24,31,32,34] In **5**, in which both qsal-5-OMe ligands are planar, 1D chains are formed by two orthogonal intermolecular π–π interactions with plane-to-plane distances of 3.28–3.32 Å, which lengthen by about 0.08 Å at room temperature (Table 3). In comparison, the plane-to-plane distances in **1** and **2** of 3.34–3.35 Å suggest that the dimers have weaker π–π interactions. The 1D chains formed in **1**–**3** are connected to each other by parallel fourfold aryl embrace (P4AE) or pseudo-P4AE interactions.[35] In the latter, the C–H···π interactions are replaced by C–H···O interactions involving the coordinated phenolate oxygen atom (Figure 4). Unusually, in **5** there are no P4AE interactions, which contrasts with all other [Fe(qsal-5-OMe)$_2$]$^+$ complexes. This may be responsible for the more gradual SCO in this compound.[23,24]

The packing in **3** is radically different to those of all the other compounds, with weak π–π interactions between the phenyl and quinoline rings forming a 1D column (Figure 5). C–H···O interactions then link these in a ladder packing motif. There are no strong interactions between the [Fe(qsal-4-OMe)$_2$]$^+$ units.

In the case of the ClO_4 and NO_3 complexes the 2D planes are connected by C–H···O interactions involving the methoxyl groups to form 3D supramolecular networks (see Figure 6). Despite the differences in the [Fe(qsal-4-OMe)$_2$]Y complexes compared with the [Fe(qsal-5-OMe)$_2$]Y analogues, there is still signif-

Table 3. Supramolecular interaction distances in **1**–**3** and **5**.

	1-ClO_4	**2**-NO_3	**3**-PF_6	**5**-108 K
π				
Cent···cent[a]	3.474	3.439	4.067	3.539
Plane···plane[b]	3.351	3.338	–	2.274
Cent···cent[a]	–	–	–	3.624
Plane···plane[b]	–	–	–	3.317
C–H···O				
In 1D chains	2.668 (O1···H18)	2.646 (O1···H18)	2.692 (O3···H2)	2.594 (O1···H132)
	2.647 (O3···H10)	2.559 (O3···H17)		2.549 (O1···H132)
OMe groups	2.551 (O2···H11)	2.542 (O2···H16)	2.636 (O4···H7)	2.630 (O4···H132)
	2.396 (O7···H16)	2.585 (O7···H25B)		
		2.586 (O7′···H25B)		
P4AE				
Cent···cent[c]	3.719	3.623	–	–
Plane···plane[d]	3.295	3.323	–	–
C–H···π	2.654	2.614 (O1···H32)	–	3.014

[a] The centroid···centroid distance between the centroids of the phenyl and quinoline rings. [b] The plane···plane distance is the distance between the phenyl and quinoline planes. [c] The centroid···centroid distance between the centroids of the quinoline rings. [d] The plane···plane distance between the quinoline planes.

© 2016 Wiley-VCH Verlag GmbH & Co. KGaA, Weinheim

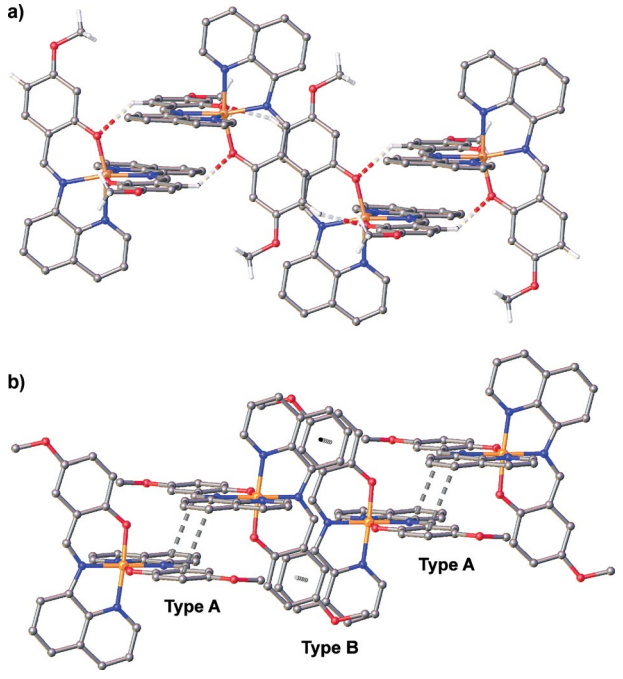

Figure 3. Top: view of the π–π and C–H···O interactions in **2**. Bottom: the π–π interactions in **5** that form the 1D chains.

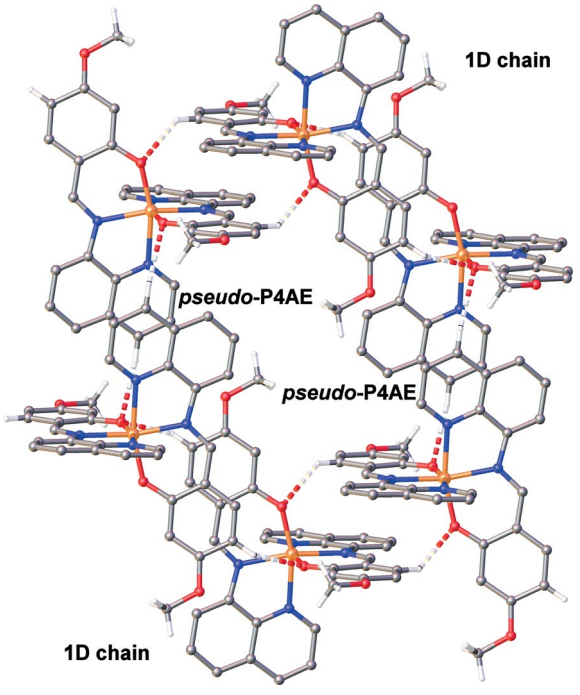

Figure 4. View of pseudo-P4AE interactions in **2**; only selected hydrogen atoms are shown in the interest of clarity.

icant cooperativity. This suggests that the lack of SCO in **1**–**4** is most probably due to the distortion in the qsal-4-OMe ligand.

Magnetic Studies on [Fe(qsal-4-OMe)$_2$]Y·Solvent

The magnetic properties of **1**–**4** were studied by SQUID magnetometry and are presented as $\chi_M T$ versus T plots in Figure 7.

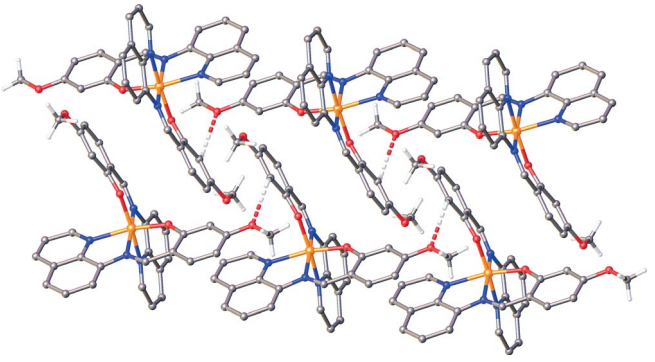

Figure 5. View of the ladder motif formed by π–π and C–H···O interactions in **3**.

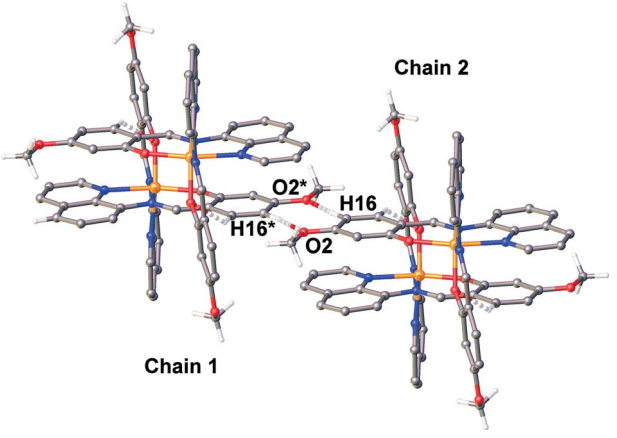

Figure 6. View of the C–H···O interactions involving the OMe groups in **2**. Only selected hydrogen atoms are shown for the sake of clarity.

The $\chi_M T$ values are in the range 4.00–4.50 cm^3 K mol^{-1} for **1**–**3** and are invariant between 30 and 300 K, indicative of the compounds being HS only. The OTf analogue shows about 25 % SCO, although this is very gradual and occurs over about 150 K. Despite repeated attempts we have been unable to get crystals of sufficient quality for a structural study on **4**.

The lack of complete SCO in **1**–**4** most likely stems from the position of the OMe group, which, as the structural studies show, results in non-planar qsal-4-OMe ligands and significant distortion at the metal centre. It is noteworthy that while **3** is HS, **5** and [Fe(qsal-5-OMe)$_2$]PF$_6$ both exhibit SCO, which confirms that qsal-4-OMe generates a weaker ligand field than qsal-5-OMe; similar conclusions have been drawn concerning [Fe(salEen-4-OMe)$_2$]PF$_6$.[25] Moreover, [Fe(qsal-3-OMe)$_2$]PF$_6$·2H$_2$O is also trapped in the HS state.[19] Indeed, in [Fe(qsal)$_2$][Ni(pddt)$_2$][36] and [Fe(qsal)$_2$][M(pds)$_2$] (pddt = 6,7-dihydro-5*H*-1,4-dithiepin-2,3-dithiolate, pds = pyrazine-2,3-diselenolate, M = Cu, Au)[37] the presence of a similar degree of distortion at the Fe centre also results in SCO being switched off. We cannot absolutely rule out solvent effects influencing SCO properties in **1** and **2**, but the fact that the structures are largely constructed by π–π and C–H···O interactions and that solvent has relatively minor effects on the SCO behaviour of related compounds suggests that in this case substituent effects are more significant.

© 2016 Wiley-VCH Verlag GmbH & Co. KGaA, Weinheim

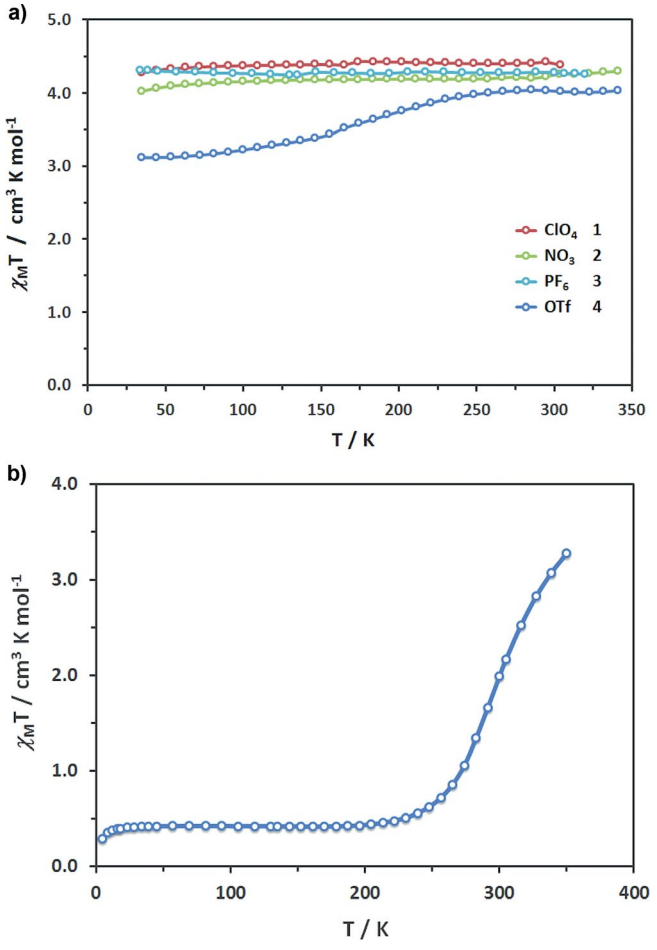

Figure 7. $\chi_M T$ versus T plots for **1**–**4** (top) and **5** (bottom).

In contrast to **1**–**4**, **5** does undergo gradual and almost complete SCO with $\chi_M T$ = 3.27 cm^3 K mol^{-1} at 350 K. This behaviour is slightly different to that of [Fe(qsal-5-OMe)$_2$]PF$_6$, for which SCO is slightly more gradual and less complete ($\chi_M T$ = 2.60 cm^3 K mol^{-1} at 350 K). This agrees with our studies on [Fe(qsal-5-I)$_2$]OTf·MeOH, in which loss of MeOH only slightly impacts $T_{1/2}$, although the non-solvated compound does exhibit broader hysteresis.[32]

Conclusions

We have prepared four Fe^{III} complexes of the new Hqsal-4-OMe ligand. Solution studies revealed that the compounds are HS at room temperature and that the OMe group does not significantly alter the electronic properties of **1**–**4** compared to the related [Fe(qsal-5-OMe)$_2$]Y compounds. Structural analysis of **1**–**3** revealed that the compounds often contain a distorted qsal-4-OMe ligand, which magnetic studies show results in loss of SCO making the complexes essentially HS. The solid-state packing is also impacted, with only weak π–π interactions observed rather than the 1D π–π chain that is common in the [Fe(qsal-5-X)$_2$]$^+$ analogues. In certain cases there are additional C–H···O interactions, which would be expected to further weaken the ligand field provided by qsal-4-OMe. Overall, it is clear that the position of the OMe group on the ligand and solvent effects significantly affect both the coordination and supramolecular sphere in [Fe(qsal-4-OMe)$_2$]$^+$. This confirms our previous findings that the position and nature of the substituent is an important consideration in successfully obtaining SCO compounds. Further studies on whether this observation is applicable to other substituent groups are underway.

Experimental Section

General Remarks: All manipulations were performed in air with reagent-grade solvents. All other chemicals were purchased from Aldrich Chemical Company and used as received. IR (as KBr discs) were recorded with a PerkinElmer Spectrum One infrared spectrophotometer in the range 400–4000 cm^{-1}. Electronic spectra were recorded in CH_2Cl_2 at room temperature with a Shimadzu UV-1700 UV/Vis spectrophotometer. ^{1}H NMR spectra were recorded with a Bruker 300 MHz FT NMR spectrometer at 25 °C in $CDCl_3$ with $SiMe_4$ added as an internal standard. Elemental analyses were carried out with a Eurovector EA3000 analyzer by staff of the School of Chemistry, University of Bristol, UK. ESI-MS was carried out with a Bruker Daltonics 7.0T Apex 4 FTICR mass spectrometer by staff at the National University of Singapore.

Hqsal-4-OMe: 8-Aminoquinoline (1.442 g, 10.0 mmol) was dissolved in diisopropyl ether (30 cm^3) to give a pale yellow solution. 2-Hydroxy-4-methoxybenzaldehyde (1.521 cm^3, 10.0 mmol) was added and the mixture stirred for 4 h to give an orange solution. The solvent was allowed to evaporate slowly to give orange crystals, which were isolated by filtration and air-dried (2.120 g, 85 %). IR (KBr): $\tilde{\nu}_{max}$ = 3060, 2937 (ν_{CH}), 1633 ($\nu_{C=N}$). λ_{max}/nm (CH_2Cl_2, ε/M^{-1} cm^{-1}) 340 (38000). ^{1}H NMR ($CDCl_3$, 295 K, 300 MHz): δ= 8.99 (dd, J_{HH} = 1.2, 3.9 Hz, 1 H$_a$), 8.71 (s, 1 H$_g$), 8.16 (d, J_{HH} = 8.1 Hz, 1 H$_c$), 7.67 (dd, J_{HH} = 1.5, 7.8 Hz, 1 H$_d$), 7.57–7.49 (m, 2H$_{e,h}$), 7.45 (dd, J_{HH} = 3.9, 8.1 Hz, H$_b$) 7.25 (d, , J_{HH} = 9.0 Hz, 1 H$_f$), 6.47 (d, , J_{HH} = 2.1 Hz, 1 H$_j$), 6.40 (dd, , J_{HH} = 2.1, 8.7 Hz, 1 H$_i$), 3.84 (s, 3 H, OCH_3) ppm. $C_{17}H_{14}N_2O_2$ (278.31): calcd. C 73.37, H 5.07, N 10.06; found C 78.40, H 5.12, N 9.93.

[Fe(qsal-4-OMe)$_2$]ClO$_4$·CH$_2$Cl$_2$ (1): Crystals of **1** were formed by diffusion. A solution of Hqsal-4-OMe (0.0248 g, 0.1 mmol) in CH_2Cl_2 (2 cm^3) was placed at the bottom of a test tube, Et_3N (0.01 cm^3, 0.1 mmol) was added and then blank MeOH (3 cm^3) was layered in the middle as a buffer layer. Finally, a solution of Fe(ClO$_4$)$_3$·6H$_2$O (0.0234 g, 0.05 mmol) in MeOH (5 cm^3) was layered on top and the test tube sealed. The tube was left for about one week at room temperature, and black crystals were obtained at the bottom. The black crystals were washed with diethyl ether (2 × 2 cm^3) and air-dried (0.065 g, 92 %). MS (ESI): m/z = 610.2 [Fe(qsal-4-OMe)$_2$]$^+$, 99 ClO_4^-. $C_{34}H_{26}ClFeN_4O_8$ (709.90): calcd. C 57.51, H 3.69, N 7.89; found C 57.87, H 3.73, N 7.70 (loss of CH_2Cl_2).

[Fe(qsal-4-OMe)$_2$]NO$_3$·CH$_2$Cl$_2$ (2): Crystals of **2** were prepared in a similar manner to those of **1** by using a solution of Fe(NO$_3$)$_3$·9H$_2$O instead of Fe(ClO$_4$)$_3$·6H$_2$O. Black crystals were obtained after one week(0.058 g, 86 %). MS (ESI): m/z = 610.2 [Fe(qsal-4-OMe)$_2$]$^+$. $C_{34}H_{26}FeN_5O_7$·0.5CH_2Cl_2: calcd. C 57.97, H 3.81, N 9.80; found C 57.87, H 3.88, N 10.39.

[Fe(qsal-4-OMe)$_2$]PF$_6$ (3): Crystals of **3** were prepared by placing a solution of Hqsal-4-OMe (0.248 g, 1.0 mmol) in CH_2Cl_2 (2 cm^3) at the bottom of a test tube and adding Et_3N (0.14 cm^3, 1.0 mmol) and then blank MeOH (3 cm^3) as a buffer layer. Finally, a solution of Fe(PF$_6$)$_3$, prepared from $FeCl_3$ (0.081 g, 0.5 mmol) and $AgPF_6$

© 2016 Wiley-VCH Verlag GmbH & Co. KGaA, Weinheim

(0.379 g, 1.5 mmol) in MeOH (5 cm^3), was layered on top and the test tube sealed. Black crystals of **4** were obtained (0.355 g, 85 %). MS (ESI): m/z = 610.2 $[Fe(qsal\text{-}4\text{-}OMe)_2]^+$, 145 PF_6^-. $C_{34}H_{26}F_6FeN_4O_4P$ (755.41): calcd. C 54.06, H 3.47, N 7.42; found C 54.61, H 3.56, N 7.27.

$[Fe(qsal\text{-}4\text{-}OMe)_2]OTf$ (4): Crystals of **4** were prepared in a similar manner to those of **3**, except that AgOTf was used instead of $AgPF_6$ to make $Fe(OTf)_3$, to give black crystals, (0.301 g, 68 %). MS (ESI): m/z = 610.2 $[Fe(qsal\text{-}4\text{-}OMe)_2]^+$, 149 OTf. $C_{35}H_{26}F_3FeN_4O_7S$ (759.51): calcd. C 55.34, H 3.45, N 7.38; found C 55.45, H 3.65, N 7.74.

$[Fe(qsal\text{-}5\text{-}OMe)_2]PF_6{\cdot}CH_2Cl_2$ (5): Crystals of **5** were prepared in a similar manner to those of **3** by using Hqsal-5-OMe instead of Hqsal-4-OMe, which gave black needles (0.298 g, 71 %). $C_{35}H_{28}Cl_2F_6FeN_4O_4P$ (840.35): calcd. C 50.03, H 3.36, N 6.67; found C 50.45, H 3.41, N 7.02. All other data were identical to those of the previously reported complex $[Fe(qsal\text{-}5\text{-}OMe)_2]PF_6$.[24]

X-ray Crystallography: Crystal data and data processing parameters for the structures of **1**–**3** are given in Tables 4 and 5. X-ray quality crystals of **1**–**3** were grown by layering a solution of FeY_3 in MeOH over a solution of Hqsal-4-OMe and NEt_3 in CH_2Cl_2. Crystals of $[Fe(qsal\text{-}5\text{-}OMe)_2]PF_6{\cdot}CH_2Cl_2$ were grown in a similar way. Crystals were mounted on a glass fibre by using perfluoropolyether oil and cooled rapidly to 97 K in a stream of cold nitrogen for **1**–**3**. The diffraction data of **1**–**3** were collected with a Bruker APEXII area detector with graphite-monochromated Mo-K_α radiation (λ = 0.71073 Å).[38] After data collection, in each case an empirical absorption correction (SADABS) was applied.[39] In the case of **5**, X-ray crystallographic data were collected at 108 and 293 K with a Rigaku Spider diffractometer equipped with a MicroMax MM007 rotating-anode generator, Cu_α radiation (λ = 1.54178 Å), high-flux Osmic multilayer mirror optics, and a curved image-plate detector.[40] The data were integrated and scaled and averaged with FS Process. The structures were then solved by direct methods and refined on all F^2 data with the SHELX suite of programs or Olex2 (in the case of **3**).[41,42] In all cases non-hydrogen atoms were refined with anisotropic thermal parameters; hydrogen atoms were included in calculated positions and refined with isotropic thermal parameters which were about 1.2 × (aromatic CH) or 1.5 × (Me, CH_2, OH) the equivalent isotropic thermal parameters of their parent carbon atoms. All pictures were generated with OLEX2.[43]

Table 5. Crystallographic data and structure refinement for **5** at 108 and 295 K.

	5-108	**5**-293
Formula	$C_{35}H_{28}Cl_2F_6FeN_4O_4P$	$C_{35}H_{28}Cl_2F_6FeN_4O_4P$
M [g mol^{-1}]	840.33	840.33
Crystal system	triclinic	triclinic
Space group	$P\bar{1}$	$P\bar{1}$
a [Å]	12.2866(4)	12.4650(4)
b [Å]	12.4452(4)	12.6584(4)
c [Å]	12.8972(9)	13.0200(9)
α[°]	81.997(6)	81.504(6)
β[°]	72.168(5)	72.483(5)
γ[°]	62.706(4)	62.160(4)
T [K]	108(2)	293(2)
V [$Å^3$]	1668.34(16)	1732.30(16)
Z	2	2
Absorption coefficient [mm^{-1}]	6.284	6.052
Reflections collected	21144	20566
Independent reflections, R_{int}	3436, 0.1174	3477, 0.0770
Max., min. transmission	0.885, 0.145	1.000, 0.474
Restraints/parameters	0/480	0/480
Final R indices [$I > 2\sigma(I)$]: R_1, wR_2	0.0937, 0.2212	0.1258, 0.3049

CCDC 1431331 (for **1**), 1431330 (for **2**), 1431329 (for **3**), 1431332 (for **5**, at 108 K)), and 1431333 (for **5**, at 293 K) contain the supplementary crystallographic data for this paper. These data can be obtained free of charge from The Cambridge Crystallographic Data Centre.

Magnetic Susceptibility Studies: Data were collected with a Quantum Design MPMS 5 SQUID magnetometer under an applied field of 1 T over the temperature range 30–350 K for **1**–**4** and 2–350 K for **5**. The powdered or polycrystalline samples were placed in gel capsules and care was taken to allow long thermal equilibration times at each temperature.

Acknowledgments

The authors thank the Thailand Research Fund (grant number RSA5580028 and RSA5880048) for funding this research and

Table 4. Crystallographic data and structure refinement for **1**–**3**.

	1	**2**	**3**
Formula	$C_{35}H_{28}Cl_3FeN_4O_8$	$C_{35}H_{28}Cl_2FeN_5O_7$	$C_{34}H_{26}F_6FeN_4O_4P$
M [g mol^{-1}]	794.81	757.37	755.41
Crystal system	triclinic	triclinic	monoclinic
Space group	$P\bar{1}$	$P\bar{1}$	$P2_1/n$
a [Å]	11.9319(5)	11.7933(7)	18.994(6)
b [Å]	12.6183(6)	12.4411(8)	8.922(3)
c [Å]	13.4637(6)	13.2728(8)	20.243(6)
α[°]	111.791(2)	111.588(3)	90.00
β[°]	105.569(2)	103.252(4)	104.25(2)
γ[°]	103.068(2)	102.646(4)	90.00
T [K]	97(2)	97(2)	97(2)
V [$Å^3$]	1688.68(13)	1660.69(18)	3324.9(18)
Z	2	2	4
Absorption coefficient [mm^{-1}]	0.744	0.67	0.58
Reflections collected	39634	41146	24728
Independent reflections, R_{int}	9266, 0.065	7527, 0.057	7650, 0.109
Max., min. transmission	–	0.0890, 0.2530	0.780, 0.888
Restraints/parameters	0/462	267/447	0/452
Final R indices [$I > 2\sigma(I)$]: R_1, wR_2	0.044, 0.114	0.101, 0.266	0.064, 0.141

© 2016 Wiley-VCH Verlag GmbH & Co. KGaA, Weinheim

financial support from the Thailand Research Fund in the form of a Royal Golden Jubilee scholarship to D. S. (PHD/0135/2554).

Keywords: Spin crossover · Iron · N,O ligands · Magnetic properties · Substituent effects

[1] M. A. Halcrow (Ed.), *Spin-Crossover Materials: Properties and Applications*, John Wiley & Sons, Chichester, UK, **2013**.
[2] P. Gütlich, H. A. Goodwin, *Top. Curr. Chem.* **2004**, *233*, 1–47.
[3] J.-F. Létard, P. Guionneau, L. Goux-Capes, *Top. Curr. Chem.* **2004**, *235*, 221–249.
[4] A. Bousseksou, G. Molnár, L. Salmon, W. Nicolazzi, *Chem. Soc. Rev.* **2011**, *40*, 3313–35.
[5] P. Gütlich, A. B. Gaspar, Y. Garcia, *Beilstein J. Org. Chem.* **2013**, *9*, 342–91.
[6] J.-F. Létard, *J. Mater. Chem.* **2006**, *16*, 2550–59.
[7] P. J. van Koningsbruggen, Y. Maeda, H. Oshio, *Top. Curr. Chem.* **2004**, *233*, 259–324.
[8] M. Nihei, T. Shiga, Y. Maeda, H. Oshio, *Coord. Chem. Rev.* **2007**, *251*, 2606–2621.
[9] M. A. Halcrow, *Chem. Soc. Rev.* **2011**, *40*, 4119–42.
[10] M. A. Halcrow, *Chem. Lett.* **2014**, *43*, 1178–1188.
[11] P. Guionneau, *Dalton Trans.* **2014**, *43*, 382–93.
[12] G. R. Desiraju, *J. Am. Chem. Soc.* **2013**, *135*, 9952–67.
[13] S. Hayami, Z. Gu, H. Yoshiki, A. Fujishima, O. Sato, *J. Am. Chem. Soc.* **2001**, *123*, 11644–50.
[14] S. Hayami, T. Kawahara, G. Juhasz, K. Kawamura, K. Uehashi, O. Sato, Y. Maeda, *J. Radioanal. Nucl. Chem.* **2003**, *255*, 443–447.
[15] S. Hayami, K. Hiki, T. Kawahara, Y. Maeda, D. Urakami, K. Inoue, M. Ohama, S. Kawata, O. Sato, *Chem. Eur. J.* **2009**, *15*, 3497–3508.
[16] K. Takahashi, H. Cui, H. Kobayashi, Y. Einaga, O. Sato, *Chem. Lett.* **2005**, *34*, 1240–1241.
[17] K. Takahashi, H.-B. Cui, Y. Okano, H. Kobayashi, Y. Einaga, O. Sato, *Inorg. Chem.* **2006**, *45*, 5739–5741.
[18] C. Faulmann, K. Jacob, S. Dorbes, S. Lampert, I. Malfant, M.-L. Doublet, L. Valade, J. A. Real, *Inorg. Chem.* **2007**, *46*, 8548–59.
[19] J. C. Dias, B. Vieira, I. C. Santos, L. C. J. Pereira, V. Da Gama, *Inorg. Chim. Acta* **2009**, *362*, 2076–2079.
[20] B. Djukic, P. A. Dube, F. Razavi, T. Seda, H. A. Jenkins, J. F. Britten, M. T. Lemaire, *Inorg. Chem.* **2009**, *48*, 699–707.
[21] B. Djukic, M. T. Lemaire, *Inorg. Chem.* **2009**, *48*, 10489–10491.
[22] A. I. S. Neves, J. C. Dias, B. J. C. Vieira, I. S. Santos, M. B. Castelo Branco, L. C. J. Pereira, J. C. Waerenborgh, M. Almeida, D. Belo, V. Da Gama, *CrystEngComm* **2009**, *11*, 2160–68.
[23] D. J. Harding, D. Sertphon, P. Harding, K. S. Murray, B. Moubaraki, J. D. Cashion, H. Adams, *Chem. Eur. J.* **2013**, *19*, 1082–90.
[24] D. Sertphon, D. J. Harding, P. Harding, K. S. Murray, B. Moubaraki, J. D. Cashion, H. Adams, *Eur. J. Inorg. Chem.* **2013**, 788–795.
[25] A. Tissot, P. Fertey, R. Guillot, V. Briois, M.-L. Boillot, *Eur. J. Inorg. Chem.* **2014**, 101–109.
[26] A. Tissot, R. Bertoni, E. Collet, L. Toupet, M.-L. Boillot, *J. Mater. Chem.* **2011**, *21*, 18347.
[27] J. Sirirak, W. Phonsri, D. J. Harding, P. Harding, P. Phommon, W. Chaoprasa, R. M. Hendry, T. M. Roseveare, H. Adams, *J. Mol. Struct.* **2013**, *1036*, 439–446.
[28] D. Sertphon, D. J. Harding, P. Harding, K. S. Murray, B. Moubaraki, H. Adams, *Aust. J. Chem.* **2014**, *67*, 1574–1580.
[29] J. K. McCusker, A. L. Rheingold, D. N. Hendrickson, *Inorg. Chem.* **1996**, *35*, 2100–2112.
[30] M. Marchivie, P. Guionneau, J. F. Létard, D. Chasseau, *Acta Crystallogr., Sect. B Struct. Sci.* **2005**, *61*, 25–28.
[31] W. Phonsri, D. J. Harding, P. Harding, K. S. Murray, B. Moubaraki, I. A. Gass, J. D. Cashion, G. N. L. Jameson, H. Adams, *Dalton Trans.* **2014**, *43*, 17509–17518.
[32] D. J. Harding, W. Phonsri, P. Harding, I. A. Gass, K. S. Murray, B. Moubaraki, J. D. Cashion, L. Liu, S. G. Telfer, *Chem. Commun.* **2013**, *49*, 6340–6342.
[33] C. Janiak, *J. Chem. Soc., Dalton Trans.* **2000**, 3885–3896.
[34] D. J. Harding, W. Phonsri, P. Harding, K. S. Murray, B. Moubaraki, G. N. L. Jameson, *Dalton Trans.* **2015**, *44*, 15079–15082.
[35] V. Russell, M. Scudder, I. Dance, *J. Chem. Soc., Dalton Trans.* **2001**, 789–799.
[36] X.-M. Li, Y. Ji, C.-F. Wang, J.-L. Zuo, X.-Z. You, *J. Coord. Chem.* **2009**, *62*, 1544–1552.
[37] J. C. Dias, A. Soriano-Portillo, M. Clemente-Léon, C. Giménez-Saiz, J. R. Galán-Mascarós, C. J. Gómez-García, E. Coronado, *Inorg. Chim. Acta* **2007**, *360*, 3843–3847.
[38] *APEXII*, Bruker AXS Inc., Madison, WI, USA, **2005**.
[39] *SADABS* and *SAINT*, Bruker AXS Inc., Madison, WI, USA, **2003**.
[40] Rigaku, Rigaku Corporation, *Rigaku XRD*, Tokyo, Japan, **1996**.
[41] G. M. Sheldrick, *Acta Crystallogr., Sect. A* **2008**, *64*, 112–22.
[42] L. J. Bourhis, O. V. Dolomanov, R. J. Gildea, J. A. K. Howard, H. Puschmann, *Acta Crystallogr., Sect. A* **2015**, *71*, 59–75.
[43] O. V. Dolomanov, L. J. Bourhis, R. J. Gildea, J. A. K. Howard, H. Puschmann, *J. Appl. Crystallogr.* **2009**, *42*, 339–42.

Received: October 16, 2015
Published Online: December 21, 2015

© 2016 Wiley-VCH Verlag GmbH & Co. KGaA, Weinheim

Coordination Chemistry Reviews 313 (2016) 38–61

Contents lists available at ScienceDirect

Coordination Chemistry Reviews

journal homepage: www.elsevier.com/locate/ccr

Review

Spin crossover in iron(III) complexes

David J. Harding[a,*], Phimphaka Harding[a], Wasinee Phonsri[b]

[a] Molecular Technology Research Unit, School of Science, Walailak University, Thasala, Nakhon Si Thammarat 80161, Thailand
[b] School of Chemistry, Monash University, Clayton, Victoria 3800, Australia

Contents

1. Introduction 39
2. Monomeric iron(III) SCO systems 39
   2.1. Bidentate ligands 39
      2.1.1. Catecholate systems 39
   2.2. Tridentate ligands 40
      2.2.1. Quinolylsalicylaldimine complexes 40
      2.2.2. Sal-R-en complexes 42
      2.2.3. Thiosemicarbazone complexes 44
      2.2.4. Other complexes 45
   2.3. Tetradentate ligands 46
      2.3.1. Salen ligands 46
      2.3.2. Hapen ligands 47
      2.3.3. Acen ligands 47
   2.4. Pentadentate ligands 47
   2.5. Hexadentate ligands 49
3. Dimeric systems 50
4. Multinuclear systems 50
5. Multifunctional systems 51
   5.1. [Fe(5-X-sal$_2$trien)][Mn{Cr(ox)$_3$}] systems 51
   5.2. [M^{III}(dithiolene)$_2$]$^-$ systems 51
   5.3. Mixed-valence [M^{III}(dithiolene)$_2$]$^-$ systems 52
6. SCO nanomaterials 53
7. Physical characteristics of selected iron(III) SCO systems 54
   7.1. Structural characteristics of SCO 54
      7.1.1. Bond length changes and octahedral distortion 54
      7.1.2. Solvent effects 54
      7.1.3. Anion effects 54
      7.1.4. Supramolecular cooperativity in iron(III) 54
   7.2. Light activation in iron(III) 56
   7.3. Mössbauer spectroscopic studies 57
   7.4. Other techniques 58
8. Conclusions 58
   Acknowledgements 59
   References 59

ARTICLE INFO

Article history:
Received 14 September 2015
Accepted 12 January 2016
Available online 29 January 2016

ABSTRACT

Spin crossover compounds are a diverse class of switchable materials with applications ranging from data storage devices to sensors. Iron(III) spin crossover complexes have received renewed attention over the last 10 years with an increasing number of abrupt and hysteretic spin crossover systems discovered. This review provides a detailed overview of this exciting and increasingly interdisciplinary area of

* Corresponding author. Tel.: +66 75672094.

http://dx.doi.org/10.1016/j.ccr.2016.01.006
0010-8545/© 2016 Elsevier B.V. All rights reserved.

Keywords:
Spin crossover (SCO)
Iron(III) complexes
Magnetic behaviour
Crystal structure
Structure-function relationships

research with a particular focus on the structures of these materials and how this impacts their magnetic performance.

© 2016 Elsevier B.V. All rights reserved.

1. Introduction

Spin crossover (SCO) can occur in transition metal complexes with a d^4–d^7 electron configuration provided that a suitable ligand field is present [1–4]. It involves switching between a high spin (HS) and a low spin (LS) state and may be achieved by changes in temperature and pressure or more rarely light irradiation, termed the LIESST effect [1,4–7]. In the case of iron(III), which has a d^5 electron configuration, the transition occurs from a high spin state ($^6A_1$, $S = 5/2$) to a low spin state ($^2T_2$, $S = 1/2$) [8,9]. This change in magnetic moment and the fact that the switching may occur at or close to room temperature make spin crossover materials ideal candidates for molecular magnetic devices, sensors and as components in multifunctional materials [10,11].

Iron(III) compounds, compared to the more common iron(II) systems [12–16] have the advantage of generally being air stable and thus would be expected to be more amenable to processing in any future devices. Another requirement for workable devices is that the spin crossover is abrupt and occurs with hysteresis ideally greater than 40 K [17,18]. Hysteresis in SCO complexes is the result of strong connectivity between the SCO centres such that the SCO propagates rapidly through the material and is achieved either through coordination bonds or more commonly supramolecular interactions [19]. It follows that successful design of SCO materials requires effective application of crystal engineering principles [20,21].

Spin crossover in iron(III) compounds results in significant shortening of the metal–ligand bonds and averages 0.10–0.13 Å, although this is often distributed unevenly across the coordination sphere [8,9]. Compared with iron(II) complexes where the difference is typically 0.20 Å [1,2] it was long believed that iron(III) compounds could not undergo LIESST as the smaller structural change leads to rapid relaxation of the metastable HS state. However, in 2000 Sato and co-workers reported $[Fe(pap)_2]ClO_4 \cdot H_2O$ which exhibits 80% LIESST due to a combination of π–π interactions and significant distortion at the Fe(III) centre in the HS state [22,23]. This was followed by the discovery in 2001 of $[Fe(qsal)_2]NCSe$ which exhibits abrupt SCO and a hysteresis of 76 K [24,25]. The hysteresis in this case is the result of extensive π–π interactions and following these discoveries research into iron(III) SCO materials has increased dramatically.

Despite the obvious interest in iron(III) spin crossover compounds, surprisingly there has not been a review of iron(III) spin crossover chemistry since 2007 [9] and in that time there have been some significant advances in the field with many more structural studies of compounds in the HS and LS state, the discovery of a substantial number of abrupt and even symmetry breaking SCO systems and the appearance of iron(III) SCO nanomaterials. Consequently, this review will focus on papers from 2007 referring to earlier work only when it is needed to understand more recent developments. We will also exclude iron(III) porphyrin systems from the review as these have been reviewed elsewhere and typically involve a transition from a $S = 3/2$ to $S = 5/2$ spin state [26]. Readers wishing to gain an insight into these earlier reports of iron(III) SCO chemistry are referred to the excellent reviews in 2004 and 2007 by van Koningsbruggen [8] and Oshio [9], respectively. While we have tried to include as many papers as possible published over the last 8 years we are particularly interested in structure–functional relationships in SCO systems and thus there is a focus on papers where structural studies have been performed; we apologise to any authors whose work is not included as a result.

The review is organized according to ligand denticity and then subdivided into ligand type to make it easier for the reader to follow and find information of particular relevance to them. This is followed by an overview of the physical characteristics of iron(III) spin crossover compounds with an emphasis on the insights the most recent findings provide. In this way we hope that this review will serve as an invaluable reference for all those interested in iron(III) SCO chemistry.

2. Monomeric iron(III) SCO systems

2.1. Bidentate ligands

Dithiocarbamate ligands with Fe(III) were the first systems to undergo spin crossover [27,28] and while their SCO behaviour is generally very gradual [8] they continue to be studied. In 2011 Ovchinnikov and co-workers studied a range of $[Fe(S_2CNR_2)_3]$ (R = Me, Et, morpholine) complexes by EPR spectroscopy and concluded that small quantities (0.5–2%) of the solvated $[Fe(S_2CNR_2)_3]$ complex trapped inside a matrix of the non-solvated $[Fe(S_2CNR_2)_3]$ complex showed subtle changes in the EPR spectra indicative of spin crossover [29]. In line with previous reports thoroughly desolvated samples or single crystals are EPR silent between 5 and 300 K. Moreover, Garg et al. demonstrated in a Mössbauer spectroscopic study that the spectra can be resolved into HS and LS doublets [30]. As expected the isomer shift of the LS state is a little lower than the HS state consistent with the more covalent bond in the former. Interestingly, in the case of the alkyl complexes there is a clear increase in the quadrupolar splitting as the molecular weight increases. The same group has also reported the mixed ligand complexes $[Fe(S_2CNEt_2)_2(phen)]NO_3$ and $[Fe(S_2CNEt_2)(phen)_2][NO_3]_2$ in which SCO is gradual according to magnetic and Mössbauer spectroscopic studies [31]. Unfortunately, no structural data has been reported on either of these compounds.

SCO has also been reported in $Na_2(NH_4)[Fe(Hbta)_3] \cdot 3DMF \cdot 2H_2O$ where unusually for Fe(III) there is an N_6 donor set [32]. The SCO is gradual and incomplete even at 400 K and due to decomposition of the complex above this temperature does not reach the full HS state. The structure reveals weak cooperativity between the Fe(III) units as they are separated by the cations and is consistent with the gradual SCO in this system.

2.1.1. Catecholate systems

SCO complexes of Fe(III) frequently possess an N_4O_2 donor set, exemplified by $[(TPA)Fe(Cat\text{-}R)]^+$ (TPA = tris(2-pyridylmethyl) amine) where unusually the oxygen donors come from a (nominally) dianionic catecholate ligand rather than the more common phenoxide. All of the systems show gradual SCO with the transition temperature dependent on the type of catecholate and the anion used (Table 1). Interestingly, both $[(TPA)Fe(cat\text{-}Cl_4)]Y$ ($Y = PF_6$, SbF_6) may be isolated as monoclinic or orthorhombic

polymorphs [33,34]. Surprisingly, despite this the two polymorphs have similar transition temperatures at *ca.* 210 K and 250 K for the PF_6 and SbF_6 polymorphs, respectively. The two polymorphs are different in shape and colour with the orthorhombic platelets deep purple and the monoclinic needles orange. The structures of both polymorphs of [(TPA)Fe(cat-Cl_4)]PF_6 reveal that the changes in the Fe—N/O bond lengths of the orthorhombic polymorph upon SCO are slightly larger than those of the monoclinic one albeit by only 0.01 Å [33]. However, the packing is remarkably similar in both polymorphs with weak interactions between the cations forming layers with the counteranions in between these layers. The weak cooperativity and similarity of the packing are thought to be responsible for the small shift in the transition temperature. These systems have also been investigated using femtosecond optical pump-probe spectroscopy and picosecond X-ray diffraction techniques [35]. In both cases SCO occurs in three steps firstly by excitation into an excited LMCT state followed by relaxation into a metastable HS state within 300 fs. This is followed by molecular swelling resulting in a shock-wave through the crystal leading to crystal expansion within 10 ns–10 μs. Finally, the optical energy is redistributed as heat resulting in further conversion to the HS state which is complete after *ca.* 50 μs. Pressure-induced SCO occurs in [(TPA)Fe(cat-Cl_4)]SbF_6 at 294 K almost 50 K higher than that observed at ambient pressure and is consistent with higher pressure favouring the LS state [36]. The comparative similarity of the thermal and pressure-induced SCO are thought to be due to the weak cooperativity that exists in these complexes.

An ESR spectroscopic study of the related compounds $[(TPA)Fe(Cat\text{-}R)]^+$ in the LS state reveals increasing anisotropy as the substituents on the catecholate ligand become more electron withdrawing [37]. This is due to increasing Fe(II)-semiquinonate character in the Fe(III)-catecholate electronic structure.

Schultz, Popescu and co-workers have recently reported [(TPA)Fe(Cat-NN)]BPh_4 where a nitronylnitroxide radical is attached to the catecholate ligand [38]. The compound undergoes very gradual and incomplete SCO that is virtually identical to the non-radical analogue [(TPA)Fe(Cat-3,5-tBu_2)]BPh_4 suggesting that there is little magnetic exchange between the radical and the Fe d-electrons. X-ray crystallography confirms this with the Fe(III) cations essentially isolated from each other.

Very recently, the TPA ligand has been replaced with bis[(2-pyridyl)methyl]-2-(2-pyridyl)-ethylamine (pmea) to give [(pmea)Fe(Cat)]BPh_4 [39]. The compound undergoes SCO to a 50% HS state compared with [(TPA)Fe(Cat)]BPh_4 where the SCO is complete but in 2 steps. The structure of [(pmea)Fe(Cat)]BPh_4 at high and low temperature is consistent with 50% HS and again shows limited cooperativity which is clearly a feature of $[(TPA)Fe(Cat\text{-}R)]^+$ complexes.

2.2. Tridentate ligands

Tridentate ligands are particularly common in Fe(III) SCO chemistry and are often derived from salicylaldehyde and amines (Fig. 1). This gives a monoanionic N_2O ligand and, with two ligands attached to the Fe centre, results in the N_4O_2 donor set that is such a feature of Fe(III) SCO chemistry (Table 1) [8].

2.2.1. Quinolylsalicylaldimine complexes

As mentioned in the introduction $[Fe(qsal)_2]NCSe$ has one of the widest hysteresis reported for any SCO compound [24,25]. In 2009 Hayami, Sato and co-workers finally succeeded in obtaining the structure of the non-solvated compounds, $[Fe(qsal)_2]NCX$ (X = S, Se) in the HS state [23]. This allowed a direct comparison of the changes at the Fe centre which proved to be on average 0.13 Å and in line with other Fe(III) systems. The presence of solvent in the LS structure sadly prevented a direct comparison of the packing. LIESST studies on $[Fe(qsal)_2]NCX$ revealed only very weak LIESST effects despite the strong π–π interactions.

Subsequent studies on $[Fe(qsal)_2]^+$ complexes have focused, until recently, on varying the anion (anion = I^- [40], N_3^- [41], I_3^- [42,43], $[Fe(qsal)Cl_3]^-$ [40]; see also Section 5.2). A feature of many of these complexes is the presence of 1D chains formed by π–π interactions between neighbouring qsal ligands (Fig. 2). Although not a guarantee of SCO, in systems where SCO does occur it is more likely to be abrupt if these are present. The iodide and $[Fe(qsal)Cl_3]^-$ complexes are trapped in the LS and HS states respectively, based on structural and magnetic susceptibility studies [40]. However, the Mössbauer spectra of $[Fe(qsal)_2]I{\cdot}H_2O$ reveal a change from 77% LS at room temperature to 44% LS at 5.6 K; the origin of this unusual behaviour is currently unclear.

The structure of the azide complex has also been reported at 200 K showing a LS Fe centre but its SCO behaviour is currently unknown [41]. Intriguingly, the triiodide forms two polymorphs α and β [42,43]. The structure of the α-polymorph has been determined in the HS and LS state and shows a slightly smaller change of ΔFe-L = 0.11 Å compared with $[Fe(qsal)_2]NCX$ [23]. The SCO is gradual and incomplete at both ends and this is probably the reason for the smaller change in the Fe–N/O bond lengths. The effect of pressure on both α-$[Fe(qsal)_2]I_3$ and $[Fe(qsal)_2]NCS$ reveals a shift in $T_{1/2}$ to higher temperatures as the pressure is increased consistent with the greater stabilization of the LS state at elevated pressures [42]. Interestingly, in $[Fe(qsal)_2]NCS$ the increase in pressure also results in less complete SCO. The β-polymorph is obtained by precipitation of the product after a few hours, compared with several days via slow diffusion for the α-polymorph. The SCO is now complete, abrupt and with $T_{1/2}\uparrow = 117$ K and $T_{1/2}\downarrow = 92$ K exhibits a hysteresis of 25 K [43]. The structure of the β-polymorph has not yet been reported but emphasizes the importance of polymorphism in SCO chemistry [21].

In 2013, Faulmann and co-workers reported a pair of $[Fe(qsal)_2]^+$ complexes where the anion was $[Fe(CN)_5(NO)]^{2-}$ or $[RuCl_5(NO)]^{2-}$ with the aim of preparing photochromic spin crossover materials [44]. In the case of $[Fe(CN)_5(NO)]^{2-}$ the authors were able to isolate two solvates $[Fe(qsal)_2]_2[Fe(CN)_5(NO)]{\cdot}sol$ (sol = MeOH, 2MeCN) with the MeOH solvate showing gradual 50% SCO while the MeCN solvate exhibits only a minor change in $\chi_M T$ from 2.8 to 2.58 $cm^3\ mol^{-1}$ K. X-ray crystallographic analysis of $[Fe(qsal)_2]_2[Fe(CN)_5(NO)]{\cdot}MeOH$ by Hayami et al. at around the same time reveals that only one of the Fe(III) sites (Fe1) is capable of undergoing SCO [45]. Unusually $[Fe(qsal)_2]_2[Fe(CN)_5(NO)]{\cdot}MeOH$ also exhibits the LIESST effect (Fig. 3). The related complex with the Ru anion undergoes almost complete SCO with a slight hysteresis of 7 K as evidenced by magnetic and Mössbauer spectroscopic studies [44].

The first complexes of a substituted qsal ligand were reported by da Gama et al. in 2009. The complexes, $[Fe(qsal\text{-}3\text{-}OMe)_2]PF_6{\cdot}sol$ (sol = none, $2H_2O$) were trapped either in the HS (H_2O) or LS state (non-solvated) [46]. The X-ray structure of $[Fe(qsal\text{-}3\text{-}OMe)_2]PF_6$ reveals a loss of the 1D π–π chains which are such a common feature of the $[Fe(qsal)_2]^+$ complexes. In contrast, almost all the related $[Fe(qsal\text{-}5\text{-}OMe)_2]Y{\cdot}sol$ (Y = Cl, NCS, BF_4, PF_6, BPh_4) complexes exhibit SCO [47,48]. The MeOH solvate, $[Fe(qsal\text{-}5\text{-}OMe)_2]Cl{\cdot}2MeOH{\cdot}0.5H_2O$, exhibits abrupt half SCO at *ca.* 140 K with a hysteresis of 10 K while the MeCN solvate, $[Fe(qsal\text{-}5\text{-}OMe)_2]Cl{\cdot}MeCN{\cdot}H_2O$ exhibits abrupt stepped SCO at 245 and 275 K with a hysteresis of 5 K in the 1st step via a 2/3 HS intermediate [47]. For the other anions, the SCO is almost complete in the case of NCS and PF_6 but is LS only for BF_4 while the large BPh_4 anion is HS only. X-ray crystallographic analysis of $[Fe(qsal\text{-}5\text{-}OMe)_2]Y$ (Y = Cl, NCS, BF_4) reveals a return of the 1D π–π chains found in many of the qsal systems above and also an additional interaction which links these chains, a parallel four-fold aryl embrace (P4AE, see Fig. 4) [48,49].

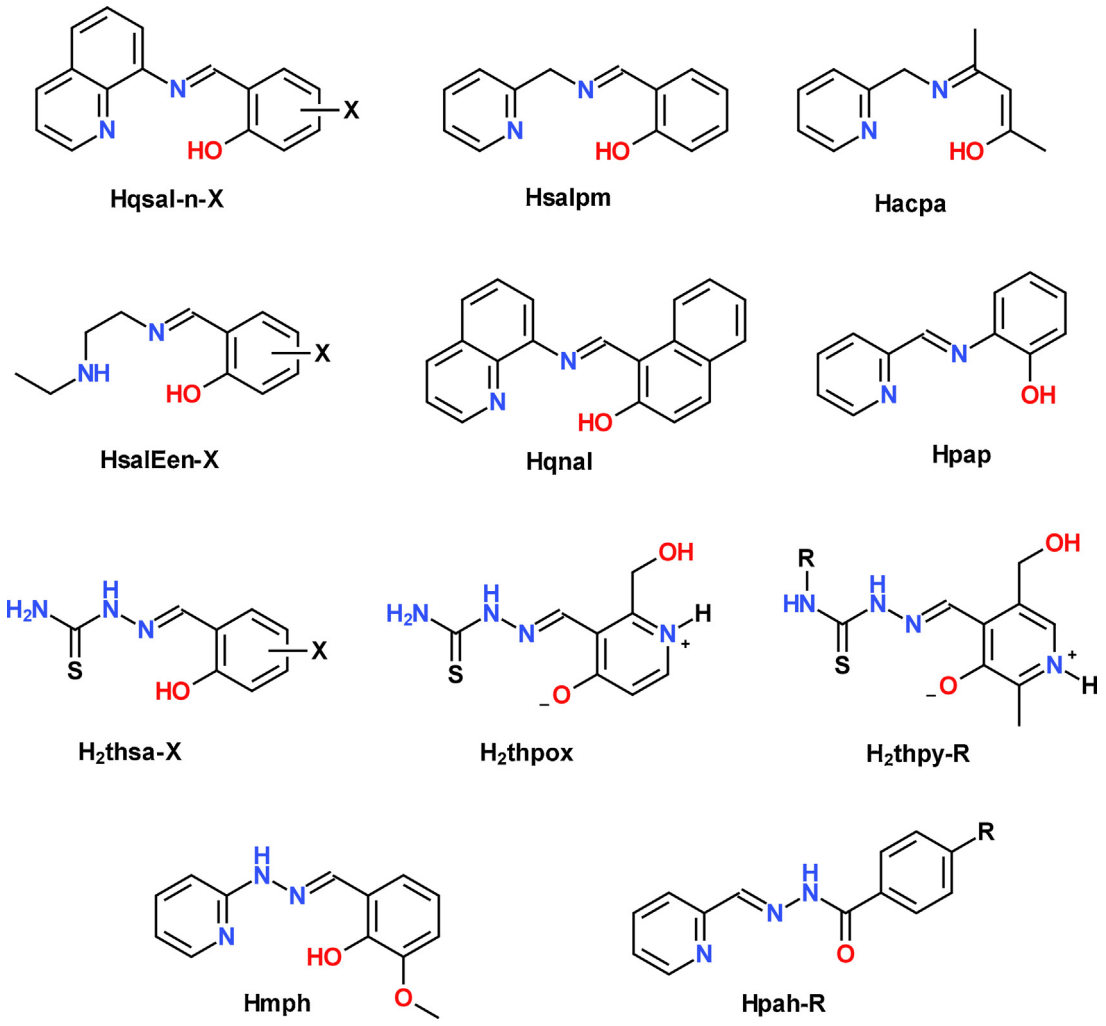

Fig. 1. Structures and abbreviations of the tridentate ligands used in iron(III) SCO systems.

While $[Fe(qsal\text{-}5\text{-}OMe)_2]PF_6{\cdot}CH_2Cl_2$ also contains 1D π–π chains the P4AE interactions are lost and the SCO is now gradual [50]. A remarkable feature of $[Fe(qsal\text{-}5\text{-}OMe)_2]Cl{\cdot}2MeOH{\cdot}0.5H_2O$ is the rare occurrence of a HS and LS Fe centre in the same asymmetric unit which is responsible for the 50% SCO. The substitutional isomers $[Fe(qsal\text{-}4\text{-}OMe)_2]Y$ (Y = ClO_4, NO_3, PF_6, OTf) are all HS except when the anion is OTf where very gradual 25% SCO occurs. The structures reveal strongly distorted qsal-4-OMe ligands, dislocated π–π chains and additional C—H···O interactions which are responsible for the loss of SCO [50].

Substituent effects are also evident in the series $[Fe(qsal\text{-}X)_2]NCS{\cdot}sol$ (X = F, Cl, Br, I) where the F and Cl compounds undergo

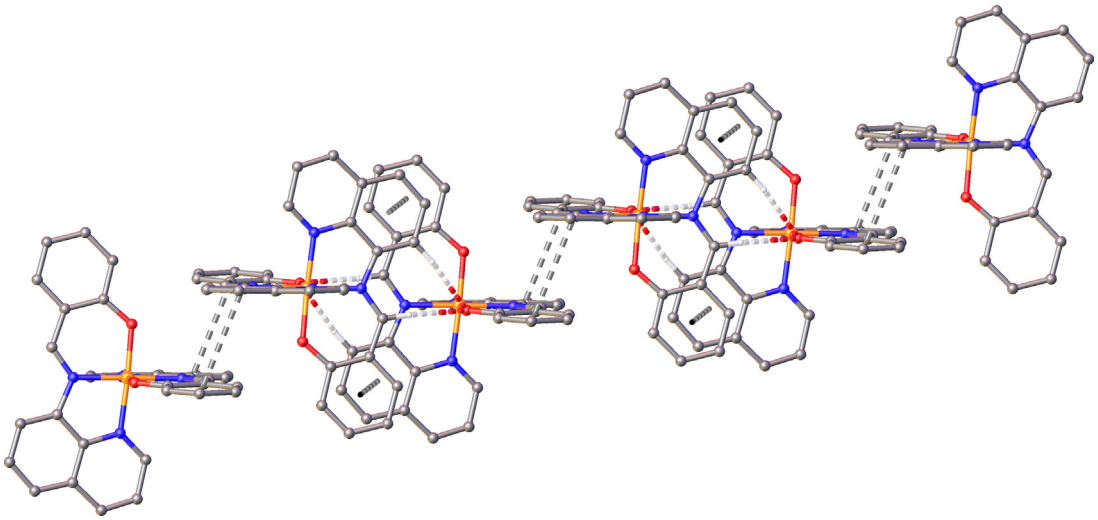

Fig. 2. View of the π–π interactions commonly observed in $[Fe(qsal)_2]^+$ complexes. Drawn from data in Ref. [24].

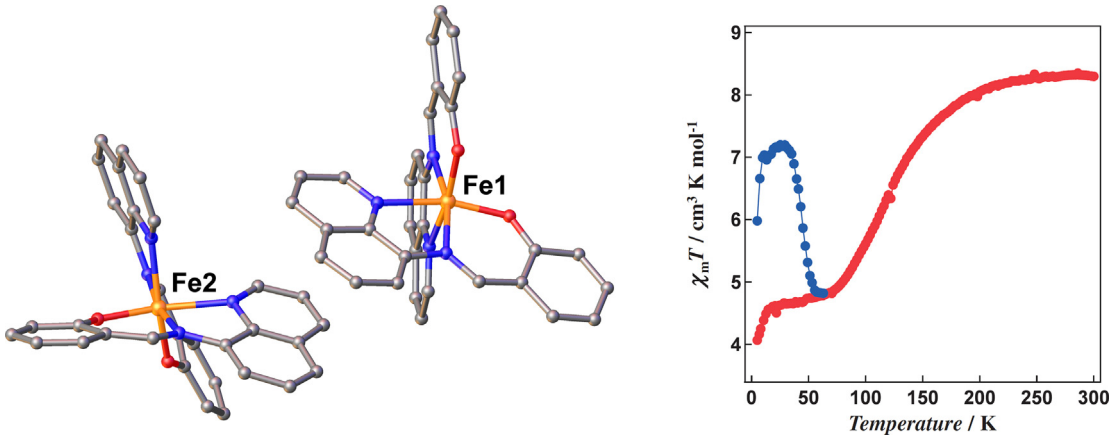

Fig. 3. (a) View of the two independent Fe(III) centres in $[Fe(qsal)_2]_2[Fe(CN)_5(NO)]\cdot MeOH$ (left) [45], (b) magnetic behaviour of $[Fe(qsal)_2]_2[Fe(CN)_5(NO)]\cdot MeOH$ (right, reproduced with permission from Ref. [45]. (Copyright The Chemical Society of Japan, 2013.)

abrupt stepped SCO through a 50% HS intermediate while the Br derivative undergoes a very gradual LS to 50% HS conversion and the iodo derivative is LS up to 300 K [52]. Structures of all the compounds reveal that the F, Br and I complexes contain two independent Fe(III) centres in the asymmetric unit of which both undergo SCO but at different temperatures for $[Fe(qsal\text{-}F)_2]NCS$ while for $[Fe(qsal\text{-}Br)_2]NCS\cdot MeOH$ only one of the Fe centres is SCO active. The stepped SCO in $[Fe(qsal\text{-}Cl)_2]NCS\cdot MeOH$ is harder to understand as there is only one Fe(III) centre in the crystal structure, although it is possible that symmetry breaking occurs in this system.

The importance of cooperativity in $[Fe(qsal\text{-}X)_2]^+$ is highlighted in $[Fe(qsal\text{-}I)_2]OTf\cdot MeOH$ and $[Fe(qsal\text{-}Br)_2]NO_3\cdot 2MeOH$ which exhibit very abrupt and abrupt symmetry breaking SCO, respectively [51,53]. Uniquely, in $[Fe(qsal\text{-}X)_2]^+$ chemistry, hysteresis is present in both steps of $[Fe(qsal\text{-}Br)_2]NO_3\cdot 2MeOH$ being 16 and 5 K in the 1st and 2nd steps, respectively with a 96 K [HS-LS] plateau (see Fig. 5) [51]. The structure of $[Fe(qsal\text{-}I)_2]OTf\cdot MeOH$ shows, to date, the smallest change in unit cell volume for any compound undergoing complete SCO of 20.6 Å^3 [53]. The structure very close to the spin transition temperature reveals subtle reorganization of the coordination and supramolecular sphere prior to actual SCO. This confirms a growing trend in SCO research that abrupt SCO does not require a crystallographic phase change or large changes in volume but rather needs extensive supramolecular interactions [17]. Moreover, it appears that symmetry breaking occurs in $[Fe(qsal\text{-}Br)_2]NO_3\cdot 2MeOH$ because these supramolecular contacts are very short which prevents SCO is a single step [54]. Indeed, loss of solvent yields $[Fe(qsal\text{-}Br)_2]NO_3$ which now undergoes a LS to 50% HS conversion but with an impressive hysteresis of 60 K [51].

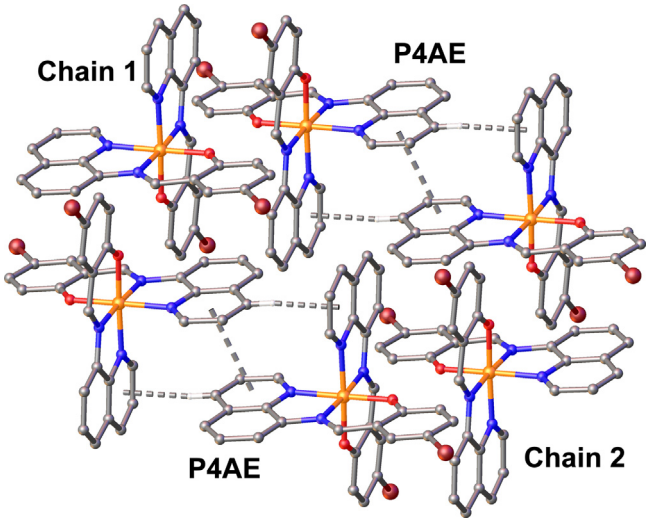

Fig. 4. View of the P4AE interactions that link the 1D π–π chains in $[Fe(qsal\text{-}X)_2]^+$ [51].

The most complex systems employing substituted qsal ligands have been developed by Lemaire et al. The two ligands devised by them were Hqsal-5-(-C≡C-3-th) (3-th = 3-thienyl) [55] and Hqsal-5-(-C≡C-3-terth) (3-terth = 3-terthienyl) [56]. The aim in both cases was to utilize the thienyl group to create polythiophene polymers with SCO groups off the polymer backbone. In the case of $[Fe\{qsal\text{-}5\text{-}(\text{-}C{\equiv}C\text{-}3\text{-}th)\}_2]Y$ (Y = PF_6, NCS, ClO_4) no electropolymerization of the thiophene was observed but SCO was present in all cases, albeit very gradual and incomplete. In the case of the NCS complex, Mössbauer spectroscopic data suggest an extremely rare $S = 5/2$ to $S = 3/2$ transition in a non-heme complex [55]. In contrast, $[Fe\{qsal\text{-}5\text{-}(\text{-}C{\equiv}C\text{-}3\text{-}terth)\}_2]PF_6$ does electropolymerize and the polymer formed undergoes a complete but extremely gradual SCO [56]. The polymer is conducting with the degree of conductivity dependent on temperature suggesting coupling between SCO and electrical conductivity.

More recently, the mixed ligand series [Fe(qsal)(thsa)]·sol (sol = 0.4 *n*-BuOH, 0.5 MeCN, 0.5 THF) has been reported where the BuOH and MeCN solvate undergo 50% SCO [57]. Structural studies of [Fe(qsal)(thsa)]·nMeCN reveal two independent Fe(III) centres with the SCO occurring between a [LS–HS] and [HS–HS] state. Remarkably, during SCO MeCN is lost in a single-crystal-to-single-crystal transformation to give [Fe(thsa)(qsal)]·0.1 MeCN which remains SCO active. Even complete solvent loss does not alter the magnetic behaviour and MeCN can be re-absorbed again without loss of crystallinity or SCO.

2.2.2. Sal-R-en complexes

The tridentate ligands, Hsal-R-en are prepared from N-alkylaminoethylamine and a salicyladehyde derivative. The presence of an NH group on the ligand helps in creating cooperativity through hydrogen bonding. Although a number of alkyl groups have previously been investigated all systems reported since 2007 utilize an ethyl group. $[Fe(salEen)_2]ClO_4$ and $[Fe(salEen)_2]ClO_4\cdot 0.5H_2O$ crystallize simultaneously from the reaction of the ligand and $Fe(ClO_4)_3$ in EtOH [58]. Both compounds undergo gradual SCO with $T_{1/2}$ higher and the SCO more abrupt for the non-solvated form. Crystal structures of both compounds unexpectedly reveal a slightly larger change in the Fe–N/O bond lengths in $[Fe(salEen)_2]ClO_4\cdot 0.5H_2O$ upon SCO. The packing in the

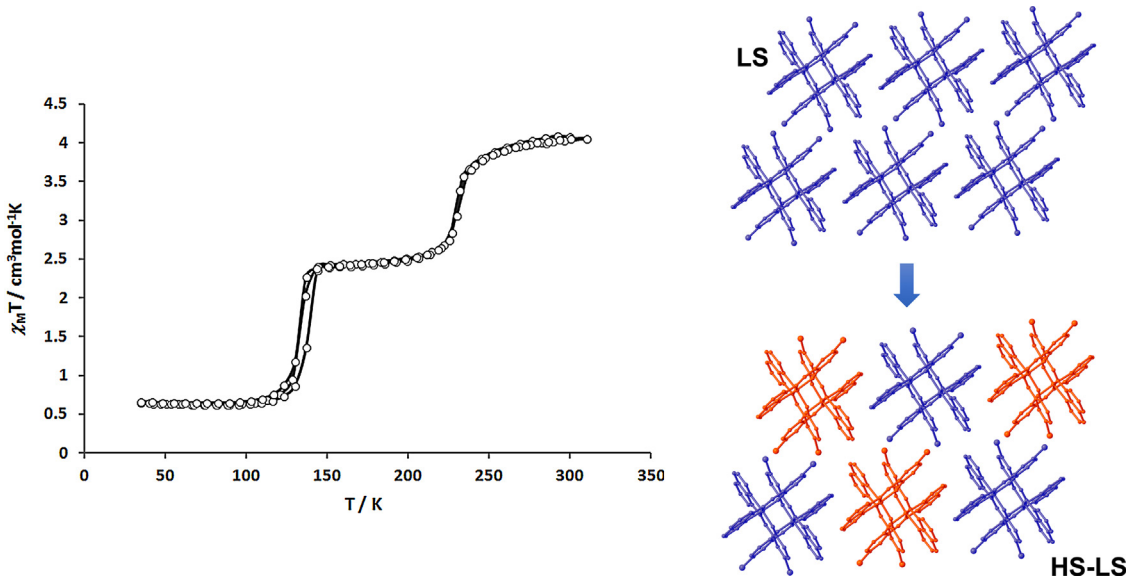

Fig. 5. View of the $\chi_M T$ vs. T plot for [Fe(qsal-Br)$_2$]NO$_3$·2MeOH (left, reproduced with permission from Ref. [51] (Copyright Royal Society of Chemistry, 2015) and the corresponding packing in the LS and [HS–LS] structures.

two structures is defined by strong N—H···anion interactions and is a feature of [Fe(salEen)$_2$]$^+$ complexes; the lack of further significant supramolecular contacts explains the very gradual nature of the SCO in both cases. Similarly, [Fe(salEen)$_2$]$_2$[Fe(CN)$_5$(NO)] undergoes very gradual SCO between 100 and 400 K [44]. Despite the different anions, the packing in the structure is little changed compared with [Fe(salEen)$_2$]ClO$_4$·sol and consequently, there is very weak connectivity between the cationic units but strong cation–anion interactions.

[Fe(3-OMe-salEen)$_2$]PF$_6$ was first prepared in 1981 [59] and undergoes very abrupt SCO at *ca.* 165 K with a hysteresis of 3 K but its structure was only recently published [60]. The structure determined at 300, 200 and 100 K shows a HS, HS and LS Fe(III) centre respectively. The Fe–N/O bond lengths change on average 0.13 Å and are a little larger than in other [Fe(salEen)$_2$]$^+$ complexes. As with [Fe(qsal-I)$_2$]OTf·MeOH, the structure close to $T_{1/2}$ shows a change in cooperativity that supports the abrupt SCO.

The closely related [Fe(4-OMe-salEen)$_2$]Y complexes (Y = NO$_3$, PF$_6$) also exhibit SCO, and when the anion is NO$_3$ this is abrupt with hysteresis (7.5 K) but centred at *ca.* 78 K [61]. The structures of both compounds have been determined in the HS and LS state revealing 2 independent Fe(III) centres for [Fe(4-OMe-salEen)$_2$]PF$_6$ and a single Fe(III) site for [Fe(4-OMe-salEen)$_2$]NO$_3$. This has a dramatic impact on the packing with a 2D supramolecular network formed by a combination of N—H···O, C—H···O interactions involving the NO$_3$ anions and partial overlap of the aromatic part of the 4-OMe-salEen ligands for [Fe(4-OMe-salEen)$_2$]NO$_3$ (see Fig. 6). In contrast, [Fe(4-OMe-salEen)$_2$]PF$_6$ contains only very weak interactions between the cations resulting in two centres that undergo SCO at similar temperatures, hence its gradual nature.

More recently, Martinho et al. have reported [Fe(3,5-Br$_2$-salEen)$_2$]Y·sol (Y = ClO$_4$, sol = EtOH; Y = BPh$_4$, sol = DMF) of which the BPh$_4$ salt shows very gradual, incomplete SCO while the ClO$_4$ complex is LS up to 350 K [62]. The structure of [Fe(3,5-Br$_2$-salEen)$_2$]BPh$_4$·DMF at 150 K reveals that the Fe(III) centre is LS and unlike most other [Fe(X-salEen)$_2$]$^+$ complexes there are no anion—N—H interactions; hydrogen bonding instead occurring between the NH groups and the DMF carbonyl O atom. This greatly reduces the cooperativity as the DMF is not involved in any further supramolecular interactions, consistent with the gradual SCO observed in this compound.

In 2015, Murray and co-workers reported moderately abrupt spin crossover in the heteroleptic complex [Fe(3-OMe-salEen)(thsa)] at 344 K [63]. The structure in the LS state shows extensive π–π and N—H···N interactions. In comparing [Fe(3-OMe-salEen)(thsa)] with related homoleptic systems the authors

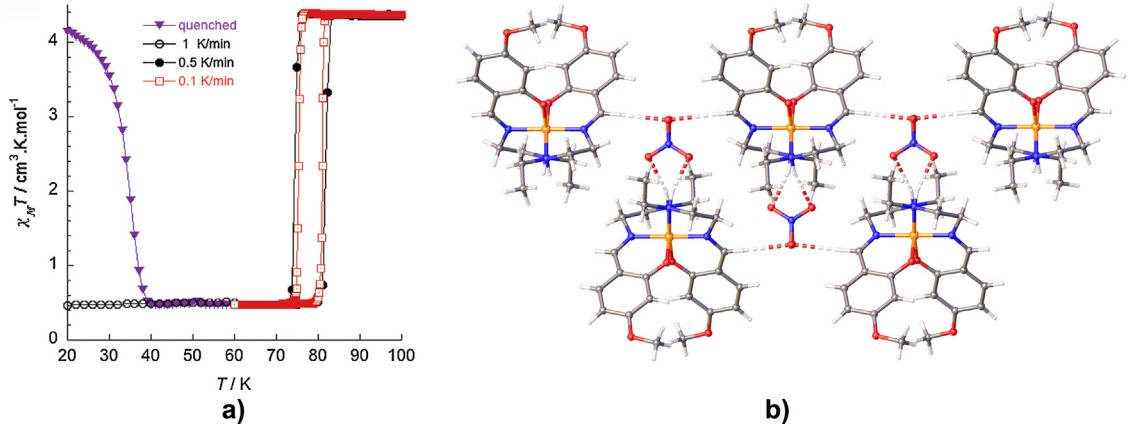

Fig. 6. (a) The magnetic profile (reproduced, slightly modified, with permission from Ref. [61] (Copyright Wiley-VCH, 2014) and (b) packing in [Fe(4-OMe-salEen)$_2$]NO$_3$ showing the 2D supramolecular network.

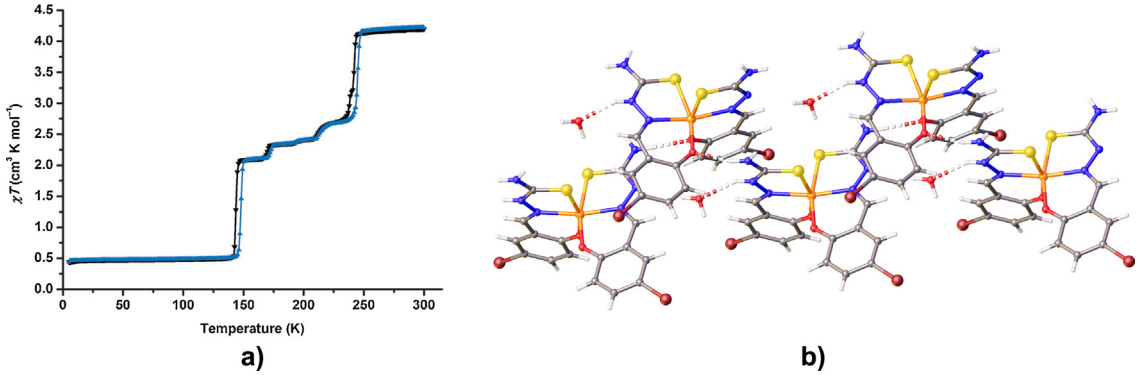

Fig. 7. (a) Multi-step spin crossover in [Fe(5-Br-Hthsa)(5-Br-thsa)]·H_2O (reproduced, slightly modified with permission from Ref. [68] (Copyright Wiley-VCH, 2013) and (b) view of the 1D hydrogen bonding chain at 123 K.

find that stronger π–π interactions lead to higher $T_{1/2}$. The SCO characteristics are improved relative to the parent compounds and represent a new strategy for preparing SCO materials.

2.2.3. Thiosemicarbazone complexes

Thiosemicarbazones, often abbreviated to X-thsa, are planar, readily derivatizable ligands which may be monoanionic or dianionic resulting in SCO complexes of the general formula, [Fe(X-Hthsa)(X-thsa)] or [Fe(X-thsa)$_2$]$^-$. Another unusual aspect of these complexes is that the Fe centre has an $N_2O_2S_2$ donor set rather than the more typical N_4O_2 donor set of other Fe(III) SCO systems. Li[Fe(5-Br-thsa)$_2$]·H_2O undergoes an abrupt SCO at $T_{1/2}\uparrow$ = 329 K and $T_{1/2}\downarrow$ = 292 K and thus a hysteresis of 37 K at its widest point [64]. Mössbauer spectroscopic studies confirm that the SCO is almost complete with a very small amount of LS species remaining at room temperature (*ca.* 3%). Later, the same authors reported a Rietveld refinement of the powder-XRD data showing that despite the large hysteresis there is no change in crystallographic space group [65]. Indeed, the large hysteresis is thought to be due to changes in the hydrogen bonding interactions involving the lattice water molecules. K[Fe(5-Br-thsa)$_2$] exhibits abrupt 2-step hysteretic SCO with ΔT = 69 K in the first cycle and 52 K thereafter [66]. The Fe–N/S bond lengths show a substantial increase upon SCO but unusually the unit cell volume only increases by 29.1 Å^3 and actually *decreases* in the SCO region. The hysteretic SCO is due to high cooperativity imparted by K coordination bonds, K–π interactions and hydrogen bonds forming a 2D network. Using [2-Me-5-Et-pyH]$^+$ results in the SCO moving to *ca.* 220 K and a loss of hysteresis according to ESR spectroscopic studies [67].

The neutral Fe(III) complexes [Fe(5-X-Hthsa)(5-X-thsa)]·nH_2O (X = H, n = 1; X = Cl, n = 1; X = Br, n = 0.5, 1) all exhibit SCO although the abruptness and degree of hysteresis is extremely sensitive to the method of preparation [68–70]. Thus, refluxing 5-Br-H_2thsa, $NHMe_2$ and $Fe(NO_3)_3$ in a MeOH/EtOH/water mixture gives [Fe(5-Br-Hthsa)(5-Br-thsa)]·H_2O which exhibits hysteretic, multi-step symmetry breaking SCO (see Fig. 7) [68] while synthesis of the compound via Li[Fe(5-Br-thsa)$_2$] and subsequent addition of [Hpy]Cl also gives [Fe(5-Br-Hthsa)(5-Br-thsa)]·H_2O but now with abrupt single step SCO [70]. Moreover, using NH_3 gives yet another compound, [Fe(5-Br-Hthsa)(5-Br-thsa)]·0.5H_2O which despite the change in the number of water molecules has a very similar magnetic profile to the compound made with pyridinium [69]. Of these only [Fe(5-Br-Hthsa)(5-Br-thsa)]·H_2O made with $NHMe_2$ has been characterized by single crystal XRD. Below 140 K and above 250 K the structure refines in monoclinic $P2_1/n$ while between these temperatures there is a change in space group to monoclinic P_n. As a consequence there are 2 Fe(III) centres, one HS and one LS, in the intermediate region and one Fe(III) centre at low and high temperatures. The Fe—N and Fe—S bond distances lengthen considerably upon SCO by 0.20 and 0.19 Å, respectively while the Fe—O bond lengths are little changed. The multi-step SCO in the intermediate region is ascribed to subtle changes in the ligand backbone coupled to resonance assisted hydrogen bonding involving the water molecule which very slightly modifies the ligand field. Interestingly, while [Fe(5-Br-Hthsa)(5-Br-thsa)]·H_2O (made with $NHMe_2$) exhibits only 5% LIESST, [Fe(5-Br-Hthsa)(5-Br-thsa)]·0.5H_2O exhibits 100% LIESST and is one of the few Fe(III) complexes to do so.

The impact of synthetic procedure is again evident in [Fe(Hthsa)(thsa)]·H_2O with van Koningsbruggen and co-workers reporting abrupt SCO in 2-steps in the cooling mode and a hysteresis of 12 and 42 K [69] while Floquet et al. [70], using pyridine as a base, report abrupt SCO in a single step with a hysteresis of only 8 K. In the heating mode the SCO occurs at *ca.* 280 K while in the cooling mode SCO occurs at from 230 to 270 K. In contrast, SCO in [Fe(5-Cl-Hthsa)(5-Cl-thsa)]·H_2O is abrupt at *ca.* 230 K with a hysteresis of 1–3 K irrespective of the base used. The structures of [Fe(5-X-Hthsa)(5-X-thsa)]·H_2O (X = H, Cl) at room temperature reveal strong hydrogen bonding between the Fe(III) centres mediated by the water molecules and π–π interactions between neighbouring aryl groups. These are slightly more planar in [Fe(Hthsa)(thsa)]·H_2O than [Fe(5-Cl-Hthsa)(5-Cl-thsa)]·H_2O reflecting the greater cooperativity observed in the former compound. Despite this it is [Fe(5-Cl-Hthsa)(5-Cl-thsa)]·H_2O that displays LIESST (33%) and not [Fe(Hthsa)(thsa)]·H_2O, thought to be due to the halogen group increasing the quantum mechanical tunnelling barrier. DSC studies reveal that ΔH = 10.5–4.3 kJ mol^{-1} and ΔS = 37.6–21.6 J K^{-1} mol^{-1} decreasing on moving from H to Cl to Br but still indicative of a substantial contribution from vibrational modes to the overall entropy and enthalpy.

Substituting one of the N–H groups for an N–Me group gives [Fe(5-Cl-Hthsa-Me)(5-Cl-thsa-Me)]·H_2O which now exhibits 2-step SCO at $T_{1/2}\uparrow$ = 249 and 278 K and $T_{1/2}\downarrow$ = 245 and 270 K and thus hystereses of 4 and 8 K [71]. X-ray crystallographic analysis at 100, 260 and 300 K indicates that the Fe centre is LS, averaged HS/LS and HS, respectively. Surprisingly, introduction of the methyl group results in only minor alterations in the packing which is again dominated by hydrogen bonding and slightly angular π–π interactions (Fig. 8). [Fe(5-Cl-Hthsa-Me)(5-Cl-thsa-Me)]·H_2O also exhibits dielectric anomalies coupled to the spin transition, demonstrating that it acts as a multifunctional material.

A Mössbauer spectroscopic study of [Fe(Hthpu)(thpu)] (H_2thpu = pyruvic acid thiosemicarbazine) has revealed that despite the low $\chi_M T$ = 3.69 cm^3 mol^{-1} K^{-1} the compound is in the full HS state undergoing a spin transition to the full LS state at 225 K. The compound also undergoes LIESST, although this is very modest at 2% [72].

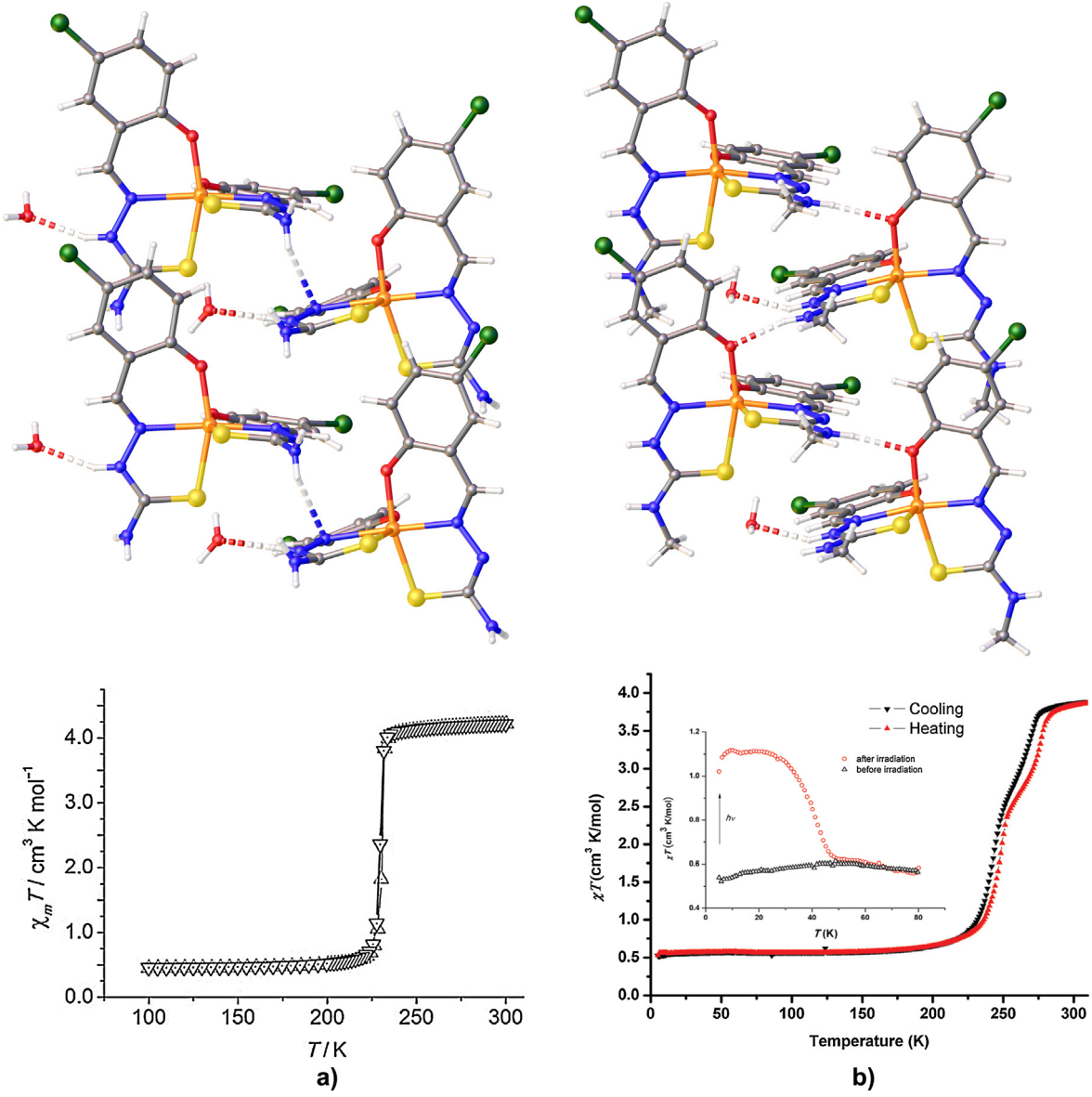

Fig. 8. (a) Comparison of the packing in [Fe(5-Cl-Hthsa)(5-Cl-thsa)]·H_2O (reproduced, slightly modified, with permission from Ref. [69] (Copyright Wiley-VCH, 2010) and (b) [Fe(5-Cl-Hthsa-Me)(5-Cl-thsa-Me)]·H_2O and the magnetic behaviour of the two complexes (reproduced with permission from Ref. [71]. (Copyright Royal Society of Chemistry, 2013.)

Two independent studies by the groups of Floquet and van Koningsbruggen have investigated a series of complexes employing pyridoxal thiosemicarbazone (H_2thpy) namely, A[Fe(thpy)$_2$]·nH_2O (A = NH_4, PPh_4, Na), [73] [Fe(Hthpy)(thpy)]·4.5H_2O, [73] [Fe(Hthpy)(thpy)]·MeOH·3H_2O, [74] [Fe(Hthpox)$_2$]Y·nsol (Y = Cl, NO_3, ClO_4, BPh_4, SO_4; sol = H_2O or MeOH) [73,75] and [Fe(H_2thpy)$_2$][Y]$_3$·nsol (Y = Cl, NO_3; sol = H_2O, EtOH) [73]. Despite the variety of protonated states, different anions and solvents none of the compounds are SCO active being either entirely HS or LS. However, some of the compounds do lose solvent converting to the HS state in the process; naturally this spin change is irreversible. What is clear from this series is that the thiolate ligands exhibit a stronger ligand field than the neutral thione ligand. Structural data for many of the compounds, show extensive hydrogen bonding involving the amide, pyridyl, hydroxyl groups and the lattice water and/or alcohol molecules.

The related compounds [Fe(Me-Hthpy)$_2$][$MeC_6H_4SO_3$]$_3$·EtOH, [75] [Fe(Me-Hthpy)(Me-thpy)]·2H_2O [74] and [Fe(Et-Hthpy)(Et-thpy)]·8H_2O [75] have also been prepared by van Koningsbruggen et al. Once again, none of the compounds undergoes SCO but it is interesting to note that [Fe(Me-H_2thpy)$_2$][$MeC_6H_4SO_3$]$_3$·EtOH is LS while [Fe(H_2thpy)$_2$][NO_3]$_3$·0.5EtOH is HS, although whether this is due to the Me group or the anion is unclear. Structural studies for all complexes show the Fe(III) is LS and once more there is strong hydrogen bonding linking the individual Fe(III) units. However, a distinct difference compared with the [Fe(Hthpy)(thpy)]·sol series is the presence of π–π interactions although these are not as extensive as in the [Fe(X-Hthsa)(X-thsa)]·H_2O series. This suggests that too many supramolecular sites lead to a loss of control of the crystal packing and consequently SCO behaviour.

2.2.4. Other complexes

The remaining complexes do not belong to a particular ligand system but are again often derived from salicylaldehyde or related derivatives. [Fe(salpm)$_2$]ClO_4·0.5EtOH is a particularly interesting example undergoing stepped SCO at 115 and 171 K through a 75% HS intermediate. The initial study of this compound revealed two independent Fe(III) centres at 100, 150 and 294 K with the centres

undergoing sequential SCO [76]. A more recent study by Morgan, Collet, Létard and co-workers revealed, using Mössbauer spectroscopy as a guide, that this explanation is too simplistic and in fact symmetry breaking SCO occurs with not *two* but *four* independent Fe(III) centres in the intermediate region [77]. It follows that at 135 K there are 3HS centres and 1LS centre consistent with the 75%HS intermediate observed in the magnetic data. Cooling results in halving of the unit cell producing two LS centres at 90 K. In addition, the compound undergoes LIESST, also in two steps reflecting the stepped SCO of the thermal transition.

The importance of supramolecular interactions is demonstrated beautifully in a study on $[Fe(acpa)_2]ClO_4$ [78]. The compound can be prepared in two forms, one where the SCO is abrupt, centered at *ca.* 370 K and with a hysteresis of 13 K and the other where it is gradual occurring between 250 and 350 K. The structures of the two polymorphs show tight packing and extensive π–π interactions in the abrupt polymorph, while these are absent in the gradual polymorph.

$[Fe(pap)_2]^+$ compounds hold the distinction of being the first Fe(III) complexes to exhibit LIESST. In 2009, structural comparison of $[Fe(pap)_2]BF_4{\cdot}H_2O$ in the HS state with $[Fe(pap)_2]PF_6{\cdot}MeOH$ which is LS, permitted, at that time, a rare insight into changes in Fe–N/O bond lengths upon SCO. A key feature was the large change in Fe–N/O bond lengths, 0.14 Å on average, and perhaps more significantly the strong structural distortion between the two spin states [23]. These combined give a LIESST activation barrier of 1,079 cm^{-1}, larger even than some Fe(II) SCO compounds and explaining the strong LIESST in $[Fe(pap)_2]ClO_4{\cdot}H_2O$ [79].

A series of compounds closely related to the $[Fe(qsal\text{-}X)_2]^+$ complexes above are $[Fe(qnal)_2]OTf{\cdot}sol$ (sol = MeOH, acetone) [80]. The compounds exhibit abrupt SCO at $T_{1/2}\uparrow = 115$ and $T_{1/2}\downarrow = 104$ K ($\Delta T = 11$ K) and $T_{1/2}\uparrow = 133$ and $T_{1/2}\downarrow = 130$ K ($\Delta T = 3$ K) for the MeOH and acetone solvates, respectively. The structure of $[Fe(qnal)_2]OTf{\cdot}MeOH$ at 80 K reveals a LS Fe(III) centre and π–π interactions formed between the quinolyl and naphthyl rings which are stronger even than those in $[Fe(qsal\text{-}X)_2]^+$ systems. Interestingly, despite the strong structural similarity and packing in the two systems, in contrast with most $[Fe(qsal\text{-}X)_2]^+$ complexes, $[Fe(qnal)_2]OTf{\cdot}sol$ are LIESST active, being 100% in the case of the acetone solvate.

Introduction of a methoxy group on the naphthyl moiety yields $[Fe(qnal\text{-}7\text{-}OMe)_2]Y{\cdot}sol$ (Y = PF_6, sol = acetone; Y = BPh_4, sol = 2MeOH) [81]. Remarkably, $[Fe(qnal\text{-}7\text{-}OMe)_2]BPh_4{\cdot}2MeOH$ has a hysteresis of 110 K at its widest point, the widest for any Fe(III) SCO system. However, in $[Fe(qnal\text{-}7\text{-}OMe)_2]PF_6{\cdot}$acetone the SCO is stepped via an 80% HS intermediate. Structural analysis of $[Fe(qnal\text{-}7\text{-}OMe)_2]PF_6{\cdot}$acetone in the HS and LS state shows an extremely large change in the Fe—O bond lengths by on average 0.08 Å while the change in the Fe—N bond lengths is more modest, 0.12 Å. In both compounds there are again strong π–π interactions which form a 1D chain with the anions linking neighbouring chains; the packing being tighter in the case of the BPh_4 complex. As with $[Fe(qnal)_2]^+$ both compounds undergo almost complete LIESST.

Hydrazone ligands have also been employed to make Fe(III) SCO complexes. The first report was by Gamez, Reedijk and colleagues on $[Fe(mph)_2]ClO_4{\cdot}0.5H_2O{\cdot}0.5MeOH$ which undergoes an unusual

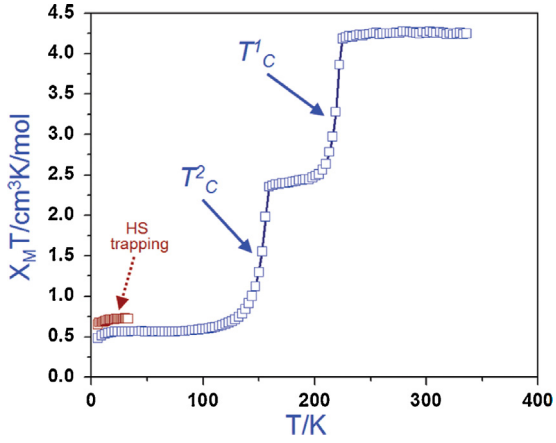

Fig. 9. Magnetic behaviour of $[Fe(mph)_2]ClO_4{\cdot}0.5H_2O{\cdot}0.5MeOH$ (reproduced from Ref. [82] with permission. (Copyright American Chemical Society, 2009.)

abrupt stepped SCO with a 45 K *ca.* 50% HS plateau (Fig. 9) [82]. The structure in the intermediate region shows that despite having two independent Fe(III) centres the Fe–N/O bond lengths are averaged across the two centres being intermediate between full HS and full LS, rather than localized as in many of the systems described above. The packing within the structure consists of H-bonded dimers which are linked to surrounding dimers by π–π interactions leading to 2D sheets.

The pyridyl aroylhydrazone Fe(III) complexes, $[Fe(pah\text{-}R)_2]ClO_4$ (R = H, *t*-Bu) required an unusual 1:1 ratio of Fe and ligand to be isolated; a 1:2 ratio of the Fe and ligand gives only the Fe(II) complex [83]. The SCO is gradual in both cases being incomplete and stepwise for $[Fe(pah)_2]ClO_4$. The structure of $[Fe(pah)_2]ClO_4$ at 100 K reveals two independent LS Fe(III) centres consistent with the stepped SCO.

The final SCO complex with a tridentate ligand is $[Fe(dammithiol)_2]Cl{\cdot}3H_2O$ which uniquely has a N_4S_2 donor set [84]. The compound exhibits a very gradual SCO, incomplete at both ends, from 50% HS at room temperature to 20% HS at 20 K according to Mössbauer spectroscopy. The structure is consistent with a LS Fe(III) centre and shows C—H···O interactions which link the Fe units into a 1D chain.

2.3. Tetradentate ligands

2.3.1. Salen ligands

Much of the most recent work on tetradentate ligands has been done by Matsumoto's group (see Table 2 and Fig. 10). The effect of the anion has been explored in $[Fe(Him)_2(3\text{-}OMe\text{-}salen)]Y{\cdot}H_2O{\cdot}EtOH$ (Y = PF_6, AsF_6, SbF_6) which show abrupt stepped SCO, half-SCO and HS only behaviour, respectively [85]. The SCO occurs at very low temperatures 20–70 K and at 40 K for the PF_6 and AsF_6, respectively. The change in SCO behaviour correlates with the size of the anion with smaller anions permitting more complete SCO. This is consistent with the void in the lattice shrinking upon SCO which can accommodate the PF_6 anion but not the larger SbF_6. Due to the low temperature of the spin crossover only the HS

Fig. 10. Structures and abbreviations of the tetradentate ligands used in iron(III) SCO systems.

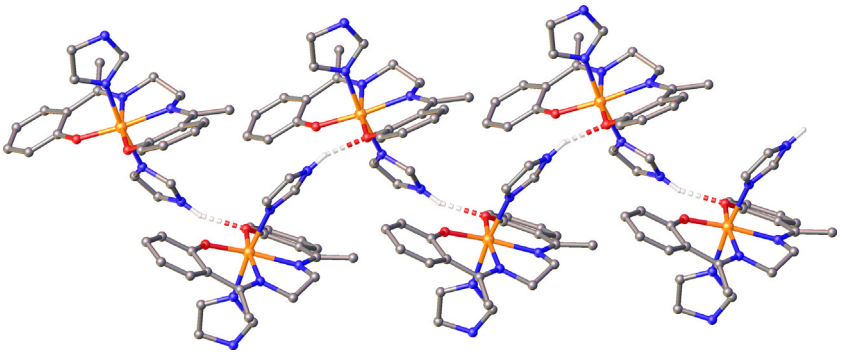

Fig. 11. The 1D hydrogen bonding chain of $[Fe(Him)_2(hapen)]AsF_6$ [87].

structures have been determined but they nevertheless show extensive 2D hydrogen bonding interactions between the Fe cations and the H_2O and EtOH molecules which accounts for the abrupt and hysteretic SCO observed in the PF_6 and AsF_6 systems.

Replacing the methoxy group with an ethoxycarbonyl group yields $[Fe(R\text{-}Im)_2(5\text{-}CO_2Et\text{-}salen)]BPh_4{\cdot}sol$ (R = H, sol = EtOH; R = 1-Me, sol = $0.5H_2O$) [86]. Both exhibit thermochromism in solution changing from red to blue-green but in the solid state only the Him complex is SCO active, although the transition is very gradual with $T_{1/2}$ = 192 K. The structure of the LS and HS forms reveals significant changes in the Fe—N bond lengths by 0.16 Å but unusually no change in the Fe—O bonds. In contrast to the structures above, there are no hydrogen bonding networks but simple hydrogen bonded dimers instead.

2.3.2. Hapen ligands

Closely related to the salen ligands above is the hapen ligand in which 2-hydroxyacetophenone is used instead of salicylaldehyde. The complexes $[Fe(Him)_2(hapen)]Y{\cdot}sol$ (Y = BF_4, ClO_4, PF_6, AsF_6, OTf, BPh_4) show a variety of magnetic behaviours with the smaller anions HS only and the larger anions SCO active [87,88]. The outstanding members of the series are the AsF_6 and PF_6 complexes which exhibit abrupt hysteretic SCO (ΔT = 4.6 K, $T_{1/2}\uparrow$ = 74 K, $T_{1/2}\downarrow$ = 69.4 K) [87] and abrupt SCO at $T_{1/2}$ = 75 K [88], respectively. In both cases the structures show a HS Fe(III) centre with a 1D hydrogen bonding zigzag chain involving the imidazole NH and coordinated phenoxy O atom that links the spin centres (Fig. 11). In its absence, the compounds are trapped in the HS state.

The position of the methoxy substituent on the hapen ligand has also been explored in $[Fe(Him)_2(n\text{-}OMe\text{-}hapen)]PF_6{\cdot}sol$ (n = 4, sol = none; 5, sol = $0.5H_2O$; 6, sol = EtOH) [89]. The 4-OMe and 5-OMe compounds undergo gradual SCO being slightly more abrupt in the former case. Both complexes exhibit thermochromism changing from deep red at room temperature to blue-green at liquid nitrogen temperatures. In contrast, the 6-OMe complex exhibits very incomplete SCO. Structural studies suggest that steric hindrance between the methyl and methoxy group results in greater distortion of the 6-OMe-hapen ligands preventing substantial SCO. The difference in the Fe—N bond lengths is *ca.* 0.14 Å upon SCO, while the Fe—O bond lengths do not change mirroring the trend observed in the $[Fe(Him)_2(salen)]^+$ complexes above. Abrupt SCO ($T_{1/2}$ = 192 K) between a single site HS state (monoclinic C2/c) and a symmetry breaking [HS–HS–HS–LS] state (triclinic $P\bar{1}$) has been reported in $[Fe(Him)_2(4\text{-}OMe\text{-}hapen)]OTf$ [90]. The packing mirrors that of the PF_6 salt with H-bonded chains of $[Fe(Him)_2(4\text{-}OMe\text{-}hapen)]^+$ bridged by the OTf anion. However, the 1D chains are interdigitated in the OTf complex but not the PF_6 analogue and this is probably responsible for the symmetry breaking SCO.

2.3.3. Acen ligands

The complexes $[Fe(acen)(n\text{-}Bu\text{-}im)_2]Y$ (Y = NTf_2, PF_6) both show SCO which is incomplete at 320 K [91]. The NTf_2 salt is an ionic liquid while the PF_6 salt is a crystalline solid. Despite the different anions the SCO profile is remarkably similar but consistent with the lack of cooperativity noted in the structure of $[Fe(acen)(n\text{-}Bu\text{-}im)_2]PF_6$.

2.4. Pentadentate ligands

Pentadentate ligands are usually dianionic Schiff bases with an N_3O_2 donor set with the final N supplied by a terminal ligand (see Fig. 12 and Table 3). The compounds, $[Fe(salten)(n\text{-}py\text{-}N{=}N\text{-}Ph)]BPh_4$ (n = 3, 4) contain photoisomerizable ligands and have been prepared with the aim of determining the effect of isomerisation on SCO characteristics [92]. Both complexes undergo gradual SCO, although it is more abrupt in the 3-py-N=N-Ph complex. In solution, photoisomerization from the *trans* to the *cis* isomer results in essentially no change in the magnetic behaviour.

$[Fe(salten\text{-}3\text{-}OMe)(Me\text{-}Im)]BPh_4$ with a methoxy group on the phenyl ring undergoes gradual SCO with $T_{1/2}$ = 215 K [93]. Structural studies show Fe–N/O bond length changes compatible with SCO with the largest difference for the Fe—N(amine) bond. The packing involves a ribbon of Fe cations connected by C—H···π interactions but surprisingly no hydrogen bonding.

Using an asymmetric ligand with ethylene and propylene linkers rather than two propylene linkers yields a range of complexes many of which undergo SCO. $[Fe(salpet\text{-}R)(NH_2\text{-}tet)]$ (R = H, 5-Cl, 5-Br, 3,5-Br_2) all show SCO although it is very gradual and incomplete even at 400 K [94]. By comparison $[Fe(salten)(NH_2\text{-}tet)]$ is HS at all temperatures. The structure of $[Fe(salpet)(NH_2\text{-}tet)]$ reveals a LS Fe(III) centre and extensive hydrogen bonding between the phenoxy O atoms and the amino N–H groups as well as an N—H···N interaction involving the tetrazole and the salpet N–H group forming a 1D chain. The N—H···O interactions, in particular, may be vital in weakening the ligand field to permit SCO.

The pseudo-halide complexes $[Fe(salpet\text{-}R)X]$ (X = NCS, NCSe, NCO, N_3) are also often SCO active [95–97]. The most abrupt SCO occurs for [Fe(salpet-3-OEt)NCS] with $T_{1/2}\uparrow$ = 84 K and $T_{1/2}\downarrow$ = 82 K and thus ΔT = 2 K, although there is a residual HS fraction even at low temperature [97]. X-ray crystallography shows two independent but structurally similar Fe(III) centres which obviously undergo SCO at the same temperature. The most interesting feature of the structure though, is the strongly asymmetric shortening of the Fe—O bond lengths by 0.01 or 0.07 Å upon SCO. The Fe—O bond distance which lengthens the most is on the propylene side of the Schiff base; this appears to be a feature of these and the [Fe(napet)X] complexes discussed below. The packing again involves H-bonding this time between the N–H amine and the oxygen atom of the ethoxy groups.

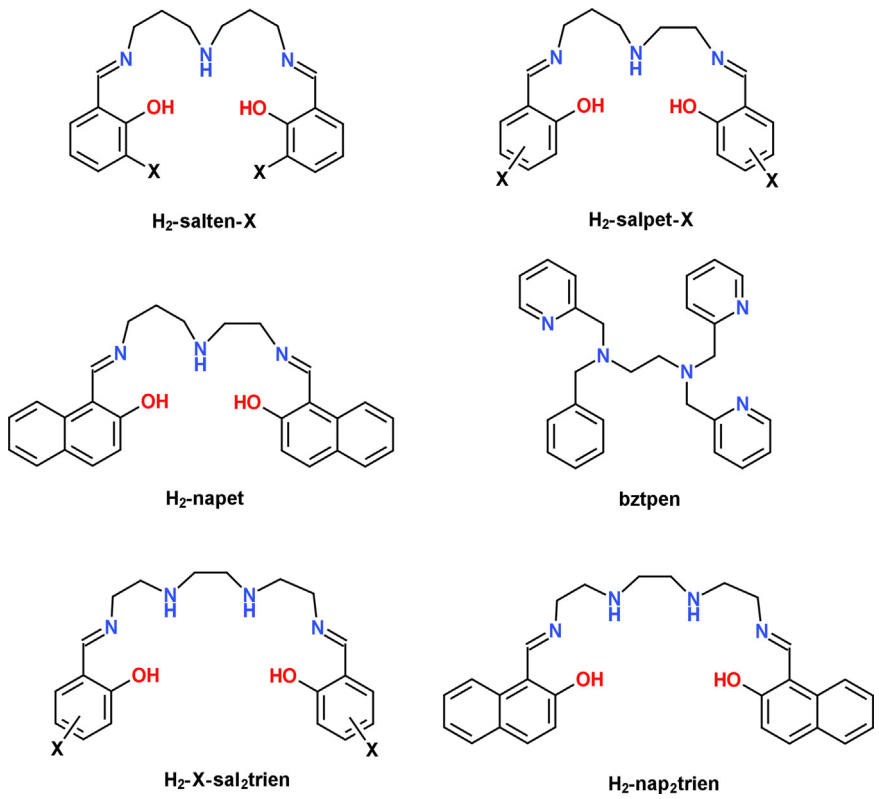

Fig. 12. Structures and abbreviations of the pentadentate and hexadentate ligands used in iron(III) SCO systems.

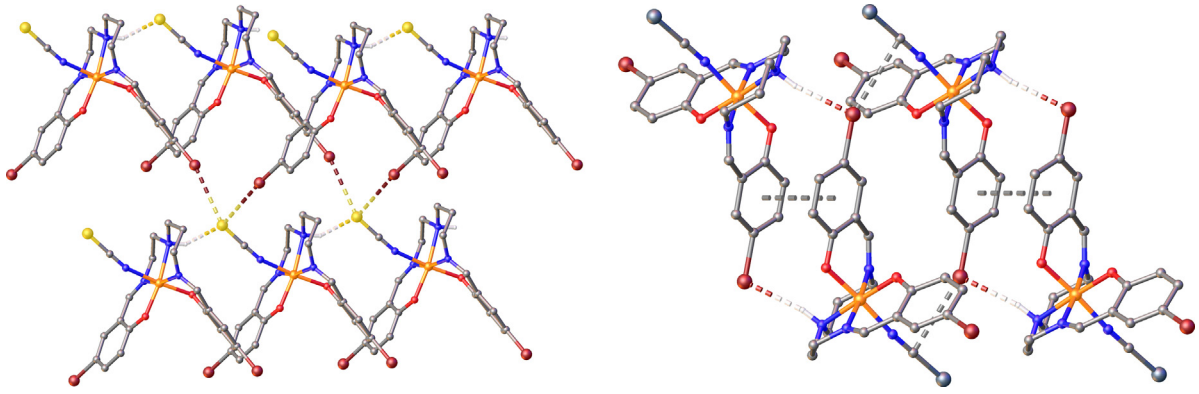

Fig. 13. Comparison of the supramolecular interactions in [Fe(salpet-Br)NCX] {X = S (HS only), Se (SCO)} [95].

[Fe(salpet-Br)X] (X = NCSe, N_3) [95] and [Fe(salpet-Cl)X] (X = NCS, NCSe) [96] show moderately abrupt SCO with $T_{1/2}$ varying from 140 to 320 K being incomplete at lower temperatures for the [Fe(salpet-Br)X] series. Structural data in either the HS or LS state for these compounds reveal once again inequivalent Fe—O bond lengths with a large change in only one of the Fe—O bond lengths. With the exception of [Fe(salpet-Br)N_3], the packing is dominated by N—H···Cl/Br interactions which are reinforced by π–π interactions (see Fig. 13). Additional C—H···Cl/Br interactions coupled with more π–π interactions form a 1D chain. In the case of [Fe(salpet-Br)N_3] the 1D chain is formed exclusively with N—H···N interactions. In either case it is clear that interactions involving the coordinated amine N–H are often key in determining SCO characteristics in [Fe(salpet-R)X] complexes.

[Fe(napet)X]·MeCN (X = NCS, NCSe) [98] and [Fe(napet)X] (X = NCS, NCO, N_3) [97,98] all exhibit quite abrupt SCO with the transition temperature varying from 117 to 174 K. For [Fe(napet)N_3] the SCO is particularly abrupt with $T_{1/2}\uparrow = 122$ K and $T_{1/2}\downarrow = 117$ K and a hysteresis of 5 K [97]. As expected [Fe(napet)NCSe]·MeCN undergoes SCO *ca.* 20 K higher than the NCS analogue [98]. The effect of solvent is evident by comparing [Fe(napet)NCS] and [Fe(napet)NCS]·MeCN where $T_{1/2}$ are 174 and 151 K, respectively. The structures of many of these complexes have been determined in both spin states with Fe–N/O bond length trends matching those of the [Fe(salpet-R)X] complexes. When the Fe—N(amine) bond length is greater than 2.20 Å the compound becomes trapped in the HS state. In terms of the packing, a feature present in all of the [Fe(napet)X] series are N—H···Y (Y = S, N or O) interactions which link the cations to form 1D chains identical to that of [Fe(salpet-Br)N_3]. When MeCN is present this chain is disrupted and N—H···N interactions form instead. Surprisingly, despite the large aromatic rings there is no evidence of π–π interactions in any of the structures.

The impact of solvent on SCO has been explored in a fascinating series of compounds [Fe(napet)NCS]·sol (sol = THF, butanone, DMF, DMSO, acetone), the first systematic structural study of

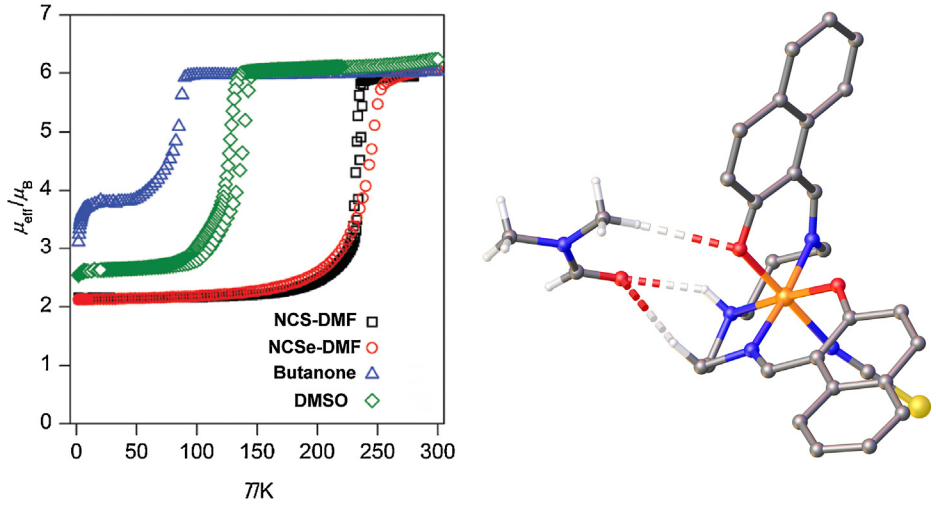

Fig. 14. Magnetic behaviour of [Fe(napet)NCS]·sol and the SCO defining N—H···O interaction in [Fe(napet)NCS]·DMF (reproduced, slightly modified, from Ref. [99]. (Copyright Royal Society of Chemistry, 2015.)

solvent effects in Fe(III) SCO chemistry [99]. All the compounds have N—H···O interactions between the coordinated amine and the oxygen atom of the solvent. The strength of this N—H···O interaction directly correlates with the transition temperature ranging from 84 to *ca.* 230 K. When the N—H···O interaction is longer than 3.0 Å, the complex is no longer SCO active (THF and acetone). In the case of [Fe(napet)NCS]·sol where the solvent is DMF and DMSO hysteresis loops of 3 and 7 K are observed, respectively (Fig. 14). The presence of hysteresis in these compounds is probably due to offset π–π, C—H···π and C—H···O interactions which form a more organized grid than that observed in other [Fe(napet)X] compounds.

Two naphthenyl ligands have been explored using 1-hydroxy-2-acetonaphthone or 2-hydroxy-1-acetonaphthone and reacting it with the asymmetric triamine to give [Fe(*n*-napet-Me)NCS] (*n* = 1 or 2) [96]. Three polymorphs of [Fe(1-napet-Me)NCS] exist with only the α-polymorph undergoing SCO, which unusually is between *S* = 3/2 and *S* = 5/2 spin states at *ca.* 42 K (Δ*T* = 4 K); the other two polymorphs are HS. The α- and γ-polymorphs both contain two independent Fe(III) centres and while for the former there is a bent and a linear NCS ligand, for the latter both are bent. In contrast, the β-polymorph has a single HS Fe(III) centre and a linear NCS ligand. Only in this polymorph is there an extended chain composed of N—H···S interactions between the coordinated amine and the thiocyanate S atom. In the α-polymorph there are no H-bonds while for the γ-polymorph a supramolecular dimer is found. A similar loss of H-bonding interactions occurs in [Fe(1-napet-Me)N_3] which is HS only and in [Fe(2-napet-Me)NCS]. The latter compound undergoes gradual and incomplete SCO with $T_{1/2}$ = 114 K, *ca.* 60 K lower than [Fe(napet)NCS] confirming that the 2-napet-Me ligand generates a weaker ligand field than napet.

Real and co-workers recently reported a series of SCO complexes which uniquely have an N_5O coordination environment, [Fe(btzpen)(OR)][PF_6]$_2$ (R = Me, Et, Pr, n-Bu, i-Bu, CH_2CH_2OH) [100,101]. It seems likely that the two tertiary amine N donors of the btzpen ligand provide a weaker ligand field than the pyridyl N donors making the complexes SCO active. All the compounds exhibit gradual SCO with $T_{1/2}$ increasing from 158 to 284 K as the ionization potential of the alkoxide decreases. The structures of the compounds in the HS and LS states reveal the expected shortening of the Fe—N bond distances between 0.09 and 0.13 Å but a lengthening of the Fe—O bond length by between 0.01 and 0.02 Å upon SCO to the LS state. The overall change in the Fe–N/O bond lengths is slightly less than that of other Fe(III) SCO complexes. The packing shows no significant cation–cation or cation–anion interactions consistent with the gradual SCO observed in these compounds.

2.5. Hexadentate ligands

The first example of symmetry breaking SCO in Fe(III) was reported in 2011 in [Fe(3,5-OMe-sal$_2$bapen)]ClO_4 [102]. The SCO is gradual and incomplete retaining 33% HS character even at low temperature but occurs in two steps with $T_{1/2}$ = 190 and 100 K with slight hysteresis in the latter step. The space group remains the same at all temperatures but trebles in size after the 1st step. This creates two Fe(III) centres one which has 50% occupancy and is LS while the other is HS with 100% occupancy and consequently an overall 67% HS state. The structure below the second step could not be determined but Mössbauer spectroscopic data mirror the magnetic studies with transitions from 100% HS to 2:1 HS:LS to 1:2 HS:LS evident.

Spin crossover has also been explored in [Fe(X-sal$_2$trien)]Y (X = Me, *i*-Pr, *t*-Bu; Y = NO_3, PF_6) [103]. The SCO is gradual and incomplete proceeding to 35–50% completeness except in [Fe(Me-sal$_2$trien)]NO_3·3/2H_2O and [Fe(Me-sal$_2$trien)]PF_6 which are LS and HS, respectively. The structure of [Fe(Me-sal$_2$trien)]PF_6 reveals two unique Fe(III) centres in which the bond lengths and angles differ significantly. This may account for the half-SCO observed in other compounds in this series, although [Fe(*t*-Bu-sal$_2$trien)]NO_3·$C_2H_4Cl_2$ contains only a single HS Fe(III) site at 100 K. However, it should be stressed that it is the non-solvated compound that undergoes SCO. In line with many [Fe(X-sal$_2$trien)]$^+$ complexes, [Fe(*t*-Bu-sal$_2$trien)]NO_3 also undergoes SCO in solution.

In [Fe(4-OH-sal$_2$trien)]Y (Y = Cl, Br and I) the SCO is gradual and incomplete going from the LS state to 20–80% HS being most complete for the iodide complex [104]. The complexes are isostructural and in the LS state, reveal extensive hydrogen bonding between the hydroxyl groups and the halide anions as well as N—H···O interactions which result in a 2D supramolecular network. As expected the hydrogen bonding is strongest for the chloride and weakest for the iodide resulting in the tightest packing for [Fe(4-OH-sal$_2$trien)]Cl and thus the poorest SCO profile. However, in solution all the compounds undergo complete SCO with clear thermochromism going from brown at 298 K to blue at 77 K (see Fig. 15).

Substituting the phenyl groups with imidazolium cations results in a SCO active ionic liquid [Fe(4-(OCH_2-imid-n-Bu)sal$_2$trien)][$(CN)_2N]_3$ with dicyanamide anions. The SCO is modest being 33% HS at 400 K but is reversible and for the first

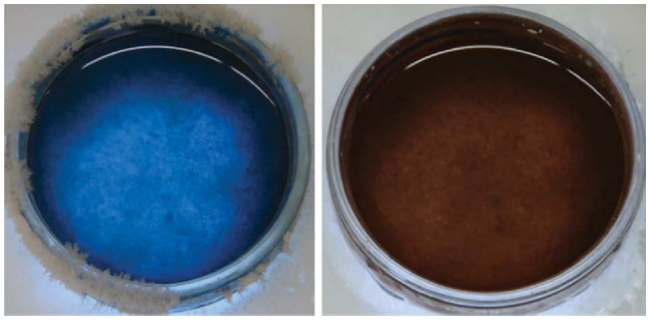

Fig. 15. Thermochromism of [Fe(4-OH-sal$_2$trien)]I in the LS (left) and HS state (right; reproduced with permission from Ref. [104]. (Copyright Royal Society of Chemistry, 2012.)

time in Fe(III) SCO chemistry the ionic liquid is thermally stable [105].

In [Fe(nap$_2$trien)]Y (Y = PF_6, NCS) where naphthenyl groups are used the PF_6 complex is LS up to 300 K [103] while the NCS complex undergoes symmetry breaking SCO that is abrupt in the first (lower temperature) step [106]. The SCO occurs at 142 and 250 K and is much broader in the second step. The structures at 50 and 298 K both contain a single Fe(III) centre which is LS and HS respectively. However, at 150 K the unit cell doubles in size with two Fe(III) centres one HS and the other LS. This type of re-entrant SCO is extremely rare and this was the first time it was reported for Fe(III). The packing within the structure is dominated by N—H···S interactions between the thiocyanate S and neighbouring amines of the nap$_2$trien ligand forming a 1D chain reminiscent of the [Fe(napet)X] and [Fe(salpet)X] systems discussed above.

[Fe($H_{1.5}$tren-imid)][ClO_4]$_{1.5}$ and [Fe(H_2tren-imid)][Co(Htren-imid)][ClO_4]$_3$ also exhibit very incomplete SCO based on Mössbauer spectroscopic studies which are 50% to 60% HS for the Fe only complex and LS to 55% HS for the Fe–Co compound [107]. [Fe($H_{1.5}$tren-imid)][ClO_4]$_{1.5}$ exists as three polymorphs trigonal, hexagonal and cubic. The trigonal polymorph has a 2D sheet supramolecular network while the cubic form is composed of supramolecular tetrahedra. In both cases the networks are held together by N—H···N hydrogen bonds involving the imidazole NH and N atoms.

3. Dimeric systems

Dinuclear systems are almost all based on the pentadentate ligands, salten and salpet [108,109]. In 2007, Matsumoto and co-workers reported [{(salten-3-OMe)Fe}$_2$(μ-bimb)][BPh_4]$_2$ (bimb = 1,4-bisimidazolylbutane) which exhibits gradual 2 step SCO with $T_{1/2}$ = 60 and 90 K [93]. The structure of the HS–HS dimer reveals only weak π–π interactions consistent with the gradual SCO. More recently, the same group has reported two related dimers [{(salten-3-OMe)Fe}$_2$(μ-4,4′-bipy)][BPh_4]$_2$ and [{(N-Me-salten-3-OMe)Fe}$_2$(μ-4,4′-bipy)][BPh_4]$_2$ which exhibit 1 and 2 step SCO, respectively being incomplete in the latter compound [110]. The 2 step SCO is due to the presence of 2 independent Fe(III) centres while in [{(N-Me-salten)Fe}$_2$(μ-4,4′-bipy)][BPh_4]$_2$ the Fe(III) centres are crystallographically equivalent. The change in the Fe–N/O bond lengths in [{(salten-3-OMe)Fe}$_2$(μ-4,4′-bipy)][BPh_4]$_2$ are rather smaller than those observed in the mononuclear compounds being 0.13 and 0.03 Å, respectively. In [{(N-Me-salten-3-OMe)Fe}$_2$(μ-4,4′-bipy)][BPh_4]$_2$ the SCO is incomplete with only one of the independent Fe centres undergoing SCO based on X-ray crystallography, although Mössbauer spectroscopy shows that at 78 K the dimer is 66% LS.

The interplay between possible magnetic exchange between the Fe(III) centres and spin crossover has been explored in a series of compounds [{(N-Me-salten)Fe}$_2$(μ-N-N)][BPh_4]$_2$ {N-N = 1,2-bis(4-pyridyl)ethane (bpe), 1,2-bis(4-pyridyl)ethane (bpea), 1,2-bis(4-pyridyl)propane (bpp), 1,4-phenylenebis (methylene)bis(imidazole)} [108]. Of these only [{(N-Me-salten)Fe}$_2$(μ-bpe)][BPh_4]$_2$ displays SCO although this is incomplete at higher temperatures. [{(N-Me-salten)Fe}$_2$(μ-N-N)][BPh_4]$_2$ (N-N = 4,4′-bipy, bpe) also exhibit thermochromism changing from dark green at low temperature to violet at room temperature. The structures of these compounds reveal crystallographically equivalent Fe(III) centres which are LS when the bridging ligands are bpe and bpea and HS with bpp.

Two asymmetric dimers [(salpet-R)Fe(μ-CN)Fe(salpet-R)]Y (R = H, Y = ClO_4·2H_2O; R = 5-Me-3t-Bu, Y = BPh_4·2MeCN) have been prepared which show gradual but complete SCO for the BPh_4 dimer and very incomplete SCO, from 62% LS to 39% LS for the ClO_4 dimer [111]. As expected, only the N-bound Fe centre undergoes SCO. The structures of the dimers are consistent with the magnetic data and interestingly in the case of the BPh_4 dimer the cyanide bridge is disordered.

The final, and to date only, Fe(III) dimer not utilizing an N_3O_2 ligand are the series [(qsal)Fe(qsal-C≡C-2,2-bith-C≡C-qsal)Fe(qsal)][Y]$_2$ (Y = Cl, NCS, PF_6, ClO_4, see Fig. 16) [112]. The SCO in these dimers is extremely gradual going from almost 100% HS to ca. 50% HS while the ClO_4 salt is incomplete at both ends (20% HS to 56% HS). The lack of structural data means that it's impossible to tell whether the SCO occurs at a single site or at both Fe centres.

4. Multinuclear systems

Multinuclear SCO systems have been prepared with the aim of producing multi-step SCO systems. The trinuclear system [(salpet)Fe(Fe(CN)$_5$NO)Fe(salpet)] shows partial and very gradual SCO in only one of the iron centres [111]. Similarly incomplete SCO is also observed in the Sn(IV) tetramer [{(salpet)Fe}$_4$Sn(CN)$_4$][Cl]$_4$ as evidenced by Mössbauer spectroscopic studies [113]. The largest member of this type is the heptanuclear cluster [Fe^{II}{(CN)Fe^{III}(salpet)}$_6$][Cl]$_2$ for which the SCO is gradual with 4 Fe(III) centres remaining HS even at 20 K [114]. The structure at room temperature is consistent with six HS

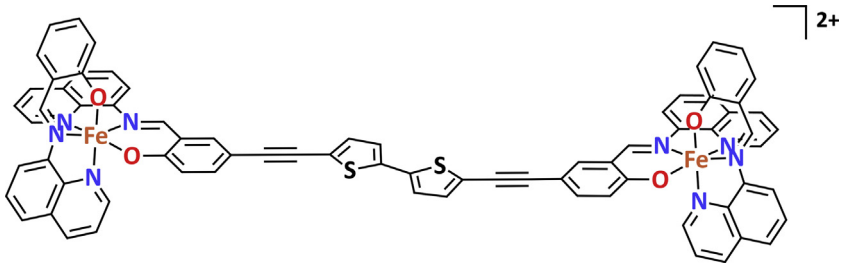

Fig. 16. View of the [(qsal)Fe(qsal-C≡C-2,2-bith-C≡C-qsal)Fe(qsal)][Y]$_2$ dimer [112].

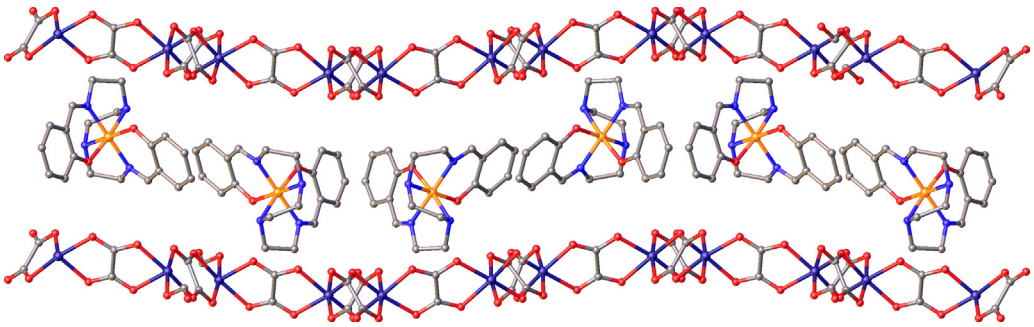

Fig. 17. Layered structure found in many [Fe(5-X-sal$_2$trien)][Mn{Cr(ox)$_3$}]·sol systems [120].

Fe(III) atoms and the close proximity of neighbouring Fe(salpet) units may explain why full SCO cannot be achieved.

In another approach Murray's group have synthesized a large number of 1D polymers [Fe(N_2O_2)L][BPh_4]$_n$ (N_2O_2 = salen, salophen, acen; L = bridging pyridyl or imidazole) with the aim of increasing cooperativity between the iron centres [115]. At almost the same time Matsumoto and co-workers reported {[Fe(acen)L][BPh_4]}$_n$ where L = 1,3-bis(4-pyridyl)propane (bpp) and 1,4-bis(N-imidazole)butane (bimb) [116]. The salen and salophen systems are almost all HS, something that in the former case is thought to be due to the *meso* configuration of the C_2N_2 backbone of the ligand. In contrast, many of the {[Fe(acen)L][BPh_4]}$_n$ systems are SCO active although they are almost all gradual and in some cases SCO is incomplete even at 350 K. The exception is {[Fe(acen)(pin)][BPh_4]}$_n$ (pin = N-(4-pyridyl)-isonicotinamide) where the SCO is relatively abrupt ($T_{1/2}$ = 135 K) possibly due to H-bonding between 1D chains [115]. Structures of {[Fe(acen)(bpp)][BPh_4]}$_n$ and {[Fe(acen)(bimb)][BPh_4]}$_n$ reveal that in spite of their identical formulas the bpp compound contains 2 crystallographically distinct 1D chains while for {[Fe(acen)(bimb)][BPh_4]}$_n$ there is only one. Changes in the Fe–N/O bond lengths are typical of SCO systems being ΔFe-N = 0.14 Å and ΔFe-O = 0.02 Å. In all these systems cooperativity is very poor despite the coordination bonds between the Fe(III) centres. The large anions may be responsible, in part, for the lack of abrupt SCO in these systems and more work is clearly needed.

5. Multifunctional systems

5.1. [Fe(5-X-sal$_2$trien)][Mn{Cr(ox)$_3$}] systems

Materials incorporating SCO centres are attractive targets as the spin crossover may be coupled to other physical properties. An elegant example of this are the series of compounds [Fe(5-X-sal$_2$trien)][Mn{Cr(ox)$_3$}]·sol (X = H, sol = CH_2Cl_2, CH_2Br_2 $CHCl_3$, $CHBr_3$, MeOH; X = Cl, Br, OMe sol = none; X = NO_2, sol = $MeNO_2$·0.5H_2O) where the SCO cation is inserted into a ferromagnetic network [117–123]. The structures are generally composed of alternating layers of the bimetallic [Mn{Cr(ox)$_3$}]$^-$ network with the [Fe(sal$_2$trien)]$^+$ cations intercalated between the layers of the 2D oxalate network (Fig. 17). In [Fe(sal$_2$trien)][Mn{Cr(ox)$_3$}]·sol (sol = CH_2Cl_2, $CHCl_3$, CH_2Br_2, $CHBr_3$) there is coexistence of ferromagnetic ordering at *ca.* 5 K and complete, gradual SCO with $T_{1/2}$ varying from 255 to 142 K [120,122]. Remarkably, all the compounds also undergo LIESST with the degree of LIESST strongly dependent on the solvent, being 40% for $CHCl_3$ and 21% for CH_2Br_2. These hybrid magnets are extremely rare and moreover, demonstrate that cooperative SCO is not a necessary requirement for the observation of LIESST in Fe(III) compounds. The structures in the HS and LS states show changes in the Fe–N/O bond lengths of *ca.* 0.15 and 0.03 Å and are similar to those of simple [Fe(sal$_2$trien)]$^+$ complexes.

The increase in the size of the cations following SCO is reflected in an increase in the distance between the oxalate layers and more extensive C—H···O interactions involving the [Fe(sal$_2$trien)]$^+$ cations which may stabilize the photogenerated metastable HS state. Solvent is critical in these systems and in contrast to the above networks [Fe(sal$_2$trien)][Mn{Cr(ox)$_3$}]·MeOH has a 3D bimetallic oxalate network which results in much more distorted [Fe(sal$_2$trien)]$^+$ units and consequently no SCO [119].

The SCO behaviour of [Fe(n-X-sal$_2$trien)][Mn{Cr(ox)$_3$}]·sol is very variable with the best coexistence of SCO and ferromagnetism occurring in [Fe(5-X-sal$_2$trien)][Mn{Cr(ox)$_3$}]·sol (X = Cl, sol = 0.5$MeNO_2$, X = Br, sol = none) [121] and [Fe(4-Br-sal$_2$trien)][Mn{Cr(ox)$_3$}]$_{0.67}$[Cl]$_{0.33}$·MeOH with 45%, 25% and 90% SCO ($T_{1/2}$ = *ca.* 340 K) respectively [123]. In contrast, [Fe(5-X-sal$_2$trien)][Mn{Cr(ox)$_3$}] where X = NO_2 and OMe, are LS and HS only, respectively [118]. Similarly, [Fe(3-X-sal$_2$trien)][Mn{Cr(ox)$_3$}] (X = Cl, Br, OMe) are essentially trapped in the HS state [123]. The structures are varied with chiral 3D bimetallic oxalate networks formed in [Fe(5-X-sal$_2$trien)][Mn{Cr(ox)$_3$}] (X = Cl, Br) while a 2D network forms for [Fe(4-Br-sal$_2$trien)][Mn{Cr(ox)$_3$}]$_{0.67}$[Cl]$_{0.33}$·MeOH. In the latter case, unusually there is a double layer of [Fe(4-Br-sal$_2$trien)]$^+$ cations in between the anionic oxalate layers. Moreover, unlike the above networks with [Fe(sal$_2$trien)]$^+$, none of the [Fe(n-X-sal$_2$trien)][Mn{Cr(ox)$_3$}]·sol systems exhibit the LIESST effect. This may be due to the more incomplete SCO, higher $T_{1/2}$ or structural differences in the networks.

More recently, the oxalate layers have been replaced by an anilate network to give [Fe(4-X-sal$_2$trien)][Mn{Cr(Cl_2An)$_3$}]·sol (X = H or OH, Cl_2An = chloroanilate), [Fe(5-Cl-sal$_2$trien)][Mn{Cr(Br_2An)$_3$}]·CH_2Cl_2·MeOH·4H_2O·1.5MeCN) (Br_2An = bromoanilate) and [Fe(sal$_2$bapen)][Mn{Cr(Br_2An)$_3$}]·4MeCN (sal$_2$bapen = N,N′-bis(salicylidene)-1,5,8,12-tetraazadodecane) [124]. These networks show ferromagnetic ordering of the anilate networks at *ca.* 10 K but no SCO being either LS or HS only. The structures are similar to those of [Fe(sal$_2$trien)][Mn{Cr(ox)$_3$}]·sol networks being composed of 2D anilate layers with the Fe(III) cations intercalated in between these layers.

Similar anilate networks, [Fe($acac_2$-trien)][Mn{Cr(Cl_2An)$_3$}]·2MeCN and [Fe($acac_2$-trien)][Mn{Cr(Br_2An)$_3$}]·2MeCN show ferrimagnetic ordering at low temperatures but no SCO at the Fe centres [125]. The [Fe($acac_2$-trien)]$^+$ cations are located in hexagonal channels provided by the anilate networks creating 2D materials. Simple Scotch tape micromechanical exfoliation yields nanosheets of the networks. The same method is also applicable to [Fe(sal$_2$trien)][Mn{Cr(ox)$_3$}]·sol despite the 3D network present in this system.

5.2. [M^{III}(dithiolene)$_2$]$^-$ systems

Another strategy towards multifunctional materials involves combining Fe(III) SCO cations with potentially conducting

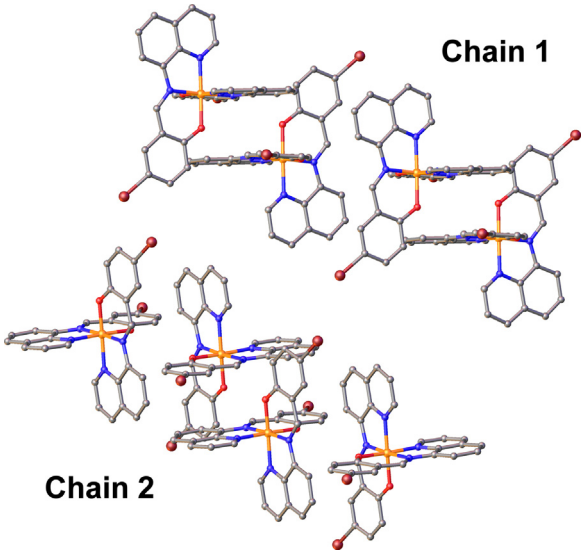

Fig. 18. View of the angular 1D chains in $[Fe(qsal\text{-}5\text{-}Br)_2][Ni(dmit)_2]\cdot CH_2Cl_2$ [132].

anions, $[M^{III}(dithiolene)_2]^-$. The most commonly used cations belong to the $[Fe(qsal\text{-}X)_2]^+$ family of SCO complexes with $[Fe(qsal)_2][Ni(dmit)_2]\cdot 2MeCN$ reported in 2005 [126]. $[Fe(qsal)_2][Ni(dmit)_2]\cdot 2MeCN$ undergoes abrupt and almost complete SCO at 194 K after the first cooling with the compound returning to the HS state at 231 K. This hysteresis is only apparent as subsequent cycles reveal SCO at 231 K in both the heating and warming modes. Despite the large anion, the structure at 273 K is strongly reminiscent of the other $[Fe(qsal)_2]^+$ complexes with 1D chains of the Fe(III) cations formed by orthogonal π–π interactions (see Fig. 2). The $[Ni(dmit)_2]^-$ anions form 1D stacks which sit in between the 1D chains of the $[Fe(qsal)_2]^+$ cations. Loss of solvent gives $[Fe(qsal)_2][Ni(dmit)_2]$ which exhibits very gradual and incomplete SCO (ca. 50% HS at 4 K) [127]. There is complete loss of the 1D $[Fe(qsal)_2]^+$ chains and alternating layers of mixed $[Fe(qsal)_2]^+$ and $[Ni(dmit)_2]^-$ units and $[Ni(dmit)_2]^-$ only stacks. It is clear that as with $[Fe(qsal\text{-}X)_2]^+$ complexes of simple anions the 1D π–π chains are essential for abrupt SCO. Cooperative SCO has been achieved in $[Fe(qsal)_2][Ni(dmise)_2]\cdot 2MeCN$ with SCO occurring at $T_{1/2}\downarrow = 241$ K and $T_{1/2}\uparrow = 256$ K and thus a hysteresis of 15 K [128]. The structure is virtually identical to that of $[Fe(qsal)_2][Ni(dmit)_2]\cdot 2MeCN$ but with the LS structure now available it is clear that in addition to the expected shortening of the Fe–N/O bond lengths (ΔFe-N = 0.169 Å, ΔFe-O = 0.032 Å) there is also reversible slippage of the $[Ni(dmise)_2]^-$ π-dimers.

A number of other anions have been used to prepare $[Fe(qsal)_2][M^{III}(dithiolene)_2]$ systems ($[M^{III}(dithiolene)_2]^- = [Cu^{III}(pds)_2]^-$, $[Au^{III}(pds)_2]^-$ [129], $[Ni(dddt)_2]^-$, $[Ni(pddt)_2]^-$ [130]). Of these only $[Fe(qsal)_2][Ni(dddt)_2]\cdot MeCN\cdot MeOH\cdot H_2O$ exhibits SCO, although it is incomplete and very gradual [130]. The structures of these compounds show high degrees of distortion at the Fe centre caused by significantly non-planar qsal ligands and it is this that is undoubtedly responsible for the lack of SCO in most of these systems. The distortion also results in weak interactions between the $[Fe(qsal)_2]^+$ cations as it is difficult to achieve effective overlap of the aromatic groups.

More recently, Takahashi et al. reported $[Fe(qsal\text{-}5\text{-}I)_2][Ni(dmit)_2]\cdot MeCN\cdot H_2O$ where the spin crossover is coupled to a spin-Peierls-like singlet formation of the paramagnetic $[Ni(dmit)_2]^-$ anions [131]. The SCO is abrupt with a hysteresis of 6 K at *ca.* 150 K. Structural data demonstrate that the SCO and spin-Peierls-like singlet formation are coupled to the reversible loss and formation of I···S interactions between the $[Fe(qsal\text{-}5\text{-}I)_2]^+$ cation and $[Ni(dmit)_2]^-$ anion. Interestingly, the packing of the $[Fe(qsal\text{-}5\text{-}I)_2]^+$ cations is via π–π and C—H···π interactions forming 1D chains rather than the more usual π–π chains. As with $[Fe(qsal)_2][Ni(dmit)_2]\cdot 2MeCN$, the $[Ni(dmit)_2]^-$ anions are present as face-to-face pairs sitting in the channels created by the network formed by the $[Fe(qsal\text{-}5\text{-}I)_2]^+$ cations.

In $[Fe(qsal\text{-}5\text{-}Br)_2][Ni(dmit)_2]\cdot sol$ (sol = CH_2Cl_2, acetone) the acetone solvate shows abrupt SCO with $T_{1/2}\downarrow = 273$ K and $T_{1/2}\uparrow = 286$ K ($\Delta T = 13$ K) while the CH_2Cl_2 solvate exhibits gradual SCO ($T_{1/2}$ *ca.* 270 K) [132]. The structures in the HS and LS states show similar changes in their Fe–N/O bond lengths upon SCO but the packing within the structures is very different. Thus, while both are composed of 1D π–π chains of the cations in the acetone solvate these are identical but in the CH_2Cl_2 solvate neighbouring chains are angled relative to each other resulting in a more open network and therefore lower cooperativity (Fig. 18).

In $[Fe(qsal\text{-}5\text{-}Cl)_2][Ni(dmit)_2]\cdot 2MeCN$ the SCO takes place in two steps at 233 and 256 K and is slightly more abrupt in the 1st lower temperature step [133]. Unusually, the unit cell doubles in size in the region of the spin transition but there is no ordering of the spin centres into HS and LS sites. The packing is virtually identical to that of $[Fe(qsal)_2][Ni(dmit)_2]\cdot 2MeCN$ with closely packed $[Fe(qsal\text{-}5\text{-}Cl)_2]^+$ cations and face-to-face pairs of the $[Ni(dmit)_2]^-$ anions. $[Fe(qsal\text{-}5\text{-}Cl)_2][Ni(\alpha\text{-}tpdt)_2]\cdot MeCN$ is also SCO active although the SCO gradual thought to be due to tight packing between the cation and anionic components of the system [134]. The packing of the $[Fe(qsal\text{-}5\text{-}Cl)_2]^+$ cations involves strong π–π interactions while the anionic units pack at right angles to each other forming zigzag chains. A combination of ferromagnetic and antiferromagnetic interactions results in glassy behaviour with a blocking temperature of 7.5 K. It is interesting to note that in all of these systems clear segregation of the cationic and anionic layers appears to be essential for SCO in $[Fe(qsal)_2][M^{III}(dithiolene)_2]$ materials.

$[Fe(3\text{-}OMe\text{-}salEen)_2][Ni(dmit)_2]\cdot MeOH$ and $[Fe(salEen)_2]_2[Ni(dmit)_2][NO_3]$ both exhibit SCO which is very gradual in the former case ($T_{1/2} = 275$ K) following solvent loss after the 1st heating and incomplete for the latter complex [135]. The structures show segregated cationic and anionic layers with $[Fe(3\text{-}OMe\text{-}salEen)_2]^+$ dimers while the $[Fe(salEen)_2]^+$ cations are linked through N—H···O interactions involving the nitrate anions. The Ni-dithiolene anions form stacks with a greater degree of overlap present in $[Fe(3\text{-}OMe\text{-}salEen)_2][Ni(dmit)_2]\cdot MeOH$. Overall the cooperativity in these systems is very weak.

5.3. *Mixed-valence $[M^{III}(dithiolene)_2]^-$ systems*

Although many of these dithiolene systems were prepared with the aim of producing SCO molecular conductors surprisingly few of the mixed-valence materials have been made. The first, $[Fe(qsal)_2][Ni(dmit)_2]_3\cdot MeCN\cdot H_2O$, was reported in 2006 with the SCO coupled to conductivity of the $[Ni(dmit)_2]$ layers ($\sigma = 2$ S cm^{-1} at 298 K)–the first example of a multifunctional Fe(III) SCO material [136]. The structure shows strong stacking of the $[Ni(dmit)_2]^-$ anions with the $[Fe(qsal)_2]^+$ cations forming a 1D π–π chain aligned with the anionic stacks. Despite this the SCO is rather gradual and incomplete at higher temperatures perhaps hindered by the $[Ni(dmit)_2]^-$ stacks. In 2007, $[Fe(salEen)_2]_2[Ni(dmit)_2]_5\cdot 6MeCN$ was reported, showing gradual but complete SCO between 50 and 300 K. The structures at 290 and 180 K reveal full HS and mostly LS Fe(III) centres, respectively with Fe–N/O bond length changes consistent with incomplete SCO over this temperature range [135]. As with $[Fe(qsal)_2][Ni(dmit)_2]_3$ the anions and cations pack into 1D stacks. However, the conductivity is an order of magnitude lower than $[Fe(qsal)_2][Ni(dmit)_2]_3$ being 0.12 S cm^{-1} at room

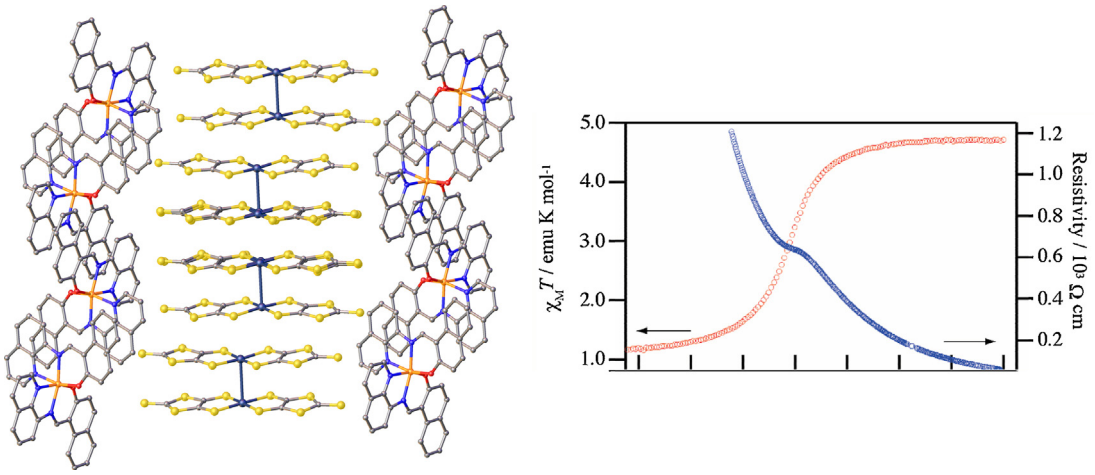

Fig. 19. View of the 1D chains and stacked $[Pd(dmit)_2]^-$ anions in $[Fe(qnal)_2][Pd(dmit)_2]_5$·acetone and the corresponding magnetic and resistivity profile (reproduced from Ref. [137] with permission. (Copyright American Chemical Society, 2008.)

temperature. $[Fe(qnal)_2][Pd(dmit)_2]_5$·acetone is the last compound of this type to be reported [137]. The SCO is moderately abrupt with $T_{1/2}$ = 220 K and shows a clear anomaly in the resistivity at the same temperature as the SCO (Fig. 19). Remarkably, the authors have been able to determine the structure in the LS and HS state which reveals columns of $[Pd(dmit)_2]^-$ and 1D π–π chains of $[Fe(qnal)_2]^+$. Upon SCO there is a considerable change in the Fe–N/O bond lengths (ΔFe-O = 0.03–0.04 Å, ΔFe-O = 0.15–0.18 Å) and more tightly packed $[Fe(qnal)_2]^+$ chains resulting in uniaxial lattice deformation. This in turn impacts the conducting $[Pd(dmit)_2]^+$ layer providing the first structural proof of cooperativity between SCO and conductivity.

6. SCO nanomaterials

SCO nanomaterials remain relatively rare in Fe(III) SCO chemistry and most materials are based on $[Fe(R\text{-}sal_2trien)]^+$. In 2008, Albrecht et al. showed a remarkable dependence of SCO *in solution* on the length of the alkyl chain in $[Fe(4\text{-}OR\text{-}sal_2trien)]NO_3$ with the C_{18} chain showing abrupt SCO ($T_{1/2}$ = 235 K) while the C_6 and C_8 groups are more gradual and incomplete at 200 K [138]. Related complexes with more branched alkyl chains varying in length from C_8 to C_{30} show increasingly abrupt and more complete SCO as the alkyl chains become longer [139] (see Fig. 20). The spin transition temperature is also tuneable over 45 K depending on the length of the alkyl group. The structure of $[Fe(4\text{-}OC_6H_{13}\text{-}sal_2trien)]PF_6$ at 173 K reveals a LS centre and supramolecular organization of the alkyl chains to form polar and non-polar layers [138]. Moreover, SEM studies show that nanorods of $[Fe(4\text{-}OR\text{-}sal_2trien)]^+$ self-assemble into spheres *ca.* 1–3 μm in diameter with these highly organized microstructures thought to be responsible for the cooperative SCO.

In another series of complexes, the sal_2trien ligand was functionalized at the amine nitrogens giving $[Fe(sal_2trien\text{-}(NR)_2)]BF_4$. $[Fe(sal_2trien)]BF_4$ is HS only while increasing the alkyl chain C_6–C_{18} results in compounds exhibiting complete SCO when R = C_{12} and C_{18} [140,141]. As with $[Fe(4\text{-}OR\text{-}sal_2trien)]^+$ increasing the alkyl chain length leads to more abrupt SCO up to C_{12} after which it becomes more gradual again. However, in solution the C_{18} analogue exhibits SCO with a hysteresis of 7 K ($T_{1/2}\downarrow$ = 195 K and $T_{1/2}\uparrow$ = 202 K)–the first observation of hysteretic SCO in solution in any Fe(III) complex. It is interesting to note that in $[Fe(sal_2trien\text{-}(NC_{18}H_{37})_2)]BF_4$ the SCO in the solid state is actually more gradual than that in solution being only 50% complete. The structure of $[Fe(sal_2trien\text{-}(NC_6H_{13})_2)]BF_4$ demonstrates that the half-SCO here is due to two independent Fe(III) centres one of which undergoes SCO while the other remains HS. $[Fe(sal_2trien\text{-}(NC_{12}H_{25})_2)][BF_4]_{0.8}[Br]_{0.2}$ has been used along with an anodic aluminium oxide template to create 1D SCO nanowires [142]. The nanowires undergo SCO but it is slightly less complete than in the bulk material.

Similar dendrimeric SCO materials have been prepared using the salEen ligand framework to make $[Fe(salEen\text{-}OCOR)_2]Cl{\cdot}H_2O$ [143]. The SCO is gradual and incomplete going from 12.5% HS to 70% at

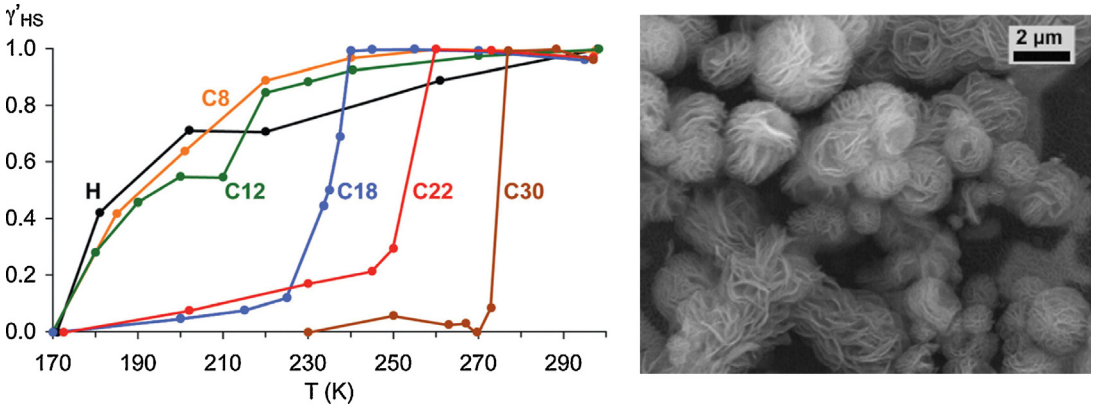

Fig. 20. Magnetic behaviour of $[Fe(4\text{-}OR\text{-}sal_2trien)]NO_3$ (left) and nanostructure (right) of $[Fe(4\text{-}OCH_2C_6H_3\text{-}(OC_{18}H_{37})_2\text{-}sal_2trien)]NO_3$ (reproduced, slightly modified, from Ref. [139] with permission. (Copyright Royal Society of Chemistry, 2012.)

340 K. A detailed ESR study reveals between 4.5 and 50 K antiferromagnetic ordering of the HS and LS Fe(III) centres while between 50 and 200 K a magnetoelectric effect is observed followed by a gradual SCO. Micro and nanomaterials of $[Fe(salEen\text{-}3\text{-}OMe)_2]PF_6$ have been prepared by simple addition of a solution of the complex to an anti-solvent [144]. The microcrystals are needle like while the nanoparticles, *ca.* 18 nm in size, are spherical. As with Fe(II) SCO nanomaterials [145], as the materials become smaller the SCO becomes more gradual with only a minor change in the spin transition temperature, 162 K (bulk) to 153 K (18 nm).

A series of $[Fe(OR\text{-}pap)_2]ClO_4$ ($R = C_8H_{17}$, $C_{10}H_{21}$, $C_{12}H_{25}$, $C_{14}H_{29}$, $C_{16}H_{33}$) dendrimers have been made with the crystal structure of $[Fe(OC_{14}H_{29}\text{-}pap)_2]ClO_4$ determined at 143 K showing a HS Fe(III) centre [146]. As expected the alkyl chains stack next to each other with π–π interactions between the pap ligands forming a 2D plane. Despite this the C_8–C_{14} compounds are all HS and become LS when $R = C_{16}$ with no evidence of significant SCO.

2D nanosheets of $[Fe(qnal)_2]^+$ and $[Fe(qsal)_2]^+$ on graphene oxide and reduced graphene oxide were recently reported by Hayami and co-workers [147]. Only the $[Fe(qnal)_2]^+$ systems are SCO active with the $[Fe(qnal)_2]^+$-reduced graphene oxide showing co-existence of SCO and conductivity, and remarkably LIESST.

7. Physical characteristics of selected iron(III) SCO systems

7.1. Structural characteristics of SCO

7.1.1. Bond length changes and octahedral distortion

As SCO involves moving electrons from the anti-bonding e_g set to the bonding t_{2g} set it is accompanied by a shortening of the Fe–L bond lengths (Tables 4 and 5). Examining all the recent structures reveals that the differences in Fe-L bond lengths vary from *ca.* 0.10–0.13 Å when SCO is complete in line with previous reports concerning iron(III) SCO systems [2,8,9]. However, in contrast with iron(II) compounds where the bond lengths changes are distributed relatively evenly around the Fe centre the changes in Fe(III) are always substantially different. In particular, the Fe—O bonds lengthen by on average only 0.035 Å between the two spin states; in some instances there is no change at all. This compares with an average difference of 0.15 Å for the Fe—N bond distances. But even here there are significant differences depending on whether the N donor is an amine, imine or aromatic nitrogen. Consequently, the average change in Fe-L bond length is too crude a measure to determine if a compound will exhibit abrupt or hysteretic SCO.

Halcrow in a recent review has argued that large changes in octahedral distortion parameters are more often correlated with abrupt SCO [148]. Recent structures reveal that these are remarkably varied with $\Delta\Sigma$ ranging from 2.1 to 47.8. $\Delta\Theta$ is even more variable being 16–148 and is not always correlated with $\Delta\Sigma$ as evidenced by $[TPAFe(cat\text{-}Cl_4)]PF_6$ [33] and the $[Fe(bztpen)(OR)][PF_6]_2$ series [100,101] where despite large $\Delta\Sigma$ values, $\Delta\Theta$ is more modest. This is almost certainly due to the different ligand denticities and donor atoms of the ligands. Nevertheless, trends are clearly evident with both $\Delta\Sigma$ and $\Delta\Theta$ generally higher when the SCO is abrupt and mirror those observed in Fe(II) systems [148]. An interesting exception is $[Fe(Him)_2(4\text{-}OMe\text{-}hapen)]PF_6$ where despite clear SCO based on Fe-L bond lengths $\Delta\Sigma$ and $\Delta\Theta$ are little changed. As has been noted by Halcrow and others [115,148], the conformation of the salen ligand is a more reliable measure of the competency of the Fe(III) to undergo SCO. Moreover, analysis of distortion pathways by Alvarez shows that distortion of octahedral $[Fe(salen\text{-}R)(L)_2]^+$ yields an equatorially vacant pentagonal bipyramid and consequently the O—Fe—O angle is a better measure of this distortion [149]. Thus, it is clear that comparisons of $\Delta\Sigma$ and $\Delta\Theta$ are only valid within specific ligand systems and care is needed in their use.

7.1.2. Solvent effects

Solvent impacts SCO characteristics in some cases quite dramatically for example $[Fe(qsal\text{-}3\text{-}OMe)_2]PF_6{\cdot}nH_2O$ ($n = 0, 2$) where the H_2O solvate is HS only while $[Fe(qsal\text{-}3\text{-}OMe)_2]PF_6$ is LS up to 300 K [46]. However, examining all recent SCO systems it is clear that more often than not different solvents modify the SCO behaviour rather than switching it off. An elegant example is [Fe(napet)NCS]·sol where changing the solvent simplify shifts $T_{1/2}$ [99]. Further insight is provided by [Fe(qsal)(thsa)]·*n*MeCN ($n = 0$, 0.1 and 0.5) where structures for all the compounds reveal that MeCN is progressively lost from a void in the lattice leaving the packing of the Fe(III) centres and consequently the magnetic behaviour unchanged [57]. This suggests that provided that the different solvent, or its loss, does not significantly impact the crystal lattice the SCO behaviour will be modified rather than switched off [47,53,58,68,69]. There is an important caveat, if the solvent tightly fills the void in the lattice then the complex will often be trapped in one spin state [57,99]. Overall, as in Fe(II) complexes [2], the effect of solvent in SCO complexes is still not well understood and whether the solvent will stabilize the LS or HS state cannot be predicted.

7.1.3. Anion effects

The use of different anions in both iron(II) and iron(III) complexes invariably alters their magnetic behaviour. Despite this surprisingly few anions have been explored with NCS, ClO_4, PF_6 and BPh_4 the most common. Moreover, there are comparatively few studies where the anion has been systematically varied. In the $[Fe(qsal\text{-}5\text{-}OMe)_2]Y$ series small anions give LS complexes and intermediate sized anions result in SCO [48]. In contrast, for $[Fe(Him)_2(hapen)]Y$ small anions result in HS behaviour while intermediate to large anions result in SCO active systems [88]. $[FeL][M^{III}(dithiolene)_2]$ complexes often exhibit abrupt and hysteretic SCO (Tables 1–3) possibly due to the fact that the $[M^{III}(dithiolene)_2]^-$ anions are planar and stack into 1D columns thereby increasing cooperativity [126,128,131–133]. It is evident from these examples that there is no general rule and each ligand system is unique in terms of which anions will promote SCO. The reason relates to the different shapes, sizes and supramolecular preferences of the anions which in most cases substantially alter the crystal lattice thereby impacting SCO behaviour. It follows that the effect of the anion on SCO properties is generally more unpredictable than solvent.

7.1.4. Supramolecular cooperativity in iron(III)

As mentioned in the introduction, cooperativity in SCO complexes is mediated by supramolecular interactions. Hydrogen bonding, π–π and C—H···X interactions are the most common supramolecular contacts in iron(III) SCO chemistry (Tables 1–3), and unsurprisingly are also found in Fe(II) [2]. While strong interactions often result in abrupt SCO systems, for instance [Fe(X-Hthsa)(X-thsa)], this is not always the case as evidenced by the $[Fe(X\text{-}salEen)_2]^+$ series. Moreover, abrupt SCO can be achieved with weak π–π interactions, as in $[Fe(qsal\text{-}X)_2]^+$ and $[Fe(qnal)_2]^+$. Interestingly, irrespective of the type of interaction that links the Fe(III) centres abrupt SCO is achieved only when the interactions form 2D sheets. A nice example is $[Fe(qsal\text{-}5\text{-}OMe)_2]Y{\cdot}CH_2Cl_2$ (Y = NCS, PF_6) where loss of the P4AE interaction in going from the NCS to the PF_6 complex results in gradual SCO for the latter [48,50]. Similar behaviour occurs in $[Fe(Him)_2(4\text{-}OMe\text{-}hapen)]Y$ (Y = PF_6, OTf) where the 1D chains are poorly linked in the PF_6 complex (gradual SCO) but closely connected in the OTf analogue (abrupt SCO) [89,90]. Another interesting feature is that many of the complexes

Table 1
SCO behaviour of selected iron(III) complexes with bi- and tridendate ligands.

Compound	Type of SCO	$T_{1/2}$ (K)	ΔT (K)	Principle interactions	Refs.
[(TPA)Fe(cat-Cl_4)]PF_6 (M)	Gradual	214	–	C—H···F	[33]
[(TPA)Fe(cat-Cl_4)]PF_6 (O)	Gradual	203	–	C—H···F	[33]
[(TPA)Fe(cat-Cl_4)]SbF_6	Gradual	250	–	C—H···F	[34]
[(TPA)Fe(cat-NN)]BPh_4	Gradual (I)	*ca.* 150	–	C—H···π	[38]
[(pmae)Fe(cat)]BPh_4	Gradual, 50%	*ca.* 130	–	C—H···π	[39]
[Fe(qsal)$_2$]NCSe	Abrupt	209 (↓), 285 (↑)	76	π–π (2D)	[24,25]
[Fe(qsal)$_2$]NCS	Gradual and abrupt, 2-steps	203 (↓) 210 (↑), 290 (↑)	83, 7	π–π (2D)	[23]
α-[Fe(qsal)$_2$]I_3	Abrupt (m)	240	–	π–π, P4AE	[42]
β-[Fe(qsal)$_2$]I_3	Abrupt	92 (↓), 117 (↑)	25	No structure	[43]
[Fe(qsal)$_2$]$_2$[Fe(NO)$(CN)_5$]	Gradual 50%	122	–	π–π (1D)	[44,45]
[Fe(qsal)$_2$]$_2$[Ru(NO)Cl_5]	Gradual 50%	187 (↓), 190 (↑)	4	No structure	[44]
[Fe(qsal-5-OMe)$_2$]Cl·2MeOH·0.5H_2O	Abrupt 50%	140 (↓), 150 (↑)	10	π–π, P4AE	[47]
[Fe(qsal-5-OMe)$_2$]Cl·MeCN·H_2O	Abrupt - 2 steps	245 (step 1), 275 (step 2)	5 (step 1)	π–π, P4AE	[47]
[Fe(qsal-5-OMe)$_2$]PF_6·sol	Gradual (I)	310 (sol = none) 280 (sol = CH_2Cl_2)	–	π–π (1D, CH_2Cl_2 solvate)	[48,50]
[Fe(qsal-5-OMe)$_2$]NCS·CH_2Cl_2	Abrupt and gradual	305	–	π–π, P4AE	[48]
[Fe(qsal-F)$_2$]NCS	Abrupt and gradual, 2 steps	157 (↓), 170 (↑)	13 (step 1)	π–π, C—H···F	[52]
[Fe(qsal-Cl)$_2$]NCS·MeOH	Abrupt 2 steps	167 (↓), 177 (↑)	10 (step 1)	π–π, P4AE, Cl···π	[52]
[Fe(qsal-Br)$_2$]NCS·MeOH	Gradual 50%	–	–		[52]
[Fe(qsal-Br)$_2$]NO_3·2MeOH	Abrupt, 2 step symmetry-breaking	128 (↓), 144 (↑) 229 (↓), 234 (↑)	16 5	π–π, P4AE	[51]
[Fe(qsal-I)$_2$]OTf	Abrupt	224 (↓), 232 (↑)	8	π–π, P4AE	[53]
[Fe(qsal)$_2$][Ni(dmise)$_2$]·2MeCN	Abrupt	241 (↓), 256 (↑)	15	π–π, C—H···π	[128]
[Fe(qsal-Cl)$_2$][Ni(dmit)$_2$]·2MeCN	Abrupt 2 steps	236, ~260	–	π–π, Cl···π, C—H···S	[133]
[Fe(qsal-Br)$_2$][Ni(dmit)$_2$]·CH_2Cl_2	Gradual	~250	–	π–π, C—H···Br, C—H···S	[132]
[Fe(qsal-Br)$_2$][Ni(dmit)$_2$]·acetone	Abrupt	273 (↓), 286 (↑)	13	π–π, C—H···S	[132]
[Fe(qsal-I)$_2$][Ni(dmit)$_2$]·MeCN·H_2O	Abrupt	150 (↓), 156 (↑)	6	C—H···π, S···I, C—H···S	[131]
[Fe(qsal)(thsa)]·sol	Gradual (I) (sol = 0.4 nBuOH, 0.5 MeCN)	320 (nBuOH), ~300 (MeCN)	–	π–π, N—H···N (MeCN)	[57]
[Fe(salEen)$_2$]ClO_4·sol	Gradual (sol = none, 0.5 H_2O)	155 (0.5 H_2O), 230 (no solvent)	–	π–π (dimer, sol = none), C—H···π (both)	[58]
[Fe(salEen)$_2$]$_2$[Fe(NO)$(CN)_5$]	Gradual	*ca.* 200		C—H···π, C—H···O	[44]
[Fe(3-OMe-salEen)$_2$]PF_6	Abrupt	162.5 (↓), 165.5 (↑)	3	P4AE, N—H···F, C—H···π	[60]
[Fe(4-OMe-salEen)$_2$]PF_6	Gradual	225		N—H···F, C—H···π	[61]
[Fe(4-OMe-salEen)$_2$]NO_3	Abrupt	75.5 (↓), 81 (↑)	7.5	π–π, N—H···O, C—H···O	[61]
[Fe(3,5-Br-salEen)$_2$]BPh_4·DMF	Gradual (I)	–	–	C—H···Br, C—H···π	[62]
[Fe(3-OMe-salEen)(thsa)]	Abrupt (m)	342 (↓), 344 (↑)	2	π–π (dimer), N—H···N	[63]
Li[Fe(5-Br-thsa)$_2$]·H_2O	Abrupt, 2 steps in heating mode	313	39	No structure	[64]
K[Fe(5-Br-thsa)$_2$]	Abrupt, 2 steps	232 (↓, 1st step), 358 (↓, 2nd step), 341 (↑)	52	N—H···O, K–O/S, K···π	[66]
[Fe(Hthsa)(thsa)]·H_2O	Abrupt, 2 steps in cooling mode	232 (↓, 1st step), 262 (↓, 2nd step), 274 (↑)	42 12	N—H···O	[69]
[Fe(5-Cl-Hthsa)(5-Cl-thsa)]·H_2O	Abrupt Abrupt	225 (↓), 228 (↑) 230 (↓), 231 (↑)	3 1	N—H···O	[70][69]
[Fe(5-Br-Hthsa)(5-Br-thsa)]·H_2O	Abrupt, stepped	193 (↓), 195 (↑)	2	No structure	[70]
[Fe(5-Br-Hthsa)(5-Br-thsa)]·H_2O	Abrupt, multistep	144 (↓), 148 (↑) 170 (↓), 173 (↑) 211 (↓), 212 (↑) 238 (↓), 245 (↑)	4 3 1 7	N—H···O	[68]
[Fe(5-Br-Hthsa)(5-Br-thsa)]·0.5H_2O	Abrupt	186 (↓), 188 (↑)	2	No structure	[69]
[Fe(5-Cl-Hthsa-Me)(5-Cl-thsa-Me)]·H_2O	Abrupt, 2 step	245 (↓), 249 (↑) 270 (↓), 278 (↑)	4 8	N—H···O	[71]
[Fe(salpm)$_2$]ClO_4·0.5EtOH	Abrupt (m), 2 steps	115, 171	–	π–π (dimer), C—H···π	[76,77]
[Fe(acpa)$_2$]ClO_4	Gradual and abrupt	265 (gradual), 365 (↓), 378 (↑)	 13	π–π (abrupt)	[78]
[Fe(qnal)$_2$]OTf·MeOH	Abrupt	104 (↓), 115 (↑)	11	π–π	[80]
[Fe(qnal)$_2$]OTf·acetone	Abrupt	130 (↓), 133 (↑)	3	π–π	[80]
[Fe(qnal)$_2$][Pd(dmit)$_2$]$_5$·acetone	Abrupt (m)	220	–	π–π, C—H···S	[137]
[Fe(qnal-7-OMe)$_2$]PF_6·acetone	Abrupt, 2 steps	130 (step 1) 194 (↓), 202 (↑)	–8	π–π, C—H···F	[81]
Fe(qnal-7-OMe)$_2$]BPh_4·2MeOH	Abrupt	194 (↓), 304 (↑)	110	π–π, C—H···π	[81]
[Fe(mph)$_2$]ClO_4·0.5H_2O·0.5MeOH	Abrupt, 2 steps	142 (step 1), 214 (step 2)	–	π–π, N—H···O	[82]
[Fe(pah)$_2$]ClO_4	Multistep (I)	–	–	π–π	[83]
[Fe(pah-*t*-Bu)$_2$]ClO_4	Gradual	280	–	No structure	[83]

I = incomplete, m = moderately.

Table 2
SCO behaviour of selected iron(III) complexes with tetradentate ligands.

Compound	Type of SCO	$T_{1/2}$ (K)	ΔT (K)	Principle interactions	Refs.
$[Fe(Him)_2(3\text{-}OMe\text{-}salen)]PF_6 \cdot H_2O \cdot EtOH$	Abrupt, 2 step	22(↓), 36(↑); 65	14	N—H···O, C—H···F	[85]
$[Fe(Him)_2(3\text{-}OMe\text{-}salen)]AsF_6 \cdot H_2O \cdot EtOH$	Abrupt, 50%	38(↓), 42(↑)	4	N—H···O, C—H···F	[85]
$[Fe(HIm)_2(5\text{-}CO_2Et\text{-}salen)]BPh_4 \cdot EtOH$	Gradual	192	–	C—H···π, C—H···O	[86]
$[Fe(Him)_2(hapen)]BPh_4 \cdot 2MeOH \cdot H_2O$	Very gradual (I)	–	–	C—H···π, N—H···O	[88]
$[Fe(Him)_2(hapen)]OTf \cdot 1.5H_2O$	Gradual (I)	–	–	N—H···O, C—H···O	[88]
$[Fe(Him)_2(hapen)]PF_6 \cdot 2H_2O$	Abrupt	78	–	N—H···O, C—H···F	[88]
$[Fe(Him)_2(hapen)]AsF_6$	Abrupt	69(↓), 74(↑)	5	N—H···O, C—H···F	[87]
$[Fe(Him)_2(4\text{-}OMe\text{-}hapen)]PF_6$	Gradual	150	–	N—H···F, C—H···F	[89]
$[Fe(Him)_2(4\text{-}OMe\text{-}hapen)]OTf$	Abrupt (I)	192(↓), 193(↑)	1	N—H···O, C—H···π	[90]
$[Fe(Him)_2(5\text{-}OMe\text{-}hapen)]PF_6$	Gradual (I)	–	–	N—H···O, C—H···F	[89]
$[Fe(Him)_2(6\text{-}OMe\text{-}hapen)]PF_6$	Gradual (I)	–	–	N—H···O, O—H···O, C—H···F	[89]

I = incomplete, m = moderately.

which contain NCS or NCSe either as ligands, [Fe(napet)NCX]·sol [98,99], or anions, $[Fe(qsal)_2]NCSe$ [23,24] and $[Fe(nap_2trien)]NCS$ [106] more often than not exhibit abrupt SCO. This seems to be due to the presence of extensive C—H···S/Se interactions which are also important in $[Fe(NCS)_2(N\text{-}N)_2]$ SCO systems [150]. The recent discovery of K–π interactions in the hysteretic SCO complex, $K[Fe(Br\text{-}thsa)_2]$ suggests that new supramolecular interactions can be used to improve cooperativity in Fe(III) SCO systems [66]. Despite this particular success, achieving predictable and highly cooperative SCO systems remains a considerable challenge and further work in varying the anion (or cation), ligand types and substituents is needed.

7.2. Light activation in iron(III)

Since 2007, a dozen new LIESST active compounds have been discovered but LIESST still remains relatively uncommon in stark contrast to the many systems for Fe(II) [151]. However, as many of the more abrupt SCO systems have yet to have their photomagnetic behaviour explored it is likely that more LIESST active compounds exist. Despite the small number of systems, T(LIESST) values range from 40 to 100 K and design strategies are becoming clearer [23,44,69,77,80,81,131]. Firstly, larger ΔFe-L values are more likely to result in LIESST as the potential energy wells are further apart thereby increasing the activation energy necessary to relax back to the LS state [151]. Secondly, a high degree of distortion in the HS state also aids LIESST [23] although this must not be too great as the compound may become trapped in the HS state. These two points emphasize that the single coordinate model is not applicable to all light activated SCO complexes and both vibrational and bending modes may need to be considered (Fig. 21). Thirdly, strong interactions while essential for the observation of LIESST in most cases are not a guarantee of it as exemplified by the $[Fe(qsal\text{-}X)_2]^+$ series where despite many hysteretic SCO systems, driven by strong π–π interactions, almost none exhibit LIESST. The reason is thought to be due to an overlap of the LIESST and reverse LIESST bands [23] and emphasizes the need to consider the type of ligand when designing light activated

Table 3
SCO behaviour of selected iron(III) complexes with penta- and hexadendate ligands.

Compound	Type of SCO	$T_{1/2}$ (K)	ΔT (K)	Principle Interactions	Ref.
$[Fe(salten)(n\text{-}py\text{-}N = N\text{-}Ph)]BPh_4$	Gradual (I)	–	–	No structure	[92]
$[Fe(salten\text{-}3\text{-}OMe)(Me\text{-}Im)]BPh_4$	Gradual	215	–	π–π (dimer)	[93]
$[Fe(salpet)(NH_2\text{-}tet)]$	Gradual (I)	–	–	N—H···O, N—H···N	[94]
[Fe(salpet-3-OEt)NCS]	Abrupt	82(↓), 84(↑)	2	C—H···π, C—H···S	[97]
[Fe(salpet-Cl)NCS]	Gradual	280	–	N—H···Cl, π-π, C—H···S	[96]
[Fe(salpet-Cl)NCSe]	Gradual	293	–	N—H···Cl, π-π, C—H···Se	[96]
$[Fe(salpet\text{-}Br)N_3] \cdot MeOH$	Gradual	140	–	N—H···N, C—H···Br	[95]
[Fe(salpet-Br)NCSe]	Gradual	317	–	N—H···Br, π-π, C—H···Se	[95]
[Fe(napet)NCS]	Gradual	174	–	N—H···S, C—H···S	[97]
[Fe(napet)NCS]·MeCN	Abrupt	151	–	N—H···N, C—H···S, C—H···π	[98]
[Fe(napet)NCS]·sol	Abrupt, 50%	84 (sol = butanone)	–	N—H···O, π-π, C—H···π	[99]
	Abrupt (DMF, DMSO)	232(↓), 235(↑) (sol = DMF)	3		
		127(↓), 138(↑) (sol = DMSO)	11		
[Fe(napet)NCSe]·MeCN	Abrupt (m)	170	–	N—H···N, C—H···Se, C—H···π	[98]
[Fe(napet)NCSe]·DMF	Abrupt (m)	244	–	N—H···O, π-π, C—H···π	[99]
[Fe(napet)NCO]	Abrupt (m)	155	–	N—H···O, C—H···π	[98]
$[Fe(napet)N_3]$	Abrupt	117(↓), 122(↑)	5	N—H···N, C—H···π	[98]
α-[Fe(1-napet-Me)NCS]	Abrupt S = 5/2 to 3/2	40(↓), 44(↑)	4	C—H···S, C—H···π	[96]
[Fe(2-napet-Me)NCS]	Gradual (I)	114	–	C—H···S, C—H···π	[96]
$[Fe(bztpen)(OR)][PF_6]_2$	Gradual	158 (OMe), 234 (OEt), 255 (O-nPr), 284 (O-nBu), 278 (O-iBu), 282 (OEtg)	–	–	[100,101]
$[Fe(5\text{-}iPr\text{-}sal_2trien)]PF_6$	Gradual, 50%	157	–	No structure	[103]
$[Fe(5\text{-}tBu\text{-}sal_2trien)]Y$	Gradual, 50% Gradual, 30%	204 –	–	N—H···O, C—H···O	[103]
$[Fe(4\text{-}OH\text{-}sal_2trien)]I$	Gradual 50%	–	–	N—H···O, O—H···I	[104]
$[Fe(3,5\text{-}OMe\text{-}sal_2bapen)]ClO_4$	Gradual, 2 step, symmetry-breaking (I)	*ca.* 110 and 190	–	N—H···O, C—H···O, C—H···π	[102]
$[Fe(nap_2trien)]NCS$	Abrupt and gradual, 2 step symmetry-breaking	142 (step 1), *ca.* 250 (step 2)	–	N—H···S, C—H···π	[106]

I = incomplete, m = moderately.

Table 4
Comparison of the Fe-L bond lengths and distortion parameters for selected iron(III) compounds in the HS and LS state (Å, °).

Compound	ΔFe-O	ΔFe-N	ΔFe-L_{ave}	ΔΣ	ΔΘ	Refs.	Note
Bidentate ligands							
[(TPA)Fe(cat-Cl_4)]PF_6 (M)	0.033	0.160	0.118	40.2	91	[33]	
[(TPA)Fe(cat-Cl_4)]PF_6 (O)	0.046	0.173	0.131	36.4	88	[33]	
Tridentate ligands							
[Fe(qsal)$_2$]NCSe	0.018	0.167	0.117	20.0	123	[24,25]	LS of CH_2Cl_2 solvate
[Fe(qsal)$_2$]NCS	0.003	0.149	0.100	15.5	104	[23]	LS of CH_2Cl_2 solvate
α-[Fe(qsal)$_2$]I_3	0.027	0.148	0.108	26.4	131	[42]	
[Fe(qsal-5-OMe)$_2$]Cl·2MeOH·0.5H_2O	0.033	0.177	0.129	32.3	139	[47]	Two Fe(III) centres
[Fe(qsal-F)$_2$]NCS	0.03	0.164	0.119	33.0	139	[52]	At 200 K, two Fe(III) centres
[Fe(qsal-Br)$_2$]NCS·MeOH	0.039	0.183	0.135	30.0	148	[52]	At 295 K, two Fe(III) centres
[Fe(qsal-Br)$_2$]NO_3·2MeOH	0.021	0.155	0.110	19.5	118	[51]	
[Fe(qsal-I)$_2$]OTf	0.031	0.158	0.116	22.6	128	[53]	
[Fe(qsal)$_2$][Ni(dmise)$_2$]·2MeCN	0.033	0.169	0.124	29.9	140	[128]	
[Fe(qsal-Cl)$_2$][Ni(dmit)$_2$]·2MeCN	0.04	0.157	0.118	36.1	139	[133]	
[Fe(qsal-Br)$_2$][Ni(dmit)$_2$]·CH_2Cl_2	0.036	0.152	0.113	27.3	142	[132]	
[Fe(qsal-Br)$_2$][Ni(dmit)$_2$]·acetone	0.022	0.149	0.107	19.2	119	[132]	
[Fe(qsal-I)$_2$][Ni(dmit)$_2$]·MeCN·H_2O	0.04	0.148	0.112	30.1	129	[131]	
[Fe(salEen)$_2$]ClO_4	0.027	0.132	0.097	11.7	56.3	[58]	
[Fe(salEen)$_2$]ClO_4·0.5H_2O	0.034	0.147	0.109	19.1	84	[58]	
[Fe(salEen)$_2$]$_2$[Fe(NO)(CN)$_5$]	0.024	0.119	0.087	13.3	99	[44]	*ca.* 80% HS at 300 K
[Fe(3-OMe-salEen)$_2$]PF_6	0.051	0.166	0.128	20.8	122	[60]	HS at 200 K
[Fe(4-OMe-salEen)$_2$]PF_6	0.040, 0.035	0.148, 0.132	0.112, 0.100	16.9	101	[61]	Fe1, Fe2
[Fe(4-OMe-salEen)$_2$]NO_3	0.036	0.169	0.125	20.2	118	[61]	293 K nearly full HS
[Fe(salpm)$_2$]ClO_4·0.5EtOH	0.044	0.167	0.126	25.8	129	[76,77]	
[Fe(acpa)$_2$]ClO_4	0.03	0.135	0.100	n/a	n/a	[78]	Gradual polymorph
[Fe(qnal)$_2$]OTf·acetone	0.05	0.12	0.097	n/a	n/a	[80]	
[Fe(qnal-7-OMe)$_2$]PF_6·acetone	0.079	0.119	0.106	18.5	70	[81]	
[Fe(qnal)$_2$][Pd(dmit)$_2$]$_5$·acetone	0.028	0.167	0.121	33.5	144	[137]	
Tetradentate ligands							
[Fe(HIm)$_2$(5-CO_2Et-salen)]BPh_4·EtOH	-0.001	0.157	0.104	2.1	34	[86]	
[Fe(Him)$_2$(4-OMe-hapen)]PF_6	0.000	0.145	0.097	8.7	20	[89]	
Pentadentate ligands							
[Fe(salpet-3-OEt)NCS]	0.040	0.150	0.113	28.2	72	[97]	
[Fe(napet)NCS]	0.044	0.145	0.111	29.3	94	[97]	
[Fe(napet)NCS]·MeCN	0.034	0.142	0.106	25.4	70	[98]	LS is close to $T_{1/2}$
[Fe(napet)NCSe]·MeCN	0.049	0.148	0.115	31.0	107	[98]	
[Fe(napet)NCSe]·DMF	0.051	0.154	0.120	31.3	94	[99]	
[Fe(napet)NCO]	0.058	0.130	0.106	25.7	69	[98]	
[Fe(bztpen)(OMe)][PF_6]$_2$	-0.009	0.116	0.095	28.1	17	[100]	
[Fe(bztpen)(OEt)][PF_6]$_2$	0.015	0.128	0.105	29.2	21	[101]	
[Fe(bztpen)(OPr)][PF_6]$_2$	0.011	0.133	0.108	23.7	16	[101]	
Hexadentate ligands							
[Fe(nap$_2$trien)]NCS	0.022	0.132	0.095	25.0	97	[106]	

SCO systems. In this regard [Fe(qnal-$X)_2$]$^+$ complexes are promising with all compounds exhibiting LIESST suggesting that qnal-X is particularly suitable for light activation [80,81]. Finally, the observation of LIESST in the [Fe(sal$_2$trien)][Mn{Cr(ox)$_3$}]·sol networks [120,122] suggests that provided that 2D and 3D networks of Fe(III) centres can be made these may also be expected to exhibit LIESST.

7.3. Mössbauer spectroscopic studies

Mössbauer spectroscopy so useful in elucidating structural details in Fe(II) SCO systems is much less effective in the case of Fe(III). This stems from the spin interconversion rate often being comparable to the Mössbauer timescale (*ca.* 10–1000 ns) resulting in broader doublets and a loss of detail [9]. Consequently, despite the large number of new SCO systems reported only a third have been studied by Mössbauer spectroscopy. As in Fe(II) systems, the isomer shift, δ and quadrupolar coupling, ΔE_Q are characteristic of the spin state. In the HS state, δ varies between 0.25 and 0.70 mms^{-1} with a small quadrupolar splitting of 0.30–1.00 mms^{-1}, the latter a consequence of the symmetric HS d^5 electronic configuration. By comparison, LS isomer shifts are between 0.05 and 0.40 mms^{-1} with ΔE_Q = 1.90–2.80 mms^{-1}; the larger quadrupolar splitting due to the t_{2g} set being incompletely filled. The slight overlap in the isomer shifts of the two spin states means that both δ and ΔE_Q are needed to correctly identify the spin state.

A particular feature of Fe(III) systems is that, in contrast to Fe(II), the spectra are often asymmetric [47,57,70,77,102,106,132]. This may occur in the HS state, LS state and sometimes both. This asymmetry has been attributed both to bond anisotropy [78] and rapid spin interconversion [47,48,53,106]. In the HS state, as the

Table 5
Comparison of the Fe-L bond lengths and distortion parameters in the HS and LS state for Fe-thsa compounds (Å, °).

Compound	ΔFe-O_{ave}	ΔFe-N_{ave}	ΔFe-S_{ave}	ΔFe-L_{ave}	ΔΣ	ΔΘ	Refs.
K[Fe(5-Br-thsa)$_2$]	0.016	0.198	0.190	0.135	47.8	145	[66]
[Fe(5-Br-Hthsa)(5-Br-thsa)]·H_2O	0.015	0.188	0.192	0.132	40.9	134	[68]
[Fe(5-Cl-Hthsa-Me)(5-Cl-thsa-Me)]·H_2O	−0.01	0.177	0.174	0.114	39.8	133	[71]

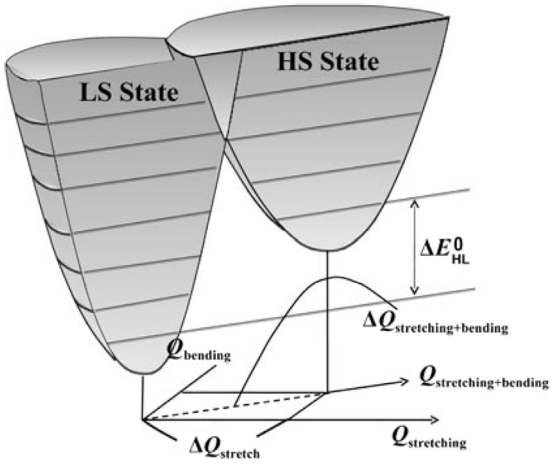

Fig. 21. Potential energy wells of the HS and LS states showing the contribution of stretching and bending (reproduced with permission from Ref. [23]. (Copyright Wiley-VCH, 2009.)

temperature is higher, spin interconversion is the more probable explanation. Indeed, in [Fe(nap_2trien)]NCS the interconversion is so rapid that the HS doublet is replaced by broad singlet [106]. A further problem is that the number of crystallographic Fe(III) sites is rarely correlated with the number of doublets. For instance, [Fe(qsal-$F)_2$]NCS [52] and [Fe(3,5-OMe-sal_2bapen)]ClO_4 [102] contain 2 and 3 sites, respectively but only a single doublet is observed. However, in [Fe(X-Hthsa)(X-thsa)]·sol (X = H, Cl, Br) despite the presence of a single crystallographic Fe(III) site two HS and LS doublets are observed [69]. In some instances Mössbauer spectroscopy can be extremely informative as it was in the identification of [Fe($salpm)_2$]ClO_4·0.5EtOH as a symmetry-breaking SCO compound [77]. Despite this Mössbauer spectroscopy in Fe(III) remains a supplementary technique. Perhaps the greater availability of synchrotron radiation will permit the use of nuclear forward scattering (NFS) or nuclear inelastic scattering (NIS) techniques to give Mössbauer parameters with higher resolution making it more widely applicable to Fe(III) SCO systems.

7.4. Other techniques

EPR spectroscopy can be valuable tool for exploring SCO in Fe(III) systems [9], although few studies have been done since 2007. These confirm earlier reports with the HS state ($S = 5/2$) characterized by a broad signal varying from $g = \sim 4.0–4.5$. The breadth and low intensity of the signal usually prevents observation of hyperfine coupling. In contrast, the LS state is generally sharp with rhombic and tetragonal systems easily distinguishable. In some cases hyperfine coupling is also observable which can provide extra information about the electronic structure of the complex. EPR spectroscopy has been particularly useful in [(TPA)Fe(Cat-R)]$^+$ where the degree of Fe(III)-catecholate character in the electronic structure can be determined [37]. Despite this, EPR spectroscopy remains much under used probably because SCO is more readily characterized by magnetic susceptibility measurements.

An area that has seen significant development in the last 10–15 years is computational modelling of SCO compounds. Several reviews have appeared recently on this subject and although, most studies have focused on Fe(II) SCO chemistry, Fe(III) systems have been considered [152–154]. DFT calculations have become the standard method for calculating the electronic structures of the two spin states and the resulting HS–LS gap. Early on it became clear that large basis sets were vital to adequately model SCO complexes [155]. Thus, basis sets such as 6-311-G** or cc-pVTZ are recommended for Gaussian type and Slater type orbitals, respectively. Extensive studies show that 'pure' functionals tend to overstabilise the LS state while Hartree–Fock (HF) methods favour the HS state [156]. Hybrid functionals fall in between these extremes and are most commonly used particularly B3LYP. In exploring the prototypical SCO complex [Fe($NCS)_2$(phen)$_2$] Reiher adjusted the HF exchange in B3LYP to 15% (termed B3LYP*) giving better agreement with experiment [157]. However, Hughes and Friesner argue that for Fe(III) this actually leads to larger spin state errors and suggest a local orbital correction to B3LYP [158]. In contrast, Jensen recommends TPSSh (10% HF exchange) [159] while Swart suggests OPBE [160] and Neese the double-hybrid orbital B2PLYP [161]. Highly accurate spin state energies have been reported for the CASPT2 method [162]. Although, the study concerned Fe(II) and Co(II) systems it should be applicable to Fe(III) systems but it is time consuming. It is clear that no single functional or method works well with every SCO system and careful validation is required in each case.

Combining molecular mechanics and ligand field parameters using an LFMM approach Deeth has been able to design and screen a series Fe(II) SCO complexes [163]. Now that there is a larger database of Fe(III) SCO systems LFMM studies could potentially lead to new Fe(III) SCO systems. Moreover, as computational methods become more efficient it is likely that structure-function relationships will become clearer permitting more rational design of SCO systems.

8. Conclusions

The last 10 years have seen significant growth in iron(III) SCO chemistry and the appearance of almost 30 hysteretic SCO systems, 12 of which exhibit hystereses greater than 10 K. The spin transition temperature in the various systems is remarkably variable ranging from 20 to 380 K probably due to the wide variety of donor sets, N_4O_2, $N_2O_2S_2$, N_3O_2S and N_5O, capable of supporting SCO. It is increasingly evident that there are more similarities between Fe(II) and Fe(III) SCO chemistry than differences, something previously noted by van Koningsbruggen et al. in 2004 [8]. Most recent research has focused on Schiff bases with tridentate N_2O and ONS ligands particularly effective in accessing abrupt SCO systems. Indeed, half of all symmetry breaking iron(III) SCO systems and [Fe(qnal-7-OMe)$_2$]BPh_4·2MeOH (110 K), which has the widest hysteresis in iron(III) chemistry, contain tridentate ligands. Part of the success of the tridentate ligand class is the effective use of supramolecular interactions including π–π, C—H···π and hydrogen bonding interactions to increase cooperativity. Halogen bonding, now finding widespread use in supramolecular chemistry, remains in its infancy in SCO research but already shows promise with I···S interactions key to the magnetic behaviour of [Fe(qsal-5-I)$_2$][Ni(dmit)$_2$]·MeCN·H_2O. Given the strength and directionality of halogen bonds further research in this area would be expected to yield many abrupt SCO systems.

As the structures of compounds in both spin states has grown it has become increasingly clear that more abrupt SCO is generally associated with larger changes in Fe-ligand bond lengths and greater changes in the distortion at the Fe(III) centre, mirroring the trend observed for iron(II). Moreover, structures close to the spin transition temperature show reorganization of the supramolecular sphere prior to actual SCO. As in Fe(II) SCO chemistry [17] the systems with the most abrupt and hysteretic SCO are mononuclear probably as a result of better control of the supramolecular connectivity in these complexes.

Light activated iron(III) SCO compounds while still rare, are now known for several ligand systems with the qnal ligand class and those incorporating metal dithiolenes the most notable. LIESST has

also been demonstrated in network materials, [Fe(X-sal$_2$trien)]-[Mn{Cr(ox)$_3$}]·sol where there is limited cooperativity and suggests a new strategy for accessing light activated materials with iron(III).

Despite these extraordinary successes, there still remain large gaps in iron(III) SCO chemistry. Dinuclear complexes are confined to two ligand systems neither of which show abrupt SCO in contrast to the many examples in iron(II) chemistry [164–167]. Higher oligomeric systems such as trinuclear, tetranuclear and above are essentially unknown for Fe(III). SCO networks are also extremely limited and no 2D or 3D networks of connected iron(III) SCO centres are yet known. Given the success that has been achieved in iron(II) SCO chemistry with [Fe(py-R)$_2${M(CN)$_4$}] [168,169] this is an area that would be expected to be developed further in the future.

Finally, iron(III) SCO nanomaterials show great potential with abrupt SCO in solution now a reality. Once again the fact that the studies of SCO nanomaterials remain very limited should provide a fruitful area of discovery as iron(III) SCO chemistry moves into a new exciting age of development.

Acknowledgements

We would like to gratefully acknowledge the Thailand Research Fund (RSA5580028 and RSA5880048) for funding our research in iron(III) spin crossover chemistry. We also thank Professor Keith Murray for comments on earlier versions of this manuscript. Structural figures for this review were drawn in OLEX2 [170] with CIF files taken from the CCDC (www.ccdc.cam.ac.uk).

References

[1] M.A. Halcrow, ed., Spin-Crossover Materials: Properties and Applications, John Wiley & Sons, Ltd, Chichester, 2013.
[2] P. Gütlich, A.B. Gaspar, Y. Garcia, Beilstein J. Org. Chem. 9 (2013) 342–391.
[3] P. Gütlich, H.A. Goodwin, Top. Curr. Chem. 233 (2004) 1–47.
[4] A. Hauser, Top. Curr. Chem. 234 (2004) 155–198.
[5] V. Ksenofontov, A.B. Gaspar, P. Gütlich, Top. Curr. Chem. 235 (2004) 23–64.
[6] J.-F. Létard, J. Mater. Chem. 16 (2006) 2550–2559.
[7] A. Cannizzo, C.J. Milne, C. Consani, W. Gawelda, C. Bressler, F. van Mourik, M. Chergui, Coord. Chem. Rev. 254 (2010) 2677–2686.
[8] P.J. van Koningsbruggen, Y. Maeda, H. Oshio, Top. Curr. Chem. 233 (2004) 259–324.
[9] M. Nihei, T. Shiga, Y. Maeda, H. Oshio, Coord. Chem. Rev. 251 (2007) 2606–2621.
[10] J.-F. Létard, P. Guionneau, L. Goux-Capes, Top. Curr. Chem. 235 (2004) 221–249.
[11] P. Gamez, J.S. Costa, M. Quesada, G. Aromí, Dalton Trans. (2009) 7845–7853.
[12] M.A. Halcrow, Coord. Chem. Rev. 253 (2009) 2493–2514.
[13] A.B. Gaspar, M. Seredyuk, P. Gütlich, J. Mol. Struct. 924–926 (2009) 9–19.
[14] Y. Sunatsuki, R. Kawamoto, K. Fujita, H. Maruyama, T. Suzuki, H. Ishida, M. Kojima, S. Iijima, N. Matsumoto, Coord. Chem. Rev. 254 (2010) 1871–1881.
[15] J. Olguín, S. Brooker, Coord. Chem. Rev. 255 (2011) 203–240.
[16] G.A. Craig, O. Roubeau, G. Aromí, Coord. Chem. Rev. 269 (2014) 13–31.
[17] M.A. Halcrow, Chem. Lett. 43 (2014) 1178–1188.
[18] S. Brooker, Chem. Soc. Rev. 44 (2015) 2880–2892.
[19] K.S. Murray, C.J. Kepert, Top. Curr. Chem. 233 (2004) 195–228.
[20] P. Guionneau, Dalton Trans. 43 (2014) 382–393.
[21] J. Tao, R.-J. Wei, R.-B. Huang, L.-S. Zheng, Chem. Soc. Rev. 41 (2012) 703–737.
[22] S. Hayami, Z. Gu, M. Shiro, Y. Einaga, A. Fujishima, O. Sato, J. Am. Chem. Soc. 122 (2000) 7126–7127.
[23] S. Hayami, K. Hiki, T. Kawahara, Y. Maeda, D. Urakami, K. Inoue, M. Ohama, S. Kawata, O. Sato, Chem. Eur. J. 15 (2009) 3497–3508.
[24] S. Hayami, Z. Gu, H. Yoshiki, A. Fujishima, O. Sato, J. Am. Chem. Soc. 123 (2001) 11644–11650.
[25] S. Hayami, T. Kawahara, G. Juhasz, K. Kawamura, K. Uehashi, O. Sato, Y. Maeda, J. Radioanal. Nucl. Chem. 255 (2003) 443–447.
[26] M. Nakamura, Coord. Chem. Rev. 250 (2006) 2271–2294.
[27] L. Cambi, L. Szegö, Chem. Ber. Dtsch. Ges. 64 (1931) 2591–2598.
[28] L. Cambi, L. Szegö, Chem. Ber. Dtsch. Ges. 66 (1933) 656–661.
[29] T.A. Ivanova, O.A. Turanova, I.V. Ovchinnikov, B. Andgheevskii, M. Augustyniak-Jablokow, Appl. Magn. Reson. 40 (2011) 21–30.
[30] A.N. Garg, S. Singhal, K. Chandra, Hyperfine Interact. 185 (2008) 151–157.
[31] S. Singhal, A.N. Garg, K. Chandra, J. Alloy. Compd. 443 (2007) 53–60.
[32] C. Cook, F. Habib, T. Aharen, R. Clérac, A. Hu, M. Murugesu, Inorg. Chem. 52 (2013) 1825–1831.
[33] E. Collet, M.L. Boillot, J. Hebert, N. Moisan, M. Servol, M. Lorenc, L. Toupet, M. Buron-Le Cointe, A. Tissot, J. Sainton, Acta Crystallogr. Sect. B Struct. Sci. 65 (2009) 474–480.
[34] W. Kaszub, M. Buron-Le Cointe, M. Lorenc, M.-L. Boillot, M. Servol, A. Tissot, L. Guérin, H. Cailleau, E. Collet, Eur. J. Inorg. Chem. (2013) 992–1000.
[35] E. Collet, N. Moisan, C. Baldé, R. Bertoni, E. Trzop, C. Laulhé, M. Lorenc, M. Servol, H. Cailleau, A. Tissot, M.-L. Boillot, T. Graber, R. Henning, P. Coppens, M.B.-L. Cointe, Phys. Chem. Chem. Phys. 14 (2012) 6192.
[36] A. Tissot, H.J. Shepherd, L. Toupet, E. Collet, J. Sainton, G. Molnár, P. Guionneau, M.L. Boillot, Eur. J. Inorg. Chem. (2013) 1001–1008.
[37] J.J. Girerd, M.L. Boillot, G. Blain, E. Rivière, Inorg. Chim. Acta 361 (2008) 4012–4016.
[38] C.R. Tichnell, D.A. Shultz, C.V. Popescu, I. Sokirniy, P.D. Boyle, Inorg. Chem. 54 (2015) 4466–4474.
[39] F. Yu, Y.-M. Zhang, A.-H. Li, B. Li, Inorg. Chem. Commun. 51 (2015) 87–89.
[40] B. Djukic, H.A. Jenkins, T. Seda, M.T. Lemaire, Transition Met. Chem. 38 (2012) 207–212.
[41] Y. Kojima, K. Kato, Y. Yamamoto, K. Inoue, S. Hayami, Acta Crystallogr. Sect. E Struct. Rep. 66 (2010) m204.
[42] K. Takahashi, T. Sato, H. Mori, H. Tajima, O. Sato, Physica B 405 (2010) S65–S68.
[43] K. Takahashi, T. Sato, H. Mori, H. Tajima, Y. Einaga, O. Sato, Hyperfine Interact. 206 (2012) 1–5.
[44] C. Faulmann, J. Chahine, L. Valade, G. Chastanet, J.F. Létard, D. De Caro, Eur. J. Inorg. Chem. 5 (2013) 1058–1067.
[45] T. Togo, S.A. Amolegbe, R. Yamaguchi, T. Kuroda-Sowa, M. Nakaya, K. Shimayama, M. Nakamura, S. Hayami, Chem. Lett. 42 (2013) 1542–1544.
[46] J.C. Dias, B. Vieira, I.C. Santos, L.C.J. Pereira, V. Da Gama, Inorg. Chim. Acta 362 (2009) 2076–2079.
[47] D.J. Harding, D. Sertphon, P. Harding, K.S. Murray, B. Moubaraki, J.D. Cashion, H. Adams, Chem. Eur. J. 19 (2013) 1082–1090.
[48] D. Sertphon, D.J. Harding, P. Harding, K.S. Murray, B. Moubaraki, J.D. Cashion, H. Adams, Eur. J. Inorg. Chem. (2013) 788–795.
[49] V. Russell, M. Scudder, I. Dance, J. Chem. Soc., Dalton Trans. (2001) 789–799.
[50] D. Sertphon, D.J. Harding, P. Harding, K.S. Murray, B. Moubaraki, H. Adams, A. Alkaş, S.G. Telfer, Eur. J. Inorg. Chem. (2016) 432–438.
[51] D.J. Harding, W. Phonsri, P. Harding, K.S. Murray, B. Moubaraki, G.N.L. Jameson, Dalton Trans. 44 (2015) 15079–15082.
[52] W. Phonsri, D.J. Harding, P. Harding, K.S. Murray, B. Moubaraki, I.A. Gass, J.D. Cashion, G.N.L. Jameson, H. Adams, Dalton Trans. 43 (2014) 17509–17518.
[53] D.J. Harding, W. Phonsri, P. Harding, I.A. Gass, K.S. Murray, B. Moubaraki, J.D. Cashion, L. Liu, S.G. Telfer, Chem. Commun. 49 (2013) 6340–6342.
[54] M. Shatruk, H. Phan, B.A. Chrisostomo, A. Suleimenova, Coord. Chem. Rev. 289–290 (2015) 62–73.
[55] B. Djukic, P.A. Dube, F. Razavi, T. Seda, H.A. Jenkins, J.F. Britten, M.T. Lemaire, Inorg. Chem. 48 (2009) 699–707.
[56] B. Djukic, M.T. Lemaire, Inorg. Chem. 48 (2009) 10489–10491.
[57] W. Phonsri, C.G. Davies, G.N.L. Jameson, B. Moubaraki, K.S. Murray, Chem. Eur. J. 22 (2016) 1322–1333.
[58] C.-F. Sheu, S.-M. Chen, G.-H. Lee, Y.-H. Liu, Y.-S. Wen, J.-J. Lee, Y.-C. Chuang, Y. Wang, Eur. J. Inorg. Chem. (2013) 894–901.
[59] M.S. Haddad, M.W. Lynch, W.D. Federer, D.N. Hendrickson, Inorg. Chem. 20 (1981) 123–131.
[60] A. Tissot, R. Bertoni, E. Collet, L. Toupet, M.-L. Boillot, J. Mater. Chem. 21 (2011) 18347.
[61] A. Tissot, P. Fertey, R. Guillot, V. Briois, M.-L. Boillot, Eur. J. Inorg. Chem. (2014) 101–109.
[62] P.N. Martinho, A.I. Vicente, S. Realista, M.S. Saraiva, A.I. Melato, P. Brandão, L.P. Ferreira, M.D.D. Carvalho, J. Organomet. Chem. 760 (2014) 48–54.
[63] W. Phonsri, V. Martinez, C.G. Davies, G.N.L. Jameson, B. Moubaraki, K.S. Murray, Chem. Commun. 52 (2016) 1443–1446.
[64] S. Floquet, M.-L. Boillot, E. Rivière, F. Varret, K. Boukheddaden, D. Morineau, P. Négrier, New J. Chem. 27 (2003) 341–348.
[65] S. Floquet, N. Guillou, P. Négrier, E. Rivière, M.-L. Boillot, New J. Chem. 30 (2006) 1621–1627.
[66] S. Kang, Y. Shiota, A. Kariyazaki, S. Kanegawa, K. Yoshizawa, O. Sato, Chem. Eur. J. 22 (2016) 532–538.
[67] A. Krupska, M.A. Augustyniak-Jablokow, V.V. Yablokov, Y.V. Zelentsov, V.A. Ulanov, J. Mrozinski, Acta Phys. Pol. A 110 (2006) 81–95.
[68] Z.-Y. Li, J.-W. Dai, Y. Shiota, K. Yoshizawa, S. Kanegawa, O. Sato, Chem. Eur. J. 19 (2013) 12948–12952.
[69] E.W.T. Yemeli, G.R. Blake, A.P. Douvalis, T. Bakas, G.O.R. Alberda van Ekenstein, P.J. van Koningsbruggen, Chem. Eur. J. (2010), http://dx.doi.org/10.1002/chem.201002100.
[70] S. Floquet, E. Rivière, K. Boukheddaden, D. Morineau, M.L. Boillot, Polyhedron 80 (2014) 60–68.
[71] Z.-Y. Li, J.-W. Dai, K.J. Gagnon, H.-L. Cai, T. Yamamoto, Y. Einaga, H.-H. Zhao, S. Kanegawa, O. Sato, K.R. Dunbar, R.-G. Xiong, Dalton Trans. 42 (2013) 14685–14688.
[72] S. Hayami, K. Hashiguchi, K. Inoue, Y. Maeda, J. Nucl. Radiochem. Sci. 5 (2004) N1–N3.
[73] S. Floquet, M.C. Muñoz, R. Guillot, E. Rivière, G. Blain, J.A. Réal, M.L. Boillot, Inorg. Chim. Acta 362 (2009) 56–64.
[74] E.W.Y. Tido, G.O.R.A. van Ekenstein, A. Meetsma, P.J. van Koningsbruggen, Inorg. Chem. 47 (2008) 143–153.
[75] E.W.Y. Tido, C. Faulmann, R. Roswanda, A. Meetsma, P.J. van Koningsbruggen, Dalton Trans. 39 (2010) 1643–1651.

[76] M.S. Shongwe, B.A. Al-Rashdi, H. Adams, M.J. Morris, M. Mikuriya, G.R. Hearne, Inorg. Chem. 46 (2007) 9558–9568.
[77] K.D. Murnaghan, C. Carbonera, L. Toupet, M. Griffin, M.M. Dîrtu, C. Desplanches, Y. Garcia, E. Collet, J.-F. Létard, G.G. Morgan, Chem. Eur. J. 20 (2014) 5613–5618.
[78] S. Hayami, D. Urakami, Y. Yamamoto, K. Kato, Y. Kojima, S. Nakashima, K. Inoue, Chem. Lett. 39 (2010) 328–329.
[79] H. Ando, Y. Nakao, H. Sato, S. Sakaki, J. Phys. Chem. A 111 (2007) 5515–5522.
[80] T. Shimizu, Y. Komatsu, H. Kamihata, Y.H. Lee, A. Fuyuhiro, S. Iijima, S. Hayami, J. Incl. Phenom. Macrocycl. Chem. 71 (2011) 363–369.
[81] M. Nakaya, K. Shimayama, K. Takami, K. Hirata, A.S. Alao, M. Nakamura, L.F. Lindoy, S. Hayami, Chem. Lett. 43 (2014) 1058–1060.
[82] J. Tang, J. Sánchez Costa, S. Smulders, G. Molnár, A. Bousseksou, S.J. Teat, Y. Li, G.A. van Albada, P. Gamez, J. Reedijk, Inorg. Chem. 48 (2009) 2128–2135.
[83] M.S. Shongwe, S.H. Al-Rahbi, M.A. Al-Azani, A.A. Al-Muharbi, F. Al-Mjeni, D. Matoga, A. Gismelseed, I.A. Al-Omari, A. Yousif, H. Adams, M.J. Morris, M. Mikuriya, Dalton Trans. 41 (2012) 2500–2514.
[84] R. Saha, S. Biswas, I.M. Steele, K. Dey, G. Mostafa, Dalton Trans. 40 (2011) 3166–3175.
[85] K. Hanahara, H. Ono, T. Fujinami, N. Matsumoto, Y. Sunatsuki, Inorg. Chim. Acta 429 (2015) 93–98.
[86] T. Fujinami, D. Hamada, N. Matsumoto, Y. Sunatsuki, R. Irie, Inorg. Chim. Acta 430 (2015) 239–244.
[87] T. Fujinami, M. Koike, N. Matsumoto, Y. Sunatsuki, A. Okazawa, N. Kojima, Inorg. Chem. 53 (2014) 2254–2259.
[88] M. Koike, K. Murakami, T. Fujinami, K. Nishi, N. Matsumoto, Y. Sunatsuki, Inorg. Chim. Acta 399 (2013) 185–192.
[89] T. Fujinami, M. Ikeda, M. Koike, N. Matsumoto, T. Oishi, Y. Sunatsuki, Inorg. Chim. Acta 432 (2015) 89–95.
[90] K. Miyano, T. Nishida, H. Ono, D. Hamada, T. Fujinami, N. Matsumoto, Y. Sunatsuki, Inorg. Chim. Acta 439 (2016) 49–54.
[91] M. Okuhata, Y. Funasako, K. Takahashi, T. Mochida, Chem. Commun. 49 (2013) 7662–7664.
[92] A. Bannwarth, S.O. Schmidt, G. Peters, F.D. Sönnichsen, W. Thimm, R. Herges, F. Tuczek, Eur. J. Inorg. Chem. (2012) 2776–2783.
[93] S. Imatomi, T. Sato, T. Hamamatsu, R. Kitashima, N. Matsumoto, Bull. Chem. Soc. Jpn. 80 (2007) 2375–2377.
[94] R. Herchel, Z. Trávníček, Dalton Trans. 42 (2013) 16279–16288.
[95] C. Krüger, P. Augustín, L. Dlháň, J. Pavlik, J. Moncol', I. Nemec, R. Boča, F. Renz, Polyhedron 87 (2015) 194–201.
[96] C. Krüger, P. Augustín, I. Nemec, Z. Trávníček, H. Oshio, R. Boča, F. Renz, Eur. J. Inorg. Chem. (2013) 902–915.
[97] P. Masárová, P. Zoufalý, J. Moncol, I. Nemec, J. Pavlik, M. Gembický, Z. Trávníček, R. Boča, I. Šalitroš, New J. Chem. 39 (2015) 508–519.
[98] I. Nemec, R. Herchel, R. Boča, Z. Trávníček, I. Svoboda, H. Fuess, W. Linert, Dalton Trans. 40 (2011) 10090–10099.
[99] I. Nemec, R. Herchel, Z. Trávníček, Dalton Trans. 44 (2015) 4474–4484.
[100] N.A. Ortega-Villar, M.C. Muñoz, J.A. Real, Eur. J. Inorg. Chem. (2010) 5563–5567.
[101] N. Ortega-Villar, A.Y. Guerrero-Estrada, L. Pin˜eiro-Loípez, M.C. Mun˜oz, M. Flores-álamo, R. Moreno-Esparza, J.A. Real, V.M. Ugalde-Saldívar, Inorg. Chem. 54 (2015) 3413–3421.
[102] M. Griffin, S. Shakespeare, H.J. Shepherd, C.J. Harding, J.-F. Létard, C. Desplanches, A.E. Goeta, J.A.K. Howard, A.K. Powell, V. Mereacre, Y. Garcia, A.D. Naik, H. Müller-Bunz, G.G. Morgan, Angew. Chem. Int. Ed. 50 (2011) 896–900.
[103] R. Pritchard, S.A. Barrett, C.A. Kilner, M.A. Halcrow, Dalton Trans. (2008) 3159–3168.
[104] I. Nemec, R. Herchel, I. Šalitroš, Z. Trávníček, J. Moncol, H. Fuess, M. Ruben, W. Linert, CrystEngComm 14 (2012) 7015–7024.
[105] A.J. Fitzpatrick, H.M. O'Connor, G.G. Morgan, Dalton Trans. 44 (2015) 20839–20842.
[106] B.J.C. Vieira, J.T. Coutinho, I.C. Santos, L.C.J. Pereira, J.C. Waerenborgh, V. da Gama, Inorg. Chem. 52 (2013) 3845–3850.
[107] G. Brewer, L.J. Alvarado, C.T. Brewer, R.J. Butcher, J. Cipressi, C. Viragh, P.Y. Zavalij, Inorg. Chim. Acta 421 (2014) 100–109.
[108] I. Nemec, R. Boča, R. Herchel, Z. Trávníček, M. Gembický, W. Linert, Montash. Chem. 140 (2009) 815–828.
[109] R. Boča, I. Nemec, I. Šalitroš, J. Pavlik, R. Herchel, F. Renz, Pure Appl. Chem. 81 (2009) 1357–1383.
[110] T. Fujinami, K. Nishi, R. Kitashima, K. Murakami, N. Matsumoto, S. Iijima, K. Toriumi, Inorg. Chim. Acta 376 (2011) 136–143.
[111] I. Šalitroš, R. Boča, L. Dlháň, M. Gembický, J. Kožíšek, J. Linares, J. Moncol, I. Nemec, L. Perašínová, F. Renz, I. Svoboda, H. Fuess, Eur. J. Inorg. Chem. (2009) 3141–3154.
[112] B. Djukic, P.K. Poddutoori, P.A. Dube, T. Seda, H.A. Jenkins, M.T. Lemaire, Inorg. Chem. 48 (2009) 6109–6116.
[113] F. Renz, S. Jung, M. Klein, M. Menzel, A.F. Thünemann, Polyhedron 28 (2009) 1818–1821.
[114] R. Boča, I. Šalitroš, J. Kožíšek, J. Linares, J. Moncol, F. Renz, Dalton Trans. 39 (2010) 2198–2200.
[115] T.M. Ross, S.M. Neville, D.S. Innes, D.R. Turner, B. Moubaraki, K.S. Murray, Dalton Trans. 39 (2010) 149–159.
[116] S. Imatomi, S. Hashimoto, N. Matsumoto, Eur. J. Inorg. Chem. 2009 (2009) 721–726.
[117] M. Clemente-León, E. Coronado, M.C. Giménez-López, A. Soriano-Portillo, J.C. Waerenborgh, F.S. Delgado, C. Ruiz-Pérez, Inorg. Chem. 47 (2008) 9111–9120.
[118] M. Clemente-León, E. Coronado, M. López-Jordà, Dalton Trans. 39 (2010) 4903–4910.
[119] M. Clemente-León, E. Coronado, M. López-Jordà, G. Mínguez Espallargas, A. Soriano-Portillo, J.C. Waerenborgh, Chem. Eur. J. 16 (2010) 2207–2219.
[120] M. Clemente-León, E. Coronado, M. López-Jordà, C. Desplanches, S. Asthana, H. Wang, J.-F. Létard, Chem. Sci. 2 (2011) 1121.
[121] M. Clemente-León, E. Coronado, M. López-Jordà, J.C. Waerenborgh, Inorg. Chem. 50 (2011) 9122–9130.
[122] M. Clemente-León, E. Coronado, M. López-Jordà, J.C. Waerenborgh, C. Desplanches, H. Wang, J.F. Létard, A. Hauser, A. Tissot, J. Am. Chem. Soc. 135 (2013) 8655–8667.
[123] M. Clemente-León, E. Coronado, M. López-Jordà, Eur. J. Inorg. Chem. (2013) 753–762.
[124] A. Abhervé, M. Clemente-León, E. Coronado, C.J. Gómez-García, M. Verneret, Inorg. Chem. 53 (2014) 12014–12026.
[125] A. Abhervé, S. Mañas-Valero, M. Clemente-León, E. Coronado, Chem. Sci. 2 (2015) 4665–4673.
[126] K. Takahashi, H. Cui, H. Kobayashi, Y. Einaga, O. Sato, Chem. Lett. 34 (2005) 1240–1241.
[127] C. Faulmann, S. Dorbes, S. Lampert, K. Jacob, B. Garreau De Bonneval, G. Molnár, A. Bousseksou, J.A. Real, L. Valade, Inorg. Chim. Acta 360 (2007) 3870–3878.
[128] K. Takahashi, H. Mori, H. Kobayashi, O. Sato, Polyhedron 28 (2009) 1776–1781.
[129] J.C. Dias, A. Soriano-Portillo, M. Clemente-Léon, C. Giménez-Saiz, J.R. Galán-Mascarós, C.J. Gómez-García, E. Coronado, Inorg. Chim. Acta 360 (2007) 3843–3847.
[130] X.-M. Li, Y. Ji, C.-F. Wang, J.-L. Zuo, X.-Z. You, J. Coord. Chem. 62 (2009) 1544–1552.
[131] K. Fukuroi, K. Takahashi, T. Mochida, T. Sakurai, H. Ohta, T. Yamamoto, Y. Einaga, H. Mori, Angew. Chem. Int. Ed. 53 (2014) 1983–1986.
[132] B.J.C. Vieira, J.C. Dias, I.C. Santos, L.C.J. Pereira, V. da Gama, J.C. Waerenborgh, Inorg. Chem. 54 (2015) 1354–1362.
[133] B.J.C. Vieira, J.T. Coutinho, J.C. Dias, J.C. Nunes, I.C. Santos, L.C.J. Pereira, V. da Gama, J.C. Waerenborgh, Polyhedron 85 (2015) 643–651.
[134] A.I.S. Neves, J.C. Dias, B.J.C. Vieira, I.S. Santos, M.B. Castelo Branco, L.C.J. Pereira, J.C. Waerenborgh, M. Almeida, D. Belo, V. Da Gama, CrystEngComm 11 (2009) 2160–2168.
[135] C. Faulmann, K. Jacob, S. Dorbes, S. Lampert, I. Malfant, M.-L. Doublet, L. Valade, J.A. Real, Inorg. Chem. 46 (2007) 8548–8559.
[136] K. Takahashi, H.-B. Cui, Y. Okano, H. Kobayashi, Y. Einaga, O. Sato, Inorg. Chem. 45 (2006) 5739–5741.
[137] K. Takahashi, H.-B. Cui, Y. Okano, H. Kobayashi, H. Mori, H. Tajima, Y. Einaga, O. Sato, J. Am. Chem. Soc. 130 (2008) 6688–6689.
[138] C. Gandolfi, C. Moitzi, P. Schurtenberger, G.G. Morgan, M. Albrecht, J. Am. Chem. Soc. 130 (2008) 14434–14435.
[139] C. Gandolfi, G.G. Morgan, M. Albrecht, Dalton Trans. 41 (2012) 3726–3730.
[140] P.N. Martinho, C.J. Harding, H. Müller-Bunz, M. Albrecht, G.G. Morgan, Eur. J. Inorg. Chem. (2010) 675–679.
[141] P.N. Martinho, Y. Ortin, B. Gildea, C. Gandolfi, G. McKerr, B. O'Hagan, M. Albrecht, G.G. Morgan, Dalton Trans. 41 (2012) 7461–7463.
[142] P.N. Martinho, T. Lemma, B. Gildea, G. Picardi, H. Müller-Bunz, R.J. Forster, T.E. Keyes, G. Redmond, G.G. Morgan, Angew. Chem. Int. Ed. 51 (2012) 11995–11999.
[143] N.E. Domracheva, A.V. Pyataev, V.E. Vorobeva, E.M. Zueva, J. Phys. Chem. B 117 (2013) 7833–7842.
[144] A. Tissot, L. Rechignat, A. Bousseksou, M.-L. Boillot, J. Mater. Chem. 22 (2012) 3411.
[145] A. Bousseksou, G. Molnár, L. Salmon, W. Nicolazzi, Chem. Soc. Rev. 40 (2011) 3313–3335.
[146] M. Nakaya, K. Shimayama, K. Takami, K. Hirata, S. Amolegbe, M. Nakamura, L. Lindoy, S. Hayami, Crystals 4 (2014) 104–112.
[147] Y. Murashima, M.R. Karim, N. Saigo, H. Takehira, R. Ohtani, M. Nakamura, M. Koinuma, L.F. Lindoy, K. Kuroiwa, S. Hayami, Inorg. Chem. Front. 2 (2015) 886–892.
[148] M.A. Halcrow, Chem. Soc. Rev. 40 (2011) 4119–4142.
[149] S. Alvarez, Chem. Rev. 115 (2015) 13447–13483.
[150] P. Guionneau, M. Marchivie, G. Bravic, J.-F. Létard, D. Chasseau, Top. Curr. Chem. 234 (2004) 97–128.
[151] J.-F. Létard, G. Chastanet, P. Guionneau, C. Desplanches, in: M.A. Halcrow (Ed.), Spin Crossover Materials: Properties and Applications, John Wiley & Sons, Ltd, Chichester, 2013, pp. 475–506.
[152] R.J. Deeth, C.M. Handley, B.J. Houghton, in: M.A. Halcrow (Ed.), Spin-Crossover Materials: Properties and Applications, John Wiley & Sons, Ltd, Chichester, 2013, pp. 443–454.
[153] R.J. Deeth, in: M. Swart, M. Costas (Eds.), Spin States in Biochemistry and Inorganic Chemistry: Influence on Structure and Reactivity, John Wiley & Sons, Ltd, Oxford, UK, 2016, pp. 85–102.
[154] K.P. Kepp, Coord. Chem. Rev. 257 (2013) 196–209.
[155] M. Güell, J.M. Luis, M. Solà, M. Swart, J. Phys. Chem. A 112 (2008) 6384–6391.
[156] M. Reiher, O. Salomon, B. Artur Hess, Theor. Chem. Acc. 107 (2001) 48–55.
[157] M. Reiher, Inorg. Chem. 41 (2002) 6928–6935.
[158] T.F. Hughes, R.A. Friesner, J. Chem. Theory Comput. 7 (2011) 19–32.
[159] K.P. Jensen, J. Cirera, J. Phys. Chem. A 113 (2009) 10033–10039.

[160] M. Swart, J. Chem. Theory Comput. 4 (2008) 2057–2066.
[161] S. Ye, F. Neese, Inorg. Chem. 49 (2010) 772–774.
[162] L. Daku, F. Aquilante, T.W. Robinson, A. Hauser, J Chem. Theory Comput. 6 (2012) 4216–4231.
[163] R.J. Deeth, A.E. Anastasi, M.J. Wilcockson, J. Am. Chem. Soc. 132 (2010) 6876–6877.
[164] A. Bousseksou, G. Molnár, J.A. Real, K. Tanaka, Coord. Chem. Rev. 251 (2007) 1822–1833.
[165] C.M. Grunert, S. Reiman, H. Spiering, J.A. Kitchen, S. Brooker, P. Gütlich, Angew. Chem. Int. Ed. 47 (2008) 2997–2999.
[166] Y. Garcia, F. Robert, A.D. Naik, G. Zhou, B. Tinant, K. Robeyns, S. Michotte, L. Piraux, J. Am. Chem. Soc. 133 (2011) 15850–15853.
[167] R. Kulmaczewski, J. Olguín, J.A. Kitchen, H.L.C. Feltham, G.N.L. Jameson, J.L. Tallon, S. Brooker, J. Am. Chem. Soc. 136 (2014) 878–881.
[168] M.C. Muñoz, J.A. Real, Coord. Chem. Rev. 255 (2011) 2068–2093.
[169] M.C. Muñoz, J.A. Real, in: M.A. Halcrow (Ed.), Spin-Crossover Materials: Properties and Applications, John Wiley & Sons, Ltd, Chichester, 2013, pp. 121–146.
[170] O.V. Dolomanov, L.J. Bourhis, R.J. Gildea, J.A.K. Howard, H. Puschmann, J. Appl. Cryst. 42 (2009) 339–342.

ChemComm

COMMUNICATION

Check for updates

Cite this: *Chem. Commun.*, 2017, 53, 9801

Received 1st August 2017,
Accepted 14th August 2017

DOI: 10.1039/c7cc05998a

rsc.li/chemcomm

Hysteretic spin crossover driven by anion conformational change†

Natnaree Phukkaphan,[a] Dyanne L. Cruickshank,[b] Keith S. Murray,[c] Wasinee Phonsri,[c] Phimphaka Harding[a] and David J. Harding*[a]

A new air stable Fe^{III} spin crossover (SCO) complex has been synthesized. The compound undergoes abrupt SCO near room temperature with $T_{1/2}$ (↓) = 244 K and $T_{1/2}$ (↑) = 278 K. Structural studies of the complex in the high spin and low spin state show that the strong cooperativity and thus the wide hysteresis is driven by an unprecedented anionic conformational change.

Molecular bistability is much sought in the development of new materials as two or more states are accessible under a wide range of external stimuli.[1–6] Spin crossover (SCO) complexes are an important family of bistable materials switching between a high spin (HS) and a low spin (LS) state under temperature, pressure or light perturbation.[7–10] It can occur in d^4–d^7 transition metal complexes provided that a suitable ligand field is present but is most commonly studied in iron(II)[11–15] and iron(III)[16,17] complexes.

Our group has been working on one particular ligand system quinolylsalicylaldimine, Hqsal-X which combined with iron(III) gives SCO active materials.[18–22] Our interest in these ligands stems from the report of $[Fe(qsal)_2]NCSe{\cdot}CH_2Cl_2$ which after solvent loss exhibits spin crossover with a hysteresis of 70 K.[23,24] The impressive hysteresis is thought to be due to extensive π–π interactions and in seeking to supplement these we, and others, have been exploring the SCO chemistry of $[Fe(qsal\text{-}X)_2]$anion {qsal-X = (*N*-8-quinolyl)-5-X-salicylaldiminate} systems. In the course of these studies while interesting systems displaying abrupt,[18] symmetry breaking[20] and stepped SCO[19,25] have been discovered the hystereses of these systems remain modest. Moreover, in many cases the SCO behaviour is changeable as a result of solvent loss, polymorphism or other effects.[26] What has become clear is that as with iron(II) SCO complexes multiple factors influence both the abruptness and the cooperativity of the spin crossover.

Of the different factors that affect SCO perhaps the most important is the anion because the different sizes and shapes can lead to significant changes in the crystal lattice and the subsequent magnetic behaviour of the compound.[27] Anions can also be important in driving SCO. One of the first reports of an order–disorder of anion leading to cooperative SCO was in $[Fe(DAPP)(abpt)][ClO_4]_2$ {DAPP = bis(3-aminopropyl)(2-pyridylmethyl)amine, abpt = 4-amino-3,5-bis(pyridin-2-yl)-1,2,4-triazole}.[28] Similar order–disorder of the anion is found in $[Fe\{3\text{-}bpp\text{-}(5\text{-}C_6H_3OH)_2\}_2][ClO_4]_2{\cdot}H_2O{\cdot}2$acetone {3-bpp-(5-$C_6H_3OH)_2$ = 2,6-bis[5-(2′-phenol)pyrazol-3-yl]-pyridine},[29] *fac*-$[Fe(2\text{-}Me\text{-}4\text{-}ima\text{-}n\text{-}Pr)_3]Cl{\cdot}PF_6$ (2-Me-4-ima-*n*-Pr = 2-methylimidazol-4-yl-methylideneamino-*n*-propyl)[30] and $[Mn(sal_2bapen)]PF_6$ {(sal_2bapen = 2,6,9,13-tetraazatetradeca-1,13-diene-1,14-diyl)-bis(phenolate)}.[31] In all the above cases the SCO is abrupt and with hysteresis, up to 40 K for $[Fe\{3\text{-}bpp\text{-}(5\text{-}C_6H_3OH)_2\}_2]\text{-}[ClO_4]_2{\cdot}H_2O{\cdot}2$acetone. Even in stepped SCO systems such as $[Fe(picpzpz)_2][BF_4]_2{\cdot}$MeOH {picpzpz = 3-(2-pyrazinyl)-1-[(2-pyridyl)methyl]pyrazole} the first abrupt SCO step is coupled to an anion order–disorder transition.[32] While in $[Co(4\text{-terpridone})_2][OTf]_2{\cdot}H_2O$ the reverse cooperative SCO is also coupled to an order–disorder of the triflate.[33] Moreover, recent studies have shown that such order–disorder transitions may be induced by high pressure.[34]

It is evident that the anion can have a profound influence on SCO characteristics and help in promoting hysteresis. However, to date there have been no reports of the impact of the anion's conformation on SCO. In this communication we report $[Fe(qsal\text{-}I)_2]NTf_2$ which undergoes an abrupt SCO close to room temperature with a hysteresis of 34 K. We demonstrate that this unusually broad and stable hysteresis is due to an unprecedented anion conformational change in which the anion is ordered in both spin states.

The complex was prepared by adding a MeOH solution of $LiNTf_2$ to a warmed MeOH solution of $[Fe(qsal\text{-}I)_2]NO_3$ resulting in precipitation of $[Fe(qsal\text{-}I)_2]NTf_2$ **1**. Recrystallization by slow evaporation of a $MeCN/CH_2Cl_2$ solution of **1** gives fine black

[a] *Functional Materials and Nanotechnology Center of Excellence, Walailak University, Thasala, Nakhon Si Thammarat, 80160, Thailand. E-mail: hdavid@g-mail.wu.ac.th; Tel: +66-75-672094*
[b] *Rigaku Oxford Diffraction, Kemsing, Sevenoaks, TN15 6QY, UK*
[c] *Monash University, Clayton, Melbourne, Victoria, 3800, Australia*

† Electronic supplementary information (ESI) available: Synthetic procedure, structural pictures, DSC measurements, and IR and Raman spectroscopic details. CCDC 1552831–1552833. For ESI and crystallographic data in CIF or other electronic format see DOI: 10.1039/c7cc05998a

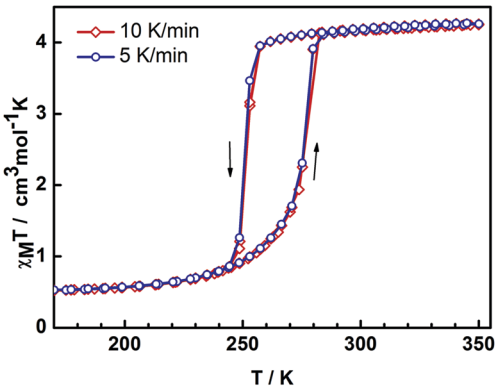

Fig. 1 $\chi_M T$ *vs.* T plot of [Fe(qsal-I)$_2$]NTf$_2$.

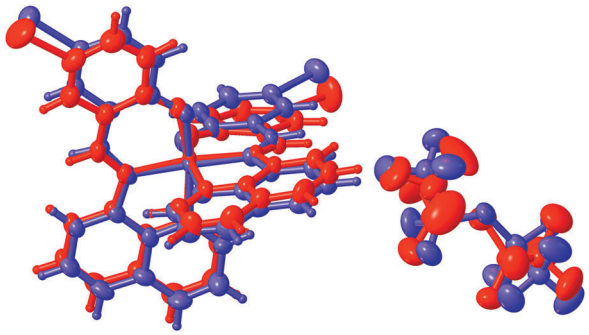

Fig. 2 Overlay of the molecular structures of [Fe(qsal-I)$_2$]NTf$_2$ at 245 K (blue) and 275 K (red) showing the more twisted qsal-I ligands in the HS state and the marked changes in the anion conformation.

needles. The absence of solvent in the lattice and the ability to synthesize the compound in air make **1** an ideal candidate for readily processable SCO materials.

Magnetic susceptibility measurements of **1** have been performed between 170–350 K at heating and cooling rates of 5 and 10 K min^{-1} (Fig. 1). At 170 K $\chi_M T$ is 0.52 cm^3 mol^{-1} K and typical of LS Fe^{III}. $\chi_M T$ gradually increases upon warming until 270 K when it increases very abruptly reaching 4.19 cm^3 mol^{-1} K at 300 K with $T_{1/2}$ = 278 K and characteristic of HS Fe^{III}. Cooling results in another abrupt transition this time at $T_{1/2}$ = 248 K giving a hysteresis of 30 K. The hysteresis loop is repeatable over successive cycles and shows no scan rate dependence. Photomagnetic measurements reveal that **1** does not undergo LIESST and given the near 100% LIESST in [Fe^{II}(qsal-I)$_2$]·CH$_2$Cl$_2$[35] this is likely due to the rapid relaxation of the light induced metastable HS state back to the LS state in Fe^{III}. This has previously been ascribed to the smaller differences in the Fe–ligand bond distances for Fe^{III} compared to Fe^{II} which permits more effective tunneling to the LS state.[36] Nevertheless, **1** is one of very few compounds that exhibit abrupt SCO with significant hysteresis close to room temperature (Table S1, ESI†).[37–39]

DSC measurements show a peak at 278 K in the warming mode and a peak at 244 K in the cooling mode giving a hysteresis of 34 K and slightly larger than that observed in the magnetic susceptibility studies, something not uncommon in SCO systems (Fig. S1, ESI†).[40] The average enthalpy and entropy values are 5.00 kJ mol^{-1} and 19.5 J mol^{-1} K^{-1}, respectively (Table S2, ESI†) and are typical of Fe^{III} systems.[16,17] The latter is significantly higher than that expected based on electronic considerations only {^{2}T$_2$ to ^{6}A$_1$ transition, Rln(6/2) = 9.13 J mol^{-1} K^{-1}} and suggests strong vibrational contributions to the entropy of SCO of *ca.* 10 J mol^{-1} K^{-1}.

To elucidate the structural contributions to SCO the crystal structure was determined at 245, 255 (upon cooling from 275 K) and 275 K. At all temperatures **1** crystallizes in triclinic $P\bar{1}$ with crystallographic data and refinement parameters given in Table S3 (ESI†). The asymmetric unit contains one octahedral Fe^{III} centre coordinated by two meridional qsal-I ligands and a single triflimide anion (Fig. 2). The Fe–N/O bond lengths are 2.099–2.137(4) and 1.918–1.921(4) Å, respectively at 275 and 255 K and characteristic of the HS state.[18,21] As is common in this family of compounds the Fe–N$_{quin}$ bond lengths are *ca.* 0.03 Å longer than the Fe–N$_{imine}$ bonds. At 245 K the bond lengths are very slightly longer than is usual for full LS Fe^{III} (normal LS Fe–N bond lengths = 1.96–1.97 Å)[18,21] suggesting that a small amount HS Fe^{III} is still present at this temperature (Table 1).[18,21] The change in Fe–O bond lengths is 0.028(6) Å while the Fe–N bond distances are 0.137(8) Å confirming that SCO has occurred. This is supported by the change in the octahedral distortion parameters which are $\Delta\Sigma$ = 18.6° and $\Delta\Theta$ = 101° and again indicative of almost complete SCO (Table 1). The final feature of note is the increased non-planarity of the qsal-I ligands upon transition to the HS state. Interestingly, similar changes occur in the strongly hysteretic SCO compound [Fe(qsal-I)$_2$]OTf·EtOH (ΔT = 80 K).[18]

The most striking difference between the HS and LS structures is a remarkable change in the conformation of the triflimide from a *syn* conformation (C–S···S–C torsion angle = 8.7(3)° and 9.3(4)° at 255 and 275 K) in the HS state to an intermediate conformation in the LS state (C–S···S–C torsion angle = 94.5(6)°, see Fig. 3). The *anti* conformation is inaccessible on steric grounds as this would place the CF$_3$ group and the quinoline ring of the qsal-I ligand in the same place. A search of the CCDC reveals that this intermediate conformation

Table 1 Fe–N/O bond lengths, octahedral distortion parameters and supramolecular contact distances (Å) or angles (°) in **1**

T	245 K	255 K	275 K
Fe–O	1.890(6)	1.918(3)	1.921(4)
Fe–N$_{quin}$	2.003(8)	2.130(4)	2.137(4)
Fe–N$_{imine}$	1.967(8)	2.099(4)	2.110(5)
Σ^a	50.4(9)	66.2(4)	69.0(4)
Θ^b	92.9	184.2	193.9
π–π	3.323(8) (type A)	3.316(4) (type A)	3.341(4) (type A)
	3.329(7) (type B)	3.345(3) (type B)	3.336(3) (type B)
C–H···π	2.804(11)	2.695(5)	2.715(6)
O···π	3.013(8)	3.194(4)	3.201(5)
α^c	4.6(3) (type A)	10.2(1) (type A)	10.1(1) (type A)
	6.3(3) (type B)	14.1(1) (type B)	13.9(1) (type B)

^{a} $\Sigma = \sum_{i=1}^{12} |90 - \alpha_i|$, where α_i are the twelve *cis* N/O–Fe–N/O angles.[43] ^{b} $\Theta = \sum_{i=1}^{24} |60 - \theta_i|$, where θ_i are the 24 unique N/O–Fe–N/O angles measured on the projection of two triangular faces of the octahedron along their common pseudo-threefold axis.[44] ^{c} α = the angle between planes of the quinoline and phenolate rings.

 This journal is © The Royal Society of Chemistry 2017

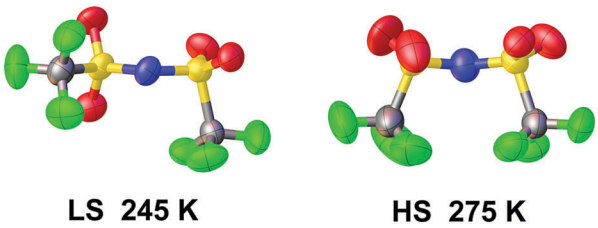

Fig. 3 View of the anion conformational change in **1** between the HS and LS states.

is very rare with only two other examples previously reported.[41,42] The anion is also involved in a O···π interaction involving the quinoline ring that shortens significantly by *ca.* 0.2 Å upon transition to the LS state (see Fig. S2, ESI†).

The packing in **1** mirrors other $[Fe(qsal\text{-}X)_2]^+$ complexes with two types of π–π interactions, type A and B, formed between neighbouring qsal-I ligands forming a 1D chain (Fig. 4 and Fig. S3, ESI†).[18–20] The type A and type B interactions are orthogonal to each other and in contrast to most $[Fe(qsal\text{-}X)_2]^+$ systems, SCO in **1** results in almost no change in the plane-to-plane distance (Table 1). Instead the qsal-I ligands become bent as the Fe^{III} centre becomes HS. The 1D chains are linked by a pair of C–H···π interactions rather than the more common P4AE contacts (Fig. S4, ESI†). Beyond this a combination of C–H···O/F interactions all involving the anion create a 3D supramolecular network. It is notable that when viewed down the 1D π–π chains there is a considerable change in the shape of the central channel from almost square to rhombus like (Fig. S5 and S6, ESI†). The close structural similarity between **1** and other less hysteretic $[Fe(qsal\text{-}X)_2]^+$ systems strongly suggests that the large hysteresis observed here is primarily due to the anionic conformational change.

To better understand the vibrational contributions to SCO we undertook variable temperature IR and Raman spectroscopic studies between 293 and 228 K (Fig. 5 and Fig. S7, S8, ESI†). The IR and Raman spectra both show significant changes between 1570–1600 cm^{-1} with the imine stretch moving from 1601 to 1606 cm^{-1} (1594 to 1600 cm^{-1} for the Raman; Fig. 5 and Fig. S7–S9, ESI†) in going from the HS to the LS state. The most striking difference though is in the S=O stretches in the IR spectra which appear at 1367 and 1381 cm^{-1} in the HS state but are absent in the LS state. The bands presumably move to lower wavenumbers as the anion undergoes conformational change[45] and are now masked by the vibrations of the qsal-I ligand.

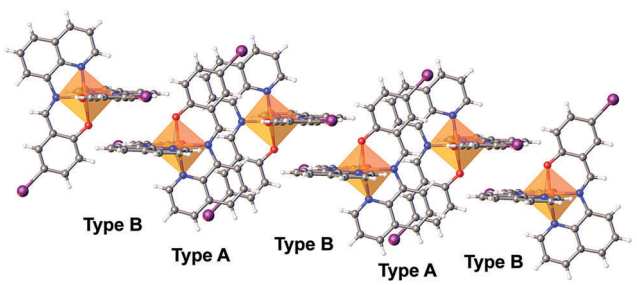

Fig. 4 View of the type A and type B interactions that form the 1D π–π chains in **1**.

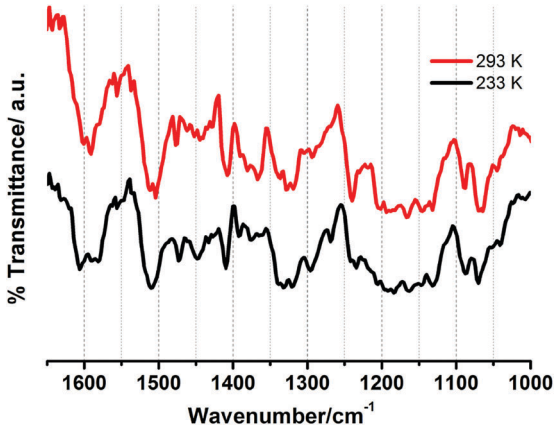

Fig. 5 View of the IR stretches in **1** in the HS (293 K) and LS state (233 K).

The Raman spectra in the cooling and heating modes show considerable differences with the spectra broader in the heating mode suggesting a mixture of HS and LS states (Fig. S9, ESI†). This is consistent with the slightly more gradual nature of the SCO in this region, upon heating, observed in the magnetic studies of **1** (Fig. 1). As in $[Fe(3\text{-}OMe\text{-}salEen)_2]PF_6$ the large changes in the HS and LS IR and Raman spectra in **1** are thought to arise from the significant differences in the skeletal vibrations of the two spin states.[46] This is supported by the fact that $[Fe(qsal\text{-}Br)_2]NO_3{\cdot}2MeOH$ which exhibits far smaller enthalpy and entropy differences shows only very minor changes in the IR spectra of the two spin states.[20]

In summary, we have prepared a solvent free, air-stable Fe^{III} SCO complex which undergoes abrupt SCO close to room temperature with an impressive hysteresis of 34 K. Structural studies indicate that the hysteresis is driven by a unique change in the anion conformation. Given the range of conformationally flexible anions available we believe this new way of achieving cooperativity in a SCO material may be expected to lead to the discovery of further cooperative SCO systems. Efforts along these lines are already underway in these laboratories.

We thank the Thailand Research Fund (RSA5880048) and the Australian Research Council for their generous support of this research. Finlay Shanks at Monash University is thanked for help with IR and Raman studies and Boujemaa Moubaraki for help with magnetic studies. We are also grateful to Dr Guillaume Chastanet at the Institut de Chimie de la Matière Condensée de Bordeaux, Université Bordeaux, France for photomagnetic studies.

Conflicts of interest

There are no conflicts to declare.

Notes and references

1 O. Sato, *Nat. Chem.*, 2016, **8**, 644–656.
2 M. Natali and S. Giordani, *Chem. Soc. Rev.*, 2012, **41**, 4010–4029.
3 R. Klajn, J. F. Stoddart and B. A. Grzybowski, *Chem. Soc. Rev.*, 2010, **39**, 2203–2237.
4 M. D. Manrique-Juárez, S. Rat, L. Salmon, G. Molnár, C. M. Quintero, L. Nicu, H. J. Shepherd and A. Bousseksou, *Coord. Chem. Rev.*, 2015, **308**, 395–408.

5 J. L. Zhang, J. Q. Zhong, J. D. Lin, W. P. Hu, K. Wu, G. Q. Xu, A. T. S. Wee and W. Chen, *Chem. Soc. Rev.*, 2015, **44**, 2998–3022.
6 J. Ferrando-Soria, J. Vallejo, M. Castellano, J. Martínez-Lillo, E. Pardo, J. Cano, I. Castro, F. Lloret, R. Ruiz-García and M. Julve, *Coord. Chem. Rev.*, 2017, **339**, 17–103.
7 K. S. Murray, in *Spin-Crossover Materials: Properties and Applications*, ed. M. A. Halcrow, John Wiley & Sons Ltd., Chichester, 2013, pp. 1–54.
8 M. A. Halcrow, *Chem. Lett.*, 2014, **43**, 1178–1188.
9 V. Ksenofontov, A. B. Gaspar and P. Gütlich, *Top. Curr. Chem.*, 2004, **235**, 23–64.
10 J.-F. Létard, *J. Mater. Chem.*, 2006, **16**, 2550–2559.
11 G. Aromí, L. A. Barrios, O. Roubeau and P. Gamez, *Coord. Chem. Rev.*, 2011, **255**, 485–546.
12 M. A. Halcrow, *Coord. Chem. Rev.*, 2009, **253**, 2493–2514.
13 G. A. Craig, O. Roubeau and G. Aromí, *Coord. Chem. Rev.*, 2014, **269**, 13–31.
14 P. Gütlich, A. B. Gaspar and Y. Garcia, *Beilstein J. Org. Chem.*, 2013, **9**, 342–391.
15 J. Olguín and S. Brooker, *Coord. Chem. Rev.*, 2011, **255**, 203–240.
16 M. Nihei, T. Shiga, Y. Maeda and H. Oshio, *Coord. Chem. Rev.*, 2007, **251**, 2606–2621.
17 D. J. Harding, P. Harding and W. Phonsri, *Coord. Chem. Rev.*, 2016, **313**, 38–61.
18 W. Phonsri, P. Harding, L. Liu, S. G. Telfer, K. S. Murray, B. Moubaraki, T. M. Ross, G. N. L. Jameson and D. J. Harding, *Chem. Sci.*, 2017, **8**, 3949–3959.
19 W. Phonsri, D. J. Harding, P. Harding, K. S. Murray, B. Moubaraki, I. A. Gass, J. D. Cashion, G. N. L. Jameson and H. Adams, *Dalton Trans.*, 2014, **43**, 17509–17518.
20 D. J. Harding, W. Phonsri, P. Harding, K. S. Murray, B. Moubaraki and G. N. L. Jameson, *Dalton Trans.*, 2015, **44**, 15079–15082.
21 K. Fukuroi, K. Takahashi, T. Mochida, T. Sakurai, H. Ohta, T. Yamamoto, Y. Einaga and H. Mori, *Angew. Chem., Int. Ed.*, 2014, **53**, 1983–1986.
22 B. J. C. Vieira, J. C. Dias, I. C. Santos, L. C. J. Pereira, V. da Gama and J. C. Waerenborgh, *Inorg. Chem.*, 2015, **54**, 1354–1362.
23 S. Hayami, Z.-Z. Gu, H. Yoshiki, A. Fujishima and O. Sato, *J. Am. Chem. Soc.*, 2001, **123**, 11644–11650.
24 S. Hayami, K. Hiki, T. Kawahara, Y. Maeda, D. Urakami, K. Inoue, M. Ohama, S. Kawata and O. Sato, *Chem. – Eur. J.*, 2009, **15**, 3497–3508.
25 D. J. Harding, D. Sertphon, P. Harding, K. S. Murray, B. Moubaraki, J. D. Cashion and H. Adams, *Chem. – Eur. J.*, 2013, **19**, 1082–1090.
26 S. Schlamp, B. Weber, A. D. Naik and Y. Garcia, *Chem. Commun.*, 2011, **47**, 7152–7154.
27 M. A. Halcrow, *Chem. Soc. Rev.*, 2011, **40**, 4119–4142.
28 G. S. Matouzenko, A. Bousseksou, S. A. Borshch, M. Perrin, S. Zein, L. Salmon, G. Molnar and S. Lecocq, *Inorg. Chem.*, 2004, **43**, 227–236.
29 G. A. Craig, J. S. Costa, O. Roubeau, S. J. Teat and G. Aromí, *Chem. – Eur. J.*, 2011, **17**, 3120–3127.
30 T. Fujinami, K. Nishi, D. Hamada, K. Murakami, N. Matsumoto, S. Iijima, M. Kojima and Y. Sunatsuki, *Inorg. Chem.*, 2015, **54**, 7291–7300.
31 P. N. Martinho, B. Gildea, M. M. Harris, T. Lemma, A. D. Naik, H. Müller-Bunz, T. E. Keyes, Y. Garcia and G. G. Morgan, *Angew. Chem., Int. Ed.*, 2012, **51**, 12597–12601.
32 B. A. Leita, S. M. Neville, G. J. Halder, B. Moubaraki, C. J. Kepert, J.-F. Létard and K. S. Murray, *Inorg. Chem.*, 2007, **46**, 8784–8795.
33 G. Agustí, C. Bartual, V. Martínez, F. J. Muñoz-Lara, A. B. Gaspar, M. C. Muñoz and J. A. Real, *New J. Chem.*, 2009, **33**, 1262–1267.
34 H. Shepherd, G. Tonge, L. Hatcher, M. Bryant, J. Knichal, P. Raithby, M. Halcrow, R. Kulmaczewski, K. Gagnon and S. Teat, *Magnetochemistry*, 2016, **2**, 9.
35 W. Phonsri, D. S. Macedo, K. R. Vignesh, G. Rajaraman, C. G. Davies, G. N. L. Jameson, B. Moubaraki, J. S. Ward, P. E. Kruger, G. Chastanet and K. S. Murray, *Chem. – Eur. J.*, 2017, **23**, 7052–7065.
36 R. Bertoni, M. Lorenc, A. Tissot, M. L. Boillot and E. Collet, *Coord. Chem. Rev.*, 2015, **282–283**, 66–76.
37 E. Tailleur, M. Marchivie, N. Daro, G. Chastanet and P. Guionneau, *Chem. Commun.*, 2017, **53**, 4763–4766.
38 S. Kang, Y. Shiota, A. Kariyazaki, S. Kanegawa, K. Yoshizawa and O. Sato, *Chem. – Eur. J.*, 2016, **22**, 532–538.
39 B. Weber, W. Bauer and J. Obel, *Angew. Chem., Int. Ed.*, 2008, **47**, 10098–10101.
40 S. Brooker, *Chem. Soc. Rev.*, 2015, **44**, 2880–2892.
41 H. Kim, K. Shin and S. Chang, *J. Am. Chem. Soc.*, 2014, **136**, 5904–5907.
42 Y. E. Türkmen, S. Sen and V. H. Rawal, *CrystEngComm*, 2013, **15**, 4221–4224.
43 J. K. McCusker, A. L. Rheingold and D. N. Hendrickson, *Inorg. Chem.*, 1996, **35**, 2100–2112.
44 M. Marchivie, P. Guionneau, J. F. Létard and D. Chasseau, *Acta Crystallogr., Sect. B: Struct. Sci.*, 2005, **61**, 25–28.
45 I. Rey, P. Johansson, J. Lindgren, J. C. Lassègues, J. Grondin and L. Servant, *J. Phys. Chem. A*, 1998, **102**, 3249–3258.
46 M. Sorai, R. Burriel, E. F. Westrum and D. N. Hendrickson, *J. Phys. Chem. B*, 2008, **112**, 4344–4350.

 This journal is © The Royal Society of Chemistry 2017

Chemical Science

EDGE ARTICLE

Check for updates

Cite this: *Chem. Sci.*, 2017, **8**, 3949

Solvent modified spin crossover in an iron(III) complex: phase changes and an exceptionally wide hysteresis†

Wasinee Phonsri,[a] Phimphaka Harding,[a] Lujia Liu,[b] Shane G. Telfer,[b] Keith S. Murray,[c] Boujemaa Moubaraki,[c] Tamsyn M. Ross,[d] Guy N. L. Jameson[e] and David J. Harding*[a]

Solvent effects in a series of Fe(III) spin crossover (SCO) complexes [Fe(qsal-I)$_2$]OTf·sol (sol = MeOH **1**, EtOH **2**, *n*-PrOH **3**, i-PrOH **4**, acetone **5** and MeCN **6**) are explored. SCO is abrupt in **1** (following MeOH loss) and **2**, gradual for **3** ($T_{1/2}$ = 199 K) and **4** ($T_{1/2}$ = 251 K) and incomplete, even up to 350 K, for **5** and **6**. In [Fe(qsal-I)$_2$]OTf SCO occurs at $T_{1/2}\downarrow$ = 225 K and $T_{1/2}\uparrow$ = 234 K (ΔT = 9 K), while aged samples of **2** exhibit an exceptionally wide hysteresis of 80 K ($T_{1/2}\downarrow$ = 139 K and $T_{1/2}\uparrow$ = 219 K). In contrast, fresh samples of **2** exhibit stepped SCO with hysteresis varying from 2 to 42 K. VT-PXRD (variable temperature powder X-ray diffraction) studies indicate a new phase, **2b**, is formed upon cooling below 180 K along with a minor LS phase **2c**. Phase **2c** and the HS phase **2a** undergo a spin transition at $T_{1/2}\downarrow$ = 180 K and $T_{1/2}\uparrow$ = 215 K with phase **2b** exhibiting two-step SCO. Structural studies in both spin states, except **6**, show the cations are linked through extensive π–π interactions to form 1D chains. A combination of P4AE (parallel fourfold aryl embrace) and I···X (X = I, O, π) interactions create tightly packed 3D supramolecular networks. This study emphasizes that while solvent may result in only small structural changes SCO characteristics can be impacted dramatically.

Received 5th December 2016
Accepted 20th March 2017

DOI: 10.1039/c6sc05317c

rsc.li/chemical-science

Introduction

Switchable molecules are attractive targets in the design of functional nanomaterials.[1–6] In this context spin crossover (SCO) compounds are ideal candidates as they can be switched by a range of stimuli including temperature,[7,8] pressure[9] and light,[10–13] or combinations thereof.[14] As molecular compounds they are easy to prepare and readily tunable. In SCO systems the switching occurs between two electronic states termed high spin (HS) and low spin (LS) that are close in energy. This arises from the splitting of the d-orbitals into a t_{2g} and an e_g set in an octahedral ligand field and, while theoretically possible for a $3d^4$–$3d^7$ electronic configuration, is most widely studied for Fe(II).[8,15–20] However, more recent research has shown that Fe(III) systems can be just as effective and have the advantage over Fe(II) systems of being air stable.[21–23] Moreover, with abrupt hysteretic, symmetry breaking and stepped SCO transitions all reported it is clear that functional devices are becoming a real possibility.

Nevertheless, challenges remain as no system yet exists which has a broad hysteresis at room temperature. In designing SCO complexes careful consideration needs to be given to selecting a ligand with a suitable ligand field strength and ensuring that it will form strong supramolecular contacts in the solid state. The latter is needed for the cooperative processes that underlie hysteretic switching.[24] In addition to the ligand, SCO behaviour is also influenced by the anion[25–32] and the solvent.[33–36] The effect of the anion is particularly pronounced as it often completely alters the solid state packing and consequently impacts SCO behaviour. Solvent effects tend to be more subtle but are less well understood as comparatively few studies exist. In the case of Fe(III) there is only one study of solvent effects in the series [Fe(napet)NCS]·sol (napet = 1-[((2-{3-[2-hydroxy-1-naphthyl)methylideneamino]propylamino}ethylimino)methyl]-2-naphthol); sol = tetrahydrofuran, methanol and 0.5 pyrazine, butanone, DMF, DMSO).[37]

[a]*Functional Materials and Nanotechnology Centre of Excellence (FuNTech), Walailak University, Thasala, Nakhon Si Thammarat, 80160, Thailand. E-mail: hdavid@g-mail.wu.ac.th*

[b]*MacDiarmid Institute for Advanced Materials and Nanotechnology, Institute of Fundamental Sciences, Massey University, Palmerston North, New Zealand*

[c]*School of Chemistry, Monash University, Clayton, Melbourne, Victoria, 3800, Australia*

[d]*Australian Synchrotron, 800 Blackburn Rd, Clayton, Victoria, 3168, Australia*

[e]*Department of Chemistry & MacDiarmid Institute for Advanced Materials and Nanotechnology, University of Otago, PO Box 56, Dunedin, 9054, New Zealand*

† Electronic supplementary information (ESI) available: Crystallographic details, structural figures, VT-PXRD data and figures, Mössbauer spectroscopic data, DSC and TGA results. CCDC 1519938–1519948. For ESI and crystallographic data in CIF or other electronic format see DOI: 10.1039/c6sc05317c

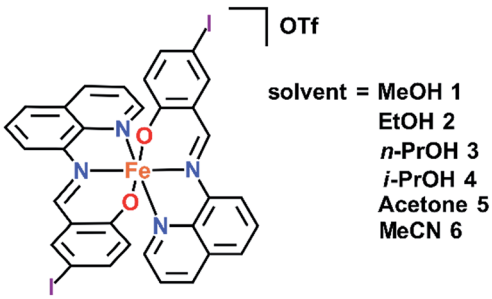

Although, only three of the compounds were SCO active[37] the authors were able to demonstrate that an N–H···O hydrogen bond between the coordinated amine and an oxygen atom from the solvent was responsible for tuning the spin transition temperature. Despite this success only one of the structures was determined in both spin states limiting the conclusions that could be drawn regarding how supramolecular connectivity is altered by SCO.

In our continuing studies on Fe(III) complexes of halogenated quinolylsalicylaldimines (qsal-X) we now report the variation of solvent in [Fe(qsal-I)$_2$]OTf·sol (sol = MeOH **1**,[38] EtOH **2**, *n*-PrOH **3**, i-PrOH **4**, acetone **5**, and MeCN **6**). The structures of all these compounds have been determined by single crystal X-ray diffraction and in many cases the structures of both the high and low spin states have been obtained. This rich data set provides insight into how subtle structural changes radically impact magnetic behaviour. In particular, [Fe(qsal-I)$_2$]OTf·EtOH is sensitive to ageing and sample treatment effects. This results in variable stepped SCO profiles with hysteresis up to 80 K. VT-PXRD studies suggest the different SCO profiles are related to a phase change that occurs following the first spin crossover. While such effects are well described in Fe(II) SCO extended framework systems[39,40] and order–disorder in Fe(II) SCO monomers[41] they are rarely reported in Fe(III).

Results and discussion

Structural overview of [Fe(qsal-I)$_2$]OTf·sol and discussion of Fe(qsal-I)$_2$]OTf·EtOH

The crystal structure of [Fe(qsal-I)$_2$]OTf·MeOH **1**, has previously been reported.[38] In this work, the crystal structures of [Fe(qsal-I)$_2$]OTf·EtOH **2**, [Fe(qsal-I)$_2$]OTf·*n*-PrOH **3**, [Fe(qsal-I)$_2$]OTf·i-PrOH **4**, [Fe(qsal-I)$_2$]OTf·acetone **5**, and [Fe(qsal-I)$_2$]OTf·MeCN **6** have been determined at two temperatures, with the exception of **6** which lost crystallinity at room temperature. The complex magnetic behaviour of [Fe(qsal-I)$_2$]OTf·EtOH **2** led us to determine the structure at 100, 170, 213 and 292 K. The crystallographic data are summarised in Table S1.† Crystals of **2** are found in phase **2a** when prepared at room temperature. Upon cooling below 170 K they shatter explosively due to a phase change to phase **2b** producing very small crystallites. Careful searching and use of synchrotron radiation allowed us to obtain the structure at 100 K, phase **2b**. Similar mechanical instability has recently been reported for [Fe(5-Br-salEen)$_2$]ClO$_4$ (5-Br-salEen = 4-bromo-2-{[2-(ethylamino)ethylimino]methyl}-phenol). In this case it is associated with a "thermosalient" effect unlike in **2**.[42] The structures of **1–6** at all temperatures belong to the triclinic space group $P\bar{1}$. The asymmetric unit contains one molecule of solvent, an [Fe(qsal-I)$_2$]$^+$ cation and a triflate anion, the first such example in Fe(III) SCO chemistry.

As **2** has the most interesting SCO characteristics we will limit the discussion at this stage to this compound. There is a remarkably anisotropic distortion of the unit cell parameters with *b* and *c* shortening by 0.845 and 0.499 Å, respectively from phase **2a** at 292 K to phase **2b** at 100 K while *a* lengthens by 0.901 Å. By comparison, the unit cell parameters in [Fe(5-Br-salEen)$_2$]ClO$_4$ exhibit changes of more than 1.0 Å.[42] Despite our smaller changes in *a*, *b* and *c*, there is a substantial reduction in the unit cell volume by 6.3%, the largest yet reported for any Fe(III) SCO complex.

The Fe centre in **2** is pseudo-octahedral with two meridionally coordinated qsal-I ligands. The Fe–ligand bond lengths for all the compounds are listed in Table 1. At 100 K the Fe–N/O bond lengths in **2b** (average 1.94 Å) are indicative of LS Fe(III).[38,43,44] At 213 and 292 K the Fe–N/O bond lengths for phase **2a** are characteristic of the HS state (average 2.06 Å at 292 K).[38,44] However, at 170 K the bond lengths of phase **2a** are a little shorter than at 213 and 292 K indicating the Fe(III) centre is mostly HS but preparing to undergo SCO. SCO results in changes of ΔFe–N = 0.170 Å and ΔFe–O = 0.023 Å and gives the largest overall change in this series.

The degree of distortion at the Fe centre, as measured by Σ and Θ,[45,46] is $\Delta\Sigma$ (HS-LS) = 23°, while $\Delta\Theta$ = 129° confirming that complete SCO occurs in **2**. Between 170 and 213 K, **2a** shows only small changes in the value of $\Delta\Sigma$ and $\Delta\Theta$, mirroring our previous findings in **1**.[38] As with the Fe–ligand bond lengths, the changes in the coordination sphere are more pronounced in **2** than in any other compound in this series as an overlay of the HS and LS structures for **1** and **2** shows in Fig. 1 (for overlays for **3–5** see Fig. S1†). The large change in unit cell volume, noted above, and the coordination sphere are most likely responsible for the large hysteresis in **2** (*vide infra*).

Magnetic studies of [Fe(qsal-I)$_2$]OTf·EtOH

Magnetic studies of **2** between 50–325 K or 50–350 K indicate that the samples exhibit age and treatment dependent SCO, as shown in Fig. 2. The previously reported magnetic profile of [Fe(qsal-I)$_2$]OTf, formed following MeOH loss from **1**, is included for comparison.[38] Two types of sample were studied, an aged and a fresh sample. Both samples were prepared by layered diffusion of Hqsal-I and NEt$_3$ in CH$_2$Cl$_2$ and Fe(OTf)$_3$ in EtOH. The difference was that the fresh sample was isolated immediately after crystallization was complete (*ca.* 3–4 days). In contrast, for the aged sample the crystals were left in the CH$_2$Cl$_2$/EtOH mother liquor for a further 2 weeks. Both samples analyse for one equivalent of EtOH. For the aged sample at 50 K $\chi_M T$ is 0.5 cm^3 K mol^{-1} and indicative of LS Fe(III), Fig. 2b. The $\chi_M T$ value gradually increases upon heating reaching 1.4 cm^3 K mol^{-1} at 235 K. After that there is an abrupt change ($T_{1/2}\uparrow$ = 252 K) becoming fully HS at 270 K where $\chi_M T$ is 4.42 cm^3 K mol^{-1}. In the cooling mode, $\chi_M T$ decreases beginning at *ca.* 210 K reaching 3.4 cm^3 K mol^{-1} at 170 K before dropping more rapidly

This journal is © The Royal Society of Chemistry 2017

Table 1 Selected Fe–N/O bond lengths (Å) and octahedral distortion parameters (°) for $[Fe(qsal\text{-}I)_2]OTf\cdot sol$

	1[a]-163 K	**1**[a]-293 K	**2b**-100 K	**2a**-170 K	**2a**-213 K	**3**-100 K	**3**-270 K	**4**-163 K	**4**-293 K	**5**-137 K	**5**-293 K	**6**-123 K
Fe1–O1	1.874(8)	1.906(6)	1.900(4)	1.907(3)	1.919(6)	1.883(2)	1.914(3)	1.887(7)	1.908(6)	1.923(6)	1.935(6)	1.868(5)
Fe1–O2	1.878(8)	1.907(7)	1.889(4)	1.908(3)	1.917(6)	1.895(2)	1.922(3)	1.893(7)	1.903(6)	1.915(6)	1.943(7)	1.884(5)
$Fe1–O_{av}$	1.876(8)	1.907(7)	1.895(4)	1.908(3)	1.918(6)	1.889(2)	1.917(3)	1.890(7)	1.906(6)	1.919(6)	1.939(7)	1.876(5)
Fe1–N1	1.965(9)	2.096(7)	1.950(4)	2.101(3)	2.102(7)	1.950(2)	2.107(3)	1.945(8)	2.071(6)	1.953(8)	2.074(8)	1.940(6)
Fe1–N2	1.939(10)	2.145(7)	1.972(5)	2.139(3)	2.143(7)	1.966(3)	2.129(4)	1.967(8)	2.084(6)	1.977(7)	2.109(7)	1.965(6)
Fe1–N3	2.010(10)	2.157(8)	1.939(4)	2.094(3)	2.115(7)	1.966(3)	2.101(3)	1.949(8)	2.067(6)	1.948(8)	2.081(8)	1.937(6)
Fe1–N4	1.948(9)	2.098(7)	1.971(5)	2.142(4)	2.152(7)	1.980(3)	2.158(4)	1.961(8)	2.110(8)	1.986(8)	2.121(7)	1.967(6)
$Fe1–N_{av}$	1.966(10)	2.124(8)	1.958(5)	2.119(4)	2.128(7)	1.966(3)	2.124(4)	1.956(8)	2.083(8)	1.966(8)	2.096(8)	1.952(6)
Σ[b]	43	65	44	60	67	47	65	48	54	41	57	47
Θ[c]	61	189	71	177	200	69	187	71	153	71	160	69

[a] Data taken from ref. 38. [b] $\Sigma = \sum_{i=1}^{12} |90 - \alpha_i|$, where α_i are the twelve *cis* N/O–Fe–N/O angles. [c] $\Theta = \sum_{i=1}^{24} |60 - \theta_i|$, where θ_i are the 24 unique N/O–Fe–N/O angles measured on the projection of two triangular faces of the octahedron along their common pseudo-threefold axis.

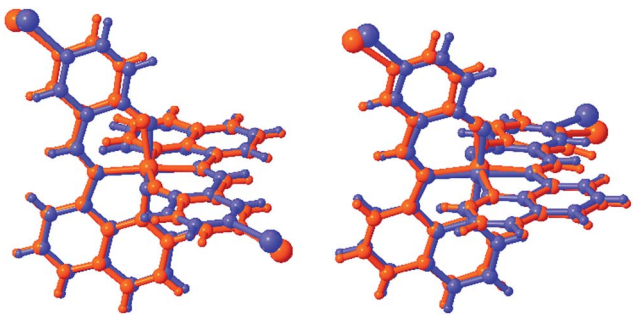

Fig. 1 Overlay of HS (red) and LS (blue) structures of **1** (left) and **2** (right).

to 0.5 cm^3 K mol^{-1} with $T_{1/2}\downarrow = 139$ K. This is consistent with the structure at 170 K which exhibits slightly shorter Fe–N/O bond lengths than at 213 K. In the second heating cycle the spin transition shifts to $T_{1/2}\uparrow = 219$ K. Upon cooling, SCO again occurs in two steps with the step less pronounced in the second cycle (at 160 K, $\chi_M T = 3.26$ and 3.72 cm^3 K mol^{-1} in 1st and 2nd cycle, respectively). Subsequent cycles do not alter the magnetic profile of the complex. Thus, the hysteresis of an aged sample of **2** is 80 K, one of the largest values ever reported for any SCO complex.

Two different magnetic measurements were performed on fresh samples of **2**. Firstly, the fresh sample was slowly cooled from room temperature. The magnetic plot in Fig. 2c shows an abrupt SCO with $T_{1/2}(\downarrow) = 175$ K and $T_{1/2}(\uparrow) = 270$ K in the first cycle. Subsequent cycles reveal two-step SCO with $T_{1/2}(\downarrow) = 213$ and 103 K with a hysteresis of about 1–2 K at each step leading to an unprecedented plateau width of *ca.* 110 K at 2.5 cm^3 K mol^{-1} and consistent with 50% HS.

In the second measurement, the sample was first quenched cooled to 100 K (Fig. 2d). Warming slowly the abrupt change at 270 K observed in the first heating cycle of the slow cooled sample is also present here. However, upon cooling the SCO profile has three steps with an extra step appearing at around 175 K with $\chi_M T = 3.30$ cm^3 K mol^{-1}, indicative of 66% HS. The second step occurs at $T_{1/2}(\downarrow) = 109$ K with $\chi_M T = 2.00$ cm^3 K mol^{-1} and consistent with 33% HS. In contrast, the heating mode is a two-step SCO process going from the LS to the HS state *via* 33% HS intermediate, resulting in an open hysteresis loop of *ca.* 42 K. The complicated SCO plots of **2** and their relationship with the phase changes are explained in the VT-PXRD section.

TGA analysis of **2** shows that it starts to lose EtOH at 353 K with solvent loss complete by 380 K (Fig. S2†). While we cannot absolutely rule out some small degree of solvent loss in fresh samples of **2** we believe that this is minimal as complete removal of EtOH requires heating under vacuum at 100 °C for 1.5 h and even then a cooling and heating cycle is required to give the magnetic profile of $[Fe(qsal\text{-}I)_2]OTf$ (Fig. S3†). Moreover, samples were sealed with Vaseline which also minimizes solvent loss.

DSC measurements of **2** on a fresh sample shows two peaks in the first cycle, one sharp at 277 K and a broader peak at 173 K with $\Delta H = 6.7$ and 7.0 kJ mol^{-1} and $\Delta S = 24$ and 40 J mol^{-1} K^{-1}, respectively (Fig. S4 and S5, Table S2†) closely matching the SCO profile observed in Fig. 2c. These calorimetric values are typical of Fe(III) SCO compounds.[21,23] In the following cycles, the peak at 173 K disappears, mirroring the magnetic studies above. VT-PXRD (*vide infra*) confirms that a phase change takes place at around 170 K. It is noteworthy that there always is a small endothermic peak at 268 K just proceeding the actual SCO possibly associated with some structural pre-organization prior to SCO. In the second cycle, the cooling mode shows only one small peak at 261 K which may correspond to the unusual flexing seen in the VT-PXRD data. The lack of other peaks in the cooling mode may be a due to the small size of the crystallites formed after the first cooling. Similar results have been reported in $[Fe(3\text{-}bpp)(3\text{-}bpp\text{-}Ph\text{-}OMe)][ClO_4]_2\cdot 1.5$-acetone (3-bbp = 2,6-bis{pyrazol-3-yl}pyridine; 3-bpp-Ph-OMe = 2,6-bis{5-(2-methoxyphenyl)pyrazol-3-yl}pyridine)[47] and $[Fe(3\text{-}bpp\text{-}Ph\text{-}OH)_2][ClO_4]_2\cdot 2$-acetone$\cdot H_2O$[48] (3-bpp-Ph-OH = 2,6-bis{5-(2-hydroxyphenyl)pyrazol-3-yl}-pyridine) which show no peaks in the cooling mode despite exhibiting abrupt SCO.

The magnetic studies reveal that samples of **2** are extremely sensitive to sample preparation and ageing. Elemental analysis confirms that both the fresh and aged samples contain one

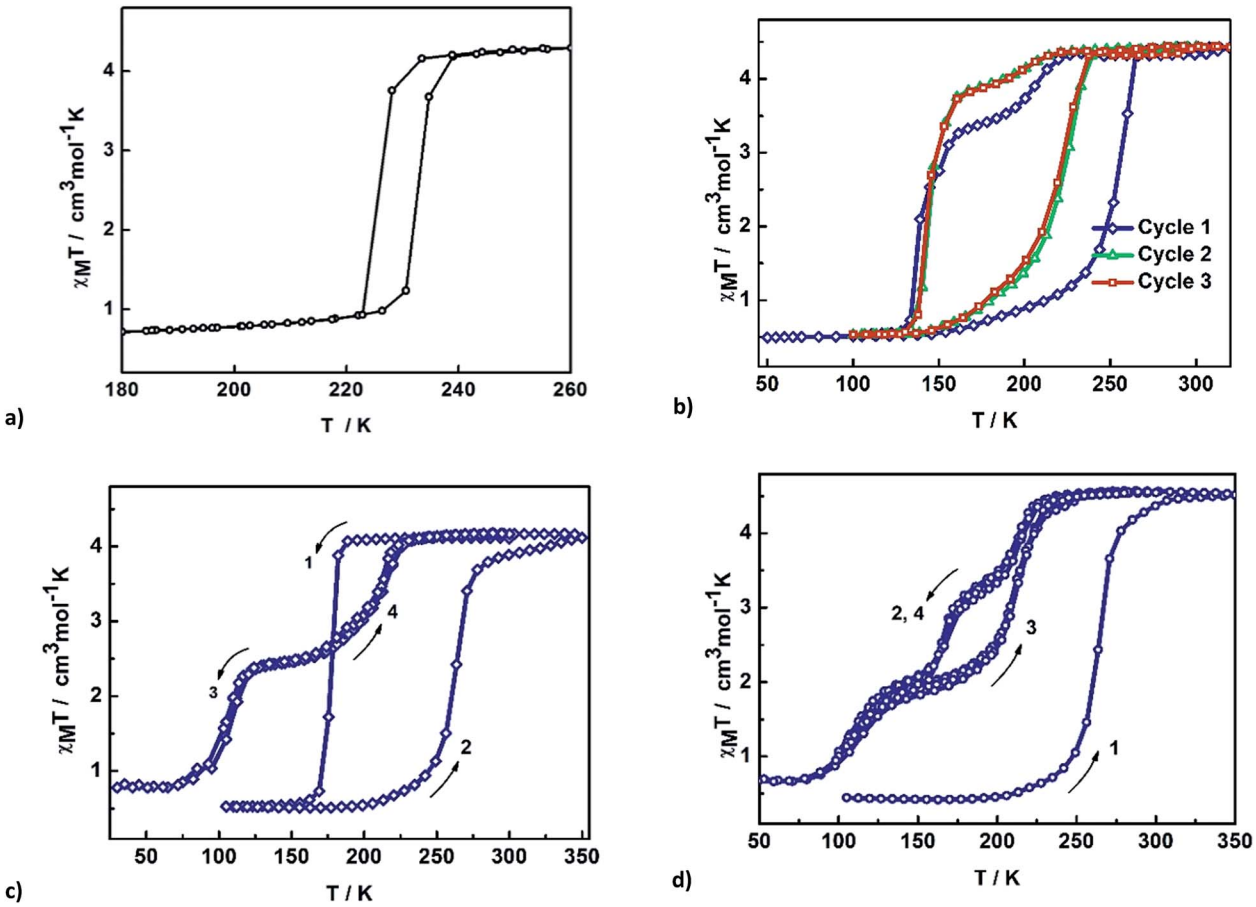

Fig. 2 Thermal variation of $\chi_M T$ *versus* T plot for (a) [Fe(qsal-X)$_2$]OTf, (b) aged EtOH **2**, (c) fresh EtOH **2**, (d) fresh EtOH **2** after flash cooling.

molecule of EtOH. Ageing effects, although uncommon, have been observed in [Fe(qsal)$_2$]NCS and [Fe(3-bpp-Ph-OH)$_2$][ClO$_4$]$_2$·2THF·H$_2$O and are generally found in hysteretic systems.[49,50] As in **2**, ageing of both these compounds results in more complete, abrupt and hysteretic SCO.

Mössbauer spectroscopic studies of [Fe(qsal-I)$_2$]OTf·EtOH

Mössbauer spectroscopy also confirms the different spin states in **2** at different temperatures (Fig. 3). The spectra show that the sample remains LS from 5.3 to 200 K due to the presence of a sharp quadrupole doublet with a wide quadrupole splitting and low isomer shift (Table S3†). By 260 K, although the signal to noise is poor, making fitting of the spectrum impossible, the presence of both HS and LS Fe(III) is visible. At 293 K the sample is fully HS with a broad quadrupole doublet with lower quadrupole splitting and higher isomer shift typical of HS Fe(III). Cooling of the sample reveals a full LS state at 220 K. The difference between the Mössbauer spectroscopic and magnetic data of the fresh sample is probably due to partial solvent loss during the measurement, something previously observed in [Fe(qsal-Br)$_2$]NO$_3$·2MeOH.[51]

VT-PXRD studies of [Fe(qsal-I)$_2$]OTf·EtOH

As the magnetic properties of **2** depend greatly on the sample age and treatment, variable temperature powder X-ray diffraction (VT-PXRD) studies of **2**, using synchrotron radiation, were used to further probe the phase changes that occur. Two experiments were designed and relate to the magnetic data of a freshly prepared sample (Fig. 2c and d). The first experiment started collecting data at high temperature (dataset A) while the other began to collect data only after quenching the sample to 100 K (dataset B). Details of the experiments are shown in Tables S4 and S5† with Pawley fits in Fig. S6 and S7.† Stacked, interpolated diffraction patterns for dataset A and B are shown in Fig. 4.

In the VT-PXRD of dataset A, Fig. 4a, only one phase, that is **2a**, is present at 300 K. On cooling down to 180 K (step 1), a majority phase **2b** and a minority phase **2c** appear while phase **2a** gradually disappears, and is completely gone at *ca.* 164 K. The calculated unit cell parameters from the PXRD patterns of phase **2a** and **2b** are consistent with the single crystal X-ray data of phases **2a** and **2b**, respectively (Tables S6 and S7,† *vide supra*). Unfortunately, attempts to obtain the single crystal X-ray structure of phase **2c** which forms upon shattering have been unsuccessful to date. After cooling to 100 K, the sample was then heated to 300 K (step 2) with phase **2b** remaining the majority phase with the suggested transformation of **2c** into **2a** occurring at around 215–220 K. The transformation of **2a** → **2c** is observed again in the following cooling mode (step 3), at *ca.* 180 K. The persistence of phase **2b** and the transformation of

 This journal is © The Royal Society of Chemistry 2017

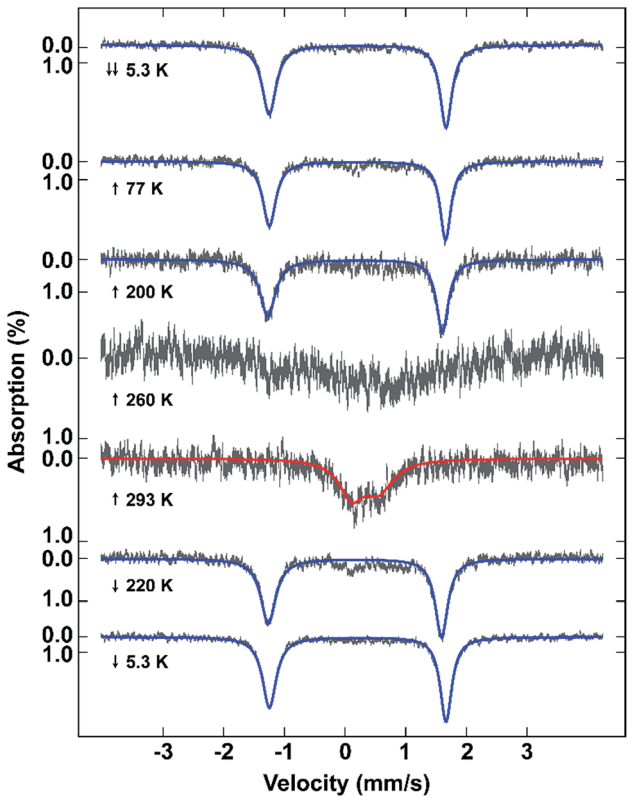

Fig. 3 ^{57}Fe Mössbauer spectra of **2** measured at the temperatures shown with a small magnetic field of 47 mT applied parallel to the γ-ray. The fits to the data are given as blue lines (LS) and red lines (HS).

the minority phase of **2c** ↔ **2a** are repeatable in the following cycles (step 4, Tables S4 and S5†). However, the emergence of the **2b** phase from **2a**, at *ca.* 180 K, takes place only once after the first cooling. As phase **2a** always exists at high temperature and transforms into phase **2c** at low temperature, it suggests that **2a** is the HS phase and **2c** is the LS phase. The temperature-dependent crystallographic phase change behaviour in **2** is summarized in Fig. 5.

For dataset B, Fig. 4b, the sample was initially quench cooled to 100 K. A mixture of phases **2b** (majority) and **2c** (minority) coexist at the beginning which contrasts with only phase **2a** being present in step 1 of dataset A. In the following cycle (steps 1 and 2), the dominant phase is **2b** which always appears together with either **2a** (HS phase) or **2c** (LS phase). Notably, the phase change temperatures between **2a** ↔ **2c** in datasets A and B are similar. However, the relatively weaker intensity of phases **2a** and **2c** in the diffraction patterns of dataset A in comparison to that in dataset B suggest there is a smaller amount of these phases in dataset A. The reason for this behaviour is unclear.

The phase transition from phase **2a** to **2b** at *ca.* 180 K, that is observed only in the first cooling (dataset A), is in accordance with the first abrupt spin transition ($T_{1/2}$ = 175 K) of the magnetic plot shown in Fig. 2c. This also agrees with the peak at 173 K from DSC results that appears distinctly in the first cooling of the experiment. For the heating mode, however, there is no phase change observed in the VT-PXRD data above 260 K where the magnetic plots in Fig. 2c and d show another abrupt SCO ($T_{1/2}$ = 270 K). There is unusual flexing of phase **2b** above 260 K in the VT-PXRD data in both dataset A and B (Fig. 4) and this might be correlated with the abrupt spin change in the magnetic data. For the following cycles, the two step SCO shown in Fig. 2c is believed to be an intrinsic magnetic property of phase **2b**.

As previously mentioned, the VT-PXRD results show relatively small amounts of phase **2a** and **2c** are present in dataset A. These two phases are expected to have minimal contribution to the magnetic plot in Fig. 2c. On the other hand, in dataset B, phases **2a** and **2c** are more pronounced. Consequently, there is

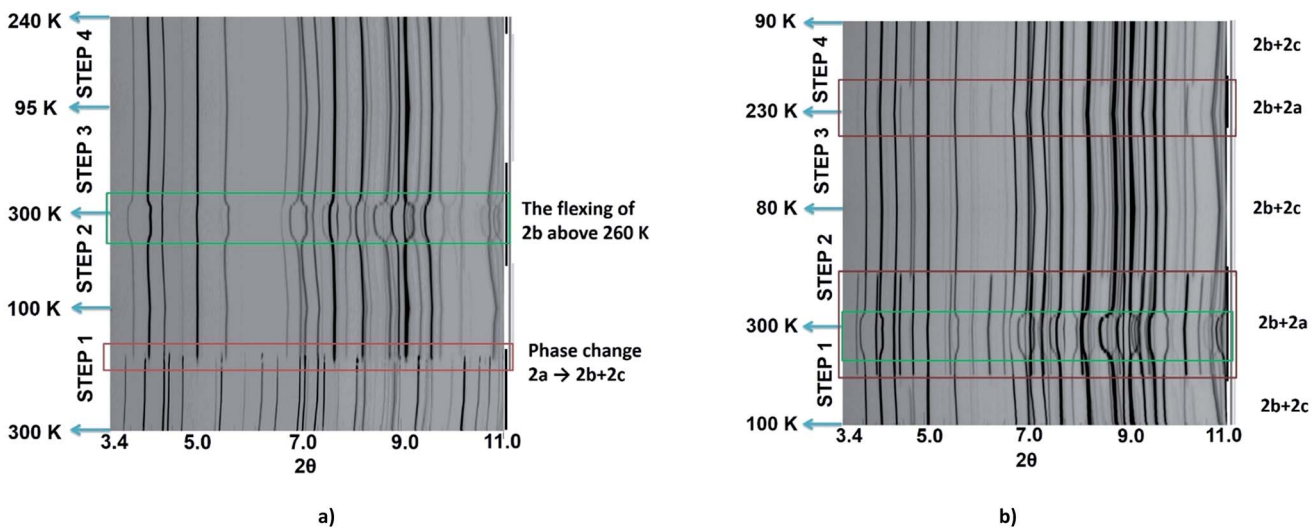

Fig. 4 Stacked, interpolated diffraction patterns of peak evolution in **2** showing the phases that are produced upon repeated heating and cooling cycles for (a) dataset A and (b) dataset B. Highlights of the phase change in the data are in the red frame, showing the presence of phase **2a** in the data. The green box shows an 'unusually large' change in the calculated unit cell parameters of **2b**. Crystallographic phases present at various temperatures (approximate) are depicted by the black (phase **2a**), dark grey (phase **2b**) and light grey (phase **2c**) lines to the right of the stack plot.

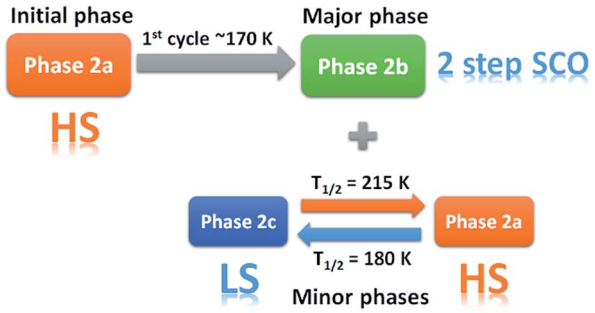

Fig. 5 Summary of the phase changes that occur in **2** from VT-PXRD studies.

Table 2 Spin transition temperatures of $[Fe(qsal\text{-}I)_2]OTf\cdot sol$

Solvent	$T_{1/2}\downarrow$/K	$T_{1/2}\uparrow$/K	ΔT/K	Note
None[a]	225	234	9	
EtOH **2** aged	139	252	113	1st cycle
	139	219	80	2nd cycle
	139	219	80	3rd cycle
n-PrOH **3**	199	199	0	
i-PrOH **4**	251	251	0	
Acetone **5**	331	332	1	
MeCN **6**	315	320	5	

[a] Data from ref. 38.

an extra step in the cooling mode of the magnetic plot at $T_{1/2} \approx$ 175 K (Fig. 2d) which is in the same region as the phase transition between **2a** → **2c**. Overall, the VT-PXRD data correlate well with the observed magnetic behaviour of **2**.

Magnetic studies of $[Fe(qsal\text{-}I)_2]OTf\cdot sol$

The impact of solvent on SCO was investigated by SQUID magnetometry of **3–6**. The results are shown in Fig. 6, while the transition temperatures of **1–6** are shown in Table 2. For **3** and **4**, the packing as well as the supramolecular interactions are almost identical (*vide infra*), resulting in very similar gradual but complete SCO. Heating the sample from 150 K, **3** continuously increases reaching a $\chi_M T$ value of 4.0 cm^3 K mol^{-1} at 275 K. For **4** the SCO is slightly more gradual. This might be due to slight alterations in the supramolecular connectivity with P4AE interactions found in **3** while only C–H···π interactions are found in **4**. The stronger cooperativity in **3** is also believed to be responsible for the lower transition temperature.

In contrast, **5** and **6** show incomplete SCO up to 350 K with a maximum of 70 and 58% HS conversion, respectively. Assuming the SCO is complete at higher temperatures the transition temperature is estimated to be 320–330 K but is rather gradual in both cases, consistent with the lower cooperativity in these compounds.

In this series, it is evident that the alcohols yield more abrupt and complete SCO, presumably due to their ability to hydrogen bond to the anion. However, the other physical properties of the solvents (volume, boiling point, dielectric constant) show no correlation with the abruptness of the SCO or the $T_{1/2}$ of the compounds. It appears that the solvent subtly alters the supramolecular connectivity in the system and it is this that is responsible for particular magnetic profiles we observe. This is explored in more detail in the following section.

Supramolecular packing in $[Fe(qsal\text{-}I)_2]OTf\cdot sol$

To try to better understand the SCO profiles of the different solvates we now examine the cooperativity in these systems. The packing in **1–6** is similar consisting of 1D chains held together by two sets of π–π interactions involving pairs of qsal-I ligands and is common for $[Fe(qsal\text{-}X)_2]^+$ complexes;[35,38,43,51,52] (Tables 3 and S8–S13†). The first set of π–π interactions (type A) contains triflate embraces (Fig. 7). The second set (type B) is supported by weak C–H···O contacts involving the alcohol solvent or C–H···N interactions in the case of MeCN. There are also C–H···O interactions between the aromatic hydrogens and the coordinated phenoxy oxygen atoms which may influence the ligand field provided by the qsal-I ligands.[53]

Upon SCO (LS to HS) the π–π distances increase by on average 0.10 Å, although there is greater range for the type B

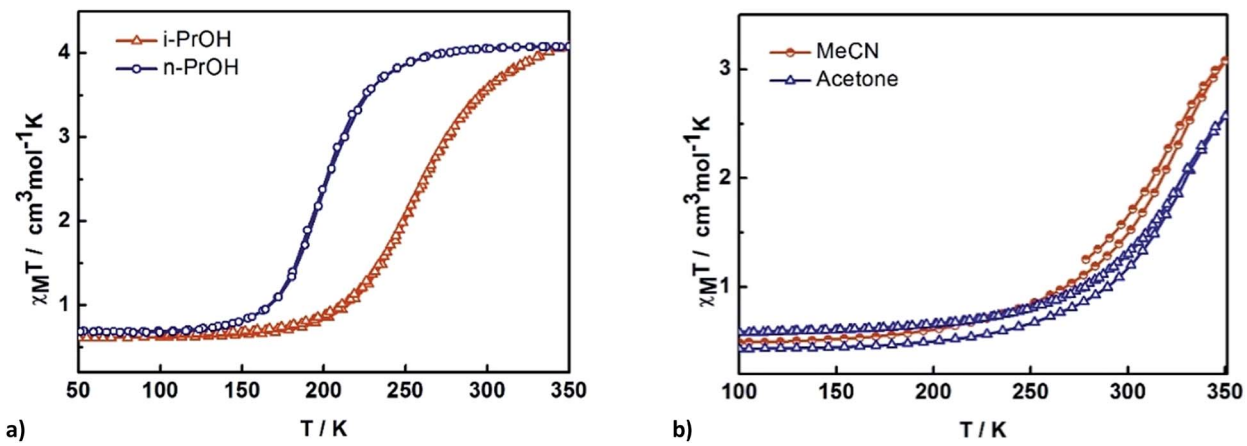

Fig. 6 Thermal variation of $\chi_M T$ *versus* T plot for $[Fe(qsal\text{-}I)_2]OTf\cdot sol$ where sol are (a) *n*-PrOH **3** and i-PrOH **4** and (b) acetone **5** and MeCN **6**.

This journal is © The Royal Society of Chemistry 2017

Table 3 Summary of the principle intermolecular interactions in [Fe(qsal-I)$_2$]OTf·sol

	1 MeOH[a]	**2** EtOH	**3** *n*-PrOH	**4** i-PrOH	**5** Acetone	**6** MeCN
In 1D	π–π, I···π, C–H···O,	π–π, I···π, C–H···O,	π–π, C–H···O	π–π, C–H···O/C	π–π, C–H···O	π–π, I···π, C–H···O
In 2D	P4AE	P4AE	P4AE	C–H···π	P4AE	P4AE
In 3D		I···I (**2a** only)		I···I	I···I	I···π
OTf	C–H···O (OTf)	I···O (OTf, **2a** only)	C–H···O (OTf)	C–H···O (OTf)	C–H···O (OTf)	C–H···O (OTf)
	C–H···F (OTf)	C–H···O (OTf)	C···O (OTf)	C···O (OTf)	C–H···F (OTf)	C–H···F (OTf)
		O···π (**2b** only)	C–H···F (OTf)		I···O (OTf)	I···O (OTf)
					I···F (OTf)	
Solvent	C–H···O (MeOH)	C–H···I (EtOH)	C–H···O (*n*-PrOH)	C–H (i-PrOH)···I	C–H···O (acetone)	C–H···N (MeCN)
		C–H···O (EtOH)	C–H (*n*-PrOH)···I	C–H (i-PrOH)···C	C–H (acetone)···I	
			C (*n*-PrOH)···I			
An–An	F···F (HS only)	F···F	F···F	F···F	O···F, O···S	
Anion–sol	O–H···O	O–H···O	O–H···O, C–H···F/O	O–H···O, C–H···F	C–H···F	C–H···O
Intra-chain/Å[b]	2.74, 2.03[c]	2.72, 2.01[d]	3.04, 2.85	3.11, 2.86	2.74, 2.46	2.92
	$\Delta = -0.71$	$\Delta = -0.71$	$\Delta = -0.19$	$\Delta = -0.25$	$\Delta = -0.28$	
Inter-chain/Å[b]	8.63, 8.83[c]	8.64, 8.71[d]	8.62, 8.82	8.81, 9.00	7.34, 7.61	9.23
	$\Delta = 0.20$	$\Delta = 0.07$	$\Delta = 0.20$	$\Delta = 0.19$	$\Delta = 0.27$	
Inter-plane/Å[b]	12.00, 12.45[c]	12.24, 12.91[d]	12.23, 12.44	12.10, 12.33	13.20, 13.48	10.99
	$\Delta = 0.45$	$\Delta = 0.67$	$\Delta = 0.21$	$\Delta = 0.23$	$\Delta = 0.28$	

[a] Data taken from ref. 38. [b] Low spin (LS), high spin (HS) distances, Δ(HS-LS). [c] At 293 K. [d] At 292 K.

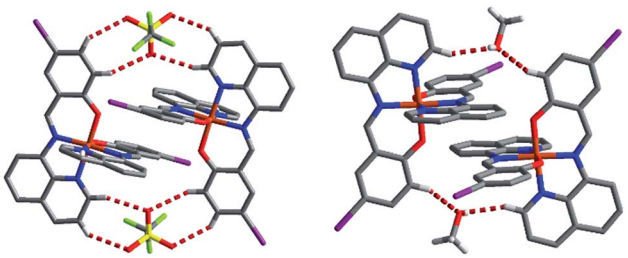

Fig. 7 (a) Type A π–π interactions showing the supporting triflate embraces and (b) type B π–π interactions showing the supporting MeOH interactions of compound **1** at 163 K.

interaction probably as this interaction involves the solvent. Interestingly, even though SCO is incomplete in **5** it shows the largest difference in π–π distances; the reason for this is unclear.

The 1D chains are further connected *via* P4AE (parallel fourfold aryl embrace) interactions[54] to create a 2D network. Uniquely for **4**, the qsal-I ligands are too offset to form a π–π interaction, and only C–H···π interactions are found (Fig. 8, Table S14†). As above the π–π distances lengthen by *ca.* 0.10 Å upon SCO. The C–H···π interactions also increase upon SCO but there appears to be an inverse relationship between the C–H···π and π–π interactions with the largest difference for **5** (*ca.* 0.12 Å, Δπ–π = 0.06 Å) and the smallest for **3** (*ca.* 0.02 Å, Δπ–π = 0.16 Å).

In addition to π–π interactions adjacent planes are linked *via* a weak I···I interaction (see Fig. S8,† a I···π bond is present in **6**). The planes are further linked by weak C–H···O and C–H···F contacts involving the triflate anions resulting in a quasi-3D network. The supramolecular interactions at 230 K for **1** and 170 K for **2a** all show subtle changes, indicative of substantial supramolecular reorganization prior to SCO.

The solvent and triflate interactions for **1–4** are very similar with two alcohol and two triflate anions bound together in a supramolecular circle (see Fig. S9 and Table S15†). The circle is composed of strong alcohol-triflate hydrogen bonds and

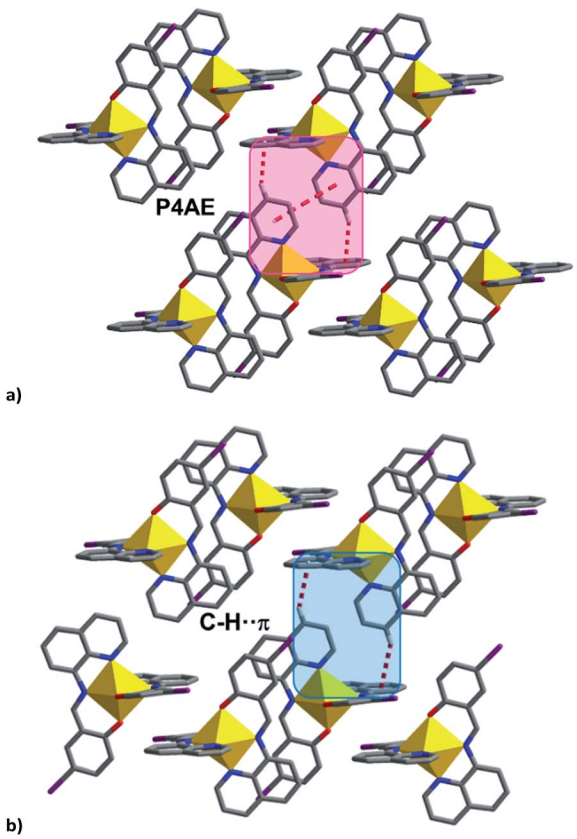

Fig. 8 (a) P4AE interactions in most [Fe(qsal-I)$_2$]OTf·sol complexes, (b) C–H···π interactions in **4** linking the chains into a plane.

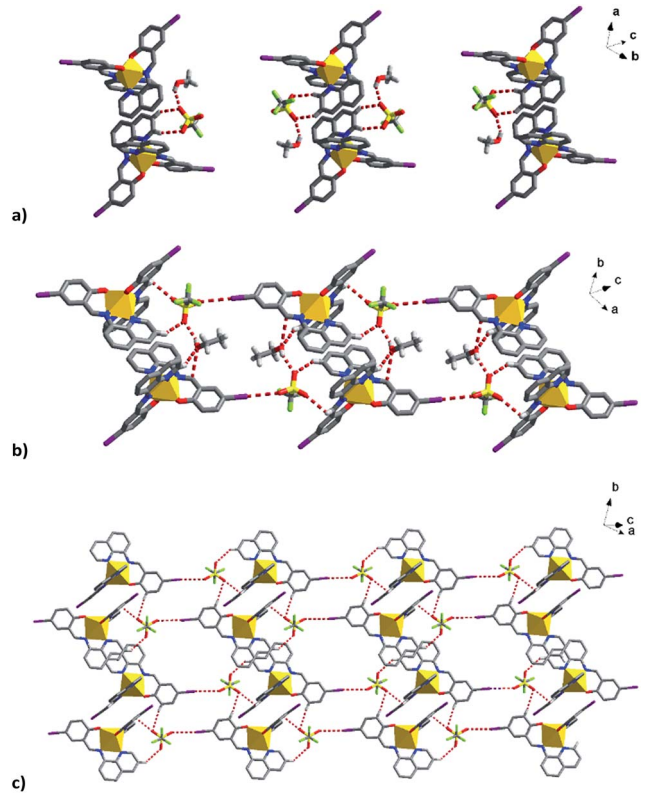

Fig. 9 Supramolecular interactions of the solvent and triflate anions in (a) **1**, (b) **2a** and (c) I···O interactions related to triflate in **2a** bridging the Fe units into a plane.

a F···F interaction[55–57] between the triflate anions. For **1** the latter is stronger at 293 K (2.867 Å) than it is at 163 K (3.005 Å) while for the other complexes it lengthens at high temperature. In **2** the difference between the HS (phase **2a**) and LS (phase **2b**) structures is almost 0.2 Å, consistent with the phase change noted above. For **3** and **4**, there are also C–H···F interactions which are generally weakened by SCO.

In **5** and **6** the solvent and triflate are linked by halogen bonding F···O and C–H···O interactions, respectively (Fig. S10†). The former are particularly strong being *ca.* 0.4 Å shorter than the van der Waals radii of F and O. This change in packing compared to **1–4** is probably responsible for the different SCO behaviour of these two solvates.

The triflate–solvent circles in **1** and **2** bridge the Fe cations that interact *via* π–π interactions as a chain through C–H···F/O interactions (Fig. S11†). In **2a** the Fe cations interact *via* P4AE and I···O interactions involving the triflate anion linking the Fe units in a plane (Fig. 9). This interaction is lost in the **2b** structure following a substantial reorientation of the triflate anion, which results in the formation of a new O···π interaction (3.022 Å, Fig. S12†). At the same time, the P4AE π–π interaction becomes more offset with neighbouring 1D chains shifted relative to each other. Similar supramolecular reorganization is found in $[Fe(qsal\text{-}I)_2][Ni(dmit)_2]\cdot MeCN\cdot H_2O$ where the loss of I···S interactions[44] also gives abrupt and hysteretic SCO.

To gain a better understanding of the 3D packing in these compounds simplified polyhedra packing diagrams have been generated viewed down the 1D π–π chains; **1** is shown in Fig. 10 as a representative example, with **2–6** shown in Fig. S13.† We define three parameters: the intra-chain, inter-chain and inter-plane distances, see Fig. 10. Looking at the different diagrams it is evident that the packing is tightest in **1** and **2**. There is also a large difference in the intra-chain distance in **1** and **2** of 0.71 Å while **3–5** exhibit much smaller values of 0.28–0.19 Å. **1** and **2** also show the smallest intra-chain distance in the HS state in this series. Moreover, the length of the 1D π–π chain, which is coincident with the *b* axis in **1**, **2** and **5** (the *a* axis for **3** and **4**), shortens most in **1** and **2** following SCO to the LS state. This confirms earlier studies that the 1D π–π chains are vital for SCO[34,38,51] and further that large differences between the two spin states will lead to abrupt SCO.[58,59]

The packing in the propanol solvates, **3** and **4**, is almost identical (see Fig. 11), although the intra- and inter-chain distances are slightly shorter in **3** than **4**. This is consistent with the magnetic studies where **4** shows slightly more gradual SCO and a higher transition temperature than **3**.

The acetone and acetonitrile solvates **5** and **6** show the most obvious gaps in the structure with the largest inter-plane and inter-chain distances in this series. These solvents are also unable to hydrogen bond with the anion and combined with the more open packing results in lower cooperativity. Overall, this

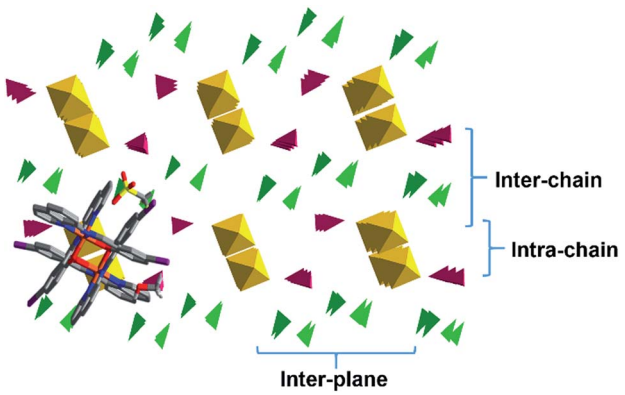

Fig. 10 Simplified packing diagram of **1** showing the intra-chain, inter-chain and inter plane distances with the $[Fe(qsal\text{-}I)_2]^+$ cations shown in yellow, the triflate anions in green and the MeOH molecules in burgundy.

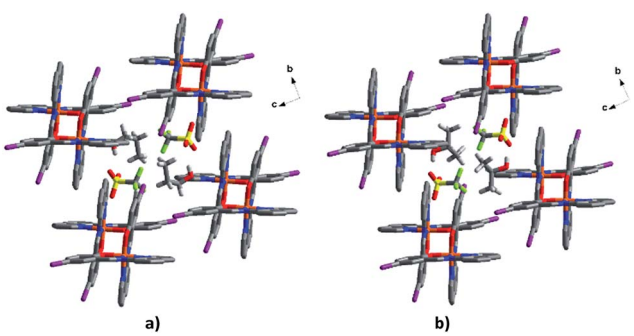

Fig. 11 The packing of the two propanol solvates in (a) **3** and (b) **4**.

This journal is © The Royal Society of Chemistry 2017

analysis reveals that the unique behaviour of **2** appears to be due to unusually tight packing which results in antagonistic interactions that favour a phase change and subsequent stepped SCO. Stepped SCO as a result of tight packing has been reported in $[Fe(qsal\text{-}Br)_2]NO_3\cdot 2MeOH$[51] and a number of Hoffmann-type networks including $[Fe_3^{II}(saltrz)_6(M^{II}(CN)_4)_3]\cdot 8H_2O$ {saltrz = 2-(((4*H*-1,2,4-triazol-4-yl)imino)methyl)-phenol},[60] $\{Fe[(Hg(SCN)_3)_2](4,4'\text{-bipy})_2\}_n$ (ref. 61) and $[Fe(dpsme)\text{-}Pt(CN)_4]\cdot 2/3dpsme\cdot x EtOH\cdot y H_2O$ (dpsme = 4,4′-di(pyridylthio)-methane).[62]

Conclusions

In summary, we have for the first time in Fe(III) SCO chemistry prepared a series of complexes that differ only in the lattice solvent, $[Fe(qsal\text{-}I)_2]OTf\cdot sol$. We have established that solvent provides a simple and valuable tool for tuning SCO properties with $T_{1/2}$ varying over nearly 200 K in **1–6**. The impact of EtOH is particularly stark with samples of **2** showing ageing and sample treatment effects. VT-PXRD studies of fresh samples show a phase change following the first cooling resulting in two-step SCO with the degree of hysteresis dependent on the amount of the minor phases **2a** and **2c** present in the sample. In contrast, the aged sample shows a remarkable hysteresis of 80 K, one of the largest values known in SCO chemistry. Surprisingly, the packing in the compounds is very similar and composed of 1D chains of the $[Fe(qsal\text{-}I)_2]^+$ cations connected by π–π interactions. Additional P4AE and I···X (X = I, O, π) interactions combine to form 3D supramolecular networks. Nevertheless, there are subtle differences which result in very different magnetic behaviour with the shortest intra-chain distances and more extensive interactions associated with more abrupt SCO. Indeed, in the case of **2** these interactions may be antagonistic thereby encouraging a phase change and stepped SCO. The startling impact that solvent has on the SCO characteristics of **1–6** should permit the development of solvent specific sensors. Moreover, the findings from this work would be expected to be applicable to other systems and will greatly aid others in the continuing search for SCO switches that operate at room temperature.

Experimental

Materials and basic characterisation

Hqsal-I was prepared as described previously.[63] All other reagents and solvents were purchased from Sigma-Aldrich Chemical Company or TCI Chemicals and used as received. Elemental analyses were carried out on a Eurovector EA3000 analyser by staff of the School of Chemistry, University of Bristol, UK. ESI-MS were carried out on a Bruker Daltonics 7.0T Apex 4 FTICR Mass Spectrometer by staff at the National University of Singapore. Infrared spectra (as KBr discs) were recorded on a Perkin-Elmer Spectrum One infrared spectrophotometer in the range 400–4000 cm^{-1}.

X-ray crystallography

Crystal data and data processing parameters for the structures of **1–6** are given in Table S1.† Crystals were mounted on a glass fibre using perfluoropolyether oil and the sample cooled to the required temperature in a stream of cold nitrogen. The diffraction data of **1**, **2** (at 170, 213 and 292 K), **4–6** were collected at 108 and 293 K on a Rigaku Spider diffractometer equipped with a MicroMax MM007 rotating anode generator, Cu_α radiation ($\lambda = 1.54178$ Å), high-flux Osmic multilayer mirror optics, and a curved image-plate detector. The data were integrated, scaled and averaged with FS Process.[64] In the case of **3** data were collected on a Bruker APEXII area detector with graphite monochromated MoKα ($\lambda = 0.71073$ Å).[65] After data collection, in each case an empirical absorption correction was applied.[66] In order to collect data for **2** at 100 K, a small amount of the sample was immersed in perfluoropolyether oil on a glass slide at room temperature, and the slide plunged into liquid nitrogen for up to one minute.

The structures were then solved by direct methods and refined on all F^2 data using the SHELX suite of programs[67] or OLEX2.[68] In all cases non-hydrogen atoms were refined with anisotropic thermal parameters; hydrogen atoms were included in calculated positions and refined with isotropic thermal parameters which were *ca.* 1.2 × (aromatic CH) or 1.5 × (Me, CH_2, OH) the equivalent isotropic thermal parameters of their parent carbon atoms. All pictures were generated using either OLEX2 or DIAMOND.[69] The CCDC numbers for the X-ray crystallographic data presented in this paper are 1519938 (**2b**), 1519939 (**2a**-170 K), 1519940 (**2a**-213 K), 1519941 (**2a**-292 K), 1519942 (**3**-100 K), 1519943 (**3**-270 K), 1519944 (**4**-163 K), 1519945 (**4**-293 K), 1519946 (**5**-137 K), 1519947 (**5**-293 K) and 1519948 (**6**).

Magnetic measurements

Data were collected using a Quantum Design MPMS 5 SQUID magnetometer under an applied field of 1 T over the temperature range 30–350 K for **1**, **3–6** and 30–325 K for **2**. The powdered or polycrystalline samples were placed in gel capsules and record at a scanning rate of nominally 10 K min^{-1}. However, care was taken to allow long thermal equilibration times at each temperature point such that the real scan rate was far lower. In the case of **2** Vaseline was used for the fresh and aged samples to ensure minimal solvent loss during the measurement.

Mössbauer spectroscopic studies

^{57}Fe Mössbauer spectra were recorded on a low field Mössbauer spectrometer from SEE Co. (Science Engineering & Education Co., MN). The sample of **2** was enclosed in Vaseline and rapidly frozen in liquid nitrogen. The sample was then placed in the spectrometer running at 5.3 K. This rapidly quenched sample was then warmed slowly to 77 K, 200 K, 260 K and 293 K. The sample was then slowly cooled to 220 K and finally returned to 5.3 K.

Synthesis of $[Fe(qsal\text{-}I)_2]OTf\cdot MeOH$, 1

Hqsal-I (154 mg, 0.4 mmol) was dissolved in CH_2Cl_2 (2 ml) giving an orange solution. NEt_3 (56 μl, 0.4 mmol) was added resulting in a change to dark orange. CH_3OH (3 ml) was layered on top of the Hqsal-I solution. In a separate flask, $FeCl_3$ (34 mg,

0.2 mmol) was dissolved in MeOH (5 ml) giving a yellow solution and AgOTf (155 mg, 0.6 mmol) added resulting in formation of a white powder (AgCl) which was filtered off. The yellow solution of $Fe(OTf)_3$ was then layered on top of the blank CH_3OH and left for 4 days. The black crystals which formed were washed with hexane (2 × 1 ml) and air dried yield 90 mg (47%). $\tilde{\nu}_{max}$(KBr)/cm^{-1} 3067 ($\nu_{Ar\text{-}H}$), 1600 ($\nu_{C=N}$), 1276 ($\nu_{S\text{-}O}$), 1139 ($\nu_{C\text{-}F}$), 1030 ($\nu_{S\text{-}O}$) cm^{-1}. *m*/*z* (ESI) 802.0 $[Fe(qsal\text{-}I)_2]^+$, 149.2 $[CF_3SO_3]^-$. Elemental analysis: calcd (found) for $C_{34}H_{24}F_3FeI_2N_4O_6S$: C, 41.51 (41.76); H, 2.46 (2.39); N, 5.70 (5.84)%.

The synthesis of the other complexes was achieved in a similar fashion by replacing MeOH with the appropriate solvent, *i.e.* EtOH, *n*-PrOH, i-PrOH, acetone and MeCN.

Synthesis of [Fe(qsal-I)$_2$]OTf·EtOH, 2

Aged sample. Prepared in a similar manner to **1** but with the crystals left in the CH_2Cl_2/EtOH mother liquor for 2 weeks. Yield 28%. $\hat{\nu}_{max}$(KBr)/cm^{-1} 3067 ($\nu_{Ar\text{-}H}$), 1600 ($\nu_{C=N}$), 1276 ($\nu_{S\text{-}O}$), 1163 ($\nu_{C\text{-}F}$), 1030 ($\nu_{S\text{-}O}$) cm^{-1}. *m*/*z* (ESI) 801.9 $[Fe(qsal\text{-}I)_2]^+$, 149.1 $[CF_3SO_3]^-$. Elemental analysis: calcd (found) for $C_{35}H_{26}F_3FeI_2N_4O_6S$: C, 42.15 (41.81); H, 2.63 (2.44); N, 5.62 (5.93)%.

Fresh sample. Crystals isolated immediately once crystallization was complete (*ca.* 3–4 days). IR and MS data matched those of the aged sample. Elemental analysis: calcd (found) for $C_{35}H_{26}F_3FeI_2N_4O_6S$: C, 42.15 (42.16); H, 2.63 (2.66); N, 5.62 (5.58)%.

Synthesis of [Fe(qsal-I)$_2$]OTf·*n*-PrOH, 3

Yield 26%. $\tilde{\nu}_{max}$(KBr)/cm^{-1} 3067 ($\nu_{Ar\text{-}H}$), 1601 ($\nu_{C=N}$), 1278 ($\nu_{S\text{-}O}$), 1159 ($\nu_{C\text{-}F}$), 1030 ($\nu_{S\text{-}O}$) cm^{-1}. *m*/*z* (ESI) 801.9 $[Fe(qsal\text{-}I)_2]^+$, 149.1 $[CF_3SO_3]^-$. Elemental analysis: calcd (found) for $C_{36}H_{28}F_3FeI_2N_4O_6S$: C, 42.75 (41.74); H, 2.79 (2.67); N, 5.54 (5.41)%.

Synthesis of [Fe(qsal-I)$_2$]OTf·i-PrOH, 4

Yield 23%. $\tilde{\nu}_{max}$(KBr)/cm^{-1} 3067 ($\nu_{Ar\text{-}H}$), 1601 ($\nu_{C=N}$), 1278 ($\nu_{S\text{-}O}$), 1159 ($\nu_{C\text{-}F}$), 1030 ($\nu_{S\text{-}O}$) cm^{-1}. *m*/*z* (ESI) 801.9 $[Fe(qsal\text{-}I)_2]^+$, 149.1 $[CF_3SO_3]^-$. Elemental analysis: calcd (found) for $C_{36}H_{28}F_3FeI_2N_4O_6S$: C, 42.75 (42.37); H, 2.79 (2.84); N, 5.54 (5.26)%.

Synthesis of [Fe(qsal-I)$_2$]OTf·acetone, 5

Yield 20%. $\tilde{\nu}_{max}$(KBr)/cm^{-1} 3044 ($\nu_{Ar\text{-}H}$), 1596 ($\nu_{C=N}$), 1261 ($\nu_{S\text{-}O}$), 1158 ($\nu_{C\text{-}F}$), 1060 ($\nu_{S\text{-}O}$) cm^{-1}. *m*/*z* (ESI) 801.9 $[Fe(qsal\text{-}I)_2]^+$, 149.1 $[CF_3SO_3]^-$. Elemental analysis: calcd (found) for $C_{36}H_{26}F_3FeI_2N_4O_6S$: C, 42.84 (43.12); H, 2.60 (2.81); N, 5.55 (6.11)%.

Synthesis of [Fe(qsal-I)$_2$]OTf·MeCN, 6

Yield 22%. $\tilde{\nu}_{max}$(KBr)/cm^{-1} 3047 ($\nu_{Ar\text{-}H}$), 1599 ($\nu_{C=N}$), 1299 ($\nu_{S\text{-}O}$), 1159 ($\nu_{C\text{-}F}$), 1042 ($\nu_{S\text{-}O}$) cm^{-1}. *m*/*z* (ESI) 801.9 $[Fe(qsal\text{-}I)_2]^+$, 149.1 $[CF_3SO_3]^-$. Elemental analysis: calcd (found) for $C_{35}H_{23}F_3FeI_2N_5O_5S$: C, 42.36 (43.62); H, 2.33 (2.54); N, 7.06 (7.17)%.

Acknowledgements

We thank the Thailand Research Fund (Grant No. RSA5580028 and RSA5880048) and the National Science and Technology Development Agency (Grant No. P-10-11181) for funding this research. KSM thanks the Australian Research Council for a Discovery Project grant to support this work. Parts of this research were undertaken on the MX2 and PD beamlines with the help of Dr Helen Brand and Dr Alan Riboldi-Tunnicliffe from the Australian Synchrotron, Victoria, Australia.

Notes and references

1 *Spin-Crossover Materials: Properties and Applications*, ed. M. A. Halcrow, John Wiley & Sons, Ltd, Chichester, 2013.
2 R. Klajn, J. F. Stoddart and B. A. Grzybowski, *Chem. Soc. Rev.*, 2010, **39**, 2203.
3 M. Natali and S. Giordani, *Chem. Soc. Rev.*, 2012, **41**, 4010.
4 M. D. Manrique-Juárez, S. Rat, L. Salmon, G. Molnár, C. M. Quintero, L. Nicu, H. J. Shepherd and A. Bousseksou, *Coord. Chem. Rev.*, 2015, **308**, 395–408.
5 J. L. Zhang, J. Q. Zhong, J. D. Lin, W. P. Hu, K. Wu, G. Q. Xu, A. T. S. Wee and W. Chen, *Chem. Soc. Rev.*, 2015, **44**, 2998–3022.
6 O. Sato, *Nat. Chem.*, 2016, **8**, 644–656.
7 K. S. Murray, in *Spin-Crossover Materials: Properties and Applications*, ed. M. A. Halcrow, John Wiley & Sons Ltd., Chichester, 2013, pp. 1–54.
8 P. Gütlich, A. B. Gaspar and Y. Garcia, *Beilstein J. Org. Chem.*, 2013, **9**, 342–391.
9 V. Ksenofontov, A. B. Gaspar and P. Gütlich, *Top. Curr. Chem.*, 2004, **235**, 23–64.
10 A. Hauser, *Top. Curr. Chem.*, 2004, **234**, 155–198.
11 J.-F. Létard, *J. Mater. Chem.*, 2006, **16**, 2550–2559.
12 J.-F. Létard, P. Guionneau and L. Goux-Capes, *Top. Curr. Chem.*, 2004, **235**, 221–249.
13 J.-F. Létard, G. Chastanet, P. Guionneau and C. Desplanches, in *Spin Crossover Materials: Properties and Applications*, ed. M. A. Halcrow, John Wiley & Sons, Ltd, Chichester, 2013, pp. 475–506.
14 M. G. Cowan, J. Olguín, S. Narayanaswamy, J. L. Tallon and S. Brooker, *J. Am. Chem. Soc.*, 2012, **134**, 2892–2894.
15 S. Brooker and J. A. Kitchen, *Dalton Trans.*, 2009, 7331–7340.
16 A. B. Gaspar, M. Seredyuk and P. Gütlich, *J. Mol. Struct.*, 2009, **924–926**, 9–19.
17 M. A. Halcrow, *Coord. Chem. Rev.*, 2009, **253**, 2493–2514.
18 Y. Sunatsuki, R. Kawamoto, K. Fujita, H. Maruyama, T. Suzuki, H. Ishida, M. Kojima, S. Iijima and N. Matsumoto, *Coord. Chem. Rev.*, 2010, **254**, 1871–1881.
19 B. Weber, in *Spin-Crossover Materials: Properties and Applications*, ed. M. A. Halcrow, John Wiley & Sons Ltd., Chichester, 2013, pp. 55–76.
20 G. A. Craig, O. Roubeau and G. Aromí, *Coord. Chem. Rev.*, 2014, **269**, 13–31.
21 M. Nihei, T. Shiga, Y. Maeda and H. Oshio, *Coord. Chem. Rev.*, 2007, **251**, 2606–2621.
22 R. Bertoni, M. Lorenc, A. Tissot, M. L. Boillot and E. Collet, *Coord. Chem. Rev.*, 2015, **282–283**, 66–76.
23 D. J. Harding, P. Harding and W. Phonsri, *Coord. Chem. Rev.*, 2016, **313**, 38–61.

 This journal is © The Royal Society of Chemistry 2017

24 K. S. Murray and C. J. Kepert, *Top. Curr. Chem.*, 2004, **233**, 195–228.
25 S. Hayami, K. Hiki, T. Kawahara, Y. Maeda, D. Urakami, K. Inoue, M. Ohama, S. Kawata and O. Sato, *Chem.–Eur. J.*, 2009, **15**, 3497–3508.
26 D. Sertphon, D. J. Harding, P. Harding, K. S. Murray, B. Moubaraki, J. D. Cashion and H. Adams, *Eur. J. Inorg. Chem.*, 2013, 788–795.
27 A. Tissot, P. Fertey, R. Guillot, V. Briois and M.-L. Boillot, *Eur. J. Inorg. Chem.*, 2014, 101–109.
28 I. Nemec, R. Herchel, R. Boča, Z. Trávníček, I. Svoboda, H. Fuess and W. Linert, *Dalton Trans.*, 2011, **40**, 10090–10099.
29 I. Nemec, R. Herchel, I. Šalitroš, Z. Trávníček, J. Moncol, H. Fuess, M. Ruben and W. Linert, *CrystEngComm*, 2012, **14**, 7015–7024.
30 C. Krüger, P. Augustín, L. Dlháň, J. Pavlik, J. Moncoĺ, I. Nemec, R. Boča and F. Renz, *Polyhedron*, 2015, **87**, 194–201.
31 M. Koike, K. Murakami, T. Fujinami, K. Nishi, N. Matsumoto and Y. Sunatsuki, *Inorg. Chim. Acta*, 2013, **399**, 185–192.
32 K. Hanahara, H. Ono, T. Fujinami, N. Matsumoto and Y. Sunatsuki, *Inorg. Chim. Acta*, 2015, **429**, 93–98.
33 J. C. Dias, B. Vieira, I. C. Santos, L. C. J. Pereira and V. Da Gama, *Inorg. Chim. Acta*, 2009, **362**, 2076–2079.
34 D. J. Harding, D. Sertphon, P. Harding, K. S. Murray, B. Moubaraki, J. D. Cashion and H. Adams, *Chem.–Eur. J.*, 2013, **19**, 1082–1090.
35 B. J. C. Vieira, J. C. Dias, I. C. Santos, L. C. J. Pereira, V. da Gama and J. C. Waerenborgh, *Inorg. Chem.*, 2015, **54**, 1354–1362.
36 T. Shimizu, Y. Komatsu, H. Kamihata, Y. H. Lee, A. Fuyuhiro, S. Iijima and S. Hayami, *J. Inclusion Phenom. Macrocyclic Chem.*, 2011, **71**, 363–369.
37 I. Nemec, R. Herchel and Z. Trávníček, *Dalton Trans.*, 2015, **44**, 4474–4484.
38 D. J. Harding, W. Phonsri, P. Harding, I. A. Gass, K. S. Murray, B. Moubaraki, J. D. Cashion, L. Liu and S. G. Telfer, *Chem. Commun.*, 2013, **49**, 6340–6342.
39 G. J. Halder, K. W. Chapman, S. M. Neville, B. Moubaraki, K. S. Murray, J.-F. Létard and C. J. Kepert, *J. Am. Chem. Soc.*, 2008, **130**, 17552–17562.
40 P. D. Southon, L. Liu, E. A. Fellows, D. J. Price, G. J. Halder, K. W. Chapman, B. Moubaraki, K. S. Murray, J. F. Létard and C. J. Kepert, *J. Am. Chem. Soc.*, 2009, **131**, 10998–11009.
41 T. M. Ross, B. Moubaraki, K. S. Wallwork, S. R. Batten and K. S. Murray, *Dalton Trans.*, 2011, **40**, 10147.
42 A. I. Vicente, A. Joseph, L. P. Ferreira, M. de Deus Carvalho, V. H. N. Rodrigues, M. Duttine, H. P. Diogo, M. E. Minas da Piedade, M. J. Calhorda and P. N. Martinho, *Chem. Sci.*, 2016, **7**, 4251–4258.
43 W. Phonsri, D. J. Harding, P. Harding, K. S. Murray, B. Moubaraki, I. A. Gass, J. D. Cashion, G. N. L. Jameson and H. Adams, *Dalton Trans.*, 2014, **43**, 17509–17518.
44 K. Fukuroi, K. Takahashi, T. Mochida, T. Sakurai, H. Ohta, T. Yamamoto, Y. Einaga and H. Mori, *Angew. Chem., Int. Ed.*, 2014, **53**, 1983–1986.
45 J. K. McCusker, A. L. Rheingold and D. N. Hendrickson, *Inorg. Chem.*, 1996, **35**, 2100–2112.
46 M. Marchivie, P. Guionneau, J. F. Létard and D. Chasseau, *Acta Crystallogr., Sect. B: Struct. Sci.*, 2005, **61**, 25–28.
47 G. Aromí, C. M. Beavers, J. Sánchez Costa, G. A. Craig, G. Mínguez Espallargas, A. Orera and O. Roubeau, *Chem. Sci.*, 2016, **7**, 2907–2915.
48 G. A. Craig, J. S. Costa, O. Roubeau, S. J. Teat and G. Aromí, *Chem.–Eur. J.*, 2011, **17**, 3120–3127.
49 H. Oshio, K. Kitazaki, J. Mishiro, N. Kato and Y. Maeda, *J. Chem. Soc., Dalton Trans.*, 1987, 1341–1347.
50 G. A. Craig, J. S. Costa, O. Roubeau, S. J. Teat and G. Aromí, *Eur. J. Inorg. Chem.*, 2013, **2013**, 745–752.
51 D. J. Harding, W. Phonsri, P. Harding, K. S. Murray, B. Moubaraki and G. N. L. Jameson, *Dalton Trans.*, 2015, **44**, 15079–15082.
52 B. J. C. Vieira, J. T. Coutinho, J. C. Dias, J. C. Nunes, I. C. Santos, L. C. J. Pereira, V. da Gama and J. C. Waerenborgh, *Polyhedron*, 2015, **85**, 643–651.
53 O. Iasco, E. Rivie, R. Guillot, M. Buron-Le Cointe, J.-F. Meunier, A. Bousseksou and M.-L. Boillot, *Inorg. Chem.*, 2015, **54**, 1791–1799.
54 V. Russell, M. Scudder and I. Dance, *J. Chem. Soc., Dalton Trans.*, 2001, 789–799.
55 K. Reichenbächer, H. I. Süss and J. Hulliger, *Chem. Soc. Rev.*, 2005, **34**, 22–30.
56 S. K. Nayak, M. K. Reddy, T. N. G. Row and D. Chopra, *Cryst. Growth Des.*, 2011, **11**, 1578–1596.
57 D. Chopra, *Cryst. Growth Des.*, 2012, **12**, 541–546.
58 M. A. Halcrow, *Chem. Soc. Rev.*, 2011, **40**, 4119–4142.
59 M. A. Halcrow, *Chem. Lett.*, 2014, **43**, 1178–1188.
60 N. F. Sciortino, K. A. Zenere, M. E. Corrigan, G. J. Halder, G. Chastanet, J.-F. Létard, C. J. Kepert and S. M. Neville, *Chem. Sci.*, 2017, **8**, 701–707.
61 E. Trzop, D. Zhang, L. Piñeiro-Lopez, F. J. Valverde-Muñoz, M. Carmen Muñoz, L. Palatinus, L. Guerin, H. Cailleau, J. A. Real and E. Collet, *Angew. Chem., Int. Ed.*, 2016, **55**, 8675–8679.
62 N. F. Sciortino, K. R. Scherl-Gruenwald, G. Chastanet, G. J. Halder, K. W. Chapman, J.-F. Létard and C. J. Kepert, *Angew. Chem., Int. Ed.*, 2012, **51**, 10154–10158.
63 J. Sirirak, W. Phonsri, D. J. Harding, P. Harding, P. Phommon, W. Chaoprasa, R. M. Hendry, T. M. Roseveare and H. Adams, *J. Mol. Struct.*, 2013, **1036**, 439–446.
64 Rigaku, *Rigaku XRD*, Rigaku Corporation, Tokyo, Japan, 1996.
65 *Bruker APEXII*, Bruker AXS Inc., Madison, WI, USA, 2005.
66 *SADABS and SAINT*, Bruker AXS Inc., Madison, WI, USA, 2003.
67 G. M. Sheldrick, *Acta Crystallogr.*, 2008, **A64**, 112–122.
68 O. V. Dolomanov, L. J. Bourhis, R. J. Gildea, J. A. K. Howard and H. Puschmann, *J. Appl. Crystallogr.*, 2009, **42**, 339–342.
69 K. Brandenberg and H. Putz, *DIAMOND, Crystal Impact*, Bonn, Germany, 2006.

Dalton Transactions

COMMUNICATION

View Article Online
View Journal

Check for updates

Cite this: DOI: 10.1039/c8dt01241e

Received 30th March 2018,
Accepted 27th April 2018

DOI: 10.1039/c8dt01241e

rsc.li/dalton

Published on 30 April 2018. Downloaded by University of Bath on 03/05/2018 11:19:01.

Self-assembly of a mixed-valence Fe^{II}–Fe^{III} tetranuclear star†

Darunee Sertphon, ‡[a] Phimphaka Harding, [a] Keith S. Murray, [b] Boujemaa Moubaraki,[b] Nicholas F. Chilton, [c] Stephen Hill,[d,e] Jonathan Marbey,[d,e] Harry Adams,[f] Casey G. Davies,[g] Guy N. L. Jameson [g,h] and David J. Harding *[a]

A unique self-assembled mixed-valence Fe^{II}–Fe^{III} tetranuclear star has been comprehensively characterised showing a large magnetic anisotropy at the peripheral Fe^{II} centres, ferromagnetic coupling between the iron centres and field-induced SMM behaviour.

The design and study of transition metal clusters with useful magnetic properties remains a considerable challenge. Single molecule magnets (SMMs) are of particular interest as they exhibit slow relaxation of magnetization with a barrier to spin reversal proportional to the uniaxial magnetic anisotropy and the squared spin of the cluster.[1–8] The magnetic bistability of these clusters potentially permits their use in data storage applications and quantum computation.[9–13] To be useful SMMs must be robust and retain their magnetic bistability when deposited on a surface.[14,15] This is often not the case, for example $[Mn_{12}O_{12}(O_2CR)_{16}(H_2O)_4]$ undergoes reduction upon deposition on Au(111) and loss of SMM behaviour.[16]

A series of particularly robust Fe_4^{III} SMMs was first reported in 1999, and is based on the star shaped $[Fe_4(dpm)_6(OMe)_6]$ (dpm = 2,2,6,6-tetramethyl-3,5-heptanedionate) molecule.[17] Replacing the methoxides with two tripodal ligands, H_3L = R-C$(CH_2OH)_3$ gives $[Fe_4(dpm)_6(L)_2]$ with improved SMM characteristics due to a change in symmetry from C_2 to D_3 resulting in an increase in the helical pitch of the $Fe(O_2Fe)_3$ core, thus increasing the magnetic anisotropy.[18,19] The robustness of these Fe_4 stars has allowed them to be deposited on gold,[20–24] silicon[25] and boron nitride.[26] Unusually, their slow magnetic relaxation is retained on surfaces, which is the first step towards making the above applications a reality.

More recently, tridentate dianionic O,N,O ligands have been used notably the chiral *R* or *S*-2-[(*o*-hydroxyphenyl)-methylideneamino]-2-phenylethanol ligands which impart their chirality on the cluster, $[Fe_4(L')_6]$.[27–29] Varying the substituents on the ligands allows tuning of the magnetic relaxation barrier (U_{eff}) from 0.5–11.0 K.[29] As with $[Fe_4(dpm)_6(L)_2]$, subtle differences in the Fe coordination spheres are responsible for the differing magnetic properties.

Similar stars are formed using the O,N,O donor ligand *N*-methyldiethanolamine (*N*-Me-dea). The star forms by self-assembly of $[Fe(N\text{-Me-dea})_2]^-$ around Fe^{III} to give $[Fe\{Fe(N\text{-Me-dea})_2\}_3]$ with U_{eff} = 14.2 K.[30,31] In an analogous way, Takahashi *et al.*, in an attempt to make spin crossover hybrid materials, instead isolated $[Fe\{Fe(phsal)_2\}_3]$ (phsal = *N*-(2-hydroxyphenyl)-salicylaldimine).[32] Despite its structural similarity to the stars above, it is not a SMM.

In our continuing interest in tridentate N_2O donor ligands we selected 2-((1*H*-imidazol-2-yl)methyleneamino)phenol (2-H_2imap)[33] with the aim of preparing Fe^{III} spin crossover complexes. Unexpectedly, the primary product is a unique mixed-valence Fe^{II}–Fe^{III} star. Herein, we report the structure, magnetic and spectroscopic properties of $[Fe_4(2\text{-Himap})_6][NO_3]_3$ **1**.

Complex **1** was synthesized by layering a MeOH solution of $Fe(NO_3)_3{\cdot}9H_2O$ on top of a warmed solution of the ligand, 2-H_2imap and NEt_3 (see ESI† for details). After one week black crystals of the self-assembled cluster $[Fe_4(2\text{-Himap})_6][NO_3]_3$ **1** are formed. Temperature and time are critical in isolating the cluster, as heating above 40 °C or harvesting the crystals too early gives the Fe^{III} monomer, $[Fe(2\text{-Himap})_2]NO_3{\cdot}0.7MeOH$ **2** (Fig. S1, S2, S8 and Table S1†). IR spectroscopic studies of **1** and **2** reveal imine and nitrate stretches in the expected posi-

[a]*Functional Materials and Nanotechnology Centre of Excellence, Walailak University, Thasala, Nakhon Si Thammarat, 80160, Thailand. E-mail: hdavid@mail.wu.ac.th*
[b]*School of Chemistry, Monash University, Clayton, Victoria, 3800, Australia*
[c]*School of Chemistry and Photon Science Institute, The University of Manchester, Oxford Road, Manchester M13 9PL, UK*
[d]*Florida State University, Department of Physics, Tallahassee, FL 32306, USA*
[e]*National High Magnetic Field Laboratory, 1800 E. Paul Dirac Drive, Tallahassee, FL 32310, USA*
[f]*Department of Chemistry, University of Sheffield, Sheffield, S3 7HF, UK*
[g]*Department of Chemistry & MacDiarmid Institute for Advanced Materials and Nanotechnology, University of Otago, PO Box 56, Dunedin, 9054, New Zealand*
[h]*School of Chemistry, Bio21 Molecular Science and Biotechnology Institute, 30 Flemington Road, The University of Melbourne, Parkville, Victoria 3010, Australia*

†Electronic supplementary information (ESI) available: Experimental details, crystallographic details & figures, magnetic fits and CASSCF-SO calculations details, Mössbauer and EPR spectroscopic figures. CCDC 1830689 and 1830690. For ESI and crystallographic data in CIF or other electronic format see DOI: 10.1039/c8dt01241e

‡Now at: Department of Chemistry, Faculty of Science, Rangsit University, Phaholyothin Rd., Muang, Pathum Thani, 12000, Thailand

Published on 30 April 2018. Downloaded by University of Bath on 03/05/2018 11:19:01.

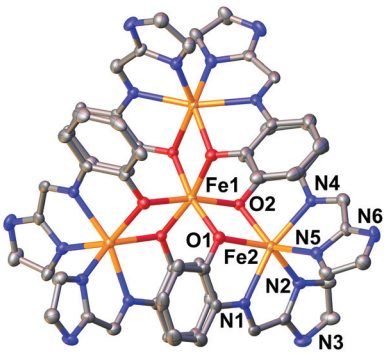

Fig. 1 View of the star shaped cluster $[Fe_4(2\text{-Himap})_6][NO_3]_3$. Hydrogen atoms are omitted for clarity.

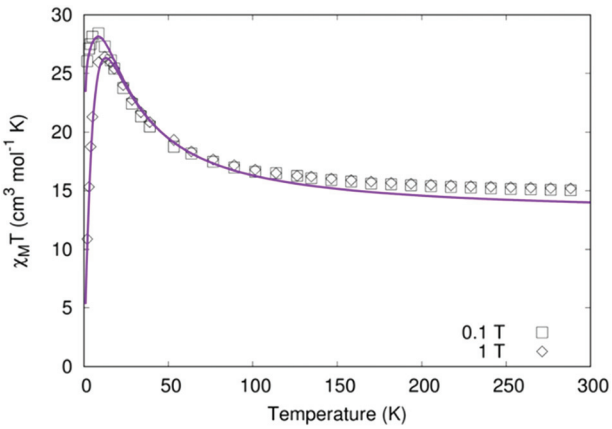

Fig. 2 $\chi_M T$ *vs.* T plot of **1**. The purple lines represent the best fit (D = −7.09 cm^{-1}) with the parameters given in the text.

tions, with $\nu_{C=N}$ being 18 cm^{-1} lower in **2** than for **1**. A similar difference in the imine stretch is observed in the Co^{II}/Co^{III} redox pair $[Co(2\text{-Himap})_2]^{0/+}$.[34] X-ray crystallography reveals that **1** is a star shaped cluster crystallizing in cubic $Pa\bar{3}$ (Fig. 1). PXRD studies indicate that the single crystal structure is representative of the bulk material and ESI-MS studies in MeOH indicate that the cluster is stable in solution (see ESI, Fig. S4 and S5†). The Fe1–O bond lengths are between 1.998–2.005(3) Å while the Fe2–N/O bond distances are much longer, 2.133–2.184(4) Å. This is consistent with the Fe1 and Fe2 centres being Fe^{III} and Fe^{II} respectively. This is, to the best our knowledge, the first example of a mixed-valence Fe star cluster. The Fe1···Fe2 distance is 3.225 Å, while the Fe2···Fe2* distance is 5.586 Å and these are similar to the equivalent distances in other Fe^{III}_4 stars. Each molecule is chiral due to intramolecular π–π interactions between the 2-Himap ligands (Fig. S3†), but as both enantiomers are present the structure overall is achiral.

Mössbauer spectra of **1** were recorded at multiple temperatures and show the presence of two subspectra above 20 K; a quadrupole doublet consistent with HS Fe^{II} and a singlet assigned to the HS Fe^{III} centre (Fig. S6 and Table S2†). The ratio of the intensity of the two species is ~2 : 1, which is lower than the expected 3 : 1 ratio. We believe this is due to differing Lamb–Mössbauer factors of the Fe^{II} and Fe^{III} centres causing the relative intensities of the two species to not be equivalent, particularly at higher temperatures.[35]

As the temperature is lowered the signals broaden, demonstrated by the temperature dependence of the full-width-at-half-maximum (FWHM) values for the transitions (Γ, Fig. S7d†). Below ~15 K, the Fe^{III} signal undergoes intermediate relaxation and broadens, but does not completely collapse into the baseline. In contrast, the Fe^{II} signal remains visible as a distinct quadrupole doublet at all investigated temperatures; these changes mirror the magnetic transition (*vide infra*).

Magnetic measurements for **1** show $\chi_M T$ = 15.02 cm^3 K mol^{-1} at 300 K with $\chi_M T$ increasing slowly to a maximum of 28.43 cm^3 K mol^{-1} at *ca.* 8 K before decreasing rapidly (Fig. 2). The $\chi_M T$ value at 300 K is consistent with one non-interacting Fe^{III} and three non-interacting Fe^{II} centres, and the low temperature data shows evidence of a ferromagnetically coupled ground state. The minor temperature dependence of $\chi_M T$ above 150 K suggests that the intramolecular magnetic interactions are relatively weak; this, coupled with the presence of a possible orbital contribution to the magnetic moment of high-spin octahedral Fe^{II} centres make the interpretation of the magnetic data fraught with difficulty. In order to get some insight into the local magnetic properties of the Fe^{II} sites to inform our interpretation, we have performed complete active space self-consistent field spin–orbit (CASSCF-SO) calculations (see ESI† for details). These show that the Fe^{II} sites are well-described as S = 2, however are subject to a significant axial zero-field splitting (ZFS, $D \sim -17$ cm^{-1}, $|E/D| \sim 0.12$), which arises from close-lying orbitally degenerate states. Interestingly, the main anisotropic axis for each of the Fe^{II} centres lies perpendicular to the plane of the Fe_4 cluster, and points towards the central Fe^{III} centre along a near-two-fold symmetry axis (Fig. S13†). Given the significant ZFS of the Fe^{II} centres and possibly weak magnetic exchange, it is important to consider the non-collinearity of the local anisotropy axes. Therefore to model our data, we employ the following spin Hamiltonian in PHI:[36]

$$\begin{aligned}\hat{H} = &-2J_1\hat{S}_1\cdot(\hat{S}_2+\hat{S}_3+\hat{S}_4) - 2J_2(\hat{S}_2\cdot\hat{S}_3+\hat{S}_3\cdot\hat{S}_4+\hat{S}_4\cdot\hat{S}_2)\\ &+D\left(\hat{S}_{z_2}{}^2+\hat{S}_{z_3}{}^2+\hat{S}_{z_4}{}^2-\frac{1}{3}(\hat{S}_2{}^2+\hat{S}_3{}^2+\hat{S}_4{}^2)\right)\\ &+g\mu_B(\hat{S}_1+\hat{S}_2+\hat{S}_3+\hat{S}_4)\cdot B\end{aligned}$$

here, $\hat{S}_1$ is the spin operator for S = 5/2 of Fe^{III}, $\hat{S}_{2-4}$ are the spin operators for S = 2 Fe^{II}, J_1 and J_2 represent the magnetic coupling between the central Fe^{III} and peripheral Fe^{II} centres (Fe1–Fe2), and the peripheral Fe atoms (Fe2–Fe2), respectively. g is the isotropic g-factor for the cluster, B is the applied magnetic field, and D is the single-ion axial ZFS of the Fe^{II} sites (we ignore E as CASSCF-SO predicts only a small rhombicity); we have rotated the local z-axis of each Fe^{II} site to point towards the central Fe^{III} ion, thus $\hat{S}_{z_{2-4}}$ are non-collinear. There are two possible solutions obtained when fitting the $\chi_M T$ and M *vs.* B

This journal is © The Royal Society of Chemistry 2018

Published on 30 April 2018. Downloaded by University of Bath on 03/05/2018 11:19:01.

data simultaneously: one with $D < 0$ (as suggested by CASSCF-SO) and one with $D > 0$. The former gives J_1 = +2.77 cm^{-1}, J_2 = −0.675 cm^{-1}, g = 1.96 and D = −7.09 cm^{-1} (Fig. 2 and S10, 11†); while the latter gives J_1 = + 2.62 cm^{-1}, and J_2 = −0.738 cm^{-1}, g = 2.03 and D = +14.0 cm^{-1} (Fig. S9–11†). Both solutions agree on the nature of the exchange interactions, where we see a weak ferromagnetic exchange between the Fe^{II} and Fe^{III} centres; antiferromagnetic coupling is observed in the related Fe^{III}_4 clusters. While the solution with $D > 0$ appears to model the high temperature $\chi_M T$ data better than the $D < 0$ solution, the low temperature magnetisation data (which is more sensitive to the details of the electronic structure) is better accounted for by the $D < 0$ solution; as $D < 0$ is also suggested by CASSCF-SO, we believe this to be the more likely description.

Given the ferromagnetic ground state and large anisotropy, we conducted ac susceptibility measurements to see if **1** showed slow magnetization relaxation and SMM behaviour. Plots of the out-of-phase susceptibilities, χ''_M, as a function of ac frequency showed zero values in zero applied dc field; however frequency dependent "tails" were noted below 5 K in a static dc field of 3000 Oe; Fig. S12.† This is in contrast with the S = 5 ground state $[Fe^{III}_4(L)_2(dpm)_6]$ stars, L = alkoxide(3-),[18] for which frequency dependent maxima in χ''_M were observed in zero dc field. Thus, our data indicate a lower U_{eff} barrier for **1** compared to the Fe^{III}_4 family of 3.5–17 K.

Variable temperature, multi-high-field/frequency EPR measurements were performed on a constrained powder of **1**.[37] Fig. 3 shows a series of field-swept dI/dB spectra recorded at different frequencies in the range from 53 to 648 GHz, and a temperature of 5 K. Meanwhile, Fig. S14† plots the positions of the features in the spectra that disperse strongly with magnetic field. These can be divided into two groupings: the first set of resonances lie on a straight line that has a slope corresponding a g-value of 2.004 ± 0.004, with zero offset (±4 GHz) on the frequency axis; the second grouping of two broad resonances observed at the highest frequencies lie on straight lines that have identical zero-field intercepts of 344 ± 4 GHz, and slopes corresponding to g-values of 1.66 ± 0.05 and 2.61 ± 0.06.

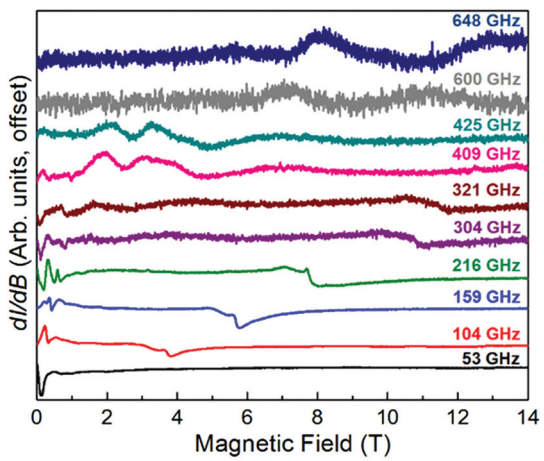

Fig. 3 Normalized high-field EPR spectra on a constrained powder of **1**; the spectra were recorded in derivative mode, dI/dB (where I is the absorption intensity), using field modulation and lock-in detection. All measurements were performed at 5 K.

The g = 2.004 resonance consists of a sharp inflection superimposed on a broader shoulder. Such a signal suggests a weakly anisotropic species, most likely corresponding to S = 5/2 Fe^{III} with an isotropic d^5 electronic configuration.[38] Were such a signal to originate from the Fe^{III} constituent within the Fe_4 cluster, it would imply essentially no exchange coupling to the Fe^{II} centres. On the basis of the magnetic measurements, we feel that this scenario is highly unlikely. Consequently, we attribute the g = 2.00 signal to the Fe^{III} monomer **2** that is likely present in small quantities in the powder sample, which shows an isotropic magnetic moment (Fig. S8†). It is difficult to compare the intensity of this signal with the broad high-frequency components because they are never observed within the same frequency/field window. However, one must recall that the dI/dB traces correspond to the 2nd derivative of the actual spin susceptibility (proportional to the number of spins). Thus, isotropic g = 2.00 resonances are strongly amplified in the dI/dB traces relative to broad anisotropic ones (see below). Therefore, it is quite possible the level of contamination in the powder sample is below the 1% level, consistent with the PXRD studies (Fig. S5†).

We also comment on a series of reproducible features observed close to zero-field (below 1 T) at the lower frequencies (<320 GHz). The origin of these signals is not presently clear. Similar signals have been observed in samples that undergo magnetic ordering and, hence, strong changes in magnetization at low fields. Again, this is not consistent with the magnetic properties of **1**, therefore likely signifying additional minor contamination of the powder sample.

The considerable zero-field splitting (ZFS) associated with the broad high-frequency signals is indicative of an appreciable magnetic anisotropy. Therefore, we associate these excitations with the coupled Fe_4 cluster **1**. Indeed, the coincidence of the zero-field offsets, and the temperature dependence of the two resonances suggest that they both originate from the ground state of the molecule. The reason there are two resonances is because the measurement was performed on a powder, *i.e.* they originate from different crystallite orientations within the powder, corresponding to turning points in the orientation dependence of the anisotropic EPR spectrum. As such, the unique zero-field intercept corresponds to the gap between the ground and first excited spin projection states of the cluster. Interestingly, simulations of the energy levels based on the $D < 0$ parameterization obtained from fits to the magnetic data suggest a ZFS of 300 GHz (10 cm^{-1}) from a set of six near-degenerate ground states to a set of six near degenerate excited states; this differs by only 13% from the value deduced by EPR measurements. Meanwhile, the $D > 0$ parameterization is completely inconsistent with the EPR results: simulations predict a ZFS of just 110 GHz (3.7 cm^{-1}) from the ground to first excited states. Therefore, the EPR measure-

Published on 30 April 2018. Downloaded by University of Bath on 03/05/2018 11:19:01.

ments strongly favour the negative D parameterization. Indeed, given the relatively low information content of the magnetic data and the level of approximation inherent in the model, agreement to within 13% is very good.

In conclusion we have prepared a unique mixed valence Fe^{II}–Fe^{III} tetranuclear star by self-assembly. The star shows weak ferromagnetic coupling between the central and peripheral Fe centres. The star is a weak field-induced SMM with magnetic, EPR and CASSCF-SO studies all suggesting $D = -7.09\ cm^{-1}$ at the peripheral Fe^{II} centres. Preliminary studies suggest that the outer Fe^{II} centres can be replaced with other metal ions and mixed metal stars of this type are now being pursued.

Conflicts of interest

There are no conflicts to declare.

Acknowledgements

We thank the Thailand Research Fund (RSA5580028 and RSA5880048), the Australian Research Council (DP140101013) and the Ramsay Memorial Trust (fellowship to NFC) for funding this research. We also thank the Thailand Research Fund for financial support in the form of a Royal Golden Jubilee scholarship to DS (PHD/0135/2554). A portion of this work was performed at the National High Magnetic Field Laboratory (NHMFL), which is supported by the NSF (DMR-1157490) and the State of Florida. SH also acknowledges the support from the NSF (DMR-1610226).

Notes and references

1 G. Christou, D. Gatteschi, D. N. Hendrickson and R. Sessoli, *MRS Bull.*, 2000, 66–71.
2 S. Dhers, H. L. C. Feltham and S. Brooker, *Coord. Chem. Rev.*, 2015, **296**, 24–44.
3 T. Glaser, *Chem. Commun.*, 2011, **47**, 116–130.
4 S. Goswami, A. K. Mondal and S. Konar, *Inorg. Chem. Front.*, 2015, **2**, 687–712.
5 K. S. Pedersen, J. Bendix and R. Clérac, *Chem. Commun.*, 2014, **50**, 4396–4415.
6 H. Miyasaka, M. Julve, M. Yamashita and R. Clérac, *Inorg. Chem.*, 2009, **48**, 3420–3437.
7 L. Rosado Piquer and E. C. Sañudo, *Dalton Trans.*, 2015, **44**, 8771–8780.
8 D. N. Woodruff, R. E. P. Winpenny and R. A. Layfield, *Chem. Rev.*, 2013, **113**, 5110–5148.
9 M. Affronte, *J. Mater. Chem.*, 2009, **19**, 1731.
10 L. Bogani and W. Wernsdorfer, *Nat. Mater.*, 2008, **7**, 179–186.
11 M. N. Leuenberger and D. Loss, *Nature*, 2001, **410**, 789–793.
12 R. E. P. Winpenny, *Angew. Chem., Int. Ed.*, 2008, **47**, 7992–7994.
13 A. Ardavan, O. Rival, J. J. L. Morton, S. J. Blundell, A. M. Tyryshkin, G. A. Timco and R. E. P. Winpenny, *Phys. Rev. Lett.*, 2007, **98**, 57201.
14 A. Cornia, M. Mannini, P. Sainctavit and R. Sessoli, *Chem. Soc. Rev.*, 2011, **40**, 3076–3091.
15 N. Domingo, E. Bellido and D. Ruiz-Molina, *Chem. Soc. Rev.*, 2012, **41**, 258–302.
16 M. Mannini, P. Sainctavit, R. Sessoli, C. Cartier dit Moulin, F. Pineider, M.-A. Arrio, A. Cornia and D. Gatteschi, *Chem. – Eur. J.*, 2008, **14**, 7530–7535.
17 A. L. Barra, A. Caneschi, A. Cornia, F. De Fabrizi Biani, D. Gatteschi, C. Sangregorio, R. Sessoli and L. Sorace, *J. Am. Chem. Soc.*, 1999, **121**, 5302–5310.
18 S. Accorsi, A.-L. Barra, A. Caneschi, G. Chastanet, A. Cornia, A. C. Fabretti, D. Gatteschi, C. Mortalo, E. Olivieri, F. Parenti, P. Rosa, R. Sessoli, L. Sorace, W. Wernsdorfer and L. Zobbi, *J. Am. Chem. Soc.*, 2006, **128**, 4742–4755.
19 A. Cornia, A. C. Fabretti, P. Garrisi, C. Mortalò, D. Bonacchi, D. Gatteschi, R. Sessoli, L. Sorace, W. Wernsdorfer and A.-L. Barra, *Angew. Chem., Int. Ed.*, 2004, **43**, 1136–1139.
20 M. Mannini, F. Pineider, P. Sainctavit, C. Danieli, E. Otero, C. Sciancalepore, A. M. Talarico, M.-A. Arrio, A. Cornia, D. Gatteschi and R. Sessoli, *Nat. Mater.*, 2009, **8**, 194–197.
21 M. Mannini, F. Pineider, C. Danieli, F. Totti, L. Sorace, P. Sainctavit, M.-A. Arrio, E. Otero, L. Joly, J. C. Cezar, A. Cornia and R. Sessoli, *Nature*, 2010, **468**, 417–421.
22 F. Pineider, M. Mannini, C. Danieli, L. Armelao, F. M. Piras, A. Magnani, A. Cornia and R. Sessoli, *J. Mater. Chem.*, 2010, **20**, 187–194.
23 S. Ninova, V. Lanzilotto, L. Malavolti, L. Rigamonti, B. Cortigiani, M. Mannini, F. Totti and R. Sessoli, *J. Mater. Chem. C*, 2014, **2**, 9599–9608.
24 M. J. Rodriguez-Douton, M. Mannini, L. Armelao, A.-L. Barra, E. Tancini, R. Sessoli and A. Cornia, *Chem. Commun.*, 2011, **47**, 1467–1469.
25 G. G. Condorelli, A. Motta, G. Pellegrino, A. Cornia, L. Gorini, I. L. Fragalà, C. Sangregorio and L. Sorace, *Chem. Mater.*, 2008, **20**, 2405–2411.
26 P. Erler, P. Schmitt, N. Barth, A. Irmler, S. Bouvron, T. Huhn, U. Groth, F. Pauly, L. Gragnaniello and M. Fonin, *Nano Lett.*, 2015, **15**, 4546–4552.
27 Y.-Y. Zhu, X. Guo, C. Cui, B.-W. Wang, Z.-M. Wang and S. Gao, *Chem. Commun.*, 2011, **47**, 8049–8051.
28 Y.-Y. Zhu, T.-T. Yin, S.-D. Jiang, A.-L. Barra, W. Wernsdorfer, P. Neugebauer, R. Marx, M. Dörfel, B.-W. Wang, Z.-Q. Wu, J. Van Slageren and S. Gao, *Chem. Commun.*, 2014, **50**, 15090–15093.
29 Y.-Y. Zhu, C. Cui, K. Qian, J. Yin, B.-W. Wang, Z.-M. Wang and S. Gao, *Dalton Trans.*, 2014, **43**, 11897–11907.
30 R. W. Saalfrank, I. Bernt, M. M. Chowdhry, F. Hampel and G. B. M. Vaughan, *Chem. – Eur. J.*, 2001, **7**, 2765–2769.
31 R. W. Saalfrank, A. Scheurer, I. Bernt, F. W. Heinemann, A. V. Postnikov, V. Schünemann, A. X. Trautwein,

 This journal is © The Royal Society of Chemistry 2018

M. S. Alam, H. Rupp and P. Müller, *Dalton Trans.*, 2006, 2865–2874.
32 K. Takahashi, K. Kawamukai, T. Mochida, T. Sakurai, H. Ohta, T. Yamamoto, Y. Einaga, H. Mori, Y. Shimura, T. Sakakibara, T. Fujisawa, A. Yamaguchi and A. Sumiyama, *Chem. Lett.*, 2015, **44**, 840–842.
33 J. Sanmartín-Matalobos, C. Portela-García, M. Fondo and A. M. García-Deibe, *Cryst. Growth Des.*, 2015, **15**, 4318–4323.
34 D. Sertphon, K. S. Murray, W. Phonsri, J. Jover, E. Ruiz, S. G. Telfer, A. Alkaş, P. Harding and D. J. Harding, *Dalton Trans.*, 2018, **47**, 859–867.
35 P. Gütlich, E. Bill and A. X. Trautwein, *Mössbauer Spectroscopy and Transition Metal Chemistry*, Springer-Verlag, Berlin/Heidelberg, 2011.
36 N. F. Chilton, R. P. Anderson, L. D. Turner, A. Soncini and K. S. Murray, *J. Comput. Chem.*, 2013, **34**, 1164–1175.
37 A. Hassan, L. Pardi, J. Krzystek, A. Sienkiewicz, P. Goy, M. Rohrer and L.-C. Brunel, *J. Magn. Reson.*, 2000, **142**, 300–312.
38 R. J. Holmberg, T. Burns, S. M. Greer, L. Kobera, S. A. Stoian, I. Korobkov, S. Hill, D. L. Bryce, T. K. Woo and M. Murugesu, *Chem. – Eur. J.*, 2016, **22**, 7711–7715.

Published on 30 April 2018. Downloaded by University of Bath on 03/05/2018 11:19:01.

Dalton Transactions

PAPER

Check for updates

Cite this: *Dalton Trans.*, 2018, **47**, 859

Slow relaxation of magnetization in a bis-*mer*-tridentate octahedral Co(II) complex†

Darunee Sertphon, ‡[a] Keith S. Murray, [b] Wasinee Phonsri, [b] Jesús Jover, [c] Eliseo Ruiz,[c] Shane G. Telfer, [d] Adil Alkaş,[d] Phimphaka Harding [a] and David J. Harding *[a]

Received 17th November 2017,
Accepted 11th December 2017

DOI: 10.1039/c7dt04335j

rsc.li/dalton

Reaction of a rigid tridentate ligand *o*-[(1*H*-imidazol-2-yl)methylideneamino]phenol (2-H_2imap) with $Co(ClO_4)_2$ in the presence of NaN_3, or $Co(NO_3)_2$ without a base yields $[Co^{II}(2\text{-Himap})_2]$ **1** and $[Co^{III}(2\text{-Himap})_2]NO_3{\cdot}MeOH$ **2**, respectively. Both complexes exhibit a *mer*-octahedral geometry with the cobalt centre being distorted along an octahedral-trigonal prismatic pathway. The packing in **1** and **2** is dominated by H-bonding forming 2D sheets and 1D chains, respectively. Detailed *dc* and *ac* magnetic studies indicate that **1** is a field-induced single-ion magnet (SIM) with D = 36.7 cm^{-1} and E = 2.0 cm^{-1}. Extensive *ab initio* calculations support these conclusions and suggest that relaxation of the magnetization occurs principally through direct quantum tunnelling in the ground state, with the Raman process dominant in an applied field. This contrasts with the recently reported series of *mer*-$[Co(L)_2]$ (L = monoanionic NNO donor ligand; *Inorg. Chem.*, 2017, **56**, 6056–6066) complexes where D is negative, as these compounds have a more ambiguous geometry, and highlights the importance of supramolecular interactions in subtly altering the coordination sphere thereby impacting the magnetic behaviour.

Introduction

Single molecule magnets are compounds which exhibit slow relaxation of their magnetism of purely molecular origin.[1] They were first discovered in the 1990s and have been extensively investigated as they have a myriad of potential applications.[2–5] Much of the early work focused on metal clusters with the aim of increasing the total spin as the barrier to spin reversal (U_{eff}) depends directly on that term: $U_{eff} = |D|S^2$, where S = the total spin of the complex and D is the axial zero-field splitting (zfs) parameter; when S is a half-integer $U_{eff} = |D|(S^2 - \frac{1}{4})$. While this was successful to some degree many of these larger spin systems still exhibited low barriers due to very small D values. In 2003, Ishikawa and co-workers discovered that the double decker complexes $[LnPc_2][NBu_4]$ (Ln = Tb,Dy) exhibit slow magnetic relaxation, with the Tb(III) complex having a barrier of 230 cm^{-1}.[6] These systems came to be known as single-ion magnets (SIMs)[7–9] and have driven much of the recent research in molecular magnetism. Indeed, very recently a Dy SIM was reported with an impressive blocking temperature of 60 K,[10,11] tantalizingly close to liquid nitrogen temperatures which could make high density data storage a reality with SIMs.

Prior to the advent of single molecule magnetism, cobalt(II) systems were some of the first complexes to be investigated for their ligand field splittings and spin–orbit coupling by Figgis *et al.*[12,13] and Gerloch *et al.*[14] These studies accounted not only for average susceptibility measurements on powders, but also explored single crystal anisotropy, generally measured at temperatures above 77 K by *dc* measurements. Cobalt(II) complexes remain interesting targets as SIMs due to the strong spin–orbit coupling of the metal ion that can, in combination with ligand field effects, lead to high magnetic anisotropy particularly in the orbitally degenerate $^4T_{1g}$ (parent) ground state octahedral species. The first Co(II) SIMs reported were distorted square pyramidal $[\{(2,6\text{-}iPr_2\text{-}PhN{=}CR)_2py\}Co(NCS)_2]$ complexes {R = Me, Ph} in which the Co(II) sitting above the basal plane is vital for observation of SMM behaviour.[15] Shortly afterwards, Long and coworkers reported the complex $[PPh_4]_2[Co(SPh)_4]$ that exhibits D = −70 cm^{-1} and U_{eff} = 21 cm^{-1}.[16] This was the

[a]*Functional Materials and Nanotechnology Centre of Excellence, Walailak University, Thasala, Nakhon Si Thammarat, 80160, Thailand. E-mail: hdavid@mail.wu.ac.th; www.funtechwu.com*
[b]*School of Chemistry, Monash University, Clayton, Victoria, 3800, Australia*
[c]*Departament de Química Inorgànica and Institut de Química Teòrica i Computacional, Universitat de Barcelona, Diagonal 645, E-08028 Barcelona, Spain*
[d]*MacDiarmid Institute for Advanced Materials and Nanotechnology, Institute of Fundamental Sciences, Massey University, Palmerston North, New Zealand*

†Electronic supplementary information (ESI) available: IR and NMR spectra, $\chi_M T$ *vs.* T and M *vs.* H plots, and extra simulations are included. CCDC 1585229 and 1585230. For ESI and crystallographic data in CIF or other electronic format see DOI: 10.1039/c7dt04335j

‡Now at Department of Chemistry, Faculty of Science, Rangsit University, 52/347 Phahonyothin Rd., Muang, Pathum Thani, 12000, Thailand.

first Co(II) SIM to show slow relaxation of magnetization in zero field. Since then a range of tetrahedral systems has been explored and a very diverse range of D values −5 to −160 cm^{-1} and relaxation barriers (14–230 cm^{-1}) has been found. In general, these systems show that use of heavier donor atoms such as S, Se, P or I increases the magnetic anisotropy.[17–21] Geometry is also important, the tight bite angle of the ligand in the tetrahedral Co(II) SIM $[NHEt_3]_2[Co(pdms)]$ {pdms = 1,2-bis(methanesulfonamido)benzene} provides significant axial distortion at the Co(II) centre, leading to large magnetic anisotropy and a relatively high barrier of 230 cm^{-1}.[22] More recently, the linear system [(NHC)Co(NDmp)] (NHC = N-heterocyclic carbene; dmp = dimesitylphenyl), has been reported to have a relaxation barrier as high as 413 cm^{-1}; a new record in transition metal based SIMs.[23]

In contrast to tetrahedral Co(II) SIMs, octahedral systems are much rarer (Table 1), with the first one reported in 2012 by Cano, Pardo and coworkers.[24] Remarkably, in their *cis*-$[Co(dmphen)_2(NCS)_2]$ complex (dmphen = 2,9-dimethyl-1,10-phenanthroline) the value of D was positive (+98 cm^{-1}), implying that the slow relaxation observed is due to transverse, or easy plane (xy) anisotropy. Since then a number of other octahedral systems have been investigated and nearly all of them show positive D values, with the magnitude dependent on the ligands used, the degree of distortion and the *cis* or *trans* geometry adopted by the cobalt centre.[25–35] Nevertheless, the explanation for the occurrence of SMM behaviour, despite positive D parameters, is still not fully understood.[36] Moreover, in employing *mer*-directing ligands Powell *et al.* were able to reverse the sign of D as a result of distortion towards a trigonal prismatic geometry.[37] In trying to better understand the different factors which favour one relaxation mechanism over another in Co(II) SIMs we now report a Co(II) SIM, $[Co(2\text{-}Himap)_2]$ **1**, with a rigid tridentate tight bite angle ligand.

Table 1 Selected examples of octahedral Co(II) complexes with positive D values

Complex	D	U_{eff}/K (H, Oe)	Ref.
cis-$[Co(dmphen)_2(NCS)_2]$	+98	22.9 (2500)	24
$[Co(\mu\text{-}L)(\mu\text{-}OAc)Y(NO_3)_2]$	+47	15.7 (1000)	25
$[Co(abpt)_2(tcm)]$	+48	86.2 (3000)	26
$[Co(acac)_2(H_2O)_2]$	+57	22.6 (various)	36
$[Co(9Accm)_2(py)_2]$	+74	Not given (500)	27
$[Co(9Accm)_2(bipy)]$	+24	Not given (700)	27
$[Co(bpy)_2(ClAn)]\cdot EtOH$	+65.9	16.6 (600)	28
$NEt_4[Co(hfac)_3]$	+118	19.5 (1000)	29
$[Co(pydm)_2][dnbz]_2$	+44	39.0 (400)	33
$[Co(bzpy)_4X_2]$	+106 (X = Cl)		34
	+90.5 (X = NCS)	27.7 (400)	
$[Co(dppm^{O,O})_3][CoBr_4]$	+147	Not given (4000)	35

dmphen = 2,9-dimethyl-1,10-phenanthroline; L = *N*,*N*′,*N*″-trimethyl-*N*,*N*″-bis(2-hydroxy-3-methoxy-5-methylbenzyl)diethylenetriamine; abpt = 4-amino-3,5-bis(2-pyridyl)-1,2,4-triazole; tcm = tricyanomethanide anion; 9Accm = 1,7-bis(9-anthryl)-1,6-heptadiene-3,5-dionate; Cl-An = chloranilate; bzpy = 4-benzylpyridine; $dppm^{O,O}$ = bis(diphenylphosphanoxido)methane; pydm = 2,6-pyridinedimethanol; dnbz = 3,5-dinitrobenzoato; hfac = hexafluoroacetylacetonate.

Results and discussion

Basic characterization and structural studies

The compound, $[Co(2\text{-}Himap)_2]$ **1** was prepared by diffusion of a solution of $Co(ClO_4)_2$ into a solution of the ligand 2-H_2imap[38] with NaN_3 added as a base. The choice of cobalt starting material and base were found to be critical in isolating **1** with $Co(NO_3)_2$ yielding instead the Co(III) compound $[Co(2\text{-}Himap)_2]NO_3\cdot MeOH$ **2** (Scheme 1).

IR spectroscopic studies indicate a strong similarity between the compounds with the imine stretch at 1587 and 1579 cm^{-1} for **1** and **2**, respectively (Fig. S1†). These values are a little lower than those previously reported by Sanmartín-Matalobos *et al.* in $[M(2\text{-}Himap)_2M(2\text{-}H_2imap)_2]^{2+}$ (M = Ni, Cu; 1610–1614 cm^{-1}).[38] The nitrate band is visible only in **2** at 1384 cm^{-1}. ^1H NMR spectroscopic studies of **2** in d^6-DMSO (Fig. S2 in the ESI†) show the typical sharp peaks of diamagnetic Co(III) in the aromatic region attributable to the 2-Himap ligand while the peak at 3.18 ppm is due to the MeOH that crystallizes in the lattice (*vide infra*).

Complex **1** crystallizes in the orthorhombic space group *Pbcn*, while complex **2** crystallizes in the triclinic group $P\bar{1}$. The structures were determined at 296 and 123 K, for **1** and **2** respectively. Crystallographic data are given in Table 2 and the relevant Co–N/O bond lengths and angles are shown in Table 3. The Co–N/O bond lengths are typical for high spin Co(II) in **1**.[28] In contrast, the bond lengths in **2** are on average 0.166 Å (Co–O) and 0.205 Å (Co–N) shorter than those in **1**, indicating that the metal centre is low spin Co(III). This is also confirmed by the octahedral distortion parameters[39,40] which show that **2** has a much more regular octahedral coordination (SHAPE[41] S-O_h parameter for **2** = 0.74) environment than **1** (see Fig. 1). The angle between the two ligands is almost 90° in both compounds and, in the case of **1**, is similar to that found in the related *mer*-$[Co(L)_2]$ systems, (L = monoanionic NNO donor ligands based on 6-hydroxymethyl-pyridin-2-ylcarboxaldehyde) reported by the Powell group.[37] SHAPE analysis[41] shows that **1** is distorted along the octahedral-trigonal prismatic pathway but is closer to octahedral (S-O_h = 3.25) than it is to trigonal prismatic geometry (S-D_{3h} = 9.50). This differs from *mer*-

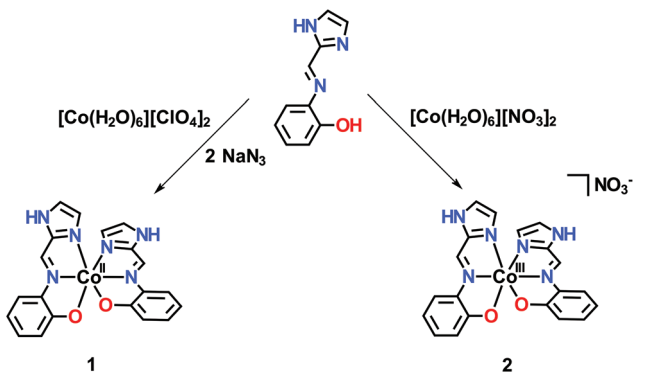

Scheme 1 Synthesis of $[Co(2\text{-}Himap)_2]$ **1** and $[Co(2\text{-}Himap)_2]NO_3$ **2**.

This journal is © The Royal Society of Chemistry 2018

Table 2 Crystallographic data and structure refinement for **1** and **2**

	1	2
Formula	$C_{20}H_{16}CoN_6O_2$	$C_{21}H_{20}CoN_7O_6$
Molecular weight/g mol^{-1}	431.32	525.36
Crystal system	Orthorhombic	Triclinic
Space group	*Pbcn*	*P*$\bar{1}$
a/Å	11.8110(7)	8.4486(5)
b/Å	9.2017(5)	10.2104(7)
c/Å	17.5762(9)	12.8436(9)
α/°	90.00	96.875(7)
β/°	90.00	98.442(7)
γ/°	90.00	101.045(7)
T/K	296	123
Cell volume/Å^3	1910.20(18)	1063.09(13)
Z	4	2
Absorption coefficient/mm^{-1}	0.928	6.836
Reflections collected	6022	6524
Independent reflections, R_{int}	1693, 0.062	2662, 0.0946
Max. and min. transmission	0.746, 0.685	1.00, 0.099
Restraints/parameters	0/136	43/317
Final *R* indices [$I > 2\sigma(I)$]: R_1, wR_2	0.0414, 0.1058	0.0934, 0.2337

Table 3 Selected bond lengths and octahedral distortion parameters (Å, °) for **1** and **2**

	1	2
Co1–O1	2.071(2)	1.897(4)
Co1–O20	—	1.924(6)
Co1–N1	2.070(3)	1.934(5)
Co1–N3	2.159(3)	1.892(6)
Co1–N20		1.950(7)
Co1–N22	—	1.885(6)
Co···Co	7.4862(3)	6.239(2)
		8.157(2)
Σ^a	103.4	49.3
Θ^b	321.4	165.3
Plane-to-plane	88.6	88.7

[a] $\Sigma = \sum_{i=1}^{12} |90 - \alpha_i|$, where α_i are the twelve *cis* N/O–Co–N/O angles.[39] [b] $\Theta = \sum_{i=1}^{24} |60 - \theta_i|$, where θ_i are the 24 unique N/O–Co–N/O angles measured on the projection of two triangular faces of the octahedron along their common pseudo-threefold axis.[40]

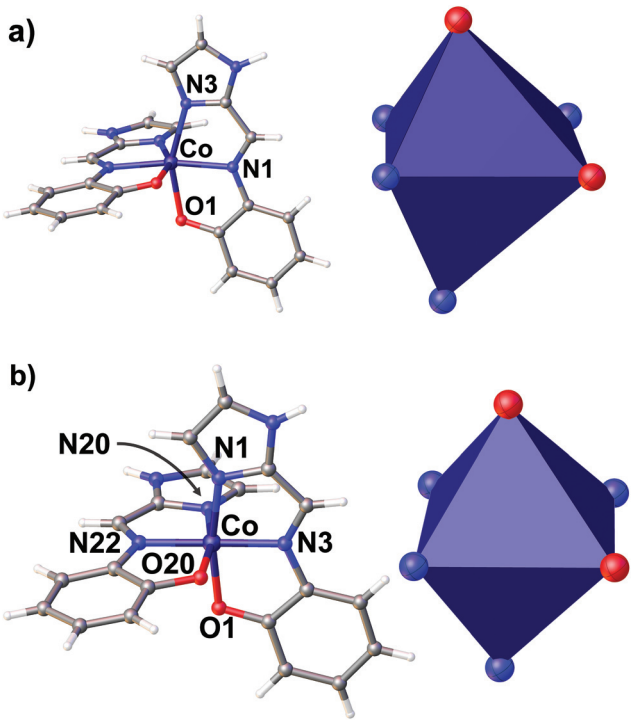

Fig. 1 View of the structures of (a) **1** and (b) **2** showing the key atom labels and the coordination polyhedra of the cobalt centres. Colour code: Co = purple, C = gray, N = blue, O = red.

[Co(L)$_2$] where the geometry is much more ambiguous and intermediate between octahedral and trigonal prismatic (S-O_h = 4.99–5.91; S-D_{3h} = 6.56–7.82) but closely mirrors the Co(II) centre in [Co(μ-L)(μ-OAc)Y(NO$_3$)$_2$].[25]

The individual Co(II) centres in **1** are linked by strong N–H···O hydrogen bonds (N2···O1 = 2.641(4) Å, N2–H2···O1 = 170.0°) involving the imidazole N–H and a phenoxy oxygen atom. The H-bond donors and acceptors are arranged to give a 2D sheet (see Fig. 2). An interesting feature of this structure is that the two [Co(2-Himap)$_2$] enantiomers self-sort into strips, with only one enantiomer present in each strip. This differs from the previously reported [Cd(2-Himap)$_2$] where the enantiomers are arranged into a 1D chain.[42] This difference seems to be due to the greater distortion at the Cd centre that permits π–π interactions which support the N–H···O hydrogen bonds.

The crystal packing of **2** is again dominated by hydrogen bonding this time between the nitrate counteranions, methanol molecules and the [Co(2-Himap)$_2$]$^+$ cations. In addition, there are now π–π interactions {plane-to-plane distance: 3.537(9) Å} which collectively link the [Co(2-Himap)$_2$]$^+$ cations into a 1D chain (Fig. 3). The 1D chains are then linked by C–H···O interactions involving the nitrate anion giving a strongly cooperative 3D supramolecular network.

Magnetic properties of [Co(2-Himap)$_2$]

Dc magnetic studies were undertaken on **1** between 2–300 K with applied fields of 0.1 T (2–70 K) and 1.0 T (2–300 K). These data are presented as $\chi_M T$ *vs.* *T* and magnetization isotherm *M* *vs.* *H* plots in Fig. S3 in the ESI.† The $\chi_M T$ values are independent of the applied field indicating a lack of magnetic impurity or Zeeman level population effects. At 300 K, $\chi_M T$ = 2.40 cm^3 mol^{-1} K and is significantly higher than the expected value of 1.875 cm^3 mol^{-1} K for an isolated *S* = 3/2 Co(II) where *g* = 2.0. This indicates a considerable orbital angular momentum contribution as expected in a $^4T_{1g}$ system that exhibits magnetic anisotropy. The $\chi_M T$ value for **1** is similar to that reported in other octahedral Co(II) complexes where $\chi_M T$ is in the range 2.30–3.05 cm^3 mol^{-1} K.[25–35] $\chi_M T$ values remain independent of temperature between 300 and ~100 K suggestive of a large distorted ligand field contribution, and spin–orbit coupling, which transform the $^4T_{1g}$ state into a lowest-energy $^4A_{2g}$ term (compressed tetragonal). Below 80 K $\chi_M T$ decreases rapidly reaching 1.30 cm^3 mol^{-1} K at 2 K which is also indicative of zfs

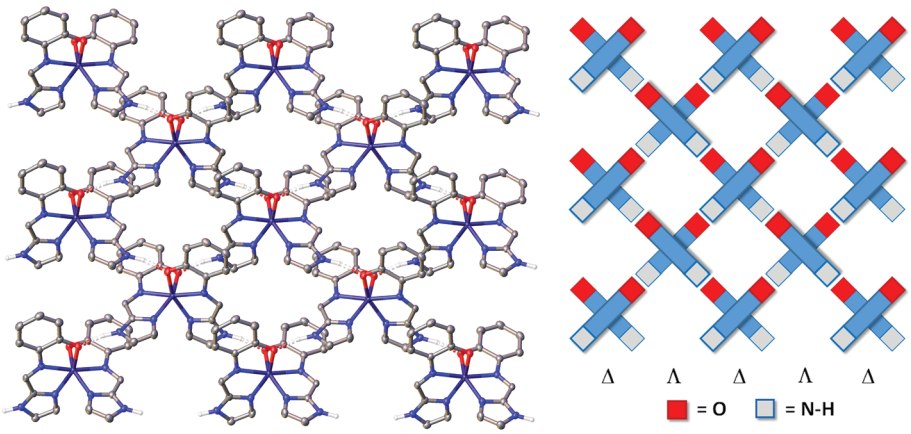

Fig. 2 View of the 2D H-bonding sheet in **1** (left) and a simplified representation of the packing motif (right).

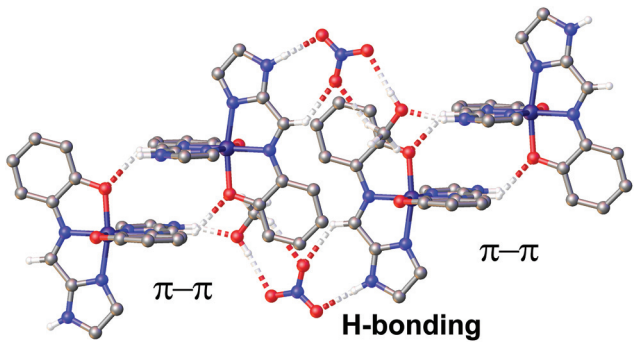

Fig. 3 View of the 1D chain formed by H-bonding and π–π interactions in **2**, for clarity selected H atoms have been removed.

of the $^4A_{2g}$ state, perhaps combined with remnant orbital degeneracy. The magnetization data reveal that the *M vs. H* curve at 2 K becomes almost saturated at higher fields with $M = 2.05N\beta$ at 2 K and 5 T. This is lower than the expected value for a $S = 3/2$ system where $g > 2.0$, probably because of spin–orbit coupling and magnetic anisotropy in **1**.

There are two approaches currently used to simultaneously fit the $\chi_M T$ *vs. T* and *M vs. H* plots. The first one assumes that zero field splitting is dominant and uses the giant spin Hamiltonian approach to obtain *D* (and *E*) and *g* values.[37] The second approach uses the Figgis approach[12,13] that yields ligand field splitting and spin–orbit coupling values.[32,35] We have used the spin Hamiltonian, shown below, with a spin of 3/2, in the program PHI[43]

$$H = D(S_z^2 - [S(S+1)/3]) + E(S_x^2 - S_y^2) + \mu_B S \cdot g \cdot H \quad (1)$$

where *D* is the axial zero field splitting (zfs) parameter; *E* is the rhombic zfs, μ_B the Bohr magneton, *H* is the applied dc field. The *g* values were either kept isotropic or anisotropic, although the latter option is more appropriate for a Co(II) complex. The fits were very good for both the $\chi_M T$ *vs. T* and the *M vs. H* plots at temperatures of 2, 3, 4 and 5.5 K; Fig. 4. The parameters obtained from the fits are: $D = +36.7$ cm^{-1}; $E = 2.0$ cm^{-1}; $g = 2.11, 2.48, 2.12$. The use of a negative *D* value gave unrealistic values of *E*, and thus this possibility can be discarded.

To better understand and quantify the magnetic anisotropy in **1** we undertook *ab initio* calculations using a multireference methodology; the computed second-order anisotropy parameters and excitation energies are collected in Table 4 ($\chi_M T$ *vs. T* and *M vs. H* plots from the simulations are shown in Fig. S4 and S5 in the ESI†). These values have been obtained from two different electronic structure calculations using the ORCA[44] and MOLCAS[45–47] software packages. ORCA produces two sets of results: CASSCF and CASSCF + NEVPT2 (which introduces the dynamic correlation effects), both including spin–orbit contributions. MOLCAS has been employed to provide CASSCF results, including spin–orbit effects that have been introduced with the SO-RASSI method. Positive, and similar, *D* values are found with the three methods, as expected for an octahedral Co(II) complex.[46] The best agreement with the experimental data is found with the ORCA/NEVPT2 calculation: $D = 39.3$ cm^{-1} and $E = 1.8$ cm^{-1}. In all cases, a 3/2 ground state is found before including spin–orbit effects. Under these conditions, the calculations show the existence of relatively low-lying spin–orbit free excited states (δ in Table 4) with energies around 1000–2000 cm^{-1} above the ground state, which may be responsible for the observed anisotropy. This is also confirmed by the anisotropic *g*-values for the ground state. Once spin–orbit effects are included a set of Kramers' doublets (KDs, Δ) is obtained; the three methods again produce very similar results, indicating a low-lying KD around 100 cm^{-1} above the ground state, which may participate in the spin relaxation processes (see below). The second KD is located at higher energies in all cases (1200–1800 cm^{-1}) and would not be expected to participate in the spin relaxation mechanism.

The sign and value of the *D* parameter can be rationalized using the spin–orbit operator, which couples the ground and excited states. When the excited state results from the excitation between orbitals with the same $|m_l|$ values, the $M_S = \pm 3/2$ components are stabilized and a negative contribution to *D* is obtained. However, an excitation between orbitals involving

 This journal is © The Royal Society of Chemistry 2018

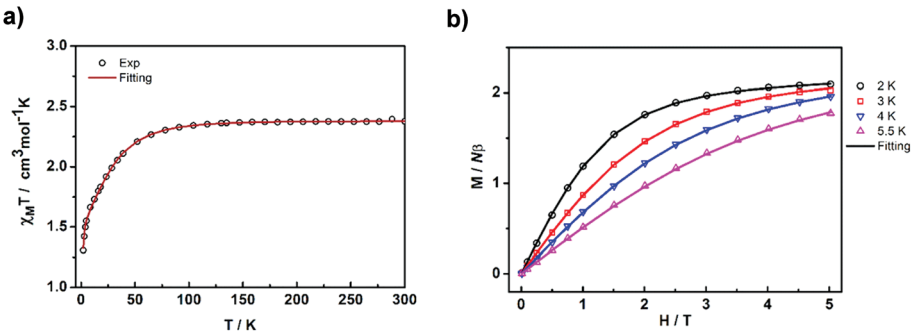

Fig. 4 Best fits of (a) $\chi_M T$ *vs.* *T* in field of 1 T and of (b) *M* *vs.* *H* isotherms using the ZFS Hamiltonian in program PHI[43] with the parameter set given in eqn (1).

Table 4 ORCA/CASSCF, ORCA/CASSCF + NEVPT2, and MOLCAS/CASSCF + RASSI computed *D*, |*E*|, and *g*-values for the ground state of **1**. δ and Δ are the computed first excitation energies before and after including the spin–orbit effects, respectively. The Δ-value corresponds to the energy difference between the ground and the first excited Kramers' doublets

Method	D_{calc} (cm^{-1})	$\|E\|_{calc}$ (cm^{-1})	δ (cm^{-1})	Δ (cm^{-1})	g_{xx}, g_{yy}, g_{zz}
ORCA/CASSCF	50.4	3.1	1339.8	101.3	2.03, 2.45, 2.53
ORCA/NEVPT2	39.3	1.8	1919.8	78.8	2.03, 2.36, 2.41
MOLCAS/CASSCF	48.2	2.8	1439.9	96.8	2.03, 2.45, 2.51

a $|\Delta m_l| = 1$ change, *i.e.* stabilizing the $M_S = \pm 1/2$ components, leads to a positive contribution to the *D* value.[48] **1** displays a distorted octahedral core, which produces the d-orbital splitting shown in Fig. 5. This orbital arrangement is obtained with the ORCA/CASSCF + NEVPT2 calculation by using the *ab initio* ligand field theory (AILF)[49,50] method. We find that the

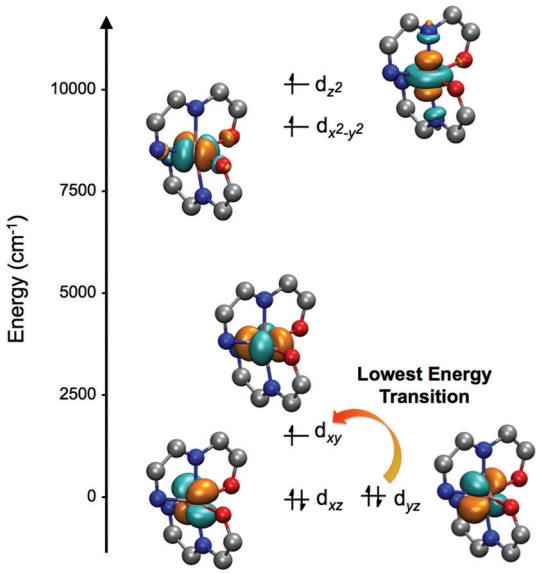

Fig. 5 AILF computed d-orbital splitting for **1** (orbital energies: d_{xz} 0.0 cm^{-1}, d_{yz} 83.9 cm^{-1}, d_{xy} 1573.4 cm^{-1}, $d_{x^2-y^2}$ 9066.1 cm^{-1}, d_{z^2} 10 150.2 cm^{-1}). Colour code: Co = pink, C = gray, N = blue, O = red; H atoms and parts of the 2-Himap ligand have been omitted for clarity.

degeneracy of the t_{2g} and e_g orbitals of the regular octahedron is broken in **1**, indicating the transformation of the initial octahedral $^4T_{1g}$ ground state into a lowest-energy $^4A_{2g}$ term, and one of the former clearly moves up in energy (1573.4 cm^{-1}), far from the last doubly occupied orbital (83.9 cm^{-1}). The AILF method allows the identification of these orbitals; the last doubly occupied orbital is d_{yz} (or d_{xz}, because these cannot be distinguished) while the first half-occupied orbital is d_{xy}; since these orbitals have a different $|m_l|$ value *i.e.* ±1 and ±2, respectively, the *D* value should be positive. This contrasts with the similar *mer*-[Co(L)$_2$] compounds which show negative *D* values.[37] The difference between the two systems is probably due to the greater distortion towards a trigonal prismatic geometry in *mer*-[Co(L)$_2$] when compared with **1**, and seems to be caused by H-bonding involving uncoordinated hydroxyl groups on the ligands.[37]

The dynamics of magnetization were investigated using *ac*-magnetic measurements. The data were recorded with an applied field of 0.2 T between 2–9 K and 50–1488 Hz (Fig. 6a). Under these conditions the out-of-phase magnetization shows a clear peak at higher frequencies, the signature of a single molecule magnet. As with many Co(II) SIMs at zero applied *dc* field there are no signals in the out-of-phase magnetization probably due to efficient quantum tunnelling and consistent with the calculations below.

The program CC-FIT [CC-FIT Copyright 2014, Nicholas F. Chilton] was used to fit the Cole–Cole plots (Fig. 6b) that showed semicircles at the lowest temperatures. The α values are 0.24 (1.8 K) to 0.07 (6 K) indicative of deviations from the Debye model and a range of distributions of the relevant relaxation processes. Usually, four mechanisms, as shown in eqn

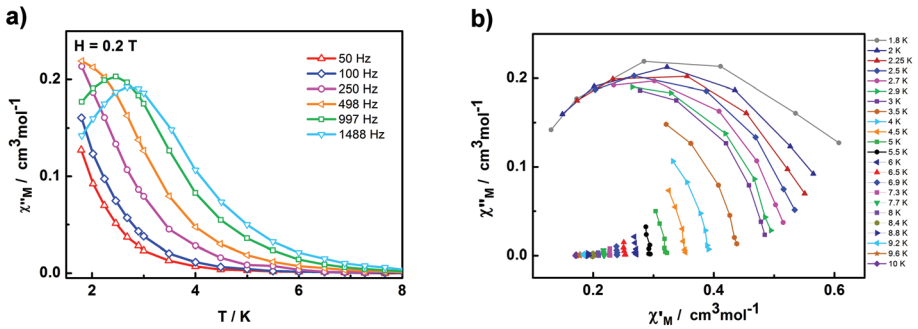

Fig. 6 (a) Variable-frequency out-of-phase components of the *ac* magnetic susceptibility and (b) Cole–Cole plot of **1** the solid lines being best fit.

(2) are considered, direct, quantum tunneling, Raman and Orbach:

$$\tau^{-1} = AH^4T + \frac{B_1}{1 + B_2H^2} + CT^n + \tau_0^{-1}\exp\left(\frac{-U_{\text{eff}}}{kT}\right) \qquad (2)$$

A common initial approach is to analyse the temperature dependence of the relaxation time τ values by plotting $\ln(\tau)$ against $1/T$ (see ESI, Fig. S6†). The best fit for **1** using only an Orbach term gives a U_{eff} value of 14 K. However, as D is calculated to be 39.3 cm^{-1} the barrier height, assuming a purely thermal relaxation pathway, should be 78.6 cm^{-1} ($2D$); this is considerably higher than the fitted barrier height. This indicates that the thermal Orbach mechanism is not the main contributor to the temperature dependence.[24,37,51] In fact, Co(II) SIMs with positive D and limited rhombicity that do exhibit Orbach relaxation are rare, with [Co(tpma)(NCMe)]BF_4 {tpma = tris(pyridylmethyl)amine} a recent example.[52]

The explanation for the occurrence of slow relaxation of magnetization with positive D values has recently been explained by a combination of a direct mechanism (due to the presence of very effective hyperfine coupling in an $I = 7/2$ Co(II) system), a Raman mechanism and a strong nuclear spin–lattice interaction which must also be taken into account.[36] In such a scenario, the temperature dependence of the spin relaxation time (see Fig. 7) can be described by a Raman term and a field-dependent mechanism contribution ${\tau_{\text{FDM}}}^{-1}$

$${\tau}^{-1} = {\tau_{\text{FDM}}}^{-1} + CT^n \qquad (3)$$

the best fit for **1** is with C = 19.12 s^{-1} $\text{K}^{-5.10}$ n = 5.10 and ${\tau_{\text{FDM}}}^{-1}$ 3685.1 s^{-1}. Although, n is smaller than the hypothetical n = 9 for a Kramers ion, the value is very similar to that reported for other easy-plane Co(II) complexes.[53]

The computed relative energies of the lowest-lying KDs and the spin relaxation pathways of **1**, obtained with the MOLCAS/CASSCF + RASSI calculation, are shown in Fig. 8. The spin relaxation mechanisms show a plausible pathway *via* direct quantum tunneling (QTM) in the ground state. The matrix elements of the transition magnetic moments found between states 1− and 1+ is 1.64, much higher than the required value of 0.1 associated with an efficient relaxation mechanism. The second KD may also be accessible (96.8 cm^{-1}) and should able

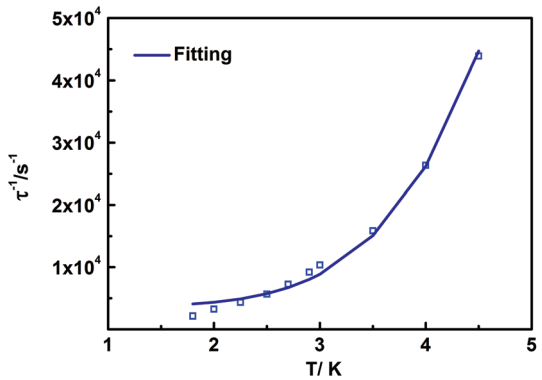

Fig. 7 Relaxation time *vs.* *T* plot and best fit as described using eqn (3) for **1** using *ac* χ''_{M} data in a *dc* field of 0.2 T.

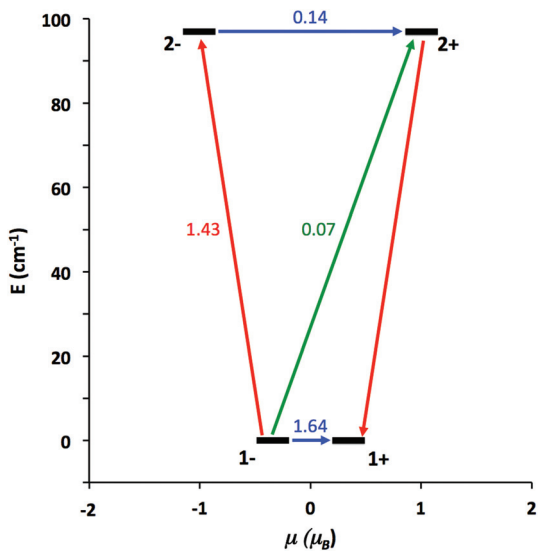

Fig. 8 Lowest two Kramers' doublets and *ab initio* computed relaxation mechanism in **1**. The thick black lines imply KDs as a function of their magnetic moment along the main anisotropy axis. Red lines indicate the magnetization reversal mechanism. The blue lines correspond to ground state QTM and thermally assisted-QTM *via* the first excited KD, and green and purple lines show the possible Orbach relaxation process. The values close to the arrows indicate the matrix elements of the transition magnetic moments (above 0.1 an efficient spin relaxation mechanism is expected).

 This journal is © The Royal Society of Chemistry 2018

to participate in alternative relaxation pathways, most probably through thermally assisted-QTM. However, the U_{eff} barrier obtained from the fit of the relaxation time (14 K) is much lower than these thermally-activated processes (139 K), and confirms the above fit that the Raman mechanism is the dominant spin relaxation process in an applied field.

Conclusions

In summary we have prepared a new Co(II) field-induced SIM featuring a rare meridional geometry. The compound shows a distorted octahedral centre and strong magnetic anisotropy. Subtle differences between **1** and similar systems previously reported result in a positive value for *D*. The difference in the sign of *D* seems to be due to the ambiguous coordination geometry in *mer*-[Co(L)$_2$] caused by H-bonding interactions and re-emphasizes the importance of supramolecular interactions in controlling not only the magnitude but the sign of *D*. In common with other octahedral Co(II) SIMs direct and Raman processes are the dominant relaxation mechanisms. With more flexible ligands and/or different donor sets a more complete picture of the magnetostructural correlations should be forthcoming and efforts along these lines are currently being explored.

Experimental

General remarks

2-H$_2$imap was prepared as previously reported.[38] All other chemicals were purchased from Sigma-Aldrich and used as received. All reactions were performed in air with reagent grade solvents. IR data were measured on a Cary 630 Agilent Technologies IR spectrometer fitted with a Specac Golden Gate diamond ATR. ^{1}H NMR spectra were collected on a Bruker 300 MHz spectrometer in d^6-DMSO at 298 K. Elemental analyses were carried out on a Eurovector EA3000 analyser by staff of the School of Chemistry, University of Bristol, UK. ESI-MS were carried out on a Bruker Daltonics 7.0T Apex 4 FTICR Mass Spectrometer by staff at the National University of Singapore.

Synthesis of [Co(2-Himap)$_2$] 1

A solution of 2-H$_2$imap (0.109 g, 0.5 mmol) in H$_2$O (3 cm^3) with NaN$_3$ (0.065 g, 1.0 mmol) was layered at the bottom of a test tube and then blank MeOH : H$_2$O (1 : 1, 10 mL) was layered in the middle as a buffer layer. Finally, a solution of [Co(H$_2$O)$_6$][ClO$_4$]$_2$ (0.183 g, 0.5 mmol) in MeOH (5 cm^3) was layered on top and the test tube sealed. The solution was left for 2 weeks at room temperature, and red brown crystals were obtained at the buffer layer. The red brown crystals were isolated, washed with diethyl ether (2 × 2 cm^3) and air dried, yield 0.065 g (30%). *m*/*z* (ESI) 429 [Co(2-Himap)$_2$]$^+$. ν_{max} (ATR)/cm^{-1} 1587, 1461, 1384, 1249, 841, 747. Anal. Calc. for **1**·H$_2$O C$_{20}$H$_{18}$N$_6$O$_3$Co: C 53.47; H 4.04; N 18.70. Found: C 53.69; H 3.82; N 19.36%.

Synthesis of [Co(2-Himap)$_2$]NO$_3$·MeOH 2

2-Himap (0.437 g, 2 mmol) was dissolved in MeOH (7 cm^3) and [Co(H$_2$O)$_6$][NO$_3$]$_2$(0.291 g, 1.0 mmol) in MeOH (5 cm^3) added dropwise into the ligand solution. The solution immediately turned deep red with a small amount of dark solid produced. After stirring for 15 minutes the solution was filtered into a test tube and left overnight at room temperature, giving dark crystals. The crystals were isolated by filtration, washed with diethyl ether (2 × 2 cm^3) and air dried, yield 0.331 g (61%). ν_{max} (ATR)/cm^{-1} 3119, 3060, 1579, 1547, 1432, 1310, 1255, 1122, 743. *m*/*z* (ESI) 429 [Co(2-Himap)$_2$]$^+$. Anal. calc. for C$_{21}$H$_{20}$N$_7$O$_6$Co: C, 48.02; H, 3.84; N, 18.66. Found: C, 47.80; H, 3.86; N, 18.63%.

X-ray crystallography

Crystals of **1** and **2** were mounted on a glass fibre using perfluoropolyether oil and in the case of **2** cooled rapidly to 123 K in a stream of cold nitrogen. The diffraction data of **1** were collected on a Bruker APEXII area detector with graphite monochromated MoKα (λ = 0.71073 Å).[54] After data collection an empirical absorption correction (SADABS) was applied.[55] In the case of **2**, data were collected at 123 K on a Rigaku Spider diffractometer equipped with a MicroMax MM007 rotating anode generator, CuK$_\alpha$ radiation (λ = 1.54178 Å), high-flux Osmic multilayer mirror optics, and a curved image-plate detector.[56] The data were integrated and scaled and averaged with FS Process. The structures were then solved by direct methods and refined on all F^2 data using the SHELX suite of programs or OLEX2.[57–59] In all cases non-hydrogen atoms were refined with anisotropic thermal parameters; hydrogen atoms were included in calculated positions and refined with isotropic thermal parameters which were *ca*. 1.2 × (aromatic CH) or 1.5 × (Me, OH) the equivalent isotropic thermal parameters of their parent carbon atoms. Crystallographic data and structure refinement parameters are given in Table 2. All pictures were generated using OLEX2.[60] The CCDC numbers for the X-ray crystallographic data presented in this paper are 1585230 and 1585229 for **1** and **2**,† respectively.

Magnetic measurements

Data were collected using a Quantum Design MPMS 7 SQUID magnetometer under applied fields of 0.1 T (2–70 K) and 1.0 T (2–300 K). The crystalline sample was placed in a gel capsule for all data collection. Magnetization isotherms were collected at 2, 3, 4, 5.5, 10 and 20 K between 0–5 T. Alternating current susceptibility measurements were undertaken in an applied field of 0.2 T between 2–9 K and 50–1488 Hz. All data were corrected for the sample holder and diamagnetic contributions.

Quantum chemical calculations

The calculation of the second-order magnetic anisotropy (or zero-field splitting) parameters (*D* and *E*) has been carried out with two different software packages: MOLCAS 8.0[45–47] and

ORCA.[44] We have employed MOLCAS (along with the SINGLE_ANISO[61,62] code) to carry out a CASSCF calculation of the energy states of the Co(II) complex. After that, the spin–orbit coupling has been introduced, as implemented in the SO-RASSI (Restricted Active Space State Interaction) approach, to mix up these energies and obtain the final energy states. In these calculations we have employed an all electron ANO-RCC basis set:[63–66] Co atoms (6s5p4d2f), N (4s3p2d1f), O (4s3p2d1f), C (3s2p) and H (2s).

A CASSCF calculation was also carried out with ORCA; the dynamic correlation effects were included through the *n*-electron valence state perturbation theory NEVPT2[67–69] method. In all cases the spin–orbit effects were included using the quasi-degenerate perturbation theory (QDPT) and the magnetic anisotropy parameters were obtained using the effective Hamiltonian method. In these calculations all the atoms are described by the def2-TZVPP basis set,[70,71] including the corresponding auxiliary basis sets for correlation and Coulomb fitting. In both sets of calculations, the active space is formed by the seven d electrons of the Co(II) centre and the five d orbitals (7,5); and all the quadruplet (10) and doublet (40) states have been taken into account.

Conflicts of interest

There are no conflicts to declare.

Acknowledgements

We gratefully acknowledge the Thailand Research Fund (RSA5880048) for funding this research and financial support from the Thailand Research Fund in the form of a Royal Golden Jubilee scholarship to D. S. (PHD/0135/2554). K. S. M. thanks the Australian Research Council for a Discovery grant. The research reported here was also supported by the Spanish *Ministerio de Economía y Competitividad* (grant CTQ2015-64579-C3-1-P, MINECO/FEDER, UE). E. R. thanks Generalitat de Catalunya for an ICREA Academia award. J. J. and E. R. gratefully acknowledge the computer resources in the Consorci Serveis Universitaris de Catalunya (CSUC). Declan Wain is thanked for curve fitting. Ivana Borilović is thanked for help with the latest version of the Program PHI and Boujemaa Moubaraki is thanked for magnetic measurements.

Notes and references

1 D. Gatteschi, R. Sessoli and J. Villain, *Molecular Nanomagnets*, Oxford University Press, 2006.
2 R. Sessoli, D. Gatteschi, A. Caneschi and M. A. Novak, *Nature*, 1993, **365**, 141–143.
3 G. Christou, D. Gatteschi, D. N. Hendrickson and R. Sessoli, *MRS Bull.*, 2000, 66–71.
4 R. E. P. Winpenny, *Angew. Chem., Int. Ed.*, 2008, **47**, 7992–7994.
5 G. A. Timco, T. B. Faust, F. Tuna and R. E. P. Winpenny, *Chem. Soc. Rev.*, 2011, **40**, 3067.
6 N. Ishikawa, M. Sugita, T. Ishikawa, S. Y. Koshihara and Y. Kaizu, *J. Am. Chem. Soc.*, 2003, **125**, 8694–8695.
7 G. A. Craig and M. Murrie, *Chem. Soc. Rev.*, 2015, **44**, 2135–2147.
8 S. Gómez-Coca, D. Aravena, R. Morales and E. Ruiz, *Coord. Chem. Rev.*, 2015, **289–290**, 379–392.
9 J. M. Frost, K. L. M. Harriman and M. Murugesu, *Chem. Sci.*, 2016, **6**, 1–22.
10 C. A. P. Goodwin, F. Ortu, D. Reta, N. F. Chilton and D. P. Mills, *Nature*, 2017, **548**, 439–442.
11 F.-S. Guo, B. M. Day, Y.-C. Chen, M.-L. Tong, A. Mansikkamäki and R. A. Layfield, *Angew. Chem., Int. Ed.*, 2017, **56**, 11445–11449.
12 B. N. Figgis, *Introduction to ligand fields*, Wiley-VCH, New York, 1966.
13 B. N. Figgis, M. Gerloch, J. Lewis, F. E. Mabbs and G. A. Webb, *J. Chem. Soc. A*, 1968, 2086.
14 R. B. Bentley, M. Gerloch, J. Lewis and P. N. Quested, *J. Chem. Soc. A*, 1971, 3751–3756.
15 T. Jurca, A. Farghal, P. H. Lin, I. Korobkov, M. Murugesu and D. S. Richeson, *J. Am. Chem. Soc.*, 2011, **133**, 15814–15817.
16 J. M. Zadrozny and J. R. Long, *J. Am. Chem. Soc.*, 2011, **133**, 20732–20734.
17 M. R. Saber and K. R. Dunbar, *Chem. Commun.*, 2014, **50**, 12266–12269.
18 L. Smolko, J. Černák, M. Dušek, J. Miklovič, J. Titiš and R. Boča, *Dalton Trans.*, 2015, **44**, 17565–17571.
19 S. Vaidya, A. Upadhyay, S. K. Singh, T. Gupta, S. Tewary, S. K. Langley, J. P. S. Walsh, K. S. Murray, G. Rajaraman and M. Shanmugam, *Chem. Commun.*, 2015, **51**, 3739–3742.
20 S. Vaidya, S. K. Singh, P. Shukla, K. Ansari, G. Rajaraman and M. Shanmugam, *Chem. – Eur. J.*, 2017, **23**, 9546–9559.
21 J. M. Zadrozny, J. Telser and J. R. Long, *Polyhedron*, 2013, **64**, 209–217.
22 Y. Rechkemmer, F. D. Breitgoff, M. van der Meer, M. Atanasov, M. Hakl, M. Orlita, P. Neugebauer, F. Neese, B. Sarkar and J. van Slageren, *Nat. Commun.*, 2016, **7**, 10467.
23 X.-N. Yao, J.-Z. Du, Y.-Q. Zhang, X.-B. Leng, M.-W. Yang, S.-D. Jiang, Z.-X. Wang, Z.-W. Ouyang, L. Deng, B.-W. Wang and S. Gao, *J. Am. Chem. Soc.*, 2017, **139**, 373–380.
24 J. Vallejo, I. Castro, R. Ruiz-García, J. Cano, M. Julve, F. Lloret, G. De Munno, W. Wernsdorfer and E. Pardo, *J. Am. Chem. Soc.*, 2012, **134**, 15704–15707.
25 E. Colacio, J. Ruiz, E. Ruiz, E. Cremades, J. Krzystek, S. Carretta, J. Cano, T. Guidi, W. Wernsdorfer and E. K. Brechin, *Angew. Chem., Int. Ed.*, 2013, **52**, 9130–9134.
26 R. Herchel, L. Váhovská, I. Potočňák and Z. Trávníček, *Inorg. Chem.*, 2014, **53**, 5896–5898.
27 R. Díaz-Torres, M. Menelaou, O. Roubeau, A. Sorrenti, G. Brandariz-de-Pedro, E. C. Sañudo, S. J. Teat, J. Fraxedas,

 This journal is © The Royal Society of Chemistry 2018

E. Ruiz and N. Aliaga-Alcalde, *Chem. Sci.*, 2016, **7**, 2793–2803.
28 R. Ishikawa, Y. Horii, R. Nakanishi, S. Ueno, B. K. Breedlove, M. Yamashita and S. Kawata, *Eur. J. Inorg. Chem.*, 2016, **2016**, 3220.
29 A. V. Palii, D. V. Korchagin, E. A. Yureva, A. V. Akimov, E. Y. Misochko, G. V. Shilov, A. D. Talantsev, R. B. Morgunov, S. M. Aldoshin and B. S. Tsukerblat, *Inorg. Chem.*, 2016, **55**, 9696–9706.
30 S. Vaidya, S. Tewary, S. K. Singh, S. K. Langley, K. S. Murray, Y. Lan, W. Wernsdorfer, G. Rajaraman and M. Shanmugam, *Inorg. Chem.*, 2016, **55**, 9564–9578.
31 C. Villa-Pérez, I. Oyarzabal, G. A. Echeverría, G. C. Valencia-Uribe, J. M. Seco and D. B. Soria, *Eur. J. Inorg. Chem.*, 2016, **2016**, 4835–4841.
32 J. Walsh, G. Bowling, A.-M. Ariciu, N. Jailani, N. Chilton, P. Waddell, D. Collison, F. Tuna and L. Higham, *Magnetochemistry*, 2016, **2**, 23.
33 D. Valigura, C. Rajnák, J. Moncol, J. Titiš and R. Boča, *Dalton Trans.*, 2017, **46**, 10950–10956.
34 C. Rajnák, J. Titiš, J. Moncol', F. Renz and R. Boča, *Eur. J. Inorg. Chem.*, 2017, **2017**, 1520–1525.
35 F. Varga, C. Rajnak, J. Titis, J. Moncol and R. Boca, *Dalton Trans.*, 2017, **46**, 4148–4151.
36 S. Gómez-Coca, A. Urtizberea, E. Cremades, P. J. Alonso, A. Camón, E. Ruiz and F. Luis, *Nat. Commun.*, 2014, **5**, 4300.
37 Y. Peng, V. Mereacre, C. E. Anson, Y. Zhang, T. Bodenstein, K. Fink and A. K. Powell, *Inorg. Chem.*, 2017, **56**, 6056–6066.
38 J. Sanmartín-Matalobos, C. Portela-García, M. Fondo and A. M. García-Deibe, *Cryst. Growth Des.*, 2015, **15**, 4318–4323.
39 J. K. McCusker, A. L. Rheingold and D. N. Hendrickson, *Inorg. Chem.*, 1996, **35**, 2100–2112.
40 M. Marchivie, P. Guionneau, J. F. Létard and D. Chasseau, *Acta Crystallogr., Sect. B: Struct. Sci.*, 2005, **61**, 25–28.
41 S. Alvarez, *Chem. Rev.*, 2015, **115**, 13447–13483.
42 A. M. García-Deibe, C. Portela-García, M. Fondo, A. J. Mota and J. Sanmartín-Matalobos, *Chem. Commun.*, 2012, **48**, 9915.
43 N. F. Chilton, R. P. Anderson, L. D. Turner, A. Soncini and K. S. Murray, *J. Comput. Chem.*, 2013, **34**, 1164–1175.
44 F. Neese, *Wiley Interdiscip. Rev.: Comput. Mol. Sci.*, 2012, **2**, 73–78.
45 G. Karlström, R. Lindh, P.-Å. Malmqvist, B. O. Roos, U. Ryde, V. Veryazov, P. O. Widmark, M. Cossi, B. Schimmelpfennig, P. Neogrady and L. Seijo, in *Computational Materials Science*, Elsevier, 2003, vol. 28, pp. 222–239.
46 V. Veryazov, P.-O. Widmark, L. Serrano-Andrés, R. Lindh and B. O. Roos, *Int. J. Quantum Chem.*, 2004, **100**, 626–635.
47 F. Aquilante, L. De Vico, N. Ferré, G. Ghigo, P.-Å. Malmqvist, P. Neogrády, T. B. Pedersen, M. Pitoňák, M. Reiher, B. O. Roos, L. Serrano-Andrés, M. Urban, V. Veryazov and R. Lindh, *J. Comput. Chem.*, 2010, **31**, 224–247.
48 S. Gómez-Coca, E. Cremades, N. Aliaga-Alcalde and E. Ruiz, *J. Am. Chem. Soc.*, 2013, **135**, 7010.
49 M. Atanasov, D. Ganyushin, K. Sivalingam and F. Neese, in *Molecular Electronic Structures of Transition Metal Complexes II. Structure and Bonding*, ed. D. M. P. Mingos, P. Day and J. P. Dahl, Springer, Berlin, 2012, pp. 149–220.
50 M. Atanasov, D. Aravena, E. Suturina, E. Bill, D. Maganas and F. Neese, *Coord. Chem. Rev.*, 2015, **289–290**, 177–214.
51 E. A. Buvaylo, V. N. Kokozay, O. Y. Vassilyeva, B. W. Skelton, A. Ozarowski, J. Titiš, B. Vranovičová and R. Boča, *Inorg. Chem.*, 2017, **56**, 6999–7009.
52 T. J. Woods, M. F. Ballesteros-Rivas, S. Gómez-Coca, E. Ruiz and K. R. Dunbar, *J. Am. Chem. Soc.*, 2016, **138**, 16407–16416.
53 M. A. Palacios, J. Nehrkorn, E. A. Suturina, E. Ruiz, S. Gómez-Coca, K. Holldack, A. Schnegg, J. Krzystek, J. M. Moreno and E. Colacio, *Chem. – Eur. J.*, 2017, **23**, 11649–11661.
54 *Bruker APEXII*, Bruker AXS Inc., Madison, USA, 2005.
55 *SADABS and SAINT*, Bruker AXS Inc., Madison, USA, 2013.
56 *Rigaku, Rigaku XRD*, Rigaku Corporation, Tokyo, Japan, 1996.
57 G. M. Sheldrick, *Acta Crystallogr., Sect. A: Found. Crystallogr.*, 2015, **71**, 3–8.
58 G. M. Sheldrick, *Acta Crystallogr., Sect. C: Struct. Chem.*, 2015, **71**, 3–8.
59 L. J. Bourhis, O. V. Dolomanov, R. J. Gildea, J. A. K. Howard and H. Puschmann, *Acta Crystallogr., Sect. A: Found. Adv.*, 2015, **71**, 59–75.
60 O. V. Dolomanov, L. J. Bourhis, R. J. Gildea, J. A. K. Howard and H. Puschmann, *J. Appl. Crystallogr.*, 2009, **42**, 339–342.
61 L. F. Chibotaru, L. Ungur and A. Soncini, *Angew. Chem., Int. Ed.*, 2008, **47**, 4126–4129.
62 L. F. Chibotaru, L. Ungur, C. Aronica, H. Elmoll, G. Pilet and D. Luneau, *J. Am. Chem. Soc.*, 2008, **130**, 12445–12455.
63 B. O. Roos, V. Veryazov and P.-O. Widmark, *Theor. Chem. Acc.*, 2004, **111**, 345–351.
64 B. O. Roos, R. Lindh, P.-Å. Malmqvist, V. Veryazov and P.-O. Widmark, *J. Phys. Chem. A*, 2004, **108**, 2851–2858.
65 B. O. Roos, R. Lindh, P.-Å. Malmqvist, V. Veryazov and P.-O. Widmark, *J. Phys. Chem. A*, 2005, **109**, 6575–6579.
66 B. O. Roos, R. Lindh, P.-Å. Malmqvist, V. Veryazov and P.-O. Widmark, *Chem. Phys. Lett.*, 2005, **409**, 295–299.
67 C. Angeli, R. Cimiraglia, S. Evangelisti, T. Leininger and J.-P. Malrieu, *J. Chem. Phys.*, 2001, **114**, 10252–10264.
68 C. Angeli, R. Cimiraglia and J.-P. Malrieu, *Chem. Phys. Lett.*, 2001, **350**, 297–305.
69 C. Angeli, R. Cimiraglia and J.-P. Malrieu, *J. Chem. Phys.*, 2002, **117**, 9138–9153.
70 F. Weigend and R. Ahlrichs, *Phys. Chem. Chem. Phys.*, 2005, **7**, 3297.
71 F. Weigend, *Phys. Chem. Chem. Phys.*, 2006, **8**, 1057.

ChemPubSoc Europe

DOI: 10.1002/ejic.201501188

EurJIC European Journal of Inorganic Chemistry

Full Paper

Spin Crossover

Substituent-Influenced Spin Crossover in Fe^{III} Quinolylsalicylaldiminates

Darunee Sertphon,[a] David J. Harding,*[a] Phimphaka Harding,[a] Keith S. Murray,[b] Boujemaa Moubaraki,[b] Harry Adams,[c] Adil Alkaş,[d] and Shane G. Telfer[d]

Abstract: The new ligand Hqsal-4-OMe was synthesized, and four iron(III) complexes, $[Fe(qsal\text{-}4\text{-}OMe)_2]Y{\cdot}CH_2Cl_2$ [Hqsal-4-OMe = 4-methoxy-*N*-(8-quinolyl)salicylaldimine; Y = ClO_4 (**1**), NO_3 (**2**)] and $[Fe(qsal\text{-}4\text{-}OMe)_2]Y$ (Y = PF_6 (**3**), OTf (**4**)] as well as the isomer $[Fe(qsal\text{-}5\text{-}OMe)_2]PF_6{\cdot}CH_2Cl_2$ (**5**), were prepared. UV/Vis spectroscopic studies indicated that the complexes are high-spin in solution and exhibit a ligand-to-metal charge-transfer band around 400 nm. X-ray crystallographic studies on $[Fe(qsal\text{-}4\text{-}OMe)_2]Y{\cdot}CH_2Cl_2$ (Y = ClO_4, NO_3) and $[Fe(qsal\text{-}4\text{-}OMe)_2]PF_6$ at 97 K revealed high-spin Fe^{III} centres with one of the qsal-4-OMe ligands significantly distorted from planarity. In contrast, in **5** the Fe^{III} centre is low-spin at low temperature, and the room-temperature structure of **5** shows about 25 % spin crossover (SCO). The structure of $[Fe(qsal\text{-}4\text{-}OMe)_2]Y{\cdot}sol$ shows weak π–π interactions between neighbouring cations, while **5** exhibits stronger π–π interactions that link it into a 1D chain. SQUID magnetometric studies revealed that **1**–**4** are essentially high-spin, whereas **5** undergoes gradual and almost complete SCO up to 350 K. A combination of distortions to the qsal-4-OMe ligand and intermolecular C–H···O interactions involving both the coordinated phenolate oxygen atom and the OMe group seem to be responsible for the loss of SCO.

Introduction

Spin crossover (SCO) complexes remain the subject of much interest owing to their relative simplicity, ease of modification and wide applicability.[1–5] The basis of SCO is the presence of two magnetic states, termed high-spin (HS) and low-spin (LS), which are close in energy.[1,2] Switching between these states may be accomplished by changes in temperature or pressure, and at lower temperatures by light irradiation.[6] Designing compounds in which the HS and LS states are close in energy involves selecting a ligand with the required ligand field appropriate to the metal concerned. In the case of Fe^{III}, suitable ligands generally have an N_4O_2 donor set with SCO between the $S = 1/2$ (LS) and $S = 5/2$ (HS) spin states.[7,8] While finding a ligand set capable of promoting SCO in a given complex is relatively easy, for the material to have any practical use, the SCO should be abrupt and occur close to room temperature with significant hysteresis. This requires a high degree of co-operativity and is generally achieved by favourable supramolecular contacts.[9–11] It follows that designing hysteretic SCO systems is principally a crystal-engineering challenge.[12] An elegant example of this that is of particular relevance to the current work is $[Fe(qsal)_2]NCSe$ [Hqsal = *N*-(8-quinolyl)salicylaldimine]. This complex exhibits an extremely broad hysteresis of 70 K just below room temperature, which has been ascribed to strong π–π interactions between neighbouring qsal ligands forming tightly packed 2D planes.[13–15]

This success led to a large number of subsequent studies mostly focusing on changing the anion,[16–18] and it was not until 2009 that complexes of substituted qsal-X ligands appeared.[19–22] The first to be reported was $[Fe(qsal\text{-}3\text{-}OMe)_2]PF_6{\cdot}nH_2O$ (n = 0 or 2), in which the water solvate is HS whereas the non-solvated compound is LS.[19] Following this study, in 2013 we reported $[Fe(qsal\text{-}5\text{-}OMe)_2]Y$ (Y = Cl, BF_4, NCS, PF_6 and BPh_4), of which many of the compounds exhibit SCO, in three cases with hysteresis.[23,24] At about the same time Boillot and co-workers reported $[Fe(salEen\text{-}4\text{-}OMe)_2]Y$ (HsalEen = *N*-ethyl-*N*-(2-aminoethyl)salicylaldimine; Y = PF_6, NO_3), which in the case of the nitrate shows improved hysteresis compared to the prototypical compound in this family, $[Fe(salEen\text{-}3\text{-}OMe)_2]PF_6$.[25,26] In both systems it is clear that the position of the substituent is crucial in controlling SCO characteristics. In seeking to better understand how minor structural modifications of the ligand affect SCO, we have now prepared $[Fe(qsal\text{-}4\text{-}OMe)_2]Y$ (Y = ClO_4, NO_3, PF_6, OTf). We demonstrate how this subtle change at the ligand radically impacts both the local

[a] *Molecular Technology Research Unit, Walailak University, Thasala, Nakhon Si Thammarat, 80161, Thailand*
E-mail: hdavid@wu.ac.th
www.mtruwu.com
http://tandfonline.com/tcme
[b] *School of Chemistry, Monash University, Clayton, Melbourne, Victoria, 3800, Australia*
[c] *Department of Chemistry, University of Sheffield, Sheffield, S3 7HF, UK*
[d] *MacDiarmid Institute for Advanced Materials and Nanotechnology, Institute of Fundamental Sciences, Massey University, Palmerston North, New Zealand*

Supporting information and ORCID(s) from the author(s) for this article are available on the WWW under http://dx.doi.org/10.1002/ejic.201501188.

© 2016 Wiley-VCH Verlag GmbH & Co. KGaA, Weinheim

coordination environment and the supramolecular packing and consequently the SCO properties of the compounds in this series.

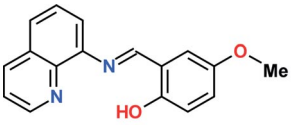

Hqsal-5-OMe

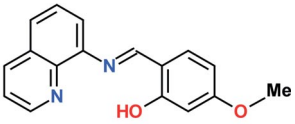

Hqsal-4-OMe

Results and Discussion

Ligand Synthesis

The ligand Hqsal-4-OMe was prepared by our standard procedure from diisopropyl ether.[27] IR and ^{1}H NMR spectroscopic data are consistent with the proposed structure of the ligand (see Supporting Information). Interestingly, the imine stretching frequency is almost 20 cm^{-1} higher than that of the related Hqsal-5-OMe ligand, while the electronic spectrum shows a single $\pi\rightarrow\pi^*$ transition at 340 nm and is essentially identical to that of Hqsal-5-OMe.[23]

Synthesis and Characterization of [Fe(qsal-4-OMe)$_2$]Y

The complexes were all synthesized by layered diffusion of a solution of FeY_3 in MeOH on top of a solution of Hqsal-4-OMe and NEt_3 in CH_2Cl_2. In the case of Y = PF_6 and OTf, the FeY_3 solution was prepared in situ from $FeCl_3$ and an appropriate potassium or silver salt. After 3–5 d, air-stable black or dark brown crystals of the products [Fe(qsal-4-OMe)$_2$]Y·CH_2Cl_2 [Y = ClO_4 (**1**), NO_3 (**2**)] and [Fe(qsal-4-OMe)$_2$]Y [Y = PF_6 (**3**), OTf (**4**)] were isolated. For further comparison, we also synthesized [Fe(qsal-5-OMe)$_2$]PF_6·CH_2Cl_2 (**5**), which is the CH_2Cl_2 solvate of the previously reported [Fe(qsal-5-OMe)$_2$]PF_6.[24] The difference from our previous synthesis lies in the use of $AgPF_6$ instead of KPF_6, which yields a much more crystalline product.[24]

IR spectroscopy revealed stretches between 1601 and 1608 cm^{-1} for **1**–**4** (Table 1), which are typical values for the imine stretch in [Fe(qsal-X)$_2$]$^+$ complexes.[23,24] The stretches of the anions were also readily identified and confirmed the proposed formulation. The UV/Vis spectra of **1**–**4** (Figure 1) were recorded in CH_2Cl_2 and display intense absorption bands at 340 and about 400 nm, which are assigned to $\pi\rightarrow\pi^*$ and ligand-to-metal charge-transfer (LMCT) transitions, respectively, by comparison with the related [Fe(qsal-X)$_2$]$^+$ complexes.[23,24] The minor differences in extinction coefficients reflect the different solubilities of the complexes. The absence of a peak around 830 nm suggests that the complexes are HS in solution at room temperature.[20]

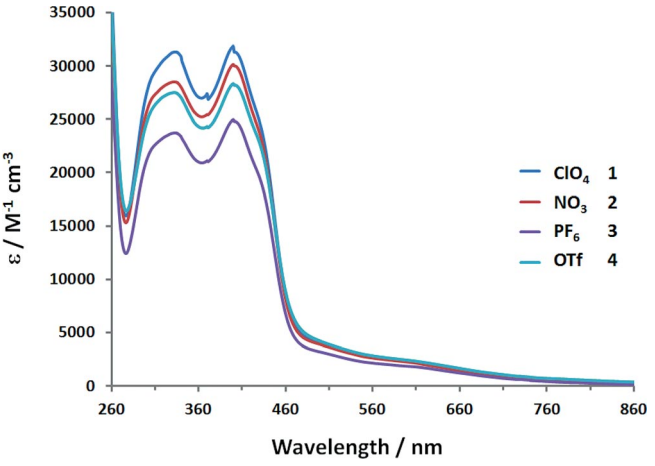

Figure 1. UV/Vis spectra of [Fe(qsal-4-OMe)$_2$]Y in CH_2Cl_2.

Structural Studies on [Fe(qsal-4-OMe)$_2$]Y·Solvent

Crystals of [Fe(qsal-4-OMe)$_2$]ClO_4·CH_2Cl_2 (**1**) and [Fe(qsal-4-OMe)$_2$]NO_3·CH_2Cl_2 (**2**) crystallized from MeOH/CH_2Cl_2 in the triclinic space group $P\bar{1}$ (Figure 2). [Fe(qsal-4-OMe)$_2$]PF_6 (**3**) crystallized in the monoclinic space group $P2_1/n$. The structures were determined at 97 K, and in all cases the Fe centre is six-coordinate with four nitrogen and two oxygen atoms from two meridional qsal ligands, leaving the oxygen atoms *cis* to each other. The Fe–ligand bond lengths and other coordination parameters are given in Table 2. The Fe–N/O bond lengths in **1**–**3** are in the ranges 2.087–2.183 and 1.936–1.904, respectively, and are close to the corresponding distances for the HS Fe^{III} centre in [Fe(qsal-5-OMe)$_2$]Cl·2MeOH·0.5H_2O.[23] However, the Fe–N bond lengths in [Fe(qsal-5-OMe)$_2$]Cl·2MeOH·0.5H_2O are more similar to each other than those in [Fe(qsal-4-OMe)$_2$]$^+$, which may influence the ability of the Fe centre to undergo SCO.

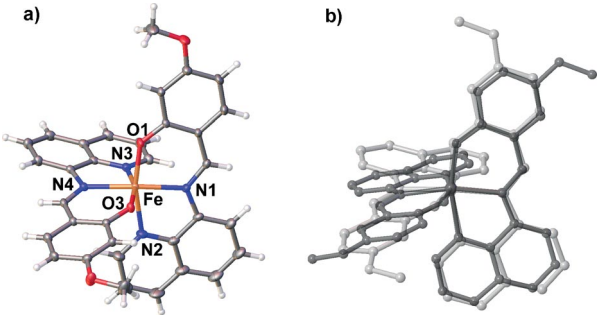

Figure 2. Left: view of the asymmetric unit of [Fe(qsal-4-OMe)$_2$]ClO_4·CH_2Cl_2 **1**; thermal ellipsoids are drawn at 50 % probability. Right: overlay of **1** (light grey) and the HS centre of [Fe(qsal-5-OMe)$_2$]Cl·2MeOH·0.5H_2O (dark grey).

Table 1. Spectroscopic data of **1**–**4**.

Compound	IR [cm^{-1}][a]		λ_{max} [nm] (ε_{max} [M^{-1} cm^{-1}])[b]
	$\nu_{C=N}$	ν_{anion}	
[Fe(qsal-4-OMe)$_2$]ClO_4 (**1**)	1608	1091	340 (24000), 406 (25000)
[Fe(qsal-4-OMe)$_2$]NO_3 (**2**)	1605	1365	340 (27000), 407 (28000)
[Fe(qsal-4-OMe)$_2$]PF_6 (**3**)	1607	845	340 (31000), 406 (32000)
[Fe(qsal-4-OMe)$_2$]OTf (**4**)	1601	1276, 1149	340 (27000), 407 (28000)

[a] As KBr discs. [b] In CH_2Cl_2.

Moreover, in **1**–**3** one of the qsal-4-OMe ligands is significantly distorted, as shown by the angle of 17–23° between the quinoline and phenolate rings. By comparison [Fe(qsal-5-

© 2016 Wiley-VCH Verlag GmbH & Co. KGaA, Weinheim

Table 2. Selected bond lengths [Å] and octahedral distortion parameters [°] for **1**–**3** at 97 K and **5** at 108 and 293 K.

	1-ClO_4	**2**-NO_3	**3**-PF_6	**5**-108	**5**-293
Fe1–O1	1.921(1)	1.920(3)	1.936(2)	1.886(6)	1.895(9)
Fe1–O3	1.923(1)	1.921(3)	1.904(2)	1.881(7)	1.862(8)
Fe1–O_{av}	1.922(1)	1.921(3)	1.920(2)	1.884(7)	1.879(9)
Fe1–N1	2.106(2)	2.107(3)	2.117(3)	1.979(7)	2.04(1)
Fe1–N2	2.164(2)	2.161(4)	2.157(3)	1.94(1)	1.98(1)
Fe1–N3	2.183(2)	2.166(3)	2.182(3)	1.978(8)	2.024(9)
Fe1–N4	2.087(2)	2.096(3)	2.095(3)	1.937(9)	1.98(1)
Fe1–N_{ave}	2.135(2)	2.133(3)	2.139(3)	1.96(1)	2.01(1)
Σ[a]	69.7	68.7	74.9	47.7	50.1
Θ[b]	198.7	195.9	213.9	74.4	107.7
α[c]	19.2	16.7	22.7	1.0	3.1
α	5.3	2.6	3.8	0.9	1.6

[a] $\Sigma = \sum_{i=1}^{12} |90-\alpha_i|$, where α_i are the twelve *cis* N/O–Fe–N/O angles.[29] [b] $\Theta = \sum_{i=1}^{24} |60-\theta_i|$, where θ_i are the 24 unique N/O–Fe–N/O angles measured on the projection of two triangular faces of the octahedron along their common pseudo-threefold axis.[30] [c] α= the angle between the planes of the quinoline and phenolate rings.

OMe)$_2$]Cl·2MeOH·0.5H_2O and **5** (at 293 K, see below) have values of 0.9–5.6°. We have previously shown for [Fe(qsal-5-*t*Bu)$_2$]$^+$ that strong distortions in the qsal-X ligands frequently result in systems in which SCO is switched off.[28] In [Fe(qsal-5-*t*Bu)$_2$]$^+$ the distortion is caused by the large steric bulk of the *t*Bu group, while in the current system the distortion may be due to the solid-state packing, which necessitates ligand distortion for C–H···O interactions to form.

The structure of **5** was determined at 108 and 293 K. At both temperatures the structure belongs to the triclinic space group $P\bar{1}$. The Fe–N/O bond lengths at 108 K are characteristic of LS Fe^{III} and become longer by about 0.03 Å on average at room temperature (Table 2), which suggests the onset of SCO. This is in agreement with magnetic susceptibility studies (see below).[31] As in [Fe(qsal-F)$_2$]NCS,[31] the incomplete SCO (ca. 25 % between 108 and 293 K) is best represented by the octahedral distortion parameter Θ, the change in which is about 33 (cf. $\Delta\Theta$= 128 for complete SCO in [Fe(qsal-I)$_2$]OTf·MeOH).[32]

In addition to the changes at the Fe centre, there are also significant differences in the two unit cells with the *a* and *b* axes increasing in length by about 0.20 Å, while the change in the *c* axis is modest (ca. 0.12 Å). This leads to a change in the unit-cell volume of 64 Å^3 and is comparable with the change that occurs in [Fe(qsal-F)$_2$]NCS between 100 and 200 K, whereby 50 % of the centres undergo SCO.[31]

The solid-state packings in **1** and **2** are very similar with intermolecular π–π interactions forming dimers (Table 3).[33] The twist in the other qsal-4-OMe ligand prevents substantial overlap such that the π–π interaction is replaced by a pair of C–H···O interactions resulting in dislocation of the 1D chain that is such a common feature of [Fe(qsal-5-X)$_2$]$^+$ complexes (Figure 3).[23,24,31,32,34] In **5**, in which both qsal-5-OMe ligands are planar, 1D chains are formed by two orthogonal intermolecular π–π interactions with plane-to-plane distances of 3.28–3.32 Å, which lengthen by about 0.08 Å at room temperature (Table 3). In comparison, the plane-to-plane distances in **1** and **2** of 3.34–3.35 Å suggest that the dimers have weaker π–π interactions. The 1D chains formed in **1**–**3** are connected to each other by parallel fourfold aryl embrace (P4AE) or pseudo-P4AE interactions.[35] In the latter, the C–H···π interactions are replaced by C–H···O interactions involving the coordinated phenolate oxygen atom (Figure 4). Unusually, in **5** there are no P4AE interactions, which contrasts with all other [Fe(qsal-5-OMe)$_2$]$^+$ complexes. This may be responsible for the more gradual SCO in this compound.[23,24]

The packing in **3** is radically different to those of all the other compounds, with weak π–π interactions between the phenyl and quinoline rings forming a 1D column (Figure 5). C–H···O interactions then link these in a ladder packing motif. There are no strong interactions between the [Fe(qsal-4-OMe)$_2$]$^+$ units.

In the case of the ClO_4 and NO_3 complexes the 2D planes are connected by C–H···O interactions involving the methoxyl groups to form 3D supramolecular networks (see Figure 6). Despite the differences in the [Fe(qsal-4-OMe)$_2$]Y complexes compared with the [Fe(qsal-5-OMe)$_2$]Y analogues, there is still signif-

Table 3. Supramolecular interaction distances in **1**–**3** and **5**.

	1-ClO_4	**2**-NO_3	**3**-PF_6	**5**-108 K
π				
Cent···cent[a]	3.474	3.439	4.067	3.539
Plane···plane[b]	3.351	3.338	–	2.274
Cent···cent[a]	–	–	–	3.624
Plane···plane[b]	–	–	–	3.317
C–H···O				
In 1D chains	2.668 (O1···H18)	2.646 (O1···H18)	2.692 (O3···H2)	2.594 (O1···H132)
	2.647 (O3···H10)	2.559 (O3···H17)		2.549 (O1···H132)
OMe groups	2.551 (O2···H11)	2.542 (O2···H16)	2.636 (O4···H7)	2.630 (O4···H132)
	2.396 (O7···H16)	2.585 (O7···H25B)		
		2.586 (O7′···H25B)		
P4AE				
Cent···cent[c]	3.719	3.623	–	–
Plane···plane[d]	3.295	3.323	–	–
C–H···π	2.654	2.614 (O1···H32)	–	3.014

[a] The centroid···centroid distance between the centroids of the phenyl and quinoline rings. [b] The plane···plane distance is the distance between the phenyl and quinoline planes. [c] The centroid···centroid distance between the centroids of the quinoline rings. [d] The plane···plane distance between the quinoline planes.

© 2016 Wiley-VCH Verlag GmbH & Co. KGaA, Weinheim

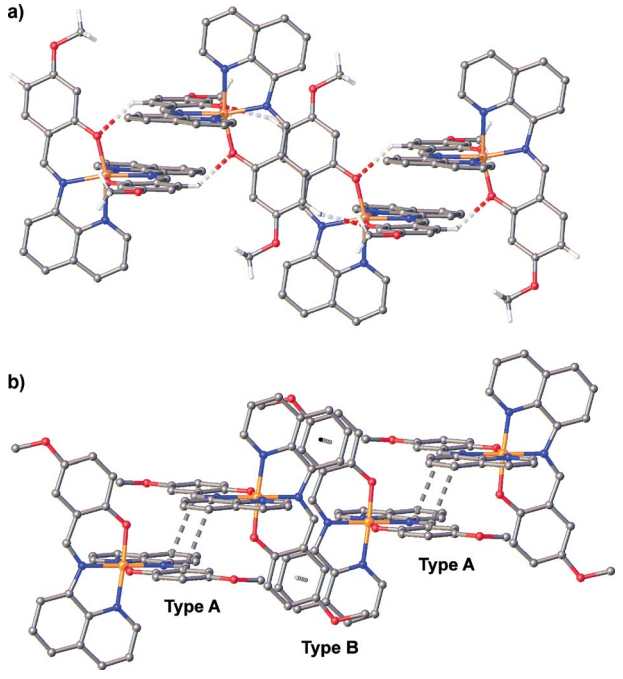

Figure 3. Top: view of the π–π and C–H···O interactions in **2**. Bottom: the π–π interactions in **5** that form the 1D chains.

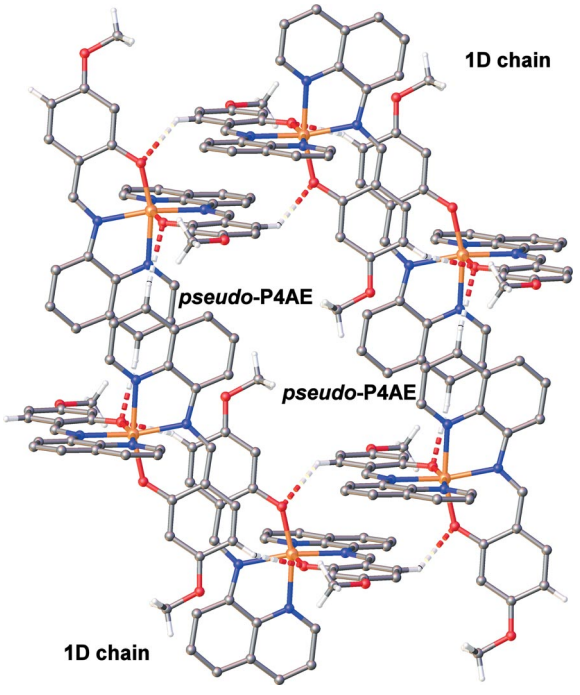

Figure 4. View of pseudo-P4AE interactions in **2**; only selected hydrogen atoms are shown in the interest of clarity.

icant cooperativity. This suggests that the lack of SCO in **1**–**4** is most probably due to the distortion in the qsal-4-OMe ligand.

Magnetic Studies on [Fe(qsal-4-OMe)$_2$]Y·Solvent

The magnetic properties of **1**–**4** were studied by SQUID magnetometry and are presented as $\chi_M T$ versus T plots in Figure 7.

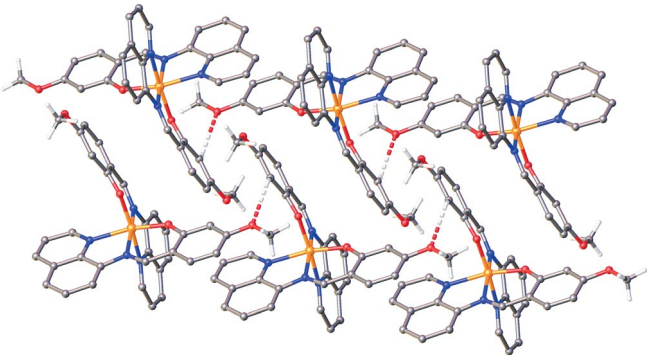

Figure 5. View of the ladder motif formed by π–π and C–H···O interactions in **3**.

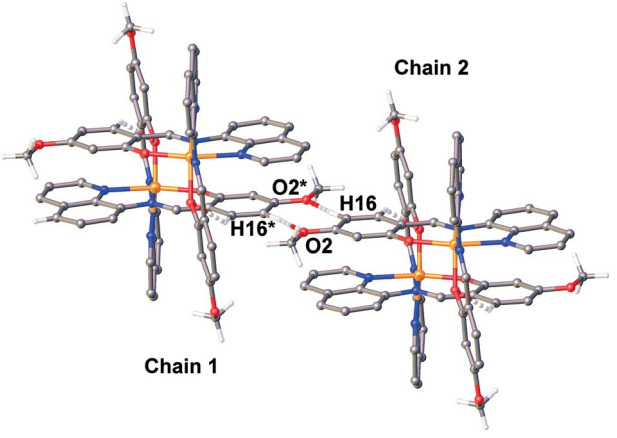

Figure 6. View of the C–H···O interactions involving the OMe groups in **2**. Only selected hydrogen atoms are shown for the sake of clarity.

The $\chi_M T$ values are in the range 4.00–4.50 cm^3 K mol^{-1} for **1**–**3** and are invariant between 30 and 300 K, indicative of the compounds being HS only. The OTf analogue shows about 25 % SCO, although this is very gradual and occurs over about 150 K. Despite repeated attempts we have been unable to get crystals of sufficient quality for a structural study on **4**.

The lack of complete SCO in **1**–**4** most likely stems from the position of the OMe group, which, as the structural studies show, results in non-planar qsal-4-OMe ligands and significant distortion at the metal centre. It is noteworthy that while **3** is HS, **5** and [Fe(qsal-5-OMe)$_2$]PF$_6$ both exhibit SCO, which confirms that qsal-4-OMe generates a weaker ligand field than qsal-5-OMe; similar conclusions have been drawn concerning [Fe(salEen-4-OMe)$_2$]PF$_6$.[25] Moreover, [Fe(qsal-3-OMe)$_2$]PF$_6$·2H$_2$O is also trapped in the HS state.[19] Indeed, in [Fe(qsal)$_2$][Ni(pddt)$_2$][36] and [Fe(qsal)$_2$][M(pds)$_2$] (pddt = 6,7-dihydro-5*H*-1,4-dithiepin-2,3-dithiolate, pds = pyrazine-2,3-diselenolate, M = Cu, Au)[37] the presence of a similar degree of distortion at the Fe centre also results in SCO being switched off. We cannot absolutely rule out solvent effects influencing SCO properties in **1** and **2**, but the fact that the structures are largely constructed by π–π and C–H···O interactions and that solvent has relatively minor effects on the SCO behaviour of related compounds suggests that in this case substituent effects are more significant.

© 2016 Wiley-VCH Verlag GmbH & Co. KGaA, Weinheim

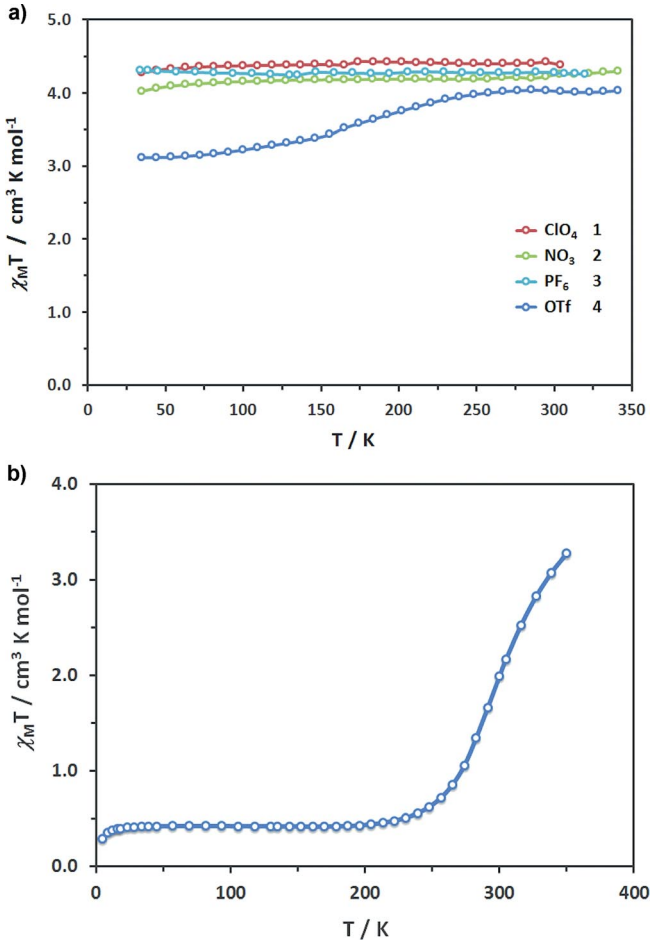

Figure 7. $\chi_M T$ versus T plots for **1**–**4** (top) and **5** (bottom).

In contrast to **1**–**4**, **5** does undergo gradual and almost complete SCO with $\chi_M T$ = 3.27 cm^3 K mol^{-1} at 350 K. This behaviour is slightly different to that of [Fe(qsal-5-OMe)$_2$]PF$_6$, for which SCO is slightly more gradual and less complete ($\chi_M T$ = 2.60 cm^3 K mol^{-1} at 350 K). This agrees with our studies on [Fe(qsal-5-I)$_2$]OTf·MeOH, in which loss of MeOH only slightly impacts $T_{1/2}$, although the non-solvated compound does exhibit broader hysteresis.[32]

Conclusions

We have prepared four Fe^{III} complexes of the new Hqsal-4-OMe ligand. Solution studies revealed that the compounds are HS at room temperature and that the OMe group does not significantly alter the electronic properties of **1**–**4** compared to the related [Fe(qsal-5-OMe)$_2$]Y compounds. Structural analysis of **1**–**3** revealed that the compounds often contain a distorted qsal-4-OMe ligand, which magnetic studies show results in loss of SCO making the complexes essentially HS. The solid-state packing is also impacted, with only weak π–π interactions observed rather than the 1D π–π chain that is common in the [Fe(qsal-5-X)$_2$]$^+$ analogues. In certain cases there are additional C–H···O interactions, which would be expected to further weaken the ligand field provided by qsal-4-OMe. Overall, it is clear that the position of the OMe group on the ligand and solvent effects significantly affect both the coordination and supramolecular sphere in [Fe(qsal-4-OMe)$_2$]$^+$. This confirms our previous findings that the position and nature of the substituent is an important consideration in successfully obtaining SCO compounds. Further studies on whether this observation is applicable to other substituent groups are underway.

Experimental Section

General Remarks: All manipulations were performed in air with reagent-grade solvents. All other chemicals were purchased from Aldrich Chemical Company and used as received. IR (as KBr discs) were recorded with a PerkinElmer Spectrum One infrared spectrophotometer in the range 400–4000 cm^{-1}. Electronic spectra were recorded in CH_2Cl_2 at room temperature with a Shimadzu UV-1700 UV/Vis spectrophotometer. ^{1}H NMR spectra were recorded with a Bruker 300 MHz FT NMR spectrometer at 25 °C in $CDCl_3$ with $SiMe_4$ added as an internal standard. Elemental analyses were carried out with a Eurovector EA3000 analyzer by staff of the School of Chemistry, University of Bristol, UK. ESI-MS was carried out with a Bruker Daltonics 7.0T Apex 4 FTICR mass spectrometer by staff at the National University of Singapore.

Hqsal-4-OMe: 8-Aminoquinoline (1.442 g, 10.0 mmol) was dissolved in diisopropyl ether (30 cm^3) to give a pale yellow solution. 2-Hydroxy-4-methoxybenzaldehyde (1.521 cm^3, 10.0 mmol) was added and the mixture stirred for 4 h to give an orange solution. The solvent was allowed to evaporate slowly to give orange crystals, which were isolated by filtration and air-dried (2.120 g, 85 %). IR (KBr): $\tilde{\nu}_{max}$ = 3060, 2937 (ν_{CH}), 1633 ($\nu_{C=N}$). λ_{max}/nm (CH_2Cl_2, ε/M^{-1} cm^{-1}) 340 (38000). ^{1}H NMR ($CDCl_3$, 295 K, 300 MHz): δ= 8.99 (dd, J_{HH} = 1.2, 3.9 Hz, 1 H$_a$), 8.71 (s, 1 H$_g$), 8.16 (d, J_{HH} = 8.1 Hz, 1 H$_c$), 7.67 (dd, J_{HH} = 1.5, 7.8 Hz, 1 H$_d$), 7.57–7.49 (m, 2H$_{e,h}$), 7.45 (dd, J_{HH} = 3.9, 8.1 Hz, H$_b$) 7.25 (d, , J_{HH} = 9.0 Hz, 1 H$_f$), 6.47 (d, , J_{HH} = 2.1 Hz, 1 H$_j$), 6.40 (dd, , J_{HH} = 2.1, 8.7 Hz, 1 H$_i$), 3.84 (s, 3 H, OCH_3) ppm. $C_{17}H_{14}N_2O_2$ (278.31): calcd. C 73.37, H 5.07, N 10.06; found C 78.40, H 5.12, N 9.93.

[Fe(qsal-4-OMe)$_2$]ClO$_4$·CH$_2$Cl$_2$ (1): Crystals of **1** were formed by diffusion. A solution of Hqsal-4-OMe (0.0248 g, 0.1 mmol) in CH_2Cl_2 (2 cm^3) was placed at the bottom of a test tube, Et_3N (0.01 cm^3, 0.1 mmol) was added and then blank MeOH (3 cm^3) was layered in the middle as a buffer layer. Finally, a solution of Fe(ClO$_4$)$_3$·6H$_2$O (0.0234 g, 0.05 mmol) in MeOH (5 cm^3) was layered on top and the test tube sealed. The tube was left for about one week at room temperature, and black crystals were obtained at the bottom. The black crystals were washed with diethyl ether (2 × 2 cm^3) and air-dried (0.065 g, 92 %). MS (ESI): m/z = 610.2 [Fe(qsal-4-OMe)$_2$]$^+$, 99 ClO_4^-. $C_{34}H_{26}ClFeN_4O_8$ (709.90): calcd. C 57.51, H 3.69, N 7.89; found C 57.87, H 3.73, N 7.70 (loss of CH_2Cl_2).

[Fe(qsal-4-OMe)$_2$]NO$_3$·CH$_2$Cl$_2$ (2): Crystals of **2** were prepared in a similar manner to those of **1** by using a solution of Fe(NO$_3$)$_3$·9H$_2$O instead of Fe(ClO$_4$)$_3$·6H$_2$O. Black crystals were obtained after one week(0.058 g, 86 %). MS (ESI): m/z = 610.2 [Fe(qsal-4-OMe)$_2$]$^+$. $C_{34}H_{26}FeN_5O_7$·0.5CH_2Cl_2: calcd. C 57.97, H 3.81, N 9.80; found C 57.87, H 3.88, N 10.39.

[Fe(qsal-4-OMe)$_2$]PF$_6$ (3): Crystals of **3** were prepared by placing a solution of Hqsal-4-OMe (0.248 g, 1.0 mmol) in CH_2Cl_2 (2 cm^3) at the bottom of a test tube and adding Et_3N (0.14 cm^3, 1.0 mmol) and then blank MeOH (3 cm^3) as a buffer layer. Finally, a solution of Fe(PF$_6$)$_3$, prepared from $FeCl_3$ (0.081 g, 0.5 mmol) and $AgPF_6$

© 2016 Wiley-VCH Verlag GmbH & Co. KGaA, Weinheim

(0.379 g, 1.5 mmol) in MeOH (5 cm^3), was layered on top and the test tube sealed. Black crystals of **4** were obtained (0.355 g, 85 %). MS (ESI): m/z = 610.2 $[Fe(qsal\text{-}4\text{-}OMe)_2]^+$, 145 PF_6^-. $C_{34}H_{26}F_6FeN_4O_4P$ (755.41): calcd. C 54.06, H 3.47, N 7.42; found C 54.61, H 3.56, N 7.27.

$[Fe(qsal\text{-}4\text{-}OMe)_2]OTf$ (4): Crystals of **4** were prepared in a similar manner to those of **3**, except that AgOTf was used instead of $AgPF_6$ to make $Fe(OTf)_3$, to give black crystals, (0.301 g, 68 %). MS (ESI): m/z = 610.2 $[Fe(qsal\text{-}4\text{-}OMe)_2]^+$, 149 OTf. $C_{35}H_{26}F_3FeN_4O_7S$ (759.51): calcd. C 55.34, H 3.45, N 7.38; found C 55.45, H 3.65, N 7.74.

$[Fe(qsal\text{-}5\text{-}OMe)_2]PF_6{\cdot}CH_2Cl_2$ (5): Crystals of **5** were prepared in a similar manner to those of **3** by using Hqsal-5-OMe instead of Hqsal-4-OMe, which gave black needles (0.298 g, 71 %). $C_{35}H_{28}Cl_2F_6FeN_4O_4P$ (840.35): calcd. C 50.03, H 3.36, N 6.67; found C 50.45, H 3.41, N 7.02. All other data were identical to those of the previously reported complex $[Fe(qsal\text{-}5\text{-}OMe)_2]PF_6$.[24]

X-ray Crystallography: Crystal data and data processing parameters for the structures of **1**–**3** are given in Tables 4 and 5. X-ray quality crystals of **1**–**3** were grown by layering a solution of FeY_3 in MeOH over a solution of Hqsal-4-OMe and NEt_3 in CH_2Cl_2. Crystals of $[Fe(qsal\text{-}5\text{-}OMe)_2]PF_6{\cdot}CH_2Cl_2$ were grown in a similar way. Crystals were mounted on a glass fibre by using perfluoropolyether oil and cooled rapidly to 97 K in a stream of cold nitrogen for **1**–**3**. The diffraction data of **1**–**3** were collected with a Bruker APEXII area detector with graphite-monochromated Mo-K_α radiation (λ = 0.71073 Å).[38] After data collection, in each case an empirical absorption correction (SADABS) was applied.[39] In the case of **5**, X-ray crystallographic data were collected at 108 and 293 K with a Rigaku Spider diffractometer equipped with a MicroMax MM007 rotating-anode generator, Cu_α radiation (λ = 1.54178 Å), high-flux Osmic multilayer mirror optics, and a curved image-plate detector.[40] The data were integrated and scaled and averaged with FS Process. The structures were then solved by direct methods and refined on all F^2 data with the SHELX suite of programs or Olex2 (in the case of **3**).[41,42] In all cases non-hydrogen atoms were refined with anisotropic thermal parameters; hydrogen atoms were included in calculated positions and refined with isotropic thermal parameters which were about 1.2 × (aromatic CH) or 1.5 × (Me, CH_2, OH) the equivalent isotropic thermal parameters of their parent carbon atoms. All pictures were generated with OLEX2.[43]

Table 5. Crystallographic data and structure refinement for **5** at 108 and 295 K.

	5-108	**5**-293
Formula	$C_{35}H_{28}Cl_2F_6FeN_4O_4P$	$C_{35}H_{28}Cl_2F_6FeN_4O_4P$
M [g mol^{-1}]	840.33	840.33
Crystal system	triclinic	triclinic
Space group	$P\bar{1}$	$P\bar{1}$
a [Å]	12.2866(4)	12.4650(4)
b [Å]	12.4452(4)	12.6584(4)
c [Å]	12.8972(9)	13.0200(9)
α[°]	81.997(6)	81.504(6)
β[°]	72.168(5)	72.483(5)
γ[°]	62.706(4)	62.160(4)
T [K]	108(2)	293(2)
V [$Å^3$]	1668.34(16)	1732.30(16)
Z	2	2
Absorption coefficient [mm^{-1}]	6.284	6.052
Reflections collected	21144	20566
Independent reflections, R_{int}	3436, 0.1174	3477, 0.0770
Max., min. transmission	0.885, 0.145	1.000, 0.474
Restraints/parameters	0/480	0/480
Final R indices [$I > 2\sigma(I)$]: R_1, wR_2	0.0937, 0.2212	0.1258, 0.3049

CCDC 1431331 (for **1**), 1431330 (for **2**), 1431329 (for **3**), 1431332 (for **5**, at 108 K)), and 1431333 (for **5**, at 293 K) contain the supplementary crystallographic data for this paper. These data can be obtained free of charge from The Cambridge Crystallographic Data Centre.

Magnetic Susceptibility Studies: Data were collected with a Quantum Design MPMS 5 SQUID magnetometer under an applied field of 1 T over the temperature range 30–350 K for **1**–**4** and 2–350 K for **5**. The powdered or polycrystalline samples were placed in gel capsules and care was taken to allow long thermal equilibration times at each temperature.

Acknowledgments

The authors thank the Thailand Research Fund (grant number RSA5580028 and RSA5880048) for funding this research and

Table 4. Crystallographic data and structure refinement for **1**–**3**.

	1	**2**	**3**
Formula	$C_{35}H_{28}Cl_3FeN_4O_8$	$C_{35}H_{28}Cl_2FeN_5O_7$	$C_{34}H_{26}F_6FeN_4O_4P$
M [g mol^{-1}]	794.81	757.37	755.41
Crystal system	triclinic	triclinic	monoclinic
Space group	$P\bar{1}$	$P\bar{1}$	$P2_1/n$
a [Å]	11.9319(5)	11.7933(7)	18.994(6)
b [Å]	12.6183(6)	12.4411(8)	8.922(3)
c [Å]	13.4637(6)	13.2728(8)	20.243(6)
α[°]	111.791(2)	111.588(3)	90.00
β[°]	105.569(2)	103.252(4)	104.25(2)
γ[°]	103.068(2)	102.646(4)	90.00
T [K]	97(2)	97(2)	97(2)
V [$Å^3$]	1688.68(13)	1660.69(18)	3324.9(18)
Z	2	2	4
Absorption coefficient [mm^{-1}]	0.744	0.67	0.58
Reflections collected	39634	41146	24728
Independent reflections, R_{int}	9266, 0.065	7527, 0.057	7650, 0.109
Max., min. transmission	–	0.0890, 0.2530	0.780, 0.888
Restraints/parameters	0/462	267/447	0/452
Final R indices [$I > 2\sigma(I)$]: R_1, wR_2	0.044, 0.114	0.101, 0.266	0.064, 0.141

© 2016 Wiley-VCH Verlag GmbH & Co. KGaA, Weinheim

financial support from the Thailand Research Fund in the form of a Royal Golden Jubilee scholarship to D. S. (PHD/0135/2554).

Keywords: Spin crossover · Iron · N,O ligands · Magnetic properties · Substituent effects

[1] M. A. Halcrow (Ed.), *Spin-Crossover Materials: Properties and Applications*, John Wiley & Sons, Chichester, UK, **2013**.
[2] P. Gütlich, H. A. Goodwin, *Top. Curr. Chem.* **2004**, *233*, 1–47.
[3] J.-F. Létard, P. Guionneau, L. Goux-Capes, *Top. Curr. Chem.* **2004**, *235*, 221–249.
[4] A. Bousseksou, G. Molnár, L. Salmon, W. Nicolazzi, *Chem. Soc. Rev.* **2011**, *40*, 3313–35.
[5] P. Gütlich, A. B. Gaspar, Y. Garcia, *Beilstein J. Org. Chem.* **2013**, *9*, 342–91.
[6] J.-F. Létard, *J. Mater. Chem.* **2006**, *16*, 2550–59.
[7] P. J. van Koningsbruggen, Y. Maeda, H. Oshio, *Top. Curr. Chem.* **2004**, *233*, 259–324.
[8] M. Nihei, T. Shiga, Y. Maeda, H. Oshio, *Coord. Chem. Rev.* **2007**, *251*, 2606–2621.
[9] M. A. Halcrow, *Chem. Soc. Rev.* **2011**, *40*, 4119–42.
[10] M. A. Halcrow, *Chem. Lett.* **2014**, *43*, 1178–1188.
[11] P. Guionneau, *Dalton Trans.* **2014**, *43*, 382–93.
[12] G. R. Desiraju, *J. Am. Chem. Soc.* **2013**, *135*, 9952–67.
[13] S. Hayami, Z. Gu, H. Yoshiki, A. Fujishima, O. Sato, *J. Am. Chem. Soc.* **2001**, *123*, 11644–50.
[14] S. Hayami, T. Kawahara, G. Juhasz, K. Kawamura, K. Uehashi, O. Sato, Y. Maeda, *J. Radioanal. Nucl. Chem.* **2003**, *255*, 443–447.
[15] S. Hayami, K. Hiki, T. Kawahara, Y. Maeda, D. Urakami, K. Inoue, M. Ohama, S. Kawata, O. Sato, *Chem. Eur. J.* **2009**, *15*, 3497–3508.
[16] K. Takahashi, H. Cui, H. Kobayashi, Y. Einaga, O. Sato, *Chem. Lett.* **2005**, *34*, 1240–1241.
[17] K. Takahashi, H.-B. Cui, Y. Okano, H. Kobayashi, Y. Einaga, O. Sato, *Inorg. Chem.* **2006**, *45*, 5739–5741.
[18] C. Faulmann, K. Jacob, S. Dorbes, S. Lampert, I. Malfant, M.-L. Doublet, L. Valade, J. A. Real, *Inorg. Chem.* **2007**, *46*, 8548–59.
[19] J. C. Dias, B. Vieira, I. C. Santos, L. C. J. Pereira, V. Da Gama, *Inorg. Chim. Acta* **2009**, *362*, 2076–2079.
[20] B. Djukic, P. A. Dube, F. Razavi, T. Seda, H. A. Jenkins, J. F. Britten, M. T. Lemaire, *Inorg. Chem.* **2009**, *48*, 699–707.
[21] B. Djukic, M. T. Lemaire, *Inorg. Chem.* **2009**, *48*, 10489–10491.
[22] A. I. S. Neves, J. C. Dias, B. J. C. Vieira, I. S. Santos, M. B. Castelo Branco, L. C. J. Pereira, J. C. Waerenborgh, M. Almeida, D. Belo, V. Da Gama, *CrystEngComm* **2009**, *11*, 2160–68.
[23] D. J. Harding, D. Sertphon, P. Harding, K. S. Murray, B. Moubaraki, J. D. Cashion, H. Adams, *Chem. Eur. J.* **2013**, *19*, 1082–90.
[24] D. Sertphon, D. J. Harding, P. Harding, K. S. Murray, B. Moubaraki, J. D. Cashion, H. Adams, *Eur. J. Inorg. Chem.* **2013**, 788–795.
[25] A. Tissot, P. Fertey, R. Guillot, V. Briois, M.-L. Boillot, *Eur. J. Inorg. Chem.* **2014**, 101–109.
[26] A. Tissot, R. Bertoni, E. Collet, L. Toupet, M.-L. Boillot, *J. Mater. Chem.* **2011**, *21*, 18347.
[27] J. Sirirak, W. Phonsri, D. J. Harding, P. Harding, P. Phommon, W. Chaoprasa, R. M. Hendry, T. M. Roseveare, H. Adams, *J. Mol. Struct.* **2013**, *1036*, 439–446.
[28] D. Sertphon, D. J. Harding, P. Harding, K. S. Murray, B. Moubaraki, H. Adams, *Aust. J. Chem.* **2014**, *67*, 1574–1580.
[29] J. K. McCusker, A. L. Rheingold, D. N. Hendrickson, *Inorg. Chem.* **1996**, *35*, 2100–2112.
[30] M. Marchivie, P. Guionneau, J. F. Létard, D. Chasseau, *Acta Crystallogr., Sect. B Struct. Sci.* **2005**, *61*, 25–28.
[31] W. Phonsri, D. J. Harding, P. Harding, K. S. Murray, B. Moubaraki, I. A. Gass, J. D. Cashion, G. N. L. Jameson, H. Adams, *Dalton Trans.* **2014**, *43*, 17509–17518.
[32] D. J. Harding, W. Phonsri, P. Harding, I. A. Gass, K. S. Murray, B. Moubaraki, J. D. Cashion, L. Liu, S. G. Telfer, *Chem. Commun.* **2013**, *49*, 6340–6342.
[33] C. Janiak, *J. Chem. Soc., Dalton Trans.* **2000**, 3885–3896.
[34] D. J. Harding, W. Phonsri, P. Harding, K. S. Murray, B. Moubaraki, G. N. L. Jameson, *Dalton Trans.* **2015**, *44*, 15079–15082.
[35] V. Russell, M. Scudder, I. Dance, *J. Chem. Soc., Dalton Trans.* **2001**, 789–799.
[36] X.-M. Li, Y. Ji, C.-F. Wang, J.-L. Zuo, X.-Z. You, *J. Coord. Chem.* **2009**, *62*, 1544–1552.
[37] J. C. Dias, A. Soriano-Portillo, M. Clemente-Léon, C. Giménez-Saiz, J. R. Galán-Mascarós, C. J. Gómez-García, E. Coronado, *Inorg. Chim. Acta* **2007**, *360*, 3843–3847.
[38] *APEXII*, Bruker AXS Inc., Madison, WI, USA, **2005**.
[39] *SADABS* and *SAINT*, Bruker AXS Inc., Madison, WI, USA, **2003**.
[40] Rigaku, Rigaku Corporation, *Rigaku XRD*, Tokyo, Japan, **1996**.
[41] G. M. Sheldrick, *Acta Crystallogr., Sect. A* **2008**, *64*, 112–22.
[42] L. J. Bourhis, O. V. Dolomanov, R. J. Gildea, J. A. K. Howard, H. Puschmann, *Acta Crystallogr., Sect. A* **2015**, *71*, 59–75.
[43] O. V. Dolomanov, L. J. Bourhis, R. J. Gildea, J. A. K. Howard, H. Puschmann, *J. Appl. Crystallogr.* **2009**, *42*, 339–42.

Received: October 16, 2015
Published Online: December 21, 2015

© 2016 Wiley-VCH Verlag GmbH & Co. KGaA, Weinheim

Received: 13 August 2016 | Revised: 10 January 2017 | Accepted: 2 February 2017

DOI 10.1002/qua.25362

FULL PAPER

WILEY International Journal of QUANTUM CHEMISTRY

Comparison of density functionals for the study of the high spin low spin gap in Fe(III) spin crossover complexes

Jitnapa Sirirak[1] | Darunee Sertphon[2] | Wasinee Phonsri[2†] | Phimphaka Harding[2] | David J. Harding[2]

[1]Department of Chemistry, Faculty of Science, Silpakorn University, Muang, Nakhon Pathom 73000, Thailand

[2]Functional Materials and Nanotechnology Center of Excellence, Walailak University, Nakhon Si Thammarat, Thasala 80160, Thailand

Correspondence
David J. Harding, Functional Materials and Nanotechnology Center of Excellence, Walailak University, Nakhon Si Thammarat, Thasala 80161, Thailand.
Email: hdavid@g-mail.wu.ac.th

Funding information
We thank Walailak University for a Postdoctoral Fellowship to JS, the Thailand Research Fund (RSA5580028 and RSA5880048) and the National Science and Technology Development Agency (grant no.: P-10-11181) for funding this research.

Abstract

A detailed investigation of the accuracy of different quantum mechanical methods for the study of iron(III) spin crossover complexes is presented. The energy spin state gap between the high and low spin states; ΔE(HS-LS) of nine iron(III) quinolylsalicylaldiminate complexes were calculated with nine different DFT functionals, then compared. DFT functionals: B3LYP, B3LYP-D3, B3LYP*, BH&HLYP, BP86, OLYP, OPBE, M06L, and TPSSh were tested with six basis sets: 3-21G*, dgdzvp, 6-31G**, cc-pVDZ, Def2TZVP, and cc-pVTZ. The cations from the X-ray crystal structures of [Fe(qsal-OMe)$_2$]Cl·MeCN·H_2O, [Fe(qsal-OMe)$_2$]Cl·2MeOH·0.5H_2O, [Fe(qsal-OMe)$_2$]BF_4·MeOH, [Fe(qsal-OMe)$_2$]NCS·CH_2Cl_2, [Fe(qsal-F)$_2$]NCS, [Fe(qsal-Cl)$_2$]NCS·MeOH, [Fe(qsal-Br)$_2$]NCS·MeOH, [Fe(qsal-I)$_2$]OTf·MeOH, and [Fe(qsal)$_2$]NCS·CH_2Cl_2 were used as starting structures. The results show that B3LYP, B3LYP-D3, OLYP, and OPBE with a 6-31G**, Def2TZVP, and cc-pVTZ basis set give reasonable results of ΔE(HS-LS) compared with the experimental data. The enthalpy of [Fe(qsal-I)$_2$]$^+$ calculated with an OLYP functional and cc-pVTZ basis set (1.48 kcal/mol) most closely matches the experimental data (1.34 kcal/mol). B3LYP* yields an enthalpy of 5.92 kcal/mol suggesting it may be unsuitable for these Fe(III) complexes, mirroring recent results by Kepp (*Inorg. Chem.*, 2016, *55*, 2717–2727).

KEYWORDS
basis sets, DFT calculations, functionals, iron(III) complexes, spin crossover

1 | INTRODUCTION

Spin crossover is an elegant example of bistability with switching occurring between a high spin (HS) and a low spin (LS) state.[1–4] A particular advantage of these materials is that a variety of external stimuli including temperature, pressure or light may be used to enable switching.[5–7] Moreover, their relative simplicity and ready processability mean that they are attractive targets in the fields of molecular electronics and high density data storage.[8,9]

To be spin crossover active requires that the HS and LS states are close in energy, something that depends on the ligand, the metal and its oxidation state.[10] Accurately computing such spin state energies to enable better design or insight into systems where subtle ligand changes radically alter magnetic behavior is, however, computationally challenging.[11–13] Part of the problem lies in the fact that the spin state gap is often within the error associated with the calculation itself. While computational systems exist which can reduce this error they are typically computationally expensive and often require expert knowledge to use correctly.[14,15] Moreover, semiempirical methods such as CAPST2 have been found to have strong dependence on the value chosen for the ionization potential—electron affinity shift.[16,17]

DFT calculations have become a popular alternative to these time consuming HF methods. While successful to some degree the choice of functional used has been shown to have a significant impact on the energy gap. Thus, pure functionals such BLYP and BP86 invariably favour LS states while hybrid functionals such as B3LYP tend to overstabilize HS states.[18] Another factor shown to be critical for most common functionals is that of the basis sets. Swart has demonstrated that large basis sets are typically required to accurately reproduce experimental data.[19]

In relation to spin crossover compounds, the favouring of the HS state by B3LYP has been compensated for by adjusting the amount of

†Current address: School of Chemistry, Monash University, Clayton, Melbourne, Victoria, 3800, Australia

 © 2017 Wiley Periodicals, Inc.

HF exchange from 20% to 15% which in a large number of Fe(II) SCO systems yields reasonable results.[20] However, Friesner and Hughes recommend against altering the degree of HF exchange instead preferring a local correction model.[21] Moreover, they suggest that the reason for the success of B3LYP* in most Fe(II) SCO systems is due to the commonality of the ligands with most systems using aromatic and imine nitrogen donors. In attempting to address this we have undertaken computational studies on a series of Fe(III) SCO systems[22,23] to see what effects the choice of functional and basis set will have on these systems. The particular system we have chosen to study is [Fe(qsal-X)$_2$]Y (qsal-X = substituted quinolylsalicylaldiminate, Y = anion; see figure below) as structural data, in both the high spin and low spin states, and thermochemical data are known for a number of these compounds permitting comparison with our computational results.[24–30]

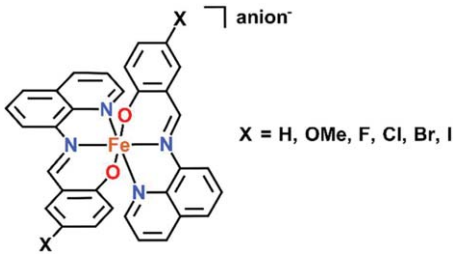

Specifically, we explore eight DFT functionals: B3LYP, B3LYP*, BH&HLYP, BP86, OLYP, OPBE, M06L, and TPSSh and six basis sets: 3-21G*, dgdzvp, 6-31G**, cc-pVDZ, Def2TZVP, and cc-pVTZ to investigate their effects on the energy differences between the high and low spin states; ΔE(HS-LS) and comparisons are drawn between the computed and experimental data.

2 | METHODS

All DFT calculations were performed using the GAUSSIAN 09 package suite[31] Using the X-ray structures as starting structures,[26–28,32] the geometries of the cations of the complexes at the lowest energy LS and HS states were fully optimized with B3LYP and 6-31G(d,p) basis set (except for the iodine atom, where a dgdzvp basis set was used).

Using the optimized structures in the HS and LS state calculated above, single point calculations were performed with seven other DFT functionals including B3LYP*, BH&HLYP, BP86, OLYP, OPBE, M06L, and TPSSh. In the case of B3LYP, we also included dispersion effects using a D3 correction[33] as such effects have recently been shown to be significant in some systems.[34] Six different basis sets: 3-21G*, dgdzvp, 6-31G**, cc-pVDZ, Def2TZVP, and cc-pVTZ were also tested. This approach is justified as beyond the geometric optimization the different functionals and basis sets result in only very minor changes to metal–ligand bond lengths and in the relative energies, as both spin states are affected in the same way by any change in method.[35,36] In the interests of simplicity, solvation, and relativistic effects are not included in the calculations as the differences between the two spin states are typically small.[21] From the electronic energies obtained from the different methods, the spin state energy differences between the high and low spin states ΔE(HS-LS) of these cations were calculated. The differences between the calculated ΔE(HS-LS) with other basis sets and those of cc-pVTZ as well as the mean of these differences from all nine complexes for each method were then calculated in order to investigate the effect of the basis set (Supporting Information Table S3). Moreover, to explore the effect of the functional on ΔE(HS-LS), the differences between the calculated ΔE(HS-LS) with other basis sets and those of cc-pVTZ along with the mean of these differences from all nine complexes for each method were calculated and compared. B3LYP was chosen as a reference functional as its performance for transition metal energetic calculations is generally very good among DFT functionals (Supporting Information Table S4).[21,37]

To obtain the thermal corrections to the enthalpy where zero-point energies were included, vibrational frequencies calculations were also performed with B3LYP, B3LYP-D3, B3LYP*, OLYP, and OPBE methods and 6-31g**, cc-pVDZ, and cc-pVTZ basis sets using the optimized structure of the cation of [Fe(qsal-I)$_2$]OTf·MeOH. Thermal corrections to the enthalpy were added to ΔE(HS-LS) computed using the above methods and compared with the experimental enthalpy.

To more accurately determine how closely the calculated structures matched the experimental ones we also determined the octahedral distortion parameters, Σ and Θ. Σ is defined as the sum of the deviation of the 12 *cis* angles (ϕ) of the complex from 90° (Equation 1),[38] while Θ is the sum of the deviation of the 24 N—Fe—N angles (θ) measured on the projection of two triangular faces of the octahedron along their common *pseudo*-three fold axes from 60° (Equation 2).[39]

$$\Sigma = \sum_{i=1}^{12} |90 - \phi_i| \quad (1)$$

$$\Theta = \sum_{i=1}^{24} |60 - \theta_i| \quad (2)$$

Finally, the frontier orbitals and more particularly the highest occupied molecular orbital (HOMO) and the lowest occupied molecular orbital (LUMO) were calculated with the aim of exploring which molecular orbitals are involved in the bonding between the iron and ligand, and how this is effected by spin crossover.

3 | RESULTS AND DISCUSSION

3.1 | Geometries of spin crossover complexes

The cations from nine X-ray crystal structures [Fe(qsal-OMe)$_2$]Cl·2MeOH·0.5H$_2$O **1**, [Fe(qsal-OMe)$_2$]Cl·2MeCN·H$_2$O **2**, [Fe(qsal-OMe)$_2$]BF$_4$·MeOH **3**, [Fe(qsal-OMe)$_2$]NCS·CH$_2$Cl$_2$ **4**, [Fe(qsal-F)$_2$]NCS **5**, [Fe(qsal-Cl)$_2$]NCS·MeOH **6**, [Fe(qsal-Br)$_2$]NCS·MeOH **7**, [Fe(qsal-I)$_2$]OTf·MeOH **8**, and [Fe(qsal)$_2$]NCS·CH$_2$Cl$_2$ **9** were used as the starting structure for structural optimization at the B3LYP/6-31G** level. Four X-ray structures have the same cation, [Fe(qsal-OMe)$_2$]$^+$ which means that there are four different starting structures of the same cation so results from these four optimized structures can be used to justify the applicability of the method. Moreover, there are four cations, in which their X-ray structures in both high spin and low spin have been reported, which are

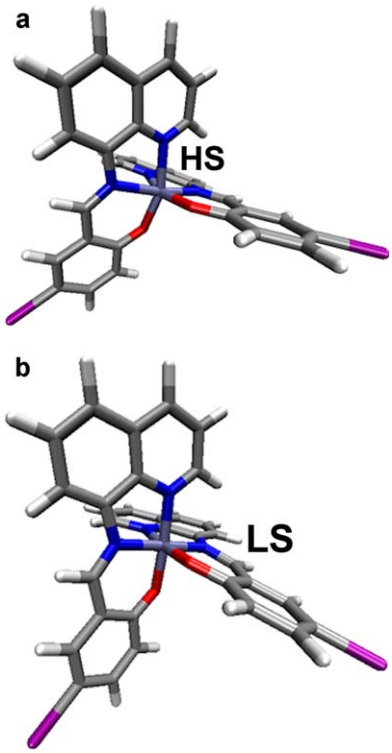

FIGURE 1 View of the molecular structure of $[Fe(qsal\text{-}I)_2]^+$ in the high spin (top) and low spin (bottom) state

$[Fe(qsal\text{-}OMe)_2]^+$, $[Fe(qsal\text{-}F)_2]^+$, $[Fe(qsal\text{-}I)_2]^+$, and $[Fe(qsal)_2]^+$,[25–28,32] permitting further comparison with the calculated structures.

The optimized structures of $[Fe(qsal\text{-}I)_2]^+$ in the HS and LS states are shown in Figure 1. Important bond lengths are listed in Table 1 (bond angles may be found in Supporting Information Table S1) while the octahedral distortion parameters Σ and Θ values are listed in Table 2.

A comparison between the X-ray and the optimized structures, reveals that the bond lengths and angles are similar as can be seen in Tables 1 and Supporting Information S1. The difference between the bond lengths and angles obtained from the X-ray structures and the optimized structures are 0.03 Å and 1.9° on average, respectively, indicating that the calculations are good models of the real structures. A comparison of **1**–**4** where the starting structures contain the same cation, $[Fe(qsal\text{-}OMe)_2]^+$ are extremely similar and further support this conclusion. Similar differences between calculated and crystal structures are observed by Jensen and Cirera in $[Fe(2\text{-}NH_2CH_2py)_3]^{2+}$ with {MAD = 0.009 Å (LS) and 0.041 Å (HS); TPSSh}[40] and Bučko et al. in $[Fe(phen)_2(NCS)_2]$ {MAD = 0.023 Å (LS) and 0.040 Å (HS); PBE + U-D2}.[41]

The degree of distortion around the Fe centre as measured by their $\sum$ and Θ values reveal that the values obtained from the X-ray structures are more similar to those of the optimized structure in the low spin state. This is expected as the exact nature of the distortion that occurs in the high spin state is often difficult to model.[42] Although the exact $\sum$ and Θ values of the optimized and X-ray structures are often significantly different, the differences between the $\sum$ and Θ values from the structures in the high and low spin state {ΔΣ (HS-LS) and ΔΘ (HS-LS)} are very similar. As octahedral distortion parameters are rarely reported, comparisons are difficult but studies on $[Fe(phen)_2(NCS)_2]$ using a PBE + U-D2 method shows that the LS differences are ca. 1° while for the HS state it is much greater at almost 28°.[41] This confirms that our calculations adequately model the $[Fe(qsal\text{-}X)_2]^+$ compounds.

3.2 | Molecular orbital analysis

The frontier orbitals of the optimized structures were also investigated (see Figures S1 and S2 in the Supporting Information). The HOMO and LUMO of the two cations: $[Fe(qsal\text{-}I)_2]^+$ and $[Fe(qsal\text{-}OMe)_2]^+$ in the high and low spin state (HS and LS) are presented as representative examples in Figures 2 and 3, respectively. The HOMO of $[Fe(qsal\text{-}OMe)_2]^+$ in both the HS and LS state has considerable electron density localized on the ligand with a relatively small metal contribution. The

TABLE 1 Comparison of the bond lengths from the X-ray crystal structures and the structures optimized at the B3LYP/6-31G** level

Bond lengths/Å	Structure	1	2	3	4	5	6	7	8	9	MAD[a]
Fe-N_{quin} (HS)	Opt	2.20	2.20	2.20	2.21	2.21	2.20	2.19	2.15	2.22	-
Fe-N_{quin} (HS)	X-ray	2.17	-	-	-	2.14[b]	-	-	2.15	2.16	0.053
Fe-N_{quin} (LS)	Opt	2.01	2.01	2.01	2.01	2.01	2.01	2.01	1.96	2.01	-
Fe-N_{quin} (LS)	X-ray	1.99	1.98	1.97	1.98	1.97	1.97	1.98	1.99	1.99	0.031
Fe-N_{imine} (HS)	Opt	2.15	2.15	2.15	2.14	2.15	2.15	2.16	2.14	2.15	-
Fe-N_{imine} (HS)	X-ray	2.11	-	-	-	2.11[b]	-	-	2.09	2.10	0.045
Fe-N_{imine} (LS)	Opt	1.96	1.96	1.96	1.96	1.96	1.96	1.96	1.93	1.96	-
Fe-N_{imine} (LS)	X-ray	1.95	1.94	1.93	1.94	1.93	1.93	1.96	1.94	1.95	0.018
Fe-O (HS)	Opt	1.90	1.90	1.90	1.90	1.89	1.90	1.90	1.88	1.89	-
Fe-O (HS)	X-ray	1.91	-	-	-	1.90[b]	-	-	1.90	1.90	0.013
Fe-O (LS)	Opt	1.86	1.86	1.86	1.86	1.86	1.86	1.86	1.85	1.86	-
Fe-O (LS)	X-ray	1.88	1.88	1.87	1.87	1.87	1.86	1.88	1.89	1.87	0.016

[a]MAD = Mean absolute deviation; in cases where experimental data are not available these points are ignored.
[b]Fe_2—N/O bond lengths at 270 K are used, taken from Ref. 27.

TABLE 2 The comparison of Σ and Θ of the X-ray crystal structures and the structures optimized at the B3LYP/6-31G** level

	Structure	1	2	3	4	5	6	7	8	9
Σ										
Σ (HS)	Opt	84.1	84.5	84.7	84.6	84.4	85.6	89.4	85.3	88.6
Σ (HS)	X-ray	74.8	-[a]	-[a]	-[a]	73.0	-[a]	-[a]	63.3	69.9
Σ (LS)	Opt	51.9	51.8	51.8	51.7	52.5	52.1	52.5	53.4	53.0
Σ (LS)	X-ray	42.4	42.5	43.6	44.4	40.1	48.2	51.4	42.0	52.1
ΔΣ (HS-LS)	Opt	32.3	32.7	33.0	32.9	31.9	33.5	36.8	31.9	35.6
ΔΣ (HS-LS)	X-ray	32.4	-[a]	-[a]	-[a]	32.9	-[a]	-[a]	21.3	17.8
Θ										
Θ (HS)	Opt	245.0	245.2	245.6	245.6	241.7	245.3	249.9	223.7	247.1
Θ (HS)	X-ray	205.5	-[a]	-[a]	-[a]	198.0	-[a]	-[a]	186.4	203.8
Θ (LS)	Opt	97.3	95.9	95.9	78.8	105.2	94.7	94.6	90.3	95.7
Θ (LS)	X-ray	62.3	64.8	58.8	61.3	80.7	67.1	74.9	61.3	81.0
ΔΘ (HS-LS)	Opt	147.7	149.3	149.7	166.7	136.6	150.6	155.3	133.4	151.3
ΔΘ (HS-LS)	X-ray	143.2	-[a]	-[a]	-[a]	117.3	-[a]	-[a]	125.1	122.8

[a]Structure not available.

HOMO of $[Fe(qsal\text{-}I)_2]^+$ (HS and LS) has more metal character than $[Fe(qsal\text{-}OMe)_2]^+$, a trend also observed for the other $[Fe(qsal\text{-}X)_2]^+$ (X = halogen) complexes. Comparing the HS and LS HOMOs, the HS HOMO is found to be a combination of a Fe $d_{x2\text{-}y2}$ orbital and O and N p-orbitals giving an Fe—O and Fe—N σ* HOMO. In contrast, the LS HOMO exhibits Fe-O π* character. This change is entirely consistent with spin crossover and electrons moving from the e_g set (Fe-ligand σ-orbitals) to the t_{2g} set (Fe-ligand π-orbitals). As expected the LUMOs of all the compounds are principally ligand based with significant electron density on the quinolyl fragment. Unlike the HOMOs the change in spin state has a relatively minor effect on the LUMOs, although there is slightly more metal participation in the LS LUMOs. Overall, the different substituent group have a relatively minor effect on the frontier orbitals consistent with the observation that all these systems undergo spin crossover.

3.3 | Spin state splitting in $[Fe(qsal\text{-}X)_2]^+$

The energy difference between the HS and LS state, Δ*E*(HS-LS) for the complexes calculated using B3LYP, B3LYP-D3, B3LYP*, BHandHLYP, BP86, OLYP, OPBE, M06L, and TPSSh, with four different basis sets each: 6-31G**, cc-pVDZ, cc-pVTZ, and Def2TZVP are presented in Table 3. These values are averages across all the complexes as the results indicate the splitting energies are relatively insensitive to the substituent group (see Supporting Information Table S2). The smaller basis sets 3-21G* and dgdzvp exhibit large standard deviations and are thus presented in Supporting Information Table S3. For all tested functionals and basis sets here, very similar Δ*E*(HS-LS) were obtained from the four different starting structures of $[Fe(qsal\text{-}OMe)_2]^+$. Figure S3 Supporting Information illustrates the comparison of Δ*E*(HS-LS) for $[Fe(qsal\text{-}OMe)_2]^+$ calculated with eight DFT functionals with 6-31G** basis set using four starting structures optimized at the B3LYP/6-31G** level. The lack of any significant difference is to be expected as the starting structures contain the same cation.

A comparison of Δ*E*(HS-LS) for the nine complexes calculated from the methods considered here, reveal similar trends as can be seen in Figure 4 for $[Fe(qsal\text{-}OMe)_2]^+$ and $[Fe(qsal\text{-}I)_2]^+$ as representative examples. The Δ*E*(HS-LS) is clearly sensitive to the DFT functional and the basis set. As can be seen in Supporting Information Tables S2–S3, when a dgdzvp basis set is used with any functional tested here, there

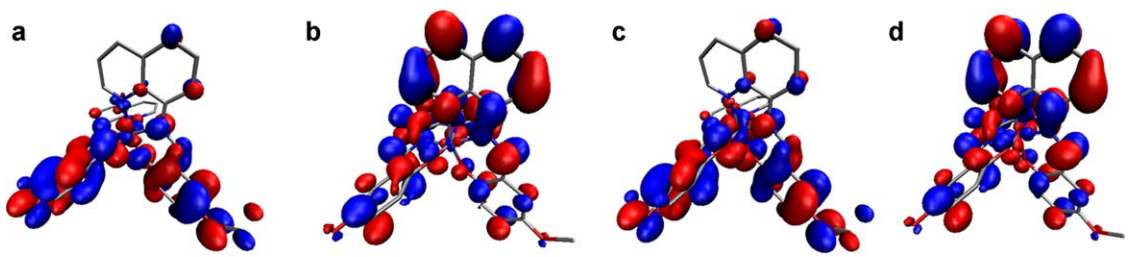

FIGURE 2 HOMO and LUMO of $[Fe(qsal\text{-}OMe)_2]^+$ in the high spin (HS) and low spin (LS) state where a = HOMO in HS, b = LUMO in HS, c = HOMO in LS, and d = LUMO in LS

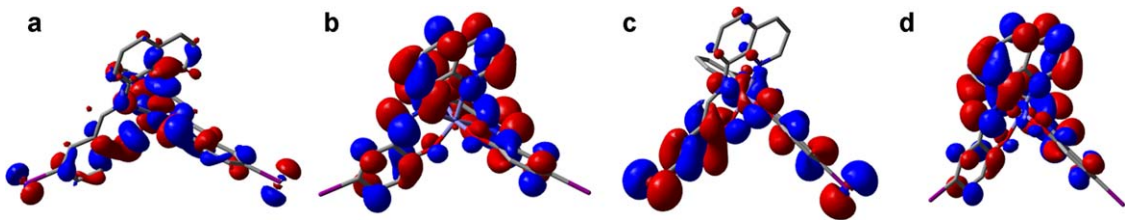

FIGURE 3 HOMO and LUMO of $[Fe(qsal\text{-}I)_2]^+$ in the high spin (HS) and low spin (LS) state where a = HOMO in HS, b = LUMO in HS, c = HOMO in LS, and d = LUMO in LS

is a large increase in ΔE(HS-LS) by 10–17 kcal/mol, compared to those of cc-pVTZ. In contrast, 3-21G* decreases ΔE(HS-LS) by 3–11 kcal/mol. This clearly shows that the dgdzvp and 3-21G* basis sets are too small for accurate calculations of the spin state energy in spin crossover systems, in line with previous reports by Swart et al.[19] The three basis sets 6-31G**, cc-pVTZ, and Def2TZVP give similar spin state splittings to each other, the difference being up to 2.5 kcal/mol but, on average, only 0.68 kcal/mol. We also note that cc-pVTZ and Def2TZVP are particularly close a trend also reported by Swart et al. in calculations on a series of $[M(Tp\text{-}R)_2]^{n+}$ (n = 0, 1, 2) compounds.[43] By comparison, cc-pVDZ yields values consistently lower than these basis sets by about 3 kcal/mol.

Looking at the effect of the functional on ΔE(HS-LS), we ignore the dgdzvp and 3-21G* basis sets due to their aforementioned failure for these spin crossover systems. As illustrated in Supporting Information Tables S2, S4, and Table 3, BH&HLYP and M06L predict negative values of ΔE(HS-LS). It follows that these two functionals favour the HS state too much, resulting in an underestimation of ΔE(HS-LS) by up to 25.2 and 7.6 kcal/mol, respectively. Jensen and Cirera report a similar favouring of the HS state by M06L in $[Fe(acac_2\text{-trien})]^+$ ($acac_2$-trien- = 4-[2-(2-{2-[3-Hydroxy-1-methyl-2-butenylideneamino]ethylamino}ethylamino)ethylimino]-2-penten-2-ol).[40] In contrast, BP86 and TPSSh favour the LS state resulting in a large positive value of HS-LS gap of 21 to 25 kcal/mol and 11 to 14 kcal/mol. The poor performance of TPSSh is puzzling given it's widespread use in iron(II) and cobalt(II) SCO materials[40,44] and suggests that it may be unsuitable for iron(III) spin crossover systems. Indeed, TPSSh has been shown to yield an enthalpy for spin crossover of 7.9 and 9.6 kcal/mol for $[Fe(acac_2\text{-trien}]^+$.[34,40] This is further supported by Bannwarth et al. who also found the LS state is favoured by TPSSh and BP86 in their iron(III) spin crossover compounds, $[Fe(salten)(n\text{-azpy})]BPh_4$ (n = 3, 4; salten = *o*-[(3-{3-[(*o*-Hydroxyphenyl)methylideneamino]propylamino}propylimino)methyl]phenol).[45] B3LYP* also seems to favour the LS state, however, using B3LYP* with cc-pVDZ gives an acceptable value of ΔE(HS-LS) (~5 kcal/mol) with the right sign, for the complexes considered here. Subtle changes in the spin state energy as a result of changes in the basis set has previously been observed by Swart et al.[19] Moreover, the general favouring of the LS state by B3LYP* is consistent with the results of with Friesner and Hughes who recommend against the use of B3LYP* in spin crossover complexes.[21] They argue that the reason B3LYP* is not suitable for all spin crossover complexes is that it was optimized using a narrow training set involving principally aromatic nitrogen donors. The system in this study involves phenoxide O donors to give an N_4O_2 donor set, compared to N_6 commonly found for Fe(II), and may explain why B3LYP* does not perform as well as expected.

As regards the remaining functionals reasonable values for the HS-LS gap (in the range of 1 to 5 kcal/mol) can be obtained from OPBE with any of these four basis sets. In addition, a HS-LS gap of 1.7 to 3.2 kcal/mol is predicted by B3LYP and OLYP with 6-31G**, cc-pVTZ, and Def2TZVP, while with cc-pVDZ these two functionals predict ΔE(HS-LS) to be −0.8 to −0.4 kcal/mol. Hence, among the functionals

TABLE 3 Average spin state splittings, ΔE(HS-LS) for the nine iron complexes, $[Fe(qsal\text{-}X)_2]^+$ calculated with nine functionals with the four largest basis sets (kcal/mol)

Functional	6-31G**	cc-pVDZ	cc-pVTZ	Def2TZVP	Mean	MAX	MIN
B3LYP	3.24	−0.74	2.01	1.67	1.54	3.24	−0.74
B3LYP-D3	3.19	0.12	2.01	1.66	1.75	3.19	0.12
B3LYP*	9.33	5.40	8.30	8.02	7.76	9.33	5.40
TPSSh	14.39	10.83	13.79	13.75	13.19	14.39	10.83
BP86	24.73	21.52	24.69	24.37	23.83	24.73	21.52
BHandHLYP	−21.08	−25.21	−22.97	−23.60	−23.60	−21.08	−25.21
OLYP	3.04	−0.39	3.00	3.10	2.18	3.10	−0.39
OPBE	3.93	1.14	4.79	5.09	3.74	5.09	1.14
M06L	−3.78	−7.57	−4.11	−3.94	−4.85	−7.57	−3.78

considered in this study, OPBE, OLYP, and B3LYP (with or without dispersion) are good choices for computing the ΔE(HS-LS) gap. The results mirror those of Swart who routinely recommends OPBE with a suitably large basis set.[46]

Comparing B3LYP and B3LYP-D3, we find that on average the difference is only 0.20 kcal/mol with a maximum deviation of 0.86 kcal/mol. While dispersion effects can be significant in spin crossover systems they are highly system dependent. In our case, it is possible that as the ligands are rigid and sterically small and there is a smaller structural difference between the two spin states for Fe(III), the dispersion effects are less significant.

3.4 | Experimental and computed enthalpies of spin crossover

For [Fe(qsal-I)$_2$]OTf·MeOH, thermochemical analysis was carried out within the harmonic approximation to estimate the enthalpy associated with the conversion between the HS and LS spin states, to compare

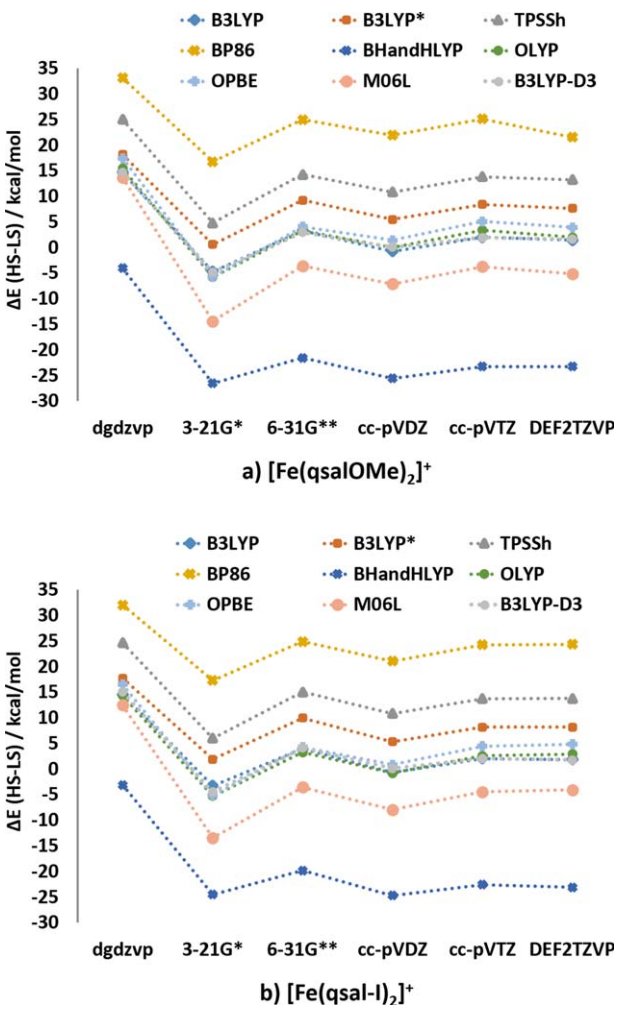

FIGURE 4 Comparison of ΔE(HS-LS) calculated with nine DFT functionals and six basis sets for a) [Fe(qsal-OMe)$_2$]$^+$ and b) [Fe(qsal-I)$_2$]$^+$ using the structures of **1** and **8** optimized at the B3LYP/6-31G** level, respectively

TABLE 4 Experimental and computed enthalpies associated with the conversion between the HS and LS spin states of [Fe(qsal-I)$_2$]$^+$ (kcal/mol)

Method		ΔH(HS-LS) Electronic energy	ΔH(HS-LS) Thermal correction to enthalpy	ΔH(HS-LS)-total
B3LYP	6-31G**	3.94	−1.82	2.12
B3LYP	cc-pVDZ	−0.68	−2.45	−3.14
B3LYP	cc-pVTZ	2.03	−1.30	0.73
B3LYP-D3	6-31G**	4.13	−1.21	2.92
B3LYP-D3	cc-pVDZ	0.10	−3.62	−3.52
B3LYP-D3	cc-pVTZ	2.07	−1.30	0.77
B3LYP*	6-31G**	9.94	−1.83	8.11
B3LYP*	cc-pVDZ	5.31	−2.49	2.82
B3LYP*	cc-pVTZ	8.19	−1.33	6.85
OLYP	6-31G**	3.25	−1.58	1.68
OLYP	cc-pVDZ	−5.29	−1.65	−6.94
OLYP	cc-pVTZ	2.57	−1.09	1.48
OPBE	6-31G**	4.27	−2.68	1.58
OPBE	cc-pVDZ	0.81	−1.57	−0.76
OPBE	cc-pVTZ	4.47	−1.62	2.85
Exp[a]				1.34

[a]Taken from Ref. 27.

with the experimental data. Five functionals: B3LYP, B3LYP-D3, B3LYP*, OLYP, and OPBE along with three basis sets: 6-31G**, cc-pVDZ, and cc-pVTZ were tested. Def2TZVP is not included as the results above shows it produces very similar spin gaps to cc-pVTZ. As shown in Table 4, the thermal corrections for enthalpies calculated from various methods are similar at −1.09 to −3.62 kcal/mol. This closely matches the value reported by Kepp in 30 spin crossover complexes of 2.15 kcal/mol.[34] The electronic energy contribution is strongly dependent on the basis set and as above it is clear that a large basis set is required to accurately model this in spin crossover systems.

The enthalpy calculated with the OLYP functional and cc-pVTZ basis set (1.48 kcal/mol) is the most similar to the experimental data (1.34 kcal/mol), followed by that of OPBE with 6-31G** (1.58 kcal/mol) and B3LYP-D3 with cc-pVTZ (0.77 kcal/mol). By comparison, B3LYP* yields a value of 5.92 kcal/mol which is a little high for Fe(III) spin crossover compounds.[23] While care is needed not to over interpret this result as it based on a single data set, an analysis of the enthalpies of six iron(III) spin crossover compounds in a recent study by Kepp revealed that the enthalpies where on average 7.64 and −0.97 kcal/mol for B3LYP* and B3LYP, respectively (see Supporting Information Table S5).[34] As Kepp's study included zero-point energies, solvation, dispersion, and relativistic effects the close agreement with the current work suggests that our conclusions are justified.

4 | CONCLUSIONS

Using the cations obtained from nine X-ray crystal structures of $[Fe(qsal\text{-}X)_2]^+$ (X = OMe, F, Cl, Br, I, H) the accuracy of different quantum mechanical methods for energetic calculations and the structure optimization of iron(III) spin crossover complexes were investigated. Reasonable results of the spin state splittings, ΔE(HS-LS) can be obtained using B3LYP (with or without dispersion), OLYP, and OPBE functionals with a 6-31G**, cc-pVDZ, cc-pVTZ, and Def2TZVP basis set. Thermodynamic parameters are also correctly predicted with the OLYP functional using a cc-pVTZ basis set (1.48 kcal/mol) giving the most similar enthalpy compared with the experimental data for $[Fe(qsal\text{-}I)_2]^+$ (1.34 kcal/mol). The over favouring of the low spin state by B3LYP* seems to suggest it may not be suitable for use with these iron(III) spin crossover systems, although further work on a broader set of compounds will be needed to confirm this. Hence, these methods are an effective tool for the prediction of spin crossover in iron(III) compounds and will be useful for other researchers seeking to explore more complex theoretical problems in iron(III) spin crossover materials.

ACKNOWLEDGMENTS

We thank Walailak University for a Postdoctoral Fellowship to JS, the Thailand Research Fund (RSA5580028 and RSA5880048) and the National Science and Technology Development Agency (grant no.: P-10-11181) for funding this research.

REFERENCES

[1] M. A. Halcrow, Ed., *Spin-Crossover Materials: Properties and Applications*, Wiley, Chichester **2013**.

[2] P. Gütlich, A. B. Gaspar, Y. Garcia, *Beilstein J. Org. Chem.* **2013**, *9*, 342.

[3] P. Gütlich, H. A. Goodwin, *Top. Curr. Chem.* **2004**, *233*, 1–47.

[4] A. Bousseksou, G. Molnár, L. Salmon, W. Nicolazzi, *Chem. Soc. Rev.* **2011**, *40*, 3313.

[5] V. Ksenofontov, A. B. Gaspar, P. GüTlich, *Top. Curr. Chem.* **2004**, *235*, 23.

[6] J. F. Létard, *J. Mater. Chem.* **2006**, *16*, 2550.

[7] J. F. Létard, G. Chastanet, P. Guionneau, C. Desplanches, in *Spin-Crossover Materials: Properties and Applications* (Ed: M. A. Halcrow), Wiley, Chichester **2013**, pp. 475–506.

[8] J. F. Létard, P. Guionneau, L. Goux-Capes, *Top. Curr. Chem.* **2004**, *235*, 221.

[9] P. Gamez, J. S. Costa, M. Quesada, G. Aromí, *Dalton Trans.* **2009**, 7845.

[10] A. Hauser, *Top. Curr. Chem.* **2004**, *233*, 49.

[11] R. J. Deeth, C. M. Handley, B. J. Houghton, in *Spin-Crossover Materials: Properties and Applications* (Ed: M. A. Halcrow), Wiley, Chichester **2013**, pp. 443–454.

[12] R. J. Deeth, in *Spin States in Biochemistry and Inorganic Chemistry: Influence on Structure and Reactivity* (Eds: M. Swart, M. Costas), Wiley, Oxford, UK **2016**, pp. 85–102.

[13] K. P. Kepp, *Coord. Chem. Rev.* **2013**, *257*, 196.

[14] K. Pierloot, S. Vancoillie, *J. Chem. Phys.* **2008**, *128*, 34104.

[15] L. Daku, F. Aquilante, T. W. Robinson, A. Hauser, *J Chem. Theory Comput.* **2012**, *6*, 4216.

[16] M. Kepenekian, V. Robert, B. Le Guennic, *J. Chem. Phys.* **2009**, *131*, 114702.

[17] M. Radoń, P. Rejmak, M. Fitta, M. Bałanda, J. Szklarzewicz, *Phys. Chem. Chem. Phys.* **2015**, *17*, 14890.

[18] M. Reiher, O. Salomon, B. Artur Hess, *Theor. Chem. Acc.* **2001**, *107*, 48.

[19] M. Güell, J. M. Luis, M. Solà, M. Swart, *J. Phys. Chem. A* **2008**, *112*, 6384.

[20] M. Reiher, *Inorg. Chem.* **2002**, *41*, 6928.

[21] T. F. Hughes, R. A. Friesner, *J. Chem. Theory Comput.* **2011**, *7*, 19.

[22] M. Nihei, T. Shiga, Y. Maeda, H. Oshio, *Coord. Chem. Rev.* **2007**, *251*, 2606.

[23] D. J. Harding, P. Harding, W. Phonsri, *Coord. Chem. Rev.* **2016**, *313*, 38.

[24] S. Hayami, Z. Gu, H. Yoshiki, A. Fujishima, O. Sato, *J. Am. Chem. Soc.* **2001**, *123*, 11644.

[25] S. Hayami, K. Hiki, T. Kawahara, Y. Maeda, D. Urakami, K. Inoue, M. Ohama, S. Kawata, O. Sato, *Chem. Eur. J.* **2009**, *15*, 3497.

[26] D. J. Harding, D. Sertphon, P. Harding, K. S. Murray, B. Moubaraki, J. D. Cashion, H. Adams, *Chem. Eur. J.* **2013**, *19*, 1082.

[27] D. J. Harding, W. Phonsri, P. Harding, I. A. Gass, K. S. Murray, B. Moubaraki, J. D. Cashion, L. Liu, S. G. Telfer, *Chem. Commun.* **2013**, *49*, 6340.

[28] W. Phonsri, D. J. Harding, P. Harding, K. S. Murray, B. Moubaraki, I. A. Gass, J. D. Cashion, G. N. L. Jameson, H. Adams, *Dalton Trans.* **2014**, *43*, 17509.

[29] D. J. Harding, W. Phonsri, P. Harding, K. S. Murray, B. Moubaraki, G. N. L. Jameson, *Dalton Trans.* **2015**, *44*, 15079.

[30] A. I. S. Neves, J. C. Dias, B. J. C. Vieira, I. S. Santos, M. B. Castelo Branco, L. C. J. Pereira, J. C. Waerenborgh, M. Almeida, D. Belo, V. Da Gama, *CrystEngComm* **2009**, *11*, 2160.

[31] M. J. Frisch, G. W. Trucks, H. B. Schlegel, G. E. Scuseria, M. A. Robb, J. R. Cheeseman, G. Scalmani, V. Barone, G. A. Petersson, H. Nakatsuji, X. Li, M. Caricato, A. Marenich, J. Bloino, B. G. Janesko, R. Gomperts, B. Mennucci, H. P. Hratchian, J. V. Ortiz, A. F. Izmaylov, J. L. Sonnenberg, D. Williams-Young, F. Ding, F. Lipparini, F. Egidi, J. Goings, B. Peng, A. Petrone, T. Henderson, D. Ranasinghe, V. G. Zakrzewski, J. Gao, N. Rega, G. Zheng, W. Liang, M. Hada, M. Ehara, K. Toyota, R. Fukuda, J. Hasegawa, M. Ishida, T. Nakajima, Y. Honda, O. Kitao, H. Nakai, T. Vreven, K. Throssell, J. A. Montgomery, Jr., J. E. Peralta, F. Ogliaro, M. Bearpark, J. J. Heyd, E. Brothers, K. N. Kudin, V. N. Staroverov, T. Keith, R. Kobayashi, J. Normand, K. Raghavachari, A. Rendell, J. C. Burant, S. S. Iyengar, J. Tomasi, M. Cossi, J. M. Millam, M. Klene, C. Adamo, R. Cammi, J. W. Ochterski, R. L. Martin, K. Morokuma, O. Farkas, J. B. Foresman, and D. J. Fox, *Gaussian 09 (Revision E.01)*, Gaussian, Inc., Wallingford CT, **2009**.

[32] D. Sertphon, D. J. Harding, P. Harding, K. S. Murray, B. Moubaraki, J. D. Cashion, H. Adams, *Eur. J. Inorg. Chem.* **2013**, 788.

[33] S. Grimme, J. Antony, S. Ehrlich, H. Krieg, *J. Chem. Phys.* **2010**, *132*, 154104.

[34] K. P. Kepp, *Inorg. Chem.* **2016**, *55*, 2717.

[35] K. P. Jensen, B. O. Roos, U. Ryde, *J. Chem. Phys.* **2007**, *126*, 14103.

[36] M. P. Waller, H. Braun, N. Hojdis, M. Bühl, *J. Chem. Theory Comput.* **2007**, *3*, 2234.

[37] M. Swart, R. Groenhof, A. W. Ehlers, K. Lammertsma, *J. Phys. Chem. A* **2004**, *108*, 5479.

[38] J. K. McCusker, A. L. Rheingold, D. N. Hendrickson, *Inorg. Chem.* **1996**, *35*, 2100.

[39] M. Marchivie, P. Guionneau, J. F. Létard, D. Chasseau, *Acta Crystallogr. Sect. B Struct. Sci.* **2005**, *61*, 25.

[40] K. P. Jensen, J. Cirera, *J. Phys. Chem. A* **2009**, *113*, 10033.

[41] T. Bučko, J. Hafner, S. Lebègue, J. G. Ángyán, *Phys. Chem. Chem. Phys.* **2012**, *14*, 5389.

[42] S. Alvarez, *Chem. Rev.* **2015**, *115*, 13447.

[43] M. Gruden-Pavlović, S. Stepanović, M. Perić, M. Güell, M. Swart, *Phys. Chem. Chem. Phys.* **2014**, *16*, 14514.

[44] J. Cirera, F. Paesani, *Inorg. Chem.* **2012**, *51*, 8194.

[45] A. Bannwarth, S. O. Schmidt, G. Peters, F. D. Sönnichsen, W. Thimm, R. Herges, F. Tuczek, *Eur. J. Inorg. Chem.* **2012**, 2776.

[46] M. Swart, *J. Chem. Theory Comput.* **2008**, *4*, 2057.

SUPPORTING INFORMATION

Additional Supporting Information may be found in the online version of this article.

How to cite this article: Sirirak J, Sertphon D, Phonsri W, Harding P, Harding DJ. Comparison of density functionals for the study of the high spin low spin gap in Fe(III) spin crossover complexes. *Int J Quantum Chem.* 2017;117:e25362. https://doi.org/10.1002/qua.25362

NJC

PAPER

Check for updates

Cite this: *New J. Chem.*, 2017, **41**, 13747

Spin crossover in mixed ligand iron(III) complexes†

Wasinee Phonsri, ‡[a] Phimphaka Harding, [a] Keith S. Murray, [b] Boujemaa Moubaraki[b] and David J. Harding *[a]

Received 25th September 2017,
Accepted 18th October 2017

DOI: 10.1039/c7nj03676k

rsc.li/njc

Mixed ligand complexes [Fe(qsal-Cl)(qsal-Br)]Y·sol (Y = NCS, sol = MeOH **1**; PF_6 **2**; BPh_4, sol = $2CH_2Cl_2$ **3**; OTf, sol = 0.5MeOH **4**) have been synthesized. X-ray crystallographic studies of **1**, **2** and **4** at 123 K reveal that the Fe(III) centres are low spin in all cases. In **2** there are two independent Fe(III) centres in the asymmetric unit cell. The structure of **3** has been determined at 100, 123 and 269 K with the Fe centre low spin, mixed spin and mostly high spin, respectively. Packing in the complexes is dominated by π–π interactions which form a 1D chain. C–H···π, C–H···Cl/Br and C–Cl/Br···π interactions link the chains to form highly cooperative supramolecular 3D networks mirroring the homoleptic complexes. SQUID magnetometric studies show almost complete, 50% complete and stepped spin crossover for **1**, **2** and **3** respectively. [Fe(qsal-Cl)(qsal-Br)]OTf·0.5MeOH **4** is low spin up to 350 K. Compared to the homoleptic complexes spin crossover behaviour is mostly intermediate between the $[Fe(qsal\text{-}Cl)_2]^+$ and $[Fe(qsal\text{-}Br)_2]^+$ systems except for **3** where spin crossover characteristics are improved compared to the homoleptic complexes.

Introduction

Iron(III) spin crossover (SCO) complexes have attracted much attention in the last few years due to an increasing number of systems that exhibit abrupt and hysteretic SCO.[1–4] Compared to the more common iron(II) SCO systems,[5–8] iron(III) shows a smaller change in the Fe-ligand bond lengths, limited colour differences between the two spin states and very often no light induced spin crossover (LIESST). Nevertheless, iron(III) compounds are usually more robust and SCO is accessible with a wide range of ligand donor sets.[1] While a range of complexes with different ligands has been reported the most successful systems incorporate tridentate ligands.[9–23] The success of these systems lies in effective control of the supramolecular interactions between the spin centres, known as the cooperativity and essential for abrupt and hysteretic SCO.[24,25] In $[Fe(qsal\text{-}X)_2]^+$ {qsal-X = (*N*-8-quinolyl)-5-X-salicylaldiminate}[9–15] complexes strong π–π interactions are involved while for $[Fe(X\text{-}salEen)_2]^+$ {X-salEen = *N*-ethyl-*N*-(2-aminoethyl)-X-salicylaldiminate}[16–18] and [Fe(5-X-Hthsa)(5-X-thsa)] (5-X-H_2thsa = 5-X-salicylaldehydethiosemicarbazone)[19–23] extensive hydrogen bonding facilitates cooperativity. In these complexes abrupt, symmetry breaking and hysteretic SCO have been reported.

In the search for systems where SCO occurs at room temperature some of us have explored the use of two different ligands. In [Fe(thsa)(qsal)]·sol (sol = 0.4*n*BuOH, 0.5MeCN, 0.5 THF) the MeCN solvate shows a reversible [LS–HS] to [HS–HS] transition with partial loss of MeCN in a single-crystal-to-single-crystal transformation.[26] The halogen substituted analogues [Fe(qsal-X)(thsa)]·*n*MeCN (X = F, *n* = 2.5; X = Cl, Br and I, *n* = 1) are also SCO active but only in the first cycle with [Fe(qsal-F)(thsa)] HS and the Br and I compounds LS.[27] The exception is [Fe(qsal-Cl)(thsa)]·MeCN which after solvent loss exhibits incomplete but hysteretic SCO. In contrast, [Fe(thsa)-(3-OMe-salEen)] shows complete SCO with a very high $T_{1/2}$.[28] In all cases, the mixed ligand complexes exhibit distinct magnetic behaviour not present in the homoleptic analogues. In attempting to more subtly alter the SCO characteristics of these complexes we have now prepared [Fe(qsal-Cl)(qsal-Br)]Y (Y = NCS, PF_6, BPh_4, OTf). The structures and magnetic profiles of the complexes are discussed and comparisons drawn with the homoleptic compounds.

Results and discussion

Synthesis of $[Fe(qsal\text{-}Cl)(qsal\text{-}Br)]^+$ complexes

The compounds [Fe(qsal-Cl)(qsal-Br)]Y·sol (Y = NCS, sol = MeOH **1**; PF_6 **2**; BPh_4, sol = $2CH_2Cl_2$ **3**; OTf, sol = 0.5MeOH **4**) have been prepared *via* layered diffusion in moderate yields (Scheme 1). The compounds are black with IR spectra showing imine

[a] *Functional Materials and Nanotechnology Centre of Excellence (FuNTech), Walailak University, Thasala, Nakhon Si Thammarat, 80160, Thailand. E-mail: hdavid@g-mail.wu.ac.th*

[b] *School of Chemistry, Monash University, Clayton, Victoria, 3800, Australia*

† Electronic supplementary information (ESI) available: TGA results, PXRD diffractograms of **3** and **4**, and supplementary X-ray crystallographic pictures. CCDC 1526771–1526776. For ESI and crystallographic data in CIF or other electronic format see DOI: 10.1039/c7nj03676k

‡ Current address: School of Chemistry, Monash University, Australia.

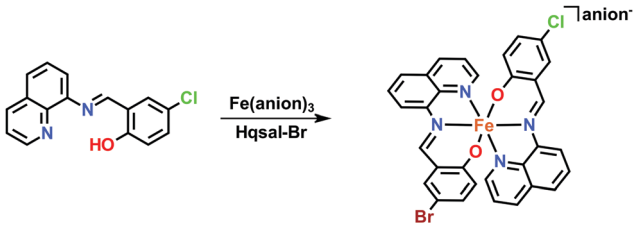

Scheme 1 Synthesis of [Fe(qsal-Cl)(qsal-Br)]$^+$.

stretches between 1598–1602 cm^{-1} and typical of chelated qsal-X ligands.[14,15,29,30] Stretches for the NCS, PF_6 and OTf anions are also evident in the IR spectra (Table 1).

TGA analysis of the compounds reveals a mass loss of 3.9% for **1** between 70–100 °C consistent with one MeOH (4.3% expected, Fig. S1, ESI†). Similarly, **3** displays a 13.7% mass loss beginning at 50 °C and complete at 90 °C, indicative of two molecules of CH_2Cl_2 (14.7%). The other complexes showed no mass loss until much higher temperatures and in the case of **4** suggests that the MeOH is readily lost, something confirmed by elemental analysis.

Structures of [Fe(qsal-Cl)(qsal-Br)]$^+$ complexes

Structures of all the mixed-ligand complexes have been determined, in some cases at multiple temperatures. The compounds all crystallize in triclinic $P\bar{1}$ except **4** which is in monoclinic $P2_1/c$ (Table 2). In all cases the Cl and Br substituents are crystallographically disordered over the two sites. This has been modelled with either fixed or variable occupancy and in both cases yields 1 : 1 ratio of the qsal-Cl and qsal-Br ligands. Interestingly, only [Fe(qsal-Cl)(qsal-Br)]PF_6 has two Fe(III) centres in the asymmetric unit with the other compounds having a single Fe(III) site (Fig. 1). By comparison, the compositions of the homoleptic compounds are [Fe(qsal-X)$_2$]NCS·MeOH, [Fe(qsal-X)$_2$]PF_6, [Fe(qsal-X)$_2$]OTf·sol (X = Cl, sol = none; X = Br, sol = 0.5MeOH) and [Fe(qsal-X)$_2$]BPh_4·sol (X = Cl, sol = H_2O; X = Br, sol = CH_2Cl_2) showing the heteroleptic species are more similar to the [Fe(qsal-Br)$_2$]$^+$ compounds.[31]

As compounds **3** and **4** differ from the homoleptic systems in terms of the solvent present in the lattice and to ensure that the bulk sample is not a mixture of the homoleptic compounds we undertook PXRD studies (Fig. S2 and S3, ESI†). The simulated and real diffractograms show remarkably good agreement and confirm that the crystal structures are reflective of the bulk material.

The Fe–N/O bond lengths of [Fe(qsal-Cl)(qsal-Br)]Y (Y = NCS, PF_6, OTf) at 123 K are between 1.945–1.969 Å and 1.850–1.880 Å, respectively indicative of LS Fe(III) (Table 3). This assignment is supported by the octahedral distortion parameters.[32,33] Interestingly, in **2** the Fe–N/O bond lengths of the two Fe(III) centres are very similar but the distortion parameters are subtly different. This may suggest that only one of the Fe centres is able to undergo spin crossover.

The most interesting member in this series is [Fe(qsal-Cl)(qsal-Br)]BPh_4·2CH_2Cl_2 where we have been able to determine the structure at three different temperatures. At 100 K the Fe–N/O bond distances are short and characteristic of a LS centre while at 123 K the Fe–N/O bond lengths elongate but are intermediate between HS and LS, termed MIX (Table 4). Note that by mixed we mean a mixture of the HS and LS states and not the intermediate S = 3/2 spin state. Only at 267 K are the Fe–N/O bonds and Σ and Θ indicative of full HS character. This suggests either gradual or stepped spin crossover is present in this compound.

The packing in **1**, **3** and **4** involves a pair of orthogonal π–π interactions which link the cations to form a 1D chain (Fig. 2 and Fig. S4–S8, ESI†). The plane-to-plane distances vary from 3.13–3.32 Å and are typical of [Fe(qsal-X)$_2$]$^+$ complexes (Table 5). In **2** the packing is substantially altered with two types of π–π interaction that form Fe1–Fe1 and Fe2–Fe2 dimers. The type A interaction is 0.13 Å shorter than type B due to the more planar qsal-X ligand in the former dimer. The dimers are linked by further π–π contacts but these have minimal overlap resulting in significantly weaker cooperativity. The 1D chains are connected by a range of other contacts principally C–H···π, C–H···Cl/Br and C–Cl/Br···π forming highly cooperative supramolecular 3D networks (Fig. 3). Many of the interactions are present in the homoleptic complexes, [Fe(qsal-X)$_2$]Y and reveal that the presence of two different ligands does not significantly impact the supramolecular connectivity.

Beyond the 1D chains, the packing in **3** is very different with multiple aryl embraces occurring between the [Fe(qsal-Cl)(qsal-Br)]$^+$ chains and the BPh_4^- anions (Fig. 4). Multiple aryl embraces are composed of a combination of C–H···π and π–π interactions in which none of the aryl groups are completely parallel or perpendicular. These interactions have been reported in a wide range of [M(2,2′-bipy)$_3$]$^{n+}$ complexes[34] and are also found in [Fe(qnal-7-OMe)$_2$]BPh_4·2MeOH.[35]

Magnetic studies of [Fe(qsal-Cl)(qsal-Br)]$^+$ complexes

The magnetic properties of **1–4** have been studied between 2–350 K by SQUID magnetometry (Fig. 5). To aid comparison, the $\chi_M T$ values of the homoleptic systems are plotted with those

Table 1 Physical and IR spectroscopic data [Fe(qsal-Cl)(qsal-Br)]Y·sol

Compound	% yield	Colour	IR[a] (cm^{-1})		
			$\nu_{C=N}$	ν_{ArH}	ν_{anion}
[Fe(qsal-Cl)(qsal-Br)]NCS·MeOH **1**	43	Black	1619	3054	2055
[Fe(qsal-Cl)(qsal-Br)]PF_6 **2**	38	Black	1614	3056	843
[Fe(qsal-Cl)(qsal-Br)]BPh_4·2CH_2Cl_2 **3**	45	Black	1619	3057	—
[Fe(qsal-Cl)(qsal-Br)]OTf·0.5MeOH **4**	35	Black	1614	3054	1297, 1164, 1084

[a] Complexes were determined in KBr.

 This journal is © The Royal Society of Chemistry and the Centre National de la Recherche Scientifique 2017

Table 2 Crystallographic data and structure refinement for **1–4**

	1	**2**		**3**		**4**
	123 K	123 K	100 K	123 K	267 K	123 K
Formula	$C_{34}H_{24}BrClFeN_5O_3S$	$C_{32}H_{20}BrClF_6FeN_4O_2P$		$C_{58}H_{44}BBrCl_5FeN_4O_2$		$C_{33.50}H_{20.50}BrClF_3FeN_4O_{3.50}S$
Molecular weight/gmol^{-1}	753.85	808.70	1152.79	1152.79	1152.79	827.31
Crystal system	Triclinic	Triclinic	Triclinic	Triclinic	Triclinic	Monoclinic
Space group	$P\bar{1}$	$P\bar{1}$	$P\bar{1}$	$P\bar{1}$	$P\bar{1}$	$P2_1/c$
a/Å	10.0889(13)	10.3803(6)	13.5484(8)	13.6206(5)	13.719(2)	14.0102(7)
b/Å	12.1516(15)	12.5570(7)	13.5845(6)	13.6929(5)	14.012(3)	19.1475(9)
c/Å	13.1028(18)	23.1729(14)	16.3212(10)	16.2779(6)	16.606(5)	12.2634(5)
α/°	105.885(3)	86.246(3)	97.290(4)	112.954(2)	113.81(2)	90
β/°	98.459(4)	81.312(3)	112.892(5)	96.785(2)	96.164(18)	111.1770(10)
γ/°	98.029(4)	89.492(3)	109.908(5)	110.518(2)	110.831(19)	90
T/K	123(2)	123(2)	100.0(1)	123(2)	267(9)	123(2)
Cell volume/Å^3	1500.6(3)	2979.4(3)	2482.6(3)	2501.27(17)	2609.3(12)	3067.6(2)
Z	2	4	2	2	2	4
Absorption coefficient/mm^{-1}	2.021	2.069	1.428	1.417	1.359	2.287
Reflections collected	9769	26 342	25 868	21 299	26 833	19 857
Independent reflections, R_{int}	6642, 0.0252	13 733, 0.1199	13 308, 0.0346	11 362, 0.0399	13 900, 0.0743	7014, 0.0399
Max. and min. transmission	0.7496 and 0.6296	0.8520 and 0.7894	0.8361 and 0.6349	0.8372 and 0.6368	0.8432 and 0.6478	0.6878 and 0.4312
Restraints/parameters	18/441	8/901	10/667	4/667	4/668	21/506
Final R indices [$I > 2\sigma(I)$]: R_1, wR_2	0.0896, 0.2389	0.0552, 0.0953	0.0491, 0.1092	0.0549, 0.1328	0.0872, 0.2282	0.0532, 0.1357

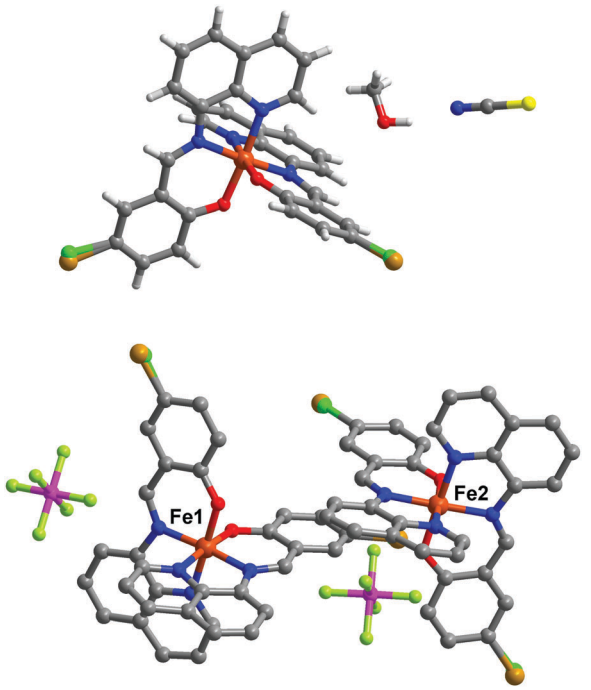

Fig. 1 The asymmetric unit of [Fe(qsal-Cl)(qsal-Br)]NCS·MeOH **1** (above) and [Fe(qsal-Cl)(qsal-Br)]PF_6 **2** (below).

Table 3 Fe–N/O bond lengths and octahedral distortion parameters of **1**, **2** and **4** at 123 K (Å, °)

	NCS-1	OTf-4	PF_6-2		
Fe1–O1	1.879(5)	1.880(3)	1.844(3)	Fe2–O3	1.855(3)
Fe1–O2	1.878(5)	1.879(3)	1.855(3)	Fe2–O4	1.858(3)
Fe1–O_{av}	1.878(5)	1.880(3)	1.850(3)	Fe2–O_{av}	1.856(3)
Fe1–N1	1.965(6)	1.948(2)	1.936(4)	Fe2–N5	1.940(4)
Fe1–N2	1.986(6)	1.962(3)	1.950(4)	Fe2–N6	1.952(4)
Fe1–N3	1.949(6)	1.946(3)	1.940(4)	Fe2–N7	1.933(4)
Fe1–N4	1.975(6)	1.962(3)	1.976(4)	Fe2–N8	1.956(4)
Fe1–N_{av}	1.969(6)	1.954(3)	1.950(4)	Fe2–N_{av}	1.945(4)
Σ	47	50	43	Σ	52
Θ	67	71	63	Θ	69

of **1–4**. In **1** the SCO is gradual reaching a plateau of *ca.* 2.5 cm^3 mol^{-1} K (60% HS) at 280–330 K before beginning to increase again. The SCO is more abrupt than [Fe(qsal-Br)$_2$]NCS·MeOH but less than the chloro analogue.[29] The onset of SCO also increases from 150 to *ca.* 200 to *ca.* 270 K in going from the Cl—only to **1** to the Br—only compound. In a similar way **2** exhibits gradual SCO behaviour intermediate between the two homoleptic analogues this time reaching 30% HS at 350 K. In the case of **4** the SCO profile more closely matches that of [Fe(qsal-Cl)$_2$]OTf than [Fe(qsal-Br)$_2$]OTf. In all of these compounds, the structures of the mixed-ligand compounds are virtually identical to the homoleptic [Fe(qsal-X)$_2$]Y systems.

In contrast, [Fe(qsal-Cl)(qsal-Br)]BPh_4·2CH_2Cl_2 exhibits a magnetic profile unlike either of the parent complexes perhaps as it contains two CH_2Cl_2 molecules rather than the single

Table 4 Fe–N/O bond lengths and octahedral distortion parameters of **3** at 100, 123 and 267 K (Å)

	100 K	123 K	267 K	ΔHS-MIX[a]	ΔHS–LS
Fe1–O1	1.876(2)	1.888(3)	1.908(3)	0.02	0.032
Fe1–O2	1.881(2)	1.887(3)	1.904(3)	0.017	0.023
Fe1–O_{av}	1.879(2)	1.888(3)	1.906(3)	0.018	0.027
Fe1–N1	1.948(2)	2.045(3)	2.131(4)	0.086	0.0183
Fe1–N2	1.977(2)	2.064(3)	2.150(4)	0.086	0.0173
Fe1–N3	1.951(2)	2.038(3)	2.129(4)	0.091	0.0178
Fe1–N4	1.983(2)	2.077(3)	2.142(4)	0.065	0.0159
Fe1–N_{av}	1.965(2)	2.056(3)	2.138(4)	0.082	0.0173
Σ	46	53	75	22	29
Θ	70	142	209	67	139

[a] ΔHS-MIX refers to the difference between the structures at 267 and 123 K.

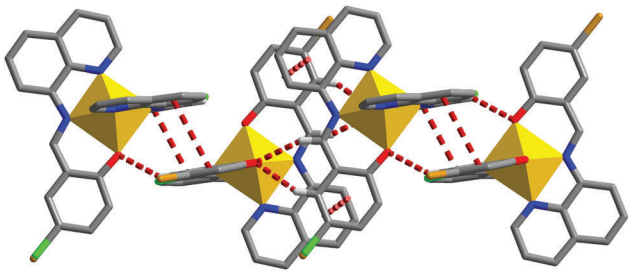

Fig. 2 View of the π–π interactions in **1**.

Table 5 Principal supramolecular contact distances and angles in **1–4** (Å, °)

	1	2	3	4
π–π[a]				
Type A	3.203	3.267 (Fe1–Fe1)	3.240[d] 3.252[e] 3.321[f]	3.248
Type B	3.272	3.393 (Fe2–Fe2)	3.131[d] 3.200[e] 3.322[f]	3.228
Br···π	3.254(8)	3.428(9)	—	—
Cl···π	3.384(5)	3.508(6)	—	—
C–H···Cl1	—	2.922(8)	—	2.857(9)
C–H···Br1	—	2.821(2)	—	2.823(3)
C–H···Cl2	—	2.723(9)	—	2.821(9)
C–H···Br2	—	2.621(3)	—	2.806(2)
α[b]		5.5, 8.5 (Fe1) 11.9, 10.0 (Fe2)	8.8, 23.1[d] 10.0, 24.9[e] 10.9, 25.4[f]	
θ[c]	89.8	83.4 (Fe1) 88.1 (Fe2)	72.6[d] 71.7[e] 72.1[f]	88.3

[a] Plane-to-distances. [b] Angle between the phenyl and quinoline rings. [c] Angle between the two planes of the qsal-X ligands. [d] At 100 K. [e] At 123 K. [f] At 267 K.

CH_2Cl_2 molecule of $[Fe(qsal\text{-}Br)_2]BPh_4$ and the H_2O in $[Fe(qsal\text{-}Cl)_2]BPh_4$.

In $[Fe(qsal\text{-}Cl)(qsal\text{-}Br)]BPh_4{\cdot}2CH_2Cl_2$ the sample was quickly cooled to 5 K and then warmed to 100 K where $\chi_M T$ = 0.45 cm^3 mol^{-1} K, consistent with LS Fe(III). Upon further heating

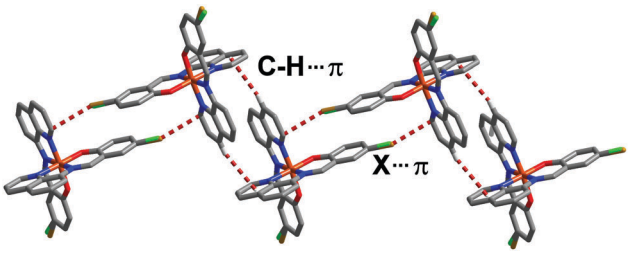

Fig. 3 View of the C–H···π and Cl/Br···π interactions that link the 1D chains in **1**.

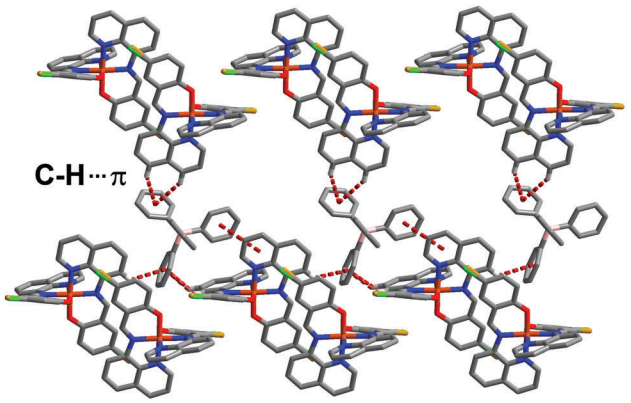

Fig. 4 View of the C–H···π interactions that link the 1D chains in **3**.

$\chi_M T$ increased to 1.40 cm^3 mol^{-1} K, indicative of 30% HS. $\chi_M T$ doesn't increase further until 300 K before an abrupt change is observed with $\chi_M T$ = 3.10 cm^3 mol^{-1} K at 350 K. TGA results (Fig. S1, ESI†) indicate that **3** loses both CH_2Cl_2 molecules in the range 320–360 K. Following this loss upon cooling we are unable to return to the full LS state with $\chi_M T$ = 1.50 cm^3 mol^{-1} K down to 30 K. Given the high vacuum of the SQUID measurements it's likely that the SCO here is coupled to partial or complete solvent loss. Comparisons with the structures at 100 and 123 K are consistent with the magnetic studies the one at 267 K is clearly different. The reason for this inconsistency is unclear but discrepancies have also been observed in other solvent sensitive SCO systems of $[Fe(qsal\text{-}X)_2]Y$.[12] Overall, the results suggest that provided that the lattice is not greatly impacted by the presence of two different ligands the SCO profile will be intermediate between the parent complexes. However, if a unique lattice is formed the mixed ligand complex can as hypothesized yield better SCO characteristics.

Conclusions

In conclusion we have successfully synthesized a series of mixed ligand $[Fe(qsal\text{-}Cl)(qsal\text{-}Br)]^+$ complexes. The heteroleptic complexes are favoured over the homoleptic systems in all cases. X-ray crystallographic studies reveal structures that are more often similar to the $[Fe(qsal\text{-}Cl)_2]^+$ complexes. In most cases the packing is little altered being strongly reminiscent of both parent $[Fe(qsal\text{-}X)_2]^+$ (X = Cl, Br) systems with strong π–π

 This journal is © The Royal Society of Chemistry and the Centre National de la Recherche Scientifique 2017

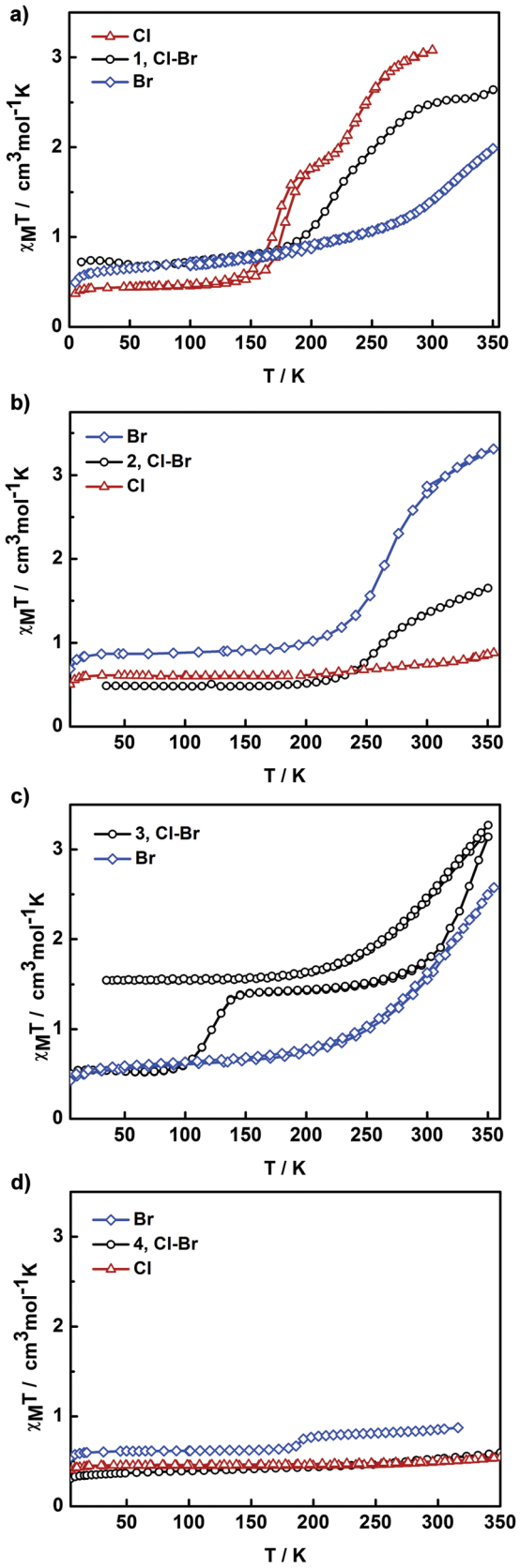

Fig. 5 $\chi_M T$ *versus* T plot for [Fe(qsal-Cl)(qsal-Br)]Y where Y are (a) NCS, (b) PF_6, (c) BPh_4, and (d) OTf.

interactions forming 1D chains. The exception is [Fe(qsal-Cl)-(qsal-Br)]$BPh_4 \cdot 2CH_2Cl_2$ where the presence of CH_2Cl_2 in the lattice, instead of H_2O, significantly impacts the packing resulting in greater cooperativity between the cations and anions. The similarity in packing for **1**, **2** and **4** with the homoleptic complexes results in the spin crossover profile being intermediate between the homoleptic $[Fe(qsal\text{-}X)_2]^+$ systems. In contrast, in **3** the alteration in the packing gives unusual stepped spin crossover behaviour surpassing both $[Fe(qsal\text{-}X)_2]BPh_4 \cdot sol$ complexes. This latter result confirms our earlier studies that mixed ligand complexes provide a valuable strategy in preparing new spin crossover systems.

Experimental

General remarks

All reactions were conducted in air using reagent grade solvents. Hqsal-Cl and Hqsal-Br were synthesized using literature procedures.[36] All other chemicals were purchased from Sigma-Aldrich Chemical Company and used as received. Infrared spectra (as KBr discs) were recorded on a Perkin–Elmer Spectrum One infrared spectrophotometer in the range 400–4000 cm^{-1}. Electronic spectra were recorded on a Shimadzu 1800 UV-visible spectrometer. Elemental analyses were carried out on a Eurovector EA3000 analyser at the School of Chemistry, University of Bristol, UK. ESI-MS were carried out on a Bruker Daltonics 7.0T Apex 4 FTICR Mass Spectrometer at the National University of Singapore.

Synthesis of [Fe(qsal-Cl)(qsal-Br)]NCS·MeOH 1. A solution of Hqsal-Br (65 mg, 0.2 mmol) and Hqsal-Cl (57 mg, 0.2 mmol) in CH_2Cl_2 (2 ml) was added to the bottom of a test tube in which NEt_3 (56 μl, 0.4 mmol) had been added as a base. $FeCl_3$ (31 mg, 0.2 mmol) was dissolved in MeOH (5 ml) and NaNCS (50 mg, 0.6 mmol) added. The solution was stirred for 5 min, filtered and then layered on blank MeOH (3 ml) which had been layered on top of the Hqsal-Cl/Br solution. After 3 days, black crystals formed which were washed with hexane (2 × 1 ml) and air dried; yield 62 mg (43%). *m*/*z* (ESI) 664.0 $[Fe(qsal\text{-}Cl/Br)_2]^+$. Elemental analysis: calcd (found) for $C_{34}H_{24}BrClFeN_5O_3S$: C, 54.17 (53.49); H, 2.79 (3.21); N, 9.70 (9.29)%.

Compounds **2–4** were prepared in a similar manner to **1** using KPF_6, $NaBPh_4$ and $NaCF_3SO_3$, respectively.

[Fe(qsal-Cl)(qsal-Br)]PF_6 2. Black crystals, 38% yield. *m*/*z* (ESI) 664.0 $[Fe(qsal\text{-}Cl/Br)_2]^+$, 144.9 $[PF_6]^-$. Elemental analysis: calcd (found) for $C_{32}H_{20}BrClF_6FeN_4O_2P$: C, 47.53 (47.41); H, 2.49 (2.91); N, 6.93 (6.96)%.

[Fe(qsal-Cl)(qsal-Br)]$BPh_4 \cdot 2CH_2Cl_2$ 3. Black crystals, 45% yield. *m*/*z* (ESI) 664.0 $[Fe(qsal\text{-}Cl/Br)_2]^+$, 319.1 $[BPh_4]^-$. Elemental analysis: calcd (found) for $C_{56}H_{40}BBrClFeN_4O_2$: C, 68.43 (68.46); H, 4.10 (4.33); N, 5.70 (5.58)% (the compound analysed without CH_2Cl_2).

Synthesis of [Fe(qsal-Cl)(qsal-Br)]$CF_3SO_3 \cdot 0.5$MeOH 4. Black crystals, 35% yield. *m*/*z* (ESI) 664.0 $[Fe(qsal\text{-}Cl/Br)_2]^+$, 149.2 $[CF_3SO_3]^-$. Elemental analysis: calcd (found) for $C_{33}H_{20}BrClF_3FeN_4O_5S$: C,

48.76 (48.82); H, 2.48 (3.07); N, 6.89 (6.97)% (the compound analysed without MeOH).

Crystallography

Crystal structures were collected on a Bruker APEXII area detector with graphite monochromated MoKα (λ = 0.71073 Å).[37] After data collection, in each case an empirical absorption correction (SADABS) was applied,[38] and the structures were then solved by direct methods and refined on all F^2 data using the SHELX suite of programs.[39] In all cases non-hydrogen atoms were refined with anisotropic thermal parameters; hydrogen atoms were included in calculated positions and refined with isotropic thermal parameters. Crystal data and data processing parameters for **1–4** are given in Table 2. Pictures were generated using DIAMOND.[40] The CCDC numbers for the X-ray crystallographic data presented in this paper are 1526771 (**1**), 1526772 (**2**), 1526773 (**3**-100 K), 1526774 (**3**-123 K), 1526775 (**3**-267 K) and 1526776 (**4**).†

Magnetic susceptibility studies

Magnetic data were collected using a Quantum Design MPMS 5 SQUID magnetometer under an applied field of 1 T over a temperature range between 340–344 K. The powdered or polycrystalline samples were placed in gel capsules and care was taken to allow long thermal equilibration times at each temperature point; often referred to as settle mode.

Conflicts of interest

There are no conflicts to declare.

Acknowledgements

We thank the Thailand Research Fund (RSA5880048) for funding this research. We also thank the Development and Promotion of Science Talents Project for a PhD scholarship to WP. KSM thanks the Australian Research Council for a Discovery grant.

Notes and references

1 D. J. Harding, P. Harding and W. Phonsri, *Coord. Chem. Rev.*, 2016, **313**, 38–61.
2 M. Nihei, T. Shiga, Y. Maeda and H. Oshio, *Coord. Chem. Rev.*, 2007, **251**, 2606–2621.
3 R. Bertoni, M. Lorenc, A. Tissot, M. L. Boillot and E. Collet, *Coord. Chem. Rev.*, 2015, **282–283**, 66–76.
4 *Spin-Crossover Materials: Properties and Applications*, ed. M. A. Halcrow, John Wiley & Sons, Ltd, Chichester, 2013.
5 P. Gütlich, A. B. Gaspar and Y. Garcia, *Beilstein J. Org. Chem.*, 2013, **9**, 342–391.
6 P. Gütlich and H. A. Goodwin, *Top. Curr. Chem.*, 2004, **233**, 1–47.
7 S. Brooker, *Chem. Soc. Rev.*, 2015, **44**, 2880–2892.
8 K. Senthil and M. Ruben, *Coord. Chem. Rev.*, 2017, **346**, 176–205.
9 S. Hayami, Z.-Z. Gu, H. Yoshiki, A. Fujishima and O. Sato, *J. Am. Chem. Soc.*, 2001, **123**, 11644–11650.
10 S. Hayami, K. Hiki, T. Kawahara, Y. Maeda, D. Urakami, K. Inoue, M. Ohama, S. Kawata and O. Sato, *Chem. – Eur. J.*, 2009, **15**, 3497–3508.
11 K. Fukuroi, K. Takahashi, T. Mochida, T. Sakurai, H. Ohta, T. Yamamoto, Y. Einaga and H. Mori, *Angew. Chem., Int. Ed.*, 2014, **53**, 1983–1986.
12 W. Phonsri, P. Harding, L. Liu, S. G. Telfer, K. S. Murray, B. Moubaraki, T. M. Ross, G. N. L. Jameson and D. J. Harding, *Chem. Sci.*, 2017, **8**, 3949–3959.
13 N. Phukkaphan, D. L. Cruickshank, K. S. Murray, W. Phonsri, P. Harding and D. J. Harding, *Chem. Commun.*, 2017, **53**, 9801–9804.
14 D. J. Harding, W. Phonsri, P. Harding, K. S. Murray, B. Moubaraki and G. N. L. Jameson, *Dalton Trans.*, 2015, **44**, 15079–15082.
15 B. J. C. Vieira, J. C. Dias, I. C. Santos, L. C. J. Pereira, V. da Gama and J. C. Waerenborgh, *Inorg. Chem.*, 2015, **54**, 1354–1362.
16 A. Tissot, R. Bertoni, E. Collet, L. Toupet and M.-L. Boillot, *J. Mater. Chem.*, 2011, **21**, 18347.
17 A. Tissot, P. Fertey, R. Guillot, V. Briois and M.-L. Boillot, *Eur. J. Inorg. Chem.*, 2014, 101–109.
18 A. I. Vicente, A. Joseph, L. P. Ferreira, M. de Deus Carvalho, V. H. N. Rodrigues, M. Duttine, H. P. Diogo, M. E. Minas da Piedade, M. J. Calhorda and P. N. Martinho, *Chem. Sci.*, 2016, **7**, 4251–4258.
19 E. W. T. Yemeli, G. R. Blake, A. P. Douvalis, T. Bakas, G. O. R. Alberda van Ekenstein and P. J. van Koningsbruggen, *Chem. – Eur. J.*, 2010, DOI: 10.1002/chem.201002100.
20 Z.-Y. Li, J.-W. Dai, Y. Shiota, K. Yoshizawa, S. Kanegawa and O. Sato, *Chem. – Eur. J.*, 2013, **19**, 12948–12952.
21 Z.-Y. Li, J.-W. Dai, K. J. Gagnon, H.-L. Cai, T. Yamamoto, Y. Einaga, H.-H. Zhao, S. Kanegawa, O. Sato, K. R. Dunbar and R.-G. Xiong, *Dalton Trans.*, 2013, **42**, 14685–14688.
22 S. Kang, Y. Shiota, A. Kariyazaki, S. Kanegawa, K. Yoshizawa and O. Sato, *Chem. – Eur. J.*, 2016, **22**, 532–538.
23 Z.-Y. Li, H. Ohtsu, T. Kojima, J.-W. Dai, T. Yoshida, B. K. Breedlove, W.-X. Zhang, H. Iguchi, O. Sato, M. Kawano and M. Yamashita, *Angew. Chem., Int. Ed.*, 2016, **55**, 5184–5189.
24 M. A. Halcrow, *Chem. Soc. Rev.*, 2011, **40**, 4119–4142.
25 K. S. Murray and C. J. Kepert, *Top. Curr. Chem.*, 2004, **233**, 195–228.
26 W. Phonsri, C. G. Davies, G. N. L. Jameson, B. Moubaraki and K. S. Murray, *Chem. – Eur. J.*, 2016, **22**, 1322–1333.
27 W. Phonsri, D. S. Macedo, C. G. Davies, G. N. L. Jameson, B. Moubaraki and K. S. Murray, *Dalton Trans.*, 2017, **46**, 7020–7029.
28 W. Phonsri, V. Martinez, C. G. Davies, G. N. L. Jameson, B. Moubaraki and K. S. Murray, *Chem. Commun.*, 2016, **52**, 1443–1446.
29 W. Phonsri, D. J. Harding, P. Harding, K. S. Murray, B. Moubaraki, I. A. Gass, J. D. Cashion, G. N. L. Jameson and H. Adams, *Dalton Trans.*, 2014, **43**, 17509–17518.
30 A. I. S. Neves, J. C. Dias, B. J. C. Vieira, I. S. Santos, M. B. Castelo Branco, L. C. J. Pereira, J. C. Waerenborgh, M. Almeida, D. Belo and V. Da Gama, *CrystEngComm*, 2009, **11**, 2160–2168.

 This journal is © The Royal Society of Chemistry and the Centre National de la Recherche Scientifique 2017

31 W. Phonsri, PhD thesis, Walailak University, 2014.
32 J. K. McCusker, A. L. Rheingold and D. N. Hendrickson, *Inorg. Chem.*, 1996, **35**, 2100–2112.
33 M. Marchivie, P. Guionneau, J. F. Létard and D. Chasseau, *Acta Crystallogr., Sect. B: Struct. Sci.*, 2005, **61**, 25–28.
34 I. Dance and M. Scudder, *J. Chem. Soc., Dalton Trans.*, 1998, 1341–1350.
35 M. Nakaya, K. Shimayama, K. Takami, K. Hirata, A. S. Alao, M. Nakamura, L. F. Lindoy and S. Hayami, *Chem. Lett.*, 2014, **43**, 1058–1060.
36 J. Sirirak, W. Phonsri, D. J. Harding, P. Harding, P. Phommon, W. Chaoprasa, R. M. Hendry, T. M. Roseveare and H. Adams, *J. Mol. Struct.*, 2013, **1036**, 439–446.
37 *Bruker APEXII*, Bruker AXS Inc., Madison, WI, USA, 2005.
38 *SADABS and SAINT*, Bruker AXS Inc., Madison, WI, USA, 2013.
39 G. M. Sheldrick, *Acta Crystallogr., Sect. A: Found. Crystallogr.*, 2008, **64**, 112–122.
40 K. Brandenberg and H. Putz, *DIAMOND, Crystal Impact*, Bonn, Germany, 2006.

Polyhedron 114 (2016) 242–248

Contents lists available at ScienceDirect

Polyhedron

journal homepage: www.elsevier.com/locate/poly

Substituent modulated packing in octahedral Ni(II) complexes

Piboonwan Insiti [a], Prapatsorn Jitthiang [a], Phimphaka Harding [a], Kittipong Chainok [b], Ratanon Chotima [c], Jitnapa Sirirak [d], Sebastian Blackwood [e], Adil Alkaş [e], Shane G. Telfer [e], David J. Harding [a,*]

[a] Molecular Technology Research Unit, School of Science, Walailak University, Thasala, Nakhon Si Thammarat 80161, Thailand
[b] Department of Physics, Faculty of Science and Technology, Thammasat University, Khlong Luang, Pathum Thani 12120, Thailand
[c] Department of Chemistry, Faculty of Science, Naresuan University, Phitsanulok 65000, Thailand
[d] Department of Chemistry, Faculty of Science, Silpakorn University, Nakhon Pathom, Thailand
[e] MacDiarmid Institute for Advanced Materials and Nanotechnology, Institute of Fundamental Sciences, Massey University, Palmerston North, New Zealand

ARTICLE INFO

Article history:
Received 22 October 2015
Accepted 14 December 2015
Available online 19 December 2015

Keywords:
Nickel(II) complexes
Schiff bases
Tridentate ligands
Structure
DFT calculations

ABSTRACT

The reaction of $NiCl_2$ with two equivalents of Hqsal-X (Hqsal-X = 5-X-*N*-(8-quinolyl)salicylaldimine) yields the octahedral complexes, $[Ni(qsal)_2]$·MeOH **1** and $[Ni(qsal\text{-}X)_2]$ (X = OMe **2**, Cl **3**, Br **4**, Me **5**, *t*-Bu **6**). UV–Vis spectroscopic studies show that the LMCT band is sensitive to the substituent, ranging from 465 to 520 nm. Crystal structures of $[Ni(qsal)_2]$·MeOH **1** and $[Ni(qsal\text{-}X)_2]$ (X = OMe **2**, Cl **3**, Br **4**) reveal that the Ni centres are octahedral, the qsal-X ligands coordinated with a meridional geometry. The packing in the structures is found to be strongly dependent on the substituent with 1D π–π chains in **3** and **4**, π–π dimers in **2** and a 1D hydrogen bonded chain in **1**. DFT calculations indicate almost identical electronic structures in **1**–**6** suggesting the difference in packing is due to the different supramolecular preferences of the substituent.

© 2015 Elsevier Ltd. All rights reserved.

1. Introduction

Schiff bases are popular ligands often formed by the reaction of amines with salicylaldehyde and related derivatives [1]. As both the amine and the salicylaldehyde can be readily modified, ligands with highly tunable steric and electronic characteristics can be prepared. Consequently, transition metal complexes of these ligands find numerous applications in a diverse set of fields including catalysis [2–5], magnetism [6,7], sensors [8,9], medical imaging [10] and optical materials [11,12]. The most popular Schiff bases continue to be either tetradentate N_2O_2 donors, which occupy the equatorial plane, or hexadentate N_4O_2 donors, which encapsulate first row transition metal ions [1]. By comparison, tridentate ligands have received less attention, and those that have been used typically incorporate simple amines as the terminal coordinating arm. For example, in Ni(II) chemistry, ligands based on *N*,*N*-dimethylethane-1,2-diamine and *N*-methyl-1,3-propanediamine have been extensively studied yielding monomeric [13–17], dimeric [18,19] and even trimeric species [14] depending on the reaction conditions, solvent and supporting anion. Moreover, the ligand may be tridentate [13,14,18] and even bidentate but with a protonated amine arm [14,17].

In contrast to these systems, the chemistry of Schiff bases with potentially coordinating aromatic amines is much less well developed. We are particularly interested in rigid ligands that enforce a meridional configuration on the metal centre, as opposed to the aminopropyl ligands above where even in the tridentate coordination mode both *fac* [13] and *mer* [15,18] configurations are encountered. The ligand system we have been exploring is 5-X-*N*-(8-quinolyl)salicylaldimine, Hqsal-X, which is a planar monoanionic ligand with a large π-surface [20]. Structures of a number of $[M(qsal\text{-}X)_2]^{0/+}$ (M = Mn, Fe, Co) complexes [21–29] reveal a tendency to form π–π interactions and bear a strong resemblance to terpyridyl embraces found in many $[M(terpy)_2]^{2+/3+}$ complexes [30]. In seeking to determine whether this is a general phenomenon for all $[M(qsal\text{-}X)_2]^{0/+}$ compounds and if the substituent group, X, plays any role in the packing we have now prepared a series of $[Ni(qsal\text{-}X)_2]$ complexes many of which have been structurally characterized.

2. Results and discussion

2.1. Synthesis and characterization of $[Ni(qsal\text{-}X)_2]$

The compounds are readily synthesized by adding a MeOH solution of $NiCl_2{\cdot}6H_2O$ to a solution of the Hqsal-X in CH_2Cl_2. Subsequent addition of NEt_3 gives red or brown microcrystals of the

* Corresponding author.

http://dx.doi.org/10.1016/j.poly.2015.12.028
0277-5387/© 2015 Elsevier Ltd. All rights reserved.

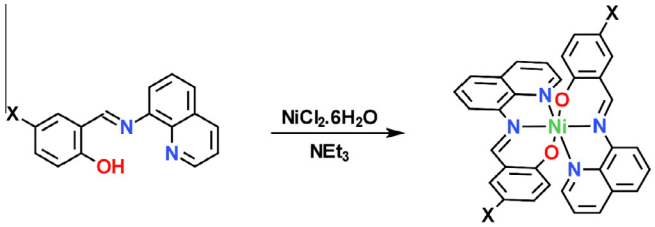

Scheme 1. Synthetic procedure for [Ni(qsal-X)$_2$] 1–6.

products [Ni(qsal)$_2$]·MeOH **1** and [Ni(qsal-X)$_2$] (X = OMe **2**, Cl **3**, Br **4**, Me **5**, *t*-Bu **6**) in good to excellent yields (Scheme 1). The compounds are insoluble in all common organic solvents except DMF and to a lesser extent DMSO. The compounds can also be prepared by diffusion of layered solutions of Hqsal-X in CH_2Cl_2, NEt_3, and Ni(OAc)$_2$·4H$_2$O in MeOH. This latter method gives deep red/brown crystals over two days. It is noteworthy that [Ni(qsal)$_2$]·0.5Me$_2$CO has previously been reported [31], although this compound was prepared from a DMF solution with a few drops of acetone added. This suggests that other solvates of [Ni(qsal)$_2$] may be accessible.

IR spectroscopic studies of **1**–**6** show a strong imine stretch between 1602–1611 cm^{-1} and are similar to values reported in other [M(qsal-X)$_2$]$^{0/+}$ complexes [21,23,25,28]. By comparison, the imine stretch of Hqsal-X is observed at 1615–1630 cm^{-1} with the lower values in **1**–**6** indicative of metal coordination [20,25,32].

The electronic spectra of **1**–**6** were recorded in DMF and are shown in Fig. 1. There are two bands in the spectra. The first occurs at *ca.* 340 nm and is assigned to a $\pi \rightarrow \pi^*$ transition of the qsal-X ligand. The UV–Vis spectra of the free ligands show a single band between 337 and 348 nm and support this assignment. The second band is found between 465 and 520 nm and is consistent with a LMCT transition. Similar results were found for [M(qsal-X)$_2$]$^{0/+}$ (M = Mn, Fe) and confirm that even in DMF the octahedral geometry around the nickel centre is preserved [21,25]. Interestingly, there is a general trend that as the substituent group becomes more electron withdrawing the transition moves to lower wavelengths, with the exception of **1**. Unfortunately, due to the poor solubility of the compounds we were unable to prepare solutions of sufficient concentration to allow us to observe the *d*–*d* transitions (Table 1).

2.2. Description of the structures of [Ni(qsal-X)$_2$]

As noted above, crystals were prepared by layered diffusion crystallizing in the monoclinic space group P2$_1$/c for **1**, while **2**–**4** all crystallize in the monoclinic space group P2$_1$/n. By comparison [Ni(qsal)$_2$]·0.5Me$_2$CO is found in the monoclinic space group C2/c [31]. Selected bond lengths are given in Table 2 while the structures of **2** and **4** are shown in Fig. 2 as representative examples. It should be noted that the poor quality of the diffraction data for **3** result in lower bond length precision, nevertheless the structure is clear and the packing mirrors that in **4** where the data is of far better quality.

As expected, the Ni centre is coordinated by two qsal-X ligands yielding an octahedral geometry and a N_4O_2 donor set. The Ni–N bond lengths vary from 2.019 to 2.120 Å with the bond to the imine nitrogen shorter than that of the quinolyl nitrogen by ~0.07 Å. Differences in Ni–N bond lengths are also observed in [Ni(salMpn-Br)$_2$] (salMpn-Br = 4-Bromo-2-{[3-(methylamino) propylimino]methyl}phenol), although the difference is greater due to the weaker coordinative ability of the amine nitrogen

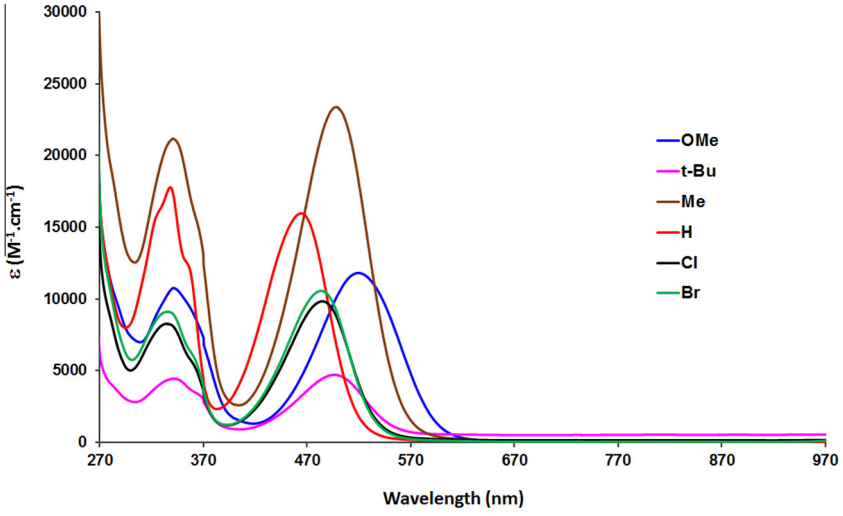

Fig. 1. UV–Vis spectra of **1**–**6** in DMF.

Table 1
Physical, IR and UV–Vis spectroscopic data for **1**–**6**.

Compound	Colour	IR (cm^{-1})			λ_{max} (nm), ε (M^{-1} cm^{-1})
		ν_{C-H}	$\nu_{C=N}$	$\nu_{C=C}$	
[Ni(qsal)$_2$]·MeOH **1**	Brown	2974(w)	1611(s)	1440(m)	330 (sh, 16600), 338 (17760), 353 (sh, 12640), 465 (15960)
[Ni(qsal-OMe)$_2$] **2**	Red	3046(w)	1602(s)	1457(s)	341 (10760), 371 (sh, 6560), 520 (11800)
[Ni(qsal-Cl)$_2$] **3**	Deep-red	3046(w)	1609(s)	1447(s)	336 (8260), 358 (sh, 5730), 485 (9830)
[Ni(qsal-Br)$_2$] **4**	Brown	3046(w)	1608(s)	1448(s)	336 (9100), 358 (sh, 6320), 484 (10560)
[Ni(qsal-Me)$_2$] **5**	Brown	3045(w)	1603(s)	1454(s)	342 (21140), 499 (23370)
[Ni(qsal-*t*-Bu)$_2$] **6**	Red	3040(w)	1602(s)	1456(s)	342 (4440), 363 (sh, 3440),496 (4720)

Table 2
Selected bond lengths and distortion parameters of [Ni(qsal-X)$_2$] **1**–**4** (Å, °).

	1	2	3	4	1·0.5Me$_2$CO[a]
Ni–O1	2.048(2)	2.046(2)	2.039(9)	2.019(2)	2.044(5)
Ni–O2[b]	2.019(2)	2.019(2)	2.018(9)	2.017(2)	2.041(4)
Ni–N1	2.104(2)	2.097(3)	2.096(10)	2.102(2)	2.082(5)
Ni–N2	2.040(2)	2.039(3)	2.026(11)	2.047(2)	2.057(5)
Ni–N3	2.120(2)	2.104(3)	2.089(11)	2.097(2)	2.101(5)
Ni–N4	2.024(2)	2.030(3)	2.019(10)	2.043(2)	2.044(5)
α[c]	17.9	6.2	4.7	4.2	8.4
	16.6	26.5	7.8	8.8	17.1
Σ[d]	53.5	53.7	44.1	44.7	53.9

[a] Data from Ref.
[b] For **2** this is O3 due to the extra O in the ligand.
[c] α = the angle between planes of the quinoline and phenolate rings.
[d] $\Sigma = \sum_{i=1}^{12} |90 - \alpha_i|$, where α_i are the twelve cis N/O–Fe–N/O angles.

[13]. There is also a slight asymmetry between the two qsal-X ligands, particularly evident in the different Ni–O bond lengths. Interestingly, in **4** and **1**·0.5Me$_2$CO the Ni–O bond lengths are almost identical.

It is evident that both ligands are significantly twisted in **1** while they are planar in **3** and **4**. In **2**, one ligand is twisted and the other is planar. This also impacts the degree of distortion at the nickel centre as measured by Σ, the sum of the deviation in the 12 *cis* angles from 90° (where $\Sigma = 0$ represents a perfect octahedron), with a decrease of almost 10° in going from **1** and **2** to **3** and **4**. The difference is clearly influenced by the substituent in the 5-position with the DFT calculations suggesting this is as result of crystal packing forces and not electronic effects (*vide infra*).

The peripheral substituent on the qsal-X ligand is found to dramatically impact the packing in the structures. Thus, in **3** and **4** the principal supramolecular motif is the formation of 1D chains composed of orthogonal π–π interactions supported by C–H···O interactions (Fig. 3). The two interactions are termed Type A and B, and range from 3.53 to 3.33 Å being different from each other by *ca.* 0.13 and 0.15 Å for **3** and **4**, respectively (Table 3). This difference in the plane to plane distances in **3** which are shorter than those of **4** by 0.07 Å may be due to the smaller chloro group which permits closer overlap of the aromatic rings. Such interactions are common in qsal-X complexes and have previously been observed in [Mn(qsal-X)$_2$] [21], [Fe(qsal-X)$_2$]$^+$ [23,26,27] and [Co(qsal-Cl)$_2$]$^+$ [29] complexes.

The 1D chains in **3** and **4** are connected to each other via C–H···X (X = Cl, Br) interactions such that neighbouring chains are slightly angular relative to each other with every second chain identically oriented (Fig. 4). This results in a 2D plane that contains only one type of C–H···Br interaction, in the case of Fig. 4 that

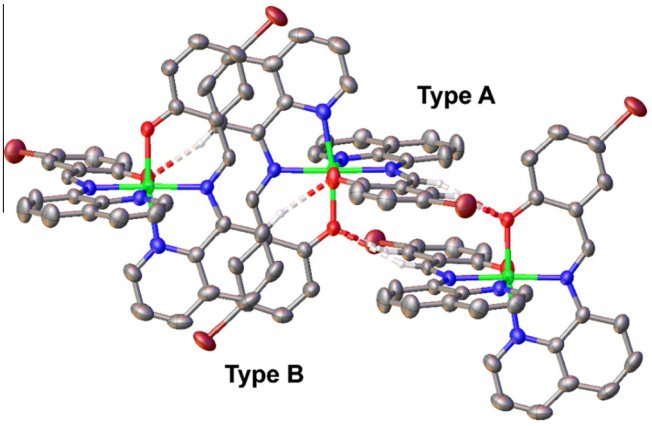

Fig. 3. View of the two orthogonal π–π interactions in [Ni(qsal-Br)$_2$] **4**.

Table 3
Distances of supramolecular interactions in **1**–**4** (Å).

	1	2	3	4
π–π				
Cg1···Cg1 (Type A)	–	3.56	3.64	3.73
Pl-to-Pl	–	3.44	3.46	3.53
Cg2···Cg2 (Type B)	–	–	3.69	3.79
Pl-to-Pl	–	–	3.33	3.39
O1···H24	2.197 (O1···H3B) 2.987 (O1···O3B)	–	2.385	2.419
O2···H10	2.004 (O1···H3A) 2.808 (O1···O3A)	2.539 (O1···H27)	2.663	2.698
O2···H12	2.553 (O2···H24)	2.533 (O1···H25)	2.663	2.673
O3A···H31	2.512	–	–	–
Quinolyl				
Cg3···Cg3	–	–	4.241	4.333
Pl-to-Pl		–	3.554	3.658
Cg4···H22		2.716 (H20)	2.695	2.816
C–H···Halogen				
H15···X1			2.765	2.839
H31···X2			2.904	3.027

involving Br2, with the second set of C–H···Br interactions linking these planes to give a 3D network (see Fig. S1). A final interaction which supports the 3D network are weak fourfold parallel embraces (P4AE [33], see Fig. S2). As with the π–π interactions all the above interactions are slightly stronger in **3** than **4** (Table 2).

The packing in **2** is strongly influenced by the fact that only one of the qsal-OMe ligands is planar with simple π–π dimers forming instead of 1D chains (Fig. 5). Nevertheless, these dimers are linked to each other by a combination of C–H···O interactions, involving

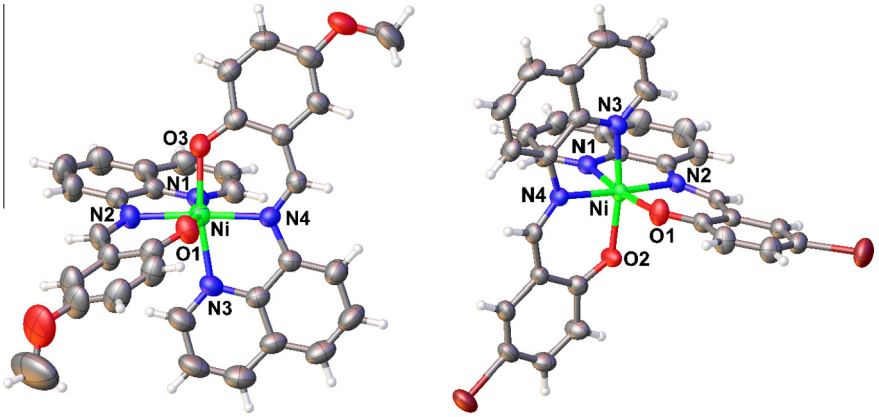

Fig. 2. View of the asymmetric unit of **2** (left) and **4** (right) with ellipsoids shown at 50% probability. Only selected atoms are labeled in the interests of clarity.

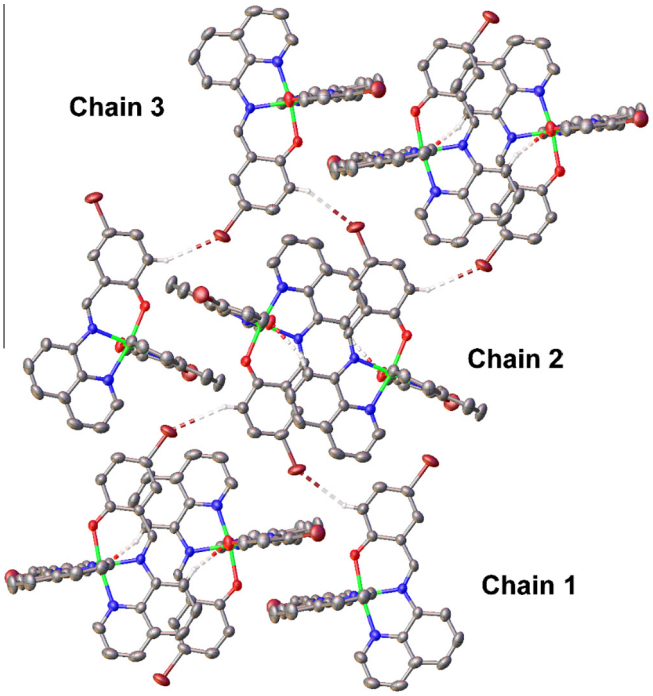

Fig. 4. View of the C–H···Br2 interactions that link the 1D chains in [Ni(qsal-Br)$_2$] **4**.

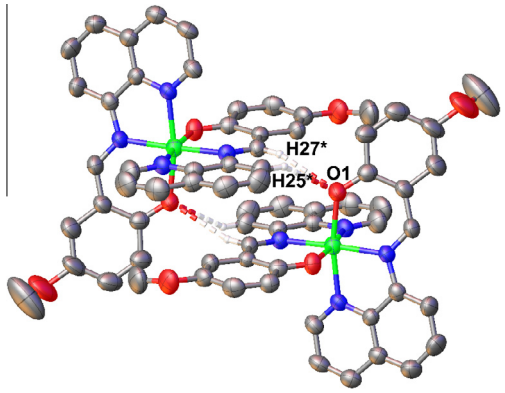

Fig. 5. View of the π–π dimer found in [Ni(qsal-OMe)$_2$] **2**. Only selected atoms are labeled in the interests of clarity.

the coordinated phenolate oxygen and a quinolyl hydrogen, and a pair of C–H···π interactions (see Fig. S3) to give a herringbone packing pattern (Fig. 6). Interestingly, this packing closely resembles that of [Ni(qsal)$_2$]·0.5Me$_2$CO but not [Ni(qsal)$_2$]·MeOH (*vide infra*).

Finally, the packing in [Ni(qsal)$_2$]·MeOH is very different to **2**–**4** with no π–π interactions in the structure. This is unsurprising given that both qsal ligands are non-planar. However, the fact that the packing in [Ni(qsal)$_2$]·0.5Me$_2$CO is almost identical to **2** suggests that for **1** the determining factor in the structure is the solvent. It follows that the substituent is important only in so far as its small size permits inclusion of solvent in the structure. The MeOH molecule is disordered over two sites and is strongly hydrogen bound to one of the phenolate oxygens and through a C–H···O interaction bridges neighbouring [Ni(qsal)$_2$] units. The other phenolate oxygen is involved in a weaker C–H···O interaction forming a 1D chain (Fig. 7). Thus, the change in packing in [Ni(qsal)$_2$]·0.5Me$_2$CO is most probably due to the fact that acetone isn't able to participate in such hydrogen bonding and 2D planes of π–π dimers are observed instead.

2.3. DFT studies

In order to investigate the impact of the substituents of **1**–**6** at the molecular level, DFT calculations were performed with the GAUSSIAN 03 software package [34]. The X-ray crystallographic data of the complexes in **1**–**4** were used as the initial structures for full optimization at the B3LYP/6-31G** level in the gas phase while the geometry optimization of **5** and **6** were performed at the B3LYP/6-31G** level in the gas phase using the modified X-ray structure of **1** as the starting structure.

The comparison of the Ni–N/O bond lengths from the DFT calculations (Table S1) with those found experimentally in the X-ray crystal structures (Table 2) shows that they are in agreement within 0.06 Å, indicating that the calculations accurately model [Ni(qsal-X)$_2$]. The frontier orbitals of **1**–**6** were also examined with the HOMO and LUMO found to be predominately ligand based π* orbitals (Fig. 8; for the remaining complexes see Fig. S4). For **1** and **3**–**4**, the HOMO and LUMO are similar; one qsal-X ligand dominating the HOMO and another qsal-X ligand dominating the LUMO. In contrast, significant electron density is found on both qsal-OMe ligands of **2**.

Given the strong similarity in the electronic structures of the [Ni(qsal-X)$_2$] complexes it seems clear that the differences in the packing motifs for **1**–**4** are due to the differing supramolecular connectivity favoured by the various substituents.

3. Conclusions

In conclusion, we have prepared six closely related [Ni(qsal-X)$_2$] complexes. The different substituents are found to have only a minor effect on the electronic structure of the complexes as evidenced by UV–Vis spectroscopic and DFT computational studies. However, the substituent significantly impacts the packing in the structures with [Ni(qsal-X)$_2$] (X = Cl, Br) favouring the 1D π–π chains that are a feature of many [M(qsal-X)$_2$]$^{0/+}$ complexes. In combination with multiple C–H···Cl/Br interactions 3D supramolecular networks are formed. [Ni(qsal-OMe)$_2$] instead forms simple π–π dimers but links them with C–H···O and C–H···π interactions resulting in a 2D plane. The incorporation of MeOH into the lattice of [Ni(qsal)$_2$] yields another motif this time dominated by strong hydrogen bonds which result in the formation of 1D chains. It is clear from this study that while 1D π–π chains remain a dominant packing motif in the structures of [M(qsal-X)$_2$]$^{0/+}$ complexes it is not the only motif that can form as the packing can be disrupted by stronger supramolecular interactions, such as hydrogen bonding in **1**. The ability of qsal-X ligands to support complexes with other co-ligands and how the X group impacts electrochemical and magnetic properties will be the subject of future studies.

4. Experimental

4.1. General remarks

All manipulations were performed in air with reagent grade solvents. All other chemicals were purchased from Aldrich Chemical Company and used as received. The Hqsal-X ligands were synthesized according to literature procedures [20,25,35,32]. Infrared spectra (as KBr discs) were recorded on a Perkin-Elmer Spectrum One infrared spectrophotometer in the range 400 to 4000 cm^{-1}. Electronic spectra were recorded in DMF at room temperature on a Shimadzu UV-1700 UV–Vis spectrophotometer. Elemental analyses were carried out on a Eurovector EA3000 analyser by staff of the School of Chemistry, University of Bristol, UK. ESI-MS were carried out on a Bruker Daltonics 7.0T Apex 4 FTICR Mass Spectrometer by staff at the National University of Singapore.

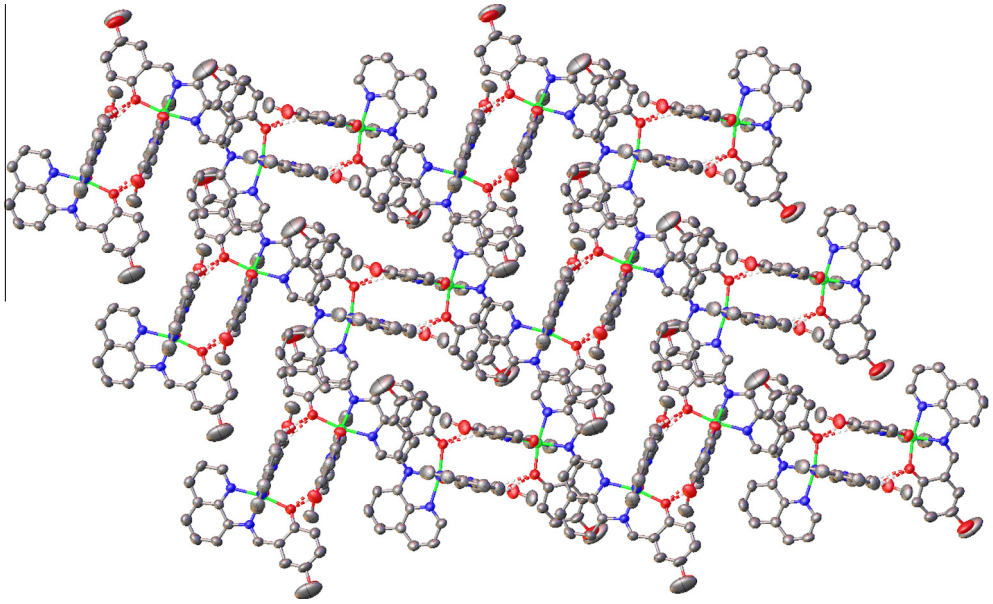

Fig. 6. Herringbone packing pattern in [Ni(qsal-OMe)$_2$] **2**.

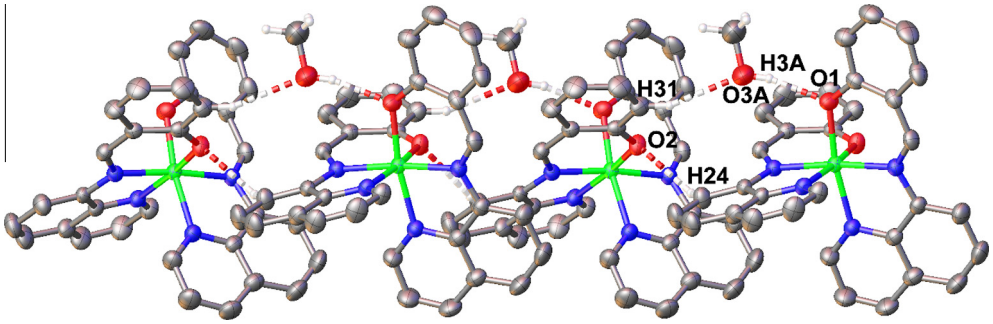

Fig. 7. View of the hydrogen bonding and C–H···O interactions that form the 1D chain in **1**. Only selected atoms are labeled in the interests of clarity.

4.2. Synthesis of [Ni(qsal)$_2$]·MeOH **1**

Hqsal (55 mg, 0.40 mmol) was dissolved in CH_2Cl_2 (10 cm^3) giving an orange solution. In a separate flask $NiCl_2{\cdot}6H_2O$ (48 mg, 0.20 mmol) was dissolved in MeOH (5 mL) to give a light green solution. The Ni(II) solution was added dropwise to the stirred Hqsal solution resulting in a yellow brown solution. NEt_3 (56 µl, 0.40 mmol) was added causing the solution to become browner. After 1 h of stirring the solution was reduced in volume to approximately 5 cm^3, filtered and then washed cold MeOH (5 mL) and Et_2O (10 mL) to give a brown solid, 91.8 mg (83%). IR (KBr): ν_{max} = 1604 ($\nu_{C=N}$). λ_{max} (CH_2Cl_2)/nm (ε/M^{-1} cm^{-1}): 328 (12010), 458 (14210) nm. ESI-MS: *m*/*z*: 553.0 [MH]$^+$. Found (calc. %) for $C_{33}H_{26}NiN_4O_3$: C 67.37 (67.72), H 4.21 (4.48), N 9.36 (9.57).

4.3. Synthesis of [Ni(qsal-OMe)$_2$] 2

2 was prepared in an identical way to **1** using Hqsal-OMe instead of Hqsal yielding deep red microcrystals in 82% yield. IR (KBr): ν_{max} = 1604 ($\nu_{C=N}$). λ_{max} (CH_2Cl_2)/nm (ε/M^{-1} cm^{-1}): 328 (12010), 458 (14210) nm. ESI-MS: *m*/*z*: 613.0 [MH]$^+$. Found (calc. %) for $C_{34}H_{26}NiN_4O_4$: C 66.84 (66.59), H 4.04 (4.27), N 8.57 (9.13).

4.4. Synthesis of [Ni(qsal-Cl)$_2$] 3

3 was prepared in an identical way to **1** using Hqsal-Cl instead of Hqsal yielding red-brown microcrystals in 74% yield. IR (KBr): ν_{max} = 1604 ($\nu_{C=N}$). λ_{max} (CH_2Cl_2)/nm (ε/M^{-1} cm^{-1}): 328 (12010), 458 (14210) nm. ESI-MS: *m*/*z*: 623.0 [MH]$^+$. Found (calc. %) for $C_{32}H_{20}Cl_2NiN_4O_2$: C 61.41 (61.78), H 3.45 (3.24), N 8.89 (9.00).

4.5. Synthesis of [Ni(qsal-Br)$_2$] 4

4 was prepared in an identical way to **1** using Hqsal-Br instead of Hqsal yielding red-brown microcrystals in 69% yield. IR (KBr): ν_{max} = 1604 ($\nu_{C=N}$). λ_{max} (CH_2Cl_2)/nm (ε/M^{-1} cm^{-1}): 328 (12010), 458 (14210) nm. ESI-MS: *m*/*z*: 711.0 [MH]$^+$. Found (calc. %) for $C_{32}H_{20}Br_2NiN_4O_2$: C 54.28 (54.06), H 3.13 (2.83), N 7.52 (7.88).

4.6. Synthesis of [Ni(qsal-Me)$_2$] 5

5 was prepared in a similar way to **1** using Hqsal-Me instead of Hqsal yielding a brown powder in 68% yield. IR (KBr): ν_{max} = 1604 ($\nu_{C=N}$). λ_{max} (CH_2Cl_2)/nm (ε/M$^{-1}\nu$cm^{-1}): 328 (12010), 458 (14210) nm. ESI-MS: *m*/*z*: 581.0 [MH]$^+$. Found (calc. %) for $C_{34}H_{26}NiN_4O_2$: C 70.44 (70.26), H 4.35 (4.51), N 9.28 (9.64).

4.7. Synthesis of [Ni(qsal-tBu)$_2$] 6

6 was prepared in a similar way to **1** using 1.0 mmol of Hqsal-*t*Bu instead of Hqsal yielding a brown powder in 66% yield. IR (KBr): ν_{max} = 1604 ($\nu_{C=N}$). λ_{max} (CH_2Cl_2)/nm (ε/M^{-1} cm^{-1}): 328 (12010), 458 (14210) nm. ESI-MS: *m*/*z*: 665.0 [MH]$^+$. Found (calc. %) for $C_{40}H_{38}NiN_4O_2$: C 71.87 (72.20), H 5.69 (5.76), N 8.09 (8.42).

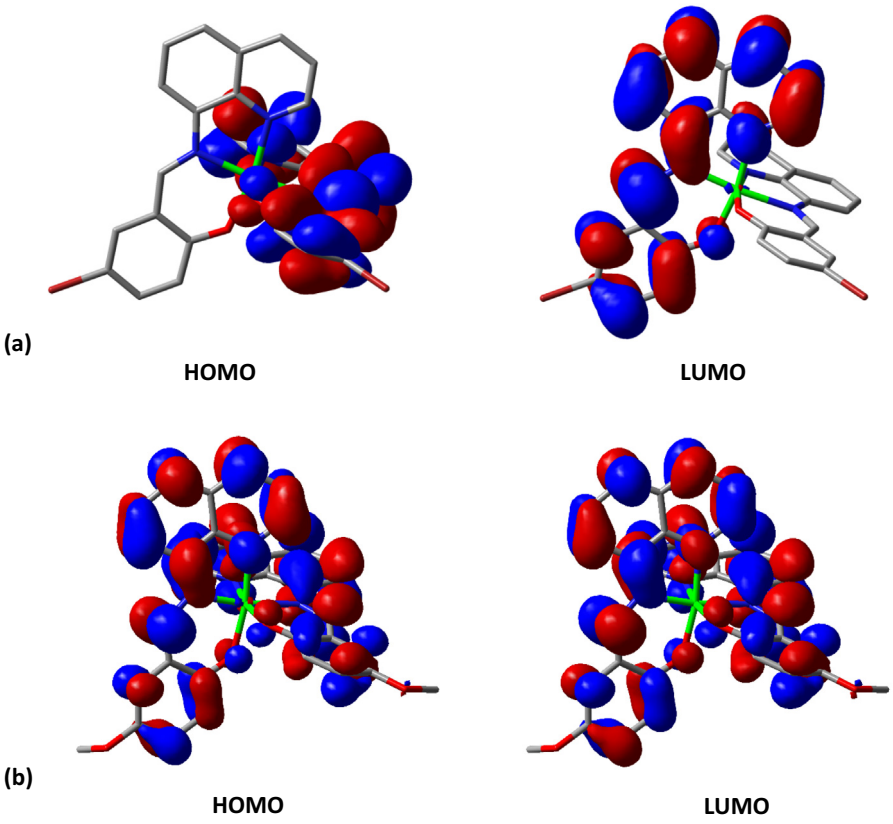

Fig. 8. HOMOs and LUMOs of (a) [Ni(qsal-Br)$_2$] **4**, (b) [Ni(qsal-OMe)$_2$] **2**.

4.8. X-ray crystallography

Crystal data and data processing parameters for the structures of **1**–**4** are given in Table 4. X-ray quality crystals of **1**–**4** were grown by layering a solution of Ni(OAc)$_2$ in MeOH over a solution of Hqsal-X and NEt_3 in CH_2Cl_2. Crystals of **1** and **4** were mounted on a glass fibre using perfluoropolyether oil. The diffraction data of **1** and **4** were collected on a Bruker D8 QUEST CMOS area detector with graphite monochromated Mo K_α (λ = 0.71073 Å) [36]. After data collection, in each case an empirical absorption correction (SADABS) was applied [37]. In the case of **2** and **3**, X-ray crystallographic data were collected at 173 and 293 K on a Rigaku Spider diffractometer equipped with a MicroMax MM007 rotating anode generator, Cu K_α radiation (λ = 1.54178 Å), high-flux Osmic multilayer mirror optics, and a curved image-plate detector [38]. The data were integrated and scaled and averaged with FS Process. The structures were then solved by direct methods and refined on all F^2 data using the SHELX suite of programs [39,40]. In all cases non-hydrogen atoms were refined with anisotropic thermal parameters; hydrogen atoms were included in calculated positions and refined with isotropic thermal parameters which were *ca.* 1.2 × (aromatic CH) or 1.5 × (Me, OH) the equivalent isotropic

Table 4
Crystallographic data and structure refinement for **1**–**4**.

	1	**2**	**3**	**4**
Formula	$C_{33}H_{26}N_4NiO_3$	$C_{34}H_{26}N_4NiO_4$	$C_{32}H_{20}Cl_2N_4NiO_2$	$C_{32}H_{20}Br_2N_4NiO_2$
Molecular weight/g mol^{-1}	585.29	613.30	622.13	711.05
Crystal system	monoclinic	monoclinic	monoclinic	monoclinic
Space group	$P2_1/c$	$P2_1/n$	$P2_1/n$	$P2_1/n$
a (Å)	8.8138(4)	12.6577(3)	10.4314(12)	10.4961(4)
b (Å)	22.6100(11)	11.6898(2)	13.0351(14)	13.1026(4)
c (Å)	13.5734(7)	18.8171(13)	19.0421(19)	19.7332(7)
α (°)	90	90	90	90
β (°)	92.8920(10)	90.420(6)	94.373(7)	94.373(7)
γ (°)	90	90	90	90
T (K)	296(2)	173(2)	293(2)	296(2)
Cell volume (Å^3)	2701.5(2)	2784.2(2)	2581.7(5)	2706.99(16)
Z	4	4	4	4
λ (Å)	0.71073	1.54178	1.54178	0.71073
Absorption coefficient/mm^{-1}	0.761	1.400	3.320	3.708
Reflections collected	33 162	27 865	19 424	34 398
Independent reflections, R_{int}	4951, 0.0827	4732, 0.0483	2687, 0.1208	5530, 0.0515
Minimum and maximum transmission	0.6653, 0.7452	0.544, 1.000	0.617, 1.000	0.383, 0.524
Restraints/parameters	1/381	0/388	0/370	0/370
Final *R* indices [$I > 2\sigma(I)$]: R_1, wR_2	0.0406, 0.0855	0.0484, 0.1015	0.1343, 0.3546	0.0346, 0.0739
CCDC number	1431228	1431229	1431227	1431226

thermal parameters of their parent carbon atoms. All pictures were generated using OLEX2 [41]. Crystals of **3** displayed limited long-range order. Diffraction was observed only to a resolution limit of 1.0 Å. The merging statistics indicated that the dataset was of mediocre quality, which results in elevated R factors and a lack of precision in determining the bond lengths. However, a clear assessment of the molecular structure and intermolecular contacts, as required for this study, can be gleaned from these data.

4.9. DFT calculations

DFT calculations were performed using GAUSSIAN 03 (Revision C.02) and employed the B3LYP density functional [34]. Calculations utilized the 6-31G** basis set with the X-ray crystallographic structures of **1**–**4** used as the starting structures for the optimization of each complex substituting the hydrogen in **1** with a methyl and *t*-butyl for **5** and **6** respectively. Pictures of the HOMO and LUMO were generated with GaussView.

Acknowledgements

We thank the Thailand Research Fund (RSA5580028 and RSA5880048) for funding this work. The Development and Promotion of Science and Technology Talents Project is thanked for undergraduate Scholarships to PI and PJ.

Appendix A. Supplementary data

CCDC 1431228, 1431229, 1431227 and 1431226 contains the supplementary crystallographic data for **1**, **2**, **3** and **4**, respectively. These data can be obtained free of charge via http://www.ccdc.cam.ac.uk/conts/retrieving.html, or from the Cambridge Crystallographic Data Centre, 12 Union Road, Cambridge CB2 1EZ, UK; fax: (+44) 1223-336-033; or e-mail: deposit@ccdc.cam.ac.uk. Supplementary data associated with this article can be found, in the online version, at http://dx.doi.org/10.1016/j.poly.2015.12.028.

References

[1] R. Hernández-Molina, A. Mederos, in: J.A. McCleverty, T.J. Meyer (Eds.), Compr. Coord. Chem. II, 2003, pp. 411–446.
[2] P.G. Cozzi, Chem. Soc. Rev. 33 (2004) 410.
[3] T. Katsuki, Chem. Soc. Rev. 33 (2004) 437.
[4] N.S. Venkataramanan, G. Kuppuraj, S. Rajagopal, Coord. Chem. Rev. 249 (2005) 1249.
[5] X.-B. Lu, D.J. Darensbourg, Chem. Soc. Rev. 41 (2012) 1462.
[6] C. Adhikary, S. Koner, Coord. Chem. Rev. 254 (2010) 2933.
[7] C. Benelli, D. Gatteschi, Chem. Rev. 102 (2002) 2369.
[8] A. Dalla Cort, P. De Bernardin, G. Forte, F. Yafteh Mihan, Chem. Soc. Rev. 39 (2010) 3863.
[9] P.D. Frischmann, M.J. MacLachlan, Chem. Soc. Rev. 42 (2013) 871.
[10] D.E. Reichert, J.S. Lewis, C.J. Anderson, Coord. Chem. Rev. 184 (1999) 3.
[11] P.G. Lacroix, Eur. J. Inorg. Chem. 2001 (2001) 339.
[12] C.J. Whiteoak, G. Salassa, A.W. Kleij, Chem. Soc. Rev. 41 (2012) 622.
[13] A. Bhattacharyya, P.K. Bhaumik, P.P. Jana, S. Chattopadhyay, Polyhedron 78 (2014) 40.
[14] P. Mukherjee, M.G.B. Drew, M. Estrader, A. Ghosh, Inorg. Chem. 47 (2008) 7784.
[15] S. Naiya, S. Biswas, M.G.B. Drew, A. Ghosh, Polyhedron 34 (2012) 67.
[16] D. Parker, E. Stephen Davies, C. Wilson, J. McMaster Inorg. Chim. Acta 360 (2007) 203.
[17] L.W. Xue, G.Q. Zhao, Y.J. Han, L.H. Chen, Q.L. Peng, Acta Crystallogr., Sect. E 66 (2010) m1352.
[18] P. Mukherjee, M.G.B. Drew, C.J. Gómez-García, A. Ghosh, Inorg. Chem. 48 (2009) 5848.
[19] P. Mukherjee, M.G.B. Drew, C.J. Gómez-García, A. Ghosh, Inorg. Chem. 48 (2009) 4817.
[20] J. Sirirak, W. Phonsri, D.J. Harding, P. Harding, P. Phommon, W. Chaoprasa, R.M. Hendry, T.M. Roseveare, H. Adams, J. Mol. Struct. 1036 (2013) 439.
[21] J. Sirirak, D.J. Harding, P. Harding, K.S. Murray, B. Moubaraki, L. Liu, S.G. Telfer, Eur. J. Inorg. Chem. (2015) 2534.
[22] D.J. Harding, W. Phonsri, P. Harding, K.S. Murray, B. Moubaraki, G.N.L. Jameson, Dalton Trans. 44 (2015) 15079.
[23] W. Phonsri, D.J. Harding, P. Harding, K.S. Murray, B. Moubaraki, I.A. Gass, J.D. Cashion, G.N.L. Jameson, H. Adams, Dalton Trans. 43 (2014) 17509.
[24] D.J. Harding, W. Phonsri, P. Harding, I.A. Gass, K.S. Murray, B. Moubaraki, J.D. Cashion, L. Liu, S.G. Telfer, Chem. Commun. 49 (2013) 6340.
[25] D.J. Harding, D. Sertphon, P. Harding, K.S. Murray, B. Moubaraki, J.D. Cashion, H. Adams, Chem. Eur. J. 19 (2013) 1082.
[26] S. Hayami, K. Hiki, T. Kawahara, Y. Maeda, D. Urakami, K. Inoue, M. Ohama, S. Kawata, O. Sato, Chem. Eur. J. 15 (2009) 3497.
[27] B.J.C. Vieira, J.C. Dias, I.C. Santos, L.C.J. Pereira, V. da Gama, J.C. Waerenborgh, Inorg. Chem. 54 (2015) 1354.
[28] O. Iasco, E. Rivie, R. Guillot, M. Buron-Le Cointe, J.-F. Meunier, A. Bousseksou, M.-L. Boillot, Inorg. Chem. 54 (2015) 1791.
[29] X.-J. Luo, C.-H. Zhang, J. Zhou, Y.-C. Liu, Acta Crystallogr., Sect. E Struct. Reports Online 69 (2013) m278.
[30] J. McMurtrie, I. Dance, CrystEngComm 11 (2009) 1141.
[31] H. Xu, Z.P. Ni, X.M. Ren, Q.J. Meng, J. Mol. Struct. 752 (2005) 153.
[32] D. Sertphon, D.J. Harding, P. Harding, K.S. Murray, B. Moubaraki, H. Adams, Aust. J. Chem. 67 (2014) 1574.
[33] V. Russell, M. Scudder, I. Dance, J. Chem. Soc., Dalton Trans. (2001) 789.
[34] M.J. Frisch, G.W. Trucks, H.B. Schlegel, G.E. Scuseria, M.A. Robb, J.R. Cheeseman, J.A. Montgomery Jr., T. Vreven, K.N. Kudin, J.C. Burant, J.M. Millam, S.S. Iyengar, J. Tomasi, V. Barone, B. Mennucci, M. Cossi, G.R. Scalmani, J.A. Pope, Gaussian 03 (Revision C.02), Gaussian Inc., Wallingford, CT, 2004.
[35] J. Wagler, D. Gerlach, G. Roewer, Inorg. Chim. Acta 360 (2007) 1935.
[36] Bruker APEXII, Bruker AXS Inc., Madison, WI, USA, 2014.
[37] SADABS and SAINT, Bruker AXS Inc., Madison, WI, USA, 2003.
[38] Rigaku, Rigaku Corporation, Rigaku XRD, Tokyo, Japan, 1996.
[39] G.M. Sheldrick, Acta Crystallogr., Sect. A64 (2008) 112.
[40] G.M. Sheldrick, Acta Crystallogr., Sect. C Struct. Chem. 71 (2015) 3.
[41] O.V. Dolomanov, L.J. Bourhis, R.J. Gildea, J.A.K. Howard, H. Puschmann, J. Appl. Crystallogr. 42 (2009) 339.

Volume 117 | Issue 9 | May 5, 2017

International Journal of QUANTUM CHEMISTRY

www.q-chem.org

WILEY